PL-TR-95-2060(II)
Special Reports, No. 274

PROCEEDINGS OF THE 17TH ANNUAL CONFERENCE ON ATMOSPHERIC TRANSMISSION MODELS, 8-9 JUNE 1994

Editors:

Gail P. Anderson
Richard H. Picard
James H. Chetwynd

24 May 1995

PHILLIPS LABORATORY
Directorate of Geophysics
AIR FORCE MATERIEL COMMAND
HANSCOM AFB, MA 01731-3010

"This technical report has been reviewed and is approved for publication"

WILLIAM A.M. BLUMBERG, Chief
Simulation Branch
Optical Environment Division

ROGER A. VAN TASSEL, Director
Optical Environment Division

This report has been reviewed by the ESC Public Affairs Office (PA) and is releasable to the National Technical Information Service (NTIS).

Qualified requestors may obtain additional copies from the Defense Technical Information Center (DTIC). All others should apply to the National Technical Information Service (NTIS).

If your address has changed, or if you wish to be removed from the mailing list, or if the addressee is no longer employed by your organization, please notify PL/TSI, 29 Randolph Road, Hanscom AFB, MA 01731-3010. This will assist us in maintaining a current mailing list.

Do not return copies of this report unless contractual obligations or notices on a specific document require that it be returned.

REPORT DOCUMENTATION PAGE

Form Approved
OMB No. 0704-0188

1. AGENCY USE ONLY *(Leave blank)*	2. REPORT DATE	3. REPORT TYPE AND DATES COVERED
	24 May 1995	Scientific

4. TITLE AND SUBTITLE
PROCEEDINGS OF THE 17th ANNUAL CONFERENCE ON ATMOSPHERIC TRANSMISSION MODELS, 8-9 JUNE 1994.

5. FUNDING NUMBERS
PE: 62101F
PR: 3054
TA: GD
WU: 01

6. AUTHOR(S)
Editors: GAIL P. ANDERSON
RICHARD H. PICARD
JAMES H. CHETWYND

7. PERFORMING ORGANIZATION NAME(S) AND ADDRESS(ES)
Phillips Laboratory/GPOS
29 Randolph Road
Hanscom AFB, MA 01731-3010

8. PERFORMING ORGANIZATION REPORT NUMBER
PL-TR-95-2060(II)
SR, No. 274

9. SPONSORING / MONITORING AGENCY NAME(S) AND ADDRESS(ES)

10. SPONSORING / MONITORING AGENCY REPORT NUMBER

11. SUPPLEMENTARY NOTES
Volume I consists of pages 1 through 467
Volume II consists of pages 468 through 822, Including A1 through A46

12a. DISTRIBUTION / AVAILABILITY STATEMENT
Approved for public release; distribution unlimited

12b. DISTRIBUTION CODE

13. ABSTRACT *(Maximum 200 words)*
CONTAINS THE VIEWGRAPHS AND OTHER MATERIALS FOR THE 45 PAPERS PRESENTED AT THE 17th ANNUAL REVIEW CONFERENCE ON ATMOSPHERIC TRANSMISSION MODELS HELD AT THE GEOPHYSICS DIRECTORATE, PHILLIPS LABORATORY (AFMC), HANSCOM AFB, MA ON:
8-9 JUNE 1994.

14. SUBJECT TERMS
Atmospheric transmittance
Aerosols
Atmospheric propagation
Clouds
Radiative transfer
Optical turbulence

15. NUMBER OF PAGES
400

16. PRICE CODE

17. SECURITY CLASSIFICATION OF REPORT	18. SECURITY CLASSIFICATION OF THIS PAGE	19. SECURITY CLASSIFICATION OF ABSTRACT	20. LIMITATION OF ABSTRACT
Unclassified	Unclassified	Unclassified	SAR

Synthetic 3-D Atmospheric Temperature Structure: A Model for Known Geophysical Power Spectra Using A Hybrid Autoregression And Fourier Technique

James H. Brown

Neil Grossbard

Memo

SYNTHETIC 3-D ATMOSPHERIC TEMPERATURE STRUCTURE: A MODEL FOR KNOWN GEOPHYSICAL POWER SPECTRA USING A HYBRID AUTOREGRESSION AND FOURIER TECHNIQUE

James H. Brown
Neil Grossbard

Abstract

Within a defined domain, geophysical phenomena often are characterized by smooth continuous power spectral densities having a negative power law slope dependence. Frequently, Fourier transform analysis has been employed to generate synthetic scenes from pseudorandom arrays by passing the stochastic data through a Fourier filter having a desired correlation structure and power spectral dependency. This report examines the possibility of producing synthetic structure by invoking autoregression analysis in conjunction with the Fourier method. Since computations that apply multidimensional fast Fourier transforms to large data arrays consume enormous resources and time, the goal of this study is to seek an alternative method to reduce the computational burden. Future editions of the Phillips Laboratory Atmospheric Radiance Codes will feature an ability to calculate structured radiance. The methods explored herein provide a process that can complement or in some cases supplement methods presently being used. Line of sight computations using the three-dimensional database will be presented.

04/18/94

Figures

1. Title Page

2. Stepping Stones - References from previous work

3. Linear Difference Equation - An autoregressive moving average (ARMA) model for a discrete spatial series, $v(n)$, that approximates deterministic and stochastic processes can be represented by the filter linear difference equation:

4. Power Spectra Model - A z transform analysis of the difference equation shows that the ARMA power spectral density ($P_{ARMA}(k)$) is contained in the equations in the slide.

5. Yule-Walker Equations - The relationship between the autocorrelation sequence and the pure autoregressive model is contained in the equations in the slide.

6. Levinson Recursion Algorithm - A standard "Levinson" algorithm that takes advantage of the Hermitian-Toeplitz matrix equation was employed to solve for the AR parameters. These are presented in the equations in the slide.

7. PSD of Simulated Series - the simulated *PSD* is obtained from the formula given in the slide. For a given altitude, the forward and backward method solves the squares problem given in the slide.

8. PSD and ACF Models - In practice, a given one-dimensional *single-sided PSD* was constructed from the *PSD* and *ACF* power law models as shown in the slide.

9. Coherence Length Parameter - the equivalent width or correlation length as a function of the *PSD* may be written as presented in the slide.

10. PSD - The model autocorrelation function used in this report leads to an isotropic two-dimensional power spectral density function given by the equation in the slide. The simulated data, $S(t, \ell)$, for a layer is described by the second equation in the slide.

11. Transverse Correction - In pursuit of avoiding the time-consuming convolution integral, an approximation was developed that modified the $PSD(k_t, k_\ell)$ at $k_t = 0$. This is given by the equation in the slide. The horizontal two-dimensional discrete Fourier Transform used in the syntheses of the database results in a well-known rectangular window sampling effect. Assuming negligible truncation of the autocorrelation function in the line-of-sight direction, truncation in the transverse direction leads to side-lobe leakage of the frequency response function of the digitized rectangular window. In the transverse direction, the effects of leakage can be computed as the convolution of the "theoretical" $PSD(k_t, k_\ell)$ with the square of the magnitude of the frequency response of a digital sinc function.

12. Line-of Sight Correction - Since the constructed database has a finite and relatively large line-of-sight data spacing, a natural truncation of the line-of-sight power spectral density function must occur that would cause significant aliasing of the line-of-sight *PSD*'s for any particular realization. Computational "aliasing" of the line-of-sight *PSD*'s was added to the "theoretical" *PSD*'s by the equations in the slide.

13. Conclusions Slide. Self-contained

Backup Table

It is anticipated that the following Table will be presented in answer to questions.

1. The chosen geometry is a segment of a sphere that consists of a volume 70 km in height by approximately 3000 km in the sensor LOS direction by approximately 51.2 km in the direction transverse to the line-of-sight. A spatial resolution element has an incremental altitude of 0.1 km by an incremental transverse distance of approximately 0.1 km by an incremental LOS distance of approximately 15.7 km. The actual data spacing in the horizontal dimension increased slightly with altitude so that points in the vertical dimension stayed on radial lines. The altitude range accounts for dominant structure effects (50-120 km). Also its vertical and transverse dimensions are sufficient to fill the field of a limb-viewing two-dimensional sensor array. The vertical and transverse spatial resolution is governed by the vertical and horizontal correlation lengths of the temperature variations but also is chosen to provide high field-of-view spatial resolution. The geometrical LOS dimensions are chosen to provide sufficient length to describe the integrated path radiance. Table 1 summarizes the database specifications.

Backup Figures

It is anticipated that the following Figures will be presented in answers to questions.

1. Database Geometry. Figure 1a illustrates the volume of the spherical segment defined by the database. The radial altitude range starts at 50 km and ends at 120 km. At 50 km altitude the curved length in the LOS direction measures 3014 km while the curved length in the transverse direction measures 51.2 km. These distances increase slightly with altitude due to the curved geometry. Figure 1b illustrates the resolution volume at 50 km. The radial altitude resolution is 0.1 km while the resolution of the curved lengths in the LOS and transverse directions is 15.7 km and 0.1 km respectively. Again the horizontal resolution lengths increase slightly with altitude.

2. Computational scheme. Correlations along the vertical lines are calculated (one layer at a time) and then the horizontal correlation calculation is applied to each layer.

3. Horizontal correlation lengths plotted as a function of altitude. A logistic dose response equation is fitted to the data. The outside curves represent the 95% confidence limits.

4. Vertical correlation lengths plotted as a function of altitude. A logistic dose response equation is fitted to the data. The outside curves represent the 95% confidence limits.

5. Root mean square values of the relative temperature fluctuations plotted as a function of altitude. A rational polynomial is fitted to the data. The outside curves represent the 95% confidence limits.

6. Graphs of Vertical, Transverse, and Line-of-Sight one-dimensional Power Spectral Densities plotted against spatial frequency. The left panel plots the vertical *PSD*'s for the theoretical model (light gray solid curve), autoregressive "generator" model (dashed curve), and the autoregressive vertical *PSD* from the simulated database (dotted curve). The middle panel plots the transverse *PSD*'s for the theoretical model (light gray solid curve), autoregressive *PSD* from the simulated database (dotted curve), and a periodogram from the simulated database (solid curve). The right panel plots the line-of-sight *PSD*'s for the theoretical model (light gray solid curve), autoregressive *PSD* from the simulated database (dotted curve), and a periodogram from the simulated database (solid curve). The plots are for 50.6 km altitude and one-dimensional high frequency spectral slope (S) = -5/3, where $\sigma^2 = 8.34 \times 10^{-4}$, L_{cv} = 1.72 km, L_{ch} = 32.9 km. The vertical spatial spacing = 0.1 km, transverse spacing = 0.1 km, and line-of sight spacing = 15.7 km. The curves show log-log plots of *PSD*'s measured in $\frac{(\delta T \,/\, Temperature)^2}{Wavenumber}$ and wavenumber measured in km^{-1}. The vertical autoregressive *PSD* for the simulation was computed by calculating a 6 coefficient forward and backward

19. PSD estimates of the horizontally scanned simulated atmosphere from Autoregressive analysis.

20. Two-Dimensional image temperature structure scene from 3-D simulation. Artificial temperature sensor located at 85 km.

autoregressive model of the vertically simulated data from layers extending from 50.0 km to 50.6 km in the forward direction and layers extending from 51.2 km to 50.6 km in the backward direction. Note that the "transverse" direction is defined as the horizontal perpendicular to the "line-of-sight" direction. The transverse and line-of-sight *PSD*'s represent the 1-D component of the 2-D horizontal *PSD* having a high frequency horizontal spectral slope = -8/3. Their autoregressive PSD's result from computing a 10 coefficient autoregressive model of the transverse and line-of-sight simulated data in the layer at 50.6 km. The transverse Nyquist frequency is approximately $1/(2x0.1) = 5\ km^{-1}$ and the line-of-sight Nyquist frequency is approximately $1/(2x15.7) = 0.032\ km^{-1}$.

7. One dimensional periodograms of the first four samples of the line-of-sight simulated data in the layer at 50.6 km.

8. Same as figure 6 except altitude = 119.3 km, $\sigma^2 = 0.0277$, $L_{cv} = 2.42$ km, and $L_{ch} = 49.1$ km. The transverse spacing is 0.101 km and LOS spacing is 15.9 km.

9. Histogram representing the probability distribution function of the simulated data at 50.6 km. Solid line is the theoretical Gaussian pdf. The variance of the data is $8.35x10^{-4}$.

10. Cumulative distribution function of the simulated data at 50.6 km compared to the theoretical curve.

11. Sample page from the database explanation file.

12. Alias branches of estimated "theoretical" LOS *PSD*.

13. "Theoretical" transverse PSD versus a 512 point PSD "corrected" for truncation of the autocorrelation function. The plot has the same input parameters previously given for 50.6 km altitude. The one-dimensional high frequency spectral slope is (*S*) = -5/3, $\sigma^2 = 8.34x10^{-4}$, L_{ch}=32.9 km, and transverse spacing = 0.1 km.

14. Approximation correction for rectangular window discrete Fourier Transform digital sinc function.

15. Viewing geometry of an imaginary temperature sensor platform located at an altitude of 85 km.

16. Integrated temperature structure along selected pixel rows comprising zenith look angles from the minimum of 94.60 to the maximum of 960

17. Integrated temperature structure along selected pixel columns comprising horizontal look angles from -.01870 to +.01870.

18. Fourier periodograms of the horizontally scanned simulated atmosphere for the same look angles of Figure 16.

GOAL - Create Synthetic 3-D Atmospheric Temperature Structure Database

- Consistent with specified PSD's, statistics, and correlation lengths
- Minimizes computational burden and storage requirements
- Applicable to Radiance Structure Models

Stepping Stones

- 1-D Model
- An Autoregressive Model for Smooth Geophysical Power Spectra with Known Autocorrelation Function, PL-TR-93-2016
-
- 2-D Model
- Atmospheric Structure Simulation: An ARMA Model for Smooth Isotropic Two-Dimensional Power Spectra, PL-TR-93-2224

Linear Difference Equation

$$x(n) = -\sum_{k=1}^{p} a(k)x(n-k) + \sum_{k=0}^{q} b(k)\varepsilon(n-k)$$

Power Spectra Model

$$P_{ARMA}(f) = T\rho_w \left| \frac{B(f)}{A(f)} \right|^2$$

$$A(f) = 1 + \sum_{k=1}^{p} a(k) \exp(-2\pi i f k T)$$

$$B(f) = 1 + \sum_{k=0}^{q} b(k) \exp(-2\pi i f k T)$$

$$x(n) = -\sum_{k=1}^{p} a(k)\, x(n-k) + \varepsilon(n)$$

$$P_{AR}(f) = \frac{T\rho_w}{|A(f)|^2} = T \sum_{k=-\infty}^{\infty} r_{xx}(k) \exp(-2\pi i f k T)$$

Yule Walker Equations

$$r_{xx}(m) = \begin{cases} -\sum_{k=1}^{p} a(k) r_{xx}(m-k) & \text{for } m > 0 \\ -\sum_{k=1}^{p} a(k) r_{xx}(-k) + \rho_w & \text{for } m = 0 \\ r_{xx}^{*}(-m) & \text{for } m < 0 \end{cases}$$

$$\begin{pmatrix} r_{xx}(0) & r_{xx}(-1) & \cdots & r_{xx}(-p) \\ r_{xx}(1) & r_{xx}(0) & \cdots & r_{xx}(-p+1) \\ \vdots & \vdots & \ddots & \vdots \\ r_{xx}(p) & r_{xx}(p-1) & \cdots & r_{xx}(0) \end{pmatrix} \begin{pmatrix} 1 \\ a(1) \\ \vdots \\ a(p) \end{pmatrix} = \begin{pmatrix} \rho_w \\ 0 \\ \vdots \\ 0 \end{pmatrix}$$

Levinson Recursion Algorithm

$$a_k[k] = -\frac{r_{xx}[k] + \sum_{\ell=1}^{k-1} a_{k-1}[\ell] r_{xx}[k-\ell]}{\rho_{k-1}}$$

$$a_k[i] = a_{k-1}[i] + a_k[k] a^*_{k-1}[k-i] \quad i = 1, 2, \cdots, k-1$$

$$\rho_k = \left(1 - |a_k[k]|^2\right)\rho_{k-1}$$

with ,

$$a_1[1] = -\frac{r_{xx}[1]}{r_{xx}[0]}$$

$$\rho_1 = \left(1 - |a_1[1]|^2\right) r_{xx}[0]$$

PSD of Simulated Series

$$PSD(f) = \frac{2\sigma_c^2 \Delta x}{\left| 1 + \sum_{i=1}^{NN} b_i e^{j2\pi f \Delta x} \right|^2}$$

Minimize ERR,

$$ERR = \left(\sum_{J=NN+1}^{M} \left(Y(J) - \sum_{i=1}^{NN} b_i Y(J-i) \right)^2 \right) + \left(\sum_{J=1}^{M-NN} \left(Y(J) - \sum_{i=1}^{NN} b_i Y(J+i) \right)^2 \right)$$

$$\sigma_c^2 = \frac{ERR}{2(M-NN)}$$

PSD and ACF Models

$$\mathrm{PSD}(k) = \frac{\sigma^2 a^{2\nu} \Gamma\left(\nu + \frac{1}{2}\right)}{\sqrt{\pi}\,\Gamma(\nu)\left(a^2 + k^2\right)^{\nu+\frac{1}{2}}}$$

$$\mathrm{ACF}(x) = \frac{\sigma^2 2^{(1-\nu)} (2\pi a x)^{\nu} K_{\nu}(2\pi a x)}{\Gamma(\nu)}$$

Coherence Length Parameter

$$L_c = \frac{\Gamma\left(\nu + \frac{1}{2}\right)}{2\sqrt{\pi}\Gamma(\nu)a}$$

2-D PSD

$$PSD_{theor}(f_x, f_y) = \frac{\sigma^2 \nu a^{2\nu}}{\pi\left(a^2 + f_x^2 + f_y^2\right)^{\nu+1}}$$

$$S(x,y) = FFT^{-1}\left(\sqrt{\frac{PSD_{theor}(f_x, f_y)}{\Delta x \Delta y}} \times FFT\left(\tilde{G}(\varepsilon_x, \varepsilon_y)\right)\right)$$

In practice, the PSD is adjusted to accord with sampling and convolution theory. For low frequency resolution along the transverse direction, the PSD is adjusted to account for rectangular windowing of decretized samples. This is the "Sinc" function effect.

For low Nyquist frequency along the LOS direction, the PSD is adjusted to account for an aliasing effect.

Transverse correction for large resolution frequency - rectangular window Sinc sampling problem

$f_y \equiv Los\ direction$

$f_x \equiv Transverse\ direction$

$Where, \quad A^2(f_x, f_y) = PSD(f_x, f_y) / \Delta x \Delta y$

$Modify\ A(0, f_y)\ to\ A_1(0, f_y)\ by:$

$$A_1(0, f_y) = gA(0, f_y) + (1 - g)A(1, f_y)$$

$such\ that$

$$\sigma^2 = \sum_{fx} \sum_{fy} A_1^2(f_x, f_y)$$

LOS correction for small Nyquist frequency

$f_y \equiv Los\ direction$

$f_x \equiv Transverse\ direction$

$For\ 0 < f_y < f_{Ny}\ \ Measured\ PSD\ at\ f_y\ is:$

$$PSD_m(f_x, f_y) = PSD(f_x, f_y) + PSD(f_x, 2f_{Ny} - f_y)$$
$$+ PSD(f_x, 2f_{Ny} + f_y) + PSD(f_x, 4f_{Ny} - f_y)$$
$$+ PSD(f_x, 4f_{Ny} + f_y) + \cdots$$

Conclusions

- Autoregressive synthesis (6 coef.) accurately models 1-D vertical geophysical PSD's
- Fast Fourier Transform synthesis accurately models 2-D horizontal geophysical PSD's
- Accounting for discretized samples, hybrid method preserves slope, coherence length, variance, and pdf (also LOS)
- Hybid system "builds in" non-stationarity
- Generation of entire 3-D database in 2.5 Hrs.

Database Specifications

Direction	Npts	Δx (km)	NΔx (km)	freq. res. 1/NΔx (cy/km)	Nyquist freq 1/2Δx (cy/km)
Vertical (50-120 km)	700	.1	70	---	---
Transverse	512	.1	51.2	.0195 (HIGH)	5
LOS	192	15.7	3014.	.00033	.0318 (LOW)

Database Geometry

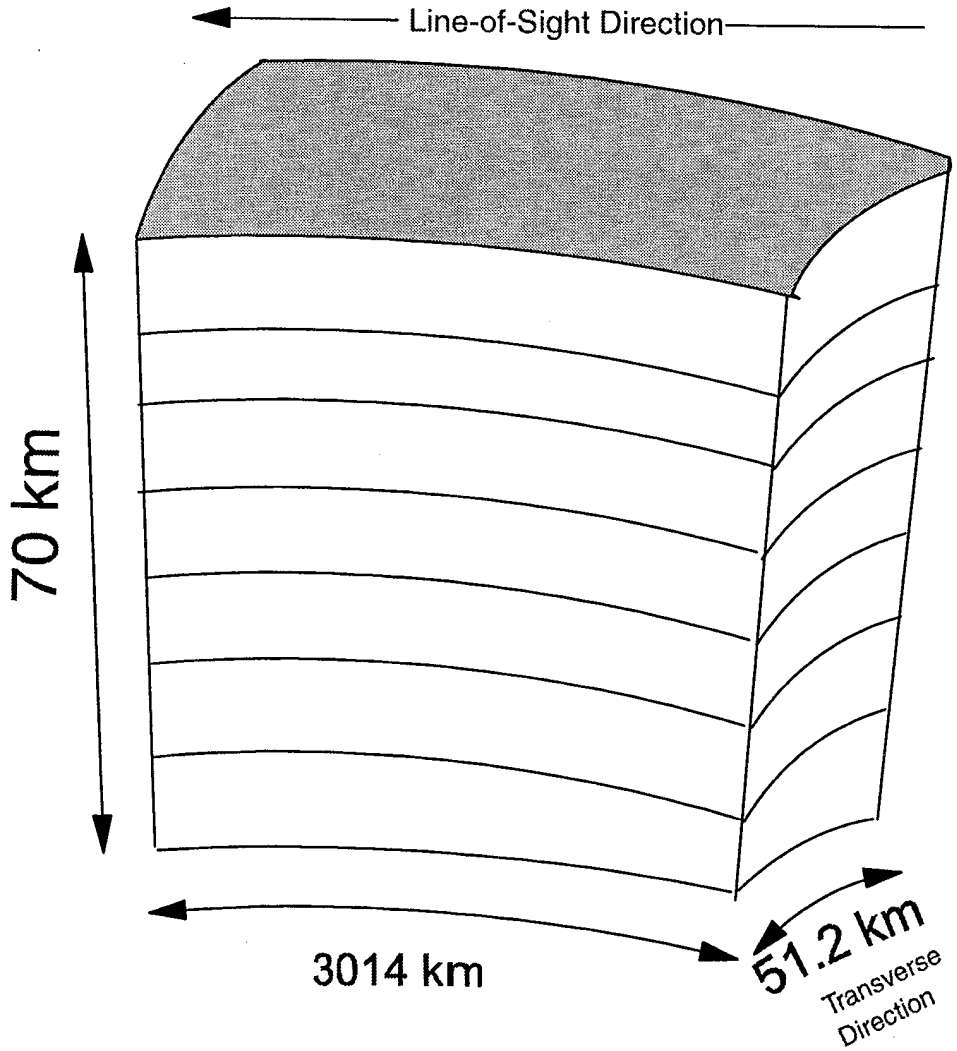

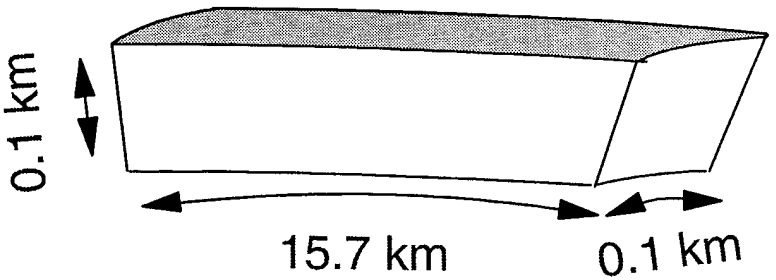

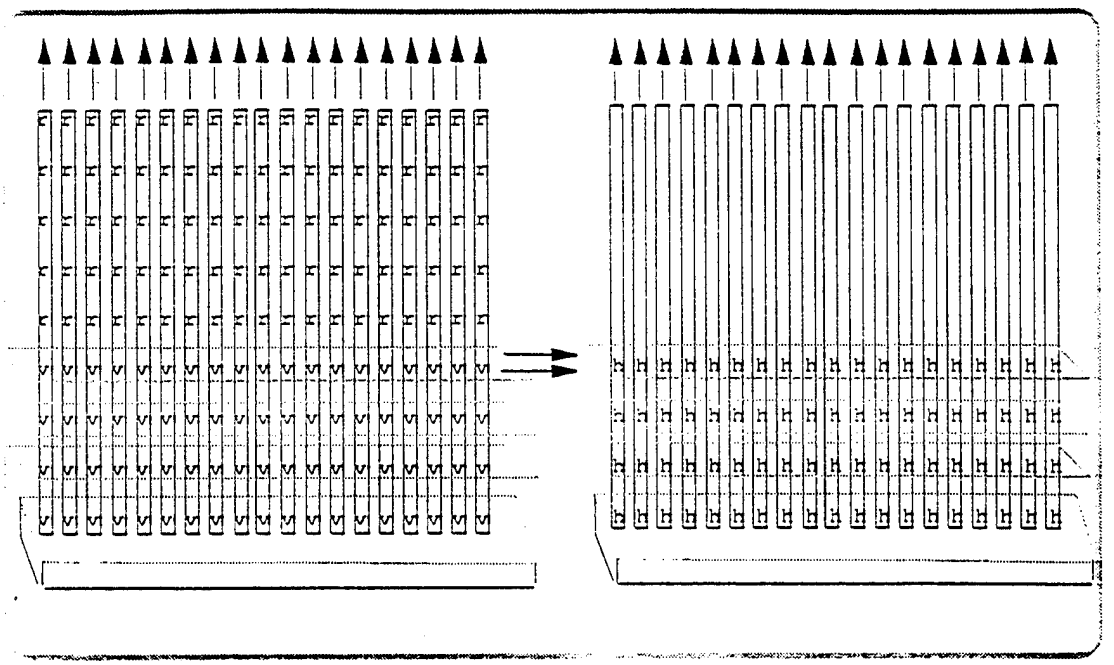

Figure 2. Calculational scheme. First, correlations along the vertical lines are calculated (one layer at a time) and then the horizontal correlation calculation is applied to each layer.

BACKUP FIG 2

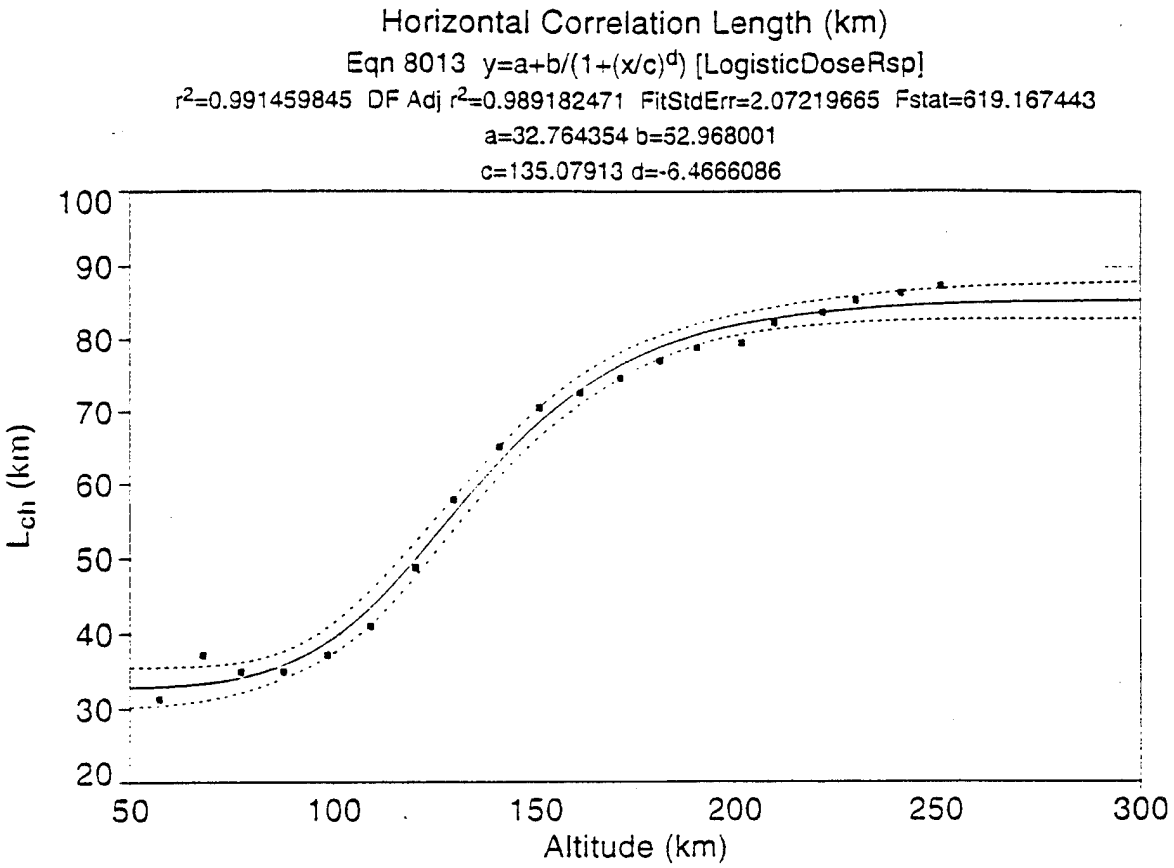

Rank 18 Eqn 8013 $y=a+b/(1+(x/c)^d)$ [LogisticDoseRsp]

r^2 Coef Det	DF Adj r^2	Fit Std Err	F-value
0.9914598452	0.9891824705	2.0721966466	619.16744310

Parm	Value	Std Error	t-value	95% Confidence Limits	
a	32.76435426	1.295628218	25.28839199	30.01210311	35.51660541
b	52.96800100	2.144297606	24.70179552	48.41295545	57.52304655
c	135.0791315	2.234742679	60.44504933	130.3319571	139.8263059
d	-6.46660858	0.680074818	-9.50867230	-7.91126428	-5.02195287

BACKUP FIG 3

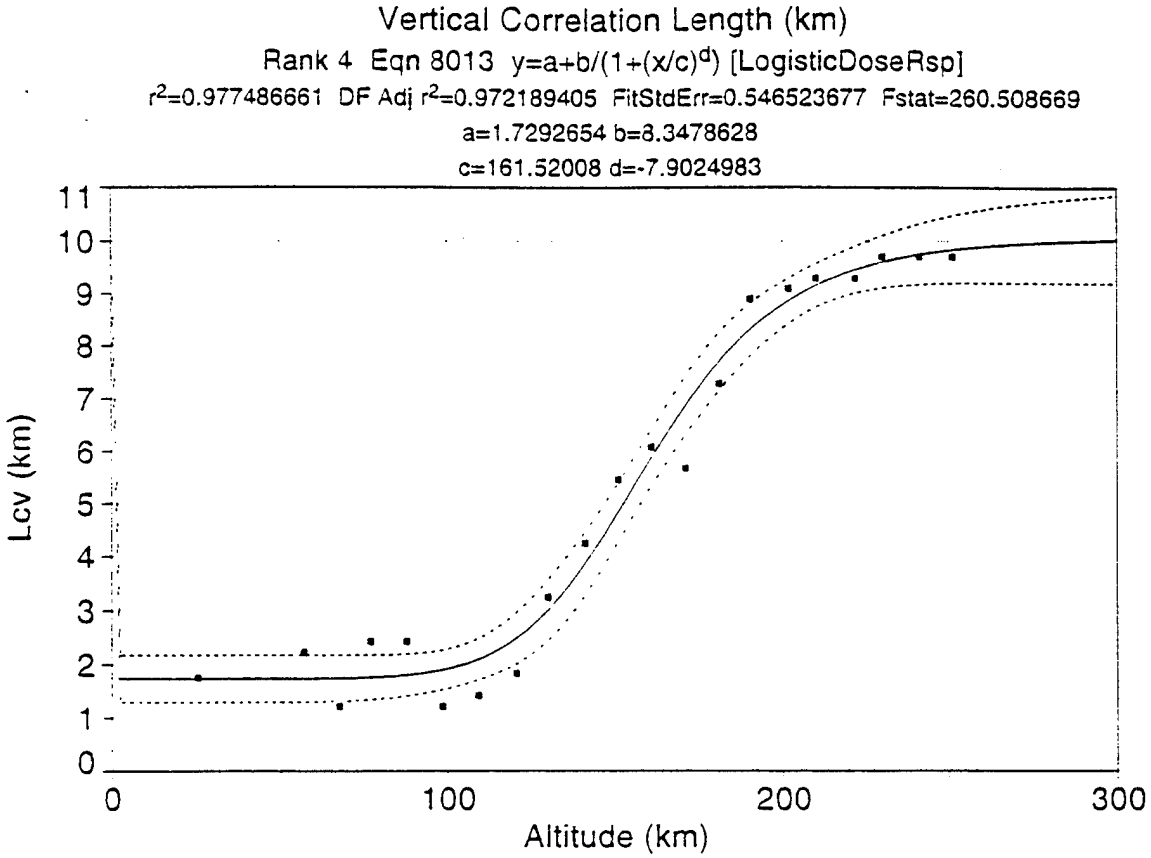

Rank 4 Eqn 8013 $y=a+b/(1+(x/c)^d)$ [LogisticDoseRsp]

r^2 Coef Det	DF Adj r^2	Fit Std Err	F-value
0.9774866610	0.9721894048	0.5465236769	260.50866885

Parm	Value	Std Error	t-value	95% Confidence Limits	
a	1.729265412	0.210585414	8.211705540	1.286422835	2.172107988
b	8.347862811	0.536310568	15.56535207	7.220048927	9.475676694
c	161.5200848	3.853308016	41.91725244	153.4169175	169.6232522
d	-7.90249825	1.339177504	-5.90100881	-10.7186706	-5.08632592

BACKUP FIG 4

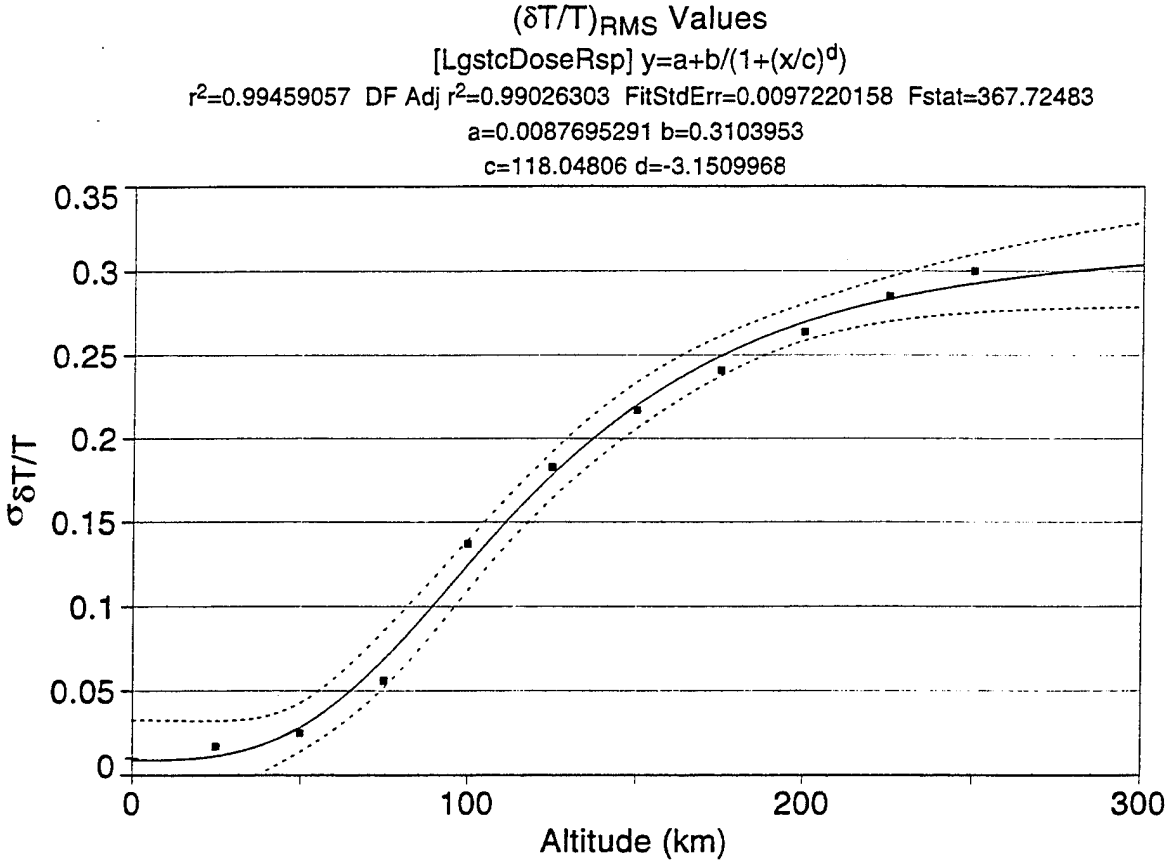

Rank 931 Eqn 8013 [LgstcDoseRsp] y=a+b/(1+(x/c)^d)

r^2 Coef Det	DF Adj r^2	Fit Std Err	F-value
0.9945905715	0.9902630287	0.0097220158	367.72482563

Parm	Value	Std Error	t-value	95% Confidence Limits	
a	0.008769529	0.009675816	0.906334825	-0.01500493	0.032543990
b	0.310395297	0.024196036	12.82835344	0.250943187	0.369847408
c	118.0480550	5.745293881	20.54691326	103.9312859	132.1648241
d	-3.15099683	0.473460616	-6.65524591	-4.31433753	-1.98765613

Date	Time	File Source
Jun 1, 1994	10:59:59 AM	d:\tcwin2\rms1.prn

BACKUP FIG 5 494

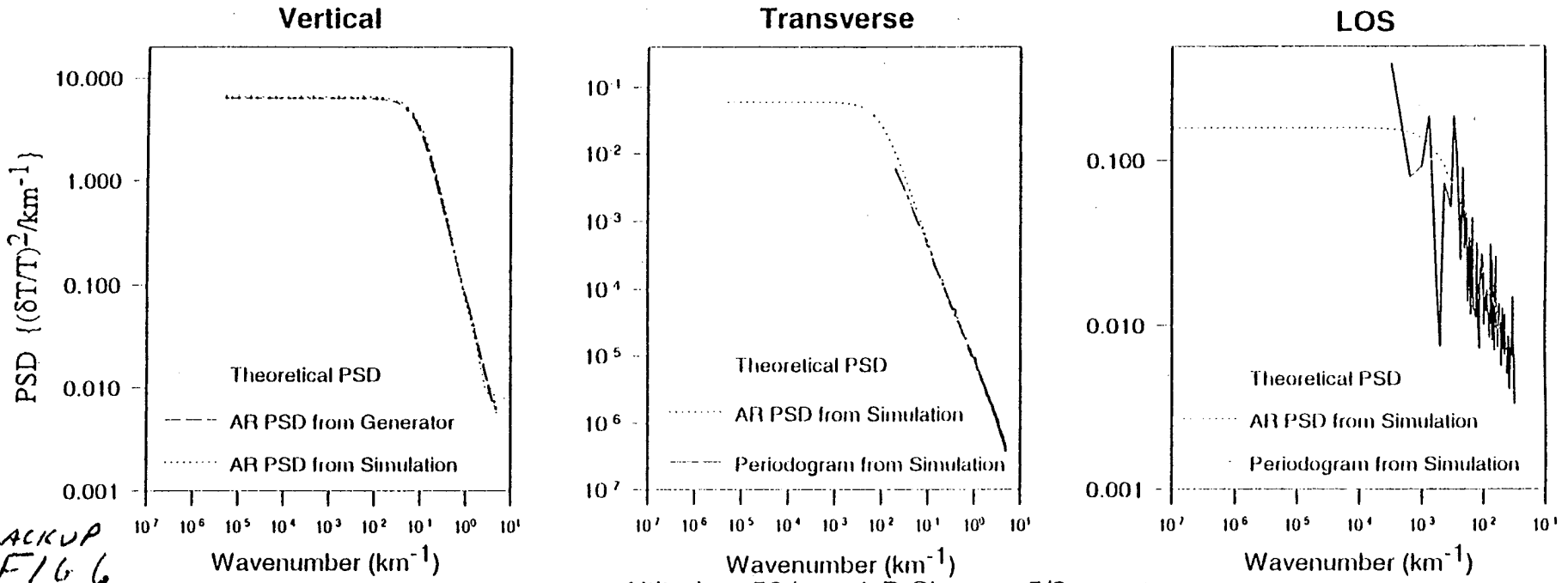

BACKUP FIG 6

Altitude = 50 km, 1-D Slope = -5/3

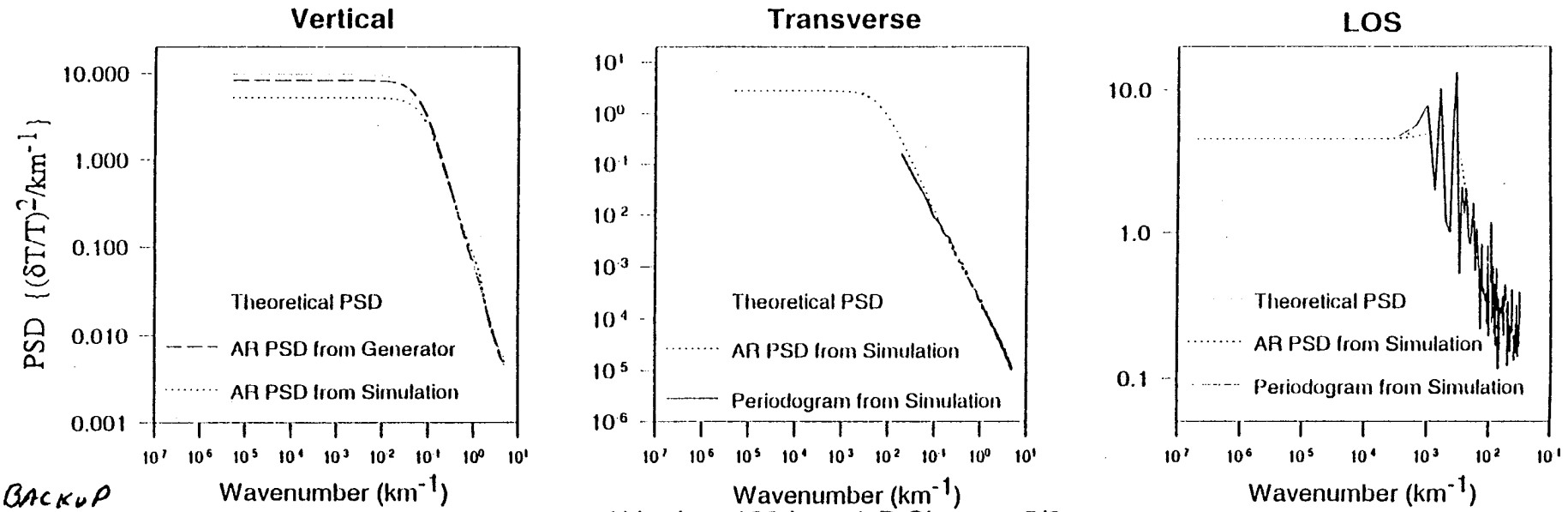

BACKUP FIG 8

Altitude = 120 km, 1-D Slope = -5/3

FILE PCRI007 7-FEB-94 NUMBER OF CYCLES USED(ALIASING) L.O.S.=157 NUMBER OF CYCLES USED(ALIASING) PER L.O.S.=1
NOTIFY ZERO FREQ TO GIVE CORRECT VARIANCE GREAT CIRCLE APPROXIMATION EARTH RADIUS= 6.370E+03
RANDOM NUMBER SEED= 12345 ALTITUDE NUMBER 7 = 5.060E+01 SLOPE(V)= 1.67E+00 THIS MEANS NU(V)= 3.33E-01 SPACING(V)= 1.00E 01
AV=6.90E-02 LCV=1.72E+00 NUMBER OF HORIZONTAL SAMPLES=98304 NUMBER OF PREDICTOR COEFFICIENTS V=6 H=10
NUMBER OF ITERATIONS=51 THIS IS ONE SHEET OF 512 PERPENDICULAR VALUES BY 192 L.O.S. VALUES SIGMA**2 WILL BE SET TO 8.34E-04
PERPENDICULAR SPACING=1.00E-01 SPACING L.O.S =1.57E+01 AH=3.62E-03 LCH=3.29E+01 SLOPE(H)=2.67E+00 THIS MEANS NU(H)=9.39E-01
INTEGRAL OF PSD= 8.99E-04

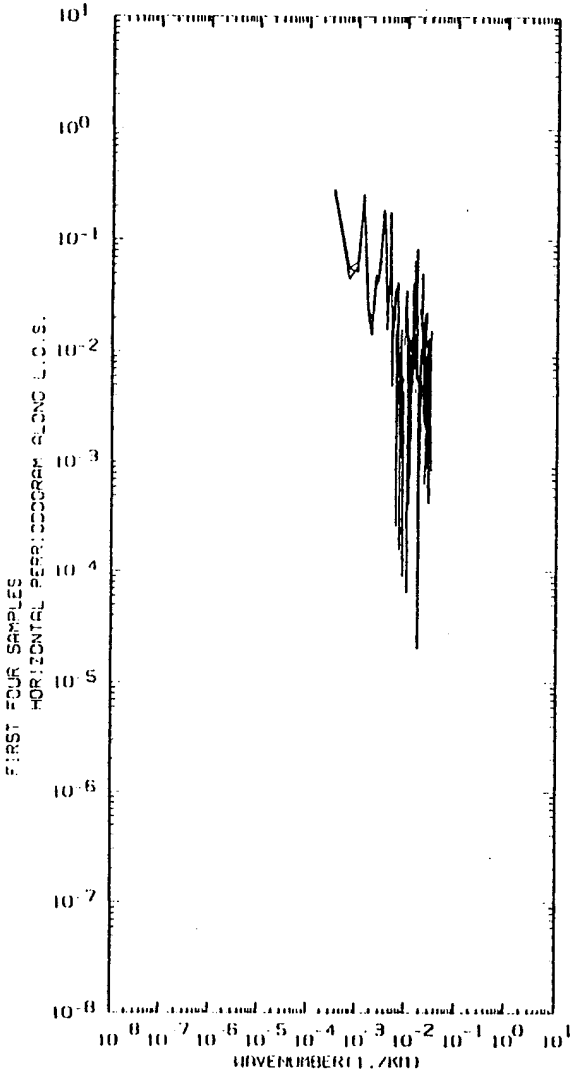

BACKUP FIG 7

FILE PCIM007 7-FEB-94 NUMBER OF CYCLES USED(ALIASING) L.O.S.=157 NUMBER OF CYCLES USED(ALIASING) PER L.O.S.=1
MODIFY ZERO FREQ TO GIVE CORRECT VARIANCE GREAT CIRCLE APPROXIMATION EARTH RADIUS= 6.370E+03
RANDOM NUMBER SEED= 12345 ALTITUDE NUMBER 7 = 5.060E+01 SLOPE(V)= 1.67E+00 THIS MEANS NU(V)= 3.33E-01 SPACING(V)= 1.00E-01
AV=6.90E-02 LCV=1.72E+00 NUMBER OF HORIZONTAL SAMPLES=98304 NUMBER OF PREDICTOR COEFFICIENTS V=6 H=10
NUMBER OF ITERATIONS=51 THIS IS ONE SHEET OF 512 PERPENDICULAR VALUES BY 192 L.O.S. VALUES SIGMA**2 WILL BE SET TO 8.34E-04
PERPENDICULAR SPACING=1.00E-01 SPACING L.O.S =1.57E+01 AH=3.62E-03 LCH=3.29E+01 SLOPE(H)=2.67E+00 THIS MEANS NU(H)=3.33E-01

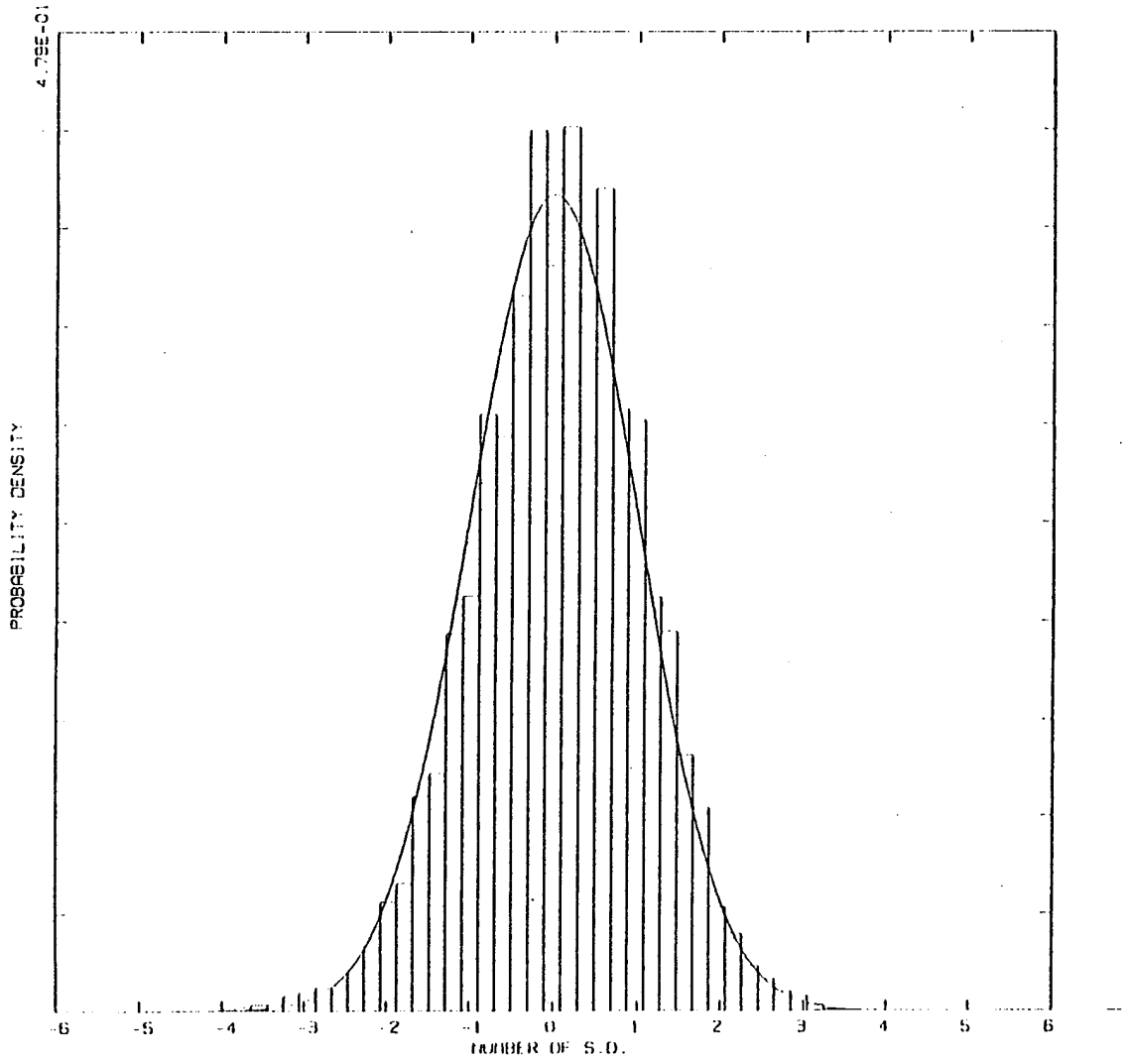

SOLID=THEORETICAL
BARS=ACTUAL
NUMBER OF POINTS=98304
WEIGHTED AVERAGE SUBTRACTED
-3.84E-03
STANDARD DEVIATION OF DATA
2.89E-02

POINTS FROM SHEET OF HORIZONTAL DATA

BACKUP FIG 9

FILE PCHMD07 7-FEB-94 NUMBER OF CYCLES USED(ALIASING) L.O.S.=157 NUMBER OF CYCLES USED(ALIASING) PER L.O.S.=1
MODIFY ZERO FREQ TO GIVE CORRECT VARIANCE GREAT CIRCLE APPROXIMATION EARTH RADIUS= 6.370E+03
RANDOM NUMBER SEED= 12345 ALTITUDE NUMBER 7 = 5.060E+01 SLOPE(V)= 1.67E+00 THIS MEANS NU(V)= 3.33E-01 SPACING(V)= 1.00E-01
AV=6.90E-02 LCV=1.72E+00 NUMBER OF HORIZONTAL SAMPLES=98304 NUMBER OF PREDICTOR COEFFICIENTS V=6 H=10
NUMBER OF ITERATIONS=51 THIS IS ONE SHEET OF 512 PERPENDICULAR VALUES BY 192 L.O.S. VALUES SIGMA**2 WILL BE SET TO 8.34E-04
PERPENDICULAR SPACING=1.00E-01 SPACING L.O.S =1.57E+01 AH=3.62E-03 LCH=3.29E+01 SLOPE(H)=2.67E+00 THIS MEANS NU(H)=3.33E-01

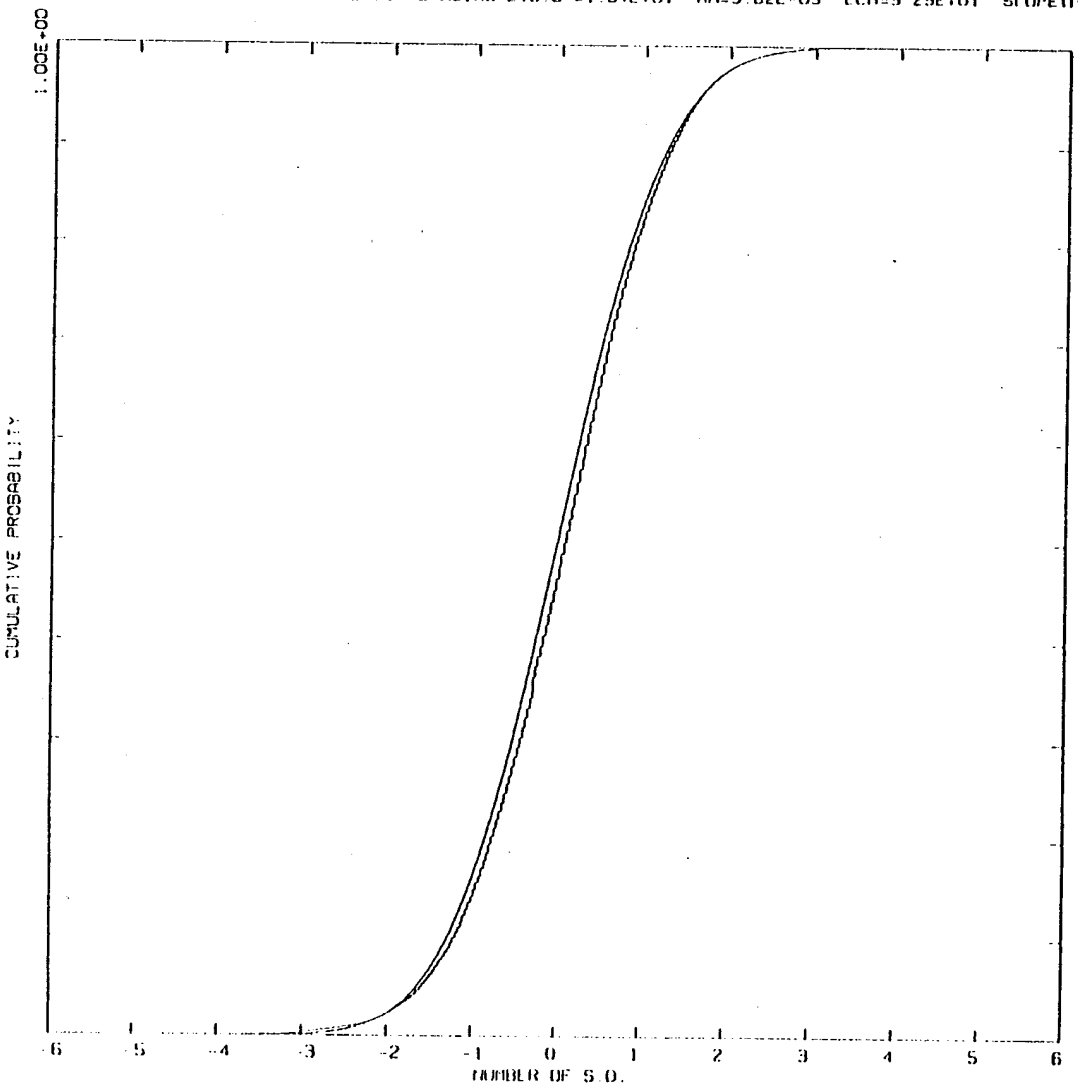

SOLID=THEORETICAL
BARS=ACTUAL
NUMBER OF POINTS=98304
WEIGHTED AVERAGE SUBTRACTED
-3.84E-03
STANDARD DEVIATION OF DATA
2.89E-02

POINTS FROM SHEET OF HORIZONTAL DATA

BACKUP FIG 10

FILE PCIM006 7-FEB-94 GREAT CIRCLE APPROXIMATION EARTH RADIUS= 6.370E+03
NUMBER OF CYCLES USED(ALIASING) L.O.S.=157 NUMBER OF CYCLES USED(ALIASING) PER L.O.S.=1
RANDOM NUMBER SEED= 12345 ALTITUDE= 5.060E+01 SLOPE(V)=1.67E+00 THIS MEANS NU(V)=3.33E-01 SPACING(V)=1.00E-01
AV=6.90E-02 LCV=1.72E+00 NUMBER OF HORIZONTAL SAMPLES=98304 NUMBER OF PREDICTOR COEFFICIENTS V=6 U=6
NUMBER OF ITERATIONS=51 THIS IS ONE SHEET OF 512 PERPENDICULAR VALUES BY 192 L.O.S. VALUES SIGMA**2 WILL BE SET TO 8.34E-04
PERPENDICULAR SPACING=1.00E-01 SPACING L.O.S =1.57E+01 AR=3.62E-03 LCU=3 29E+01 SLOPE(U)=2.67E+00 THIS MEANS NU(U)=3.33E-01
INTEGRAL OF PSD= 8.29E-04 THIS IS SHEET NUMBER 7 BIAS PSD MODEL TO GIVE CORRECT VARIANCE

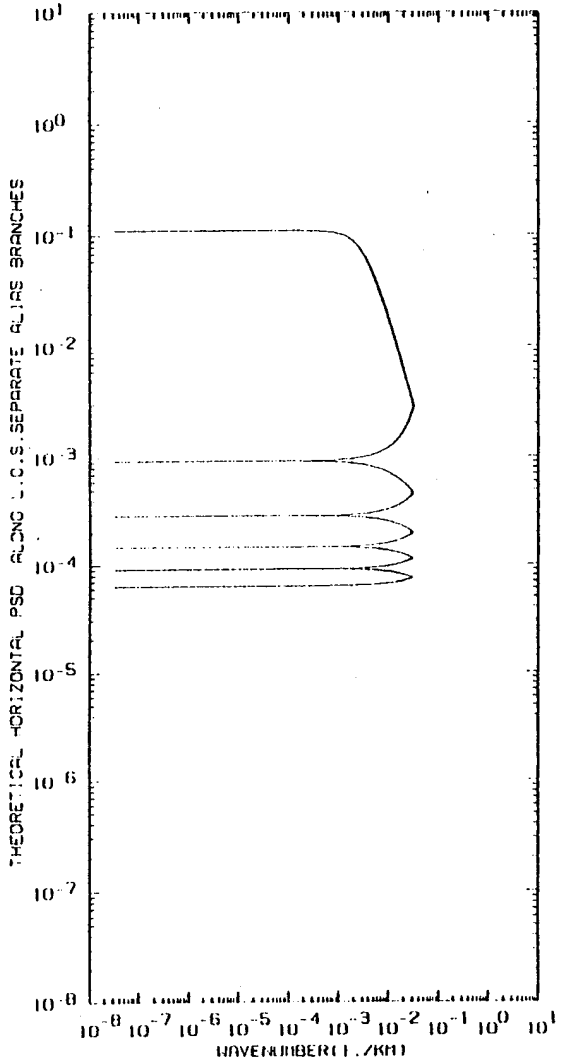

BACKUP FIG 12

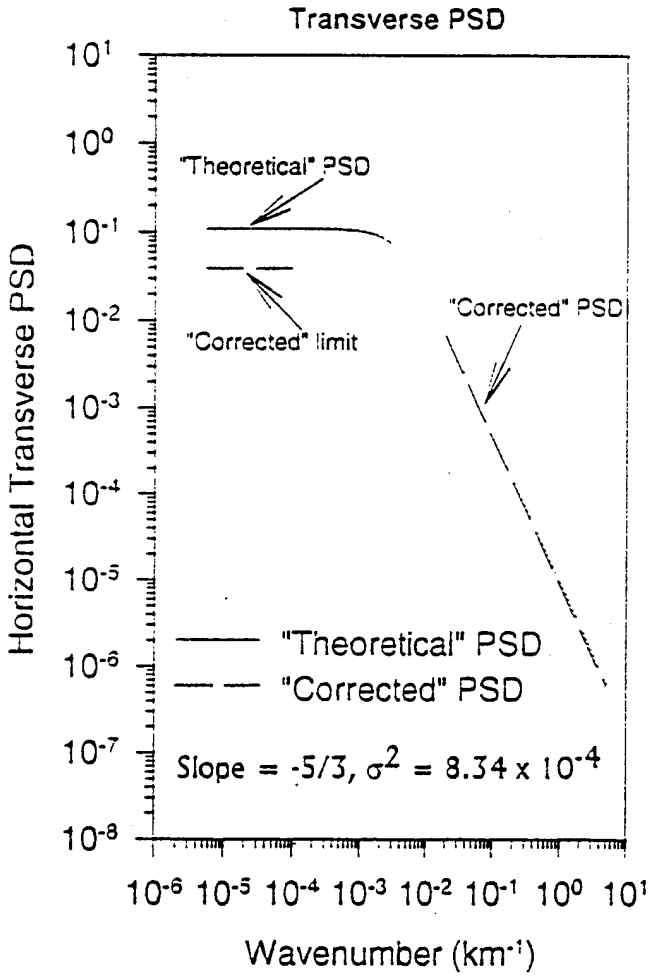

BACKUP FIG 13

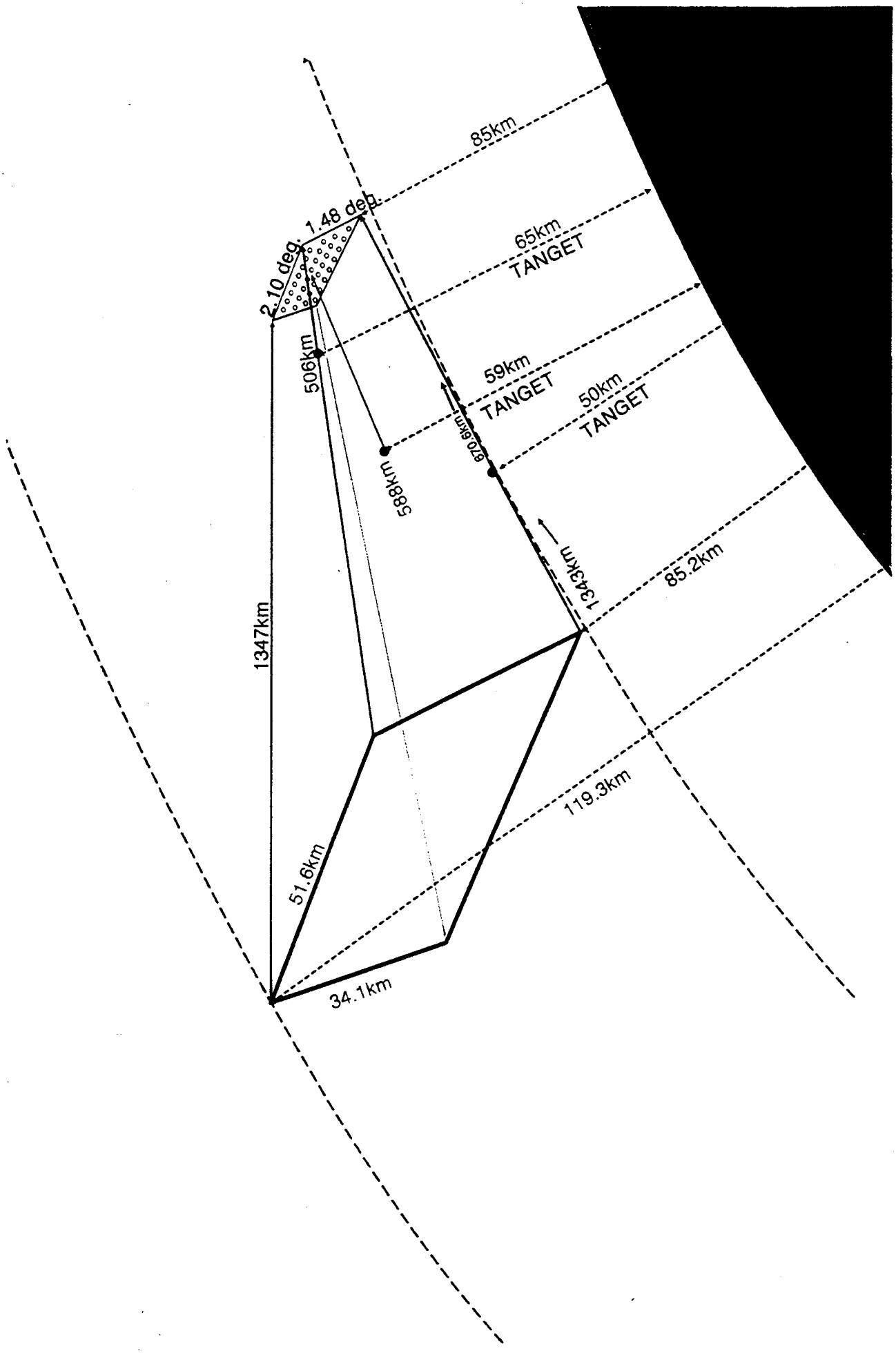
85km
1.48 deg.
2.10 deg.
65km
TANGET
506km
59km
TANGET
50km
TANGET
588km
670.6km
1343km
85.2km
1347km
119.3km
51.6km
34.1km

THIS IS FILE PINTDT6 RUN ON DATE 27-MAY-94 DATA CREATED BY FILE INTDT6 ON DATE 7-FEB-94
ALTITUDE OF OBSERVER= 8.50E+01 LOWEST ALTITUDE SIMULATED= 5.00E+01 2-D SLOPE OF PSD HORIZONTAL= 2.67E+00
1-D SLOPE OF PSD VERTICAL= 1.67E+00 TRANSVERSE SPACING AT LOWEST ALTITUDE= 1.00E-01 VERTICAL SPACING= 1.00E-01
SPACING ALONG L.O.S.= 1.57E+01 NUMBER TRANSVERSE POINTS=512 NUMBER L.O.S. POINTS=192 NUMBER OF VERTICAL SHEETS=701
MAXIMUM ANGLE L.O.S. USED= 1.19E+01 DEGREES NUMBER OF ZENITH VALUES CALCULATED=350 CENTER ZENITH VALUE= 9.52E+01 DEGREES
ZENITH SPACING= 4.20E-03 DEGREES NUMBER OF ALPHA VALUES CALCULATED=512 ALPHA SPACING= 4.20E-03

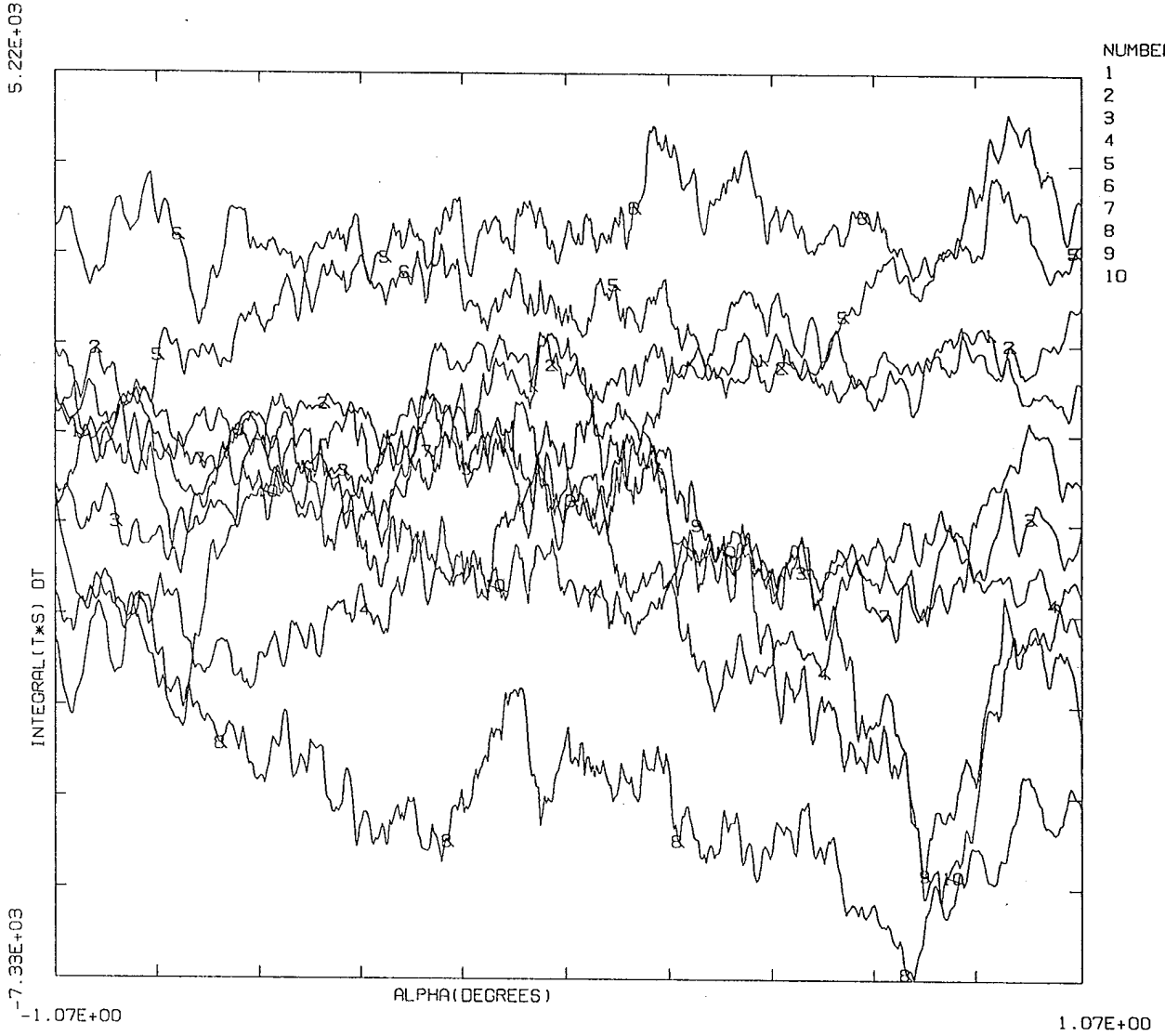

NUMBER	ZENITH
1	9.60E+01
2	9.58E+01
3	9.57E+01
4	9.55E+01
5	9.54E+01
6	9.52E+01
7	9.51E+01
8	9.49E+01
9	9.48E+01
10	9.46E+01

BACKUP 1/16/16

THIS IS FILE PINTDT6 RUN ON DATE 27-MAY-94 DATA CREATED BY FILE INTDT6 ON DATE 7-FEB-94
ALTITUDE OF OBSERVER= 8.50E+01 LOWEST ALTITUDE SIMULATED= 5.00E+01 2-D SLOPE OF PSD HORIZONTAL= 2.67E+00
1-D SLOPE OF PSD VERTICAL= 1.67E+00 TRANSVERSE SPACING AT LOWEST ALTITUDE= 1.00E-01 VERTICAL SPACING= 1.00E-01
SPACING ALONG L.O.S.= 1.57E+01 NUMBER TRANSVERSE POINTS=512 NUMBER L.O.S. POINTS=192 NUMBER OF VERTICAL SHEETS=701
MAXIMUM ANGLE L.O.S. USED= 1.19E+01 DEGREES NUMBER OF ZENITH VALUES CALCULATED=350 CENTER ZENITH VALUE= 9.52E+01 DEGREES
ZENITH SPACING= 4.20E-03 DEGREES NUMBER OF ALPHA VALUES CALCULATED=512 ALPHA SPACING= 4.20E-03

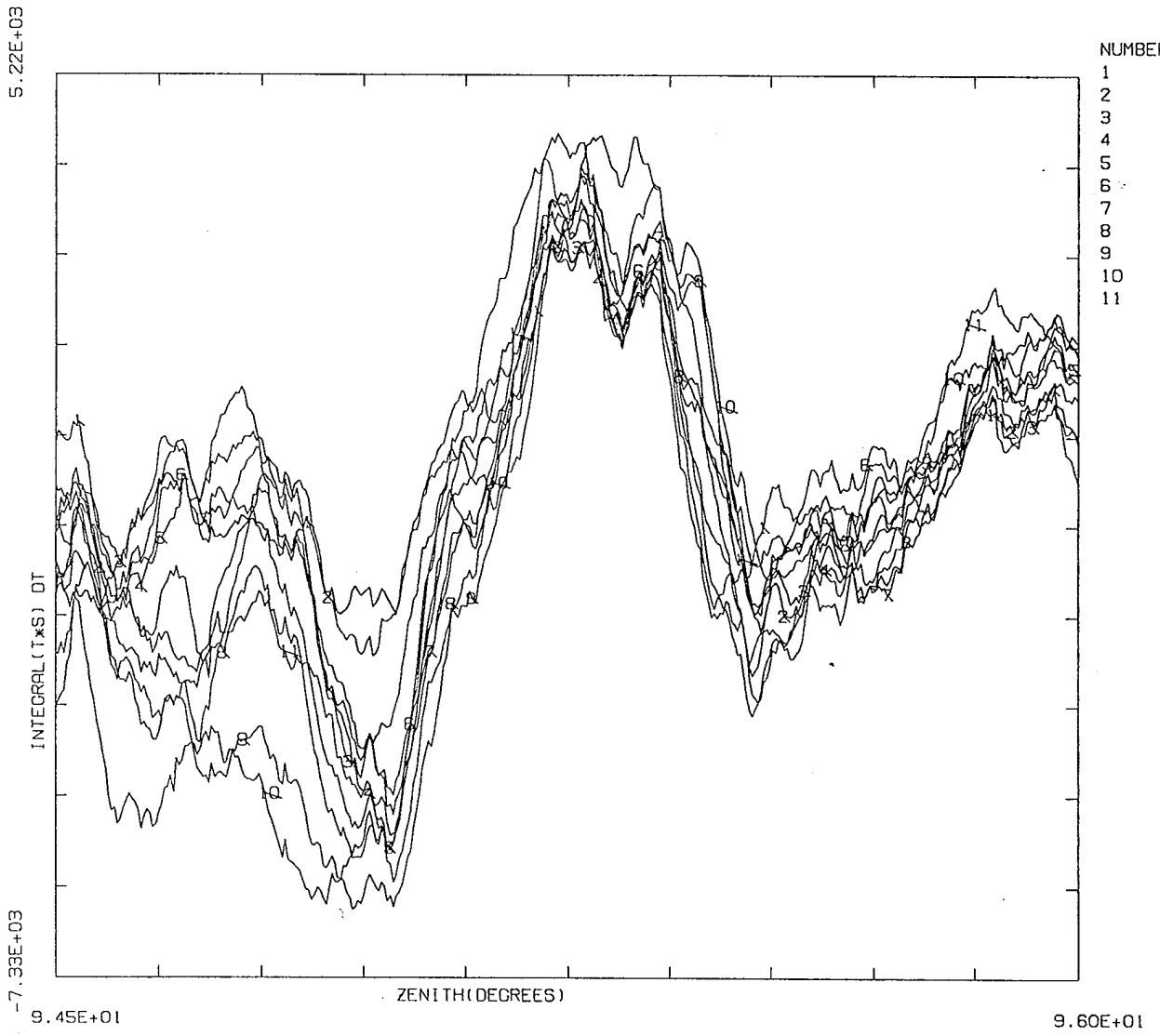

NUMBER	ALPHA
1	-1.07E+00
2	-8.59E-01
3	-6.45E-01
4	-4.31E-01
5	-2.16E-01
6	-2.10E-03
7	2.12E-01
8	4.26E-01
9	6.40E-01
10	8.55E-01
11	1.07E+00

BACKUP FIG 12

THIS IS FILE PINTDT6 RUN ON DATE 27-MAY-94 DATA CREATED BY FILE INTDT6 ON DATE 7-FEB-94
ALTITUDE OF OBSERVER= 8.50E+01 LOWEST ALTITUDE SIMULATED= 5.00E+01 2-D SLOPE OF PSD HORIZONTAL= 2.67E+00
1-D SLOPE OF PSD VERTICAL= 1.67E+00 TRANSVERSE SPACING AT LOWEST ALTITUDE= 1.00E-01 VERTICAL SPACING= 1.00E-01
SPACING ALONG L.O.S.= 1.57E+01 NUMBER TRANSVERSE POINTS=512 NUMBER L.O.S. POINTS=192 NUMBER OF VERTICAL SHEETS=701
MAXIMUM ANGLE L.O.S. USED= 1.19E+01 DEGREES NUMBER OF ZENITH VALUES CALCULATED=350 CENTER ZENITH VALUE= 9.52E+01 DEGREES
ZENITH SPACING= 4.20E-03 DEGREES NUMBER OF ALPHA VALUES CALCULATED=512 ALPHA SPACING= 4.20E-03

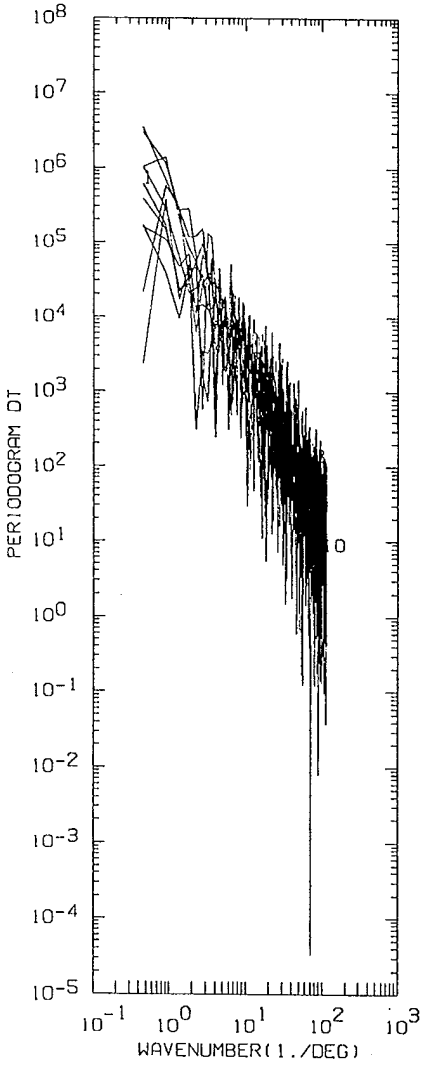

NUMBER	ZENITH
1	9.60E+01
2	9.58E+01
3	9.57E+01
4	9.55E+01
5	9.54E+01
6	9.52E+01
7	9.51E+01
8	9.49E+01
9	9.48E+01
10	9.46E+01

VALUES FOR PSD

BACKUP FIG 18

THIS IS FILE PINTDT6 RUN ON DATE 27-MAY-94 DATA CREATED BY FILE INTDT6 ON DATE 7-FEB-94
ALTITUDE OF OBSERVER= 8.50E+01 LOWEST ALTITUDE SIMULATED= 5.00E+01 2-D SLOPE OF PSD HORIZONTAL= 2.67E+00
1-D SLOPE OF PSD VERTICAL= 1.67E+00 TRANSVERSE SPACING AT LOWEST ALTITUDE= 1.00E-01 VERTICAL SPACING= 1.00E-01
SPACING ALONG L.O.S.= 1.57E+01 NUMBER TRANSVERSE POINTS=512 NUMBER L.O.S. POINTS=192 NUMBER OF VERTICAL SHEETS=701
MAXIMUM ANGLE L.O.S. USED= 1.19E+01 DEGREES NUMBER OF ZENITH VALUES CALCULATED=350 CENTER ZENITH VALUE= 9.52E+01 DEGREES
ZENITH SPACING= 4.20E-03 DEGREES NUMBER OF ALPHA VALUES CALCULATED=512 ALPHA SPACING= 4.20E-03

NUMBER	ZENITH
1	9.60E+01
2	9.58E+01
3	9.57E+01
4	9.55E+01
5	9.54E+01
6	9.52E+01
7	9.51E+01
8	9.49E+01
9	9.48E+01
10	9.46E+01

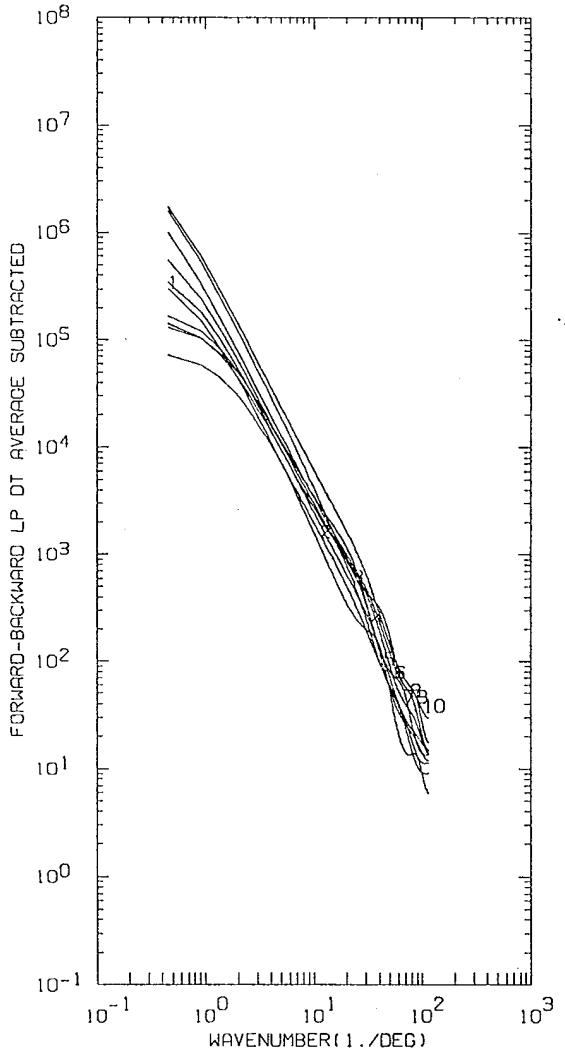

NUMBER OF LP COEFFICIENTS 6
VALUES FOR PSD

BACKUP # 19

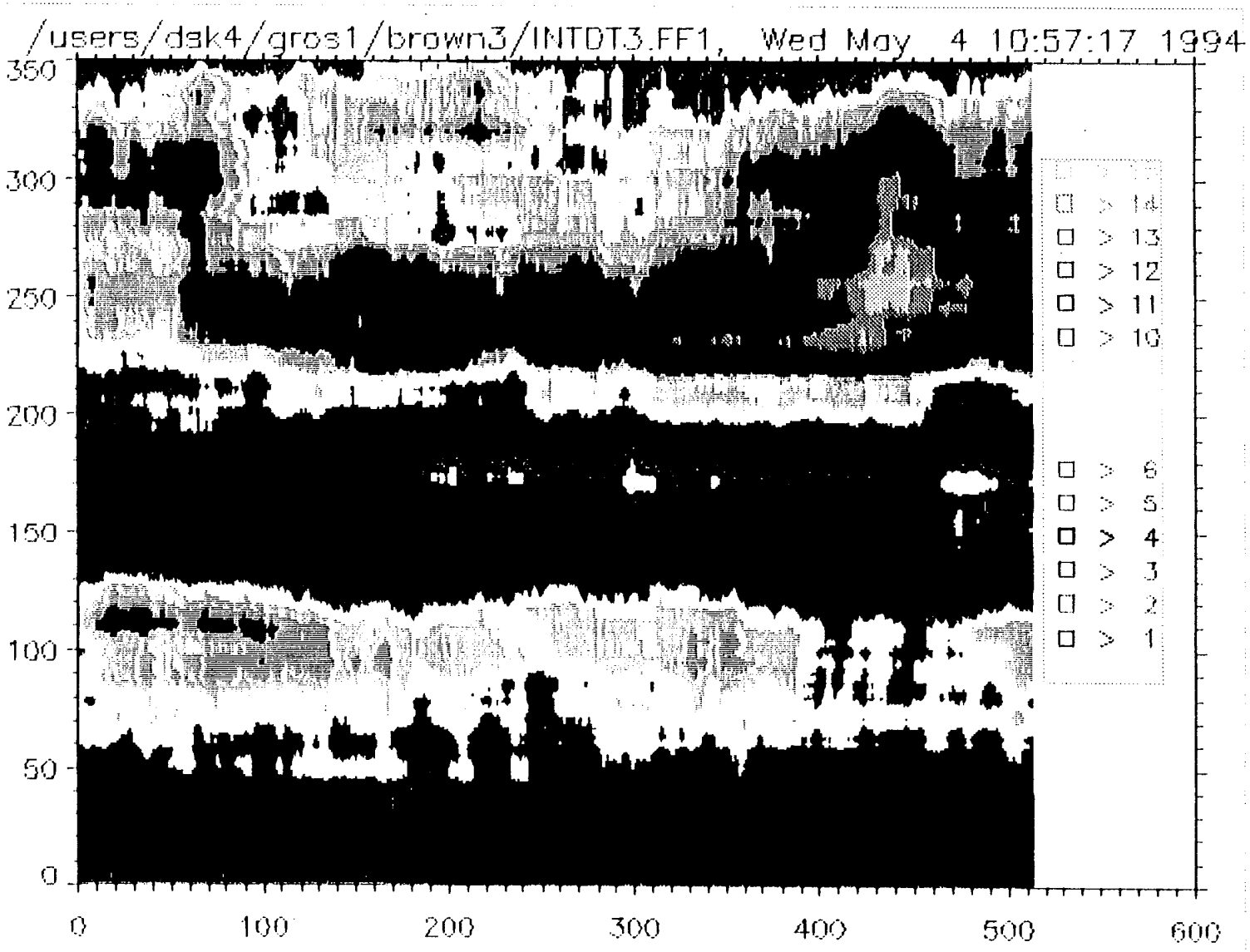

506

BACKUP FIG 20

Plane Wave Scintillation in an Onion Skin Model

Robert R. Beland
Phillips Laboratory

Geophysics Directorate
PL/GPOA
Hanscom AFB, Ma 01731
(617)-377-4604
Fax (617)-377-3661
email: beland@opus.plh.af.mil

Annual Review Conference on Atmospheric Transmission Models
7-8 June 1994

Objectives

- include horizontal variability of atmospheric turbulence through long near horizontal paths
- emphasize application to aircraft-based platforms
- derive analytic expressions for Rytov theory scintillation with onion skin model
- compare predictions with existing approaches
- investigate effects of aperture averaging and inner scale
- compare Rytov/onion skin predictions with data

Definition of Onion Skin Geometry

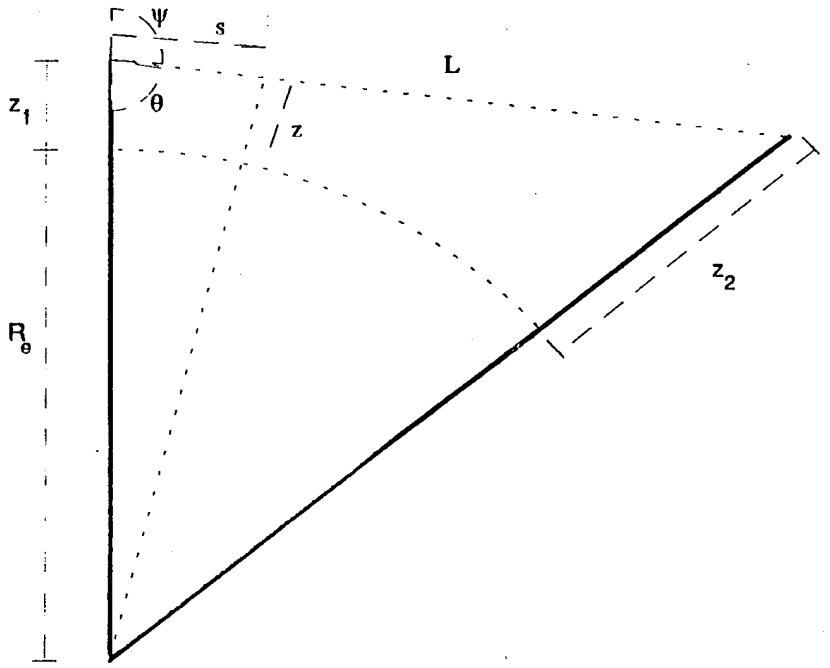

$$\cos(\psi) = \frac{R_2^2 - L^2 - R_1^2}{2R_1 L}$$

$$s = f(z,\psi)$$

$$= \sqrt{R^2 - R_1^2 \sin^2(\psi)} - R_1 \cos(\psi)$$

$$= \sqrt{(R_e + z)^2 - (R_e + z_1)^2 \sin^2(\psi)} - (R_e + z_1)\cos(\psi)$$

Altitude of the propagation path for a 12.5 km observer for various zenith angles

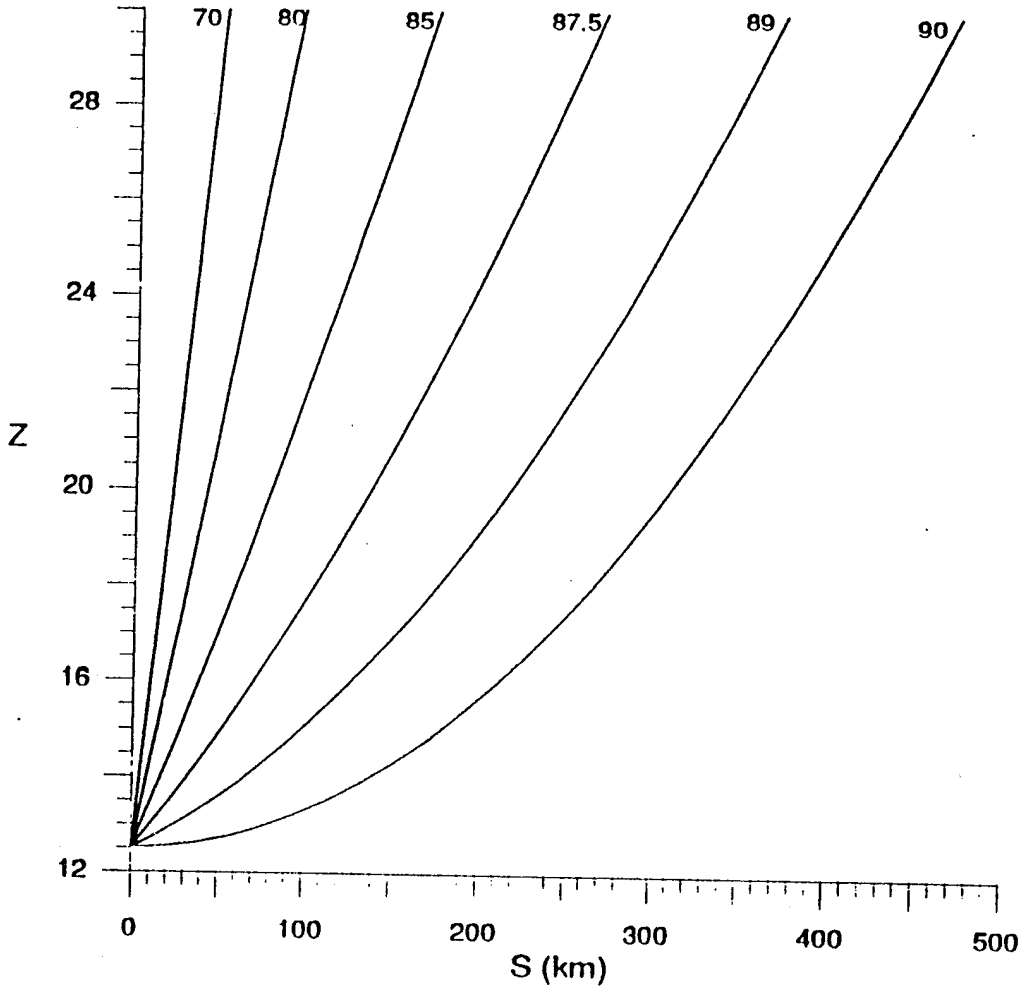

Onion Skin Model and the Log Amplitude Variance

The Rytov solution for a plane wave originating at L and observed at s=0 (point detector)

$$\sigma_\chi^2 = 4\pi^2 k^2 \int_0^L ds \int_0^\infty dK\, K\, \Phi_n(K,s) \sin^2\left(\frac{K^2 s}{2k}\right)$$

For the Kolmogorov spectrum: $\sigma_\chi^2 = 0.56 k^{7/6} \int_0^L C_n^2(s) s^{5/6} ds$

Flat Earth Model: Assume that C_n^2 is only a function of altitude. Explicitly, assume:

1) $s = (z - z_1)\sec(\psi)$

2) $C_n^2(s) = C_n^2(z)$

Then

$$\sigma_\chi^2 = 0.56 k^{7/6} \{\sec(\psi)\}^{11/6} \int_{z_1}^{z_2} C_n^2(z)(z - z_1)^{5/6} dz$$

Onion Skin Model

Assume C_n^2 is a function only of altitude, but include the earth's curvature. The atmosphere is treated as concentric shells or layers. Explicitly, assume:

1) $s = f(z,\psi)$

2) $C_n^2(s) = C_n^2(z)$

Then

$$\sigma_\chi^2 = 0.56k^{7/6}\int_{z_1}^{z_2} C_n^2(z)[f(z,\psi)]^{5/6} f'(z,\psi)\,dz$$

where

$$s = f(z,\psi) = \sqrt{(R_e+z)^2 - (R_e+z_1)^2\sin^2(\psi)} - (R_e+z_1)\cos(\psi)$$

$$f'(z,\psi) = \frac{ds}{dz} = \frac{(R_e+z)}{\sqrt{(R_e+z)^2 - (R_e+z_1)^2\sin^2(\psi)}}$$

Define the altitude weighting function, $W(z,\psi)$

$$\sigma_{\chi}^{2} = \int_{z_1}^{z_2} C_n^2(z) W(z,\psi)\, dz$$

Then, for the Onion Skin Model, for propagation beginning at z_1:

$$W(z,\psi) = \left[\sqrt{(R_e+z)^2 - (R_e+z_1)^2 \sin^2(\psi)} - (R_e+z_1)\cos(\psi)\right]^{5/6} \frac{0.56k^{7/6}(z+R_e)}{\sqrt{(z+R_e)^2 - (z_1+R_e)^2 \sin^2(\psi)}}$$

while for the Flat Earth model

$$W_F(z,\psi) = 0.56k^{7/6}\{\sec(\psi)\}^{11/6}(z-z_1)^{\frac{5}{6}}$$

Plane wave altitude weighting function for zenith angle of 60°

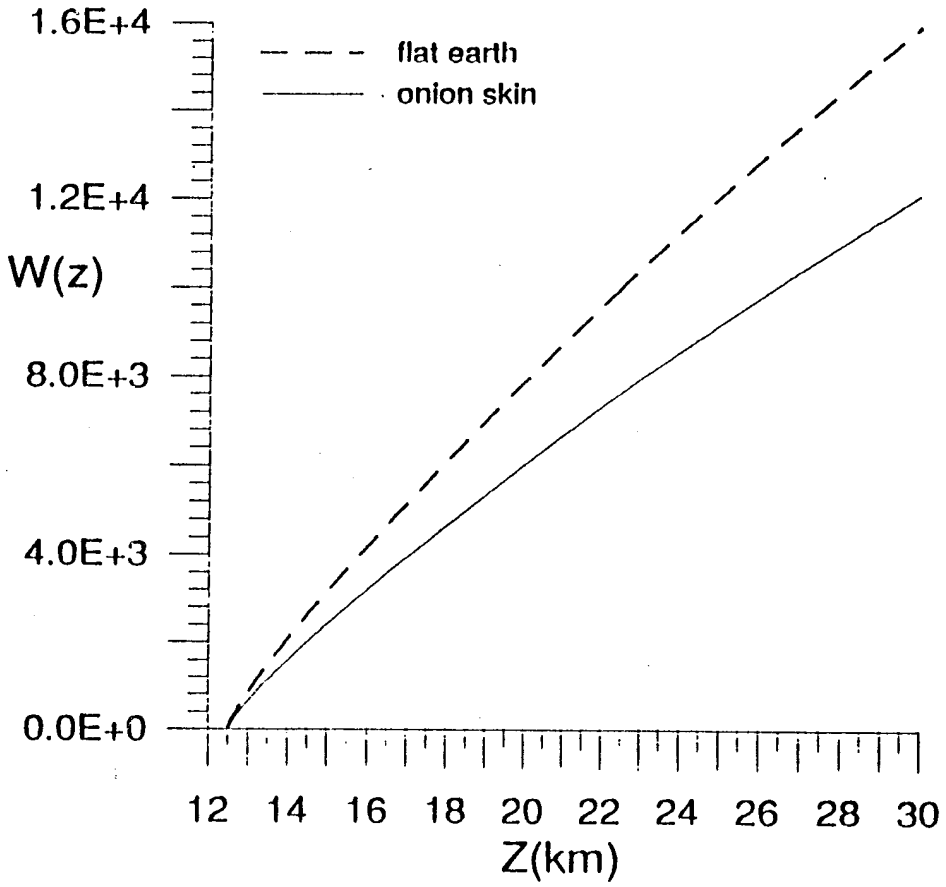

Plot of plane wave altitude weighting function for zenith angle of 89°

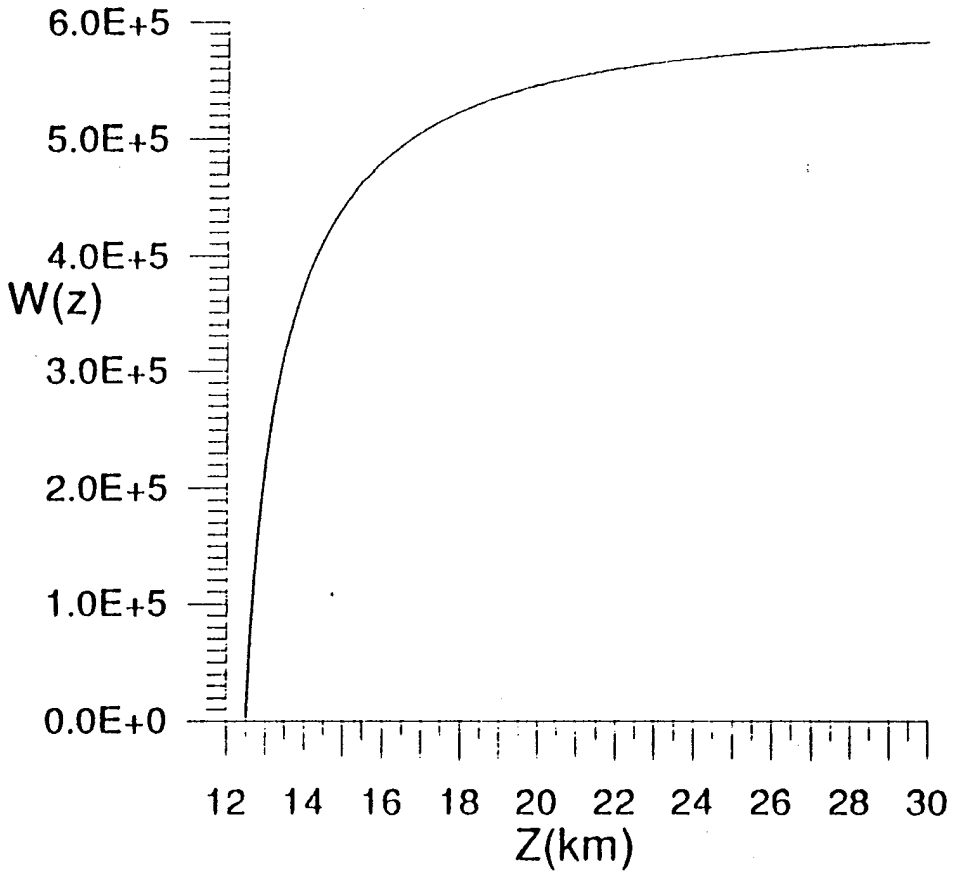

Properties of W(z,ψ)

- Onion Skin and Flat Earth Model agree exactly at $\psi = 0°$
- Onion Skin and Flat Earth Model do not significantly differ for $\psi < 30°$
- For $\psi = 90°$, Flat Earth Model is singular for all z
- For $\psi = 90°$, Onion Skin reduces to

$$W(z,90) = 0.56k^{7/6}\left[(R_e + z)^2 - (R_e + z_1)^2\right]^{-1/12}(R_e + z)$$

This has a weak singularity at the receiver, z_1. This is a mathematical singularity that is removed for any finite receiver aperture.

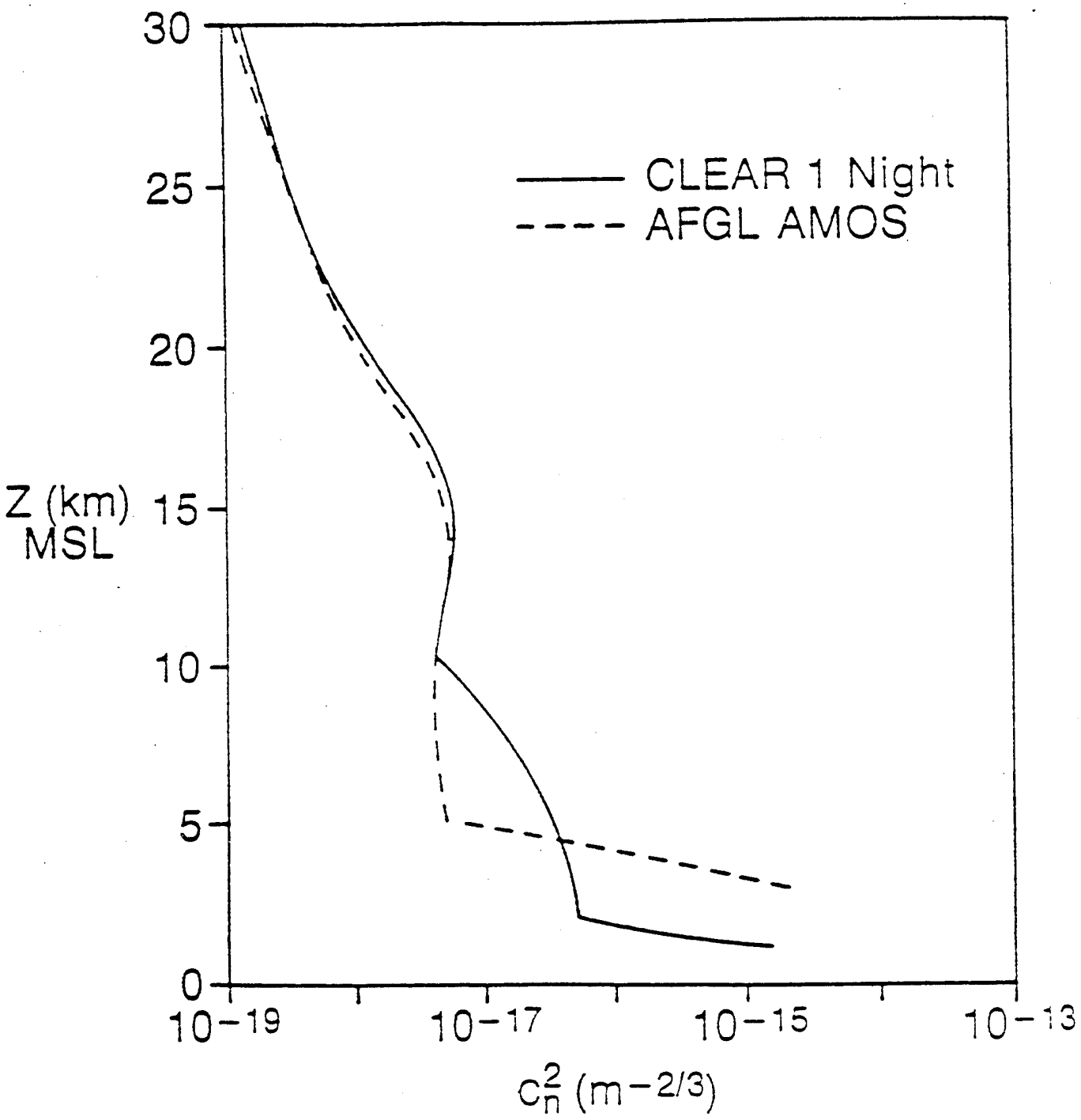
30
25
20
15
10
5
0
Z (km)
MSL
CLEAR 1 Night
AFGL AMOS
10−19
10−17
10−15
10−13
C_n^2 (m−2/3)

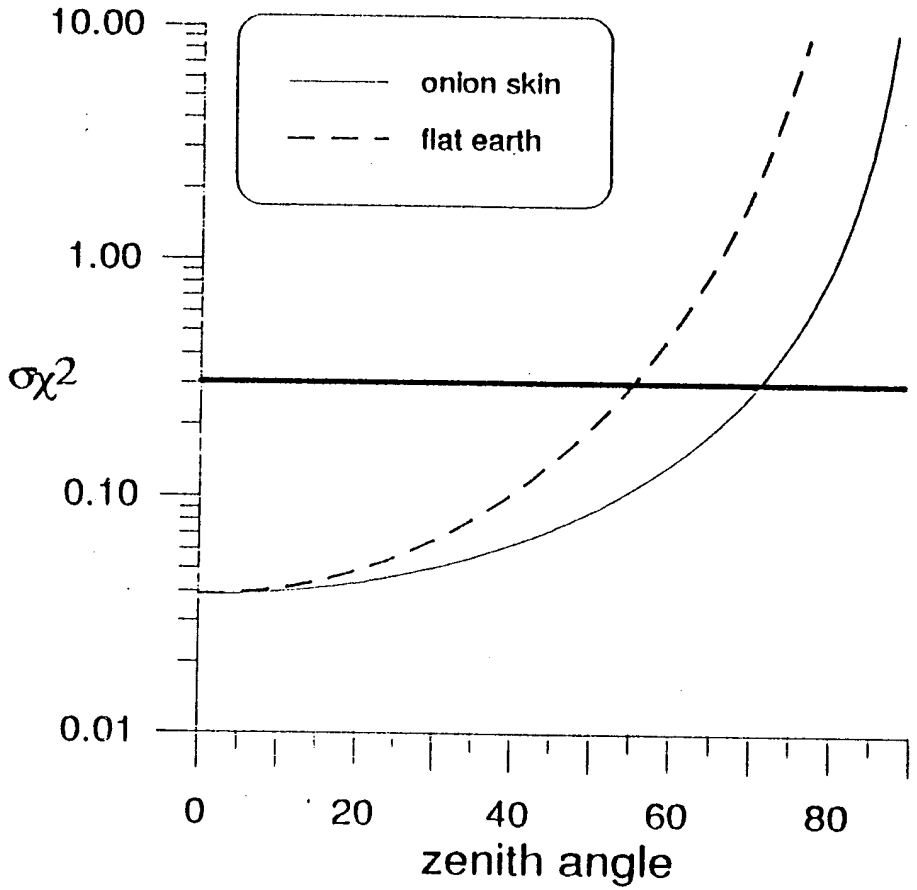

The turbulence profile used is that of CLEAR I.
The receiver is assumed to be at ground level (1.216 km MSL for CLEAR I).
This calculation assumes a point receiver.

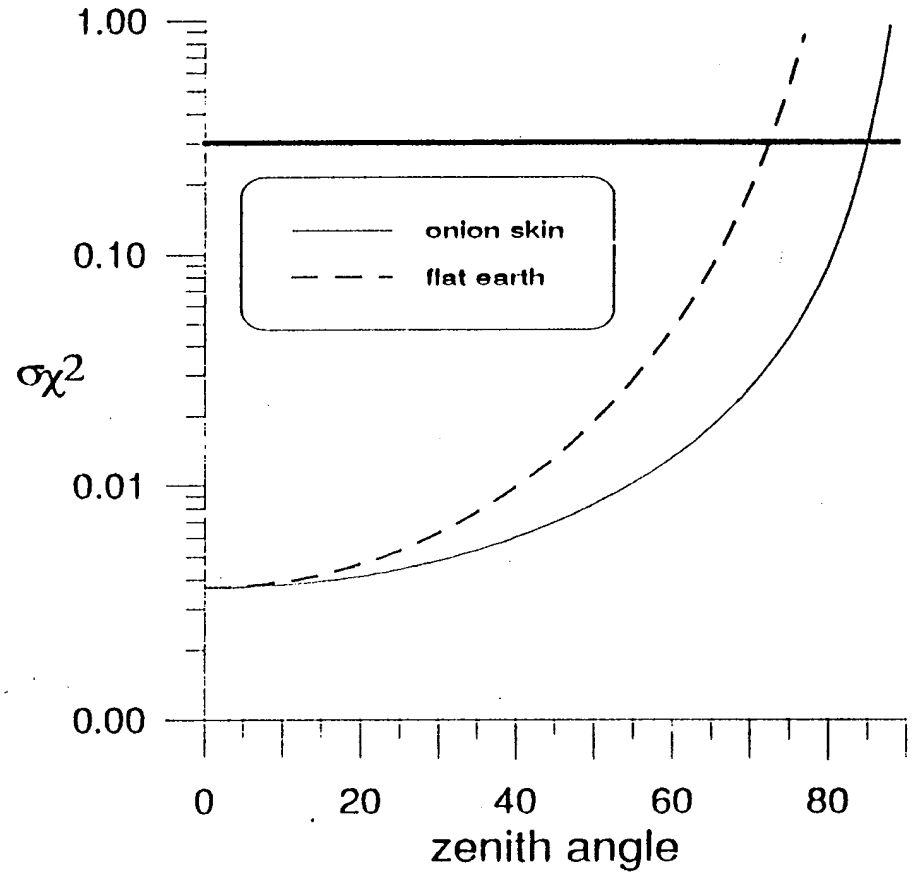

The turbulence profile used is that of CLEAR I.
The receiver is assumed to be at 12.5 km MSL.
This calculation assumes a point receiver.

Finite Aperture Effects

For a receiver is a circular aperture of radius a

$$\sigma_\chi^2 = 4\pi^2 k^2 \int_0^L ds \int_0^\infty dK\, K\, \Phi_n(K,s) \sin^2\left(\frac{K^2 s}{2k}\right)\left[\frac{2J_1(Ka)}{Ka}\right]^2$$

Using Kolmogorov spectrum, we can define a path weighting function, as before:

$$W(s,a) = 0.033\pi^2 2^{\frac{13}{6}} k^{\frac{1}{6}} a^{-2} s^{\frac{11}{6}} \int_0^\infty dK\, K^{\frac{-14}{3}} \sin^2(K^2) J_1(Ka\sqrt{\frac{2k}{s}})^2$$

and an Onion Skin altitude weighting function:

$$W(z,a,\psi) = 4\pi^2 k^2 f'(z,\psi) \int_0^\infty dK\, K\, \Phi_0(K) \sin^2\left(\frac{K^2 f(z,\psi)}{2k}\right)\left[\frac{2J_1(Ka)}{Ka}\right]^2$$

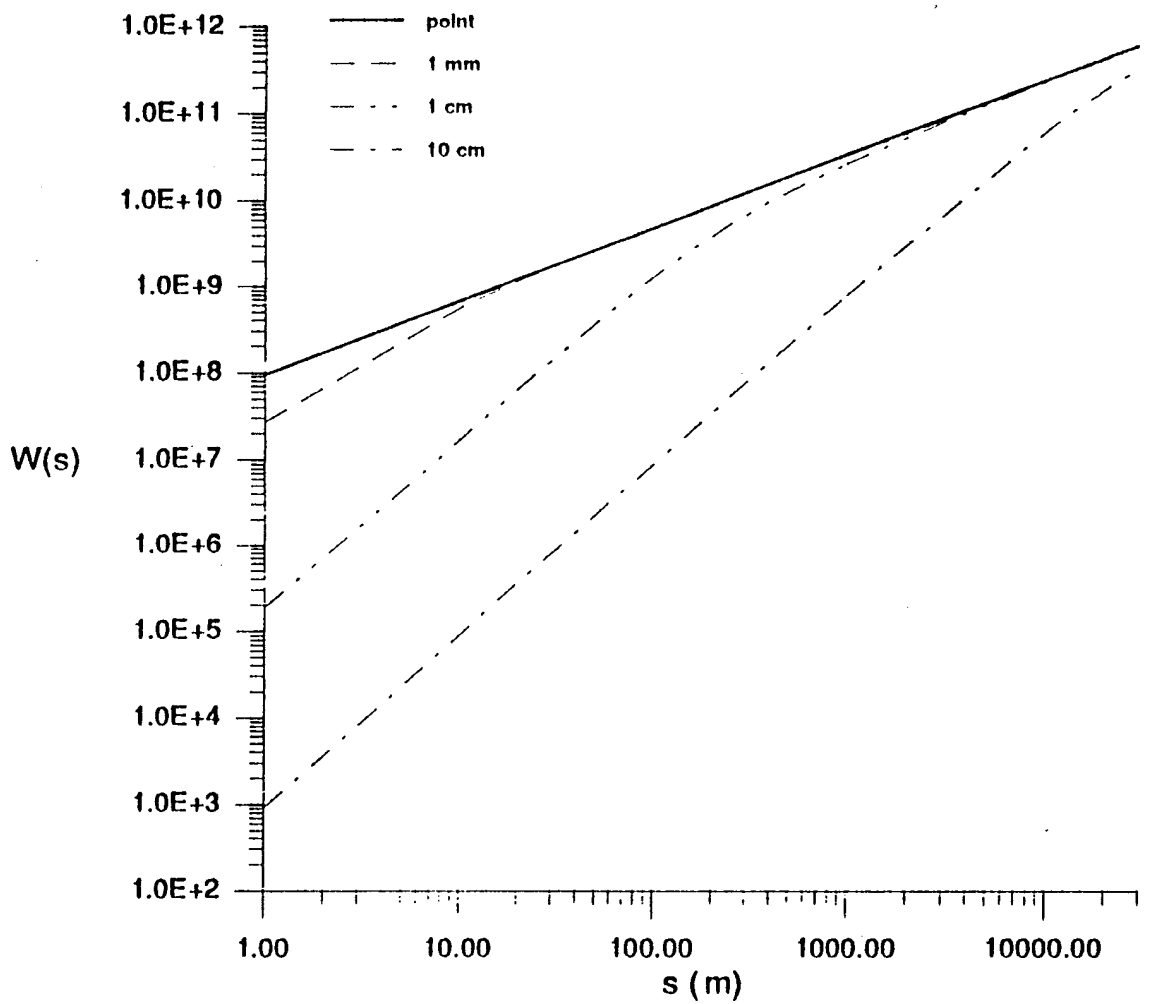

Path weighting function for plane wave scintillation. The solid curve is the usual 5/6 power weighting function.

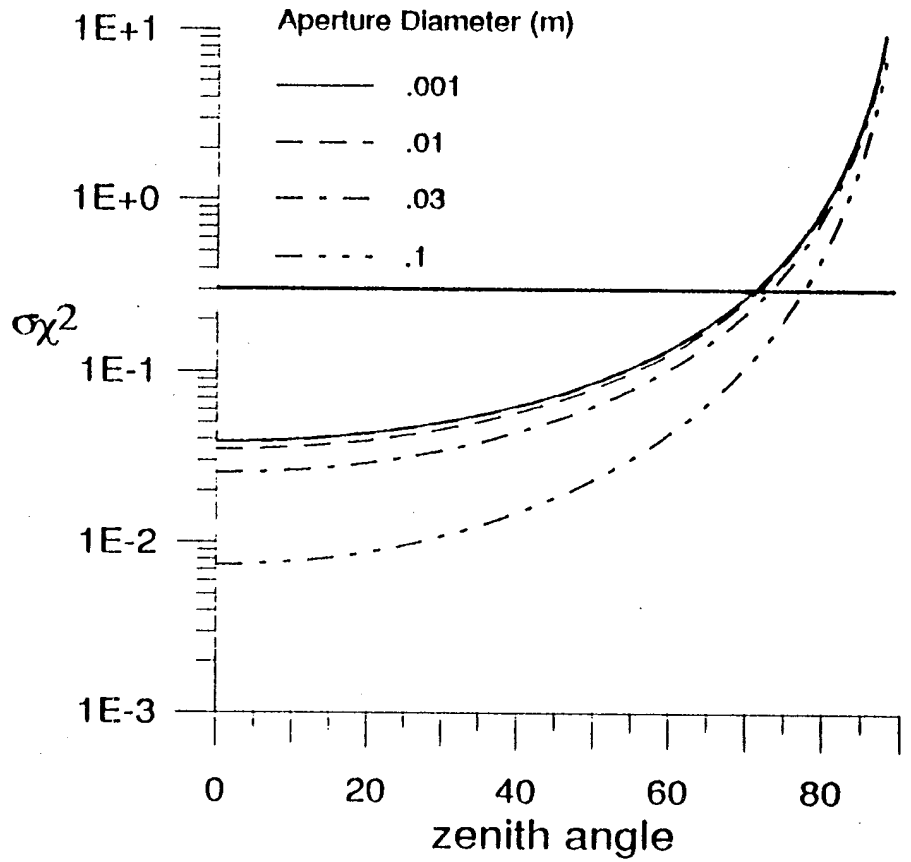

Plane wave log amplitude variance showing the effect of aperture averaging as a function of zenith angle. The calculation used the Clear 1 profile in an onion skin, with the receiver at ground level (1.216 km MSL).

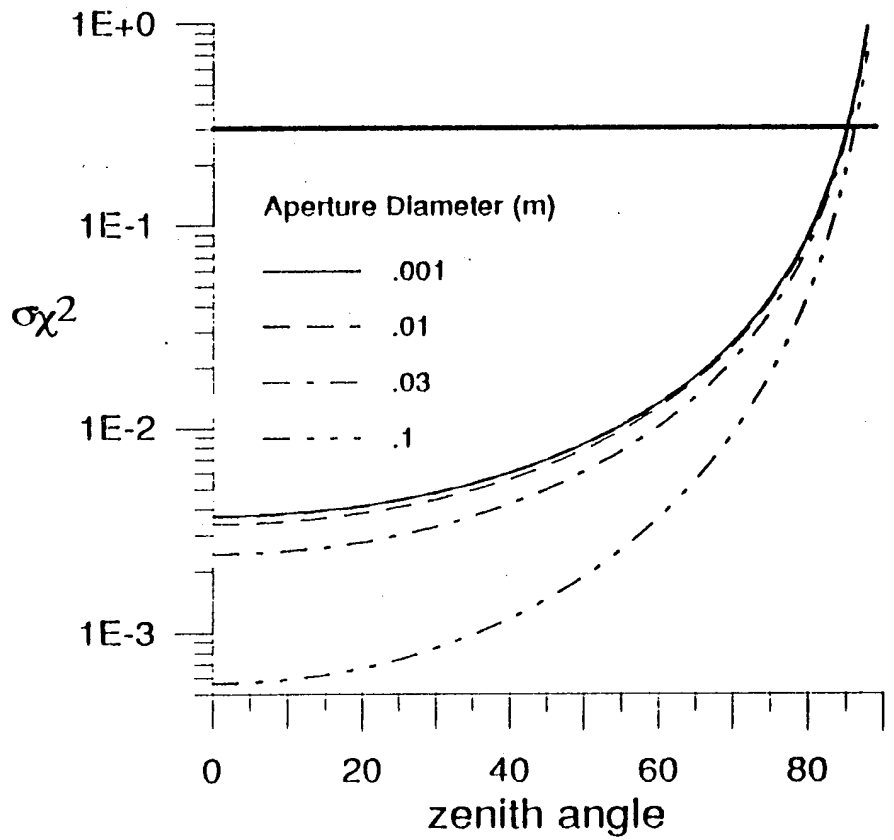

Plane wave log amplitude variance showing the effect of aperture averaging as a function of zenith angle. The calculation used the Clear 1 profile in an onion skin model, with the receiver at an altitude of 12.5 km.

Onion Skin Model Predictions for Airborne Measurements

- Rytov/onion skin model predicts
    1. that the weak fluctuation approximation applies to zenith angles $< \approx 85°$ and that larger angles are in the saturation region

- Rytov/Onion Skin model shows that there is a small difference between the 1 and 3 cm apertures at 80° (.08 vs .09) and explains the reduction of aperture averaging effect:
    1. Aperture averaging removes contribution from turbulence near the receiver.
    2. The reduction by a 1 cm aperture is due to the reduced contribution from the first km of the path. As the zenith angle increases, the atmospheric path increases and the ratio of the turbulence in the first kilometer to the rest of the path decreases.
    3. The amount of the reduction is a function of the distribution of the turbulence. A smooth distribution like CLEAR 1 produces different results than an actual profile that had a strong layer in the first kilometer of the path.

Inner Scale Effects

- Non-zero inner scale effects can included in the Rytov/Onion Skin Model by using the Tatarskii form of the spectrum

$$\Phi_n(K,s) = 0.033 C_n^2(s) K^{\frac{-11}{3}} e^{\frac{-K^2}{K_m^2}}$$

where $K_m = 5.92/l_0$ and l_0 is the inner scale.

- Log amplitude variance will be calculated as before using this spectrum with $l_0 = 10$ cm. This value is on the large side for propagation above 12.5 km, but should bound the problem.

- Inner scale is actually path dependent and increases with altitude. Only a constant value of 10 cm is used.

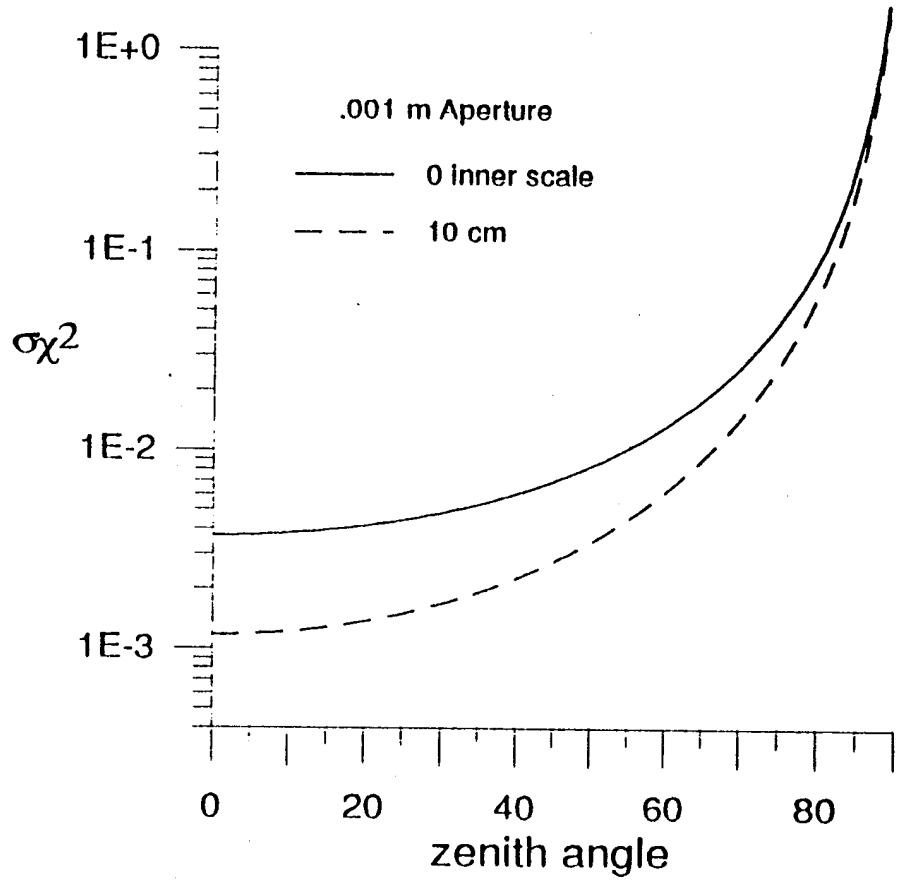

The effect of inner scale is shown for a 1 mm receiver. The calculation uses the Clear 1 profile and a receiver at 12.5 km altitude.

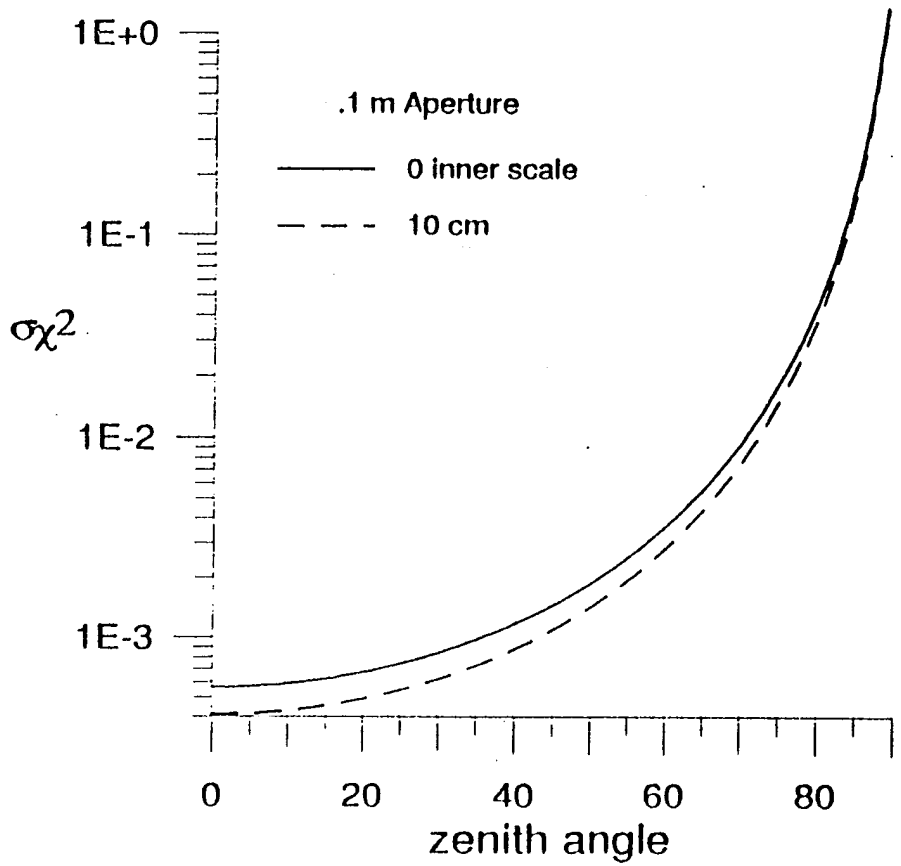

The effect of inner scale is shown for a 10 cm receiver. The calculation uses the Clear 1 profile and a receiver at 12.5 km altitude.

Inner Scale: Results

In weak fluctuations and near horizontal propagation,

- inner scale is a small corrrection to log amplitude variance; it decreases in importance as the zenith angle increases (path length increases).

- When combined with aperture averaging, inner scale is further reduced in importance.

Why ? Just like the aperture averaging effect, small scales ($<l_o$) contribute to log amplitude variance mainly from the part of the path in front of the receiver. This path forms less and less of the total turbulence as zenith angle increases. Of course, the relative magnitude of this contribution is determined by the distribution and strength of turbulence along the path.

BUT:
Inner scale is very important to log amplitude variance in the strong or saturated scinitllation domain.

Comparison to Data

- The Rytov/onion skin model can be used to compare predictions with data for zenith angles as large as about 85°.
- Airborne measurements typically made from altitudes of 40,000-50,000 ft.
- Cn2 profiles used were the Clear 1 model and actual PL/GP thermosonde profiles in order to include the effect of layering.
- Comparison of predictions to published astronomical data

Profiles used

Name	location	trop hgt (km)	comments
CLEAR 1	WSMR	17	no layers; average
MT0575	Montana	9	winter
MT0582	Montana	9	winter
L4031	Penn State	13.5	low winds; strong layers
L4032	Penn State	11	jet stream
L3998	Cape Cod	12	jet stream
AZ8809	Azores	12.5	low trop and strat Cn2

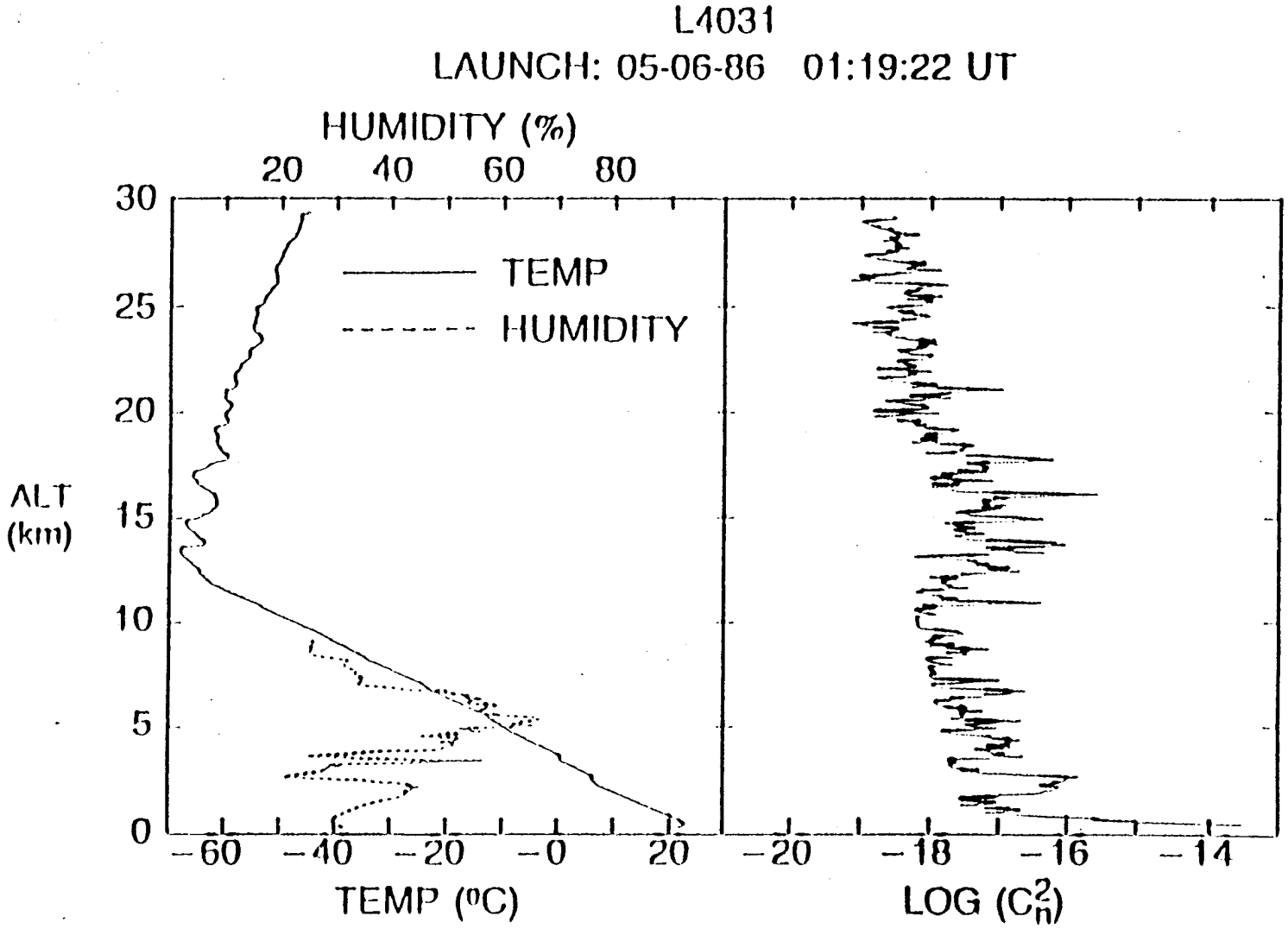
L4031
LAUNCH: 05-06-86 01:19:22 UT
HUMIDITY (%)
20
40
60
80
30
25
20
15
10
5
0
ALT (km)
TEMP
HUMIDITY
−60
−40
−20
−0
20
TEMP (°C)
−20
−18
−16
−14
LOG (C_n^2)

Predictions of σ_χ^2 with Rytov/onion skin model

Sirius (s105)

d=.03 m λ=0.5 μ z=50,200 ft ψ =83.6 °

	l_0=0	l_0=10 cm
Clear 1	0.036	0.025
MT0575	0.035	0.026
MT0582	0.042	0.031
L4031	0.139	0.098
L4032	0.089	0.069
AZ8809	0.039	0.031
L3998	0.049	0.039
data ave	0.066 +/-0.041	0.049 +/-0.029

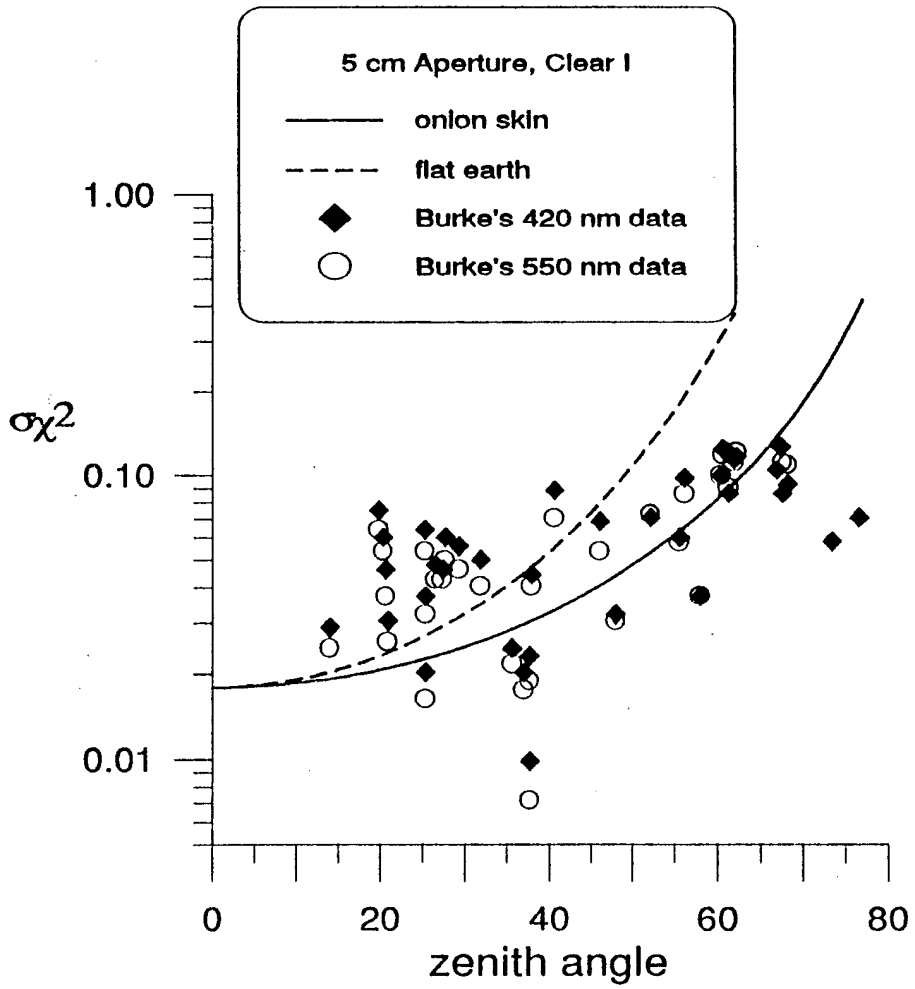

Comparison of Burke's astronomical data (Burke,J.J., JOSA,**60**, 1262-1263,1960) with predictions using CLEAR 1 and an observer at ground (1.216 km MSL)

Summary/Conclusions

- Onion skin formalism provides a model for horizontal structure of turbulence
- formalism reduces to "flat earth" model for small zenith angles and hence is an extension/refinement of the theory
- Predicts phenomena or behavior such as the reduction of inner scale and aperture averaging effects that are observed and not predictable from "flat earth" model
- Combined with Rytov theory, onion skin model yields expressions for near horizontal propagation that can be studied analytically
- formalism easily extended beyond plane wave scintillation to other optical effects such as spherical wave effects, image blurring and beam wander and broadening, etc

Extensions

Fried's plane wave transverse coherence length:

$$r_0 = 2.1\left[1.46k^2 \int_0^L C_n^2(s)ds\right]^{-3/5}$$

In the flat earth model,

$$r_0 = 2.1\left[1.46k^2 \sec(\psi) \int_{z_1}^{z_2} C_n^2(z)dz\right]^{-3/5}$$

The coherence length in the onion skin model becomes

$$r_0 = 2.1\left[1.46k^2 \int_{z_1}^{z_2} C_n^2(z) f'(z,\psi)\, dz\right]^{-3/5}$$

$$= 2.1\left[1.46k^2 \int_{z_1}^{z_2} C_n^2(z) \frac{(R_e + z)}{\sqrt{(R_e + z)^2 - (R_e + z_1)^2 \sin^2(\psi)}} dz\right]^{-3/5}$$

COMPARISON OF A MODEL DESCRIBING PROPAGATION THROUGH OPTICAL TURBULENCE (PROTURB) WITH FIELD DATA

Robert W. Smith
U.S. Army Test and Evaluation Command
Ft. Belvoir Meteorological Team
Ft. Belvoir, Virginia 22060

Jennifer C. Ricklin
U.S. Army Research Laboratory
Battlefield Environment Directorate
White Sands Missile Range, New Mexico 88002

Kevin E. Cranston and John P. Cruncleton
Physical Science Laboratory
New Mexico State University
Las Cruces, New Mexico 88003-0002

ABSTRACT

The PROTURB model, developed by the Battlefield Environment Directorate of Army Research Laboratory, calculates an estimate of optical turbulence strength and its effects on visible and infrared imaging and laser system performance. The PROTURB model was earlier compared to data obtained from the REBAL 92 field test held in Bushland, Texas, and data supplied by the Army Test and Evaluation Command Ft. Belvoir Meteorological Team[1]. Recent PROTURB updates included modifying the radiative flux portion of the energy balance model. Here we present a new comparison using data from three locations that differ greatly in meteorological conditions, including hot and moist conditions, hot and dry conditions, and moderate climatic conditions. There also exists a considerable difference in site characteristics such as ground conditions and vegetation. This latter data set was collected during the summer of 1993 at the following sites: Eglin AFB, Florida, Ft. Hunter-Liggett, California, and Ft. A.P. Hill, Virginia. We discuss the data collection and reduction effort, and show how this data compares with PROTURB predictions.

2. INTRODUCTION

The PROTURB model consists of five distinct modules; the PROTURB interface, surface boundary module, planetary boundary layer module, imaging statistics module and the laser propagation module. The PROTURB user-friendly interface controls the input of data, the calculation procedure and the display of the output data in both numerical and graphical form. The surface boundary layer module is based on a radiative-energy flux balance model[3]

that in turn drives a Monin-Obukhov similarity theory model[2] for unstable atmospheric conditions. This module is responsible for the optical turbulence profile that extends from 10 times the roughness length up to the Obukhov height. The surface boundary layer module takes into consideration the effects of moisture and gives approximations during stable atmospheric conditions and in and around the neutral events. The planetary boundary layer module is also based on Monin-Obukhov similarity theory and the Ekman spiral[4]. This module is responsible for the continuation of the optical turbulence profile from the Obukhov height to the top of the planetary boundary layer. The imaging statistics module is primarily based upon the work of D. L. Fried[5]. This module determines the image statistics that correspond to an image that has propagated over the designated path. The current laser propagation module is based on Rytov theory developed at ARL West[6]. This module is responsible for determining laser propagation statistics such as irradiance variance and beam size.

3. FIELD DATA COLLECTION

All field metorological data were collected by the TECOM Ft Belvoir Meteorological Team. The same type of instruments were used at each location and proper calibration procedures were followed. Figure 1 locates the three locations. The optical

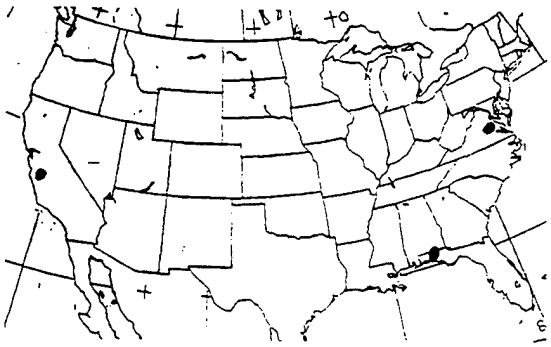

FIGURE 1 LOCATION OF DATA SITES

scintillometers used were the Lockheed model CN2. All data collection was automated and included temperature, relative humidity,pressure,rain rate and amount, visibility,soil temperature, long and short wave radiation, cloud amount, cloud height, C_n^2, and spectral atmospheric transmission.All data except clouds and transmission were collected in a single data set. An example is shown in table 1.Clouds and transmission were reported in seperate files which are not shown here.It must be pointed out that in each case, the collection system was designed for the test support and not this comparison effort. The standard measurements were taken at a location very near the scintillometer receiver while the cloud data was taken from our base site which could be several kilometers away from the other measurments. Data from Ft.

Day	Time hhmm	Press mb	WDD dg	WSP M/S	PKS M/S	Temp dg/c	RH %	Soil dg/c	Vsby km	PSP VER	PSP OUT	RNRT mm/h	SCINT VOLT	PIR VER	PIR OUT
196	15	1012.8	143	0.35	0.60	23.2	94	14.9	10.54	0.00	0.00	0.00	0.016	391.5	442.4
196	30	1012.6	20	0.04	0.40	23.1	95	14.8	9.15	0.00	0.00	0.00	0.013	390.8	441.7
196	45	1012.6	52	0.09	0.40	23.1	95	14.6	10.86	0.00	0.00	0.00	0.005	391.1	441.5
196	100	1012.4	104	0.21	0.60	23.1	95	14.6	11.51	0.00	0.00	0.00	0.017	390.2	440.3
196	115	1012.3	60	0.31	0.90	23.0	95	14.5	9.81	0.00	0.00	0.00	0.012	390.8	440.4

TABLE 1. FORMAT OF FIELD DATA

AP Hill and Eglin AFB were averaged for one minute while 10 minute data was collected at Ft. Hunter Liggett. Data was collected over the entire 24 hour period and examples of temperature,humidity,solar radiation and C_n^2 are shown in figure 2 to illustrate the differences between the locations. Since much more data was collected than could possibly be used in this effort, a few representative days were chosen from each location. Complete details are available from the Ft. Belvoir team.

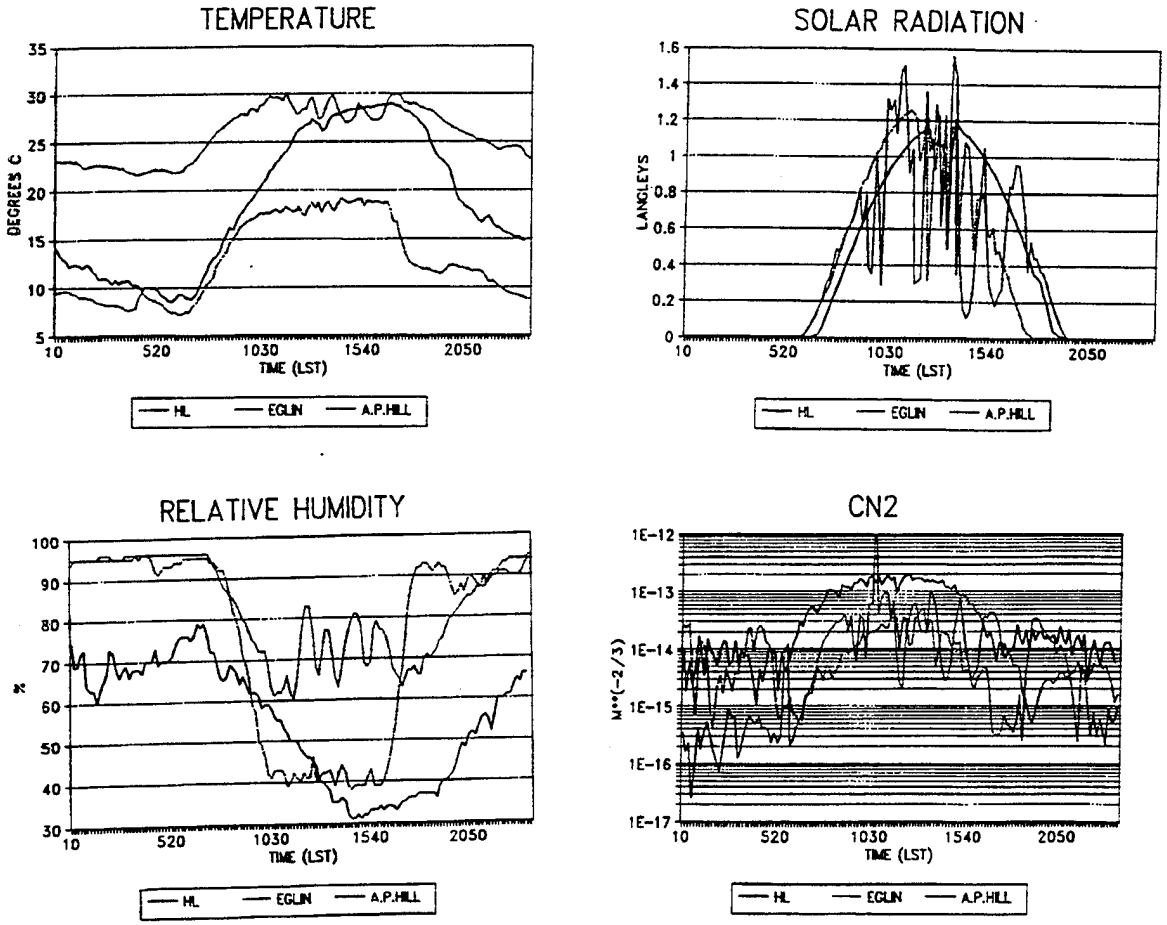

FIGURE 2 GRAPHICAL EXAMPLES OF SELECTED DATA EXAMPLES

4.PROTURB METHODOLOGY

The field data was reviewed and 10 to 15 minute averages were determined. The geographical locations of the tests were determined to within 1/4 of a degree. The data point times were converted from local time to decimal GMT time. The original values for the relative humidity, wind speed, cloud properties and reference temperature were then converted to units acceptable to PROTURB. Table 2 and 3 are samples of the results of that effort. Table 2 is the time dependent inputs and Table 3 is an example of the PROTURB inputs with an identification of the various input.

Time GMT	Temperature degrees Kelvin	Wind Speed m/sec	Relative Humidity	Cloud Cover	Cloud Type	Cloud Density	Ceiling Height
2000	289.1500	6	0.94	99	0	4	1180
2025	288.9500	.7	0.94	99	0	4	900
2050	288.7500	1.1	0.94	99	0	4	700
2075	288.7500	.3	0.95	99	0	4	650
2100	288.7500	.3	0.95	99	0	4	200

TABLE 2 AN EXAMPLE OF METEOROLOGICAL DATA PREPARED FOR PROTURB

1993	9	8	35.8	-121.2	2100.0	20	1
600	285.00	310.25	973.0	2.0	0.416	2.0	0.05
0.26	50	3.0	10.0	1000.0	1.06	2	4
0.92	3	2	3	0	284.65	10.0	4.0
0.0	32.0	0	0				

LINE 1	LINE 2	LINE 3	LINE 4	LINE 5
YEAR	CLOUD HGT	ALBEDO	GROUND EMISSIVITY	CUT OFF FREQ
MONTH	REFERENCE TEMPERATURE	INTEGRATION SUB-INTERVAL	SOIL MOISTURE	FREQ CALC INTERVAL
DAY	EST.MAX TEMPERATURE	RECEIVER HEIGHT	SOIL COMPOSITION	DEBUGGING FLAG
LATITUDE	REFERENCE PRESSURE	SOURCE HEIGHT	VEGETATION FACTOR	PLANETARY EXTENTION FLAG
LONGITUDE	WIND SPEED	PATH LENGTH	SNOW TYPE	
GMT	RELITIVE HUMIDITY	WAVE LENGTH	EST. MIN TEMPERATURE	
% CLOUD COVER	REFERENCE HEIGHT	CLOUD TYPE	FOCAL LENGTH	
GROUND COVER	ROUGHNESS ELEMENT	CLOUD DENSITY	ENTRANCE PUPIL DIA.	

TABLE 3 AN EXAMPLE OF A PROTURB INPUT DATA SET

The unstable atmosphere diurnal output from the PROTURB model was then compared to the corresponding measured values for Cn2 and the incoming solar radiation. Error analysis was performed

on the unstable atmospheric condition portion of the numerical results.

Incomplete knowledge of the test site forced the assumption of some of the values for the air pressure, the soil characteristics, and the vegetation characteristics. These values were estimated through the use of site photographs, topographic maps and data from surrounding sites. The most critical of these inputs is the estimation of soil wetness which was estimated through the use of rainfall data and on-site observations. The beam path was considered to be a constant height of 2.0 meters above the ground. The remaining parameters are presented above in the sample input cards.

5. RESULTS

The results of the comparisons are presented in Figures 3 through 5 which show both the C_n^2 and the incident shortwave radiation. Figure 3 shows comparisons from Ft. AP Hill. Agreement in solar radiation is very good. The C_n^2 does show some large differences but are still considered good when one considers the terrain of the path. The comparisons do show a vast improvement over the predecessor model "IMTURB" as discussed by Smith and Corbin[1]. Figure 4 shows Ft. Hunter-Liggett data which also looks quite good. The deviation shown on 6 September is probably due to differing cloud conditions between the base site and the observation site 3 kilometers away. Figure 5 shows Eglin AFB data. Here the cloud observation was 6 km from the data site. Again the agreement is considered very encouraging. If perfectly representative data were available, better agreement would be expected.

The daylight portion of the error analysis is presented in Tables 4 and 5. These results include only times when the atmosphere was unstable. The percent C_n^2 variation was determined by the relation %Variation = 100.0*((Measured-PROTURB)/Measured). The mean, standard variation, standard error and skewness of the percent variations were then determined. The radiation difference is presented in units of watts/meter^2 and is a straight difference between the measured and calculated values.

The values for percent variation of C_n^2 at Ft. A. P. Hill were quite large and negative. The negative values are an indication that the PROTURB model predicted larger C_n^2 values than were measured. The negative values for the skewness also indicates the presence of a systematic error. It is believed that the main source of error is in the estimation of a 2.0 meter height for the scintillometer positions. The actual site possessed several shallow canyons along the propagation path. This would mean that the actual average path height was greater than

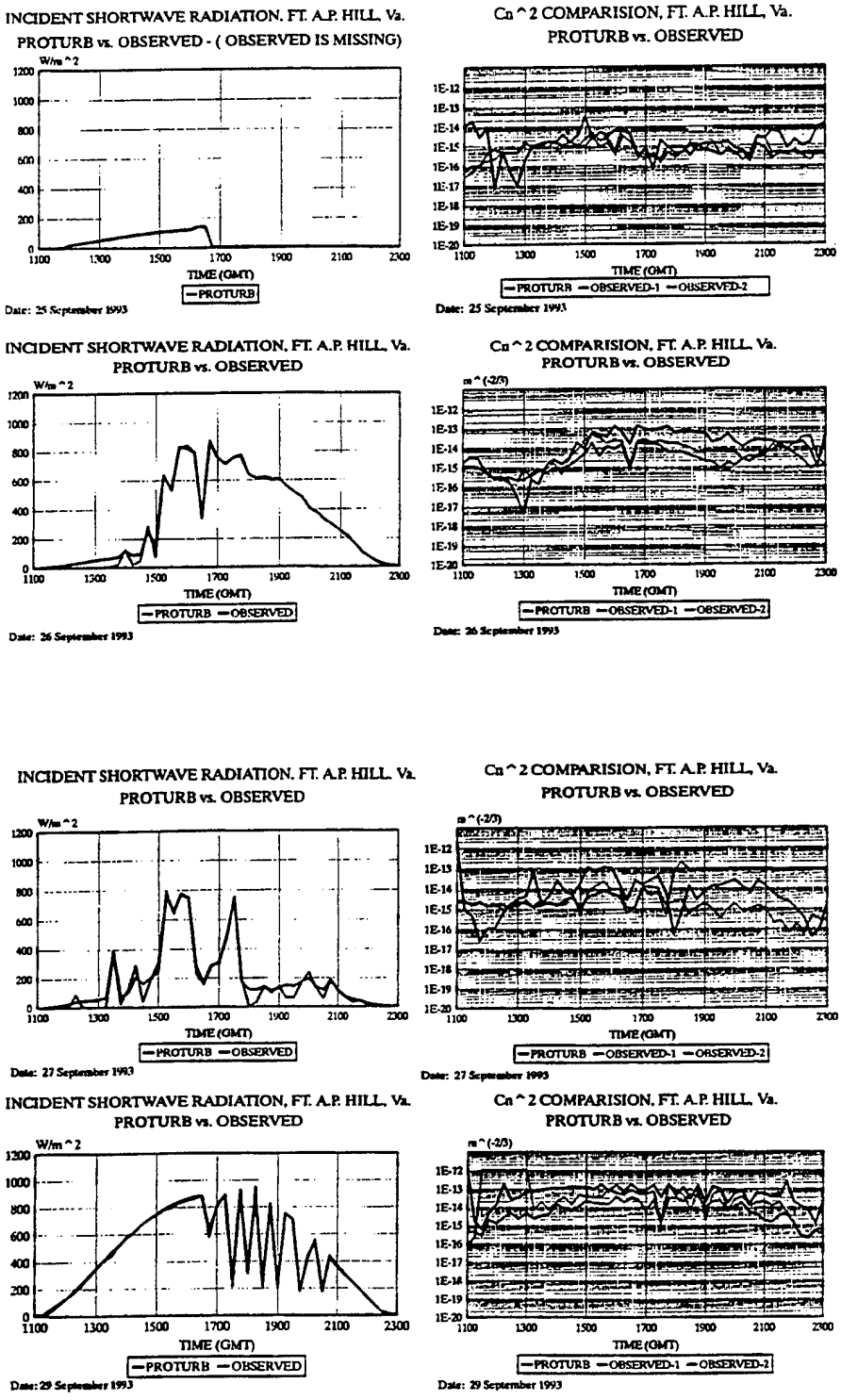

FIGURE 3. COMPARISONS FROM FT A.P. HILL,VA

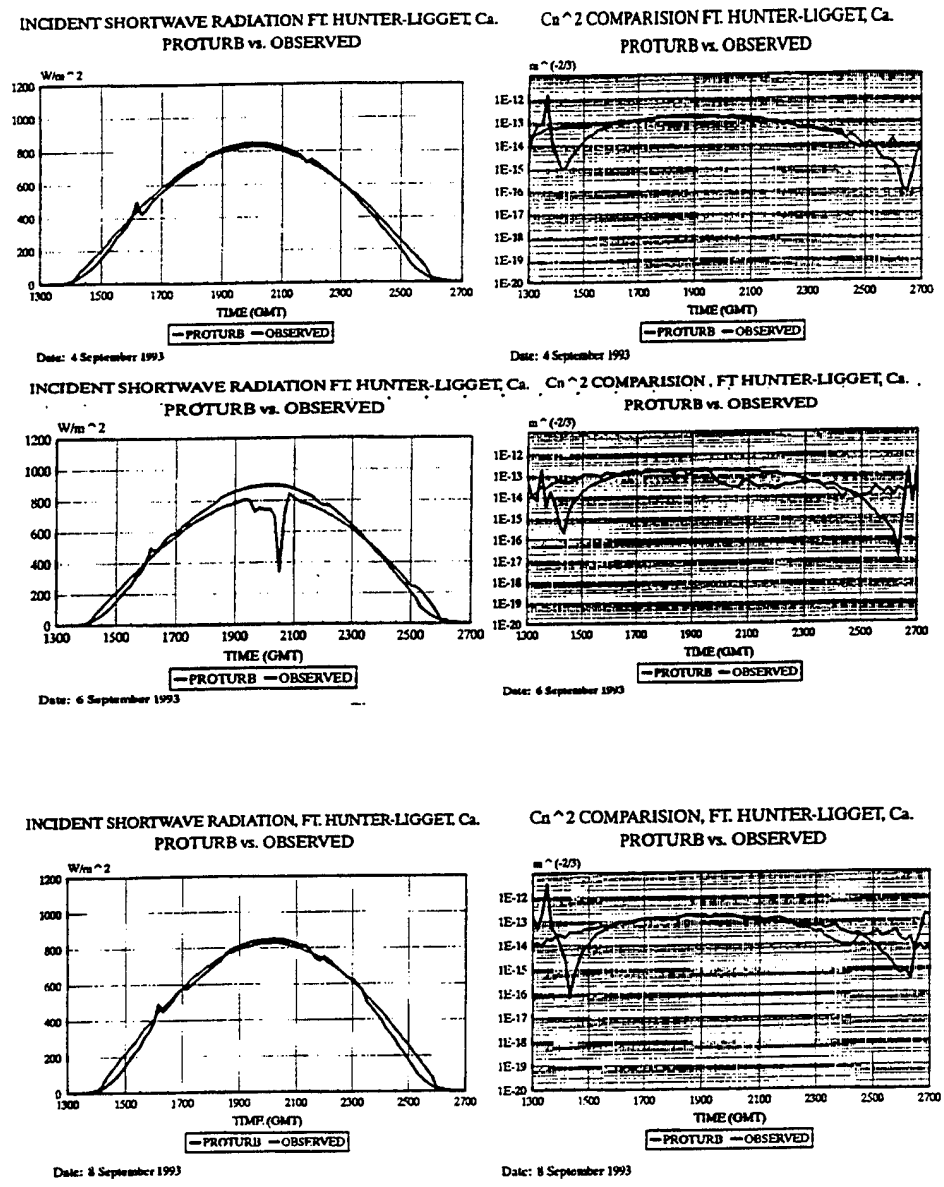

FIGURE 4. COMPARISONS FROM FT HUNTER-LIGGETT, CA

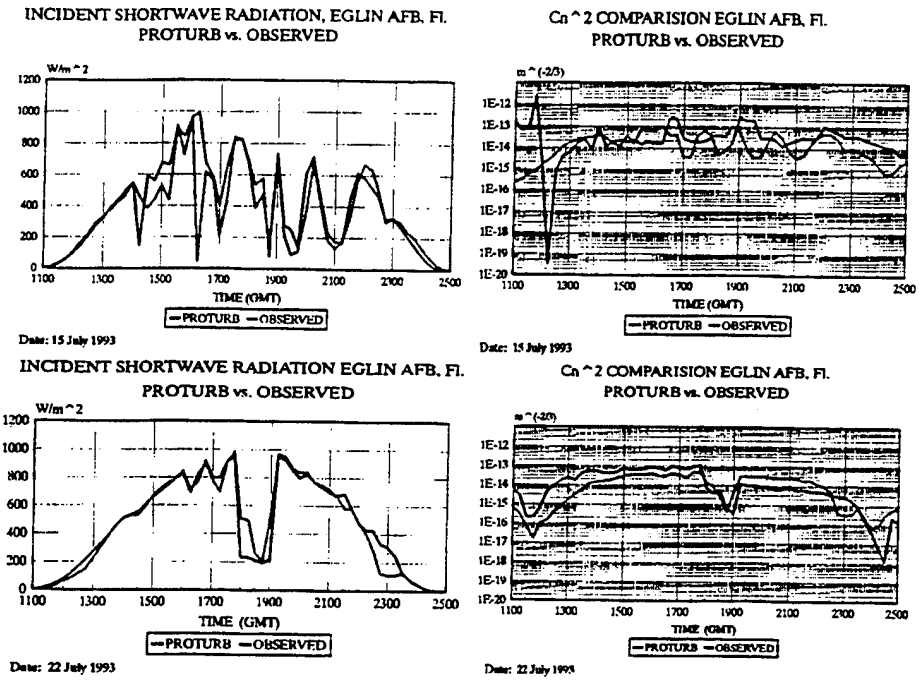

FIGURE 5. COMPARISONS FROM EGLIN AFB, FL

Test Name	Mean C_n^2 Variation	Standard Deviation	Standard Error	Skewness
A.P. Hill day 268	-254.929	484.5339	77.58751	-2.53165
A.P. Hill day 269	-310.992	396.5065	57.23050	-1.16931
A.P. Hill day 270	-869.412	1247.6720	180.08600	-1.82635
A.P. Hill day 272	-1285.680	1506.9560	217.51030	-2.19559
Ft. H-L day 247	6.5033	49.03060	5.587556	0.01920
Ft. H-L day 249	25.3578	51.54052	6.599088	-1.26270
Ft. H-L day 251	-20.3807	90.60885	11.06963	-2.32109
Eglin AFB day 196	-352.167	908.3837	128.3648	-4.95832
Eglin AFB day 203	-136.794	285.6617	43.03498	-2.44425

TABLE 4. C_n^2 Variation statistics. Data points that indicate stable or neutral conditions have been excluded from the statistical analysis. Also, experimental data that indicate equipment malfunction have been excluded.

Test Name	Mean Difference	Standard Deviation	Standard Error	Skewness
A.P. Hill day 268	NA	NA	NA	NA
A.P. Hill day 269	-11.2648	24.33080	3.511848	-1.32431
A.P. Hill day 270	-16.7757	41.56963	6.000059	-0.34138
A.P. Hill day 272	-5.7251	18.67955	2.696161	0.17929
Ft. H-L day 247	6.5033	49.03060	5.587556	0.09030
Ft. H-L day 249	-24.2058	83.46530	9.053083	-3.27868
Ft. H-L day 251	16.5451	33.65205	3.587320	0.55062
Eglin AFB day 196	-33.6366	157.24040	21.01214	-3.60090
Eglin AFB day 203	-1.83572	85.89066	11.47762	1.37096

TABLE 5. Short wave radiation difference statistics.

2.0 meters. An increase in the assumed path height would reduce the Cn2 values generated by PROTURB thus reducing the error. The occurrence of fog and rain along the path should also be considered a source of error since PROTURB does not include the actions of such atmospheric additives. In general, the PROTURB values tend to possess the same trends as the measured values and though the error is quite high the results are comparable with that of models with similar input simplicity.

The values for percent variation of C_n^2 at Ft. Hunter-Liggett were very reasonable. There appears to a sea breeze effect present in the measured data in both the morning and afternoon. The PROTURB model assumes that the atmospheric condition is generated by the surface-air interface and not influenced by outside forces such as weather fronts and nearby surface inhomogeneities such as a land-sea interface. Thus the prevailing deviations were seen in the morning and early evening were less pronounced possibly due to the effect of the nearby ocean. The surface at Ft. Hunter-Liggett was relatively flat leading to better overall results.

The values for percent variation of C_n^2 at Eglin AFB, were moderately successful. The PROTURB model was more sensitive to wind speed and cloud coverage than the measured data. In general, PROTURB would have predicted larger values for results had it not been for this sensitivity. The over prediction of C_n^2 can be attributed to PROTURB'S lack of sensitivity in relation to soil type and soil moisture effects. An upgraded soil model is currently under development and should be installed by the time of public release.

The shortwave radiation comparison at all sites were very good. The primary deviation is in the shape of the clear-sky curve directly after sun rise and before sunset. This greater measured radiation at these points can be assumed to be related to the value of the diffuse sky radiance at low solar elevation angles. It appears that the PROTURB cloud reduction factors represent reasonable approximations to the effects of clouds.

A more complete analysis is being prepared for the use of the Army Research Laboratory by Cranston and Cruncleton.

CONCLUSIONS

Given that some necessary approximations were made in transforming from a nonuniform terrain to a uniform terrain with fixed site parameters, the PROTURB model did a reasonable job in the determination of C_n^2. It was noticed that the significant decreases and increases in C_n^2, due to clouds and wind effects,

are parallel in both PROTURB and measured values, but that the PROTURB model appears to be overly sensitive to these factors. The primary factors responsible for this sensitivity are the Angus-Leppan wetness and cloud parameters, and the thermal diffusivity of the soil. These factors play important roles in the energy partition within the energy balance model and should be scrutinized further. The comparisons presented here considered only the unstable condition. Noting the collected turbulence data shown on figure 2, it is recommended that an effort be made to extend the model into night or stable conditions.

References

1. R. W. Smith and T. Corbin, "Field measurement and comparison of optical turbulence.", SPIE Vol. 1687

2. W. B. Miller and J. C. Ricklin, "A Module for Imaging Through Optical Turbulence - IMTURB", U. S. Army Atmospheric Sciences Laboratory Tech Report - 0221-27, November 1990.

3. H. Rachele and A. Tunick, "Energy Balance Model for Imagery and Electromagnetic Propagation", U. S. Army Atmospheric Sciences Laboratory Tech Report - 0311, May 1992.

4. H. Rachele, "Ekman Spiral", unpublished notes, April 20 1992.

5. D. L. Fried, "Theoretical Study of Non-Standard Imaging Concepts", Defense Technology Information Center Tech Report - RADC-TR-76-51, March 1976.

6. W. B. Miller, J. C. Ricklin and L. C. Andrews, "Log-amplitude variance and wave structure function: a new perspective for Gaussian beams", Journal Optical Society of America, Vol.10, No.4, April 1993.

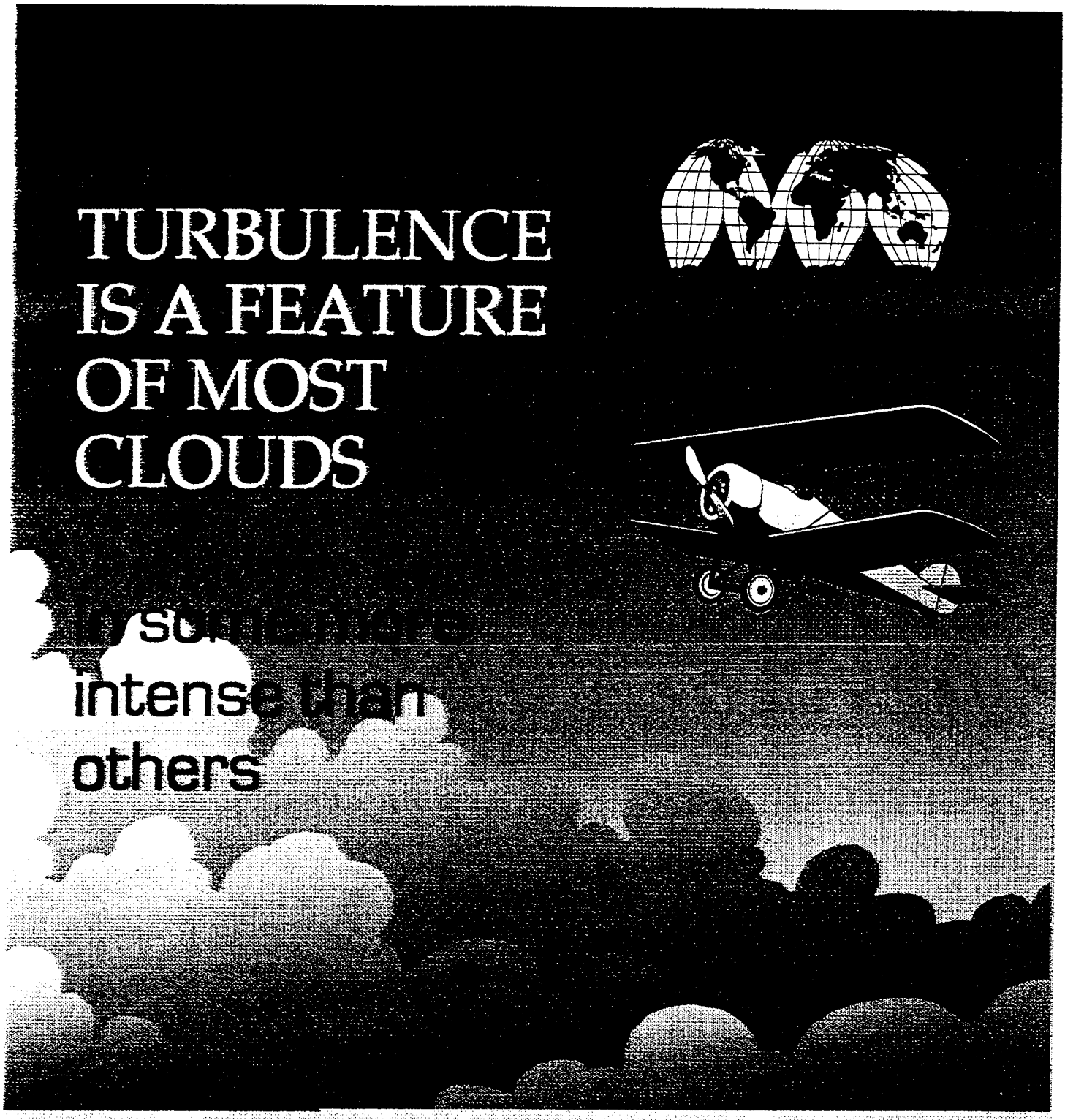

J.W. TELFORD

THE ROLE OF TURBULENCE

in Cloud Droplet Formation and Outside the Cloud

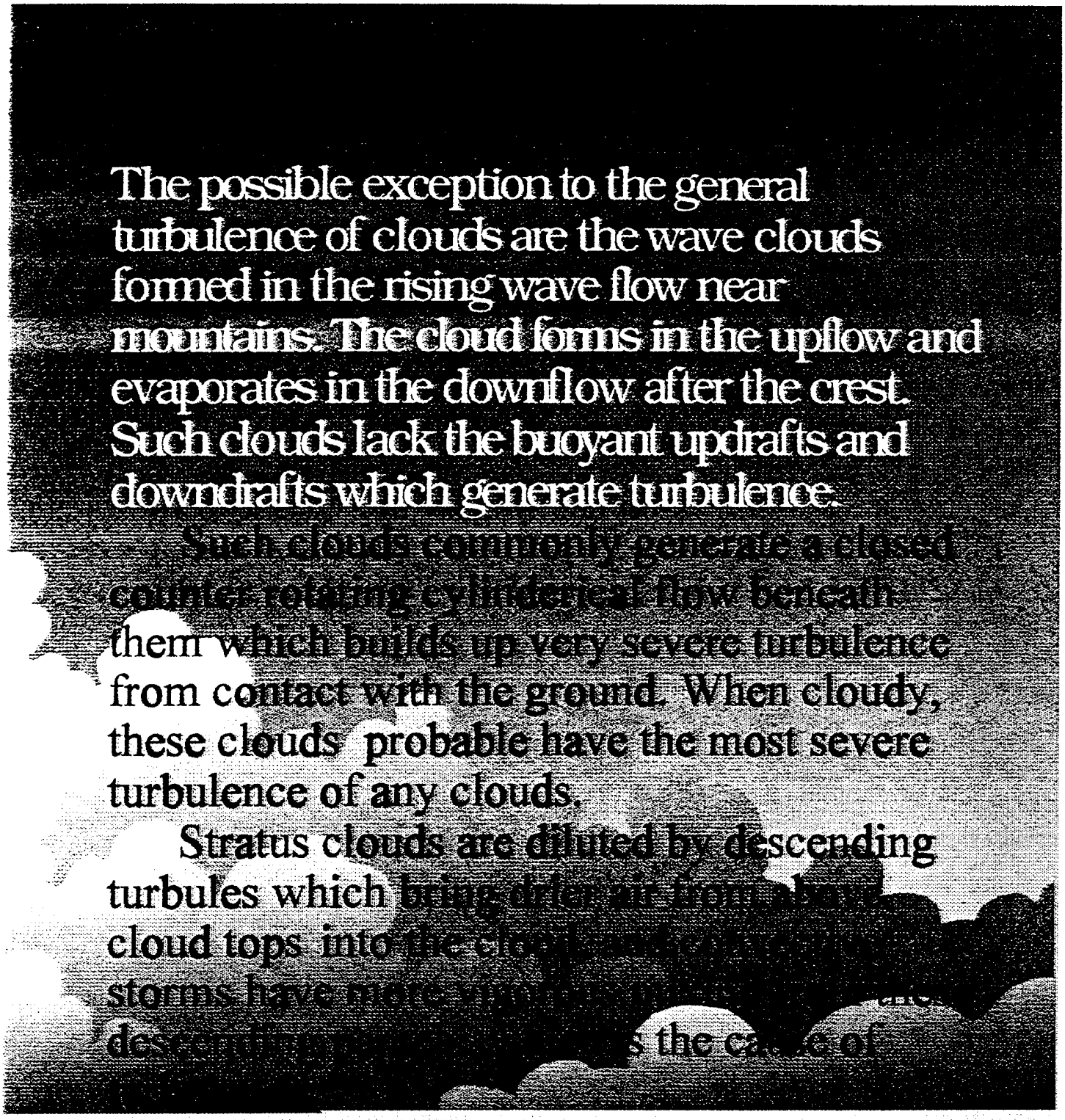

These turbules modify the cloud microphysical particles to such an extent that this is the primary controlling factor.

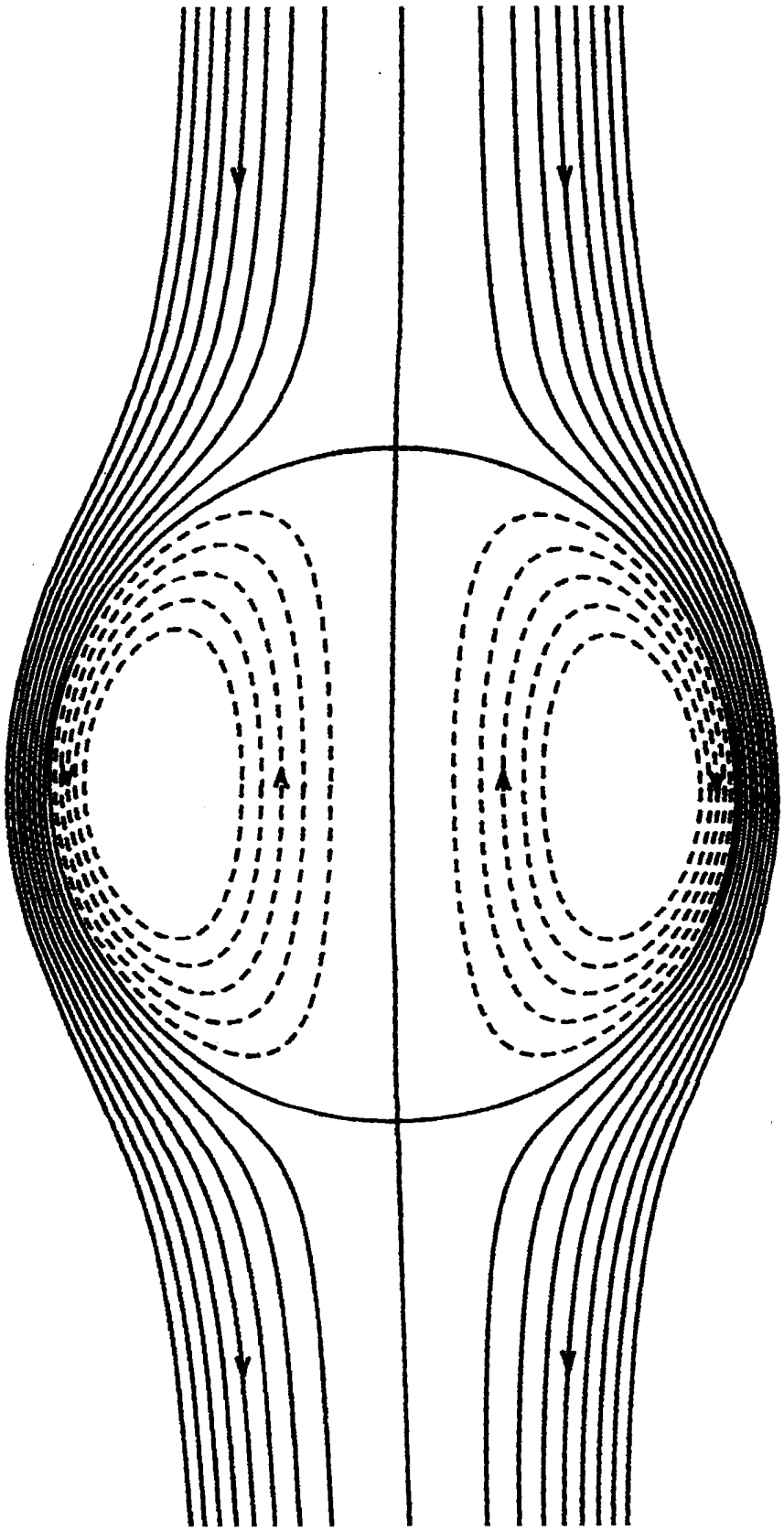

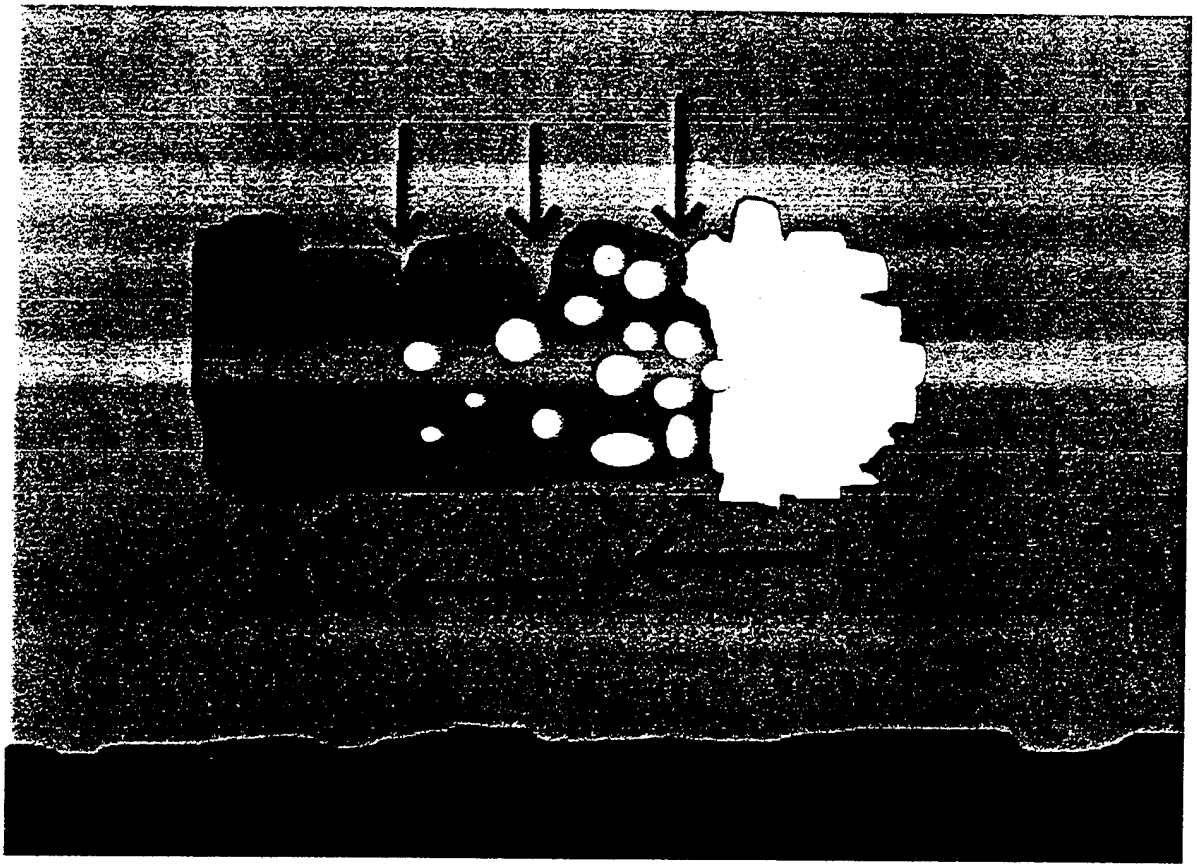

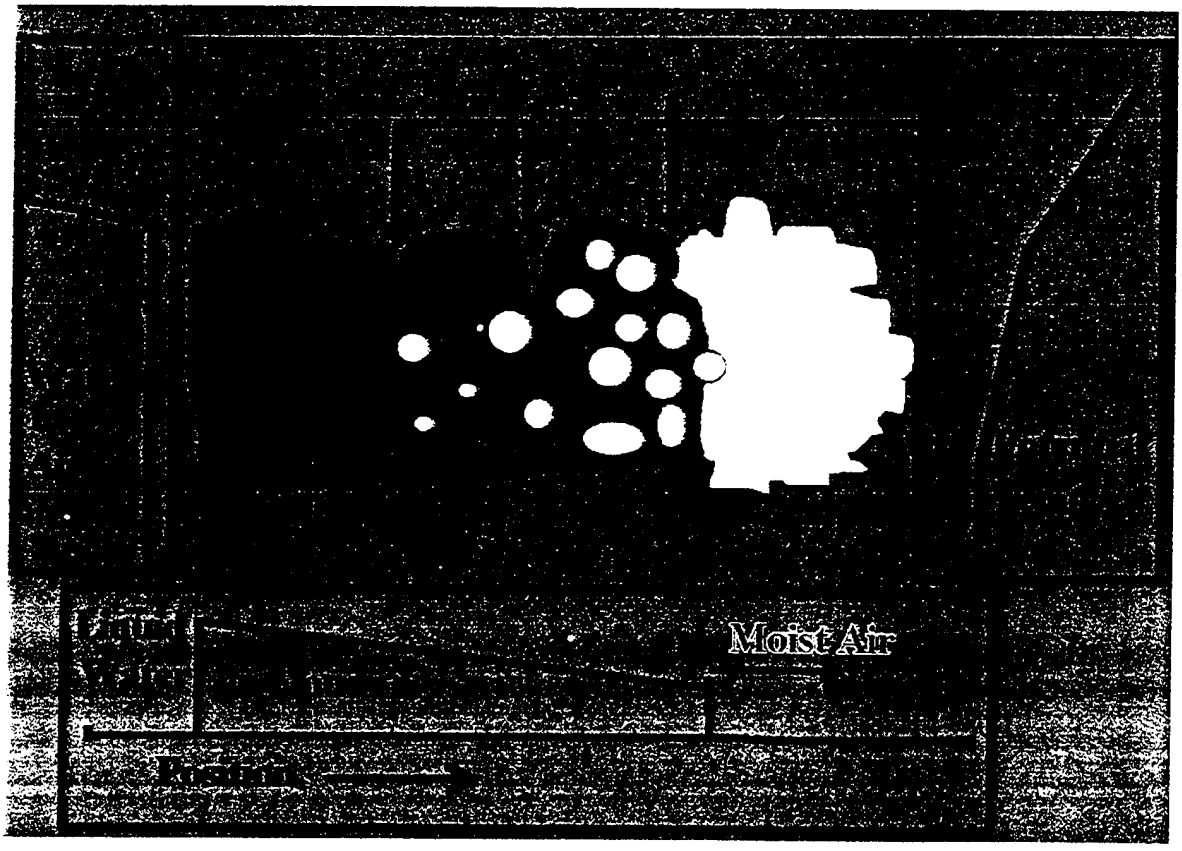
Moist Air

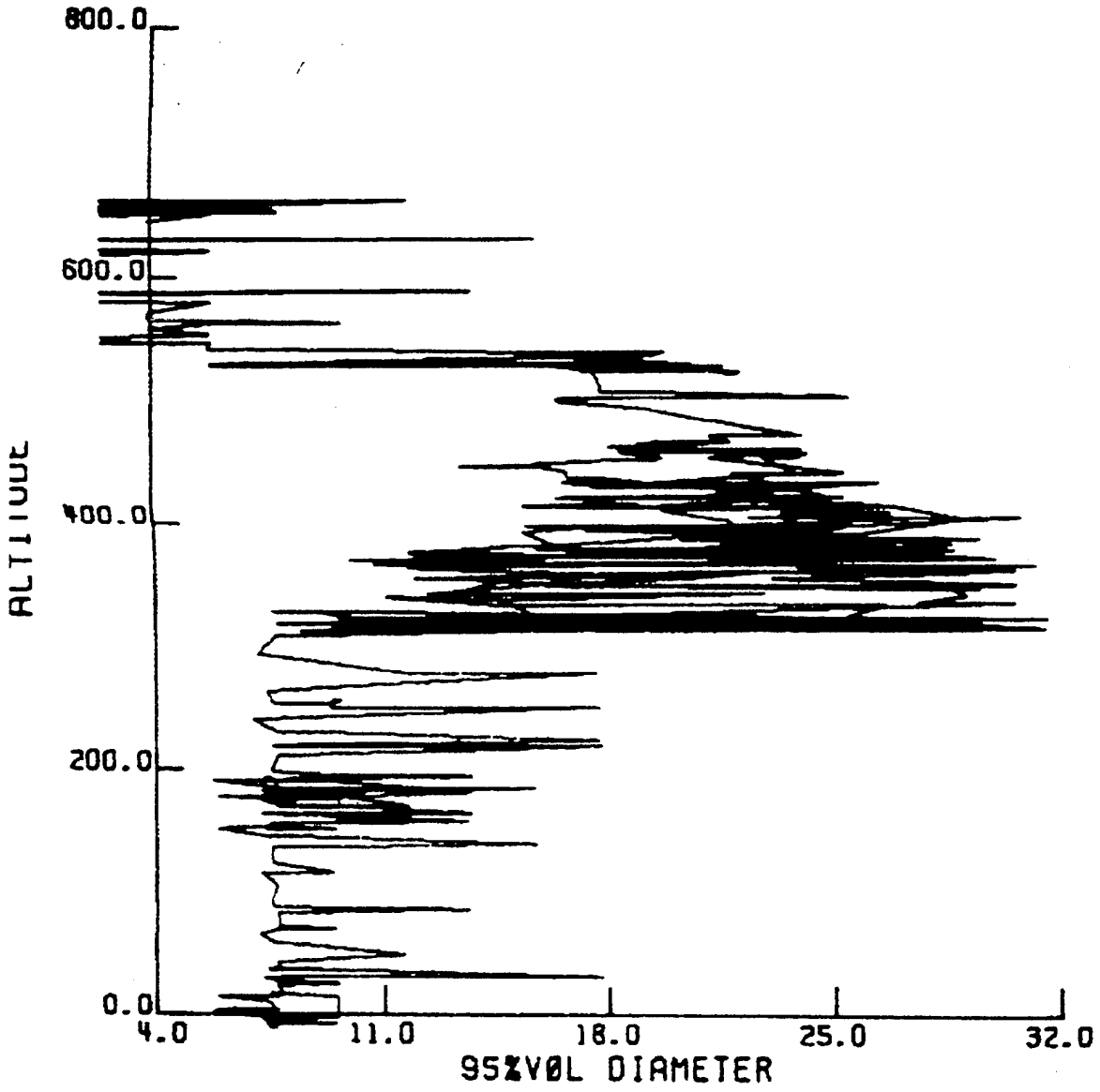

MARINE STRATUS CLOUD, LARGEST DROPS FROM PARCEL TO PARCEL

FOG OBSERVATIONS

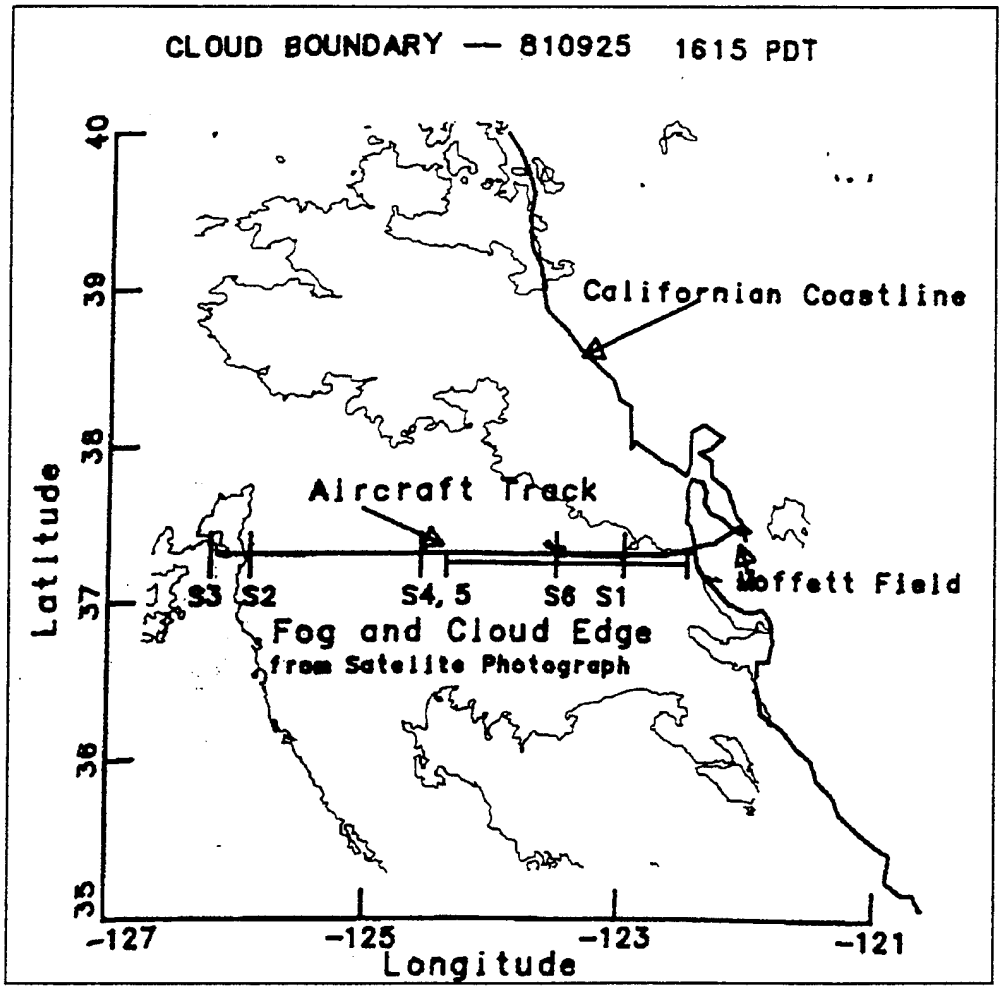

FOG IS COMPLETELY CALM

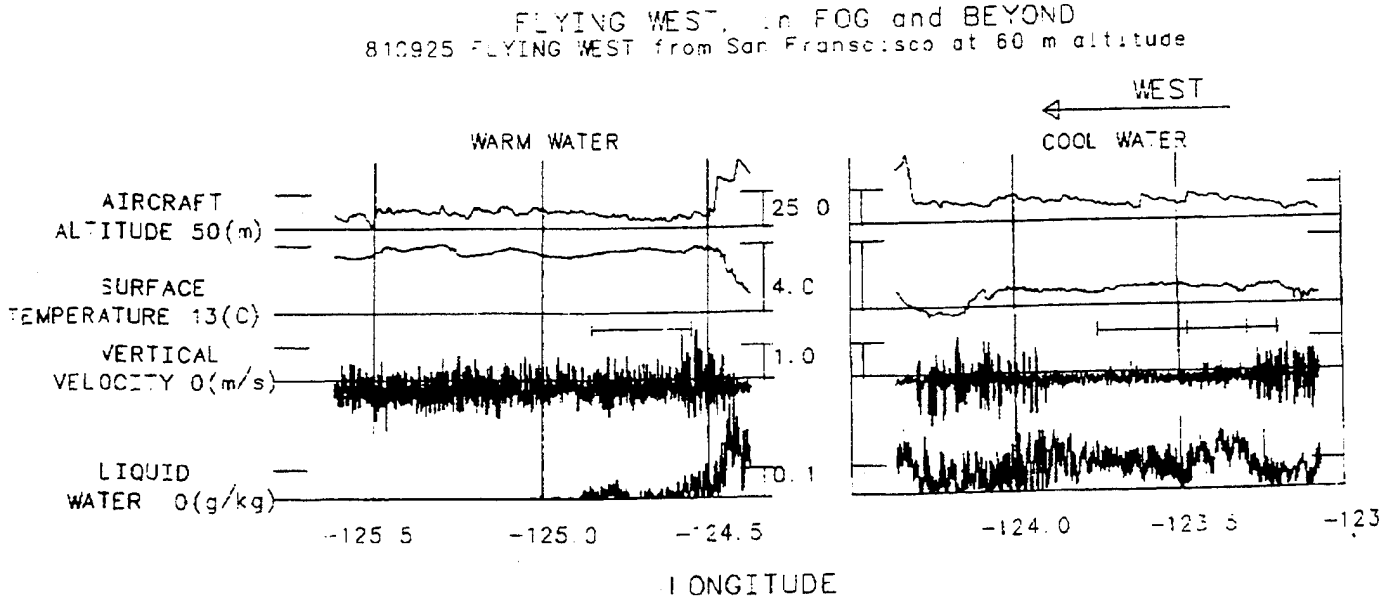

FOG

THERE ARE NO DOWNDRAFTS IN THE FOG.

HENCE THERE IS NO COOLING FLUX OF HEAT

HENCE THE FOG TOP IS NOT BEING COOLED BY RADIATION.

CONVECTING CLOUD

STILL FOG

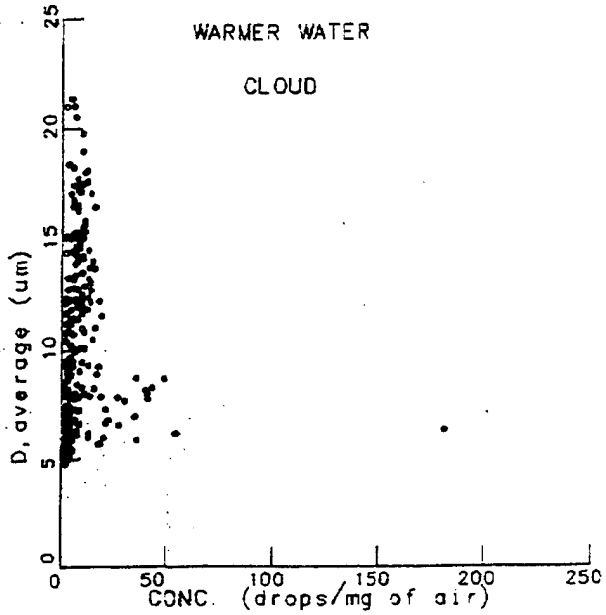

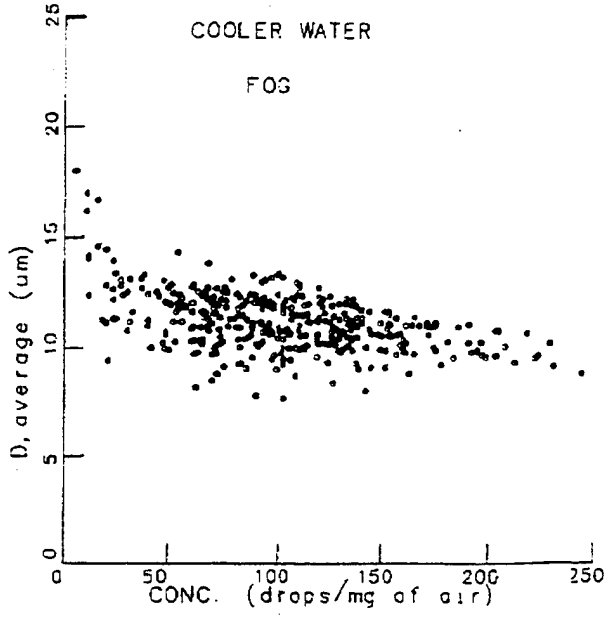

ON THE RIGHT THE FOG DROPS AVERAGE ABOUT THE SAME DIAMETER ALTHOUGH THE CONCENTRATION VARIES BY 100 : 1

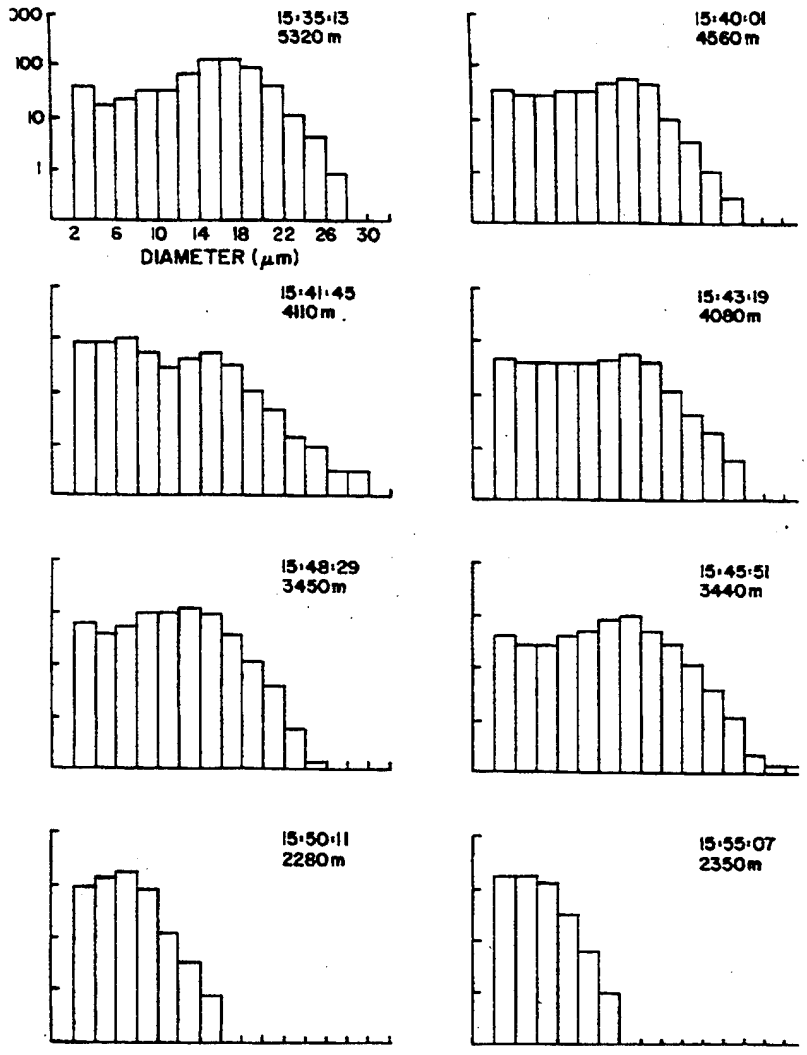

CLOUD DROP SPECTRA

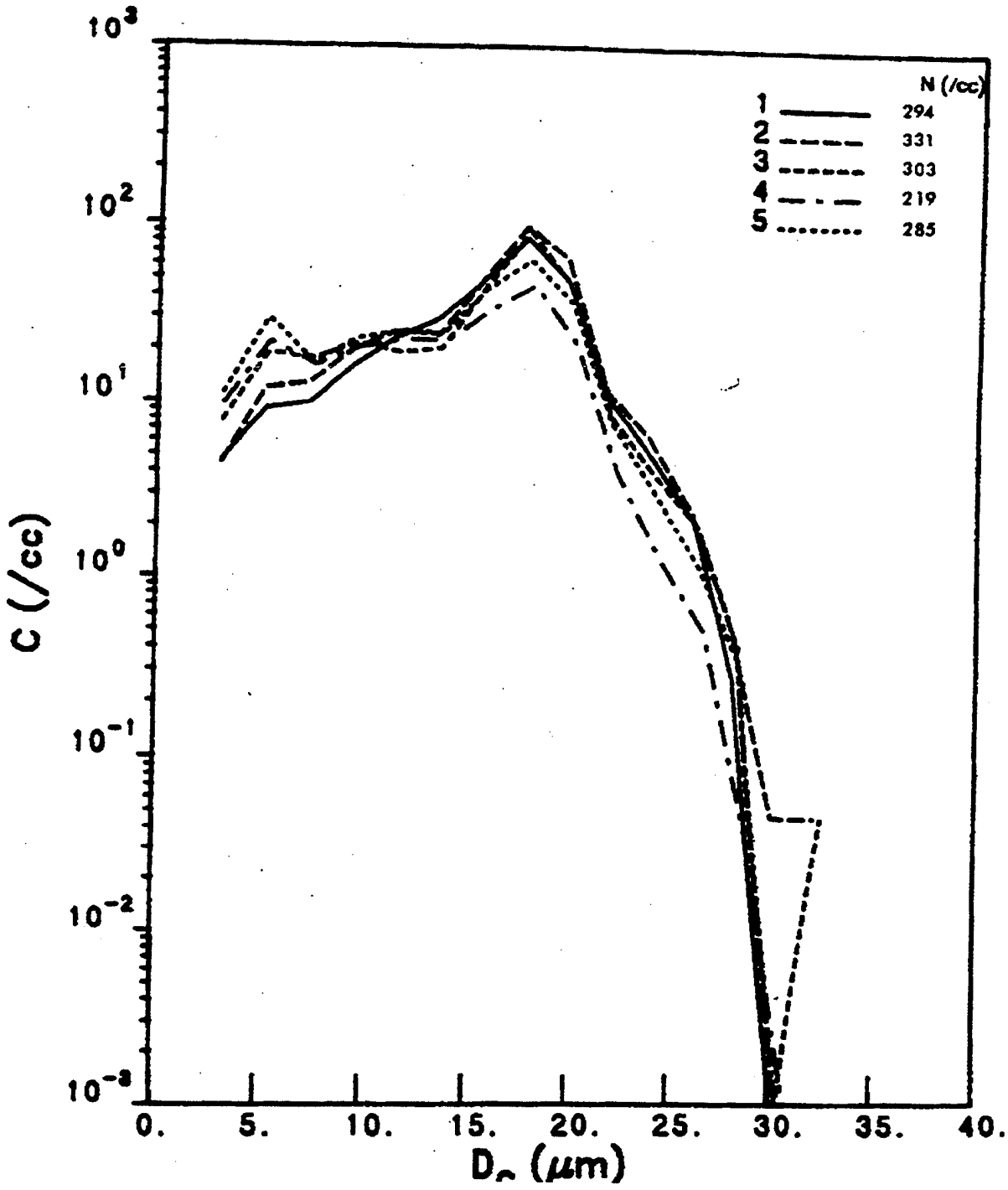

CLOUD DROP CHANGES AS CLOUD IS ENTERED

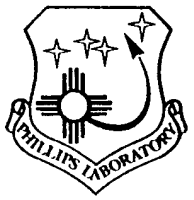

SHARC-3: A Model for Infrared Atmospheric Radiance at High Altitudes

R.D. Sharma, J.H. Brown, J.H. Gruninger, R.L. Sundberg, J.W. Duff, L.S. Bernstein, M.W. Matthew, S.M. Adler-Golden, D.C. Robertson, and R.J. Healey

17th Annual Review Conference on Atmospheric Transmission Models

Phillips Laboratory
Hanscom AFB

8 June 1994

PRESENTATION OUTLINE

- OBJECTIVE
- SHARC OVERVIEW
- SHARC MODULES
  - AMBIENT POPULATIONS
  - AURORAL ENHANCEMENT
  - SPECTRAL RADIANCE
- SHARC-DATA COMPARISONS
  - SPIRE CO_2 EMISSION
  - SPIRE AND SPIRIT NO EMISSION
  - CIRRUS H_2O AND O_3 EMISSION
- FUTURE PLANS
- SUMMARY

SHARC OBJECTIVES

- COMPUTER CODE TO CALCULATE HIGH-ALTITUDE BACKGROUNDS IN QUIESCENT AND AURORALLY DISTURBED ATMOSPHERES

- PROVIDE SPECTRAL PREDICTIONS FOR RADIANCE AND TRANSMITTANCE ALONG ARBITRARY PATHS THROUGH THE ATMOSPHERE
  - MODEL ATMOSPHERIC EMISSION PROCESSES
  - SUPPORT AF MEASUREMENTS PROGRAMS CIRRIS 1A, SPIRIT II, MSX
  - PROVIDE CALCULATIONS FOR SYSTEMS STUDIES

SHARC OVERVIEW

- SHARC CALCULATES NLTE RADIATION FROM AMBIENT AND AURORAL ATMOSPHERES

- SOME FEATURES:
  - 50-300 km ALTITUDE REGIME
  - 2-40 μm WITH A RESOLUTION OF 0.5 cm^{-1}
  - INTERACTIVE INPUT MODULE WITH ERROR CHECKING
  - ADJUSTABLE CHEMICAL KINETICS MECHANISMS/RATES
  - AUTOMATICALLY INCLUDES LTE & NLTE CONTRIBUTIONS
  - AMBIENT MOLECULES INCLUDE: H_2O, O_3, CO, NO, OH, CO_2, plus H_2O and CO_2 ISOTOPES
  - AURORAL MODULE WITH: NO^+, NO, CO_2
  - PATHS ACROSS AND AROUND THE SOLAR TERMINATOR

ILLUSTRATIVE SHARC CALCULATION

- SPACE VIEWING THROUGH A 50km LIMB PATH

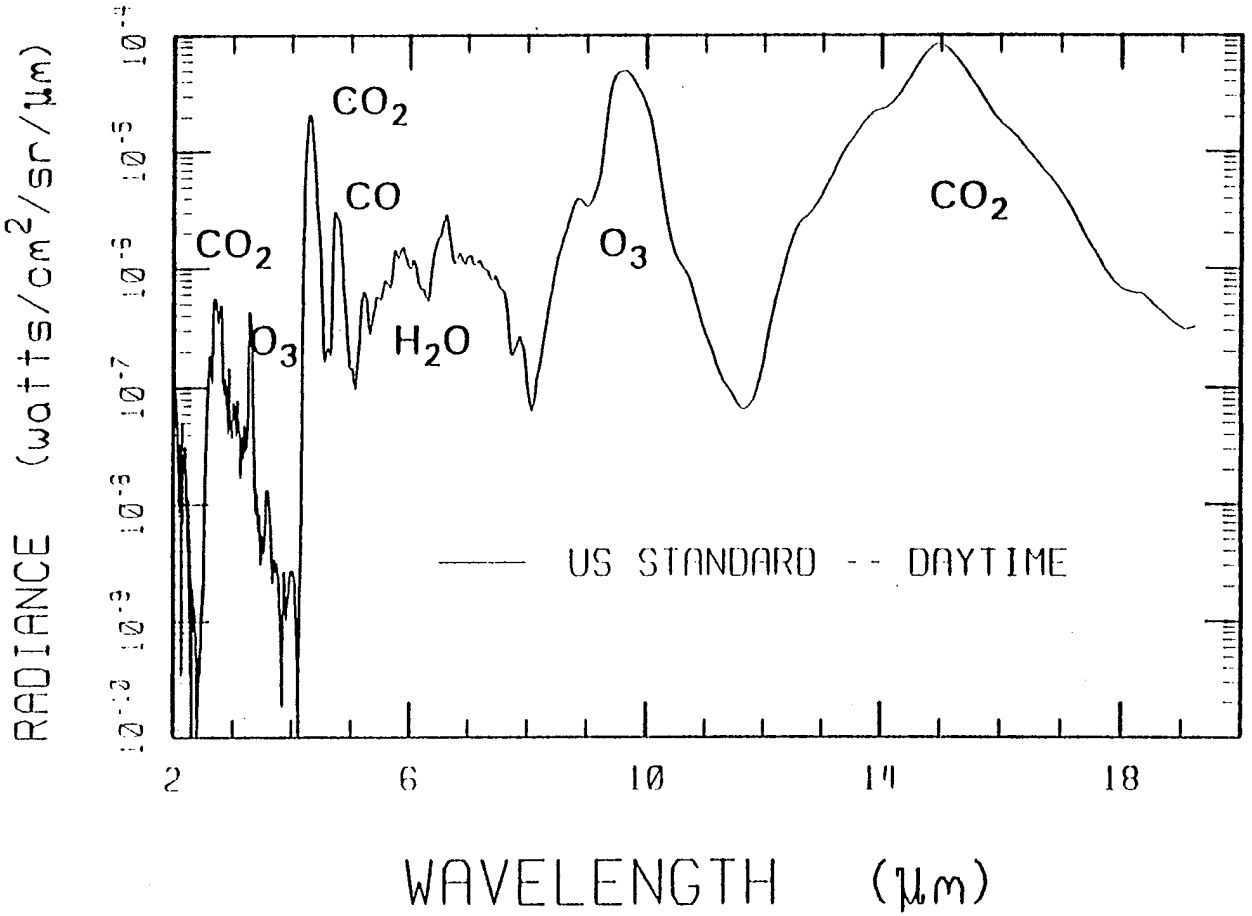

SHARC-3 FLOW CHART

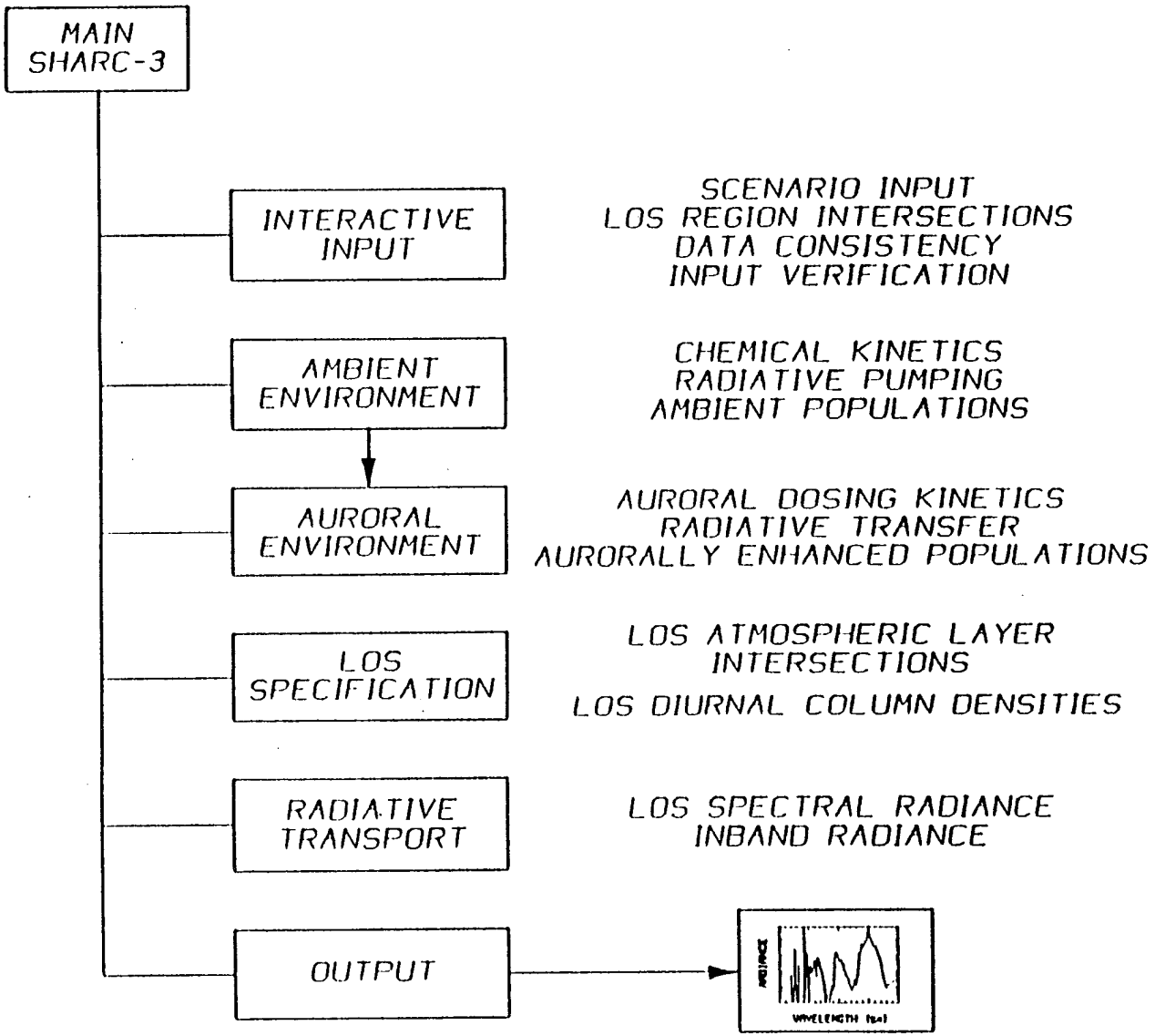

AMBIENT POPULATIONS MODULE

- SYMBOLIC DESCRIPTION OF CHEMICAL KINETICS
  - BASED ON WIDELY USED SANDIA **CHEMKIN** CODE
  - EXAMPLE: $M + O + O_2 \rightarrow M + O_3(000)$
    $M + O_3(001) \rightarrow M + O_3(000)$
    $O_3(001) \rightarrow O_3(000) + h\nu$
- RATE EQUATIONS SOLVED IN STEADY STATE
- MONTE CARLO CALCULATION FOR RADIATIVE ENHANCEMENT
  - LAYER-LAYER PUMPING
  - IMPORTANT FOR THICK BANDS (CO_2)

RADIATIVE EXCITATION MODULE (NEMESIS)

- RADIATIVE EXCITATION SIGNIFICANTLY ENHANCES EXCITED-STATE POPULATIONS OF STRONG BANDS AND HENCE THE STRENGTH OF THEIR EMISSIONS

- MONTE CARLO MODEL FOR LAYER-LAYER ABSORPTION AND EMISSION OF PHOTONS

- BASIC MODEL ASSUMPTIONS
  - SEMI-INFINITE PLANE-PARALLEL HOMOGENEOUS LAYERS
  - VOIGT LINESHAPE
  - TRANSLATIONAL-ROTATIONAL EQUILIBRIUM
  - COMPLETE LINE FREQUENCY REDISTRIBUTION
  - COMPLETE ROTATIONAL LEVEL REDISTRIBUTION
  - NO LINE OVERLAP

SHARC AURORAL MODULE

- AURORAL PHENOMENOLOGY
  - ELECTRON DEPOSITION MODELS FOR DIFFERENT STRENGTH AURORAS: CLASS II, III, III+
  - SOLVES TIME/ENERGY DEPENDENT RATE EQUATIONS TO CALCULATE BOTH SECONDARY ELECTRON DISTRIBUTIONS AND THE KINETICS FOR IR RADIATORS
  - CALCULATES PRODUCTION OF ATMOSPHERIC NO and NO^+
  - PRESENT IR MOLECULES ARE: NO, NO^+, CO_2
- SHARC AURORAL APPROACH
  - GEAR'S STIFF ODE ALGORITHM USED
  - CAN ADD NEW RADIATORS VIA USER-DEFINED INPUT FILES
  - LOCALIZED AURORAL REGION(S) EMBEDDED IN AMBIENT ATMOSPHERE
- GEOMETRY MODEL INSURES THAT LOS TRAJECTORIES INTERSECT AURORA AS DESIRED

ILLUSTRATIVE AURORAL ENHANCEMENT

- PATH 90 km - SPACE

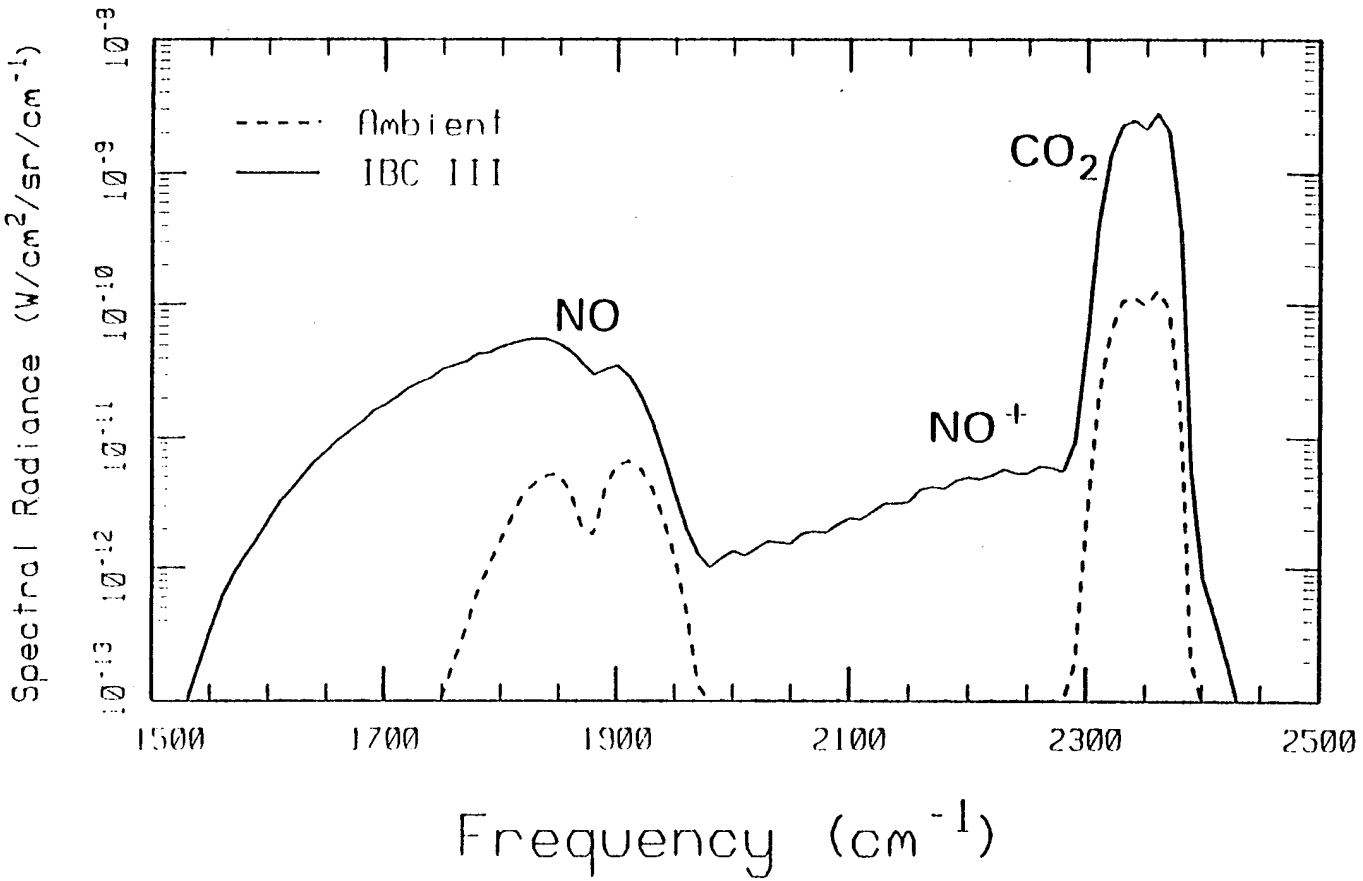

COMPARISON TO AURORAL FIELD DATA

- FWI DATA (FIELD WIDENED INTERFEROMETER)
- VERTICAL PATH 90 KM TO SPACE
- CLASS II AURORA
- $N(^2D) + O_2$ REACTION TO PRODUCE NO^*

BUT

- CURRENT WORK SUGGESTS $N(^4S)$ IMPORTANT TOO

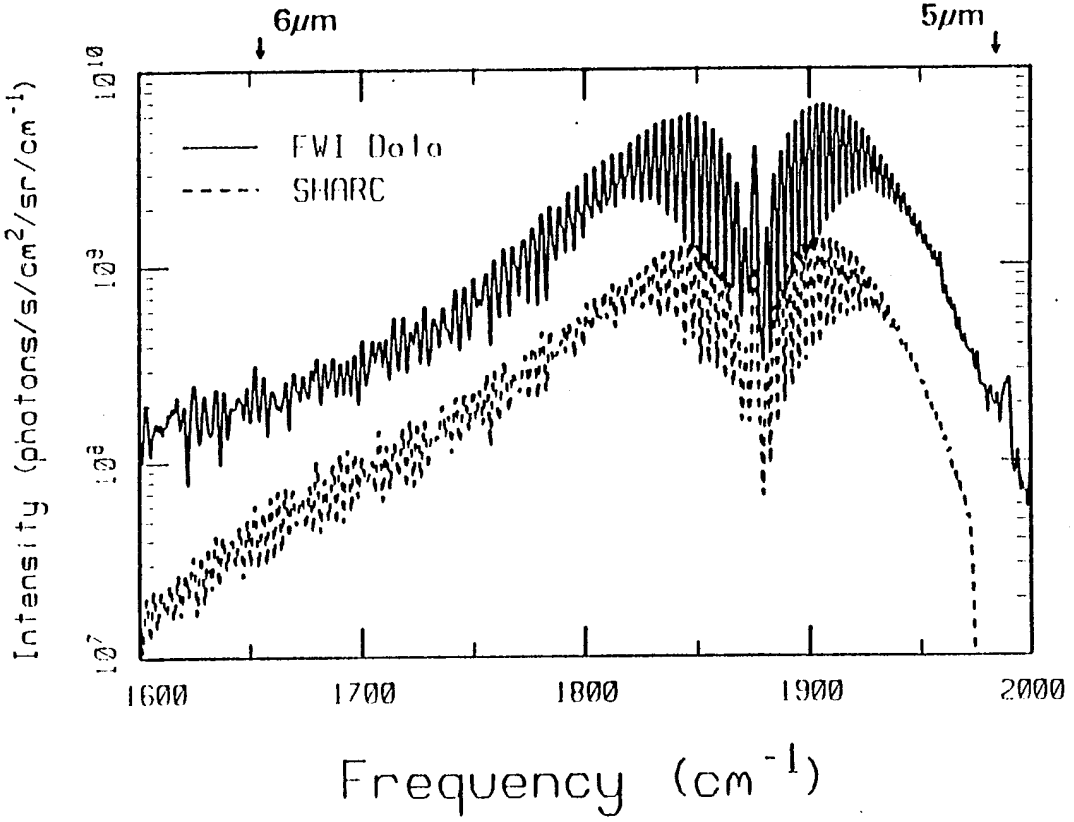

SPECTRAL RADIANCE MODULE

- RADIATION TRANSPORT CALCULATION PERFORMED FOR EACH MOLECULAR LINE
  - USES PL ATMOSPHERIC ABSORPTION LINE DATABASE (HITRAN)
- RODGERS-WILLIAMS APPROXIMATION FOR VOIGT EQUIVALENT WIDTH OF A SINGLE LINE
- LAYER-DEPENDENT LINE STRENGTHS
- CURTIS-GODSON APPROXIMATION
  - AVERAGING PROCEDURE FOR INHOMOGENEOUS PATHS
- LINE OVERLAP CORRECTION FOR DENSE REGIONS
- 50-70 TIMES FASTER THAN TRADITIONAL LBL APPROACH

SPIRE: DAYTIME CO_2 (4.3 μm)

- SOLAR PUMPED VIA EXCITATION OF SHORT WAVE IR BANDS

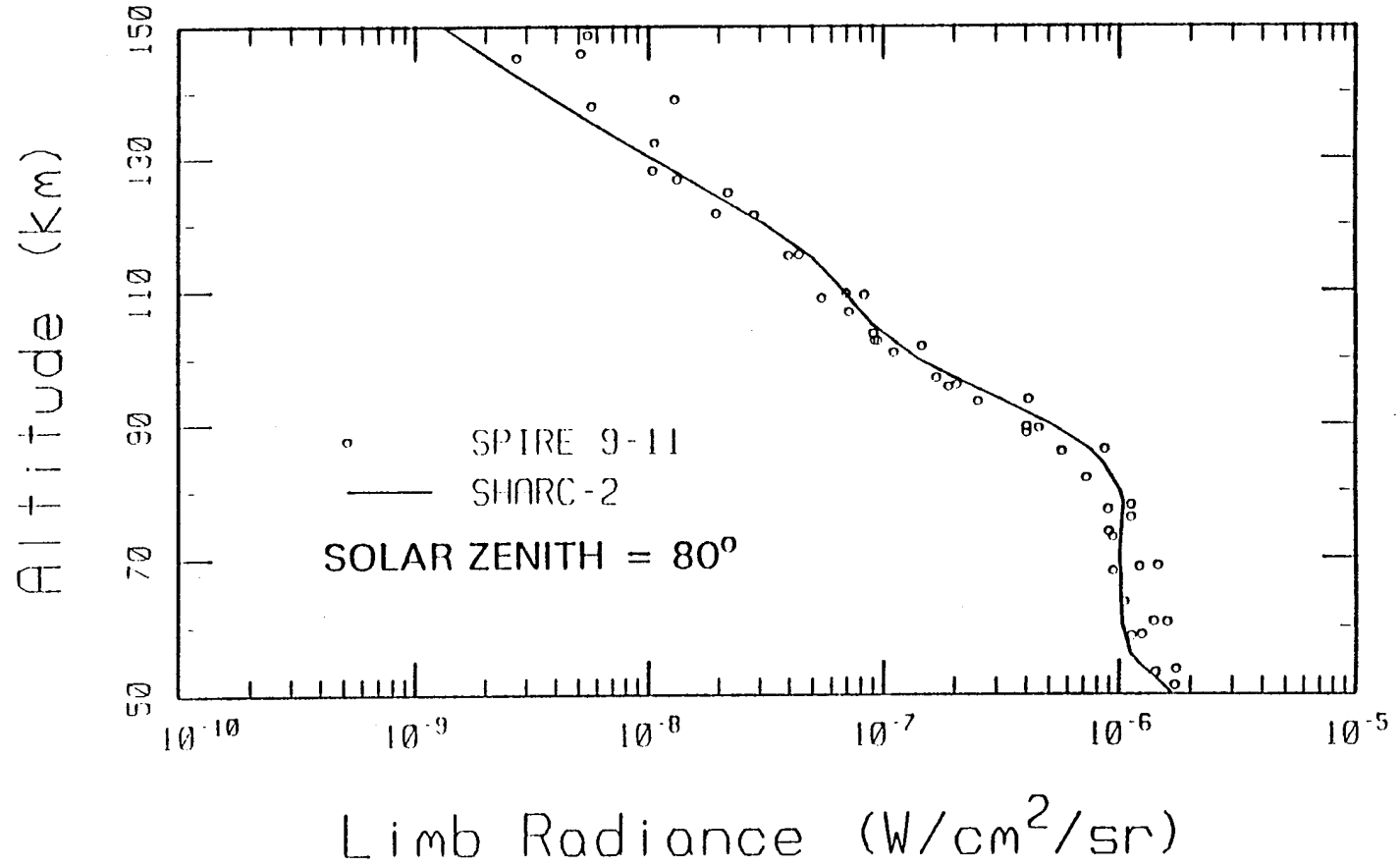

SPIRE: LONG WAVE CO_2

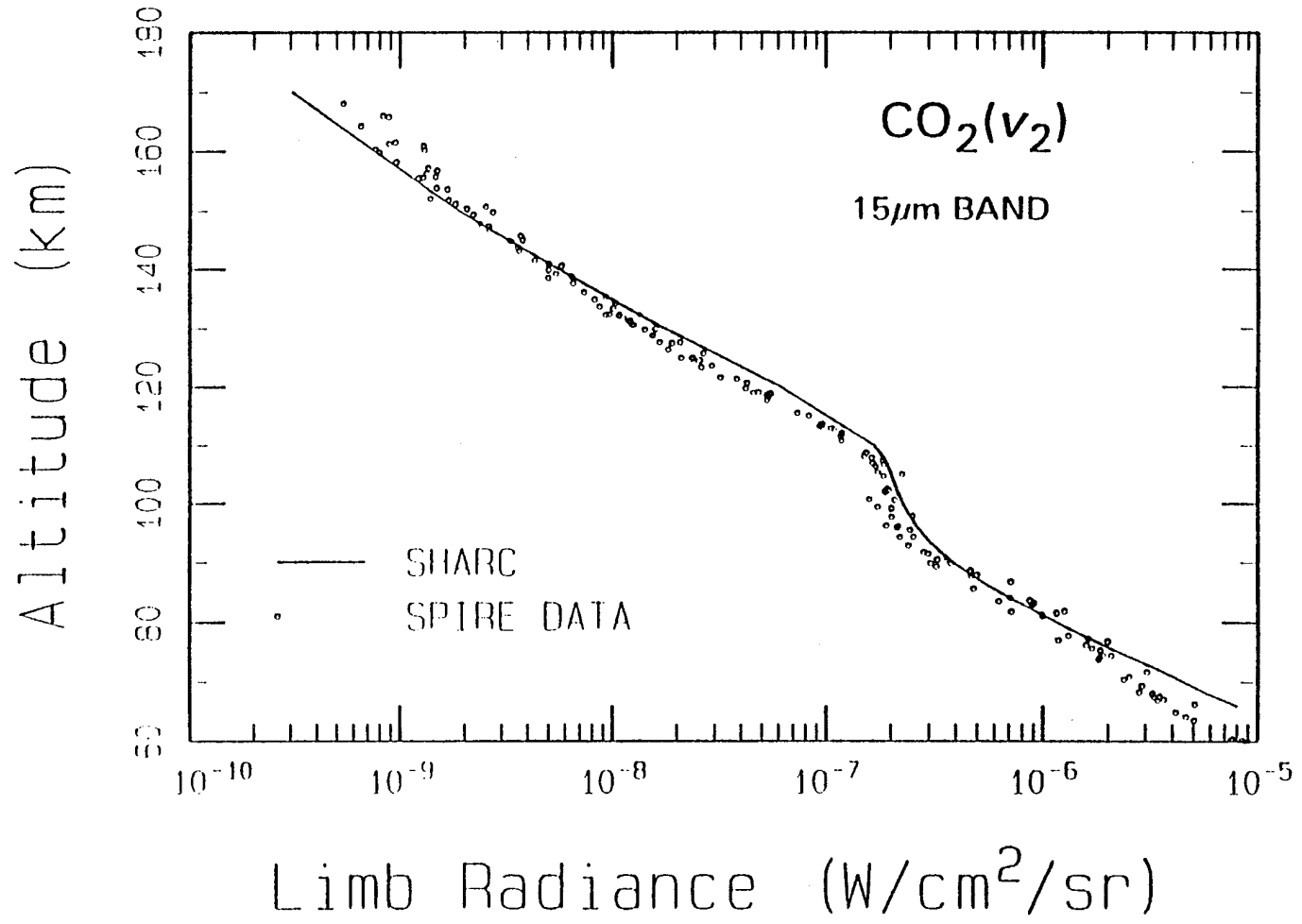

COMPARISON TO NO (5.3 μm) DATA

- SIGNIFICANT VARIABILIITY IN OBSERVED NO RADIANCES

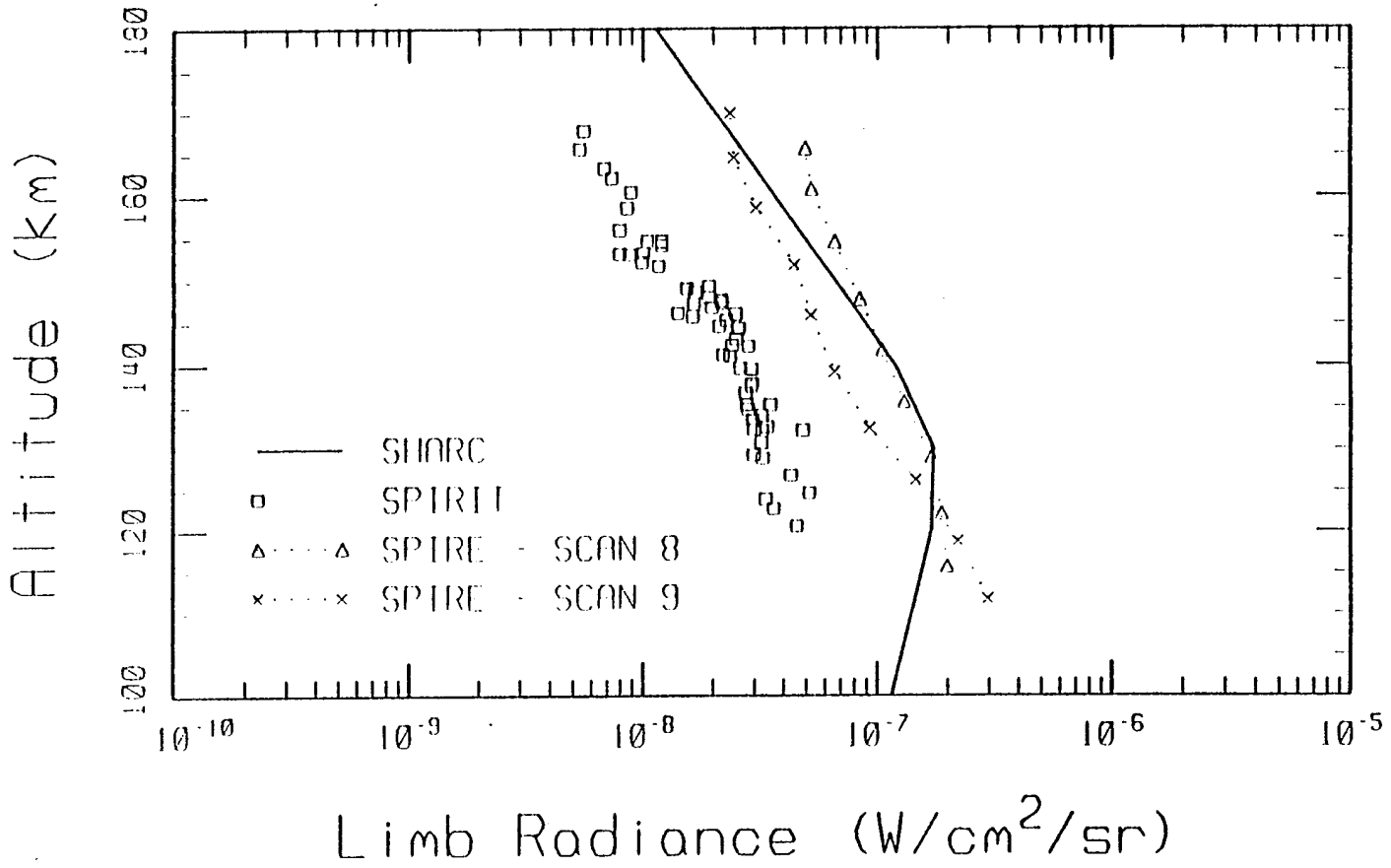

COMPARISON TO O_3(9.6 μm) DATA

- SPIRIT 1 AND SPIRE DATA FOR NIGHTTIME CONDITIONS

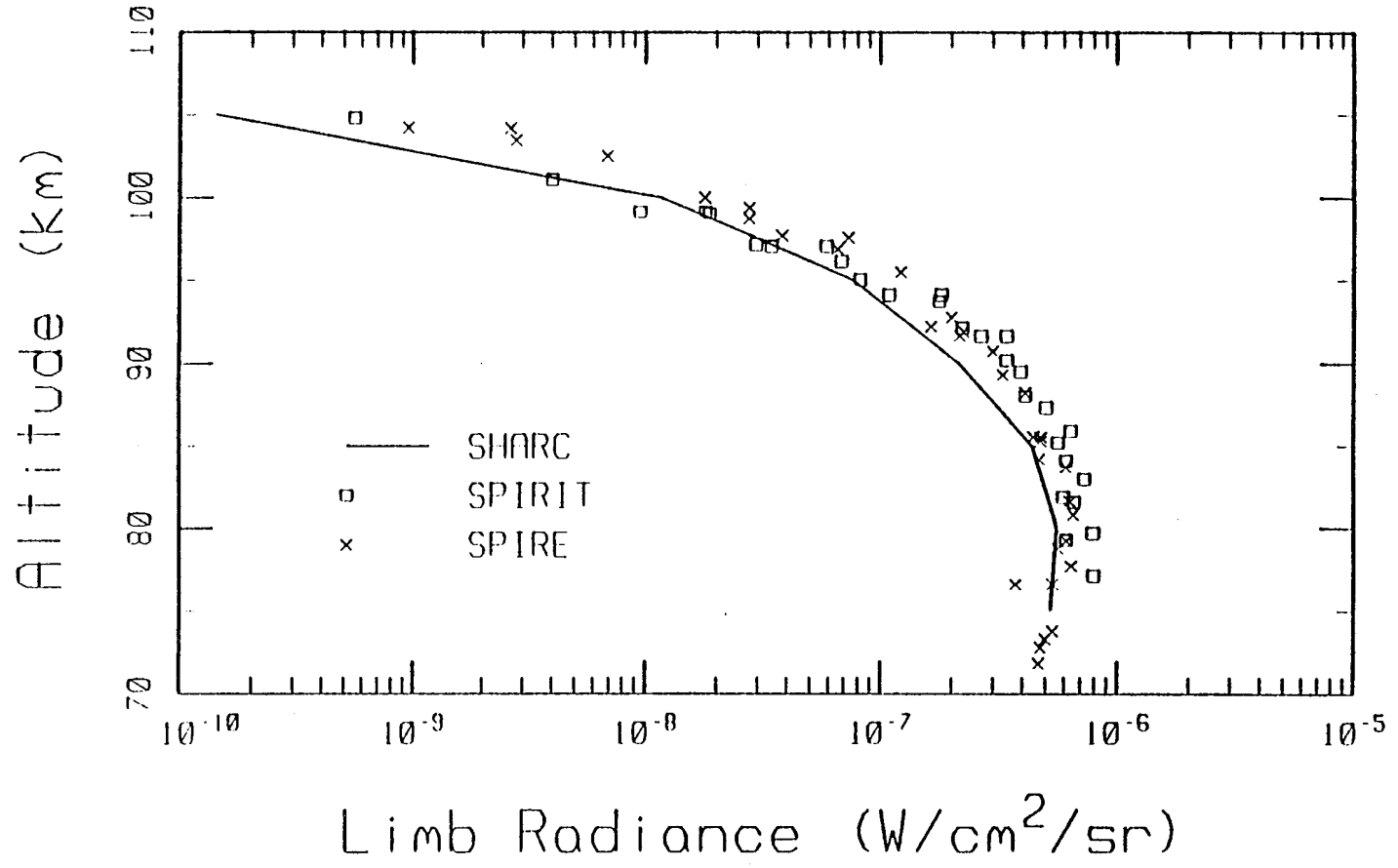

COMPARISON TO CIRRIS DATA

- ILLUSTRATIVE CIRRIS SPECTRAL DATA FOR LIMB VIEWING

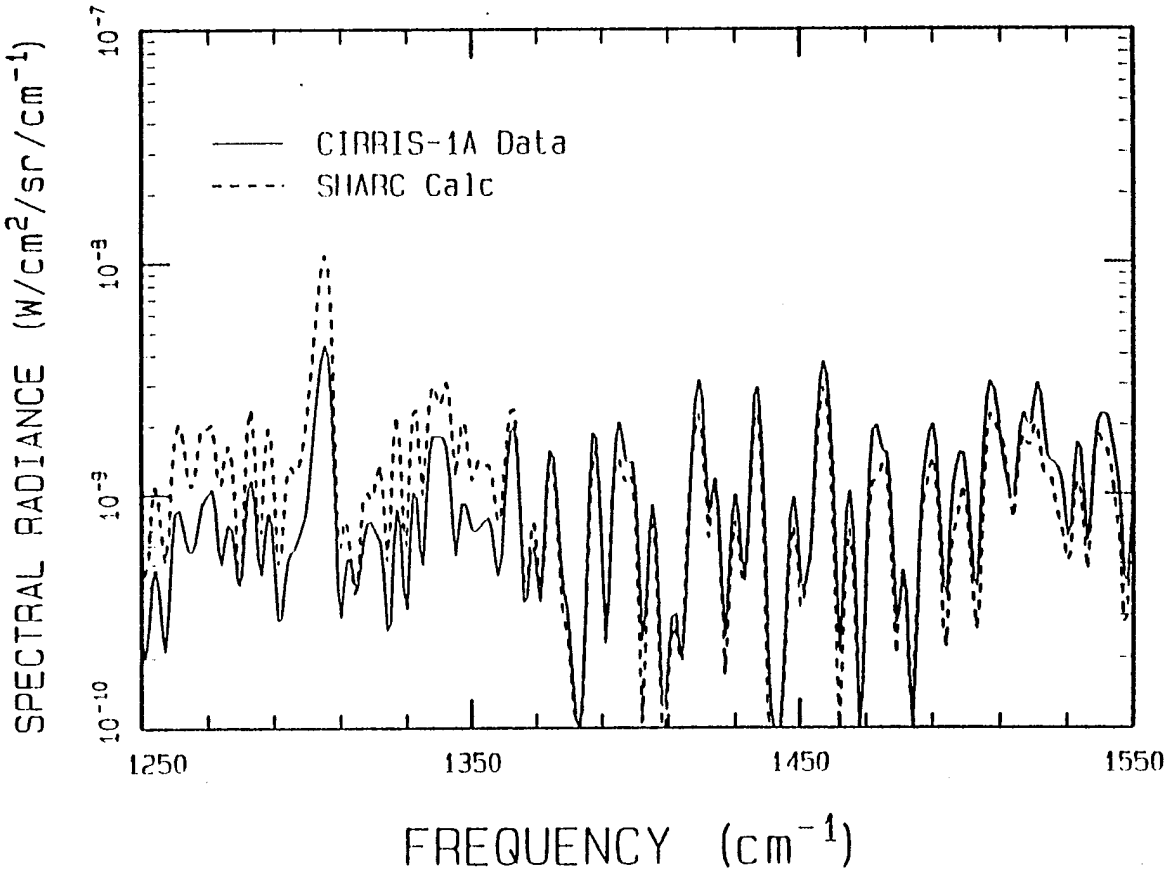

COMPARISON TO CIRRIS DATA (cont.)

- ILLUSTRATIVE CIRRIS SPECTRAL DATA FOR LIMB VIEWING

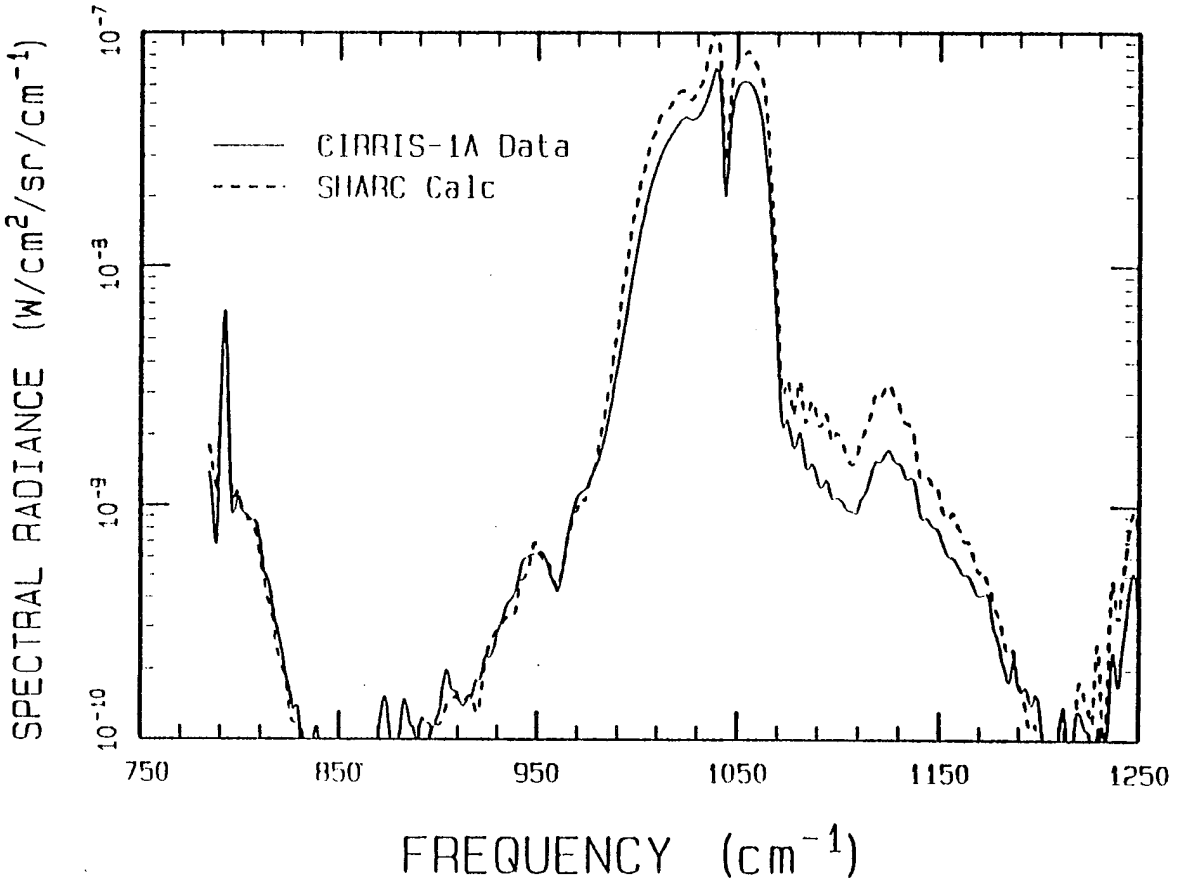

LIMB VIEWS ALONG SOLAR TERMINATOR

- CIRRIS IN-BAND DATA FOR LIMB VIEWS

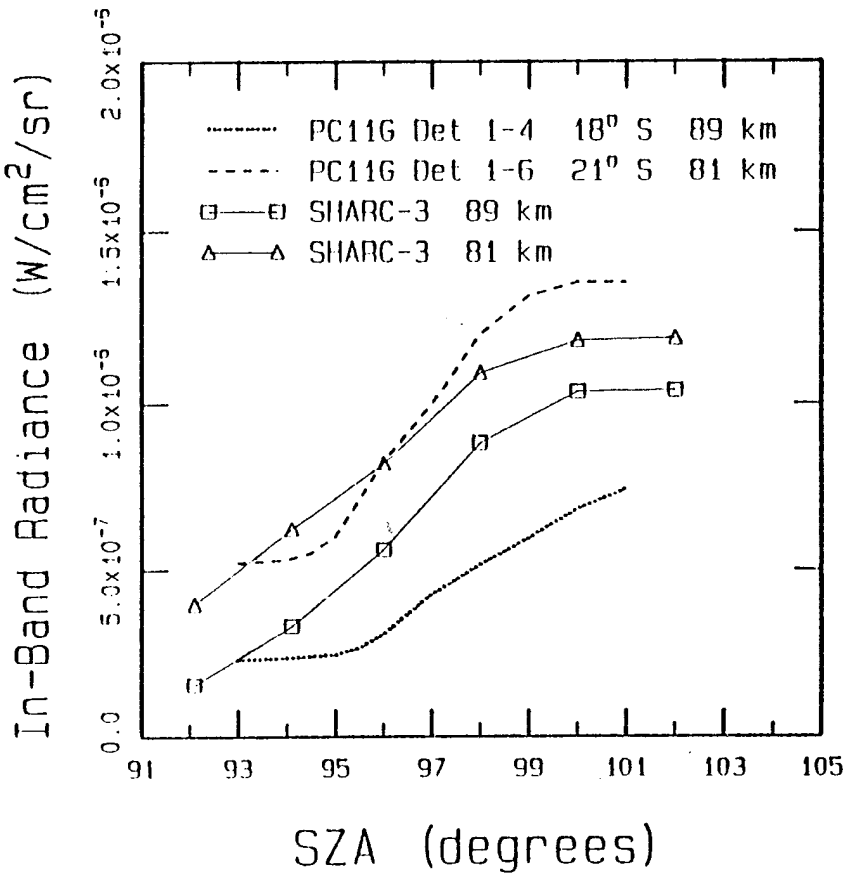

RUN TIMES - CHEMISTRY

- CHEMISTRY REPEATED ONLY FOR MODIFIED ATMOSPHERE
- AMBIENT POPULATIONS
  - 89 BANDS OF H_2O, CO_2, O_3, CO, NO, OH
    26 OF WHICH REQUIRE RADIATION TRAPPING TREATMENT
  - 66 ATMOSPHERIC LAYERS FROM 50 TO 300 KM

DATA GENERAL AViiON AV5100 (20 MIPS)	: 15.2 MIN
DEC VAX 8800	: 10.8 "
DEC VAX 780	: 80.1 "

- AURORAL POPULATIONS (ADDITIONAL TO AMBIENT)
  - 31 VIBRATIONAL STATES: NO(13), NO^+(14), CO_2(4)
  - 37 RADIATING BANDS: NO(23), NO^+(13), CO_2(1)
  - 36 LAYERS FROM 80 TO 150 KM

DATA GENERAL AViiON AV5100 (20 MIPS)	: 7-12 MIN
DEC VAX 8800	: 5- 8.5 "
DEC VAX 780	: 37-64 "

RUN TIMES - LOS RADIANCE

- SPECTRAL RADIANCE - SINGLE BAND
  - 14-16 μm BAND OF CO_2 WITH 890 LINES
  - 131 LAYERS (50 KM LIMB)

  DATA GENERAL AViiON AV5100 (20 MIPS): 5.2 SEC
  DEC VAX 8800 : 3.7 "
  DEC VAX 780 : 27.6 "

- SPECTRAL RADIANCE - MULTIPLE BANDS
  - 1-40 μm BANDPASS: H_2O, CO_2, O_3, CO, NO, OH
    84,000 LINES
  - 131 LAYERS (50 KM LIMB)

  DATA GENERAL AViiON AV5100 (20 MIPS): 6.3 MIN
  DEC VAX 8800 : 4.5 "
  DEC VAX 780 : 33.4 "

FUTURE PLANS

- VALIDATION AND UPGRADES BY COMPARISON TO THE CIRRIS-1A DATA BASE
- DEVELOPING MODULE FOR ATMOSPHERIC STRUCTURES
  - SPECTRAL-SPATIAL CLUTTER METRICS
  - SPIE PAPER 2223-26
- INTERFACED SHARC WITH THE LOW-ALTITUDE CODE
  - SAMM: SHARC AND MODTRAN MERGED
- EXTEND INTO THE NEAR INFRARED AND VISIBLE SPECTRAL REGIONS

SUMMARY

- SHARC IS A HIGH-ALTITUDE RADIANCE MODEL FOR THE INFRARED SPECTRAL REGION
  - AURORAL AND QUIESCENT ATMOSPHERES
  - DIURNAL VARIATION INCLUDING SOLAR TERMINATOR
  - MODULARIZED STRUCTURE
  - ARBITRARY PATHS ABOVE 50 km
  - LINE-BY-LINE RADIANCE CALCULATIONS
  - FULLY INTEGRATED & LOCALIZED AURORAL REGION(S)
  - CLUTTER MODULE UNDER DEVELOPMENT
- VALIDATED WITH FIELD DATA TAKEN BY THE GEOPHYSICS DIRECTORATE, PHILLIPS LABORATORY
  - CIRRIS, SPIRE, SPIRITS, FWI, etc.

Non-LTE in CO_2 in the middle atmosphere

A. A. Kutepov[1], V. P. Ogibalov[2] and G. M. Shved[2]

[1]Institute for Astronomy and Astrophysics, University of Munich
Scheinerstraße 1, 81679 Munich, Germany
tel.: +49-89-92209430, FAX: +49-89-93309427
e-mail: kutepov@usm.uni-muenchen.de

[2]Department of Atmospheric Physics, University of St. Petersburg
St. Petersburg-Petrodvorets, 198904, Russia
tel.: +7-812-4284575, FAX: +7-812-4287240
e-mail: ogibalov@lmupa.phys.lgu.spb.su

Contents

1 Introduction

- LTE
- vib. non-LTE and rot. LTE
- total non-LTE

Techniques used to model non-LTE

- Lambda iteration ($L \times L$)
- Curtis-matrix tech. ($L \times D \times L \times D$)
- ALI tech. ($L \times L$)

2 System of vibrational energy levels and radiative transitions of CO_2

We considered *all* vibrational levels and *all* ro-vibrational lines for the $C^{12}O_2^{16}$ isotope which are available from HITRAN-92: the excitation of ν_2- and ν_3- vibrations up to $5\nu_2$ and $3\nu_3$ respectively.

Radiative processes: (a) absorption of direct solar radiation and the radiation coming from the lower boundary, (b) absorption of atmospheric radiation and (c) spontaneous and stimulated emission.

Quantitative characteristics of the model:

Total number of vibrational levels: L_v=127

Total number of ro-vibrational levels: L=7499

Total number of bands: 324

Total number of ro-vibrational lines: 29993

2.1 Collisional processes

2.1.1 R-T processes

Assumption of rotational LTE (infinite large rate of the R-T exchange)

2.1.2 Intra-molecular V-V processes

$$CO_2(n^l v_3) + M(N_2, O_2) \rightarrow CO_2(n^{l''}(v_3 - 1)) + M + \Delta E, \tag{1}$$

where $n' = n + 1, n + 2, n + 3, n + 4$.

$$CO_2(n^l v_3, m) + M(N_2, O_2, O) \rightarrow CO_2(n^{l'} v_3, m') + M + \Delta E, \tag{2}$$

where m and m' denote arbitrary levels from the groups $n^l v_3$ and $n^{l''} v_3$ respectively.

2.1.3 Inter-molecular V-V processes

$$CO_2(n^l v_3) + N_2(0) \rightarrow CO_2(n^{l''}(v_3 - 1)) + N_2(1) + \Delta E \tag{3}$$

$$CO_2(n^l v_3) + O_2(0) \rightarrow CO_2((n+1)^{l''}(v_3 - 1)) + O_2(1) + \Delta E \tag{4}$$

$$CO_2(n^l v_3) + O_2(1) \rightarrow CO_2((n+2)^{l'} v_3) + O_2(0) + \Delta E \tag{5}$$

$$C^{12}O_2^{16}(n^l v_3) + C^{12}O_2^{16}(00^0 0) \rightarrow C^{12}O_2^{16}(n^{l'}(v_3 - 1)) + C^{12}O_2^{16}(00^0 1) \tag{6}$$

$$N_2(1) + O_2(0) \rightarrow N_2(0) + O_2(1) + \Delta E \tag{7}$$

2.1.4 V-T processes

$$CO_2(n^l v_3) + M(N_2, O_2) \rightarrow CO_2((n-1)^{l'} v_3) + M + \Delta E, \qquad |l - l'| = 1 \tag{8}$$

$$CO_2(n^l v_3) + O \rightarrow CO_2((n-1)^{l''} v_3) + O + \Delta E \tag{9}$$

$$CO_2(n^l v_3) + O \rightarrow CO_2(n^{l''}(v_3 - 1)) + O + \Delta E \tag{10}$$

$$N_2(1) + O \rightarrow N_2(0) + \Delta E \tag{11}$$

$$O_2(1) + M(N_2, O_2, O) \rightarrow O_2(0) + M + \Delta E \tag{12}$$

2.2 Reference atmosphere

Temperature profiles, mixing ratio profiles for N_2, O_2 and O: MSISE-90 reference atmosphere.

The volume mixing ratio for CO_2 was compiled on the basis of experimental data, presented by Trinks and Fricke (1978), Offermann et al (1981) and Rincland et al (1992).

2.3 Computational features

On each iteration step we solve the radiative transfer equation in each of 29993 ro-vibrational lines using the Feautrier technique for 16 frequency and 4 angle grid points.

In order to reach the convergence criterion 10^{-4} for vibrational populations 6 and 40 accelerated lambda iterations are required for day and night conditions respectively.

2.4 Results

2.4.1 Verification of standard approximations

1. Effect of highly excited levels

2."Emission" and "radiative temperature" approximations for week bands

3. Spontaneous emission

$$\sum_j n_{vj} A_{vj,v'j'} = n_v \sum_j W_v^{LTE}(j,T) A_{vj,v'j'} = n_v A_{v,v'}(T) \qquad (13)$$

where

$$W_v^{LTE}(j,T) = \frac{g_v(j)\, exp(-\frac{E_v(j)}{k_B T})}{Q_v(T)} \qquad (14)$$

4. Weak transitions, not presented in HITRAN-92

5. Laser transitions around 10 μm

2.4.2 Influence of collisional rate coefficients

- Rate coefficient for quenching of the ν_2 transitions by atomic oxygen: 1.5, 3 and 6×10^{-12} cm^3 s^{-1}.
- Multi-quantum and one-quantum quenching of vibrations by atomic oxygen

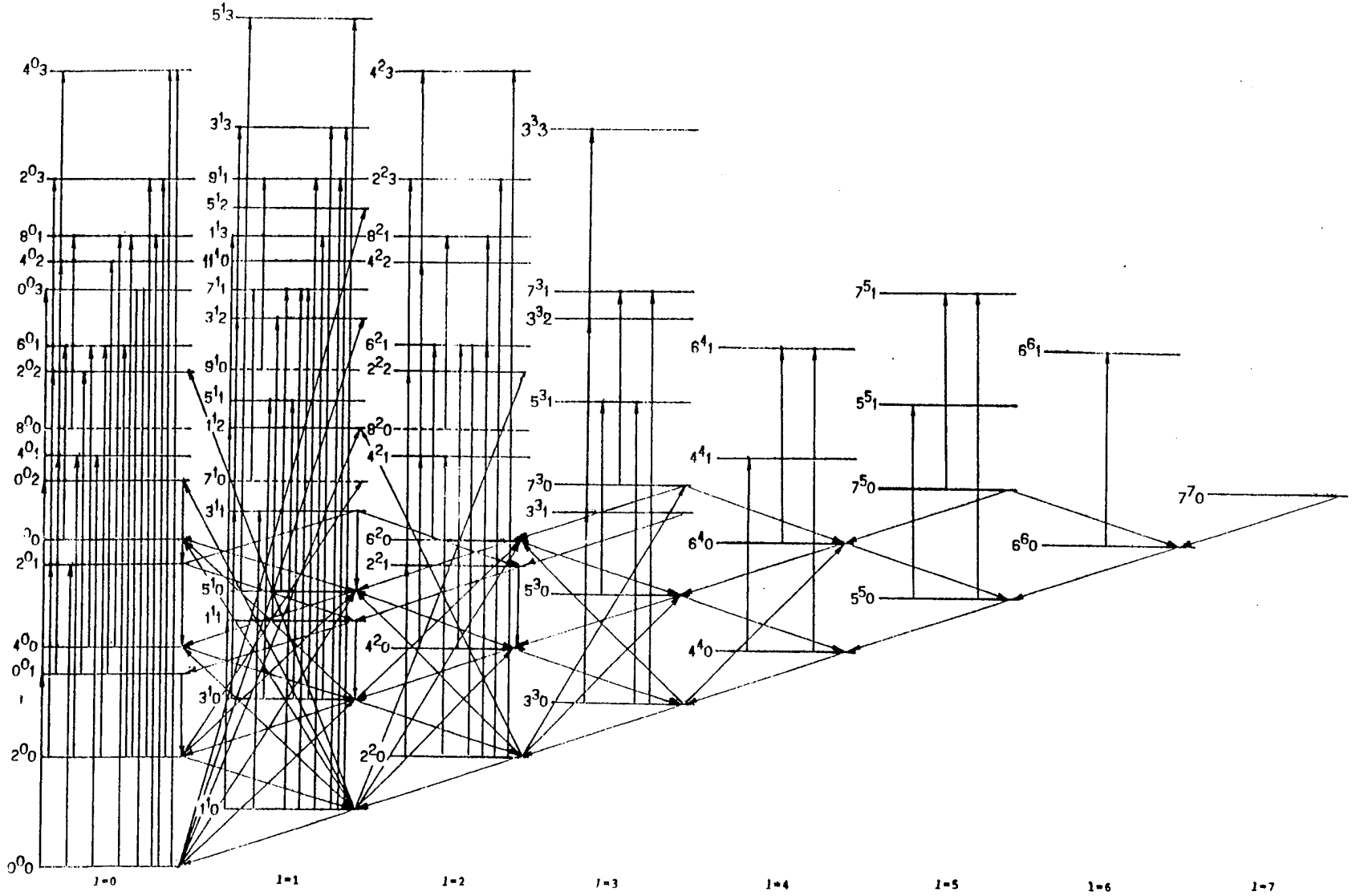
5^1_3
4^0_3
4^2_3
3^1_3
3^3_3
2^0_3
9^1_1
2^2_3
8^0_1
5^1_2
8^2_1
4^0_2
1^1_3
4^2_2
0^0_3
11^1_0
7^3_1
7^1_1
7^5_1
6^0_1
3^1_2
3^3_2
6^2_1
6^4_1
6^6_1
2^0_2
9^1_0
2^2_2
5^1_1
5^3_1
5^5_1
8^0_0
1^1_2
8^2_0
4^0_1
4^2_1
4^4_1
0^0_2
7^1_0
7^3_0
7^5_0
7^7_0
3^1_1
3^3_1
2^0_0
6^2_0
6^4_0
6^6_0
2^2_1
2^0_1
5^1_0
5^3_0
5^5_0
1^1_1
4^0_0
4^2_0
4^4_0
0^0_1
3^1_0
3^3_0
2^0_0
2^2_0
1^1_0
0^0_0
J=0
J=1
J=2
J=3
J=4
J=5
J=6
J=7

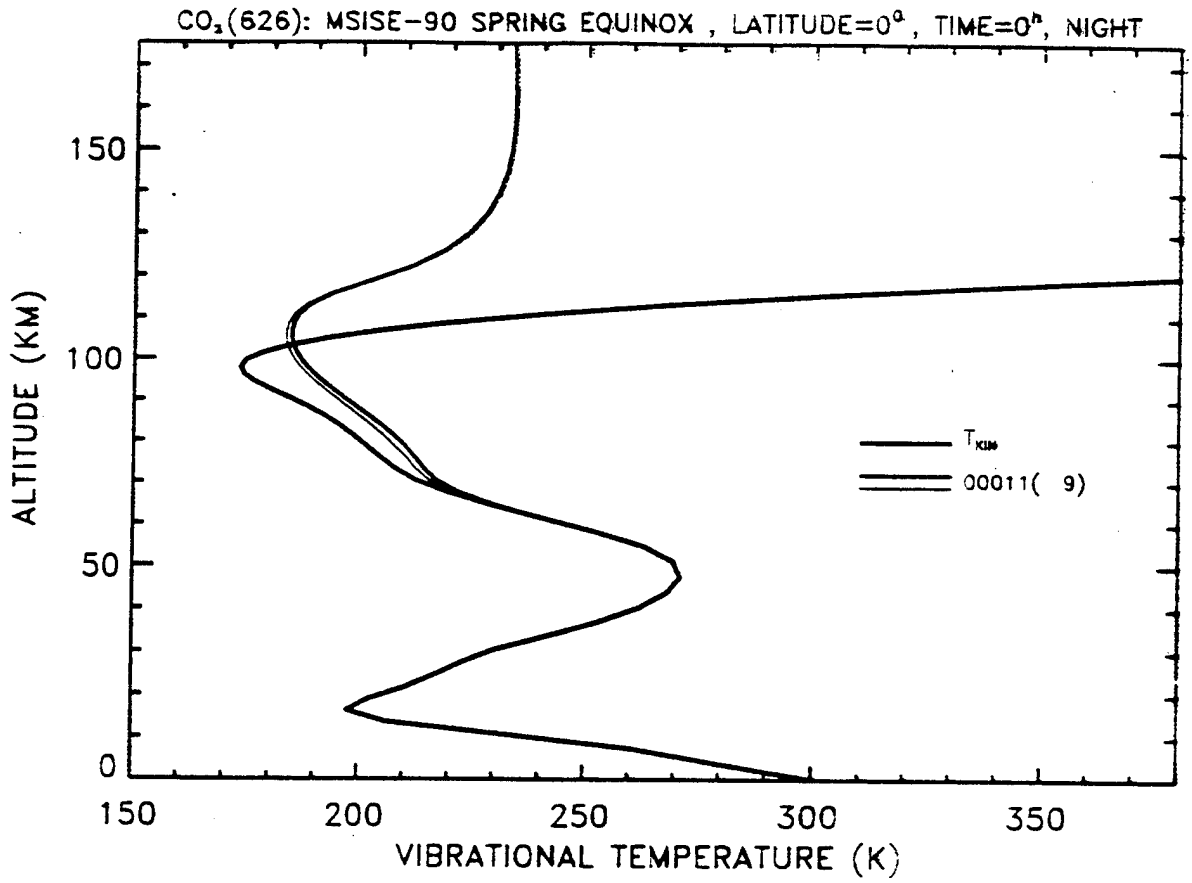
CO₂(626): MSISE-90 SPRING EQUINOX , LATITUDE=0°, TIME=0h, NIGHT
ALTITUDE (KM)
150
100
50
0
150
200
250
300
350
VIBRATIONAL TEMPERATURE (K)
T_KIN
00011(9)

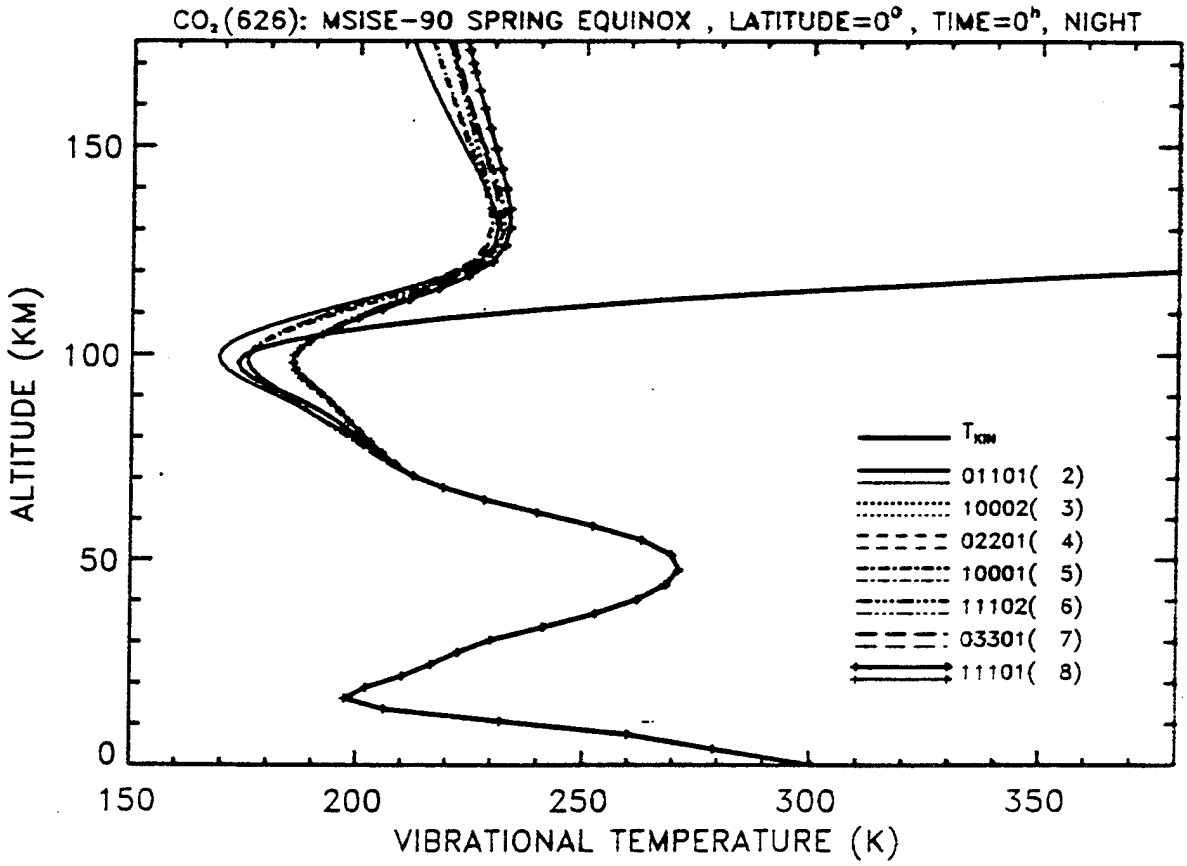
CO₂(626): MSISE-90 SPRING EQUINOX , LATITUDE=0°, TIME=0h, NIGHT
ALTITUDE (KM)
150
100
50
0
150
200
250
300
350
VIBRATIONAL TEMPERATURE (K)
T_KIN
01101(2)
10002(3)
02201(4)
10001(5)
11102(6)
03301(7)
11101(8)

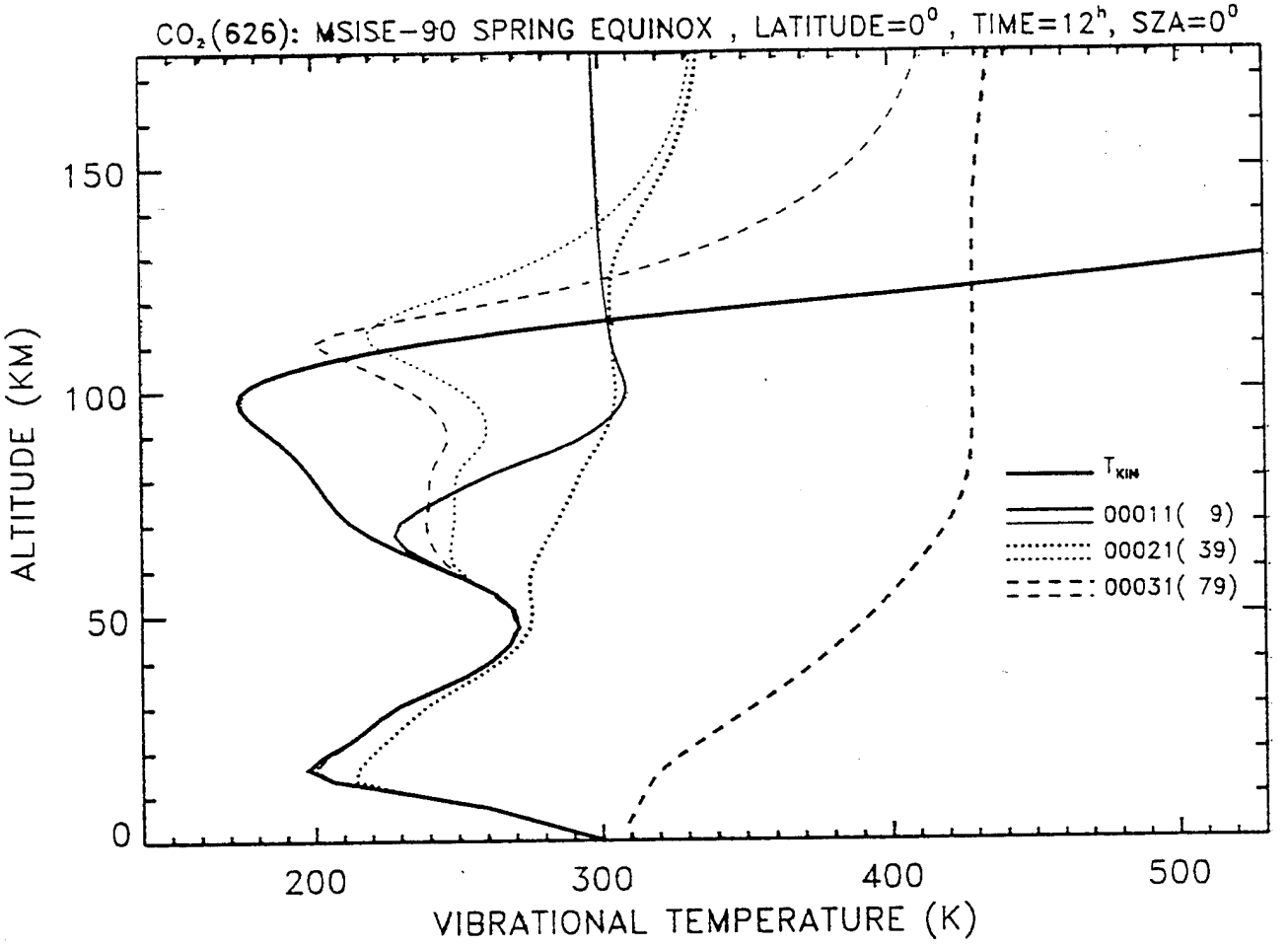
CO₂(626): MSISE-90 SPRING EQUINOX , LATITUDE=0°, TIME=12h, SZA=0°
ALTITUDE (KM)
150
100
50
0
200
300
400
500
VIBRATIONAL TEMPERATURE (K)
T_KIN
00011(9)
00021(39)
00031(79)

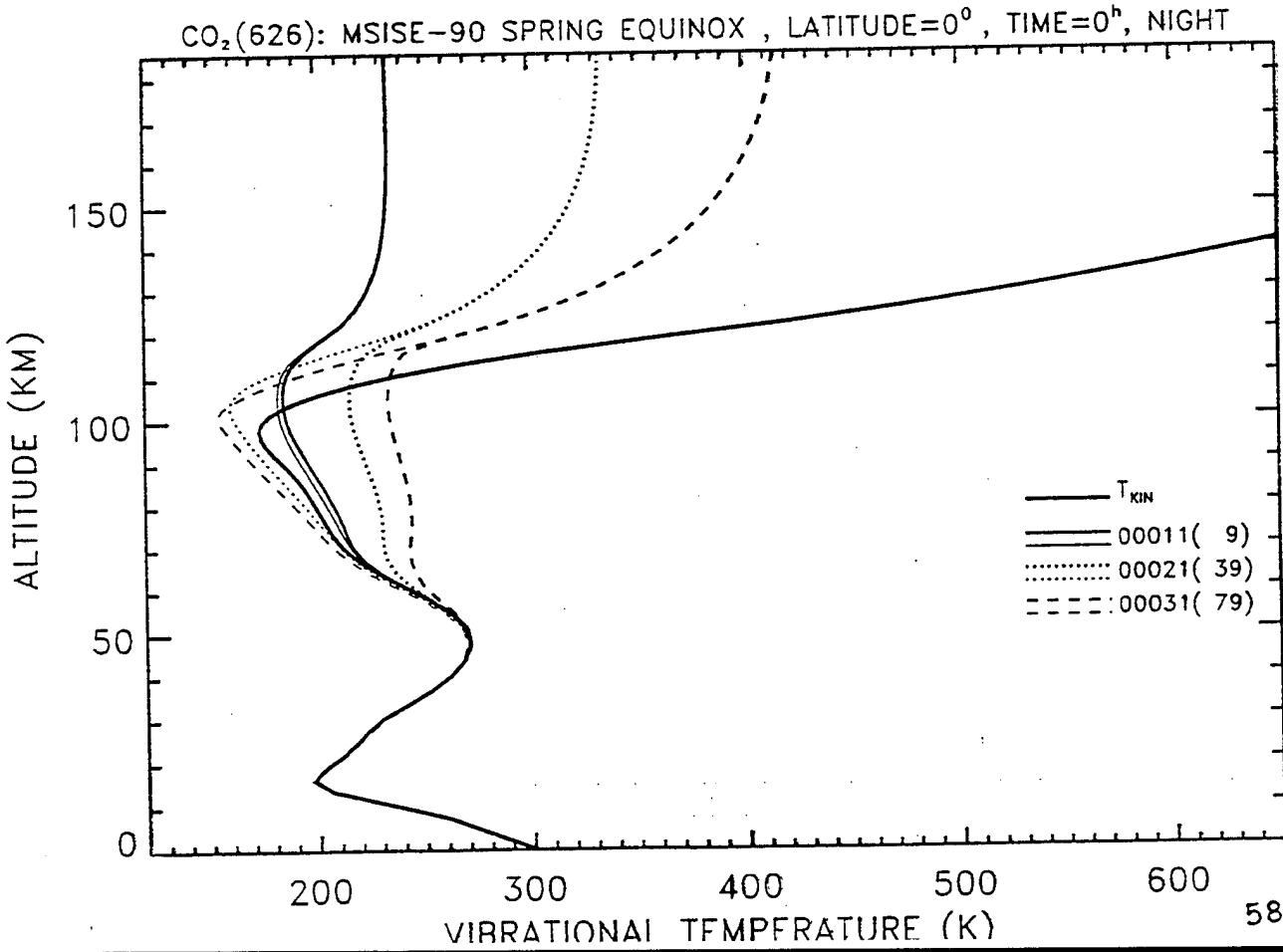
CO₂(626): MSISE-90 SPRING EQUINOX , LATITUDE=0°, TIME=0h, NIGHT
ALTITUDE (KM)
150
100
50
0
200
300
400
500
600
VIBRATIONAL TEMPERATURE (K)
T_KIN
00011(9)
00021(39)
00031(79)

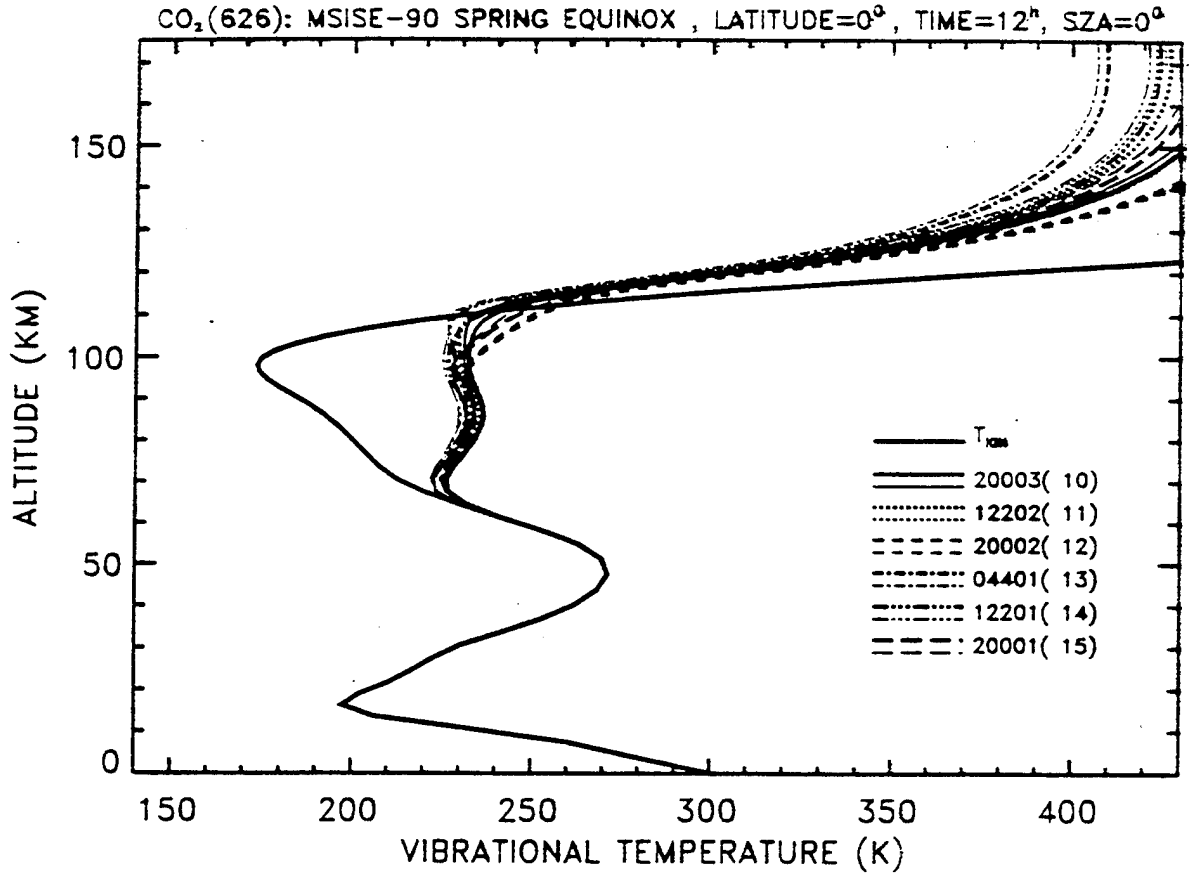
CO₂(626): MSISE-90 SPRING EQUINOX , LATITUDE=0°, TIME=12h, SZA=0°
ALTITUDE (KM)
VIBRATIONAL TEMPERATURE (K)
T_KIN
20003(10)
12202(11)
20002(12)
04401(13)
12201(14)
20001(15)

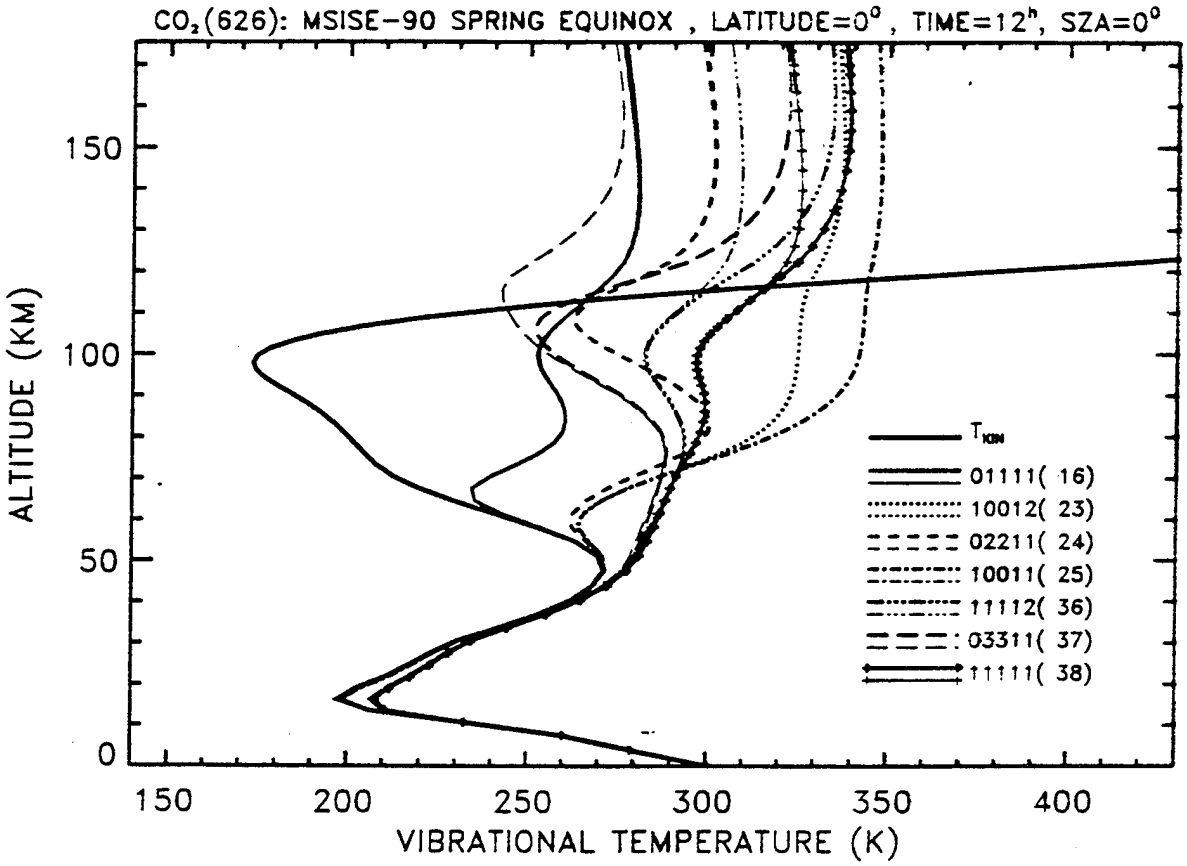
CO₂(626): MSISE-90 SPRING EQUINOX , LATITUDE=0°, TIME=12h, SZA=0°
ALTITUDE (KM)
VIBRATIONAL TEMPERATURE (K)
T_KIN
01111(16)
10012(23)
02211(24)
10011(25)
11112(36)
03311(37)
11111(38)

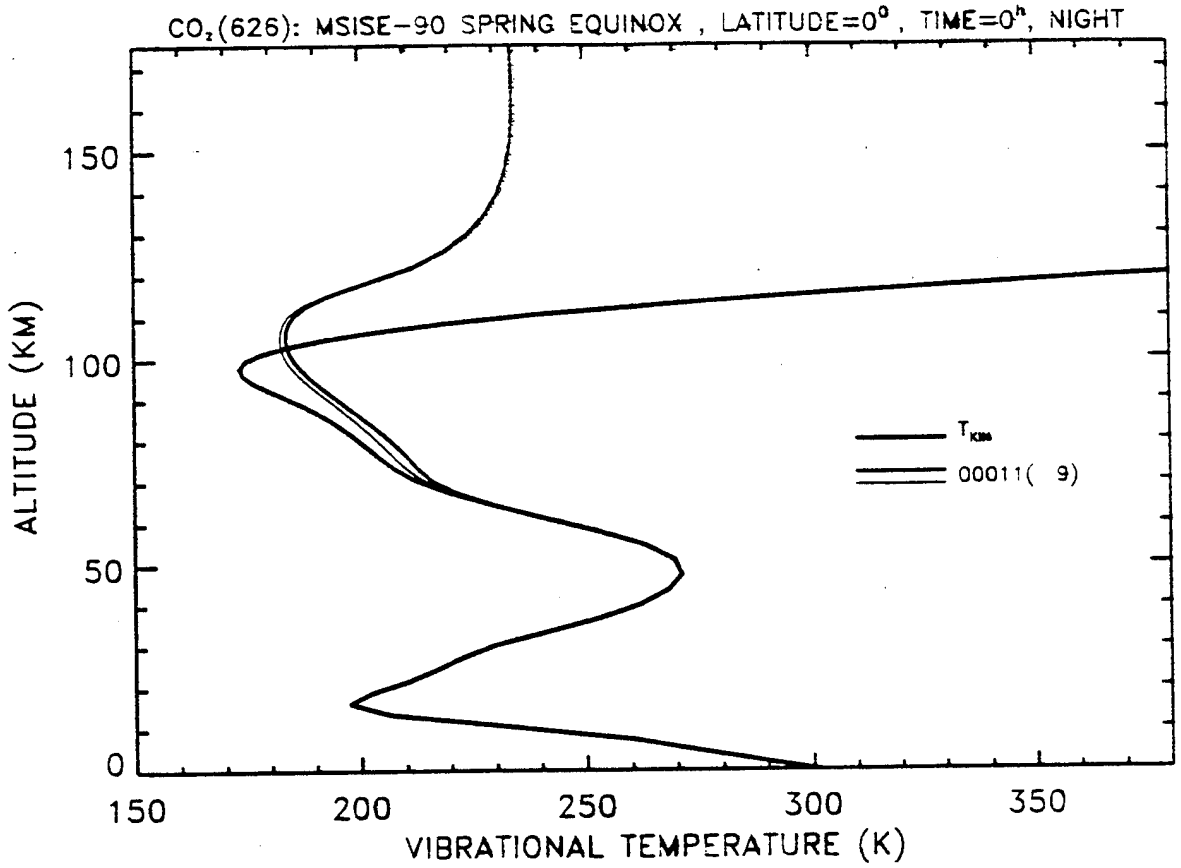
CO₂(626): MSISE-90 SPRING EQUINOX , LATITUDE=0°, TIME=0ʰ, NIGHT
ALTITUDE (KM)
150
100
50
0
150
200
250
300
350
VIBRATIONAL TEMPERATURE (K)
T_KIN
00011(9)

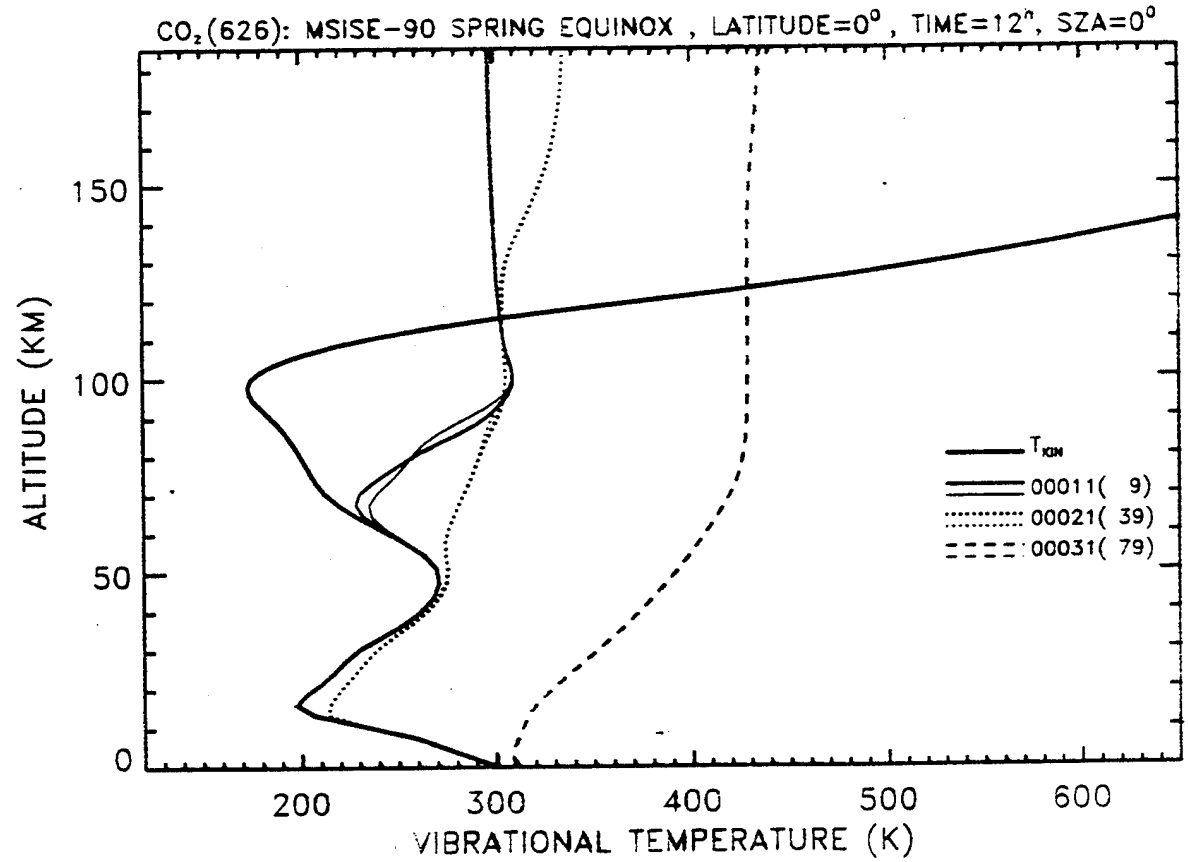
CO₂(626): MSISE-90 SPRING EQUINOX , LATITUDE=0°, TIME=12ʰ, SZA=0°
ALTITUDE (KM)
150
100
50
0
200
300
400
500
600
VIBRATIONAL TEMPERATURE (K)
T_KIN
00011(9)
00021(39)
00031(79)

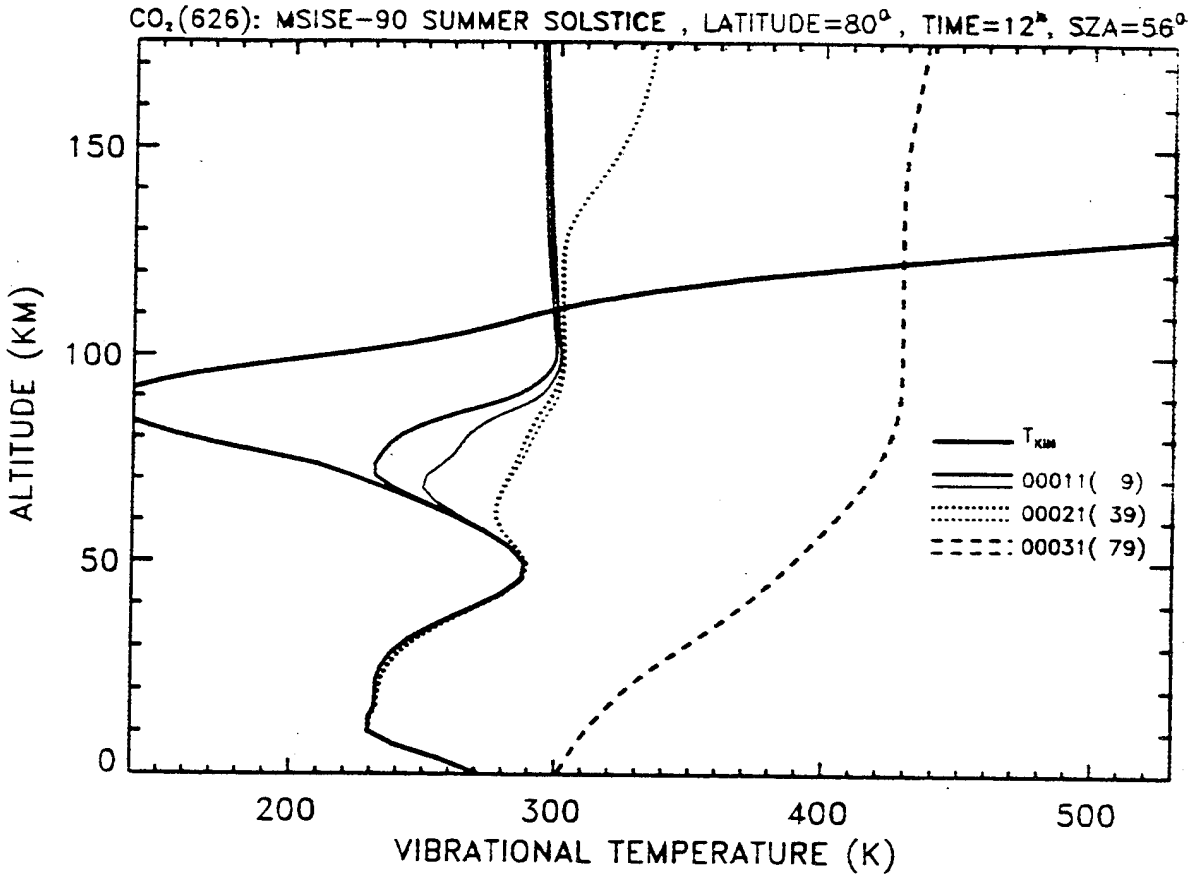
CO_2(626): MSISE-90 SUMMER SOLSTICE , LATITUDE=80°, TIME=12h, SZA=56°
ALTITUDE (KM)
150
100
50
0
200
300
400
500
VIBRATIONAL TEMPERATURE (K)
T_{KIN}
00011(9)
00021(39)
00031(79)

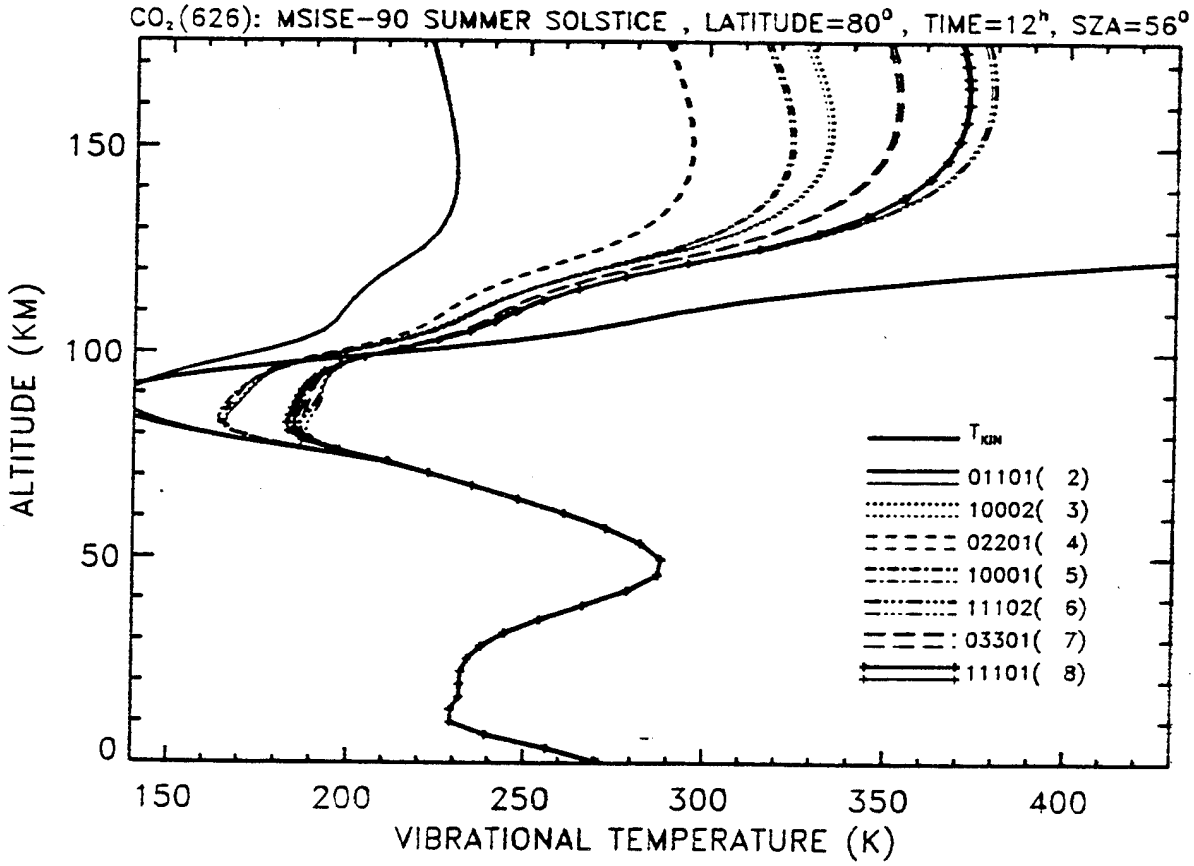
CO_2(626): MSISE-90 SUMMER SOLSTICE , LATITUDE=80°, TIME=12h, SZA=56°
ALTITUDE (KM)
150
100
50
0
150
200
250
300
350
400
VIBRATIONAL TEMPERATURE (K)
T_{KIN}
01101(2)
10002(3)
02201(4)
10001(5)
11102(6)
03301(7)
11101(8)

12

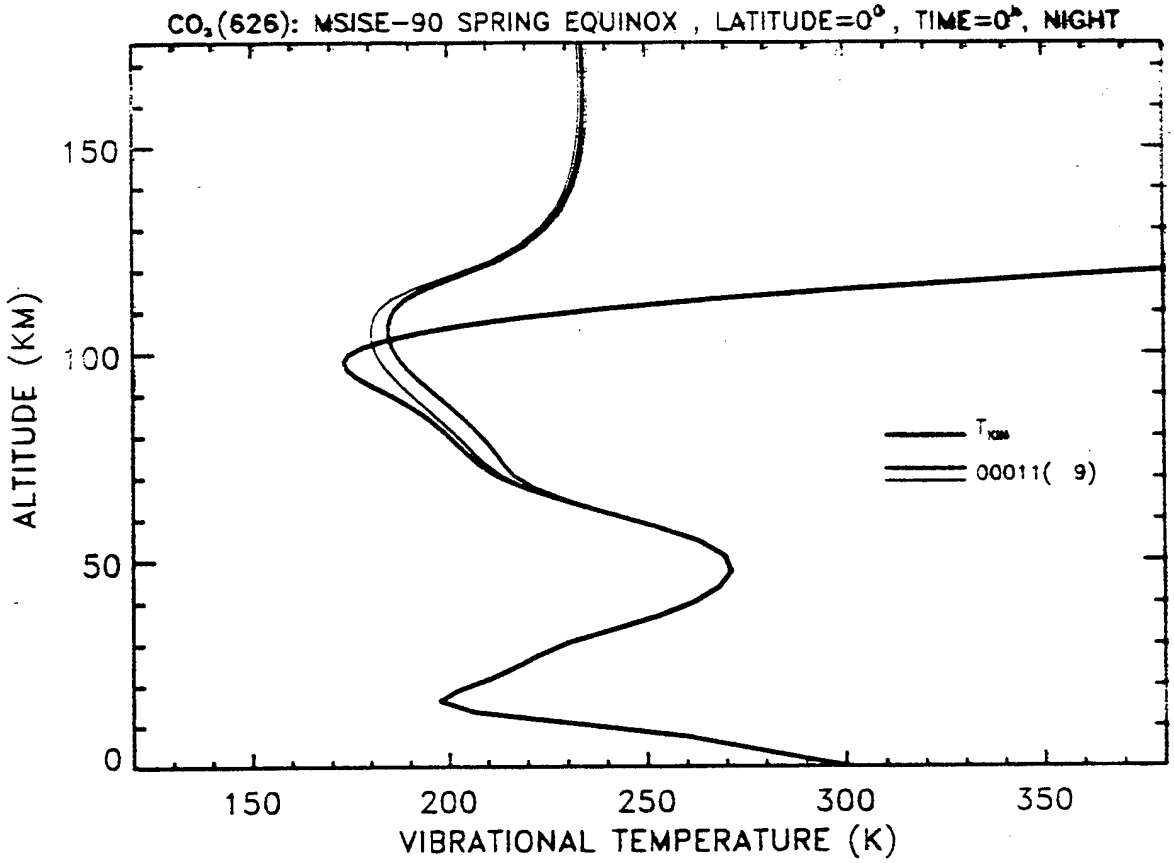
CO₂(626): MSISE-90 SPRING EQUINOX , LATITUDE=0°, TIME=0ʰ, NIGHT
ALTITUDE (KM)
150
100
50
0
150
200
250
300
350
VIBRATIONAL TEMPERATURE (K)
T_KIN
00011(9)

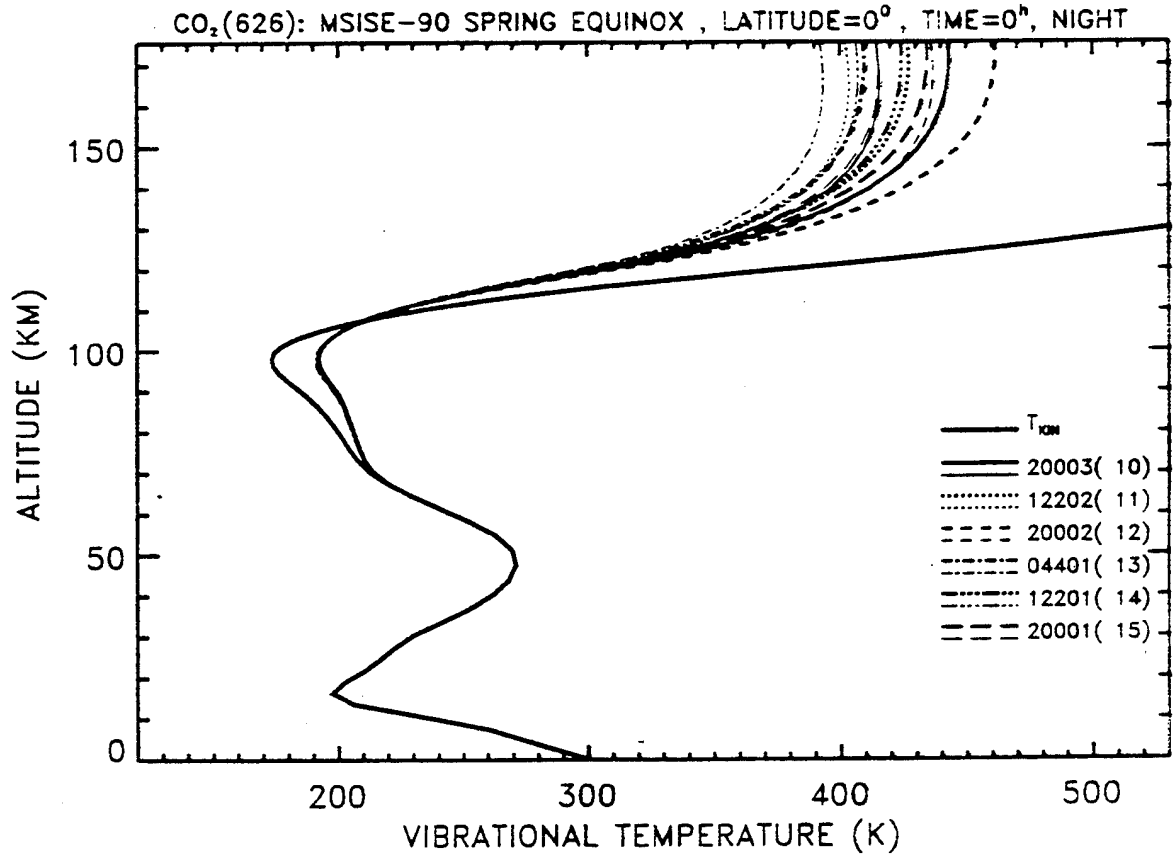
CO₂(626): MSISE-90 SPRING EQUINOX , LATITUDE=0°, TIME=0ʰ, NIGHT
ALTITUDE (KM)
150
100
50
0
200
300
400
500
VIBRATIONAL TEMPERATURE (K)
T_KIN
20003(10)
12202(11)
20002(12)
04401(13)
12201(14)
20001(15)

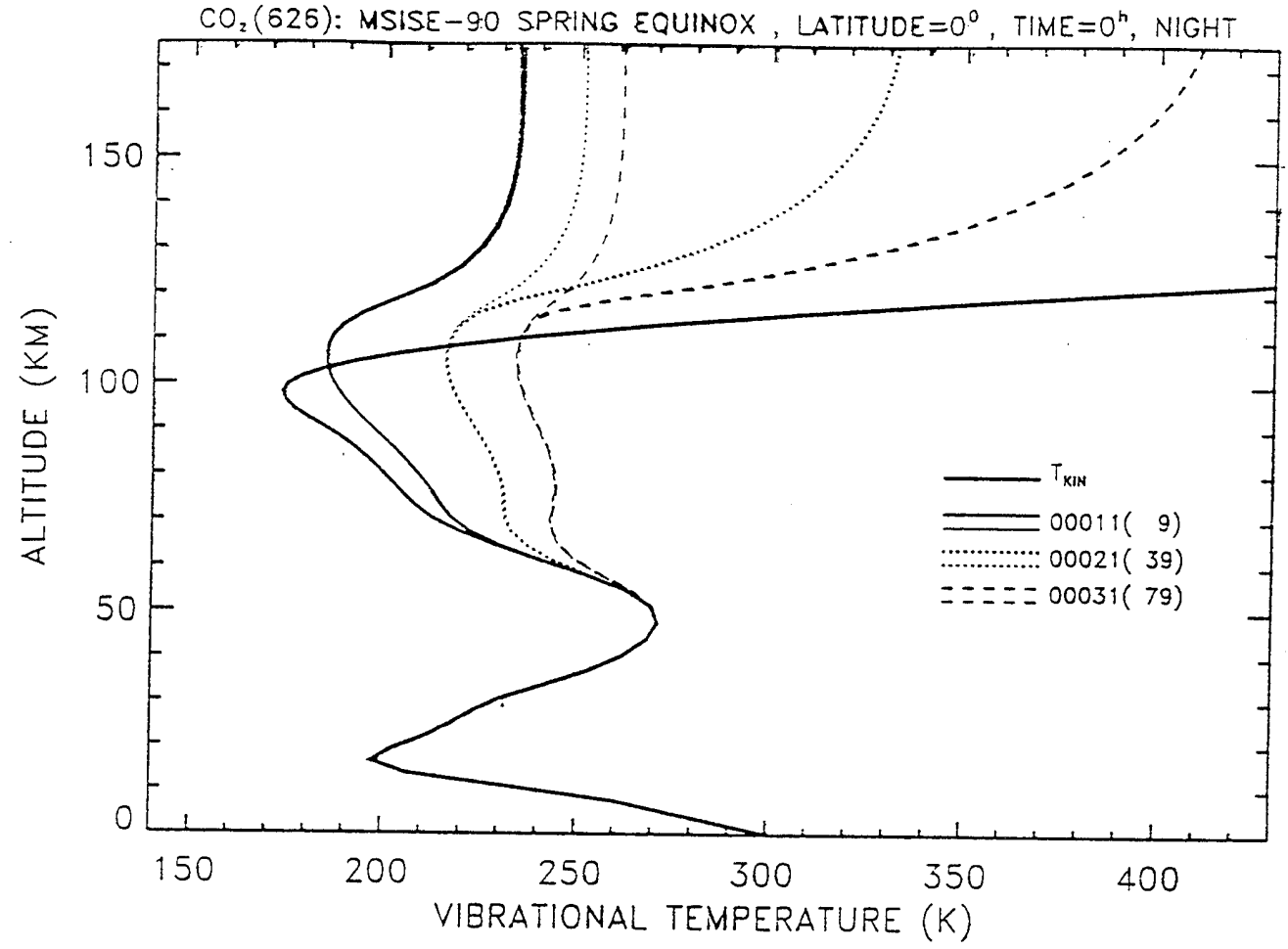
CO_2(626): MSISE-90 SPRING EQUINOX , LATITUDE=0°, TIME=0h, NIGHT
ALTITUDE (KM)
VIBRATIONAL TEMPERATURE (K)
T_{KIN}
00011(9)
00021(39)
00031(79)

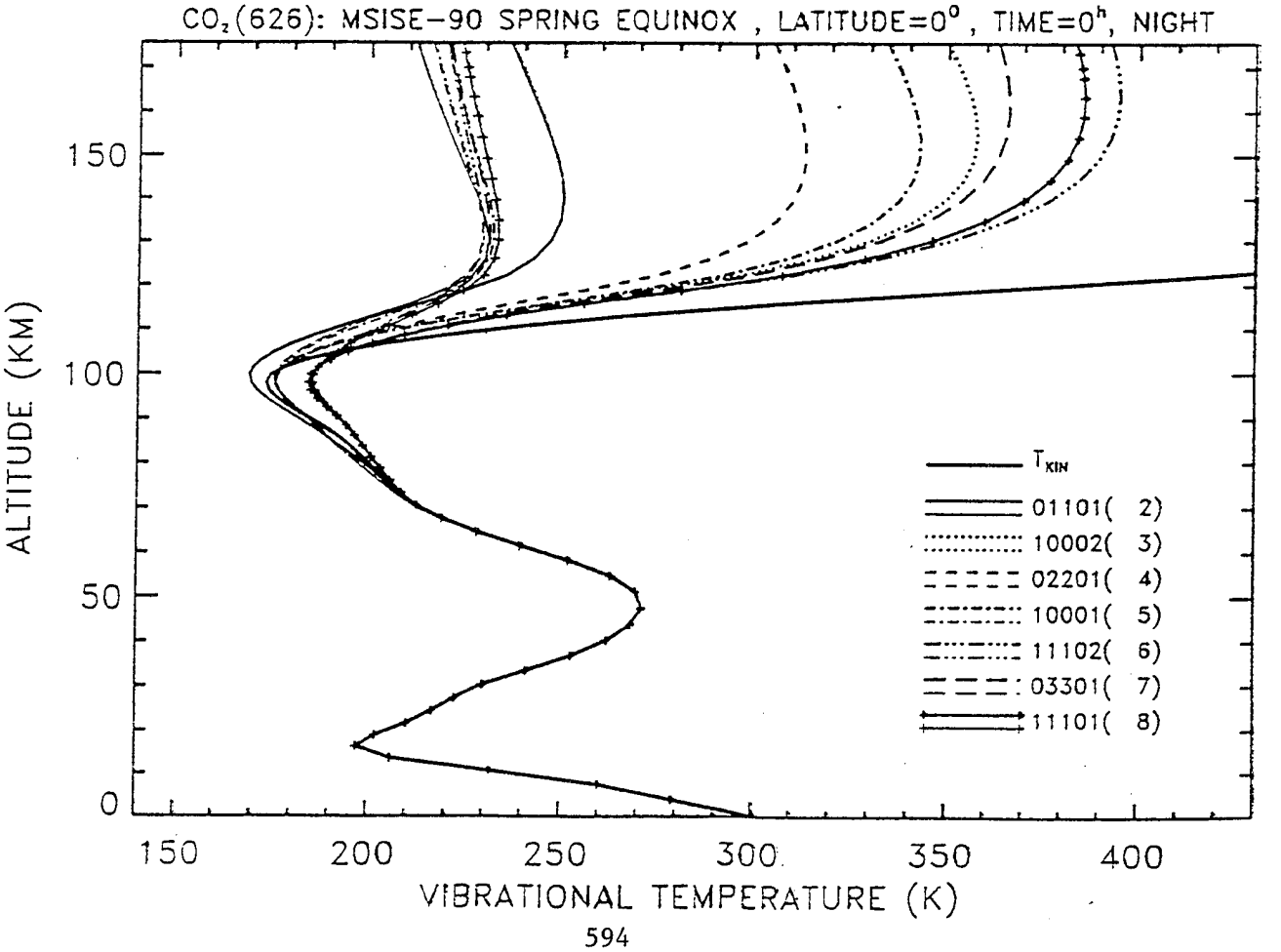
CO_2(626): MSISE-90 SPRING EQUINOX , LATITUDE=0°, TIME=0h, NIGHT
ALTITUDE (KM)
VIBRATIONAL TEMPERATURE (K)
T_{KIN}
01101(2)
10002(3)
02201(4)
10001(5)
11102(6)
03301(7)
11101(8)

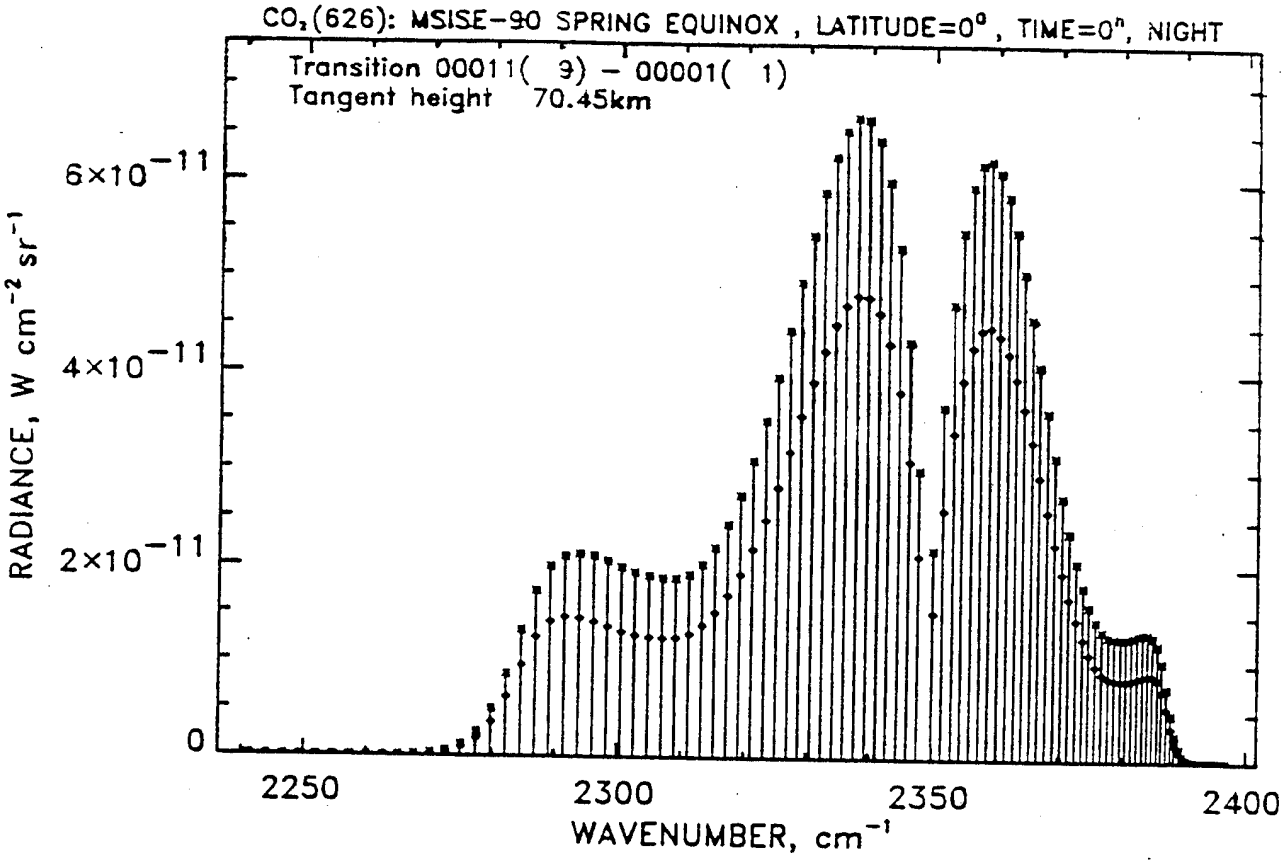
CO₂(626): MSISE-90 SPRING EQUINOX , LATITUDE=0°, TIME=0ʰ, NIGHT
Transition 00011(9) – 00001(1)
Tangent height 70.45km
RADIANCE, W cm⁻² sr⁻¹
6×10⁻¹¹
4×10⁻¹¹
2×10⁻¹¹
0
2250
2300
2350
2400
WAVENUMBER, cm⁻¹

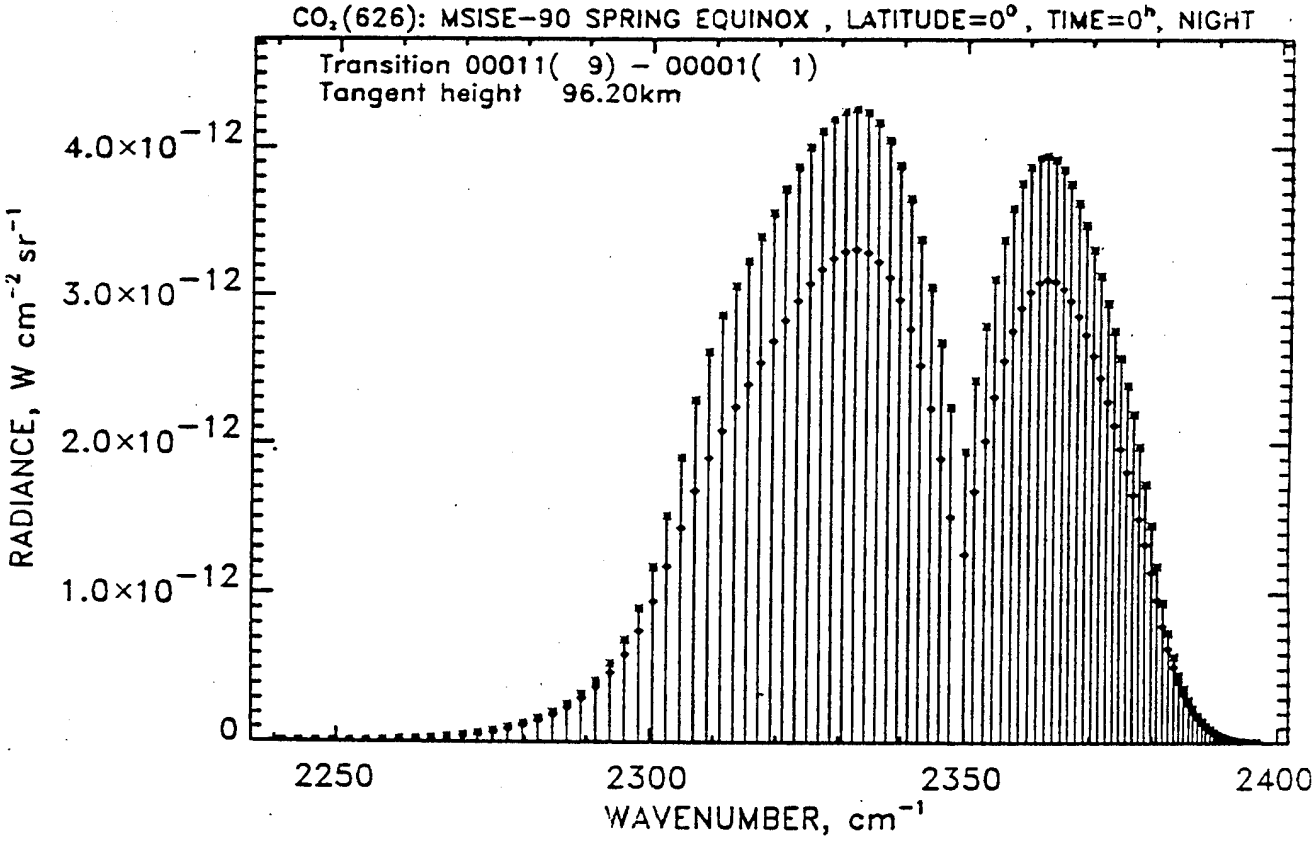
CO₂(626): MSISE-90 SPRING EQUINOX , LATITUDE=0°, TIME=0ʰ, NIGHT
Transition 00011(9) – 00001(1)
Tangent height 96.20km
RADIANCE, W cm⁻² sr⁻¹
4.0×10⁻¹²
3.0×10⁻¹²
2.0×10⁻¹²
1.0×10⁻¹²
0
2250
2300
2350
2400
WAVENUMBER, cm⁻¹

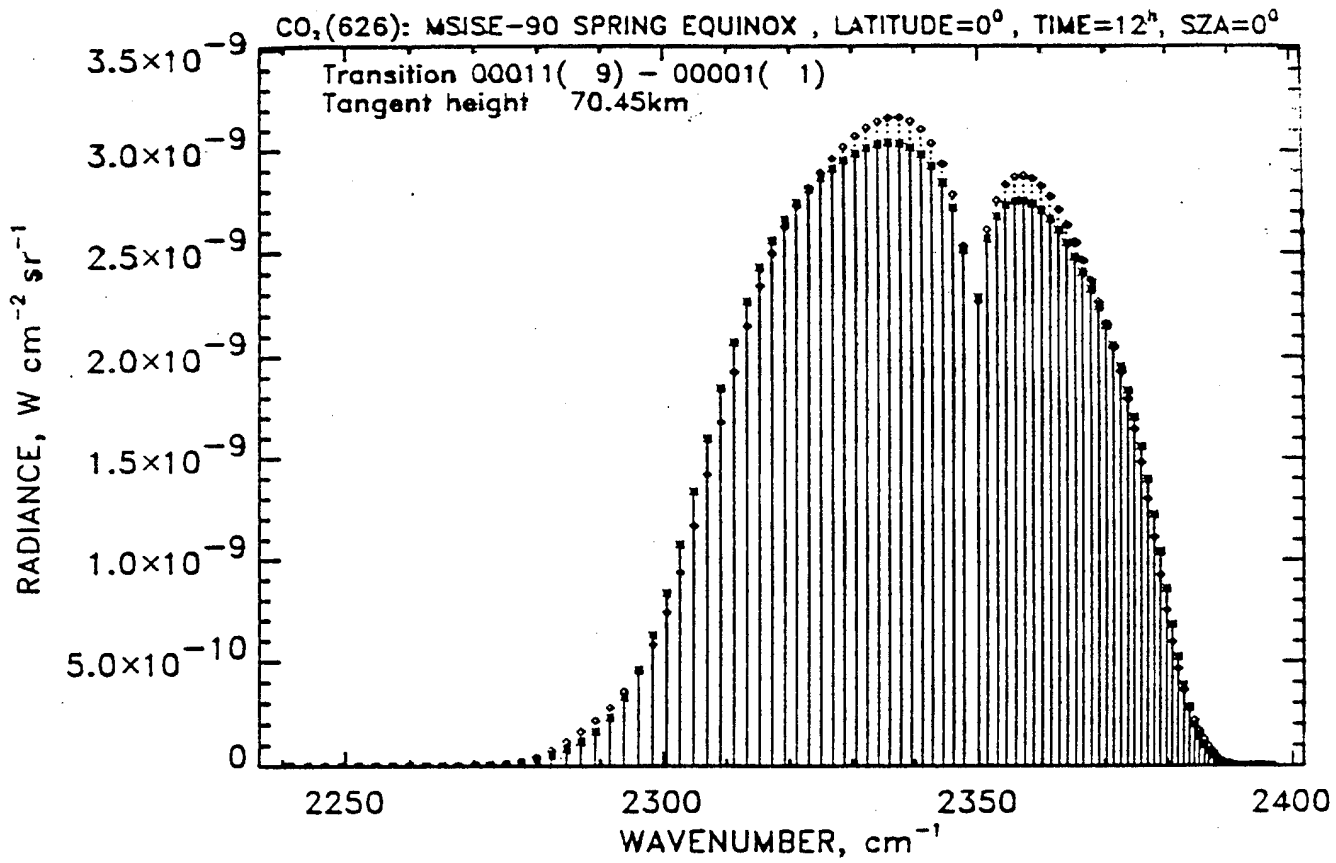
CO₂(626): MSISE-90 SPRING EQUINOX , LATITUDE=0°, TIME=12h, SZA=0°
Transition 00011(9) – 00001(1)
Tangent height 70.45km
RADIANCE, W cm⁻² sr⁻¹
3.5×10⁻⁹
3.0×10⁻⁹
2.5×10⁻⁹
2.0×10⁻⁹
1.5×10⁻⁹
1.0×10⁻⁹
5.0×10⁻¹⁰
0
2250
2300
2350
2400
WAVENUMBER, cm⁻¹

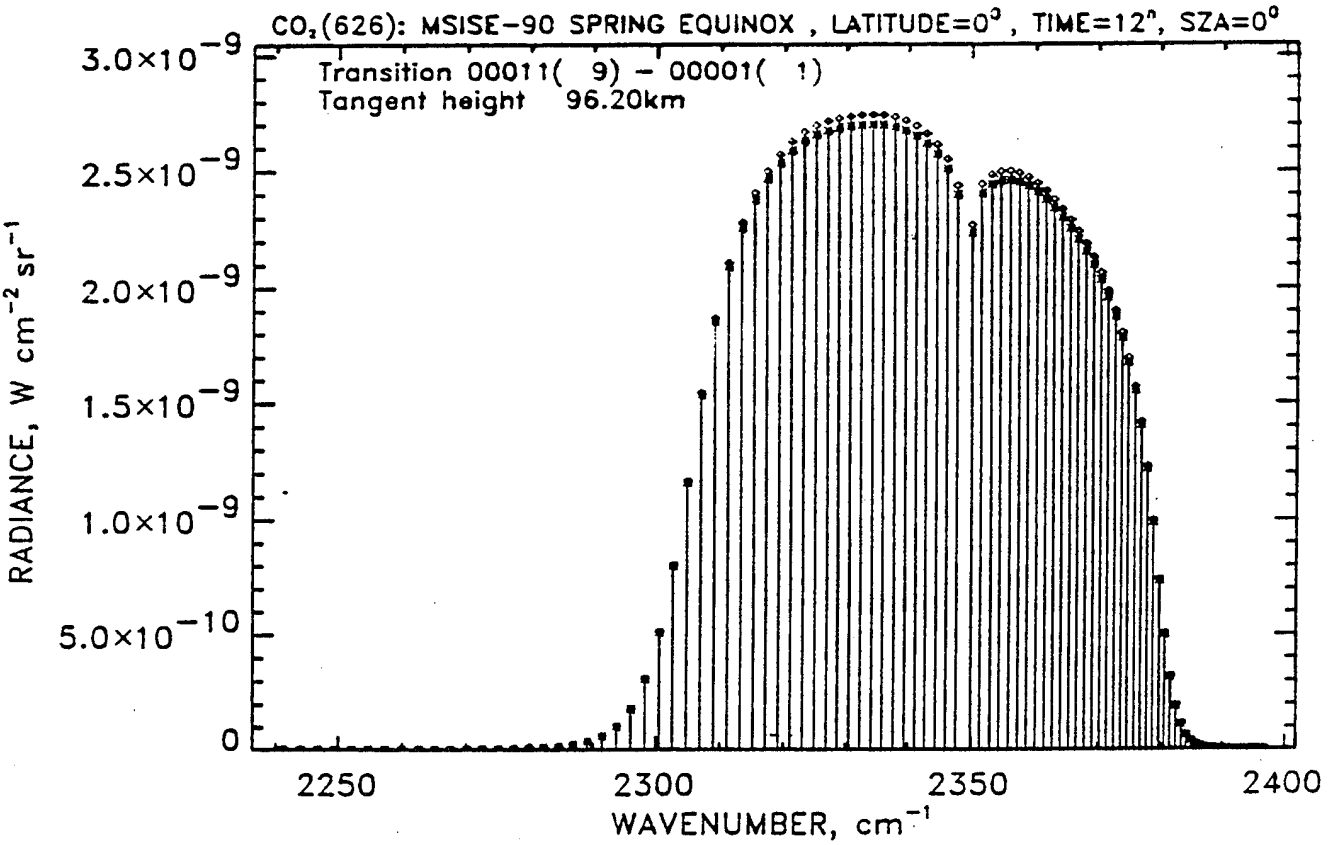
CO₂(626): MSISE-90 SPRING EQUINOX , LATITUDE=0°, TIME=12h, SZA=0°
Transition 00011(9) – 00001(1)
Tangent height 96.20km
RADIANCE, W cm⁻² sr⁻¹
3.0×10⁻⁹
2.5×10⁻⁹
2.0×10⁻⁹
1.5×10⁻⁹
1.0×10⁻⁹
5.0×10⁻¹⁰
0
2250
2300
2350
2400
WAVENUMBER, cm⁻¹

10

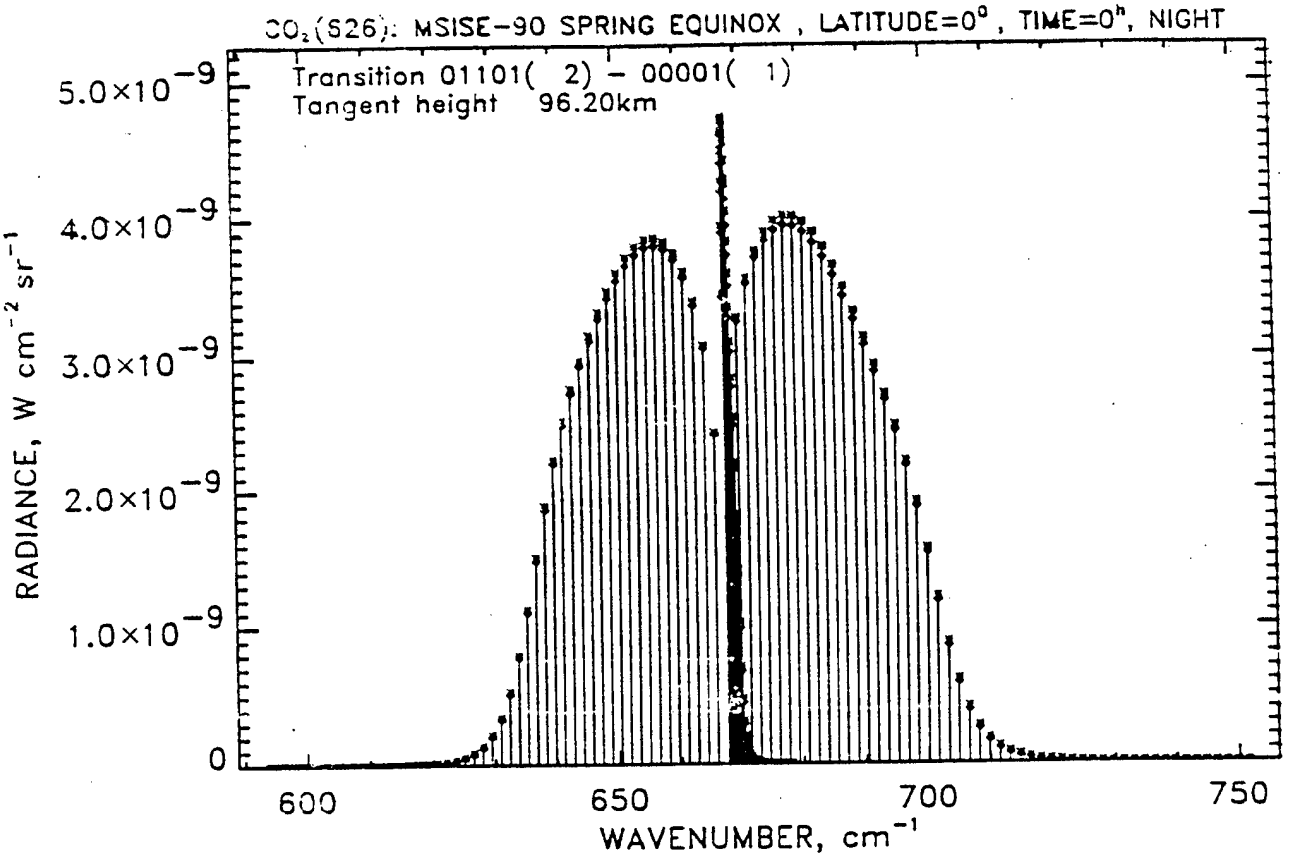
CO_2(626): MSISE-90 SPRING EQUINOX , LATITUDE=0°, TIME=0h, NIGHT
Transition 01101(2) – 00001(1)
Tangent height 96.20km
RADIANCE, W cm^{-2} sr^{-1}
5.0×10^{-9}
4.0×10^{-9}
3.0×10^{-9}
2.0×10^{-9}
1.0×10^{-9}
0
600
650
700
750
WAVENUMBER, cm^{-1}

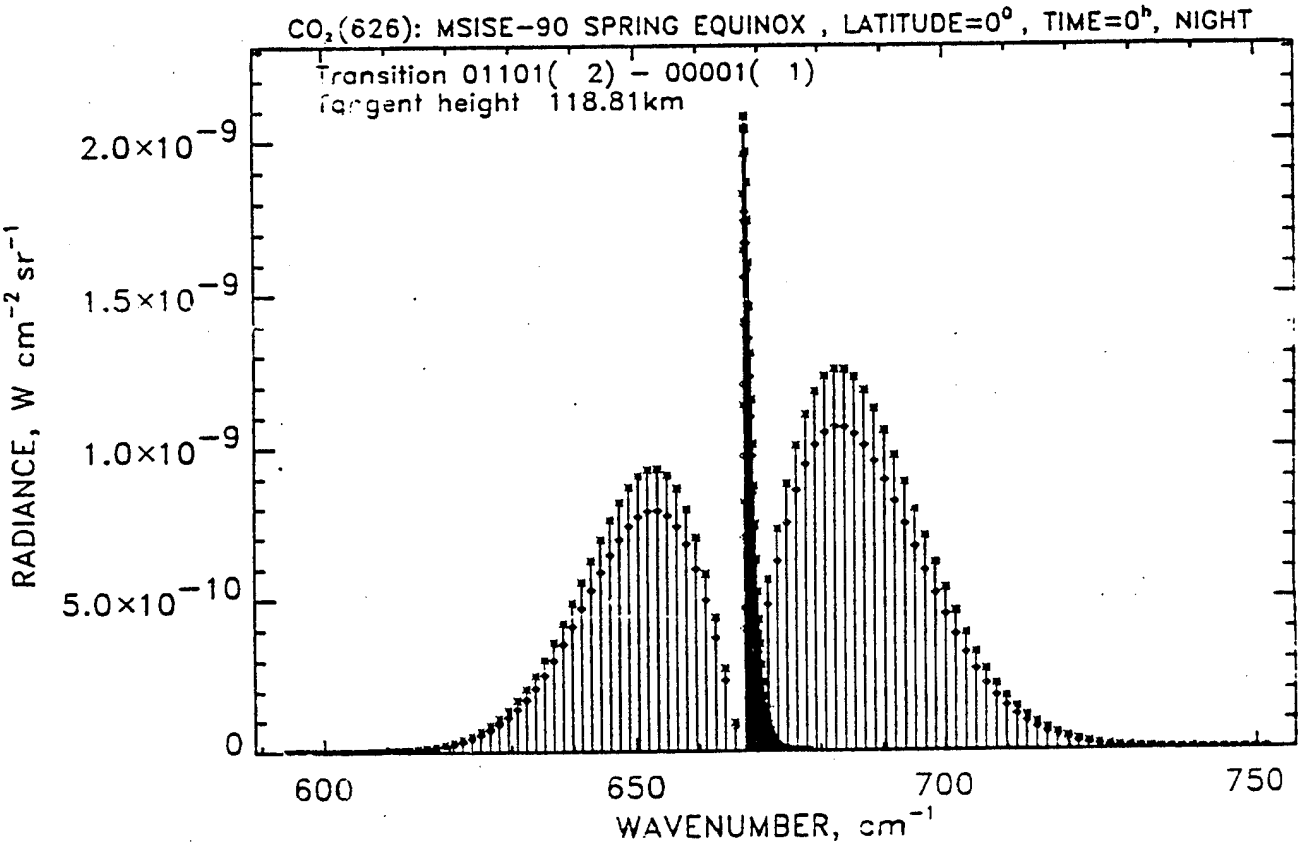
CO_2(626): MSISE-90 SPRING EQUINOX , LATITUDE=0°, TIME=0h, NIGHT
Transition 01101(2) – 00001(1)
Tangent height 118.81km
RADIANCE, W cm^{-2} sr^{-1}
2.0×10^{-9}
1.5×10^{-9}
1.0×10^{-9}
5.0×10^{-10}
0
600
650
700
750
WAVENUMBER, cm^{-1}

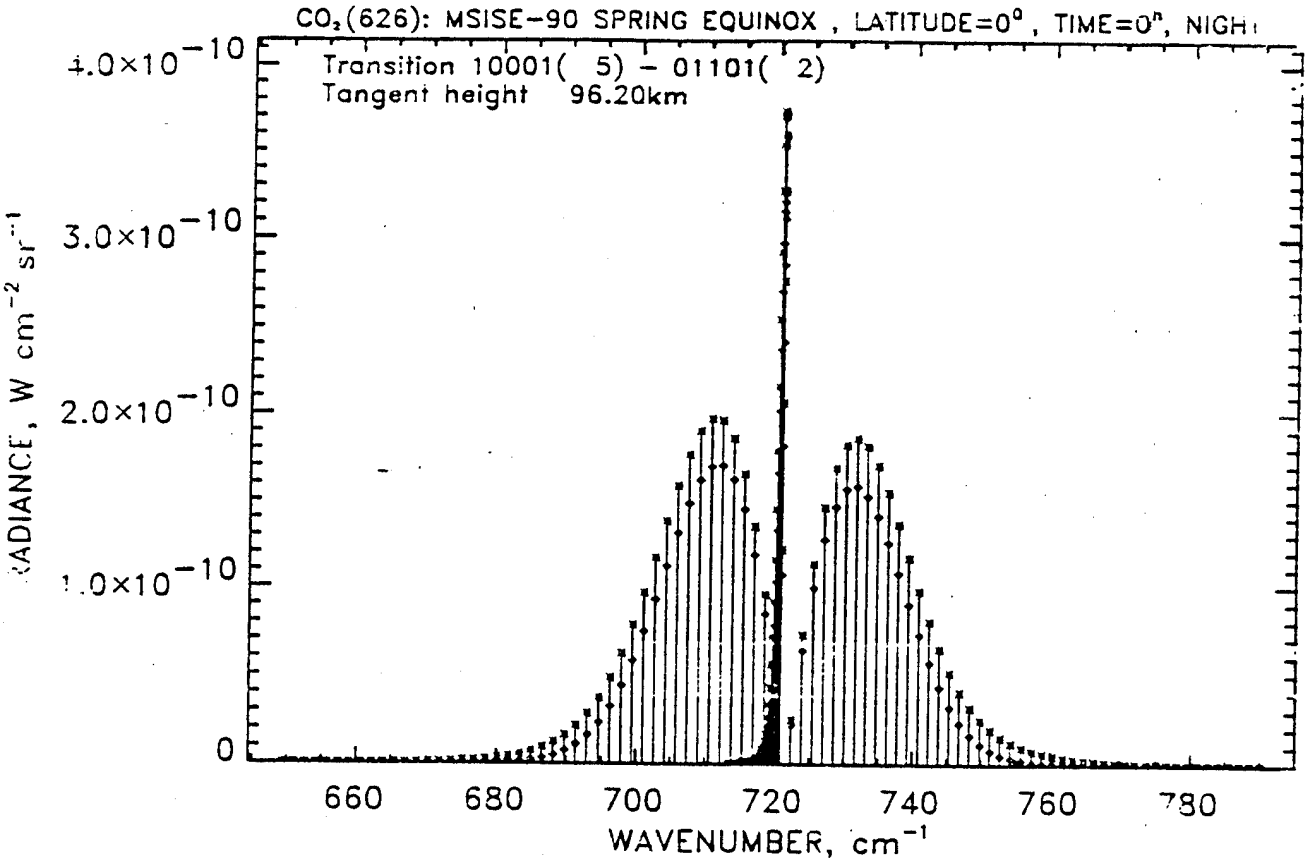
CO₂(626): MSISE-90 SPRING EQUINOX , LATITUDE=0°, TIME=0h, NIGH
Transition 10001(5) - 01101(2)
Tangent height 96.20km
4.0×10⁻¹⁰
3.0×10⁻¹⁰
2.0×10⁻¹⁰
1.0×10⁻¹⁰
0
RADIANCE, W cm⁻² sr⁻¹
660
680
700
720
740
760
780
WAVENUMBER, cm⁻¹

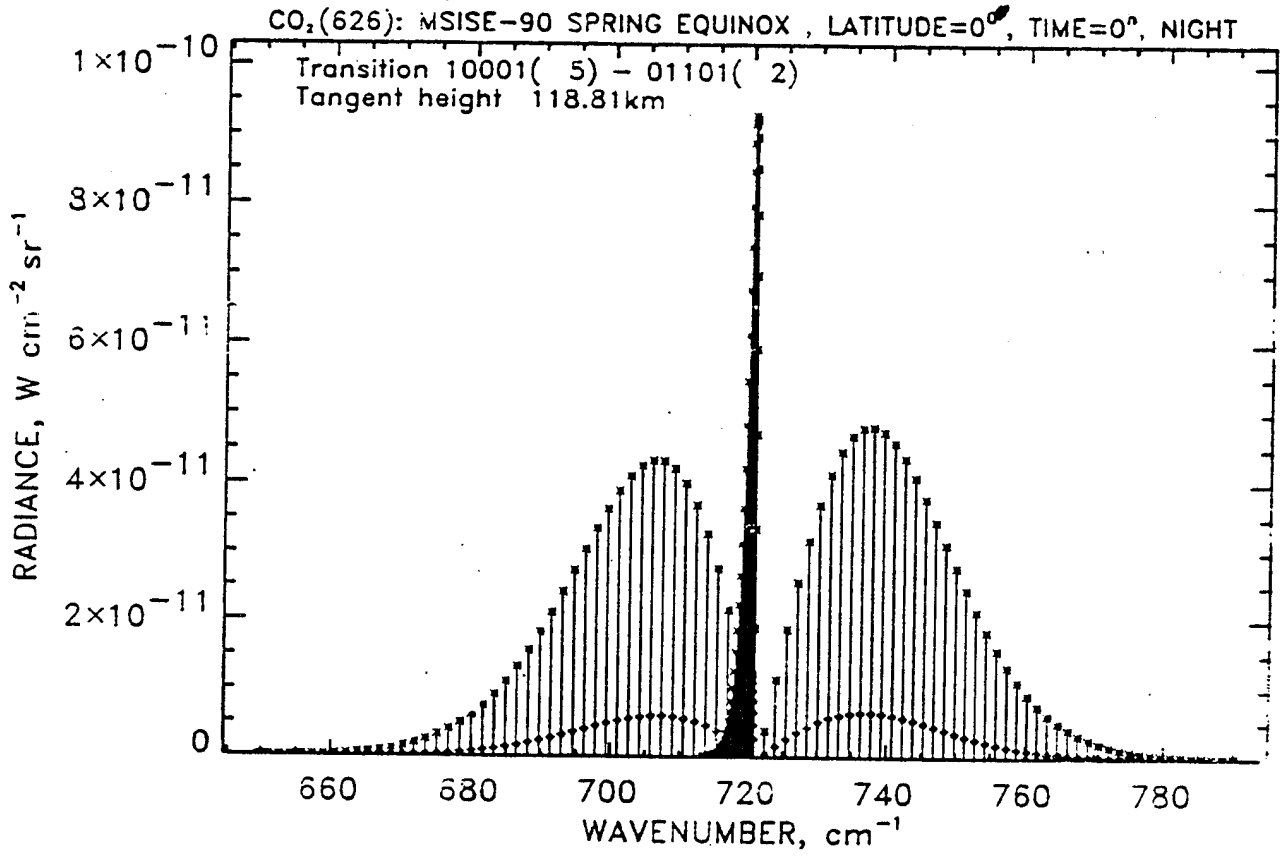
CO₂(626): MSISE-90 SPRING EQUINOX , LATITUDE=0°, TIME=0h, NIGHT
Transition 10001(5) - 01101(2)
Tangent height 118.81km
1×10⁻¹⁰
8×10⁻¹¹
6×10⁻¹¹
4×10⁻¹¹
2×10⁻¹¹
0
RADIANCE, W cm⁻² sr⁻¹
660
680
700
720
740
760
780
WAVENUMBER, cm⁻¹

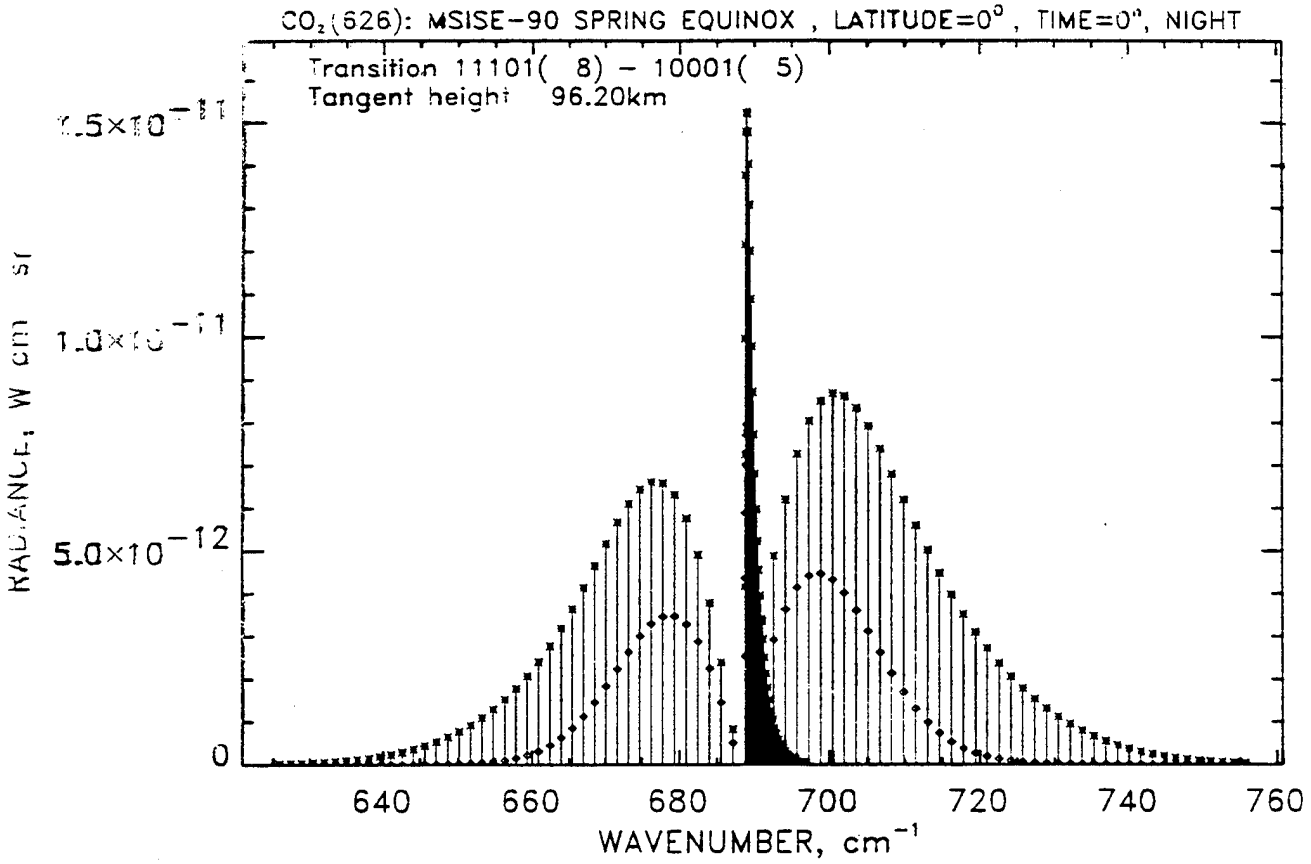
CO₂(626): MSISE-90 SPRING EQUINOX , LATITUDE=0° , TIME=0°, NIGHT
Transition 11101(8) – 10001(5)
Tangent height 96.20km
1.5×10⁻¹¹
1.0×10⁻¹¹
5.0×10⁻¹²
0
640
660
680
700
720
740
760
WAVENUMBER, cm⁻¹

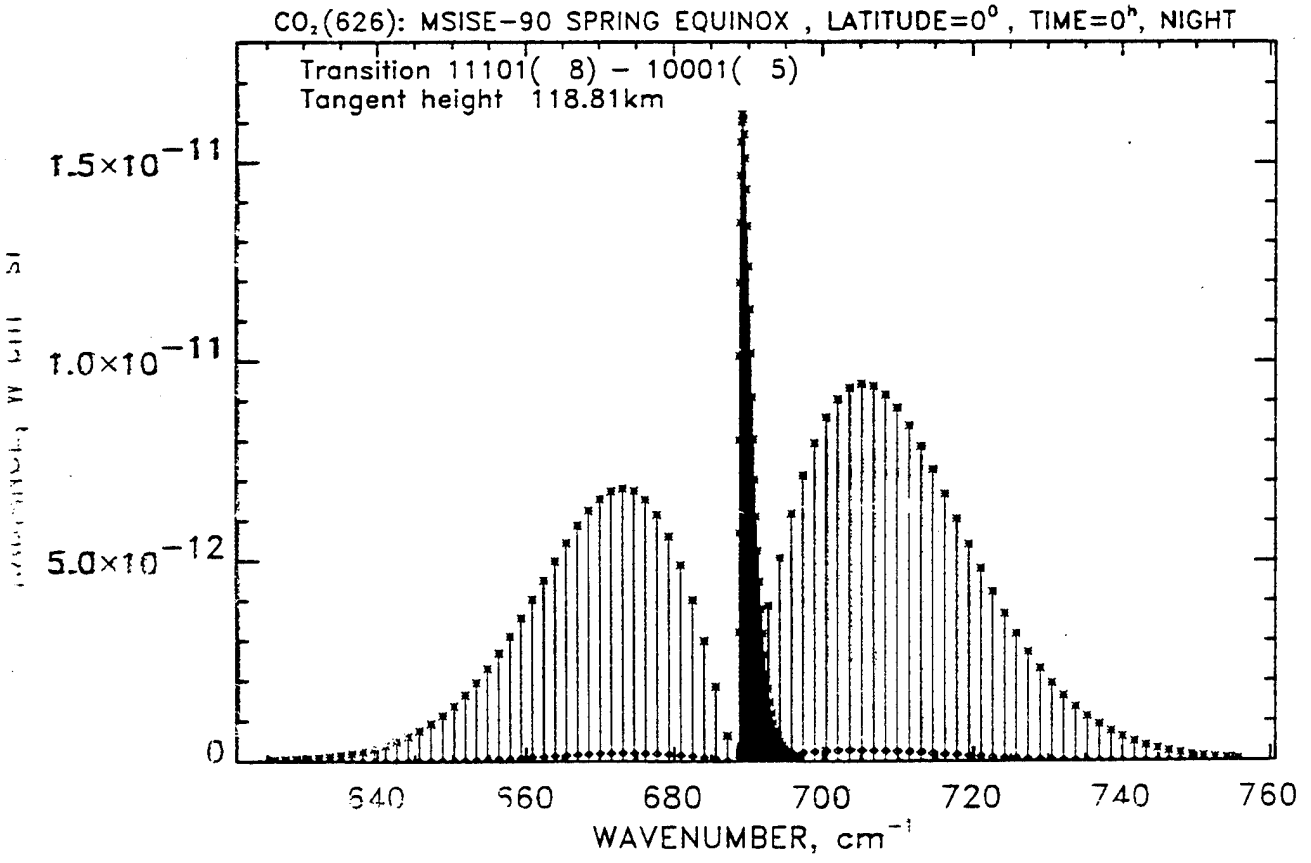
CO₂(626): MSISE-90 SPRING EQUINOX , LATITUDE=0° , TIME=0ʰ, NIGHT
Transition 11101(8) – 10001(5)
Tangent height 118.81km
1.5×10⁻¹¹
1.0×10⁻¹¹
5.0×10⁻¹²
0
640
660
680
700
720
740
760
WAVENUMBER, cm⁻¹

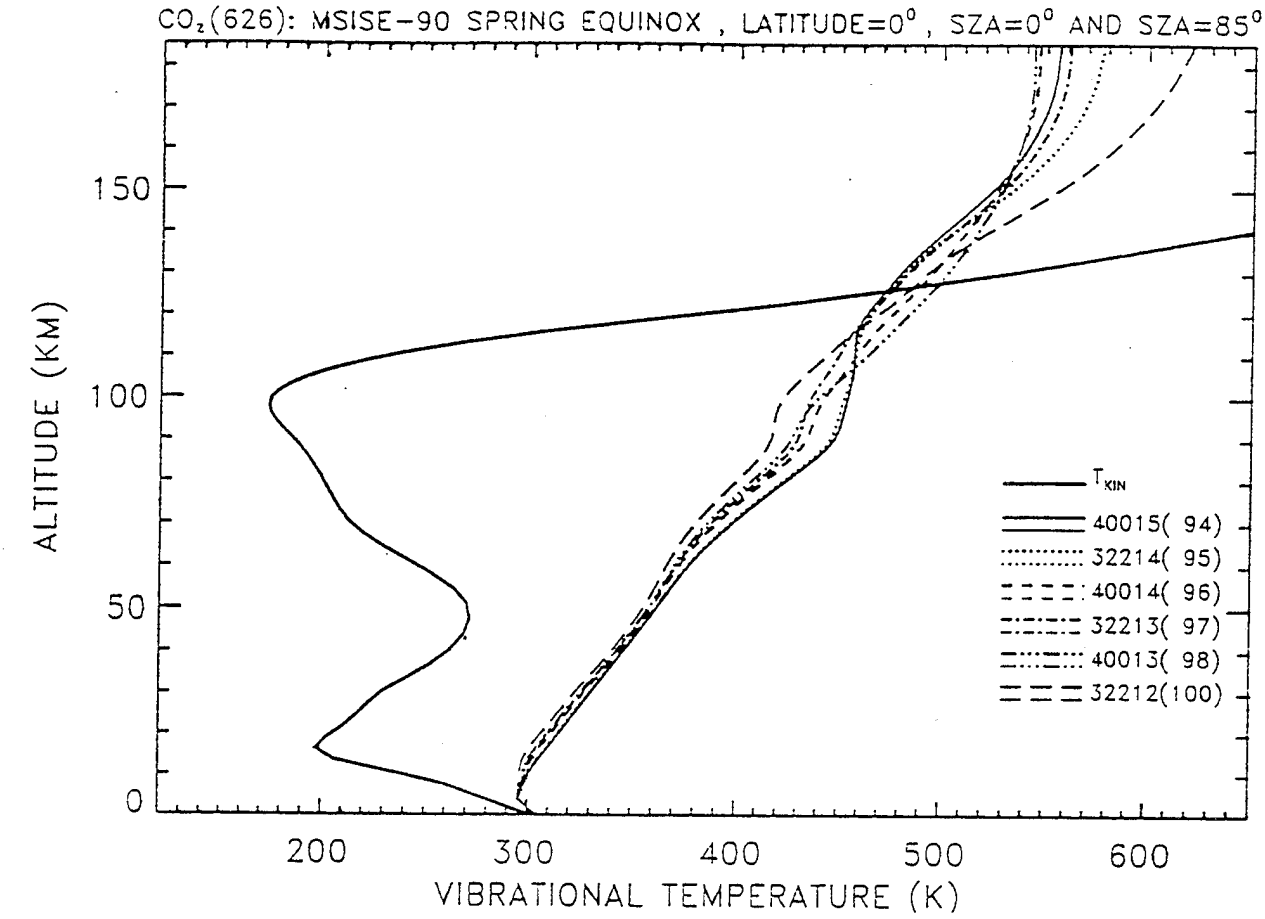
CO₂(626): MSISE-90 SPRING EQUINOX , LATITUDE=0°, SZA=0° AND SZA=85°
ALTITUDE (KM)
VIBRATIONAL TEMPERATURE (K)
T_KIN
40015(94)
32214(95)
40014(96)
32213(97)
40013(98)
32212(100)

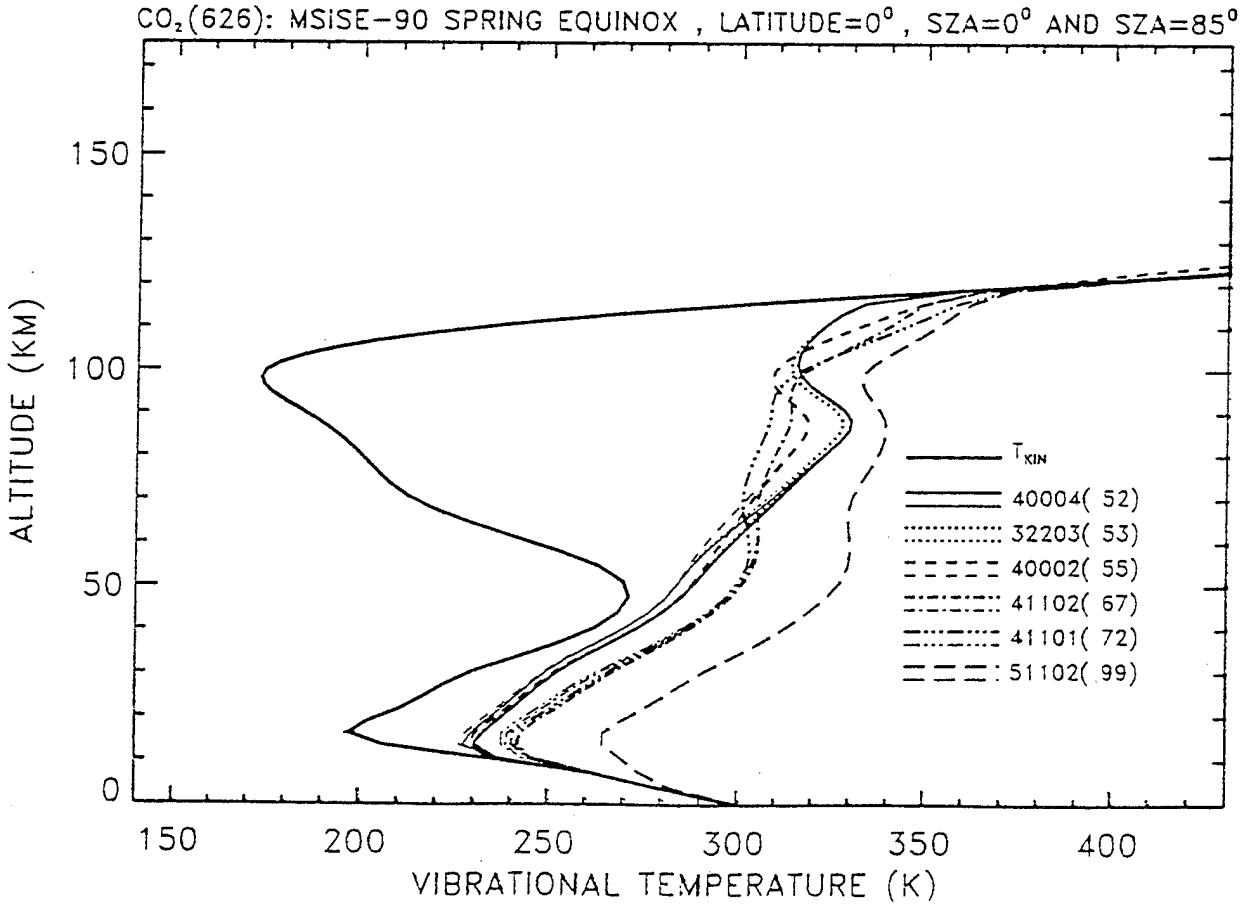
CO₂(626): MSISE-90 SPRING EQUINOX , LATITUDE=0°, SZA=0° AND SZA=85°
ALTITUDE (KM)
VIBRATIONAL TEMPERATURE (K)
T_KIN
40004(52)
32203(53)
40002(55)
41102(67)
41101(72)
51102(99)

Comparison of Line-by-Line and Modified Curtis Matrix Narrow-Band Model Approaches to Radiative Transfer in the CO_2 15 micron Bands

P.P. Wintersteiner, ARCON Corporation, Waltham, MA
M. Lopez-Puertas, Astrophysical Institute, Granada, Spain
J.R. Winick, Phillips Laboratory, Geophysics Directorate
R.H. Picard, Phillips Laboratory, Geophysics Directorate

17th Annual Review Conference
on Atmospheric Radiation Models
June 8, 1994

Objectives:

- Check validity of infrared radiative transfer methods by comparing band model with line-by-line approach
- Validate calculations of
  - CO_2 vibrational populations and emission rates
  - Atmospheric cooling by 15 micron emission
- Demonstrate capability of forward models for use with inversion/ retrieval algorithms

Approach:

- Isolate effects of the different radiative transfer methods by performing parallel calculations that are (otherwise) as nearly identical as possible
- Compare results:
  - Vibrational temperatures of CO_2 bend-stretch states
  - Atmospheric infrared cooling rates

RAD Algorithm

- Iterative algorithm
  - Method of successive substitution
    - Start with provisional vibrational temperatures
    - Calculate radiative-excitation rates
    - Recalculate vibrational temperatures assuming steady state
  - Small equation set (different altitudes not explicitly coupled)
  - Rapid convergence assured by nested iteration scheme
- Fundamental quantity: specific intensity of radiation
- Full line-by-line radiative transfer calculation
- Fully variable emission and absorption lineshapes
  - Dependence on temperature, pressure

Modified Curtis Matrix (MCM) Model

- Inversion technique
  - Curtis Matrix method
  - Simultaneous solution of linear equations
  - Larger equation set (different altitudes explicitly coupled)
- Fundamental quantity: heating rate
- "Pseudo" line-by-line algorithm
  - Numerical integration over frequency
  - Reduced number of equivalent lines, grouped by strength
- Averaging over atmospheric paths
  - Curtis-Godson approximation
  - Lineshape, temperature, density, pressure

Correlating the Models

- Input model atmospheres
  - Temperature, constituent densities
  - Layering: 80 layers, 40-160 km, 1.5 km/layer
- Thermal and vibrational mechanisms
- Rate constants for collisional processes
- Radiative transition data
  - 626 fundamental, minor isotope fundamentals, 626 hot bands
  - HITRAN'92 lines
  - Temperature dependence of line strengths
- CO_2 isotopic abundances
- Treatment of lower boundary

Test Cases

- Model Atmospheres
  - US Standard Atmosphere, 1976 (midlatitude, "average" structure)
  - CIRA 80 degrees S, December (warm stratopause, cold mesopause)
  - CIRA 80 degrees N, December (cold stratopause, warm mesopause)

- Rate constant for deactivation of bending mode by [O]
  - "Fast" case: $k_o = 6.1 \times 10^{-12}\ cm^3 / sec$ @ 300 K
    (Sharma and Wintersteiner, GRL 17, 2201, 1990)
  - "Slow" case: $k_o = 2.0 \times 10^{-13}\ cm^3 / sec$ @ 300 K

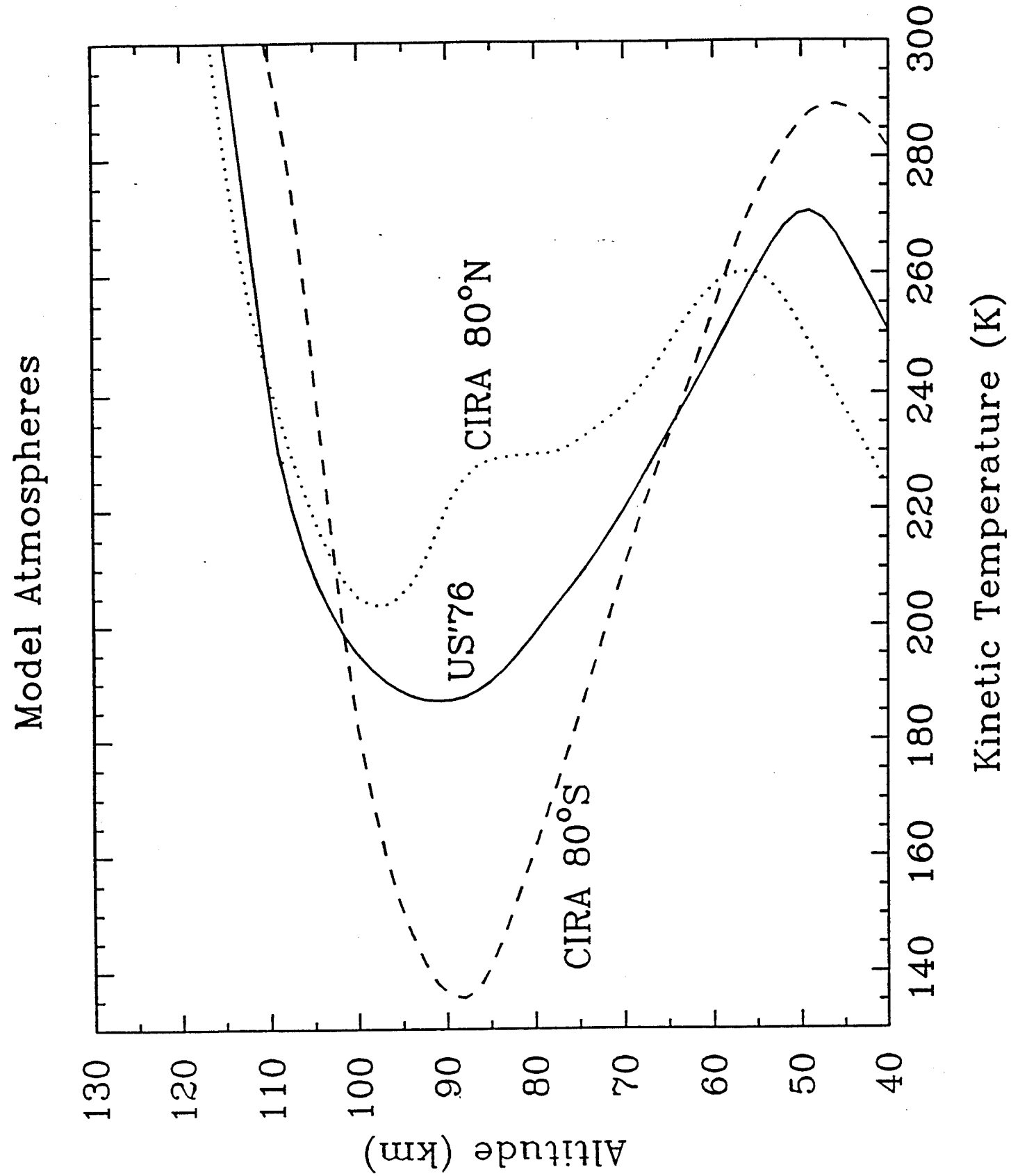
Model Atmospheres
US'76
CIRA 80°N
CIRA 80°S
Altitude (km)
130
120
110
100
90
80
70
60
50
40
Kinetic Temperature (K)
140
160
180
200
220
240
260
280
300

Fig 1

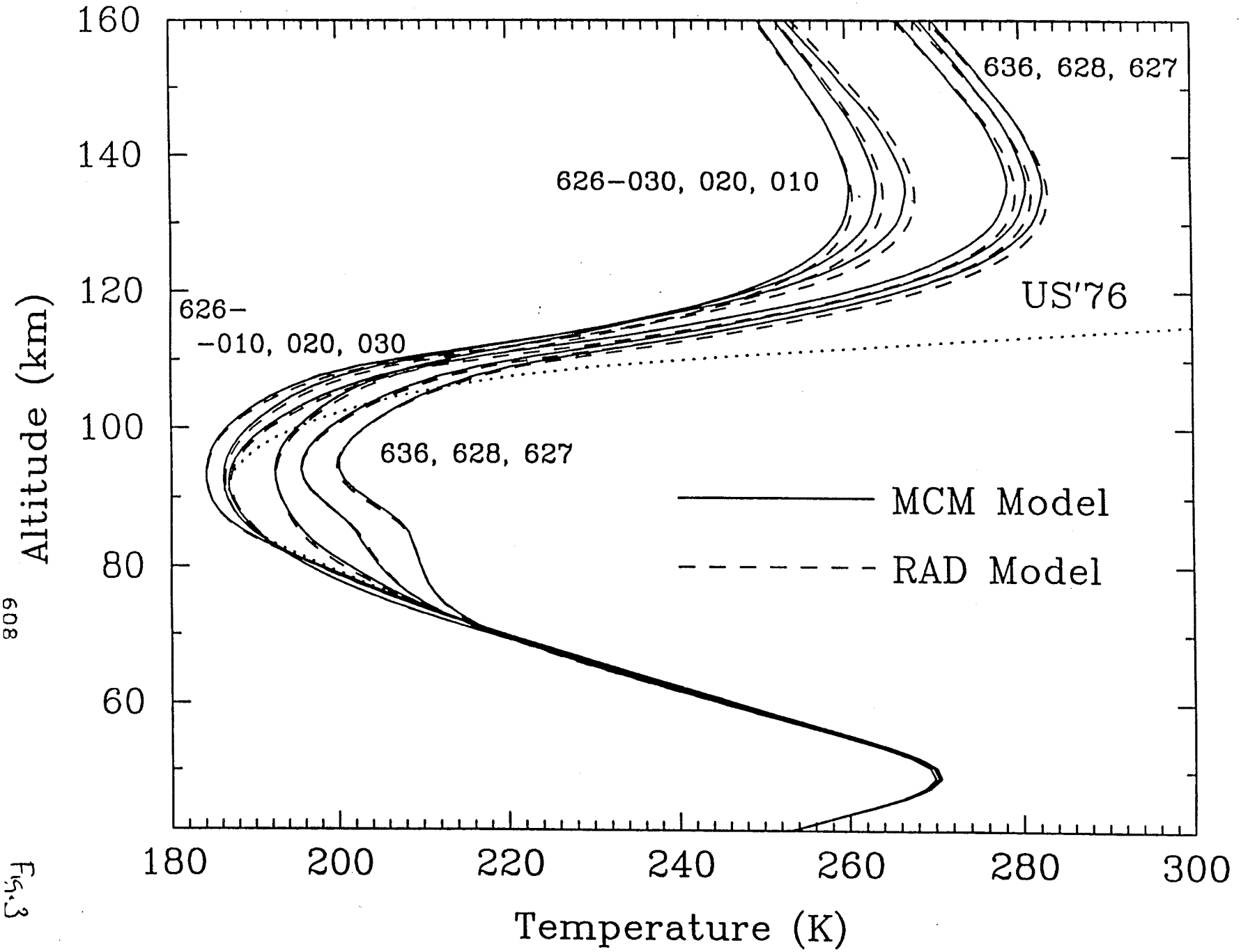
160
140
120
100
80
60
Altitude (km)
180
200
220
240
260
280
300
Temperature (K)
636, 628, 627
626–030, 020, 010
626–
–010, 020, 030
US'76
636, 628, 627
MCM Model
RAD Model

608

Fig. 3

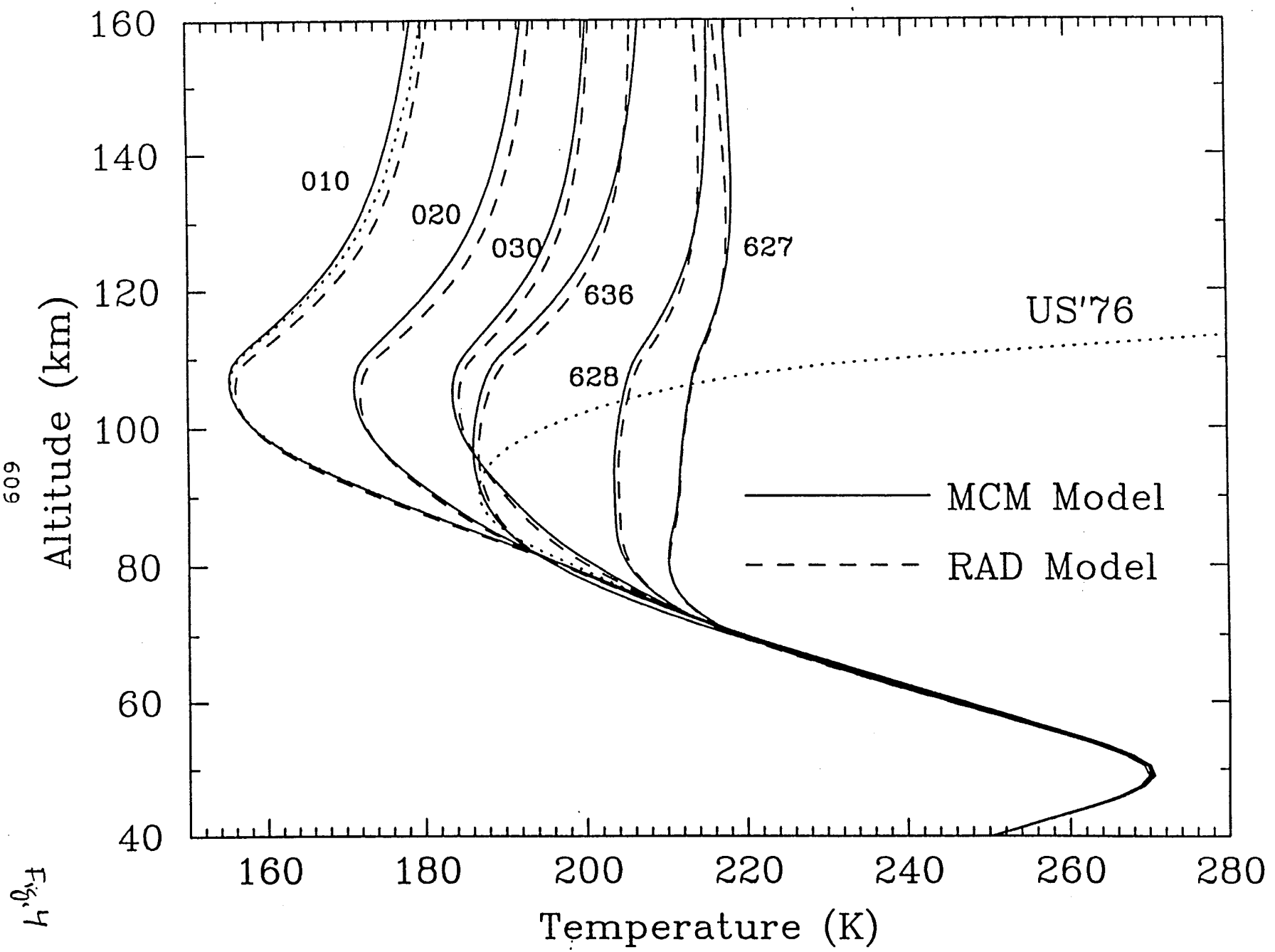
160
140
120
100
80
60
40
Altitude (km)
160
180
200
220
240
260
280
Temperature (K)
010
020
030
636
627
628
US'76
MCM Model
RAD Model

609

Fig. 7

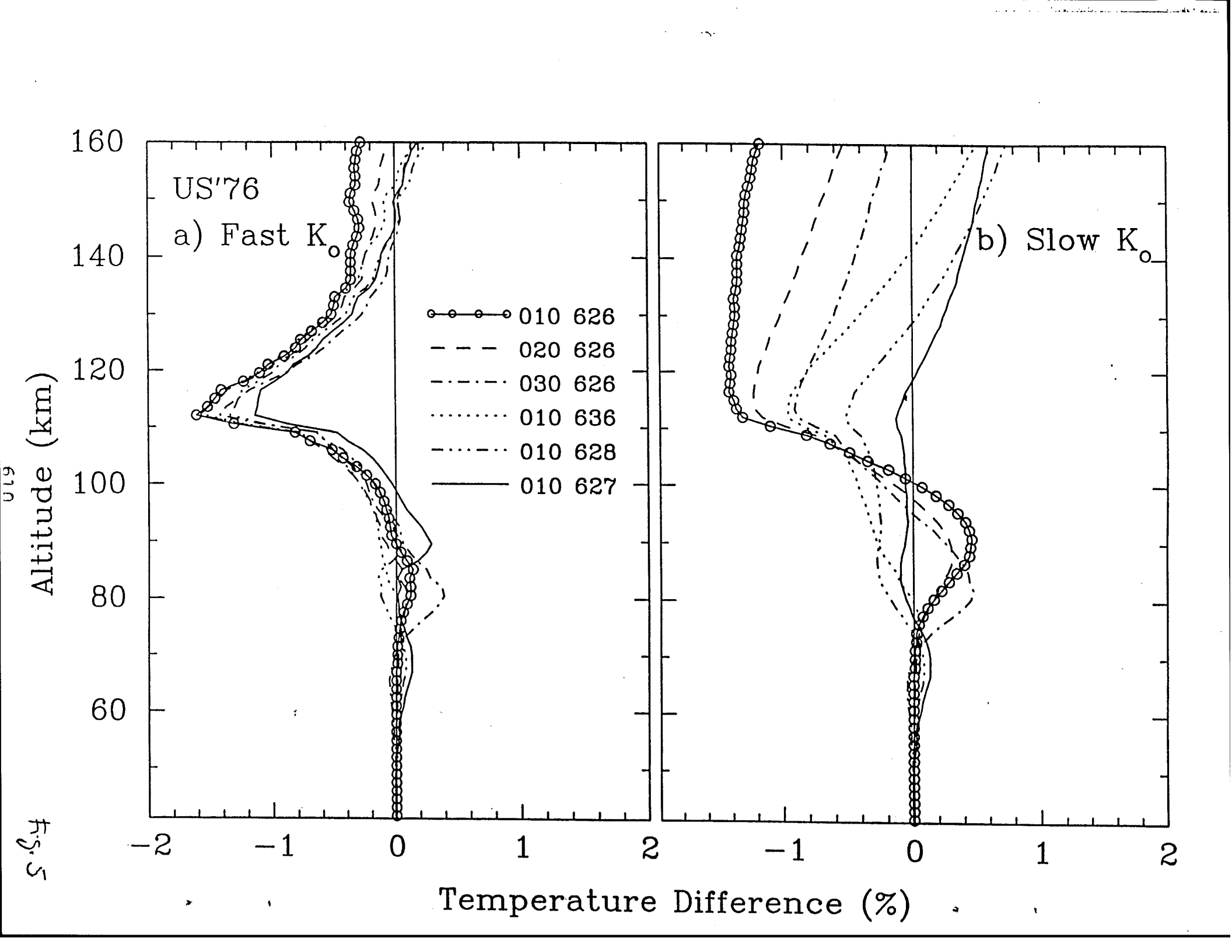
US'76
a) Fast K_o
b) Slow K_o
010 626
020 626
030 626
010 636
010 628
010 627
Altitude (km)
160
140
120
100
80
60
−2
−1
0
1
2
Temperature Difference (%)

Summary of Results, Vibrational Temperatures

- "Fast" case (realistic kinetic parameters)
  - Below 70 km, excellent agreement
  - In the upper mesosphere

    absolute differences < 1 K, for US'76 and CIRA 80 N, all bands

    absolute differences < 2 K for CIRA 80 S except 626-030 (< 3 K)

    626-010 level quite close to LTE at summer polar mesopause
  - In the thermosphere

    MCM consistently predicts lower vibrational temperatures

    peak differences < 4 K, occurring near 115-120 km
- "Slow" case (best test of radiative transfer)
  - Absolute differences < 2.5 K for US'76 and CIRA 80 N, all bands
  - Differences < 3 K (mesosphere) or 6 K (thermosphere) for CIRA 80 S
  - MCM consistently predicts

    lower vibrational temperatures in the thermosphere

    higher vibrational temperatures at the mesopause

Understanding Models' Differences

- Issue
  - MCM underestimates total radiative excitation in thermosphere
  - MCM overestimates total radiative excitation near mesopause
- Take MCM to "line-by-line limit"
  - Eliminate grouping of equivalent lines
  - Better agreement in thermosphere
  - General pattern of discrepancies persists
- Analyze total radiative excitation in thermosphere
  - Compare contributions from different source layers
  - MCM calculates

    less absorption from source layers below the mesopause

    more absorption from source layers above the mesopause

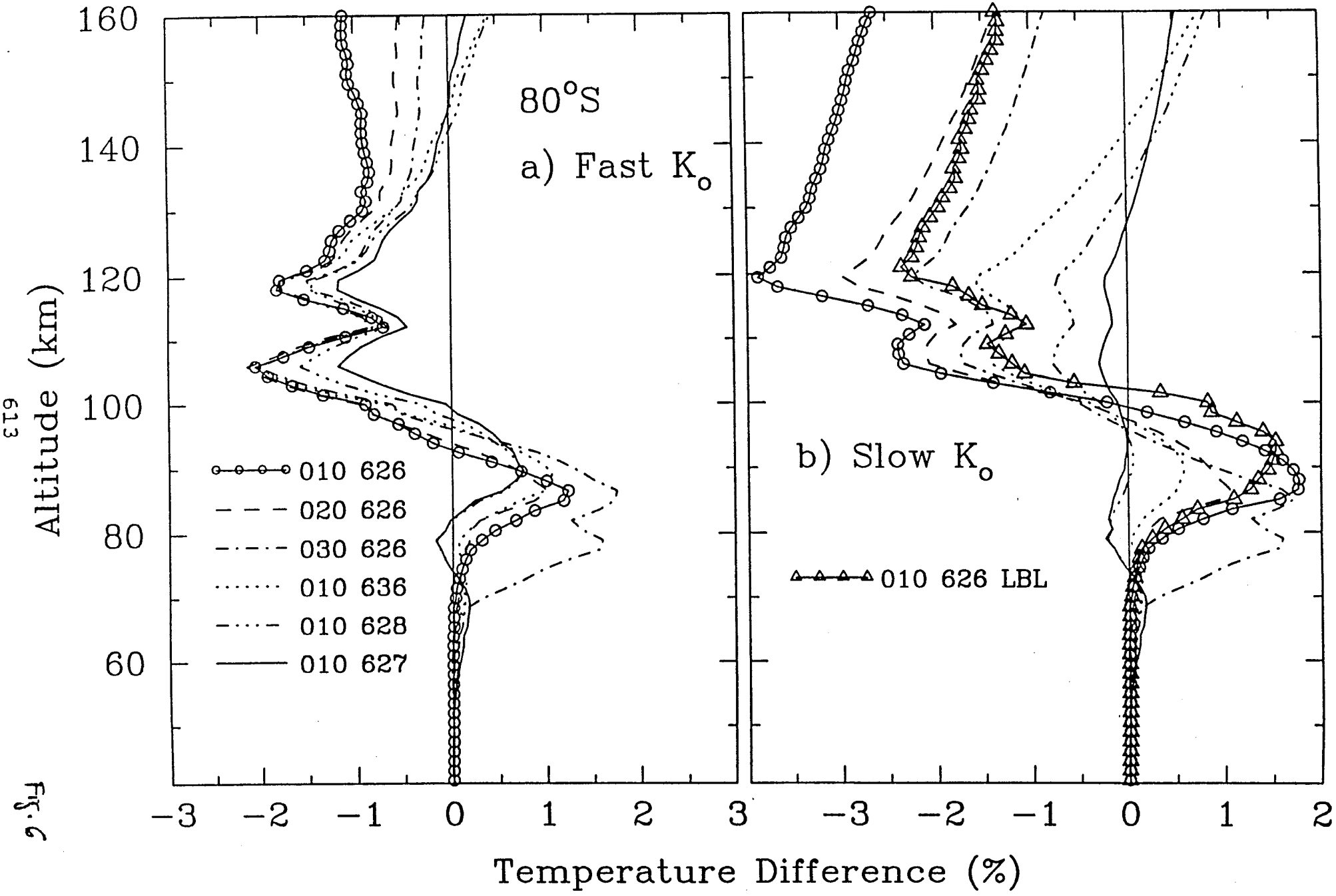
80°S
a) Fast K_o
b) Slow K_o
010 626
020 626
030 626
010 636
010 628
010 627
010 626 LBL
Altitude (km)
160
140
120
100
80
60
−3
−2
−1
0
1
2
3
Temperature Difference (%)

613

Fig. 2

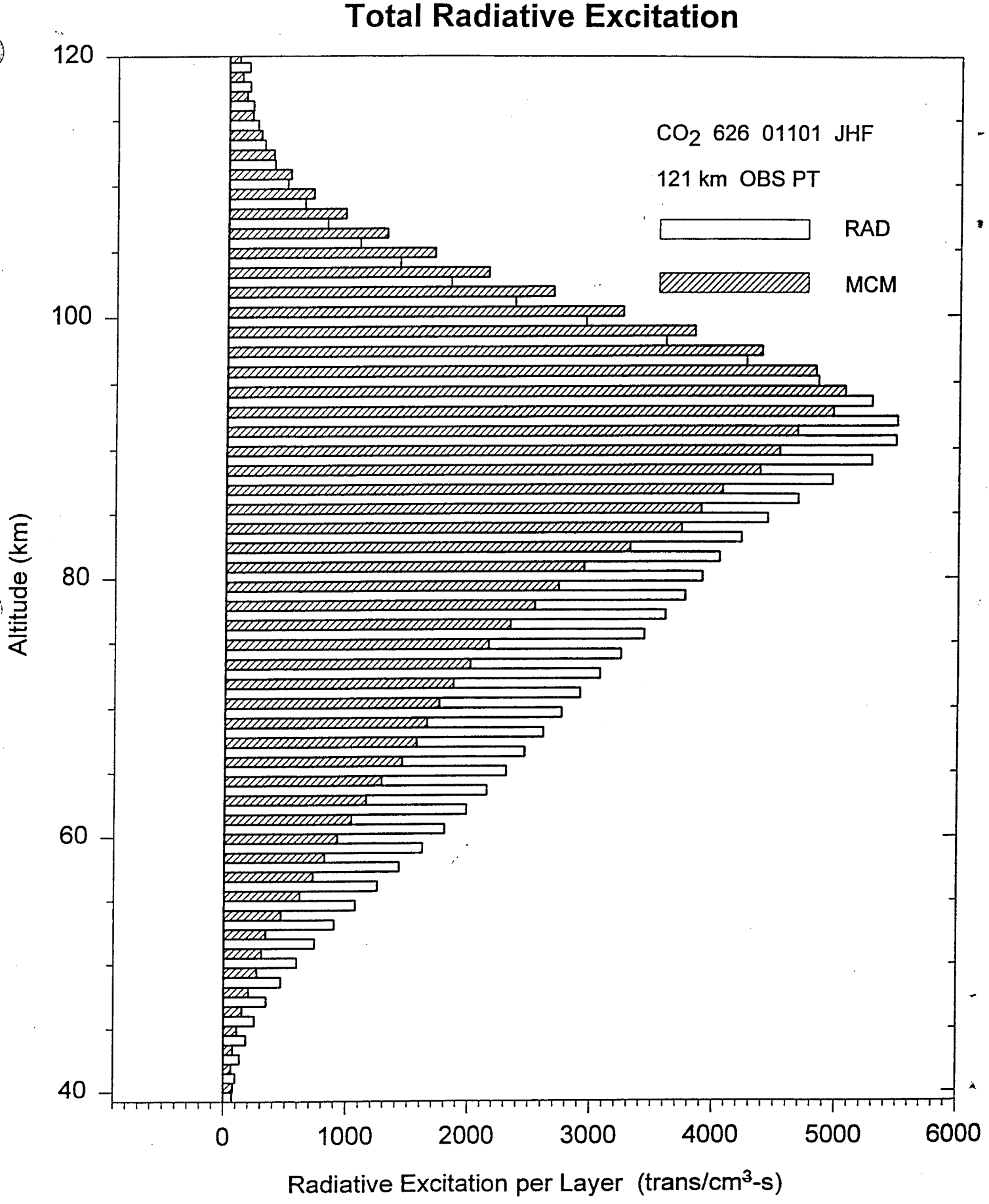
Total Radiative Excitation
CO_2 626 01101 JHF
121 km OBS PT
RAD
MCM
Altitude (km)
120
100
80
60
40
0
1000
2000
3000
4000
5000
6000
Radiative Excitation per Layer (trans/cm^3-s)

Understanding Models' Differences (cont.)

- MCM path-weighted temperature smaller than proper absorption temperature; path-weighted pressure greater
  - absorption lineshape narrower than in RAD
  - less absorption in wings (lower-altitude, warmer source regions)
  - more absorption in line centers (higher-altitude, colder source regions)
- Result: MCM calculates less total radiative excitation in thermosphere

- Analyze radiative excitation at the mesopause
  - MCM path-weighted temperature greater than proper absorption temperature; path-weighted pressure greater
    - absorption lineshape broader than in RAD
    - more absorption in wings (lower-altitude, warmer source regions)
    - less absorption in line centers (higher-altitude, colder source regions)
  - Result: MCM calculates more total radiative excitation at mesopause
- Residual discrepancies explained by MCM path-averages

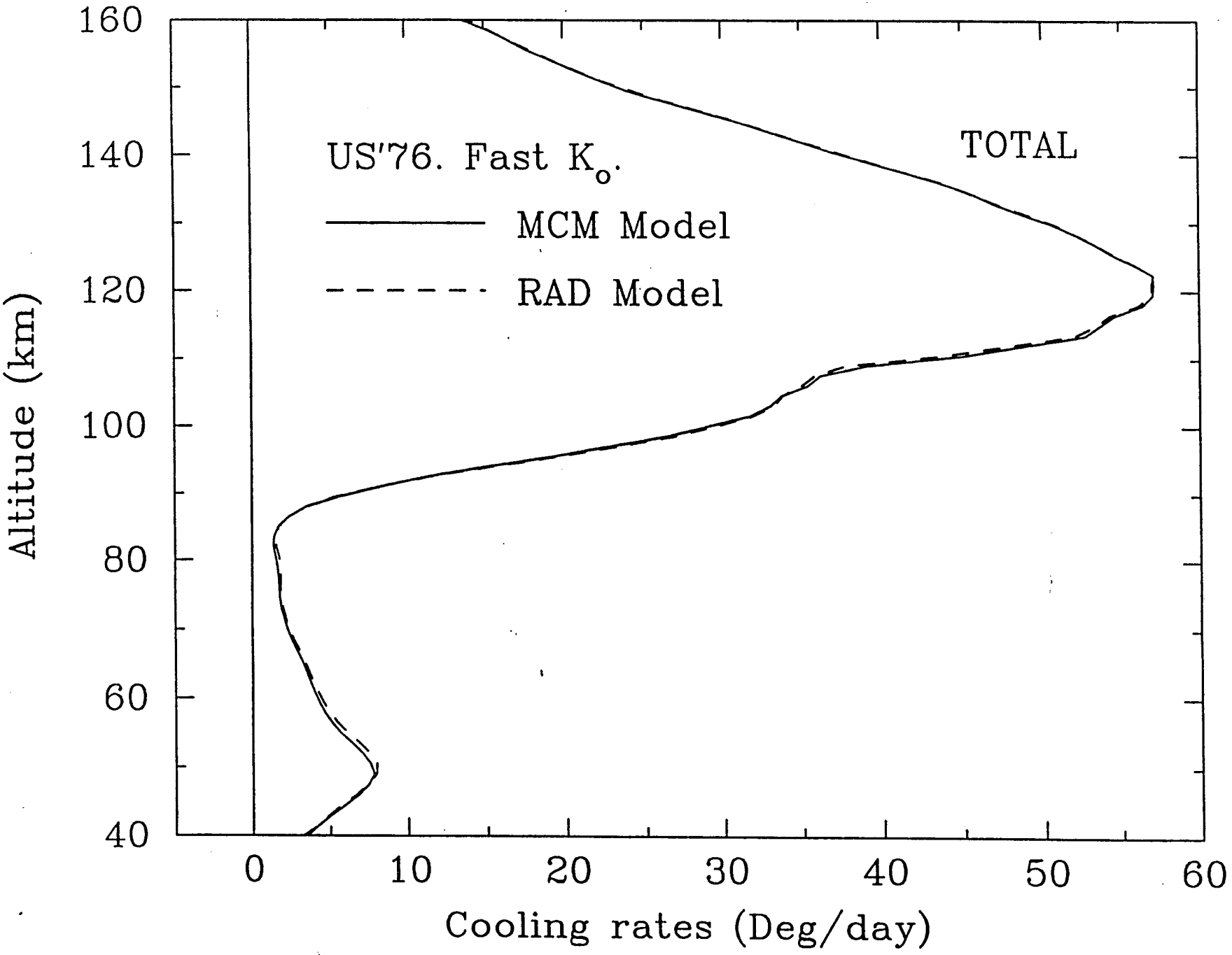
160
140
120
100
80
60
40
Altitude (km)
US'76. Fast K_o.
MCM Model
RAD Model
TOTAL
0
10
20
30
40
50
60
Cooling rates (Deg/day)

616

Fig. 9

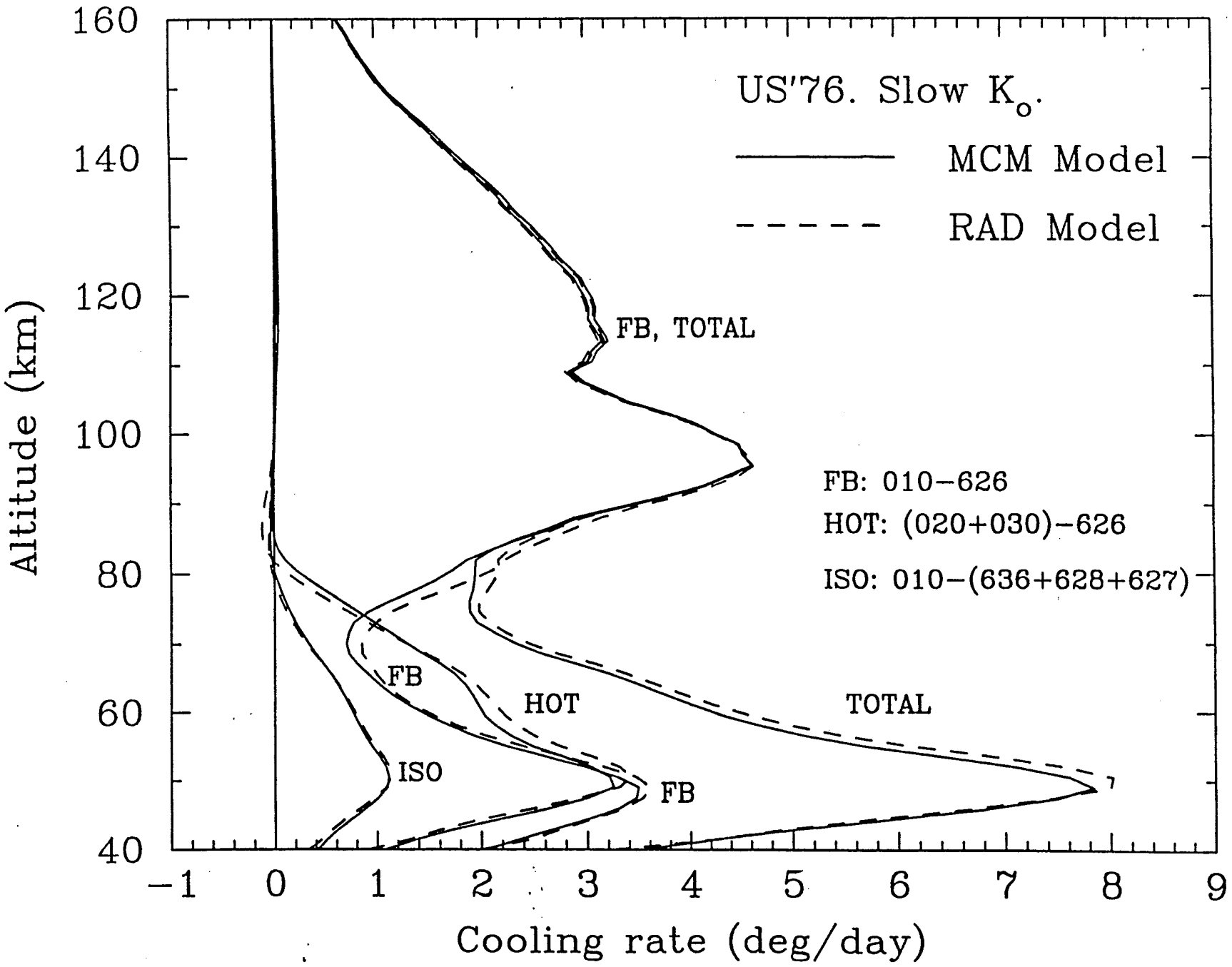
US'76. Slow K_o.
MCM Model
RAD Model
FB, TOTAL
FB: 010−626
HOT: (020+030)−626
ISO: 010−(636+628+627)
FB
HOT
TOTAL
ISO
FB
Altitude (km)
Cooling rate (deg/day)
160
140
120
100
80
60
40
−1
0
1
2
3
4
5
6
7
8
9

Summary of Results, Cooling

- Lower mesosphere
  - Absolute differences < 0.5 K/day (~ 6-8 % of total cooling)
  - Agreement consistent for all bands
    - 626 fundamental
    - isotopic fundamentals
    - hot bands
  - "Fast" and "slow" cases give the same results
- Mesopause and thermosphere
  - Differences significant only for "fast" case
  - Absolute differences < 3 K/day, all altitudes
  - Peak differences occur in narrow altitude ranges

Conclusions

- The two radiative transfer algorithms give consistent results for populations and cooling
  - Strong and weak bands
  - 120-km altitude range
  - Extreme temperature structures
  - Extreme kinetic parameters
- Small discrepancies understood
  - Grouping of equivalent lines in MCM
  - Path-average temperature, pressure, affect absorption lineshape in MCM
- Vibrational temperatures and cooling rates validated
- Results are accurate enough to be used for retrievals from non-LTE atmospheric emissions
- Cooling rates are accurate enough for use in dynamical models and thermal-balance calculations

Subthermal NO($^2\Pi_\Omega$) Spin-Orbit Distributions in the Thermosphere

S.J. Lipson, P.S. Armstrong[1], J.A. Dodd[1],
J.R. Lowell, W.A.M. Blumberg, and R.M. Nadile
Phillips Laboratory, Geophysics Directorate,
Hanscom AFB, MA
[1]Stewart Radiance Laboratory, Bedford MA

Annual Review Conference on
Atmospheric Transmission Models

June 1994

Supported by: Air Force Office of Scientific Research
and the Ballistic Missile Defense Organization

CIRRIS 1A EXPERIMENT

- **High S/N earthlimb spectra recorded by Shuttle-based Michelson interferometer (1 cm^{-1} resolution)**
- **Nitric oxide ($^2\Pi_\Omega$, $\Omega = {}^1/_2, {}^3/_2$) $\Delta v = 1$ emissions**

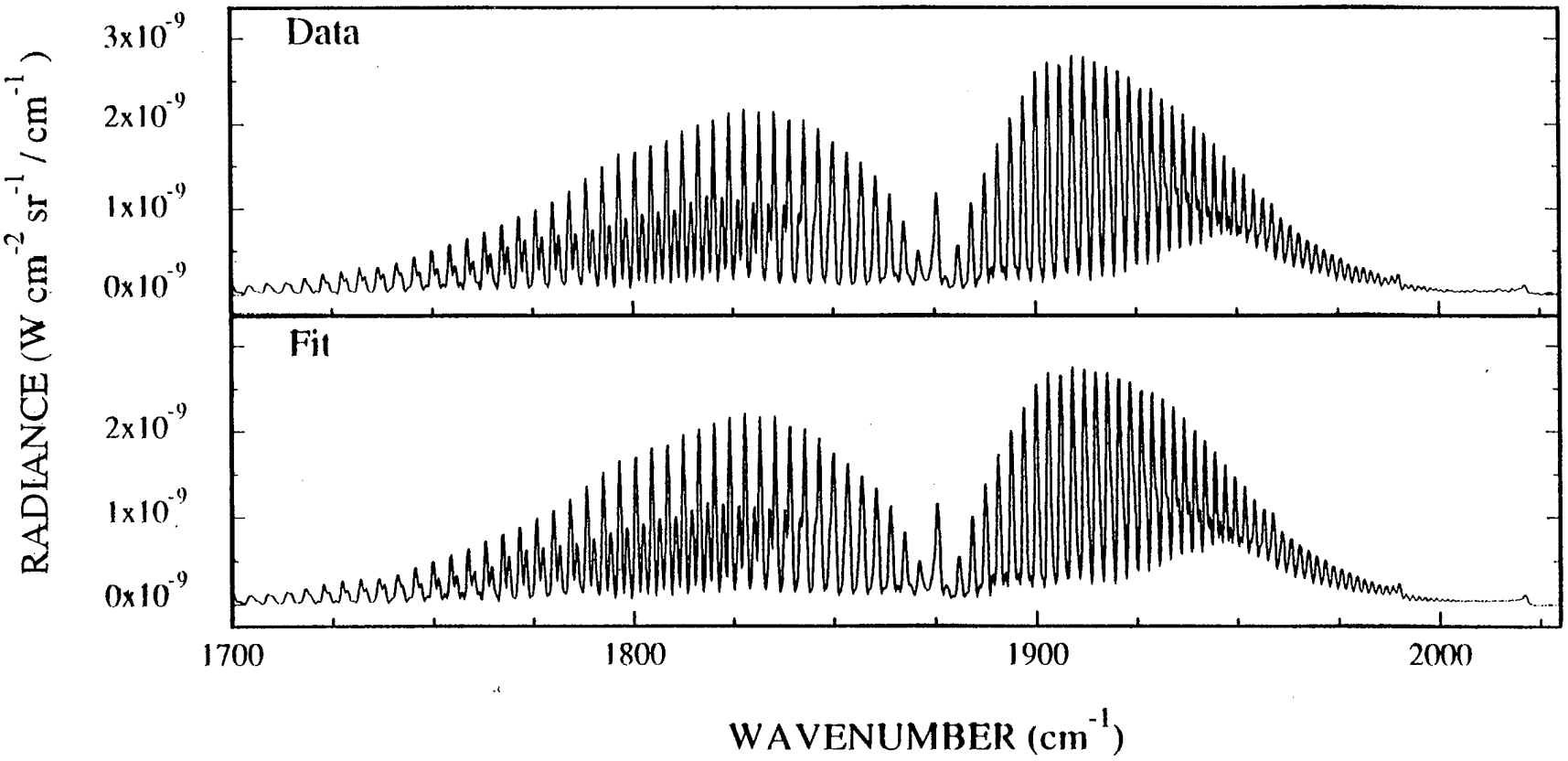

Spectral Fits

- Nonequilibrium and equilibrium synthetic spectra
- Nonequilibrium fit matches spin-orbit features

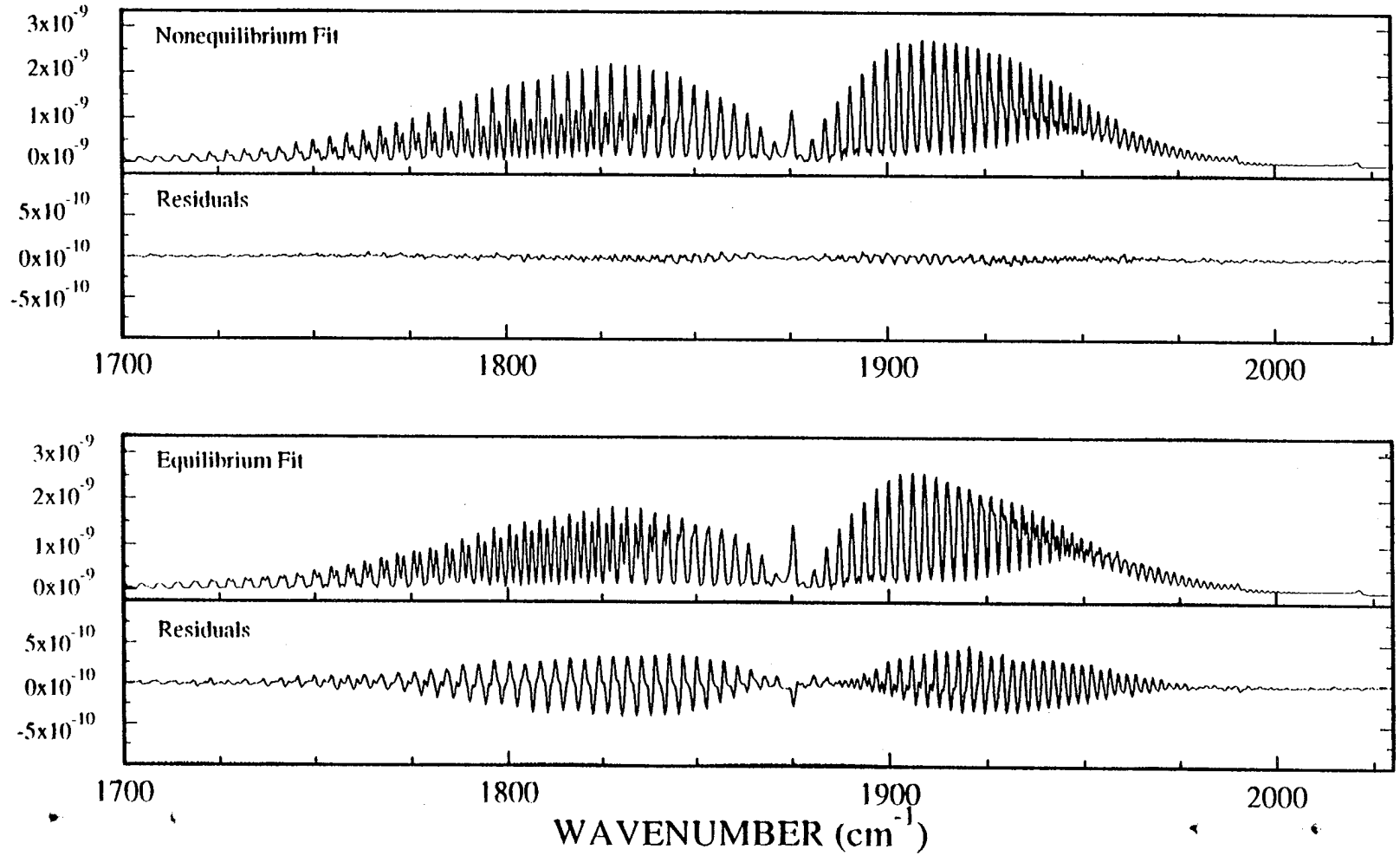

Analysis of Subthermal Nitric Oxide Spin-Orbit Population Distributions

- Populations obtained by nonlinear synthetic spectral fitting
  - Spin-orbit equilibrium at T(rotation) gives large residuals
  - Best fit obtained for independent spin-orbit populations
- Large enhancement in lower spin-orbit manifold population
  - Energy separation between manifolds is only 120 cm^{-1}
  - Effective spin-orbit temperature 200 K instead of 900 K
- Spin-orbit population enhancement increases with altitude
  - Collisional relaxation becomes dominant at lower altitudes
  - Limb view line-of-sight effects important below 135 km
- Trend of population ratio is consistent throughout data set
  - Much less variation seen than in radiance or temperature
  - Possible effect of chemical production seen in auroral data

Nitric Oxide Energy Level Diagram

- **Energies shown for the Ω=1/2, 3/2 spin-orbit manifolds for v = 0, 1**

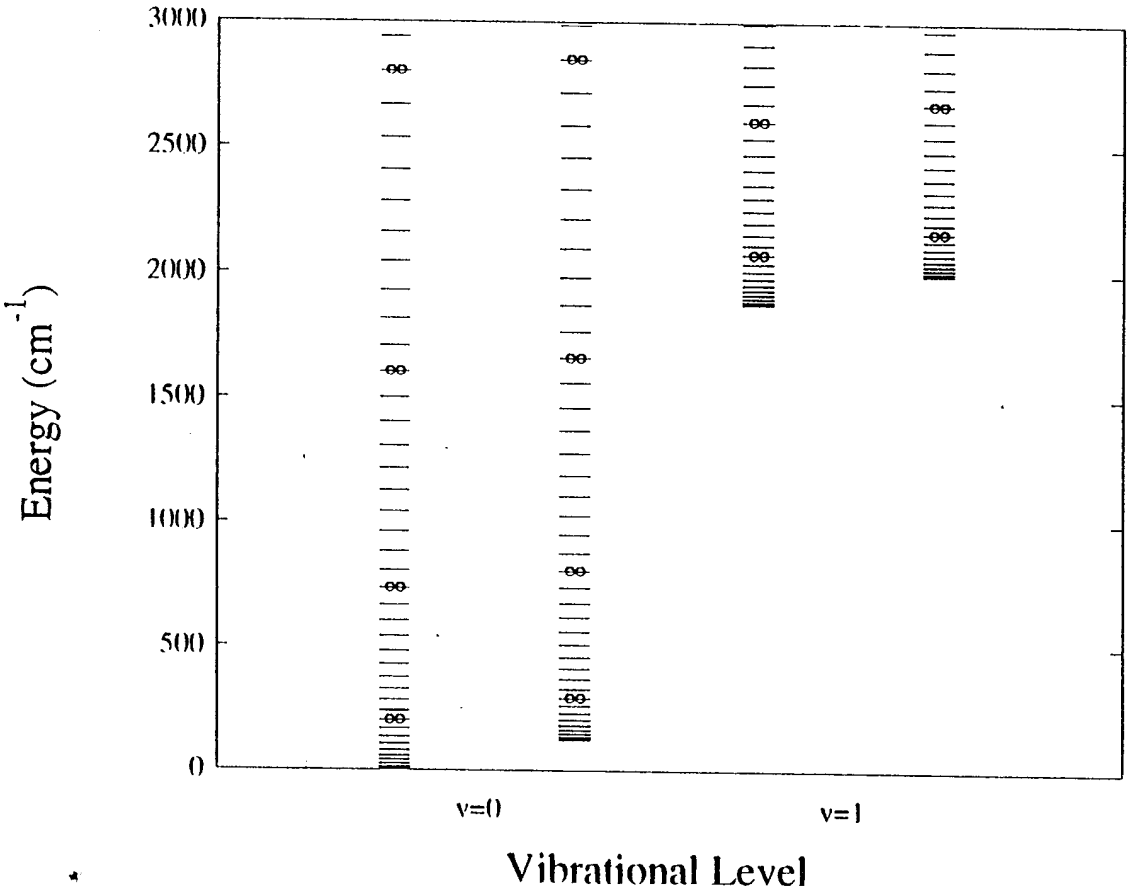

Daytime and Nighttime NO Spectra

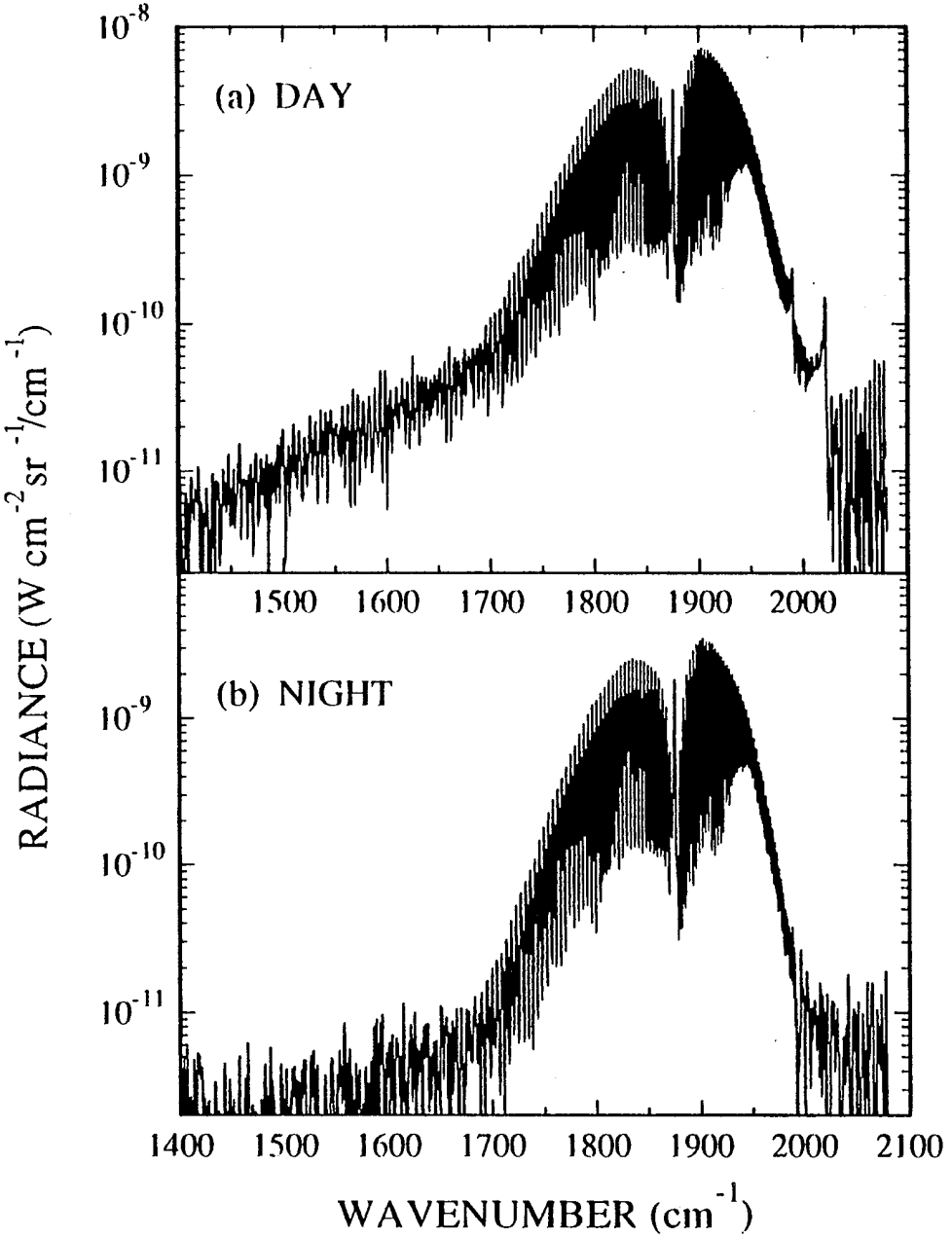

Spin-Orbit Altitude Profile

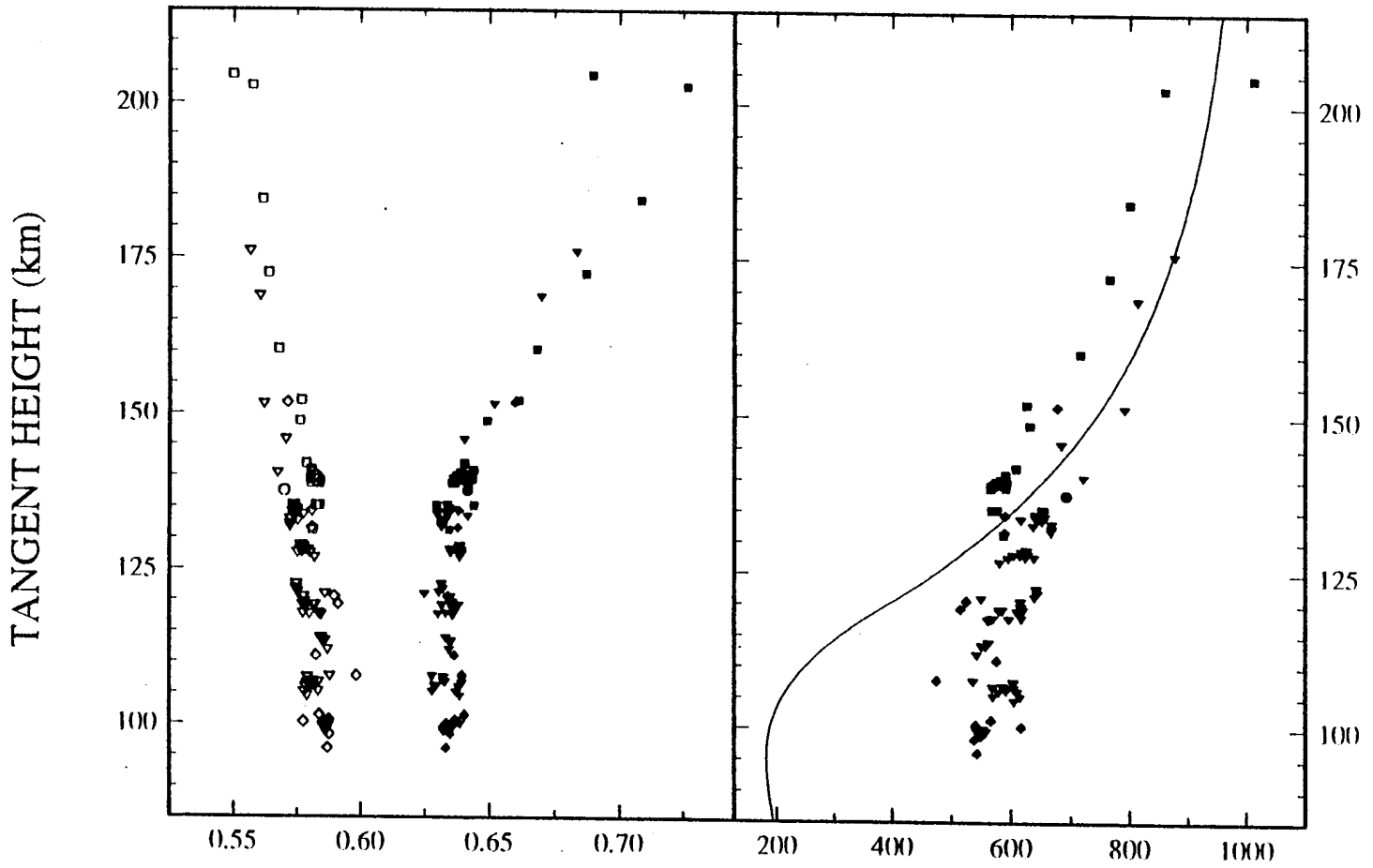

$\Omega = {}^{1}/_{2}$ FRACTION

Expectation: open symbols

Observation: filled symbols

TEMPERATURE (K)

MSIS Temperature Profile: line

Observation: symbols

Origin of Subthermal Spin-Orbit Population Distribution

- Leading candidate is collisional uppumping by O atoms, main source of NO(v=1) in thermosphere
- Radiation, primary NO(v=1) loss mechanism, does not induce spin-orbit state preference
- Collisional relaxation occurs at insufficient rate at higher altitudes
- Chemical production has diurnal variation not observed in sublevel distributions

Impact On Related Research

- Nonequilibrium OH sublevel distributions also observed in CIRRIS 1A experiment
- Subthermal NO sublevel distributions produced in laboratory NO_2 photodissociation experiments
- Ground-based microwave measurements of NO densities in the upper atmosphere
- Band-integrated satellite measurements of NO radiance using pressure-modulated absorption
- Spin-orbit nonequilibrium must be taken into account when interpreting experimental data
- May provide method of discriminating chemical production from collisional uppumping in NO

Comparison of Global Variations of the Radiance of the Stratospheric O_3, CH_4 and HNO_3 Spectra as Viewed by CIRRIS 1A with UARS/CLAES Experiment.

B K Rezai[1], G E Bingham[2], L R Megill[1], D K Zhou[2], J L Mergenthaler[3], A E Roche[3], J B Kumer[3], G P Anderson[4] and R D Nadile[4]

1 Center for Atmospheric and Space Sciences,
Utah State University, Logan, UT 84322-4405

2 Space Dynamics Laboratory,
Utah State University, Logan, UT 84322-9710

3 Lockheed Palo Alto Research Laboratory, Palo Alto, CA 94304

4 Department of the Air Force, Phillips Laboratory (AFMC)/GPOS/GP
Hanscom Air Force Base, Massachusetts 01731-3010

PRESENTED TO 17TH ANNUAL REVIEW CONFERENCE ON
ATMOSPHERIC RADIATION MODELS
HANSCOM AFB, MA
JUNE 7, 1994

ABSTRACT

The importance of the distribution of O_3, CH_4 and nitrogen compounds to stratospheric chemistry has been clearly established. We report on measurements of these species by the Cryogenic Infrared Radiation Instrumentation for Shuttle (CIRRIS 1A) which flew aboard Discovery OV-103, (STS-39) on April 28 to May 6, 1991. By looking in the limb, it was possible to obtain approximately a thousand interferograms. This made possible the identification of many important stratospheric gases, including O_3, CH_4, HNO_3 and chlorine source species CCl_2F_2 and CCl_3F. The accuracy of the CIRRIS 1A measurements is therefore of interest in polar ozone depletion studies, and validation is a major consideration. This paper reviews the CIRRIS 1A observations of O_3, CH_4 and HNO_3 spectra and deduced vertical profile concentrations, discusses their accuracy and precision. We compare the CIRRIS 1A measurements with the Cryogenic Limb Array Etalon Spectrometer (CLAES) on board the Upper Atmosphere Research Satellite. Specifically we compare CIRRIS 1A and CLAES spectra in the wavelength regions targeted for O_3, CH_4 and HNO_3 concentration retrievals, and we compare the retrieved quantities for species in the southern and northern hemispheres. Since CIRRIS 1A data were collected shortly before, and CLAES data shortly after, the Pinatubo eruption, such comparisons are of significant value both scientifically and from a validation standpoint.

CLAES - CIRRIS 1A OVERVIEW FOR CORRELATIVE STUDY

We discus data from CLAES on the UARS satellite which viewed the stratospheric observations for over 19 months beginning in October 1991.

CLAES narrow band channels of the blocker filters regions 8, 6, and 4 (centered at wavenumbers of 792 cm^{-1}, 879 cm^{-1} and 1257 cm^{-1}) were used to retrieve O_3, HNO_3 and CH_4 profiles. A multi-channel, multi-emitter retrieval scheme is used to establish the VMR [Roche et al, 1993].

CLAES spectral emission radiance measurements for a range of altitudes and their components are examined. These examples will illustrate instrument continuous scan mode spectral regions and their performance.

CLAES - CIRRIS 1A OVERVIEW FOR CORRELATIVE STUDY COUNT.

We also discus an analysis of the measurements obtained from the CIRRIS 1A payload aboard the STS-39, that viewed the stratosphere on April 28 to May 6, 1991.

The CIRRIS 1A payload consists of the two primary sensors (cryogen-cooled radiometer and interferometer), and co-aligned ancillary sensors, mounted to a two-axis gimbal system. The Interferometer is a Michelson design and features a flex-pivot mirror translation system.

The interferometer focal plane contains five Si:AS detectors behind an eight-position filter wheel that respond to radiation between 2.5 and 25 microns and provides a spectral resolution ranging between 1 and 8 cm^{-1} over an eight-order dynamic range [Coney et al, 1992].

CLAES DESIGN AND FUNCTIONAL DIAGRAM

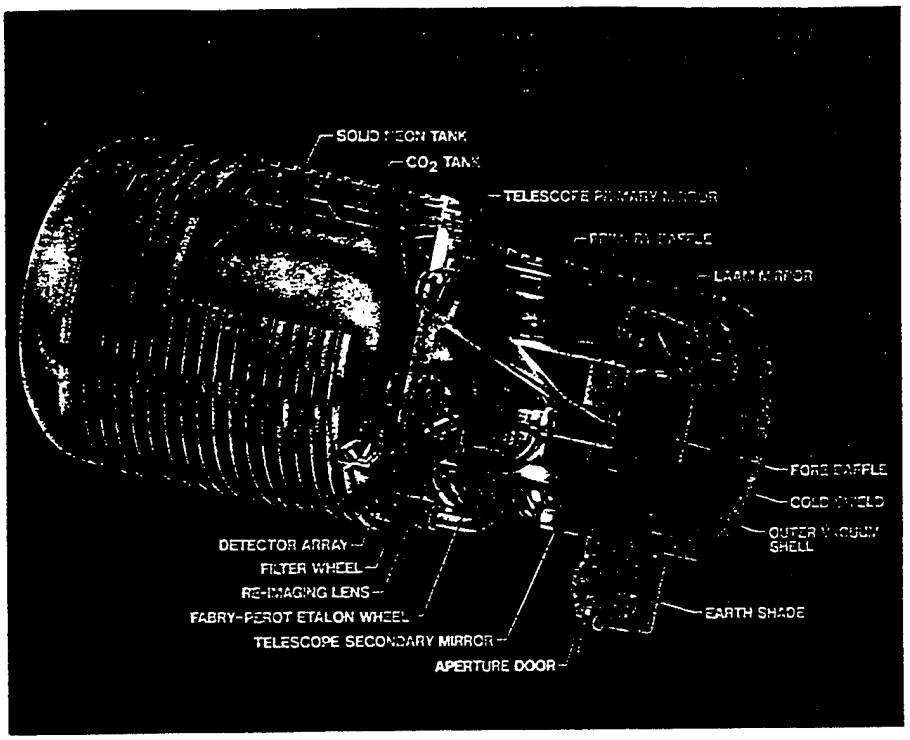

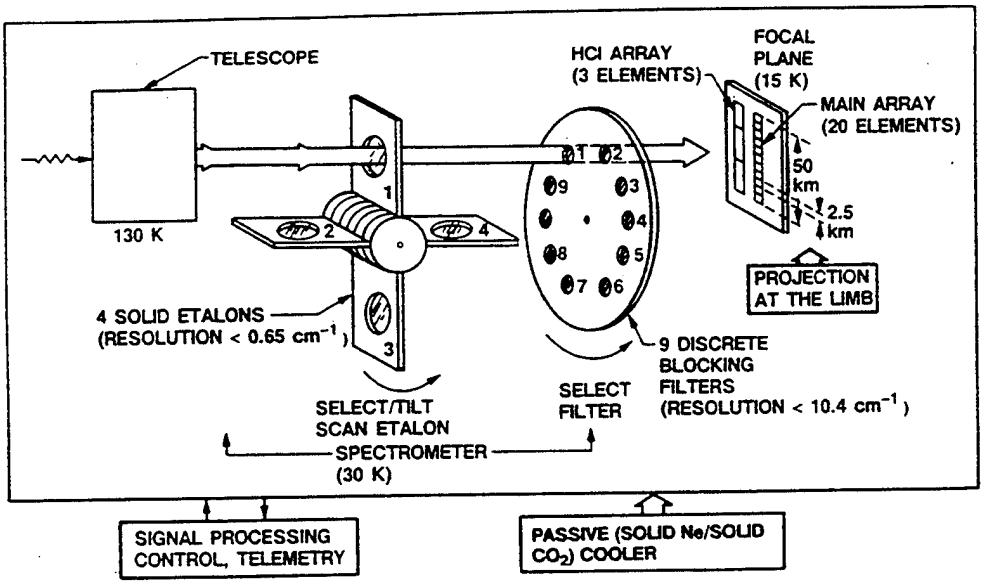

*See Roche et el.
JOURNAL OF GEOPHYSICAL RESEARCH, VOL. 98, NO. D6, PAGES 10,763-10,775, JUNE 20, 1993

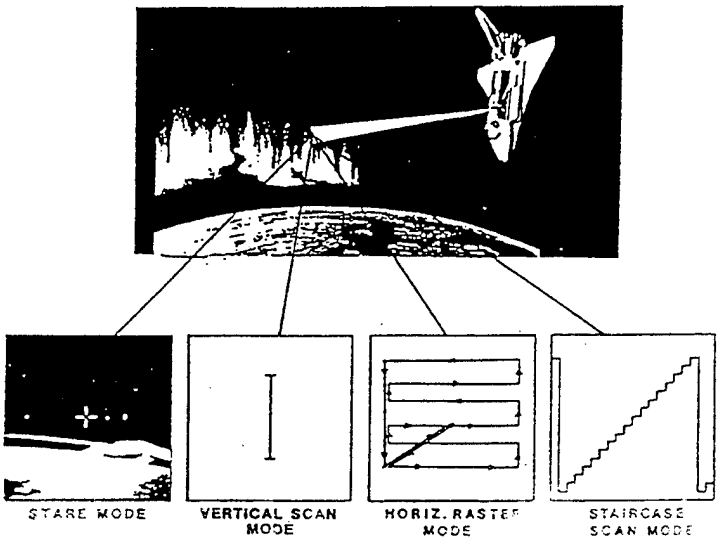

CIRRIS 1A viewing & illustration of gimbal motion for typical mode [Bartschi B. et al, 1987]

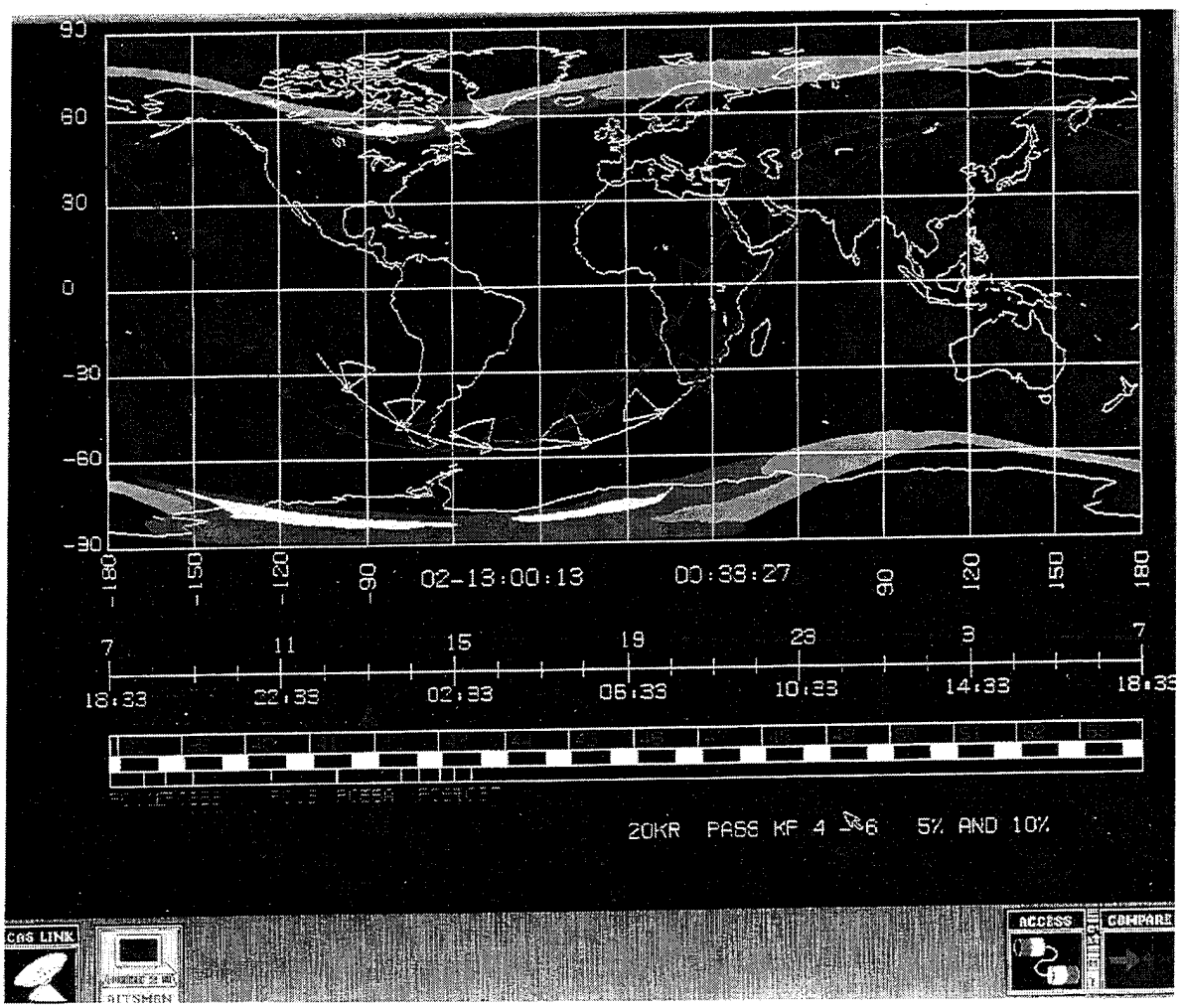

Typical course of the Shuttle during STS-39 flight for April 28 and May 6, 1991. Photograph shows CIRRIS 1A orbit and typical look angles and projected auroral intensity and locations. A portion of the CIRRIS 1A flight was dedicated to stratospheric gas measurements. Courtesy of USAF Phillips Laboratory and Radex, INC.

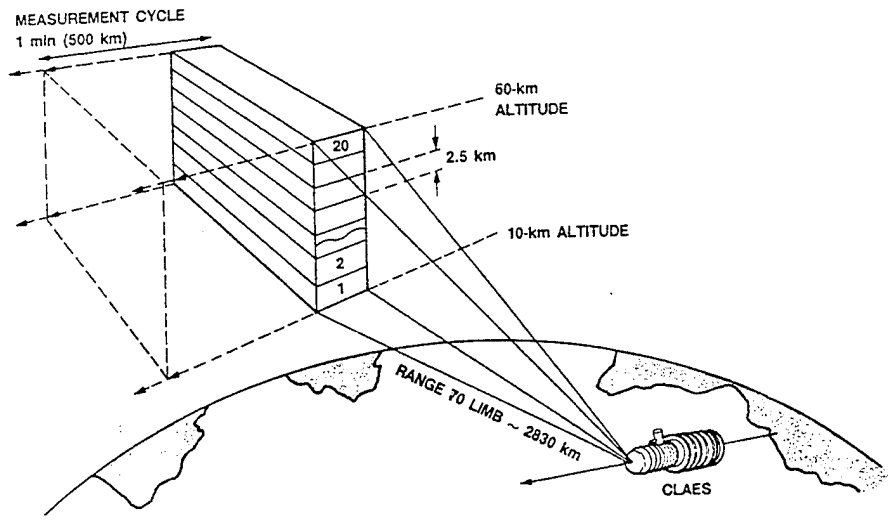

CLAES viewing geometry [Roche et al, 1993]

CLAES NORTH-SOUTH LOOKING COVERAGE DURING STRATOSPHERIC GAS MEASUREMENTS

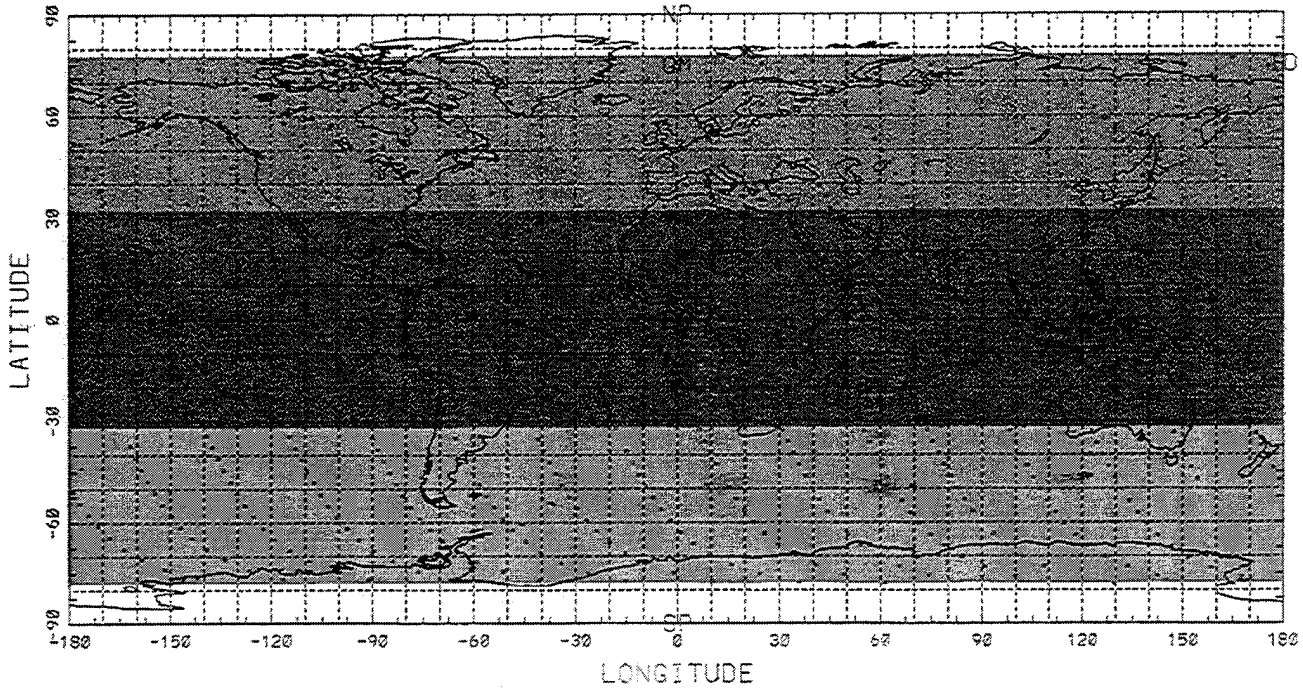

CLAES latitude versus longitude coverage for the month of April 1992. Points at which calibrations were performed for each descending day are shown. Violet indicates north looking; acqua indicates south looking; blue is the overlap regions. Upper and lower panels each contain about 600 data points from 16 orbits over a 24 hour period covering any latitude band.

SHUTTLE GROUND TRACK DURING STRATOSPHERIC GAS MEASUREMENTS

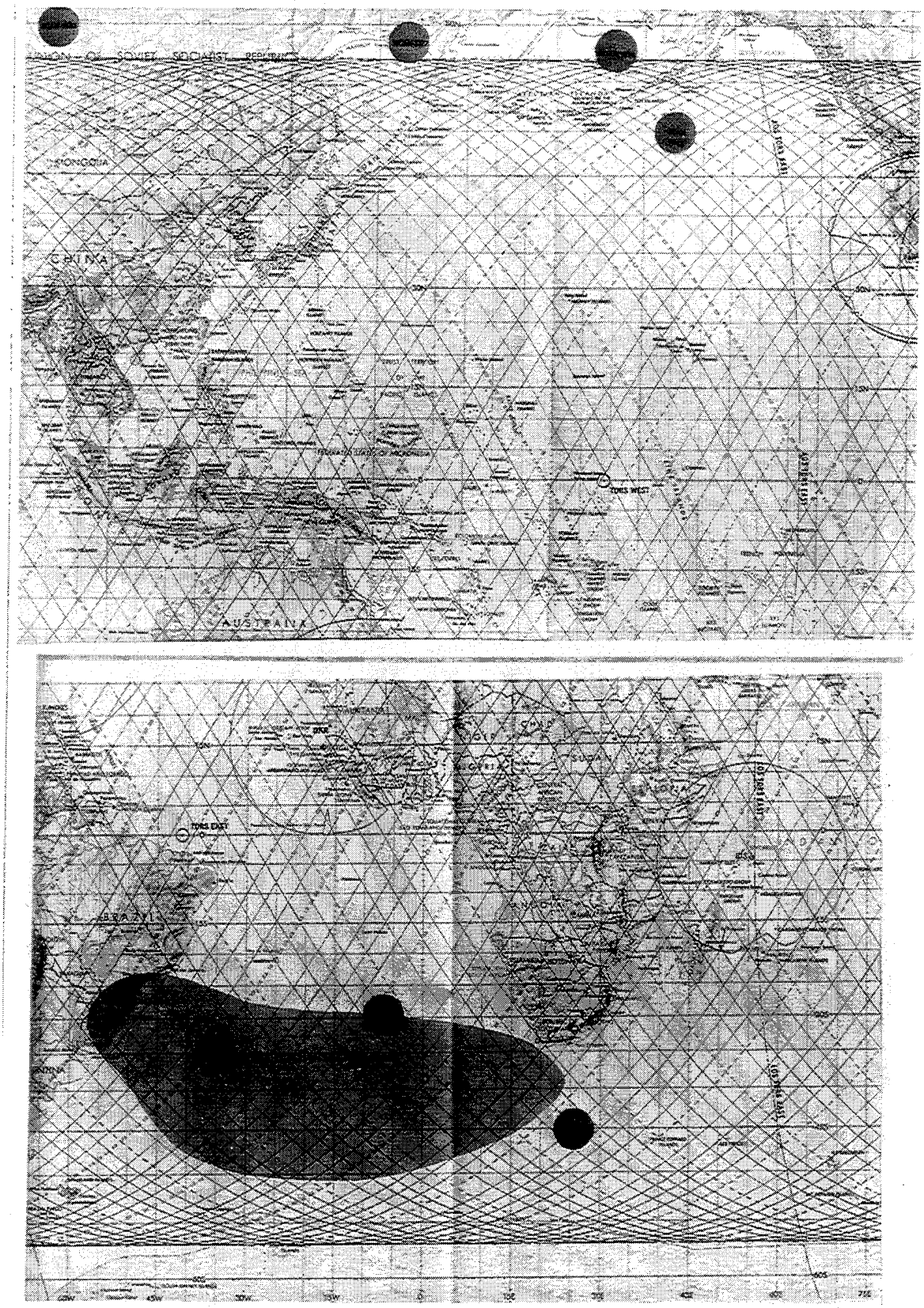

Typical course of the Shuttle during STS-39 flight for April 28 and May 6, 1991. A portion of the CIRRIS 1A flight was dedicated to stratospheric gas measurements. Points indicate seven data sampling profiles locations.

CALCULATED RADIANCE AT THE SENSOR FOR LIMB TANGENT ALTITUDE h, FREQUENCY ν_i

Lockheed

$$R_i(h, \nu_i) = -\int_{\nu_1}^{\nu_2}\int_{\phi_1}^{\phi_2}\int_{s=0}^{\infty} B(\nu_i, T)\, F(\phi)\, R(\nu_i)\, \frac{d\tau_i(\nu s)}{ds}\, d\nu d\phi dS$$

PLANCK FUNCTION AT ν_i, T, POINT S

INSTRUMENT SPATIAL RESPONSE FUNCTION

INSTRUMENT SPECTRAL RESPONSE FUNCTION AT ν_i

DERIVATIVE OF TRANSMITTANCE FROM POINT S TO SENSOR

WHERE

$$\tau_i = \exp\left[-\int_s^{\infty} k_\nu(P, T)\, q\, ds\right]$$

AND

$$K_\nu(P, T) = \frac{S\alpha}{\pi[(\nu - \nu_0)^2 + \alpha^2]} = \text{SPECTRAL ABSORPTION CROSS SECTION FOR LORENTZ LINE SHAPE}$$

THE MEASURED RADIANCE IS OBTAINED AS

$$N_i(h, \nu_i) = D_i \text{ (VOLTS)} \times CAL_i \text{ (RADIANCE/VOLTS)}$$

BY COMPARING ALL R_i AND D_i FOR EACH TANGENT ALTITUDE, SOLUTIONS ARE FOUND BY ITERATING T, P, AND q

X90907_R_JS_LC

X90907_R_JS_LC

CLAES ETALON AND BLOCKER FILTER

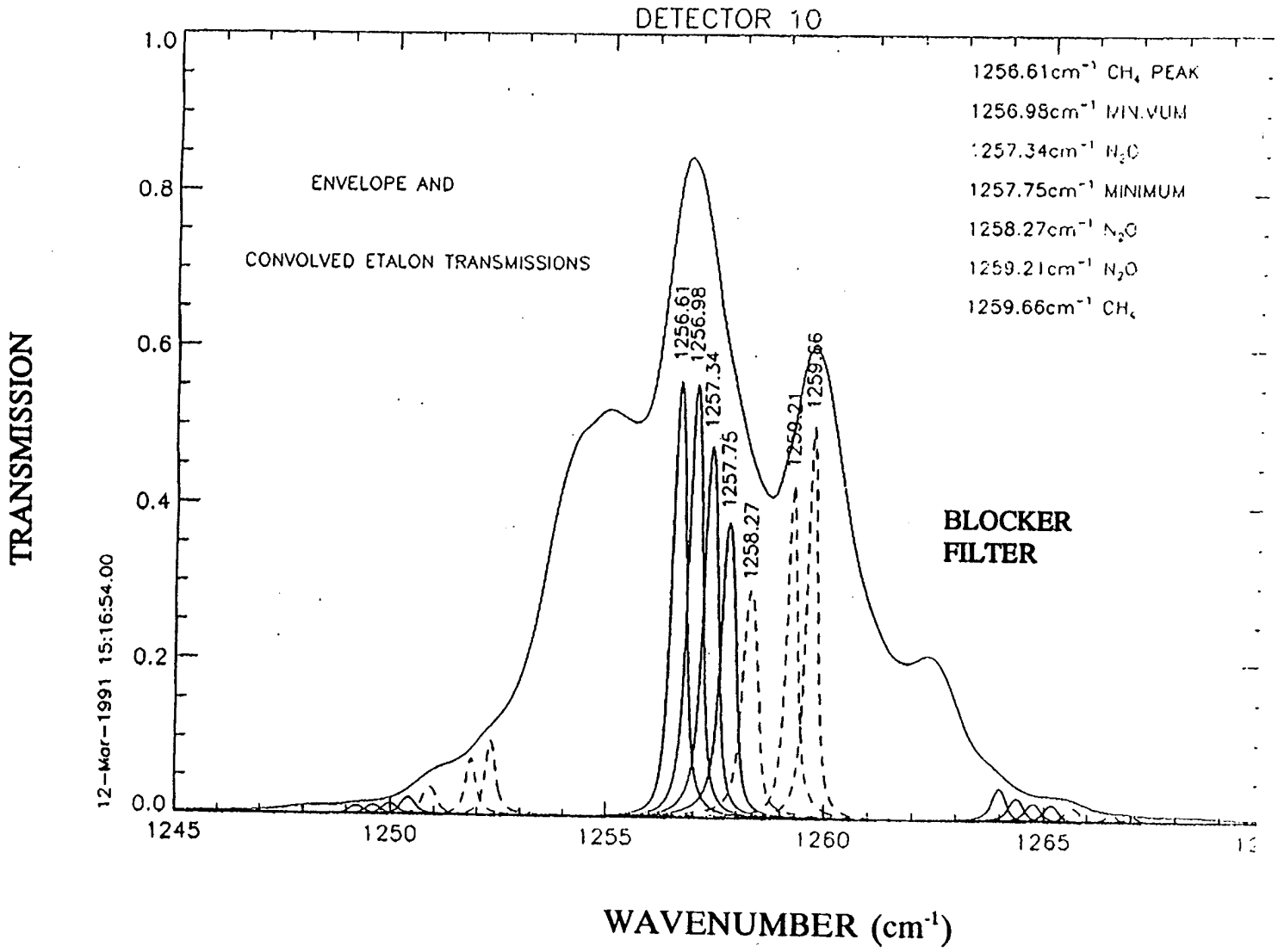

Example of CLAES blocker etalon transmittances for Etalon tilt positions for blocker filter region 4.

CIRRIS 1A INFRARED AND ATMOSPHERIC RADIATION MODEL

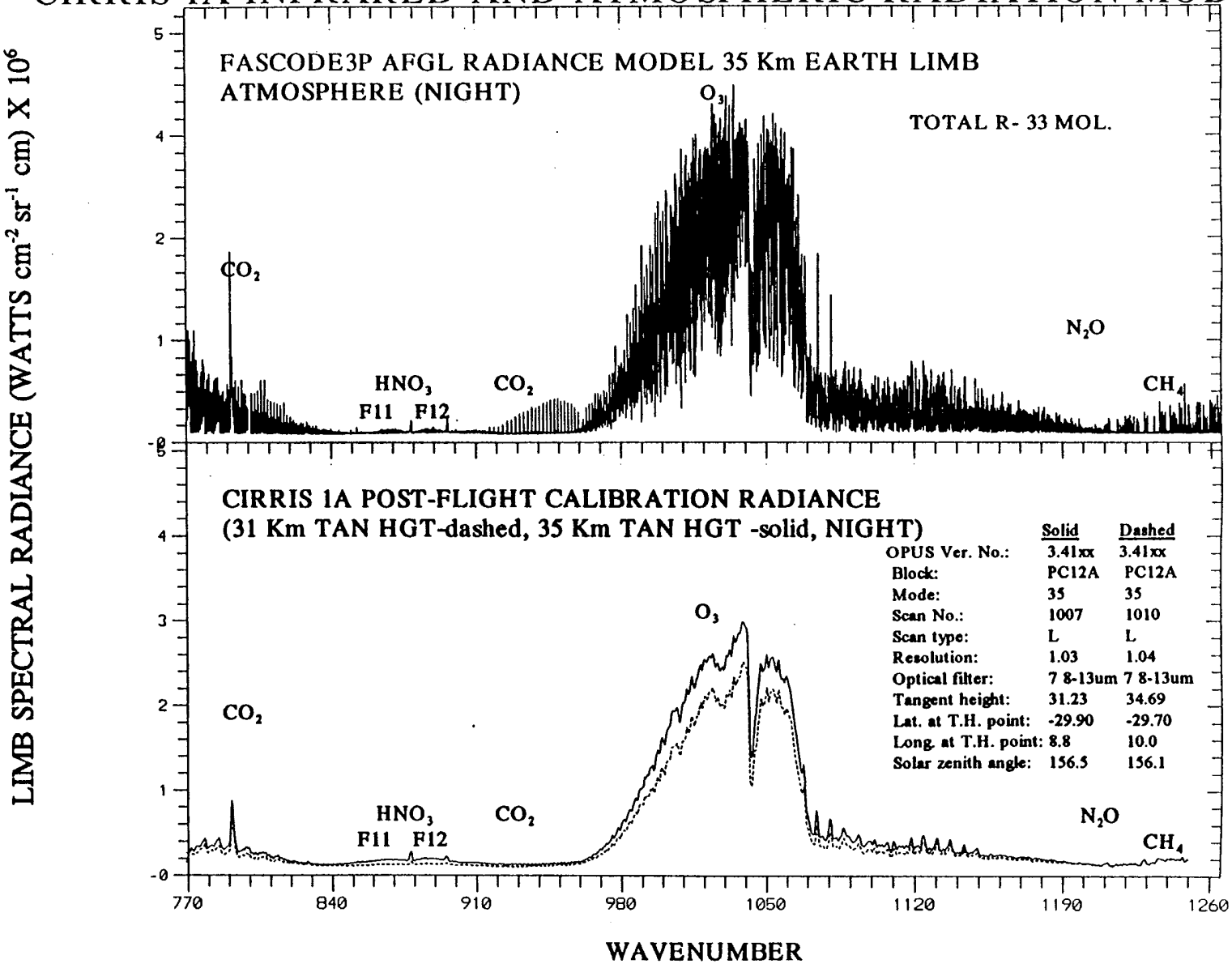

The spectral distribution of infrared emission produced by minor species in the stratosphere. The figure compares the AFGL radiance model (FASCODE3P line-by-line radiation code), with data taken by the Cryogenic Infrared Radiance Instrumentation for Shuttle (CIRRIS 1A) viewing the earth limb at altitudes of 31 and 35 km.

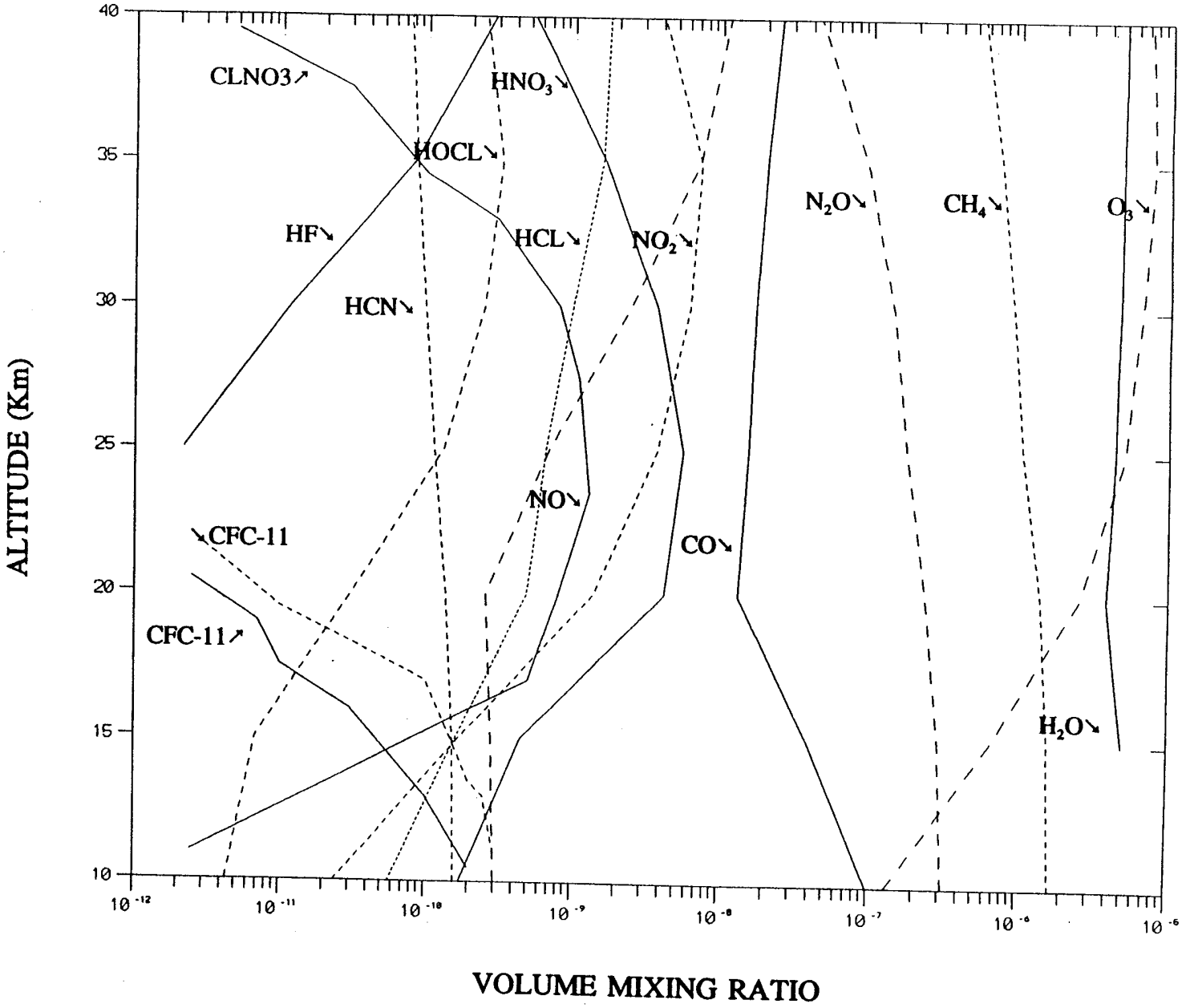

VMR profiles used in the analysis of mid-latitude spectra over the southern hemisphere.

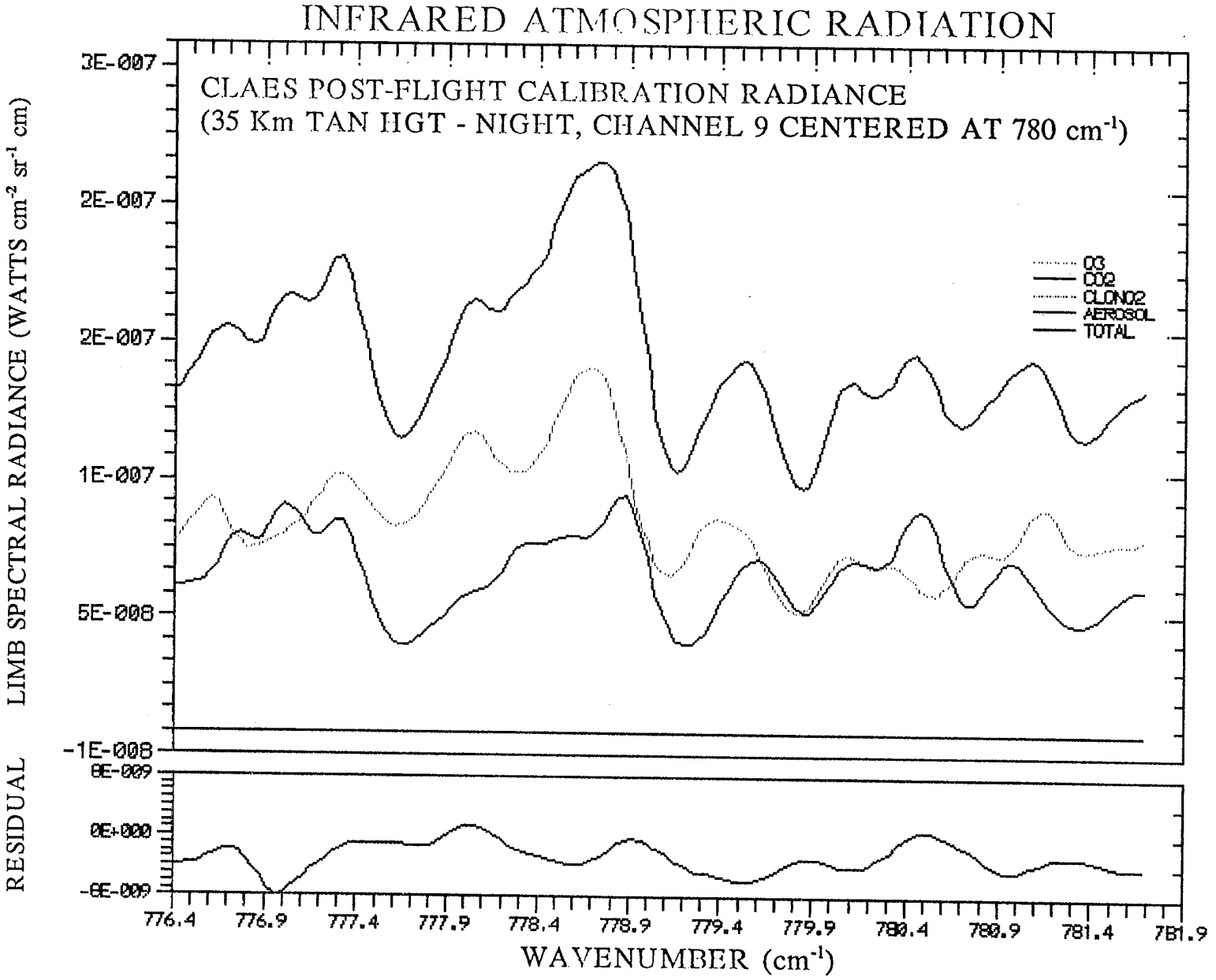

The spectral distribution of infrared emission produced by minor species in the stratosphere. The figure shows the spectral emissions measured by the Cyrogenic Array Etalon Spectrometer (CLAES) viewing the earth limb at altitude of 35 km.

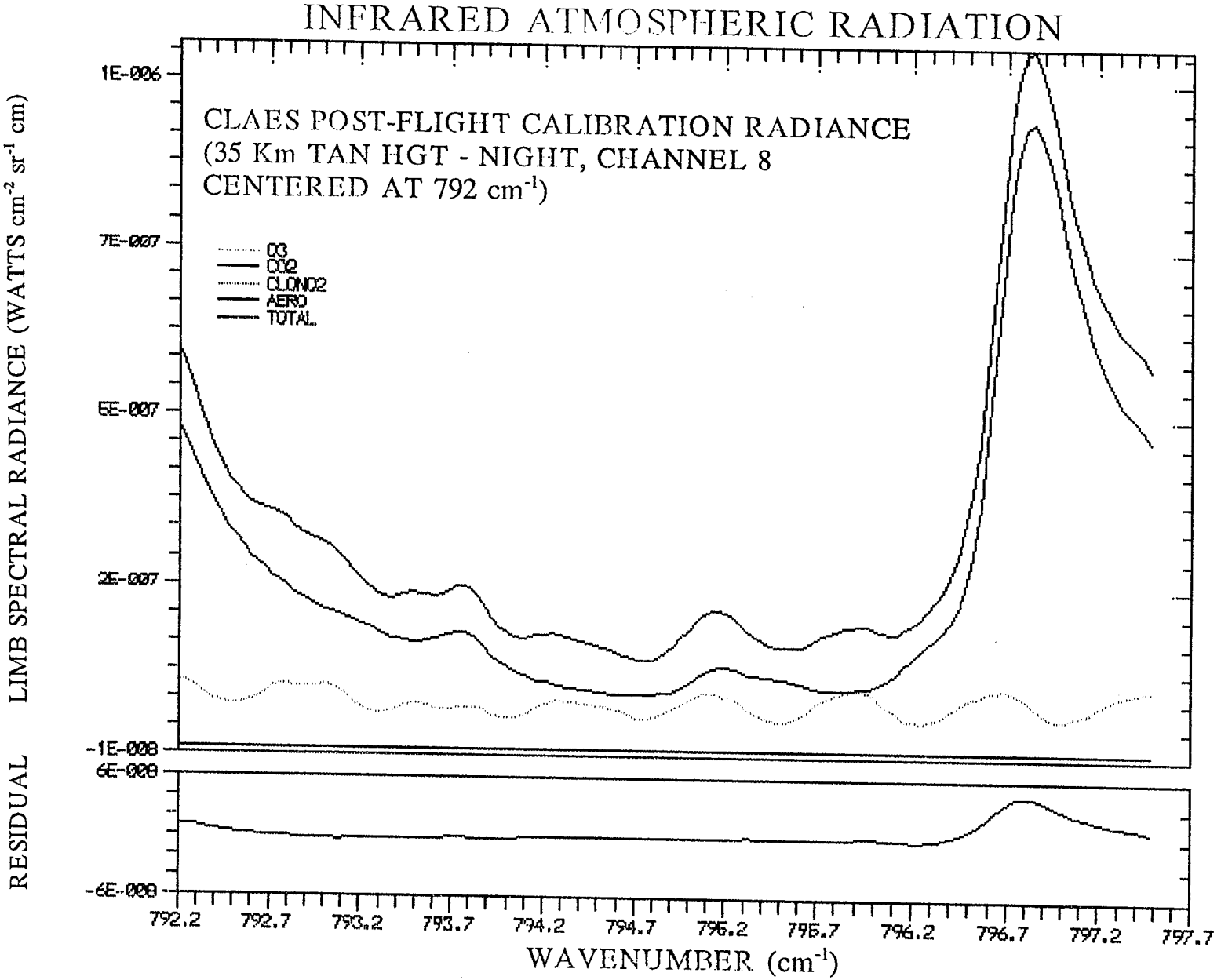

The spectral distribution of infrared emission produced by minor species in the stratosphere. The figure shows the spectral emissions measured by the Cyrogenic Array Etalon Spectrometer (CLAES) viewing the earth limb at altitude of 35 km.

CLAES, CIRRIS 1A DATA AND RADIATION MODEL COMPARISONS

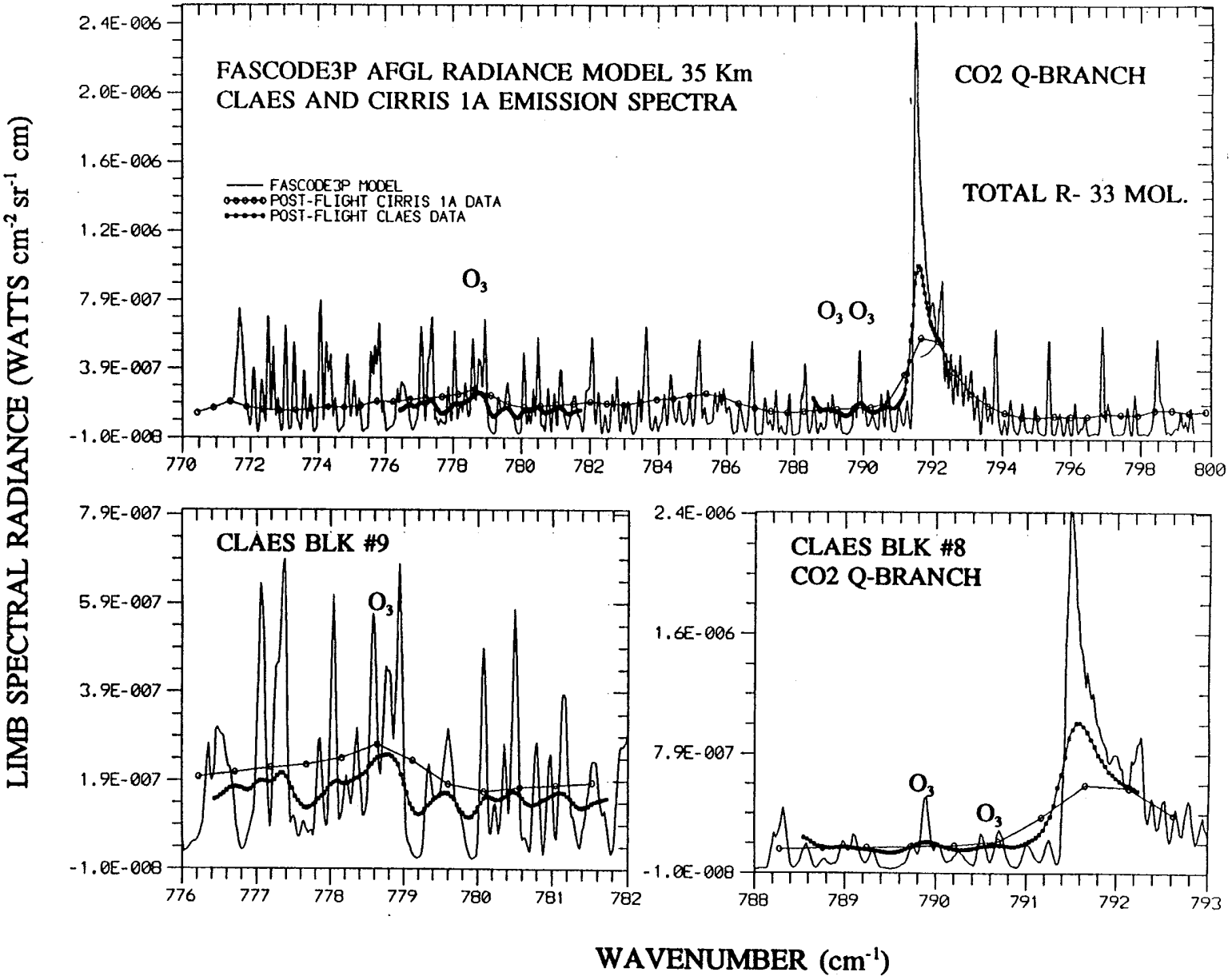

Correlation and anti-correlation between CLAES, CIRRIS 1A O3 data compared with FASCODE3P model. The figure shows that the line position, intensity and spectral distributions measured by CLAES and CIRRIS 1A agree with each other and with those of the model at this altitude.

CLAES, CIRRIS 1A DATA AND MODEL COMPARISONS

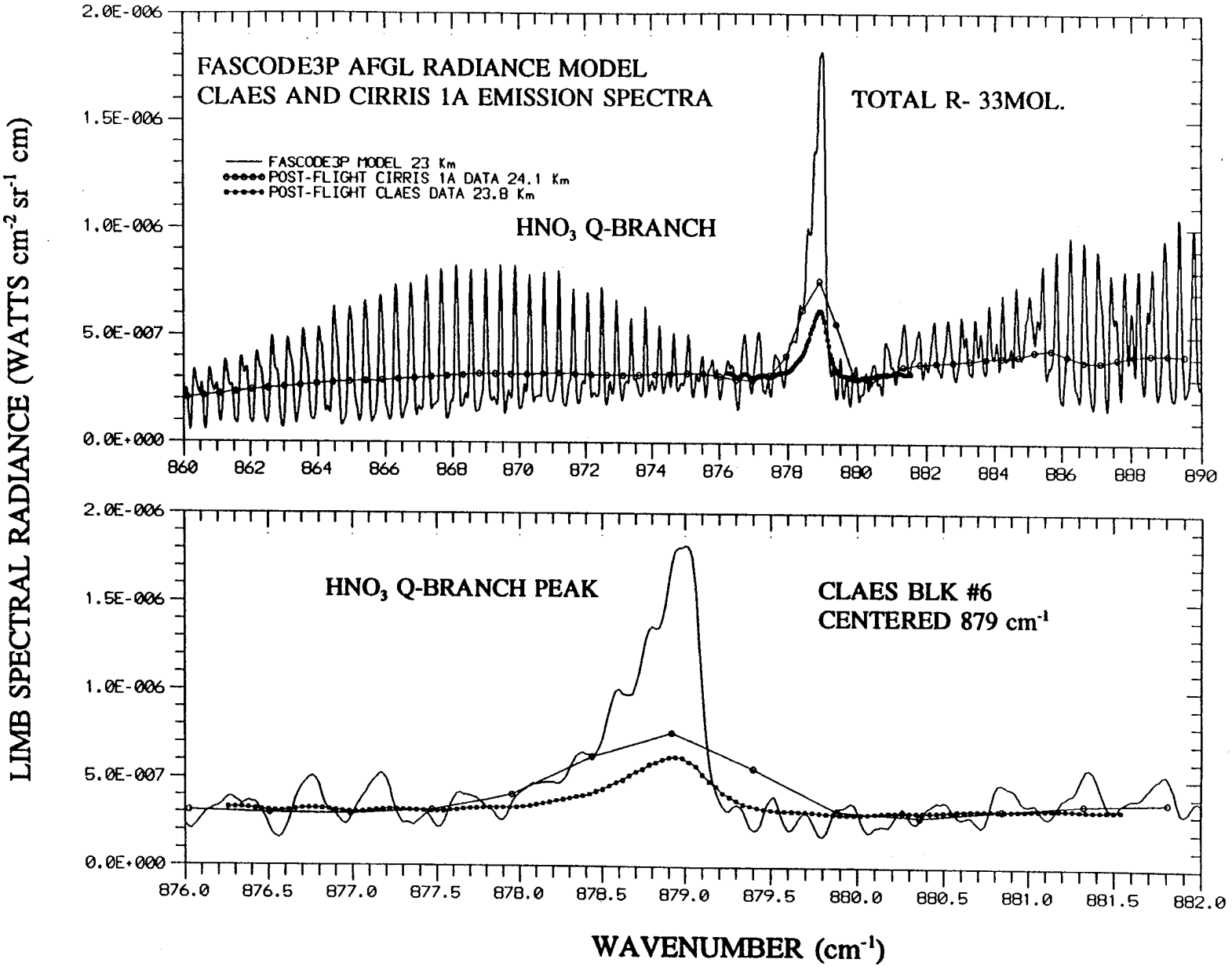

CLAES and CIRRIS 1A HNO3 spectra compared with model at 23 Km tangent height. The figure shows the measured and model spectra agree quite well. The model spectral resolution is 0.02 cm^{-1}. When intercomparing the residual spectra, the slightly different scaling should be regarded.

CLAES, CIRRIS 1A DATA AND RADIATION MODEL COMPARISONS

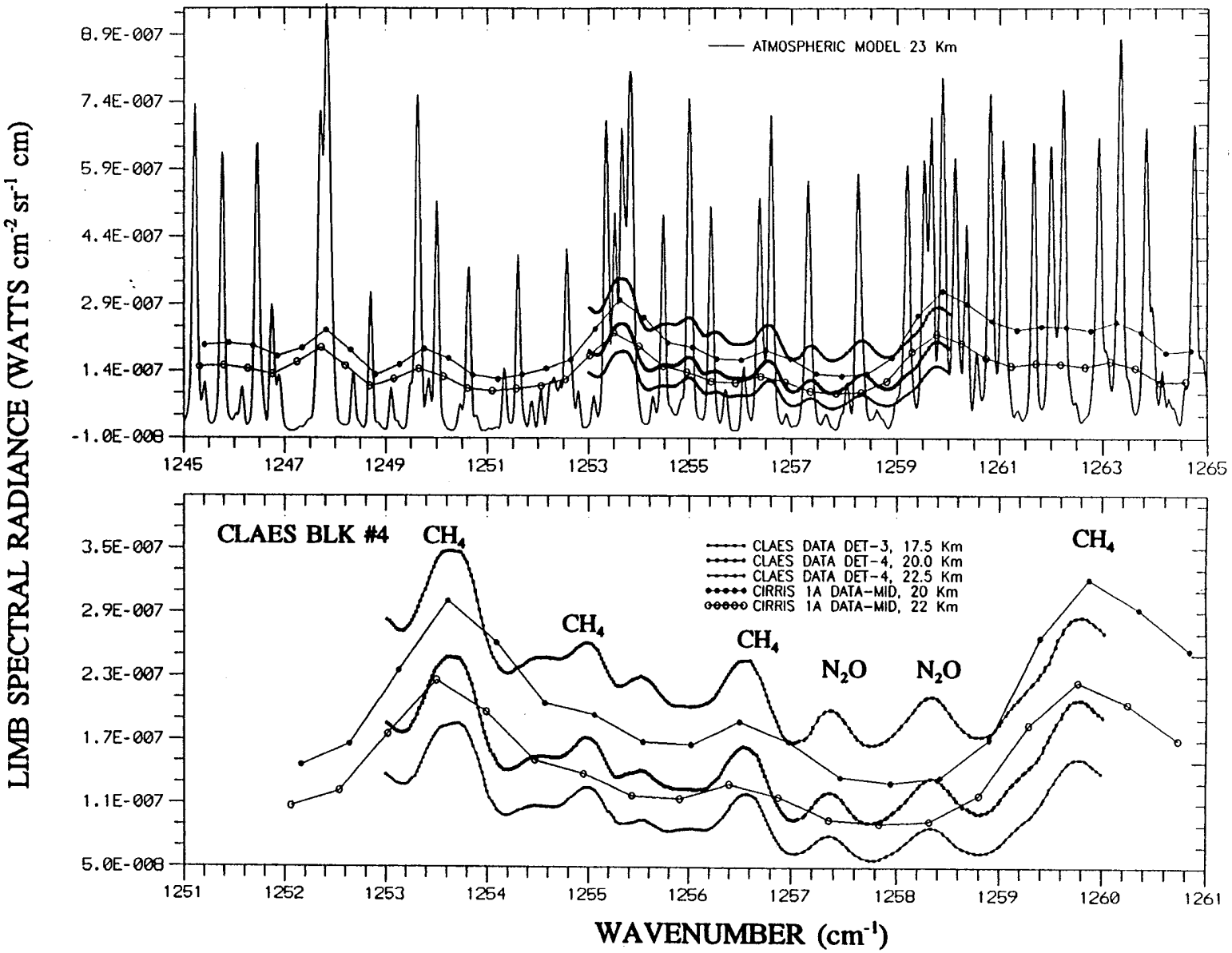

Correlation between CLAES, CIRRIS 1A CH_4/N_2O data compared with line-by-line model radiation.

SUMMARY

We have presented the analysis of CLAES spectral emission measured data and CIRRIS 1A interferometric data.

Data from the CIRRIS 1A interferometer and the CLAES spectral emission measurements (and their components of the computed fit) were used to characterize the O_3, HNO_3 and CH_4 emission.

Forward calculations of spectra were performed by the FASCOD3P line-by-line radiation code. The code was modified in order to permit the calculation of CFC's and $CLONO_2$ emissions from absorption cross-sections.

Our study of CLAES-CIRRIS 1A spectra shows that the line positions, intensity, and spectral distribution agree with each other and with those of the model at selected altitude and latitude to within experimental accuracy.

SUMMARY COUNT.

This line of investigation appears to be very promising for comparison of the techniques but more work is necessary establish additional information.

The integrated radiances of selected spectral features, are used to infer the concentration profiles of some atmospheric constituents including chlorine containing sources (CFC-11, CFC-12) as well as HNO_3, O_3, CH_4.

This presentation of stratospheric gas measurements for CLAES spectral emission and CIRRIS 1A interferometric data is preliminary. There is a wealth of excellent spectra that need to be reduced, analyzed, correlated and interpreted.

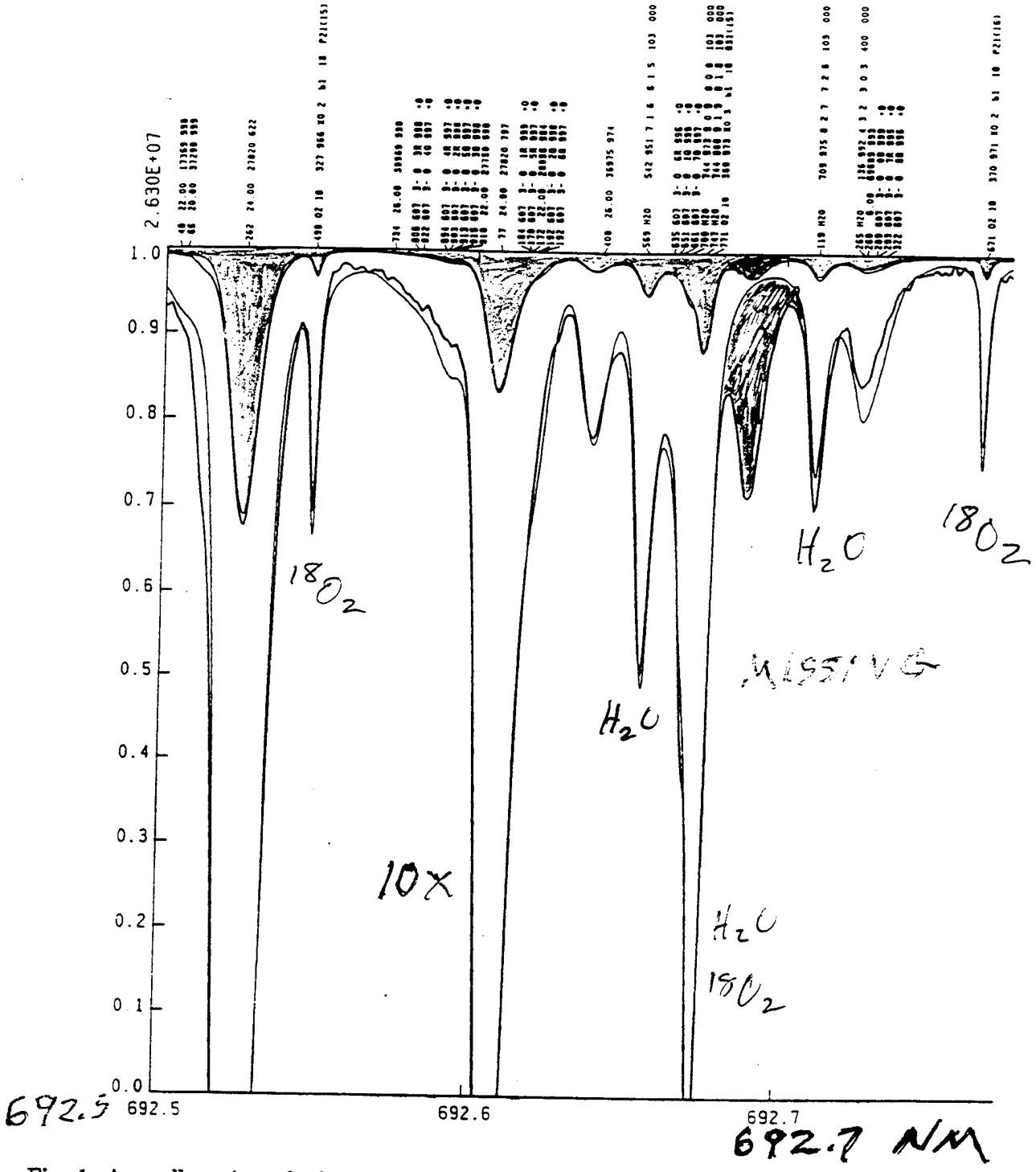

Fig. 1. A small section of solar central intensity spectrum at 692.5 nm plotted at full scale and at 10 times scale. The heavy lines are the observed FTS spectrum from James Brault at Kitt Peak. The resolution is 522000 and the signal-to-noise is about 3000 which is poor for this work. The continuum level is uncertain. The thin line is the computed spectrum. It would be possible to adjust the line data for a better match but most of the discrepencies are from missing lines. There are solar lines of Ca I, Ti I, Cr I, Fe I, C I, CN, and terrestrial lines of H_2O and $^{16}O^{18}O$. The first number in each line label is the last 3 digits of the wavelength and the 4th number is the per mil central intensity if the line were computed in isolation.

Annual Review Conference on Atmospheric Transmission Models
7-8 June 1994, Phillips Laboratory, Bedford, MA

The POAM II Experiment and Early Measurement Results

E.P. Shettle, R.M. Bevilacqua, J.S. Hornstein
Remote Sensing Division, NRL, Washington, DC 20375

W.J. Glaccum
ARC, Landover, MD

S. Krigman, J. Lumpe, M. Fromm, and D. Debrestian
CPI, Fairfax, VA

POAM II Additional Science Team Members

Eric Chassefière, Francis Dalaudier, & Carole Deniel
Service d'Aerronomie du CNRS

Jacqueline Lenoble & Collette Brogneiz
Université de Science et Technologie de Lille

David Rusch, Todd Clancy, & Cora Randall
University of Colorado

John Olivero
Embry-Riddle Aeronautical University

Polar Ozone and Aerosol Measurement (POAM II) Science Summary

POAM II uses proven visible solar occultation and techniques from a polar orbiting spacecraft - SPOT 3.

The solar occultation technique consists of measuring solar extinction as a function of frequency as the sun rises or sets relative to the spacecraft. From these measurements the abundance profile of absorbing gases and aerosol extinction profiles can be determined.

POAM II measures key constituents of the polar stratosphere: aerosols, O_3, H_2O, NO_2, and temperature.

POAM II measurements are vital to understanding the Antarctic "ozone hole" and possible development of Arctic ozone depletions.

POAM II - (Polar Ozone & Aerosol Measurement)

9 Channel Solar Occultation Instrument launched on the SPOT 3 Satellite

- Designed to measure long-term trends in ozone abundances at polar latitudes, and examine the morphology of spring-time ozone depletions in the polar regions.

- Measure stratospheric aerosol extinction profiles and obtain a climatology of Polar Stratospheric Clouds (PSC's).

- Make zonal average measurements of H_2O and NO_2 in the stratosphere.

- Make observations of the frequency of occurrence and optical thickness of high cirrus clouds.

OPTICAL HEAD ASSEMBLY

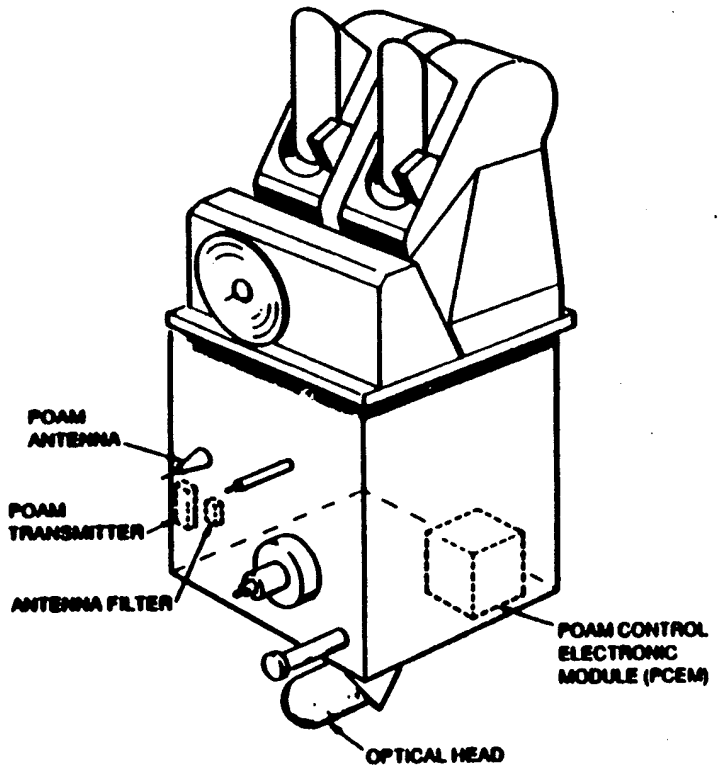

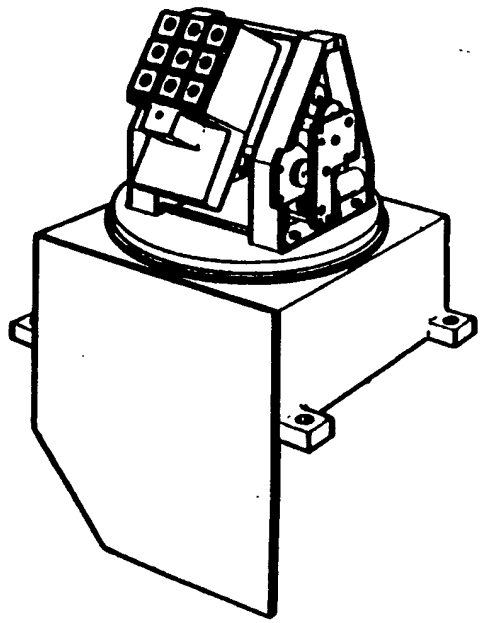

Figure 1: Schematic drawing showing the location of the POAM II instrument components integrated onto the SPOT 3 satellite (left) and schematic of the POAM II Optical Head Assembly (right).

SCIENCE SENSORS OPTICAL PATH

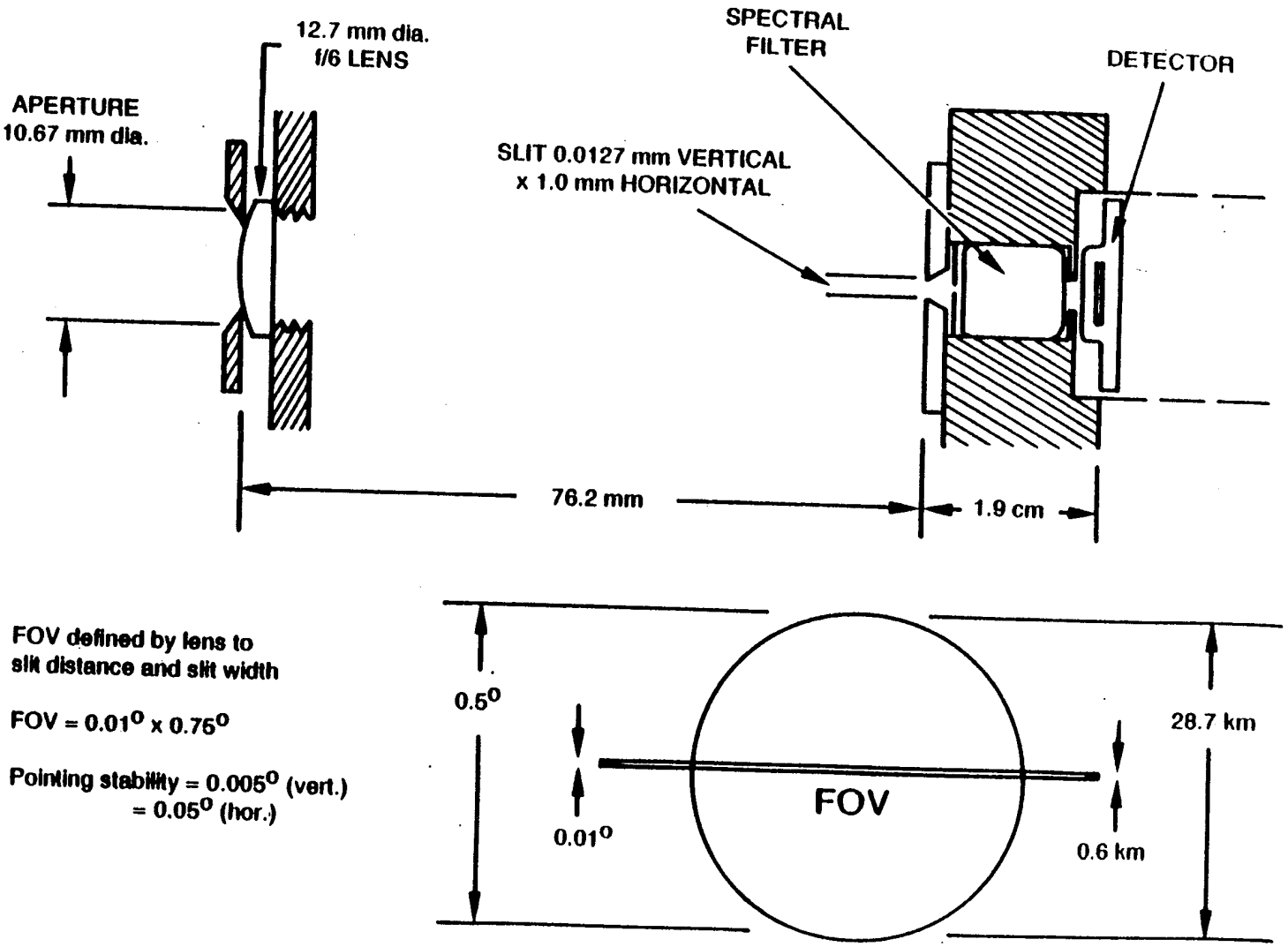

Figure 2: POAM II science sensors optical path arrangement.

Atmospheric Extinction vs Wavelength at 18 km

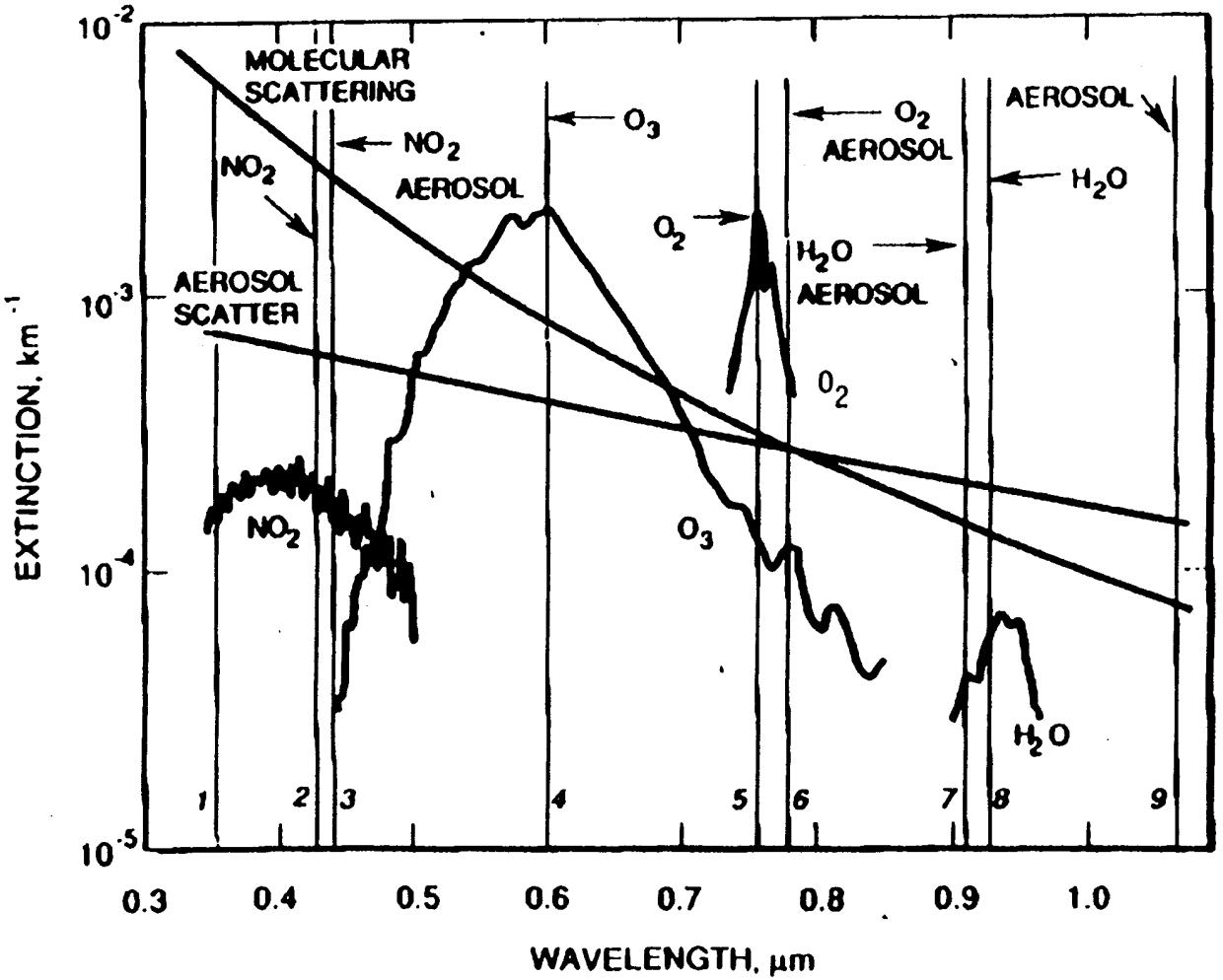

Wavelength (nm)	Width (nm)	Primary Purpose
353.0	5	Aerosols
442.0	2	NO_2 Off
448.3	2	NO_2 On
600.0	15	Ozone
760.8	2	O_2 On
780.0	15	O_2 Off
920.0	2	H_2O Off
935.5	2	H_2O On
1059.0	10	Aerosols

POAM II Sub-Tangent Latitude
1994 Sunrises

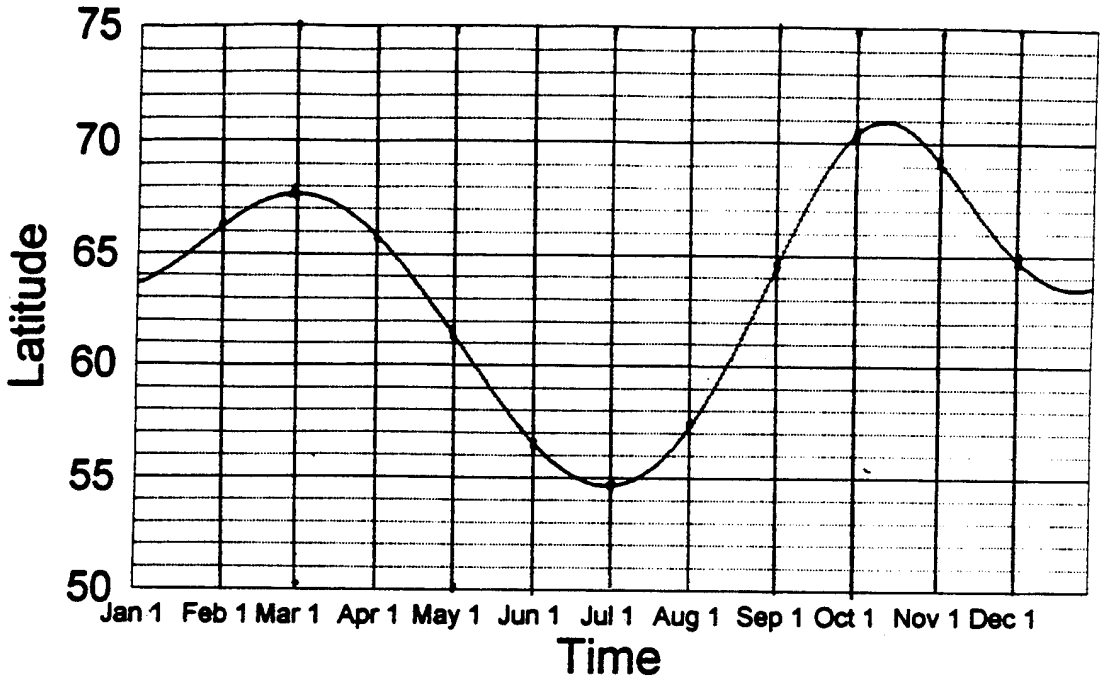

POAM II Sub-Tangent Latitude
1994 Sunset

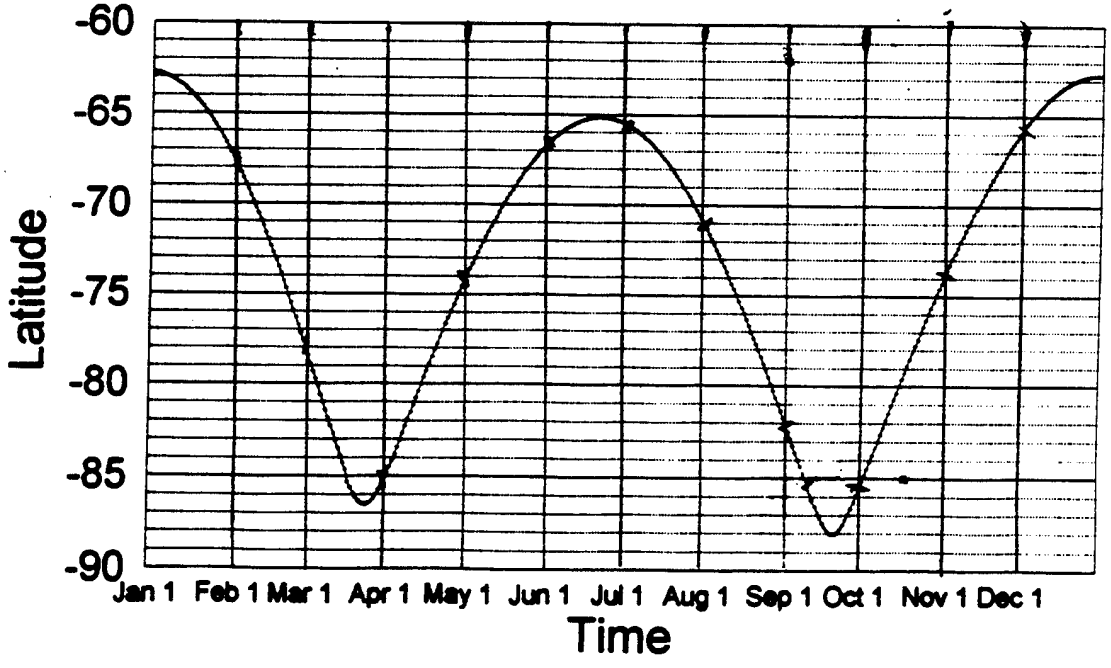

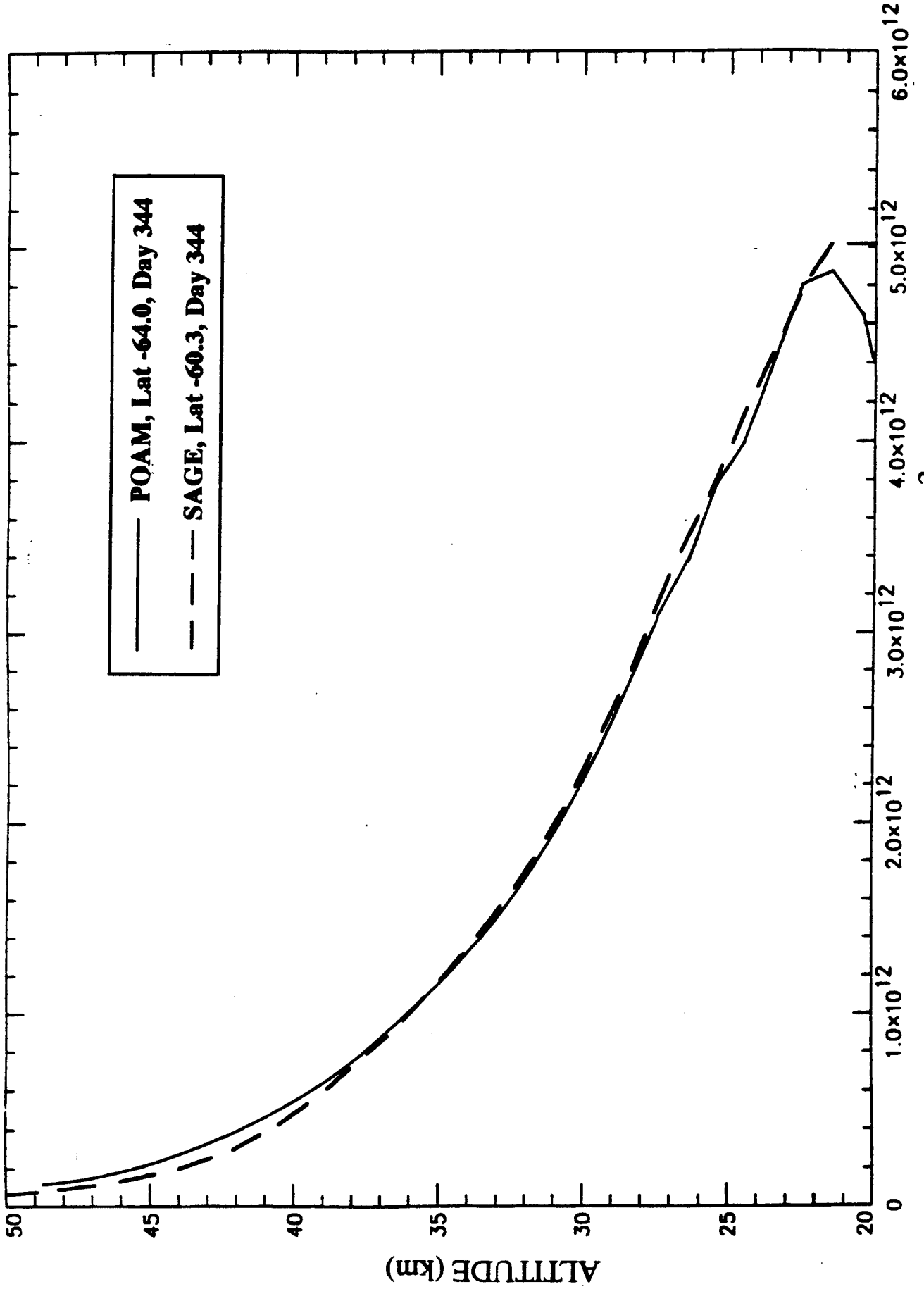
POAM, Lat -64.0, Day 344
SAGE, Lat -60.3, Day 344
ALTITUDE (km)
50
45
40
35
30
25
20
0
1.0×10^12
2.0×10^12
3.0×10^12
4.0×10^12
5.0×10^12
6.0×10^12
OZONE DENSITY cm^-3

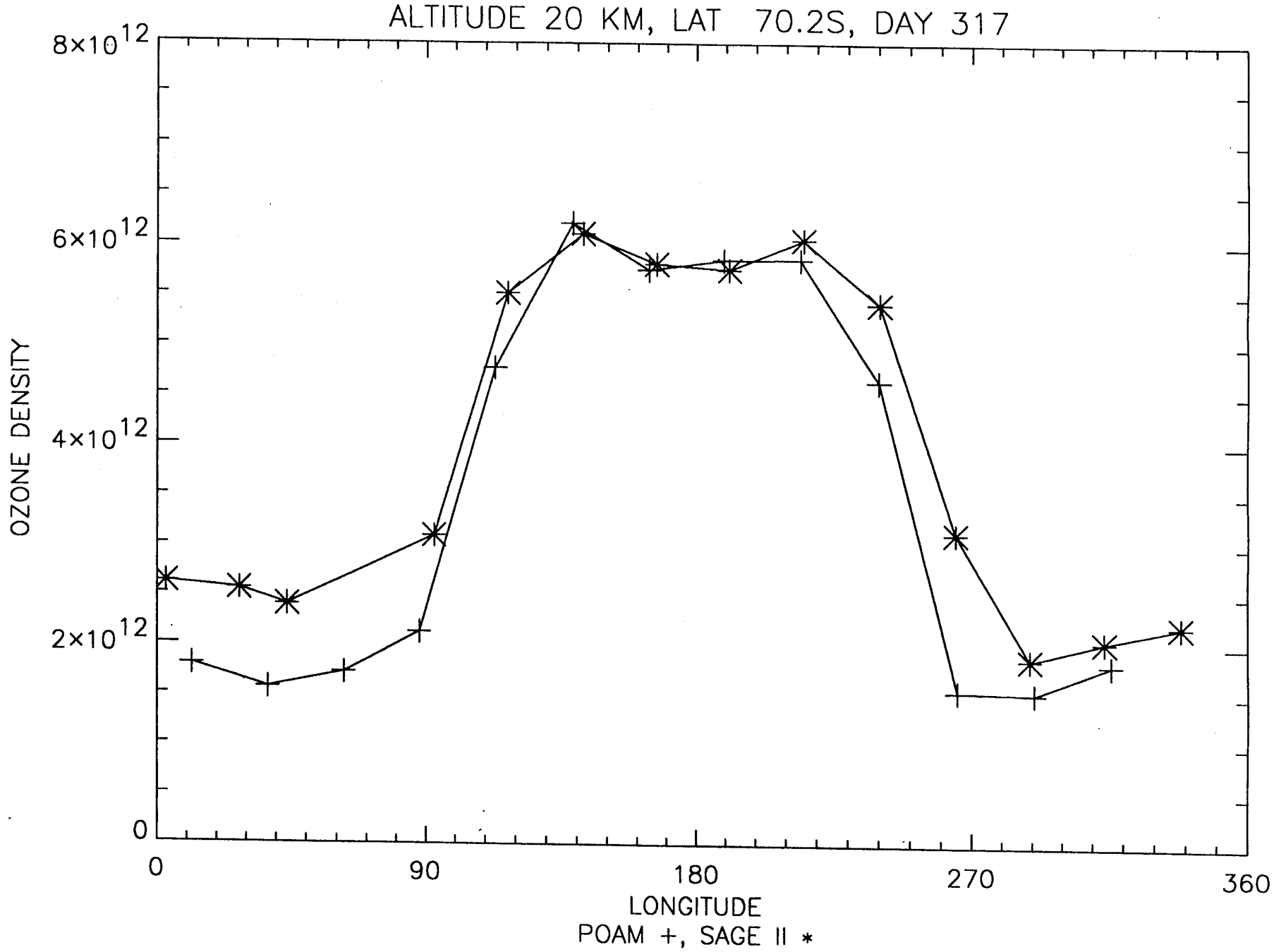
ALTITUDE 20 KM, LAT 70.2S, DAY 317
8×10^12
6×10^12
4×10^12
2×10^12
0
OZONE DENSITY
0
90
180
270
360
LONGITUDE
POAM +, SAGE II *

POAM II Comparisons with University of Wyoming Balloon Measurements near Archangel, Russia (64.62° N 40.5° E)

Measurement Dates

Date	Time (GMT)	20 km Tan. Latitude	20 km Tan. Longitude	Range (km)
Mon 29 Nov 93	1133	65.01	35.89	224
Wed 1 Dec 93	1054	64.78	45.28	229

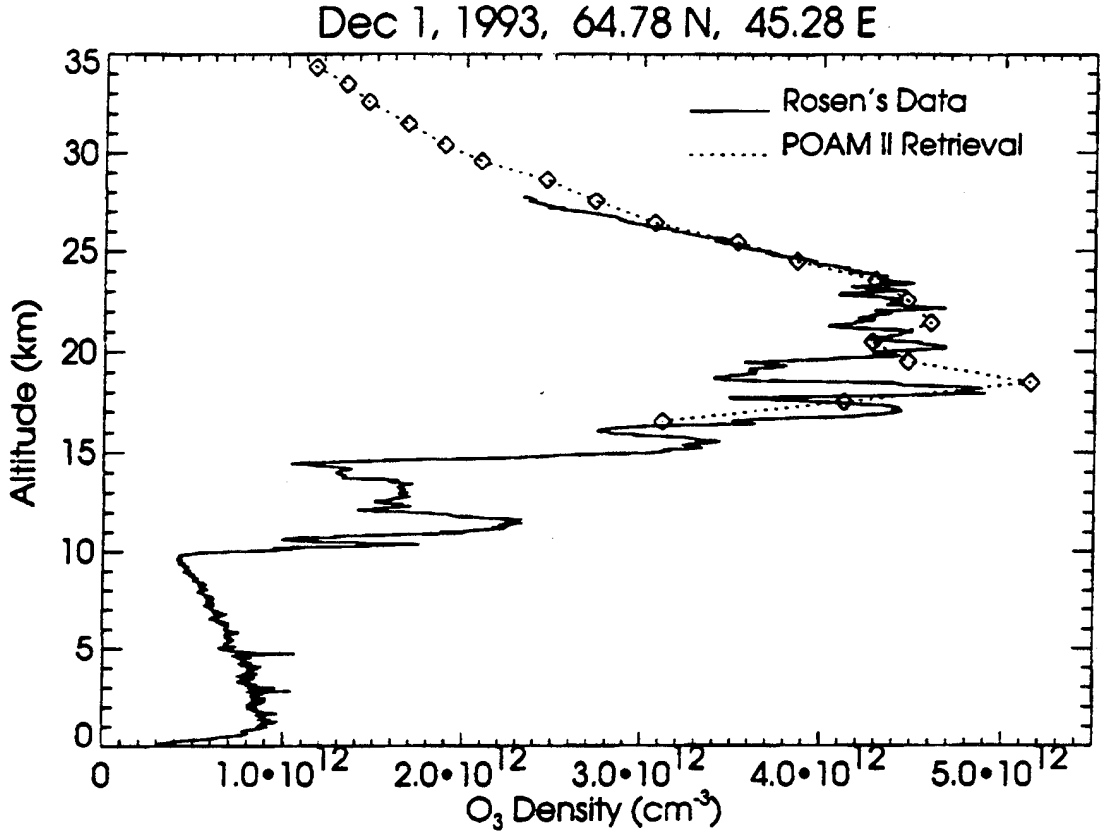
Dec 1, 1993, 64.78 N, 45.28 E
Rosen's Data
POAM II Retrieval
Altitude (km)
35
30
25
20
15
10
5
0
0
1.0•10^12
2.0•10^12
3.0•10^12
4.0•10^12
5.0•10^12
O3 Density (cm-3)

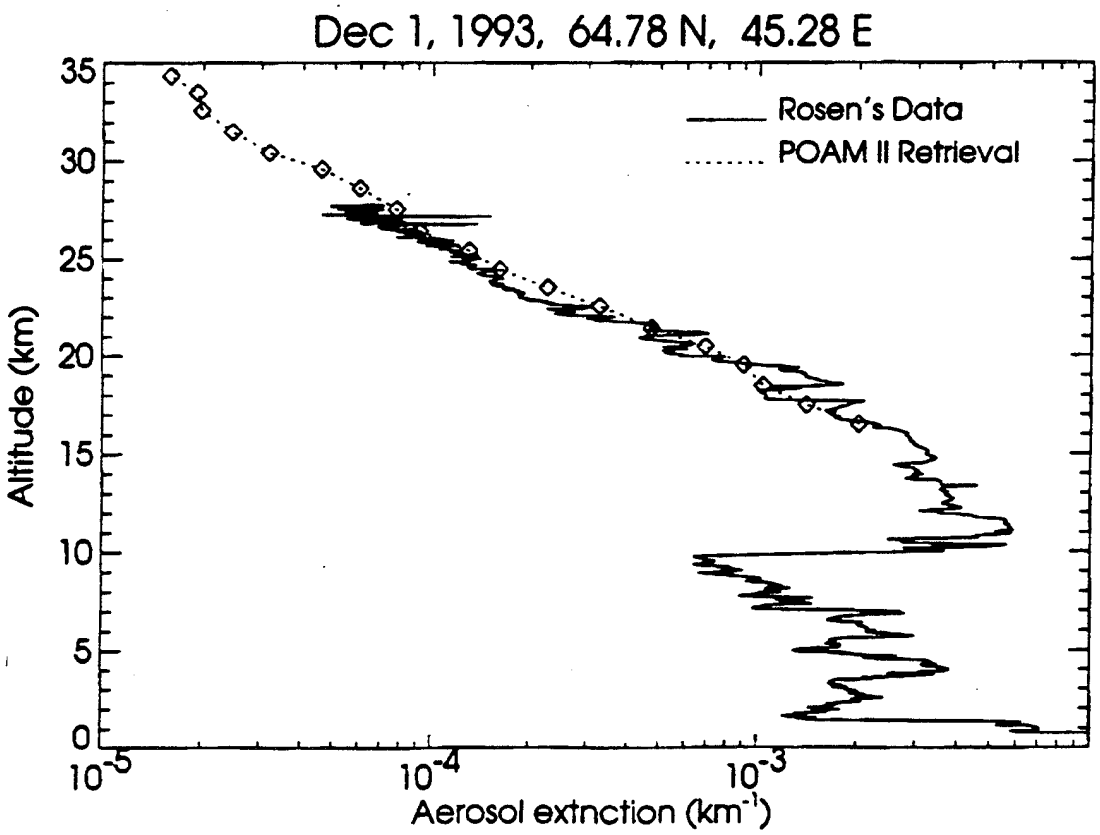
Dec 1, 1993, 64.78 N, 45.28 E
Rosen's Data
POAM II Retrieval
Altitude (km)
35
30
25
20
15
10
5
0
10-5
10-4
10-3
Aerosol extnction (km-1)

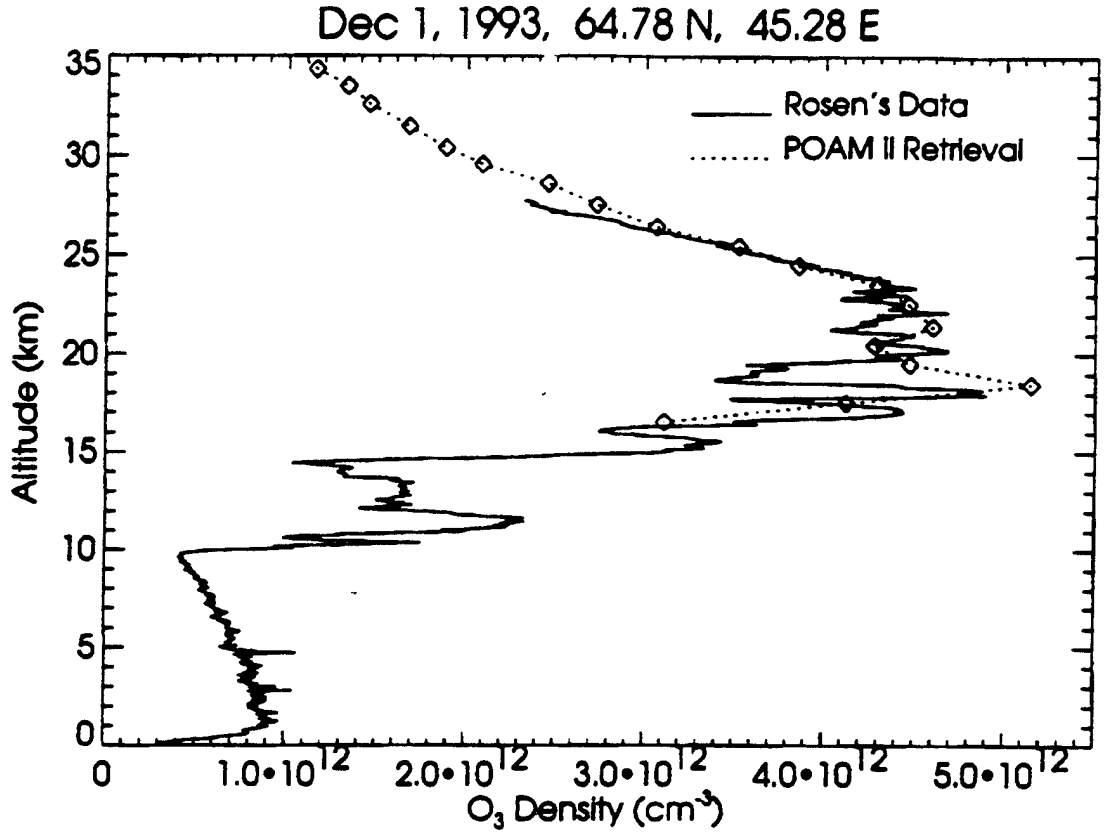
Dec 1, 1993, 64.78 N, 45.28 E
Rosen's Data
POAM II Retrieval
Altitude (km)
35
30
25
20
15
10
5
0
0
1.0•10^12
2.0•10^12
3.0•10^12
4.0•10^12
5.0•10^12
O3 Density (cm^-3)

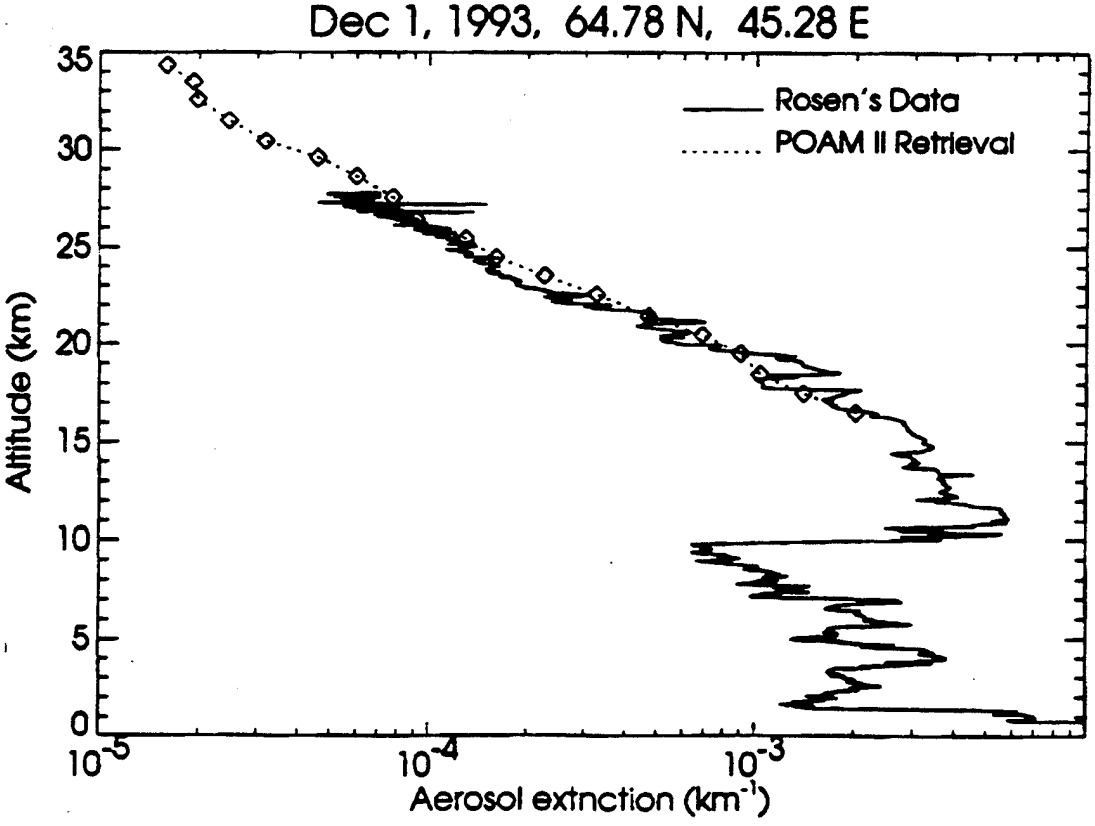
Dec 1, 1993, 64.78 N, 45.28 E
Rosen's Data
POAM II Retrieval
Altitude (km)
35
30
25
20
15
10
5
0
10^-5
10^-4
10^-3
Aerosol extnction (km^-1)

POAM II Comparisons with University of Wyoming Balloon Measurements near McMurdo (78° S 167° E)

Measurement Dates

Date	POAM II Time (GMT)	20 km Tan. Latitude	20 km Tan. Longitude	Range (km)	Balloon Time (GMT)
16 Oct 93	1002 1143	79.78 79.75	177.05 151.67	305 404	0100 15 Oct
23 Oct 93	1108	77.15	162.05	148	2200
28 Oct 93	1112	75.36	161.67	318	1100
30 Oct 93	1033	74.68	171.60	384	1000

Deshler & Johnson McMurdo profile Oct 15 compared with POAM II Oct 16

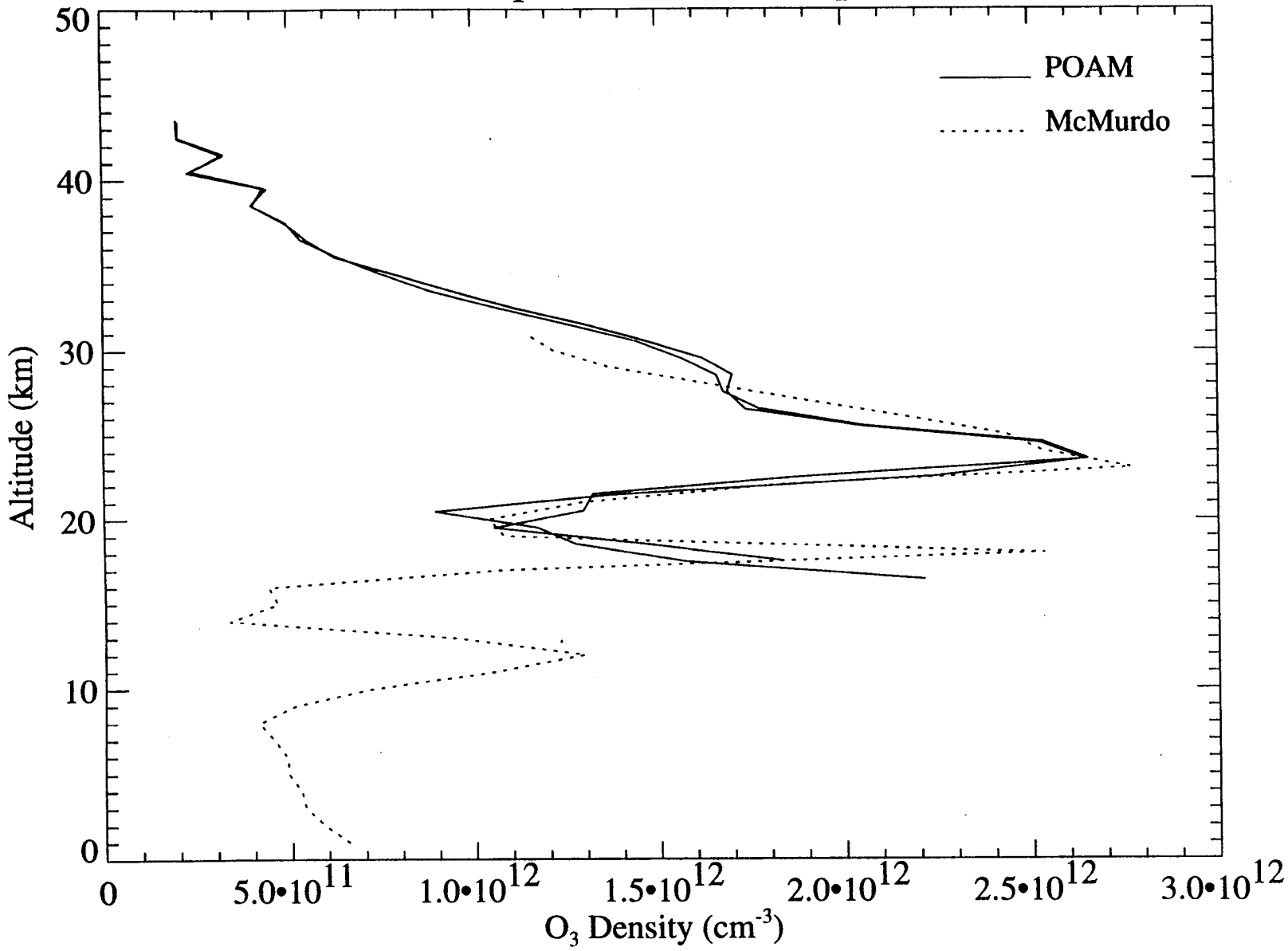

Polar Vortex & POAM Events: 931016

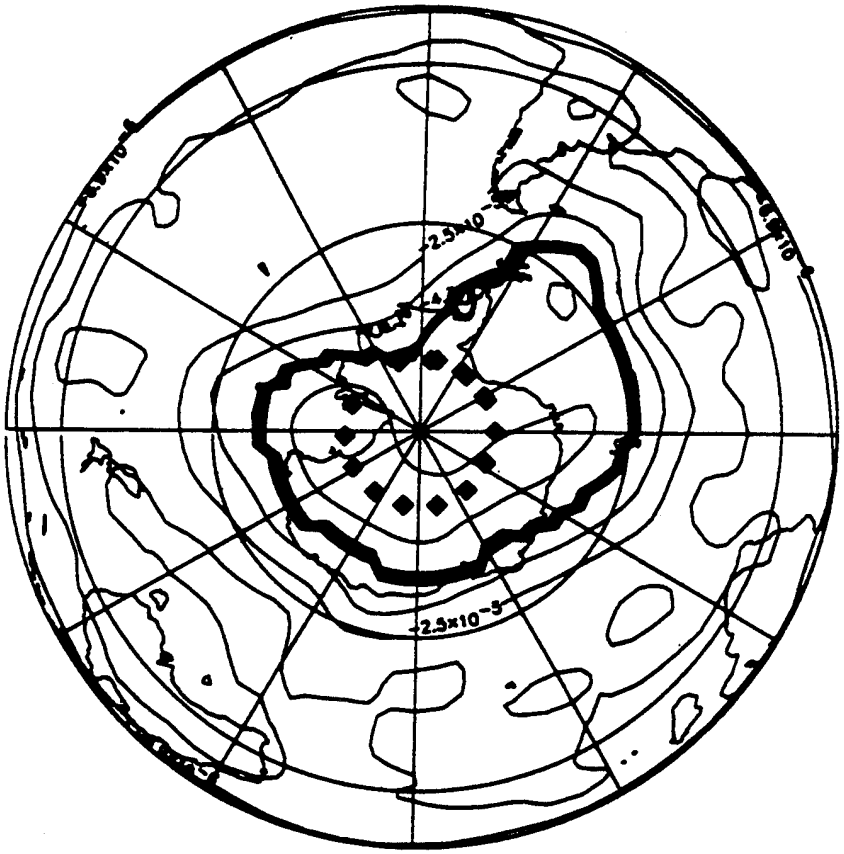

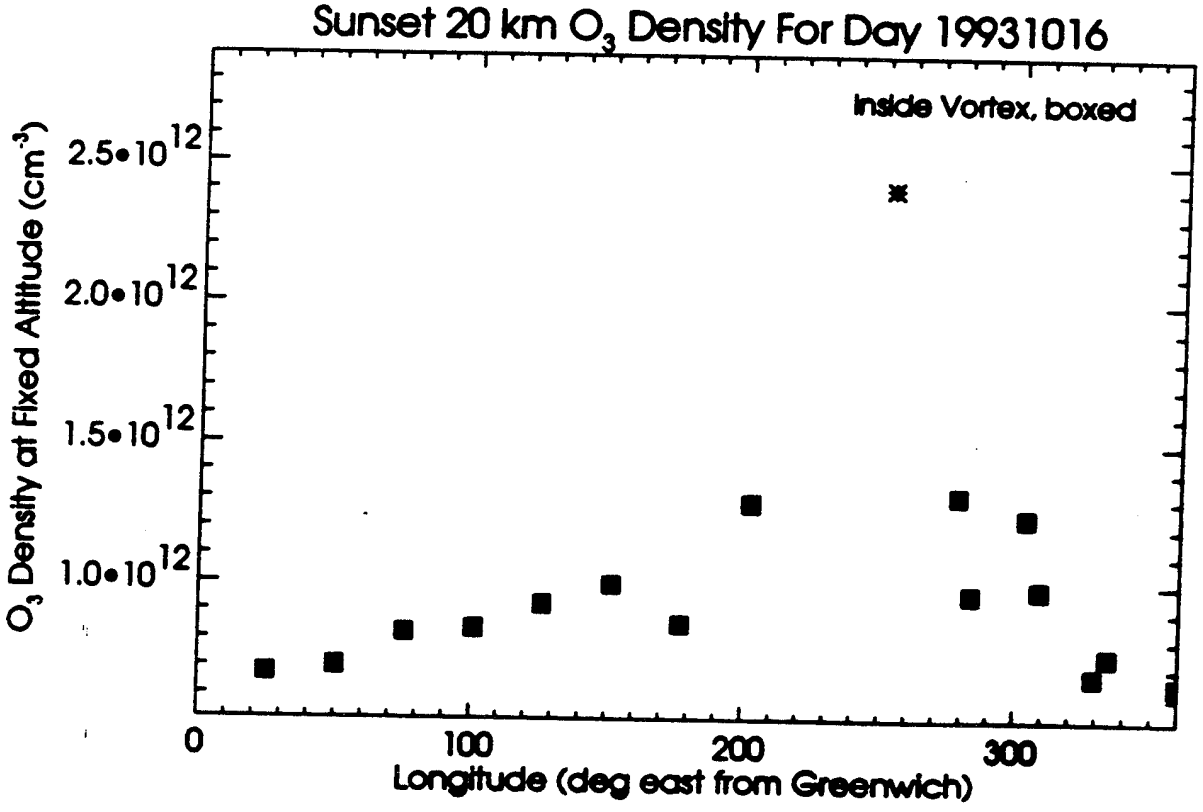

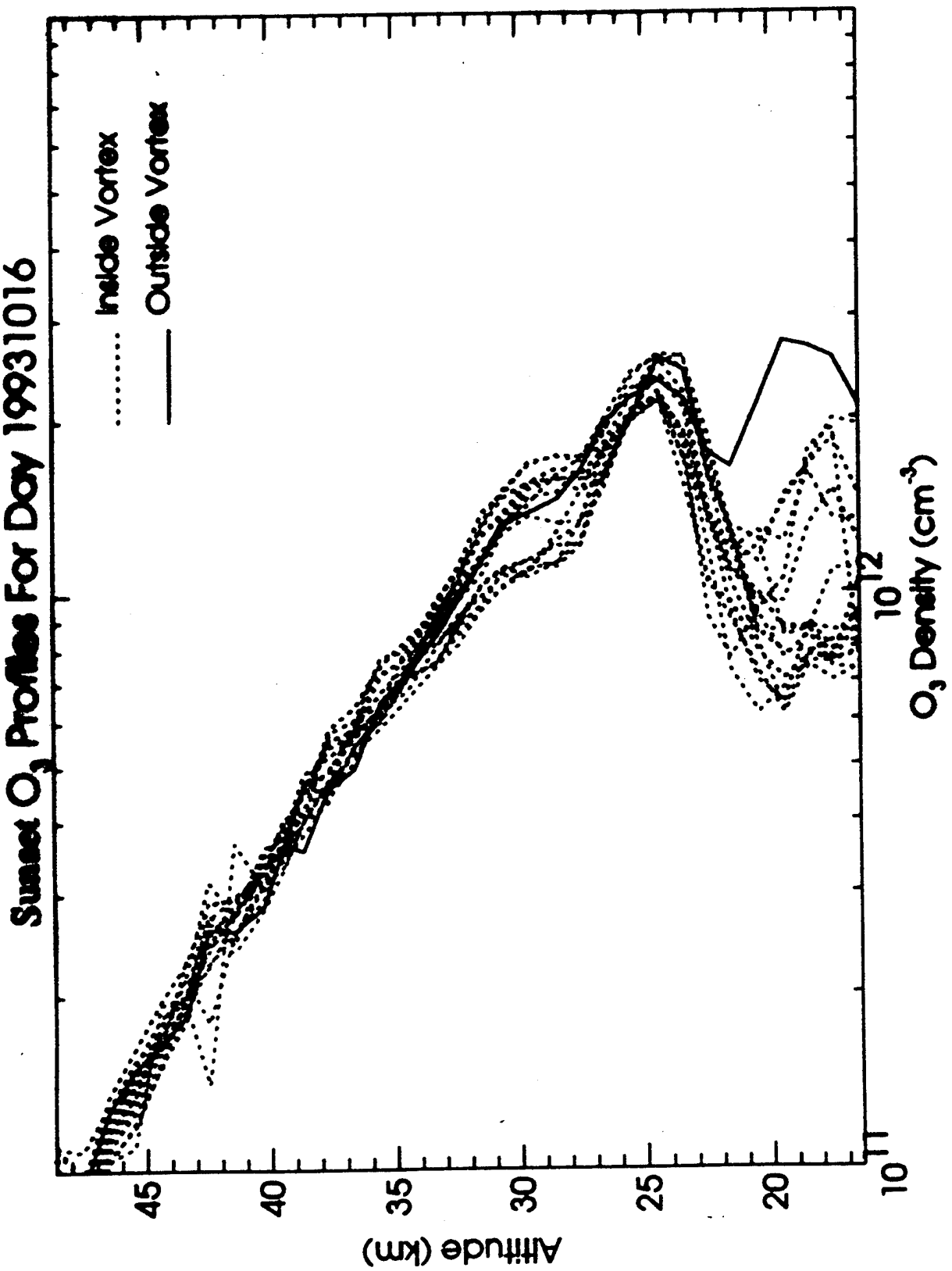
Sunset O_3 Profiles For Day 19931016
Inside Vortex
Outside Vortex
Altitude (km)
45
40
35
30
25
20
10^{11}
10^{12}
O_3 Density (cm^{-3})

Polar Vortex & POAM Events: 931108

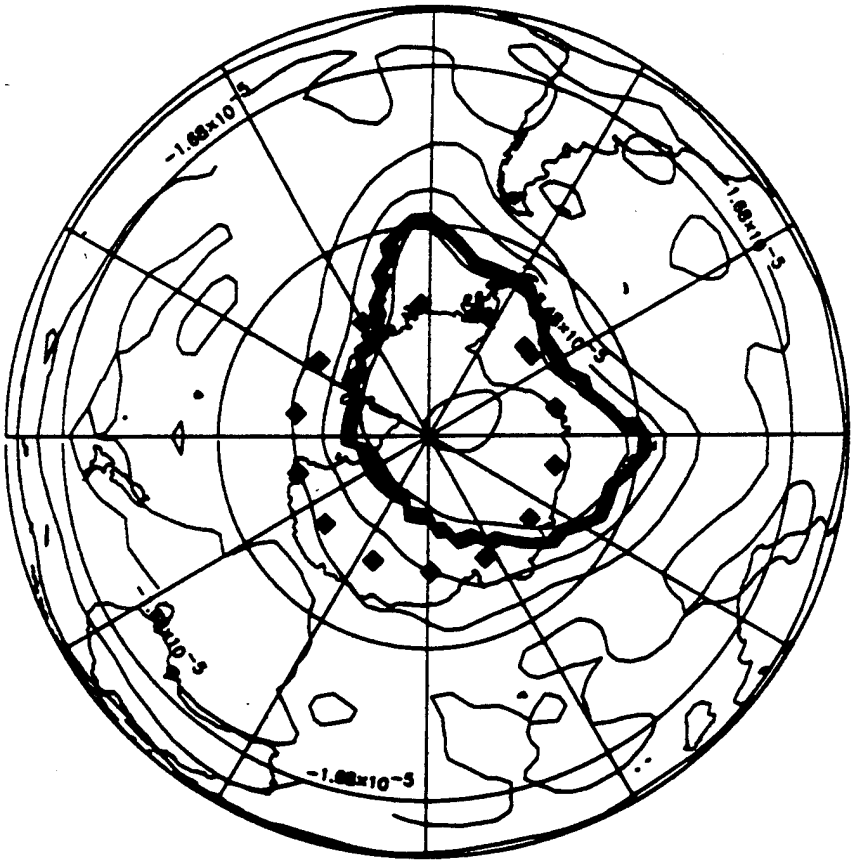

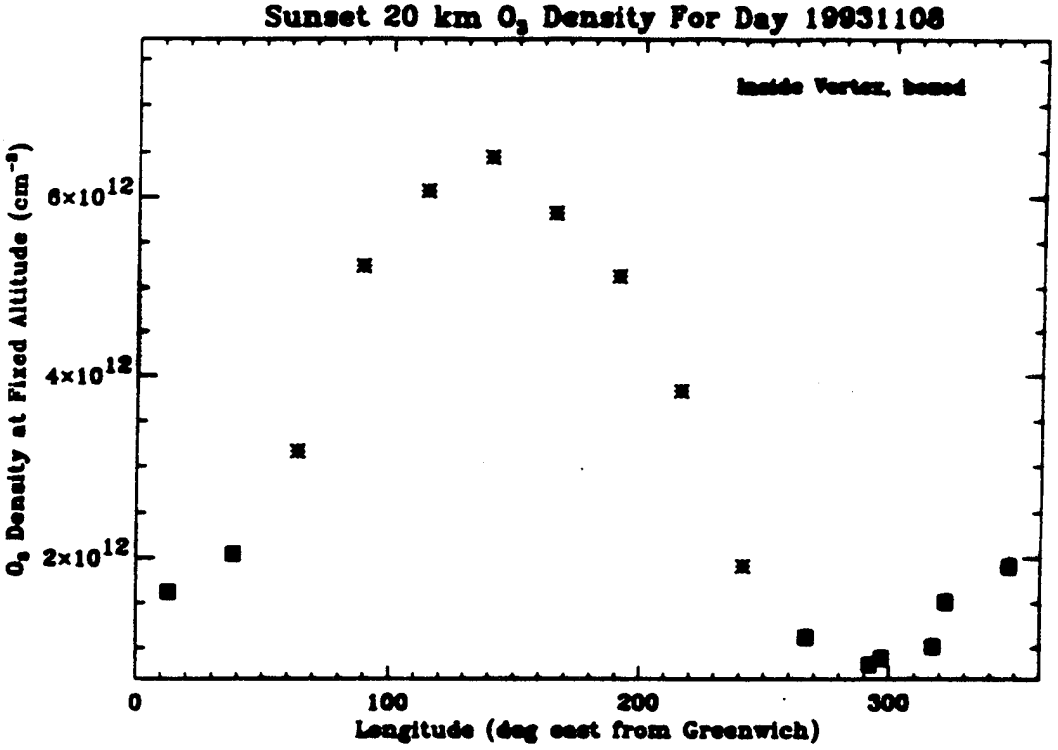

Ozone Concentration (cm^{-3}) Variation Over 1 Day
Southern Hemisphere For 10/16/93
cm^{-3}
6.0×10^{12}
5.0×10^{12}
4.0×10^{12}
3.0×10^{12}
2.0×10^{12}
1.0×10^{12}
Altitude (km)
30
25
20
50
100
150
200
250
300
350
Longitude

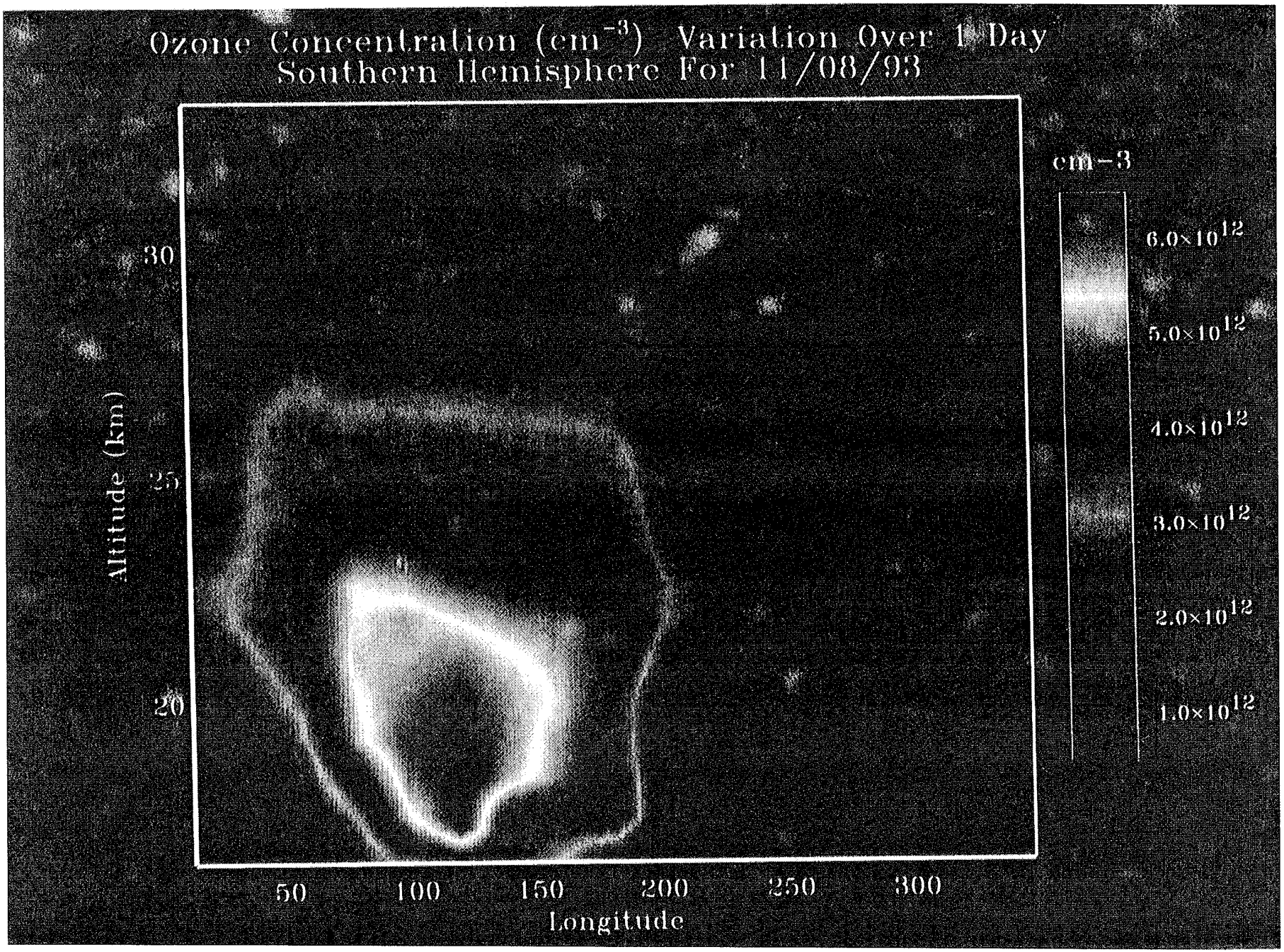
Ozone Concentration (cm^{-3}) Variation Over 1 Day
Southern Hemisphere For 11/08/93
Altitude (km)
30
25
20
50
100
150
200
250
300
Longitude
cm-3
6.0×10^{12}
5.0×10^{12}
4.0×10^{12}
3.0×10^{12}
2.0×10^{12}
1.0×10^{12}

Ozone Concentration (cm^{-3}) Variation Over 1 Day
Southern Hemisphere For 11/25/93
cm^{-3}
5.0×10^{12}
4.0×10^{12}
3.0×10^{12}
2.0×10^{12}
1.0×10^{12}
Altitude (km)
30
25
20
50
100
150
200
250
300
Longitude

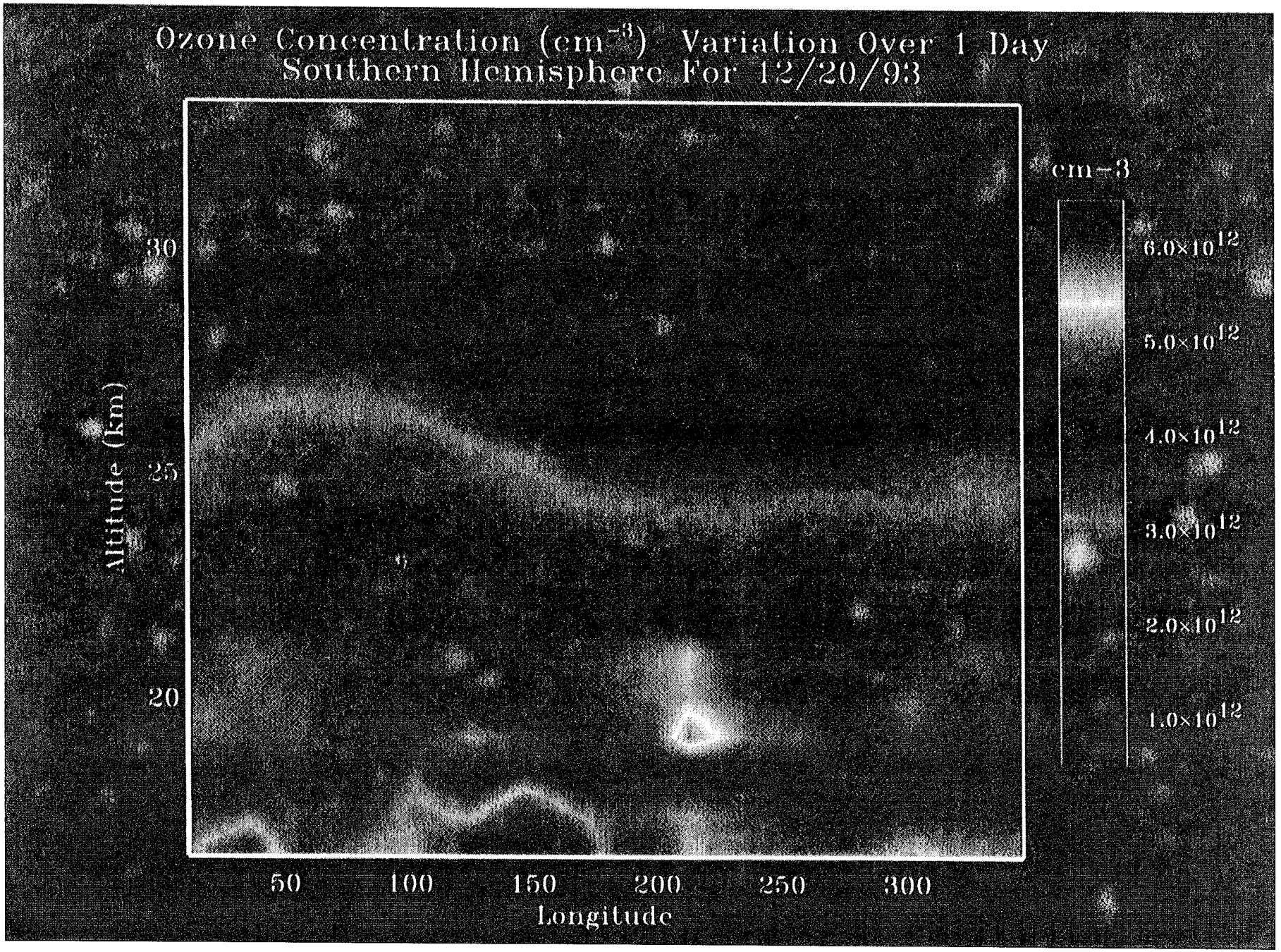
Ozone Concentration (cm^{-3}) Variation Over 1 Day
Southern Hemisphere For 12/20/93
Altitude (km)
30
25
20
50
100
150
200
250
300
Longitude
cm-3
6.0×10^{12}
5.0×10^{12}
4.0×10^{12}
3.0×10^{12}
2.0×10^{12}
1.0×10^{12}

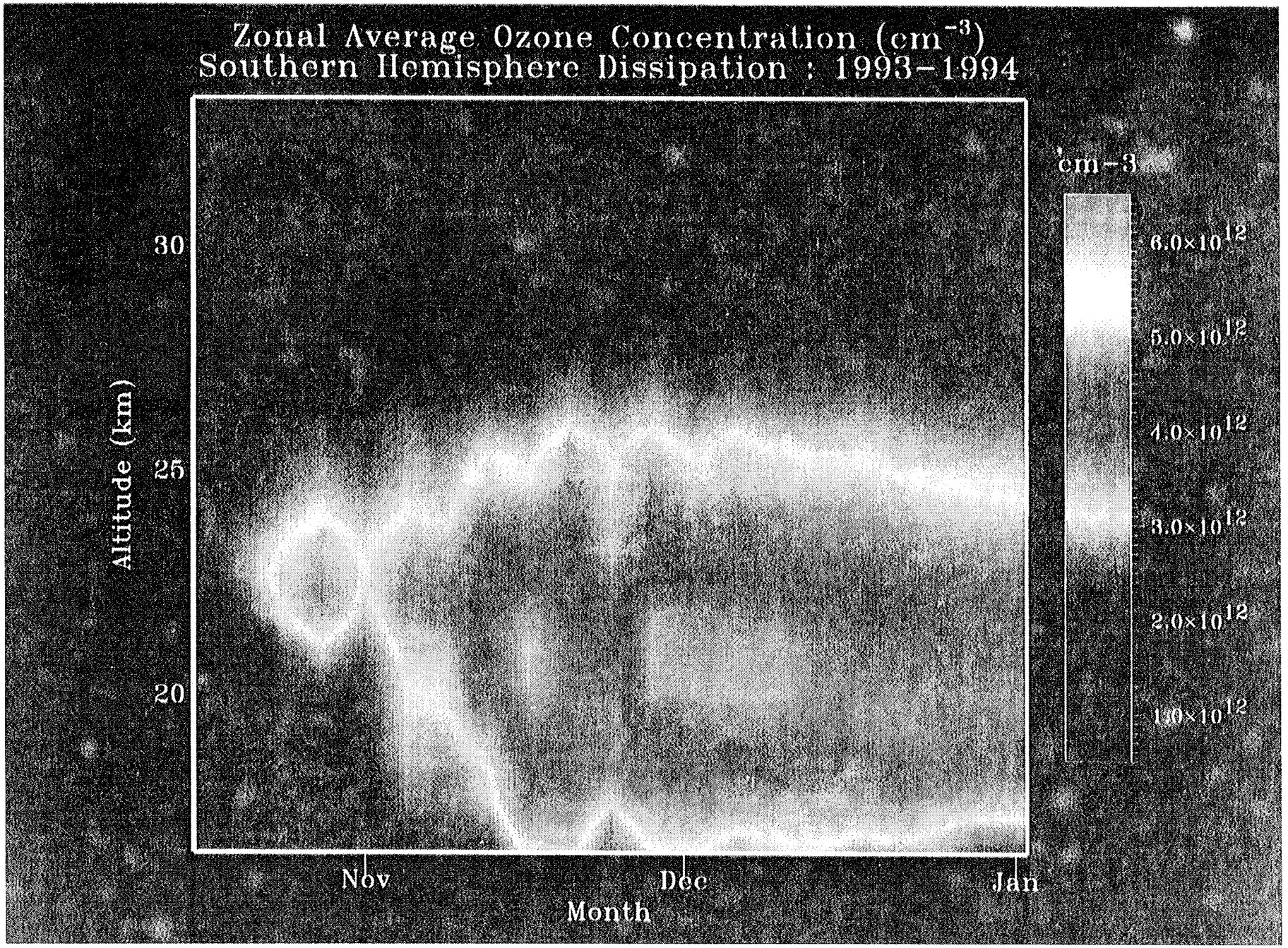
Zonal Average Ozone Concentration (cm^{-3})
Southern Hemisphere Dissipation : 1993–1994
Altitude (km)
30
25
20
Nov
Dec
Jan
Month
cm-3
6.0×10^{12}
5.0×10^{12}
4.0×10^{12}
3.0×10^{12}
2.0×10^{12}
1.0×10^{12}

Conclusions

* POAM II continues to operate well 8 months after launch.
* Validation of the Ozone retrievals is well under way.
* Validation of the other species has begun.

Large-Scale Retrieval of Atmospheric Parameter Profiles

Annual Review Conference on
Atmospheric Transmission Models

June 8, 1994

L. Sparks, J.L. Fanselow, J. McComb,
S. Nandi, J. Parker, and J.E. Patterson

Jet Propulsion Laboratory
California Institute of Technology
Pasadena, California 91109

Simulation / Data System

Functional Schematic

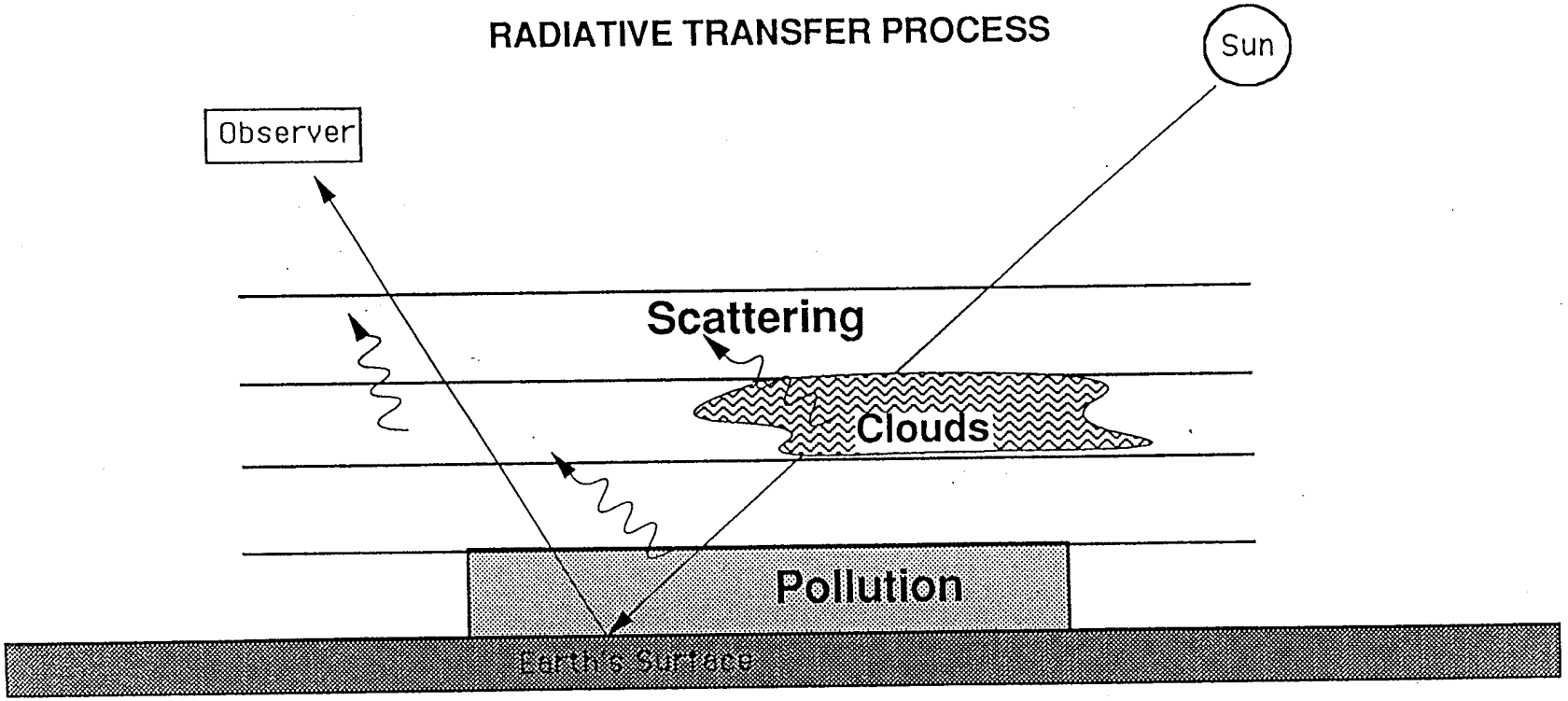

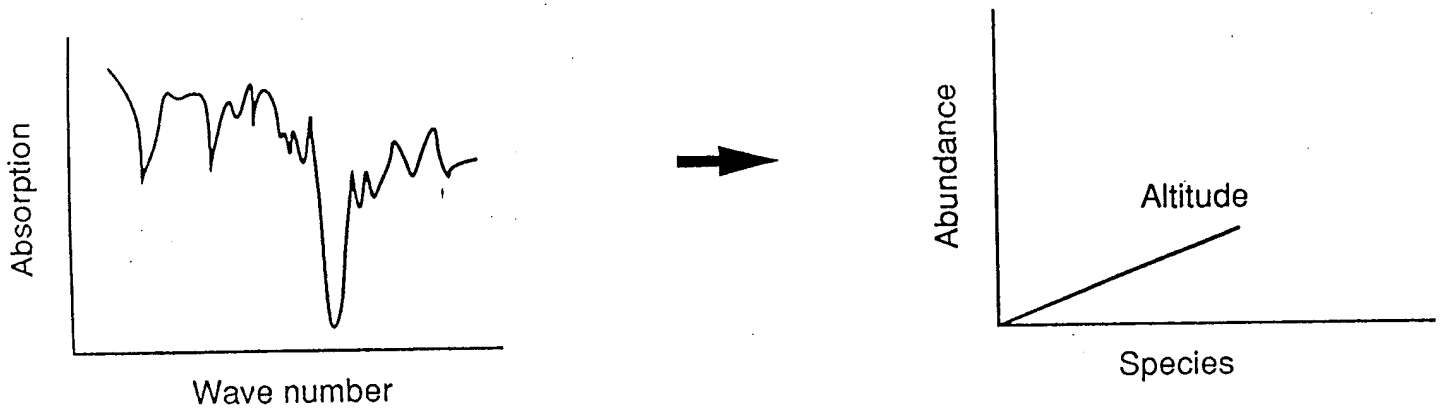

JPL

SEASCRAPE

Sequential Evaluation Algorithm for Simultaneous and Concurrent Retrieval of Atmospheric Parameter Estimates

- ***Sequential*** parameter estimation that utilizes a Square Root Information Filter, allows the specification of *a priori* data and constraints, and provides a formal error analysis.

- ***Simultaneous*** retrieval of multiple atmospheric profiles and instrument parameters.

- ***Concurrent*** data analysis on a parallel processor.

- ***Retrieval*** algorithm integrates the forward model with the inversion algorithm (the forward model can stand alone as a simulation tool).

JPL

Features of SEASCRAPE

Version 1.0

- Nadir sounding.
- Retrieval of temperature, pressure, and constituent profiles.
- Simultaneous processing of multiple spectra.
- One dimensional model (spherical symmetry).
- Homogeneous layers with arbitrary spacing.
- Refraction (discontinuous refractive index).
- Parameters defined at zone boundaries, where a zone consists of one or more layers.
- Constraints and *a priori*:
  A. Hydrostatic equilibrium.
  B. Parameter ranges.

JPL

Features of SEASCRAPE (*cont.*)

Version 1.0

- Absorption/emission spectra (modeled on a line-by-line basis).
- Continuum absorption: H_2O, CO_2, O_2, N_2.
- Absorption cross sections for species where individual lines cannot be modeled.
- Modeling and retrieval of surface brightness temperature.
- Formal, quantitative error analysis.
- SEA_Front, a menu-driven front-end for operating SEASCRAPE.
- Public domain software with anonymous FTP access.

JPL

Features of SEASCRAPE (*cont.*)

Version 2.0 and beyond

- Implementation in a parallel processing environment.
- Limb and nadir sounding.
- Ground emission and reflection.
- Multi-dimensional atmospheric model.
- Inhomogeneous cells:
  A. Improved ray-tracing.
  B. Improved integration of the equation of radiative transfer.
  C. Improved hydrostatic equilibrium.
- Clouds, aerosols, and scattering, possibility incorporating existing electromagnetic scattering codes.
- Retrieval of instrumental parameters.

JPL

Applications

- Airborne Emission Spectrometer (AES) - nadir sounding, emission spectra
- Deep Space Network (DSN) - uplooking retrieval of water vapor profiles, emission spectra
- ATMOS Fourier Transform Spectrometer (FTS) for the ATLAS Shuttle payload - limb sounding, transmission spectra
- Spectroscopic community- simulation studies
- Tropospheric Emission Spectrometer (TES) for Eos - nadir and limb sounding, emission spectra

JPL

Structure of SEASCRAPE

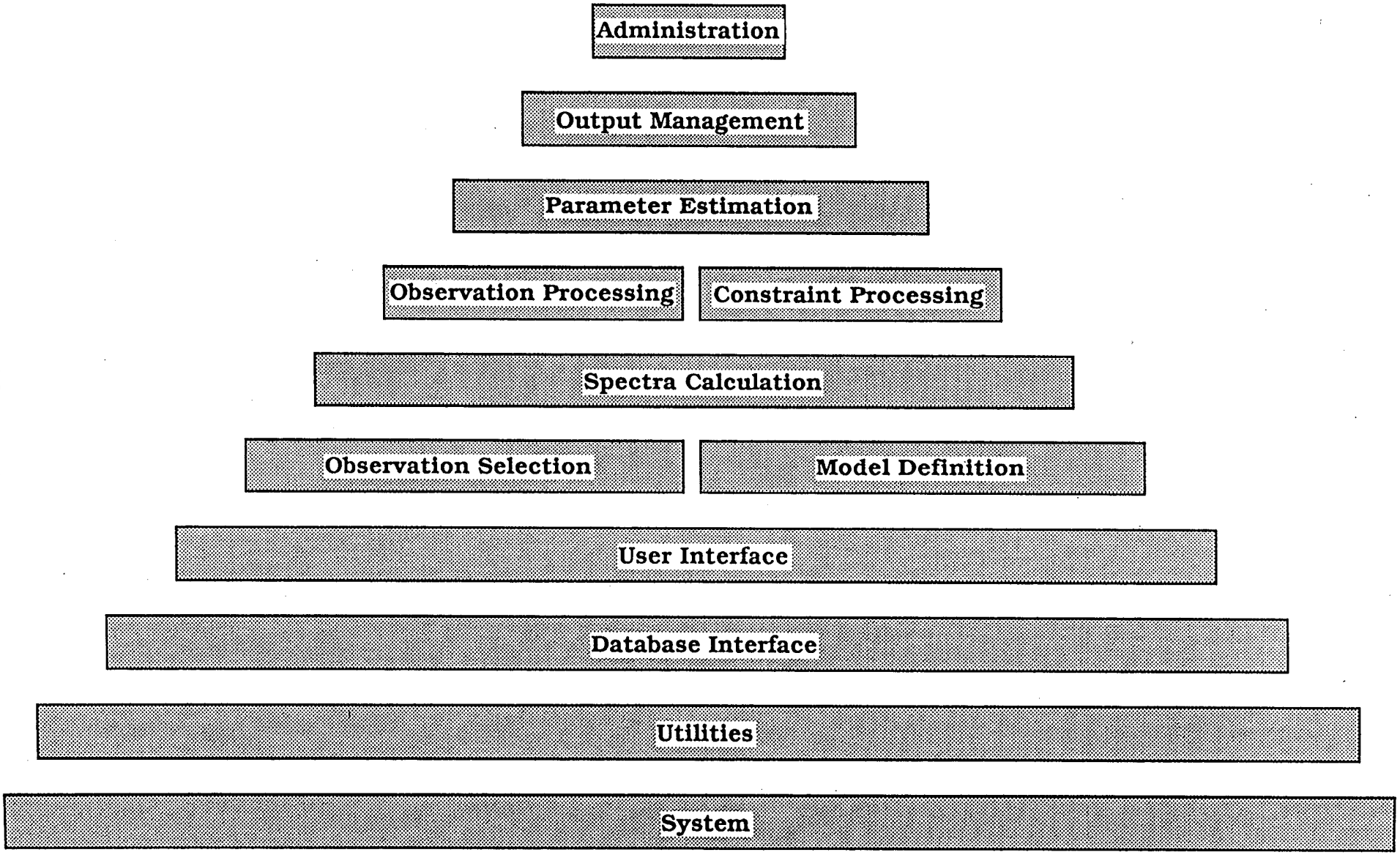

JPL

SEASCRAPE

Data Flow

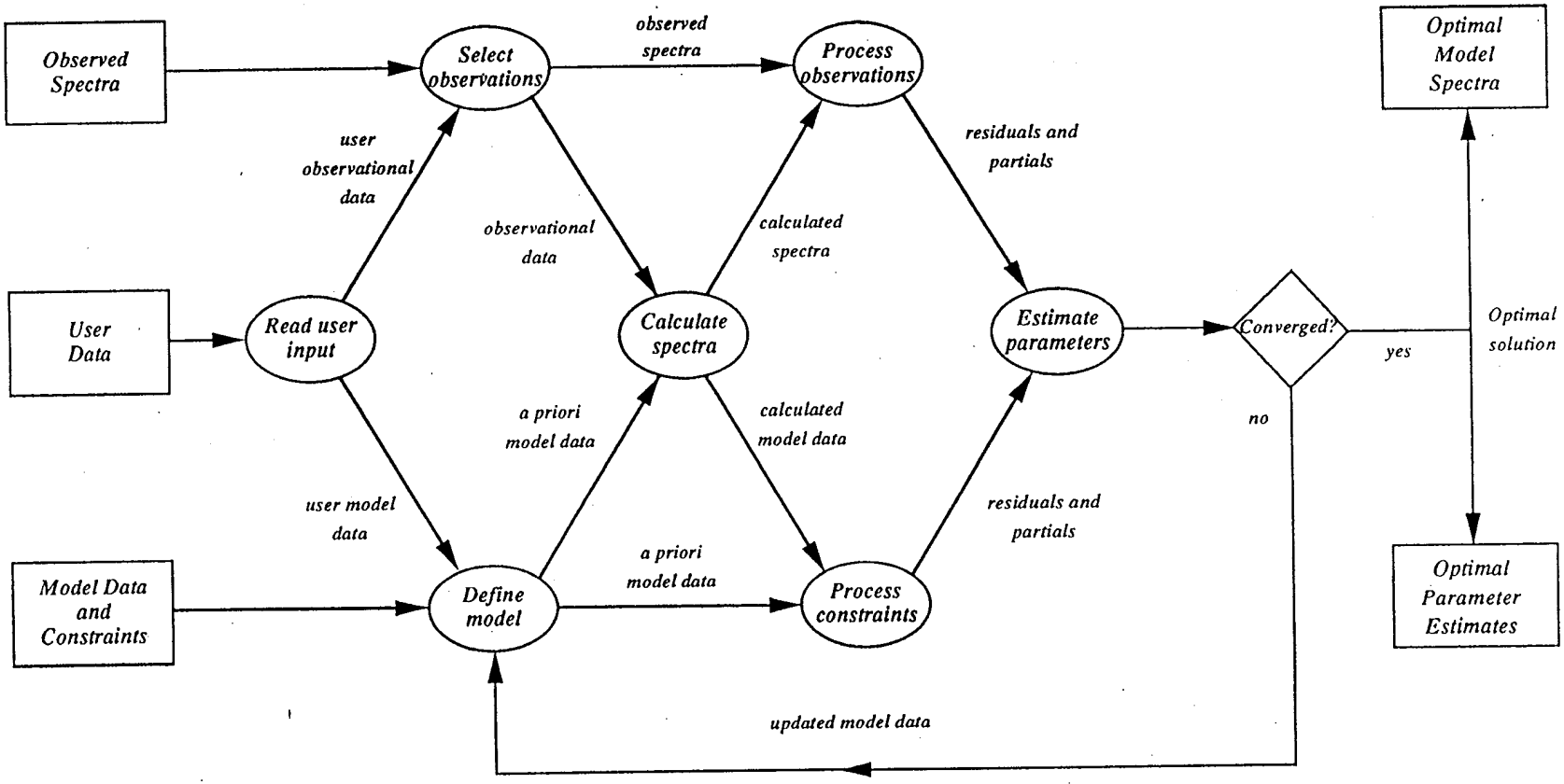

JPL

Forward Model

Radiation reaching the instrument is a function of the radiation emitted, scattered and absorbed by the atmosphere as well as the radiation emitted and reflected by the background.

Equation of radiative transfer:

$$\frac{\partial J(\nu,s)}{\partial s} = -\kappa(\nu,s)[J(\nu,s) - B(\nu,s)]$$

where

$J(\nu,s)$ ≡ radiance;
$\kappa(\nu,s)$ ≡ extinction coefficient;
$B(\nu,s)$ ≡ thermal emission;
ν ≡ frequency;
s ≡ path length;

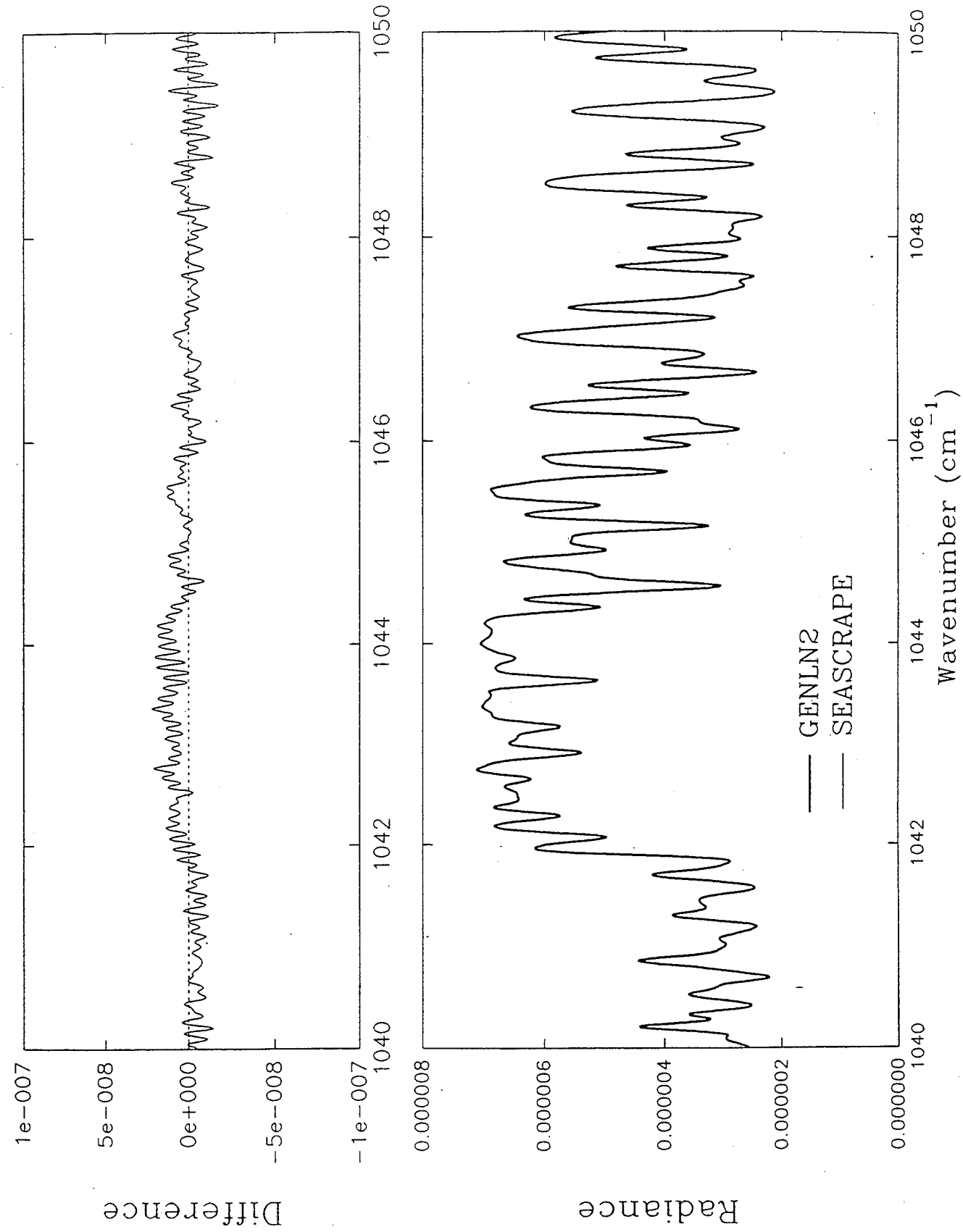
GENLN2 vs. SEASCRAPE – Case 2aa
Difference
1e-007
5e-008
0e+000
-5e-008
-1e-007
1040
1042
1044
1046
1048
1050
Radiance
0.000008
0.000006
0.000004
0.000002
0.000000
GENLN2
SEASCRAPE
Wavenumber (cm^{-1})

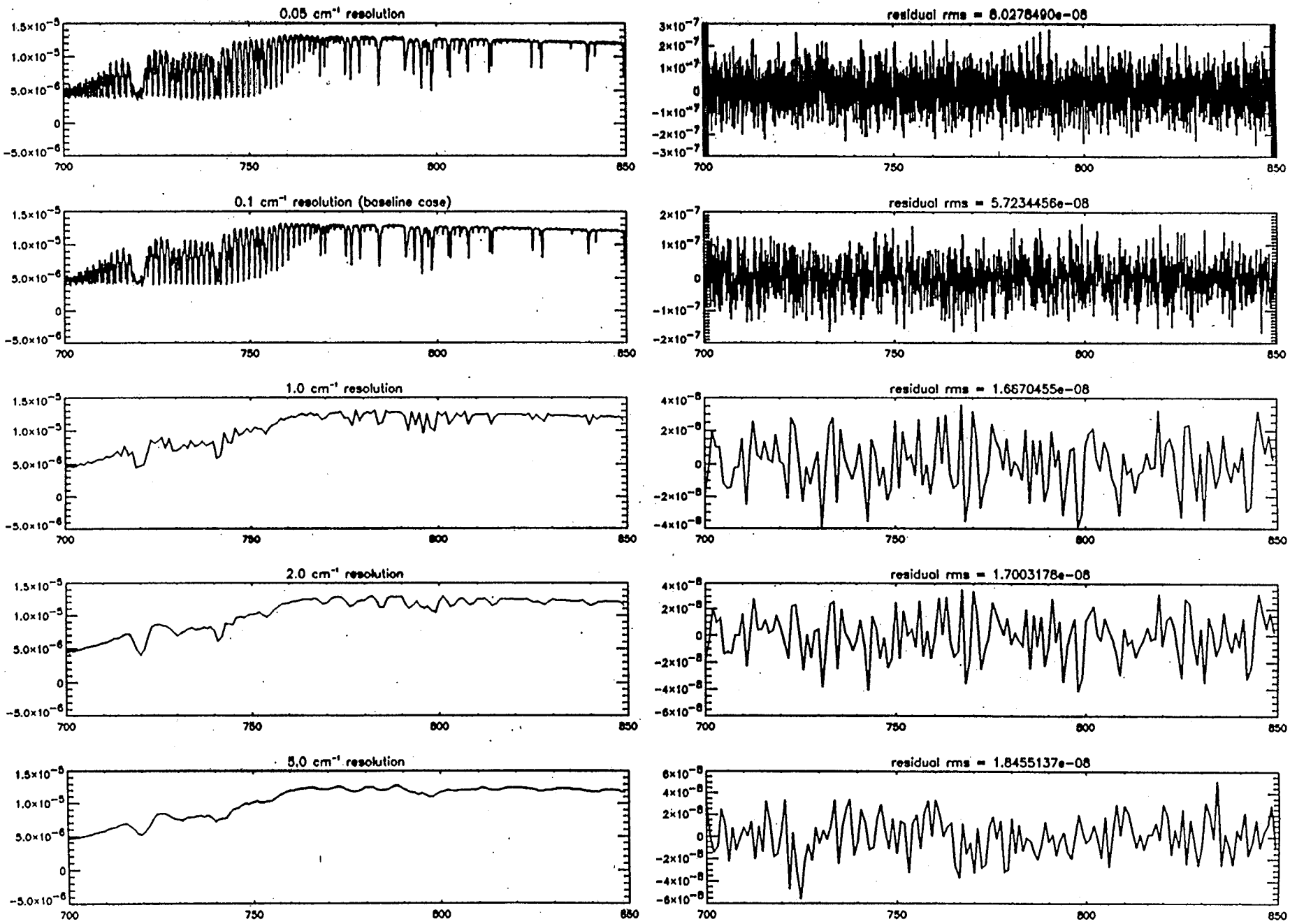

S. Nandi 4/13/94

JPL

Parameter Estimation

Processing observations:

$$\bar{J}_\nu = J_\nu + \sum_{n=0}^{N} \frac{\partial J_\nu}{\partial \Lambda_n} \Delta\Lambda_n + \varepsilon_\nu$$

where $\bar{J}_\nu$ ≡ observed radiance; Λ_n ≡ parameters to be estimated;
J_ν ≡ modeled radiance; ε_ν ≡ error;

Processing constraints:

$$\bar{f} = f + \sum_{n=0}^{N} \frac{\partial f}{\partial \Lambda_n} \Delta\Lambda_n + \varepsilon$$

where $\bar{f}$ ≡ imposed value of constraint; ε ≡ error.
f ≡ estimated value of constraint;

Solve for $\Delta\Lambda_n$.

Least Squares Process

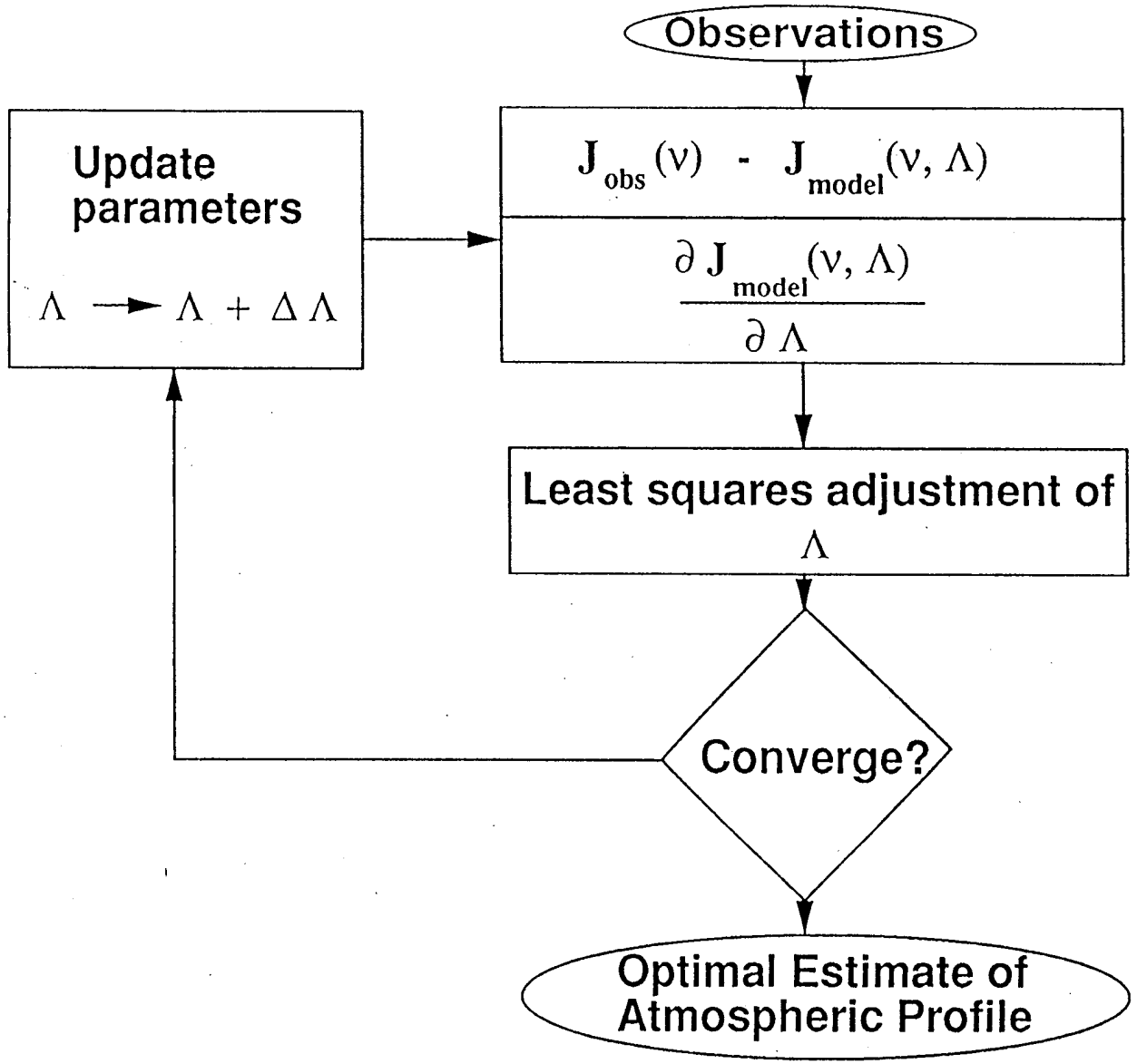

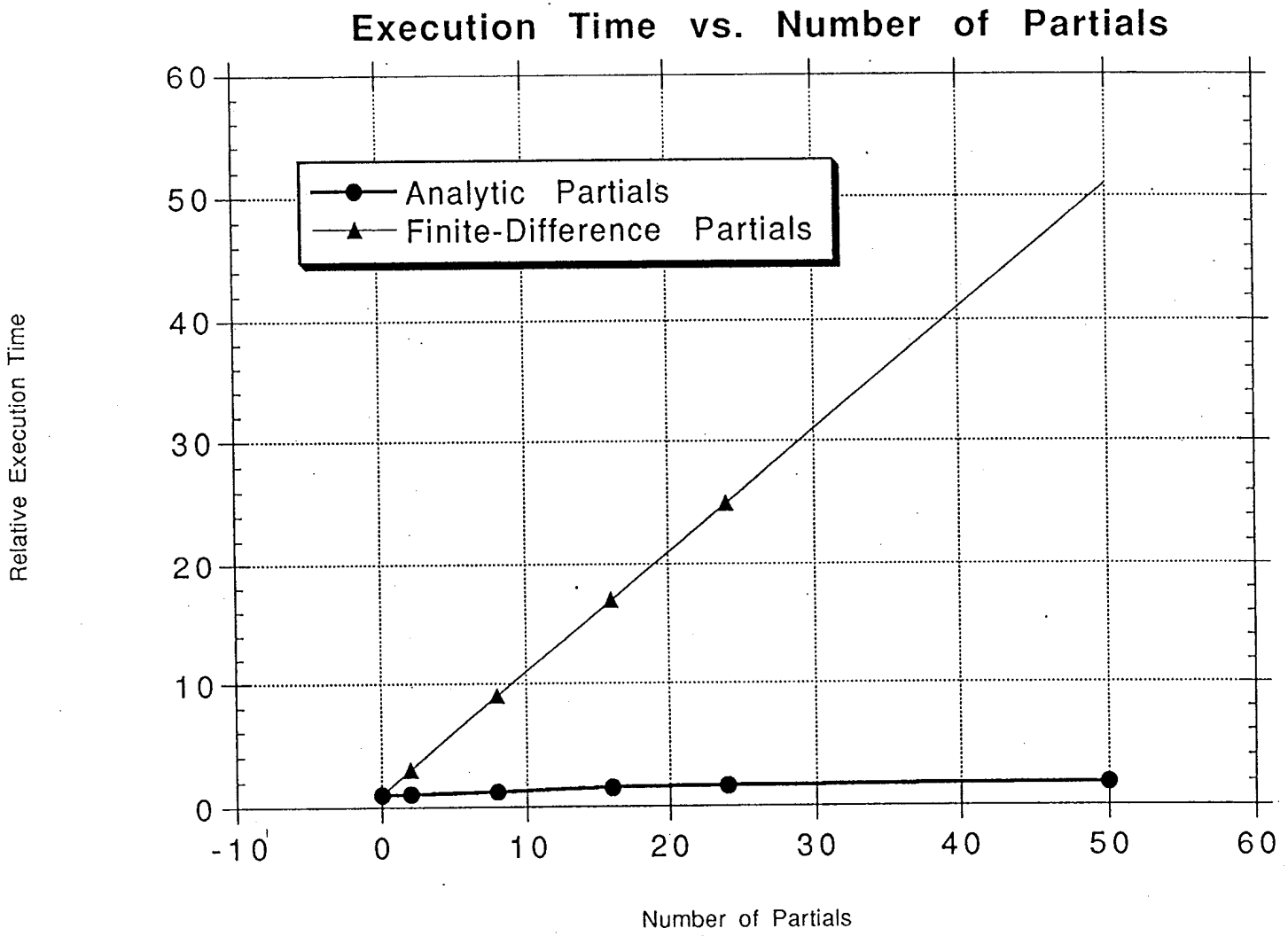
Execution Time vs. Number of Partials
Analytic Partials
Finite-Difference Partials
Relative Execution Time
Number of Partials
60
50
40
30
20
10
0
-10
0
10
20
30
40
50
60

JPL

Error Analysis

In addition to retrieving parameter profiles, the estimation algorithm provides a systematic, quantitative error analysis:

Observational error (i.e., noise)
A priori model error
$\Rightarrow$ Parameter error

The output parameter error covariance matrix describes quantitatively:

- the uncertainty of the retrieved parameters;
- correlations between the errors in the retrieved parameters;
- the optimal parameterization of the observational model.

JPL

Parallel Implementation of SEASCRAPE

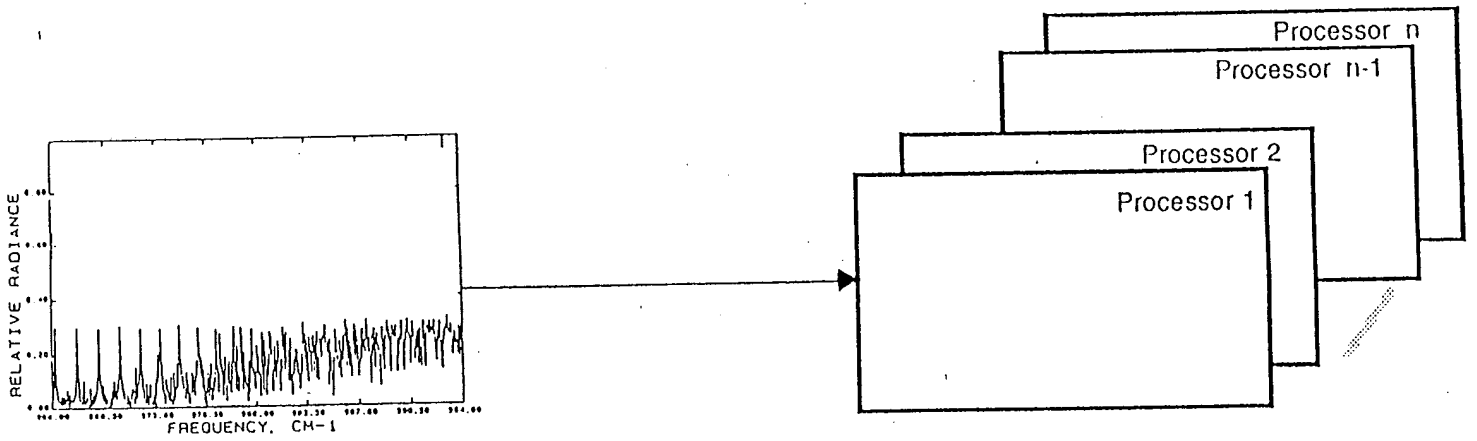

In the parallel decomposition of SEASCRAPE, each processor

- *receives a frequency window of the observed spectrum*
- *has resident in memory its section of the line list data base*
- *forms it own SRIF matrix for the estimated parameters which is then combined with the SRIF matrices from the other processors*

Processor attributes:

- *MIMD (each processor must be independent to avoid serious load imbalance)*
- *high performance (10 - 30 MFLOPS)*
- *large DRAM (16-64 megabytes)*

aer

A GENERAL INVERSION PACKAGE FOR ADVANCED RETRIEVAL OF ATMOSPHERIC SPECIES FROM HIGH SPECTRAL RESOLUTION MEASUREMENTS

J.L. MONCET
W.O. GALLERY

ATMOSPHERIC AND ENVIRONMENTAL RESEARCH, INC.

Annual Review Conference on Transmission Models
Phillips Laboratory, Hanscom AFB, MA
June 7-8, 1994

aer

Introduction

- Goal: to develop a generic research grade inversion code
  - Simultaneous retrieval of atmospheric temperature and/or atmospheric species concentration (water vapor and trace species)
  - Applied to high spectral resolution radiance measurements.

- Main Features:
  - Based on non-linear least-squares inversion technique
  - Radiative transfer (forward model)
    - Currently uses optical depth calculation from FASCODE plus internal layer looping/interface for user-supplied forward model: exact (line-by-line) or approximate (e.g. MODTRAN)

- Applicable to any viewing geometry: upward/downward/limb and can accommodate any instrument type from microwave to IR sounder (satellite or balloon borne, or ground based)

aer

Introduction (continued)

- Some Requirements:
  - Computationally fast
  - Flexible user input (can easily select retrievable species, atmospheric layering, viewing geometry, instrument characteristics,...)
  - Allows the retrieval of non-atmospheric parameters (spectroscopic parameters, calibration parameters, tangent height for limb case ...)

- Applications
  - Actual data analysis and exploration fo the retrieval capability of particular instrument designs (e.g. DBIS, SCRIBE, CIRRIS, MSX)
  - Retrieval simulations for sensor design trade studies (MOES, AIRS, ITS)
  - Benchmarking fast forward model parameterizations or non-optimal retrieval approaches (e.g. onion peeling) used in operational applications

aer

Comparison with Current Operational Retrieval Algorithms

- A number of specialized non-linear inversion codes are already available or being developed for various applications (e.g. AIRS program, UARS)
- These codes use fast parameterizations of the atmospheric transmission for each individual molecular species (e.g. McMillin and Fleming, 1976, Eyre and Woolf)
- Issues:
  - Process of parameterizing the forward model may be expensive (requires multiple runs of reference line-by-line model and validation)
  - Algorithm bound to a specific instrument design and atmospheric representation (vertical layering,...etc.)
  - Parameterization of the forward model not error free and the impact on the retrieval product is generally not known

=> Fast parameterization is impractical at an exploratory stage

  - Dificult/expensive to vary instrument characteristics and to revise spectroscopic parameters and atmospheric representation
- Answer:
  - Need to sacrifice actual execution time for enhanced flexibility and versatility

aer

General Code Description

- 4 separate modules:
  - Radiative transfer (XFWS)
  - Filtering
  - Pre-inversion processor
  - Inversion (XINV)
- Can be run interactively and independently or run together controlled by script
- Atmospheric layering implicit in the definition of the first-guess
- Unique input control file for all 4 modules used to:
  - Select viewing geometry (by specifying instrument altitude and viewing angle(s))
  - Select instrument function from preset filter bank
  - Select any of the 35 standard HITRAN molecular species to be retrieved simultaneously over specified altitude range (extended in the future to heavy molecules)
- XFWD uses atmospheric optical depths generated by an external forward model (runs currently with FASCODE routine HIRAC1). Radiative transfer is done internally by XFWD
- Interface for external forward model (e.g. MODTRAN)

Block Diagram of Retrieval Algorithm

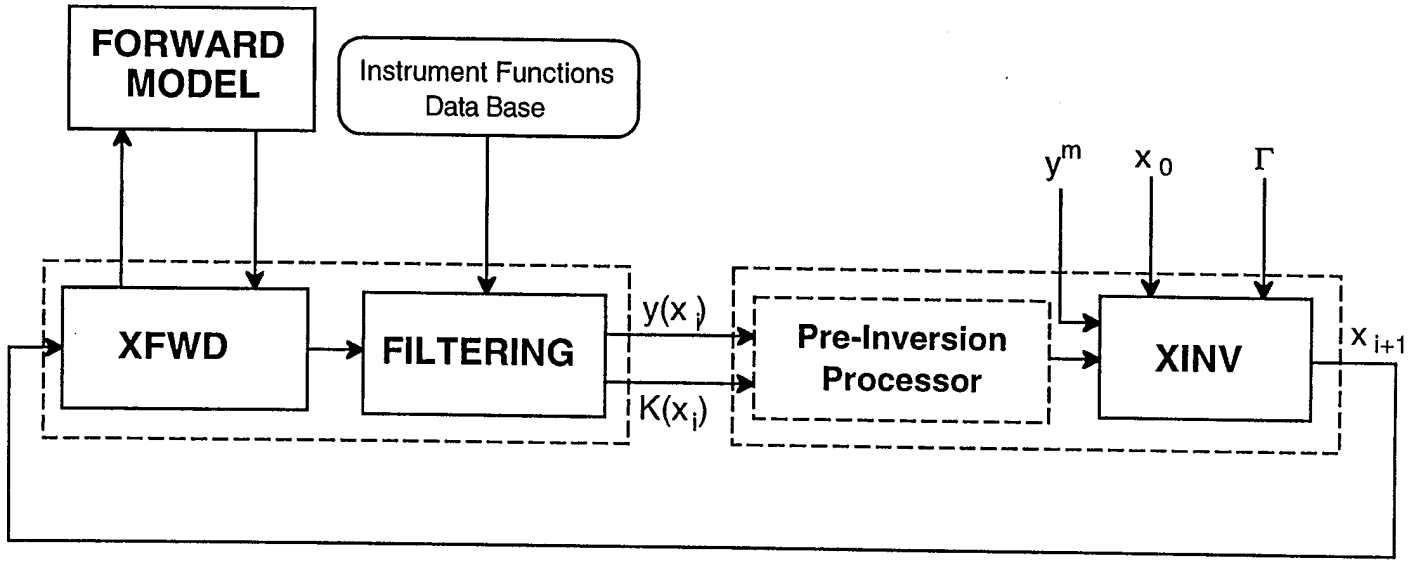

x_0 = background (first-guess) atmospheric profile

x_i = estimated atmospheric profile at iteration i

$y(x_i)$ = calculated radiances

y^m = radiance measurements

$K(x_i)$ = Jacobian or sensitivity matrix

Γ = matrix of "damping" coefficients

aer

Optimal Retrieval Approach (see Rodgers, 1976 and Eyre, 1989)

- Simultaneous retrieval of all species concentration at all atmospheric levels from available measurements
- Non-linear least-squares method based on Newton iteration procedure
- Optimal solution $\hat{x}$ is such that the following cost function is minimized

$$J(x) = \left(y^m - y(x)\right)^t w\left(y^m - y(x)\right) + \left(x - x_o\right)^t \Gamma\left(x - x_o\right)$$

- Solved by linearizing forward model around current guess at each iteration step:
  $\delta y = K\delta x$; K is the Jacobian - calculated in XFWD

- The optimal solution is

$$x_i = x_{i-1} + H^{-1}\left[K^t W\left(y^m - y\left(x_{i-1}\right)\right) + \Gamma\left(x_0 - x_{i-1}\right)\right]$$

where

$$H = \left(K^t W K + \Gamma\right)$$

- Γ can be manually tuned or evaluated from background error statistics when available (maximum probability solution (see Rodgers, 1976)

Radiative Transfer Algorithm

- **Start with layer furthest away from the observer (layer 1 in upward looking case)**

LAYER 1

1a) calculate ε_1 **and** $\frac{\partial \varepsilon_1}{\partial \tau_1}$

1b) calculate $\frac{\partial y}{\partial q_{1,m}} = \frac{\partial \varepsilon_1}{\partial \tau_1} \times \frac{\partial \tau_1}{\partial u_{1,m}} \times \frac{\partial u_{1,m}}{\partial q_{1,m}}$

for m = 1,...M (number of constituents)

1c) update $\sigma_1 = \varepsilon_1$

LAYER 2

2a) calculate ε_2 **and** $\frac{\partial \varepsilon_2}{\partial \tau_2}$

2b) calculate $\frac{\partial y}{\partial q_{1,m}} = \frac{\partial y}{\partial q_{1,m}} + \left(\frac{\partial \varepsilon_2}{\partial \tau_2} - \sigma_1\right) \times \frac{\partial \tau_2}{\partial u_{2,m}} \times \frac{\partial u_{2,m}}{\partial q_{1,m}}$

and $\frac{\partial y}{\partial q_{2,m}} = \left(\frac{\partial \varepsilon_2}{\partial \tau_2} - \sigma_1\right) \times \frac{\partial \tau_2}{\partial u_{2,m}} \times \frac{\partial u_{2,m}}{\partial q_{2,m}}$

for m= 1,...M (number of constituents)

2c) update $\sigma_2 = \sigma_1 + \varepsilon_2$

REPEAT 2a,b,c FOR LAYER 3 AND SUBSEQUENT LAYERS

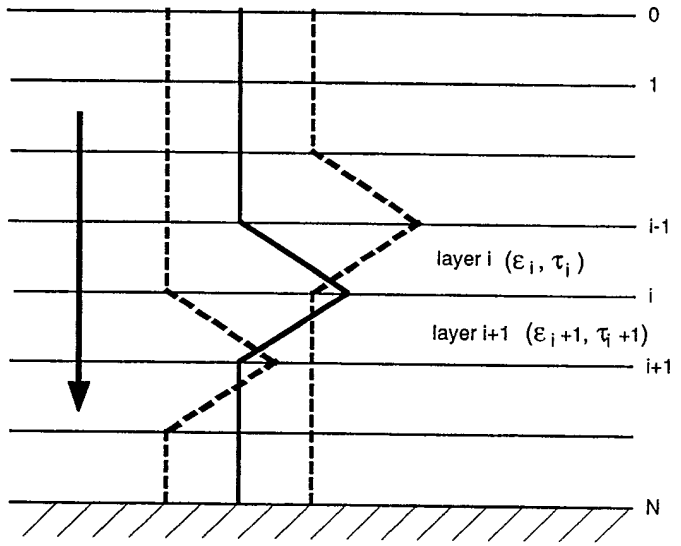

τ_i = layer optical depth

$\varepsilon_i = \varepsilon_i\left(\tau_i, \overline{T}, T_{bound}\right)$ contribution of layer i to observed radiance y

$\sigma_i = \sum_{j=1}^{i} \varepsilon_j$; contribution of atmosphere above level i to the observed radiance $(\sigma_i = y)$

u_i = absorber amount for layer i

q_i = mixing ratio at boundary i

aer

Accelerated Numerical Implementation

- Existing "Path Characterization" algorithm (Isaacs et al,1990) calculates Jacobian by finite differencing on radiances - i.e. computes as many radiances as there are retrieved parameters
- New approach: calculates Jacobian analytically
- Gain in computation is achieved by

  1) eliminating the redundancy in the radiative transfer calculations

	Current	New	Gain (for N=20, M=2)*
# of opt. depth calculations	N + MxN**2	N + MxN	~14
# of layer emission calculations	N + MxN**2	<2N	~20**

* N = number of levels, M = number of constituents (e.g. M=2 for simultaneous retrieval of temperature and water vapor); gain = current/new operations

** Looses roughly a factor 2 over Path Characterization algorithm due to the fact that current code operates at finest DV.

aer

Accelerated Numerical Implementation (continued)

2) efficient vectorization (each step in the radiative transfer calculations operates simultaneously on 2400 spectral elements)

3) minimization of I/O's

PRELIMINARY TIMING FIGURES

Derivative calculations for temperature (at 23 levels) and water vapor (18 levels) - continuous spectral coverage from 500 to 1400 cm^{-1} at full spectral resolution: 30 min. with old version on Convex at Phillips Lab.(Goal with improved version: <10 min).

aer

Examples of Application

- SIMULTANEOUS RETRIEVAL OF LOW ALTITUDE TEMPERATURE AND WATER VAPOR FROM GROUND BASED IR MEASUREMENTS (DBIS, J.M. Theriault et al.,1993)

- RETRIEVAL OF HIGH ALTITUDE OH PROFILES FROM BALLOON BORNE MICROWAVE SOUNDER (Steve Miller, PL/OS)

aer

SIMULTANEOUS RETRIEVAL SIMULATION:
Hot Dry Case-jl02a
709 Channels (2 cm-1 res) : First Guess Estimation :
Tuned Damping (4, 100, 2)

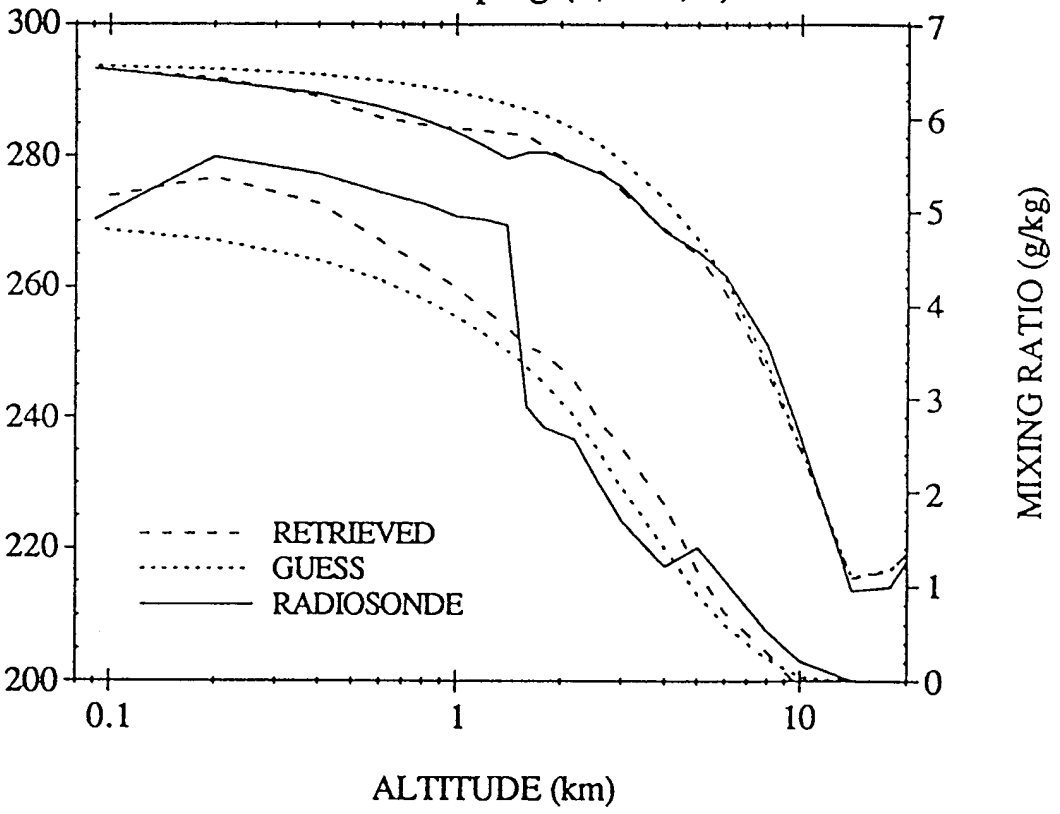

701

aer

SIMULTANEOUS RETRIEVAL (jl02a simulation):
FASCODE / VS / MODRAN-L JACOBIANS

Spectral Band 500 1400 cm^{-1}
Damping-T=100 : Damping-H=4

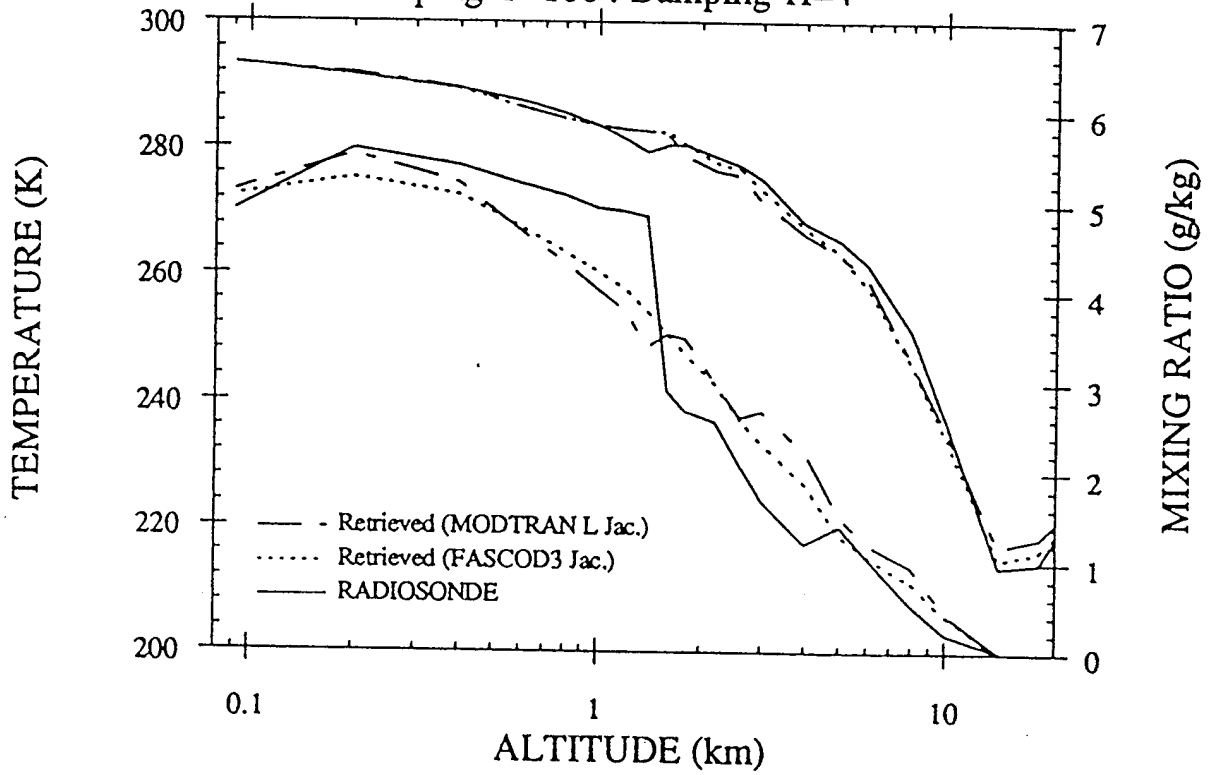

aer

Future Work

- Develop limb retrieval capabilities:
  - already incorporates sphericity and atmospheric refraction
  - explore ways to speed up radiative transfer calculations
- Extend the code to include cross-sections for heavy molecules
- Continue work on user interface
- Continue to improve speed:
  - progressive spectral degradation of the transfer calculations through filtering operation
  - analytical derivations of the Jacobian for molecular mixing ratios and eventually temperature
- Long term: treatment of clouds and aerosol by coupling the code with CHARTS (Moncet and Clough,1992)
- Parallelization

aer

Acknowledgements

This work is supported by the U.S. Air Force/Phillips Lab under contract F19628-93-C-0040.

Our thanks to Gail Anderson and Steve Miller of the Optical Science Division of the Phillips Lab for their support and collaboration.

SIMULATION OF STELLAR OCCULTATION MEASUREMENTS

Liisa Oikarinen

Erkki Kyrölä, Elina Sihvola, and Johanna Tamminen

Finnish Meteorological Institute

Department of Geophysics

1. Stellar occultation method
2. GOMOS instrument
3. Atmospheric model
4. Data inversion

GOMOS = Global Ozone Monitoring by Occultation of Stars

- An ESA Developed Instrument (EDI), funded under the ENVISAT-1 programme
- Main objective of GOMOS: trend studies of ozone
- Measurement: global mapping of stratospheric O_3, NO_2, NO_3, aerosols, H_2O, temperature (O_2)
- Launch 1998

Role of FMI in GOMOS:

- Scientific help in instrument development
- Development of data retrieval methods
- Data center

The stellar occultation measurement principle

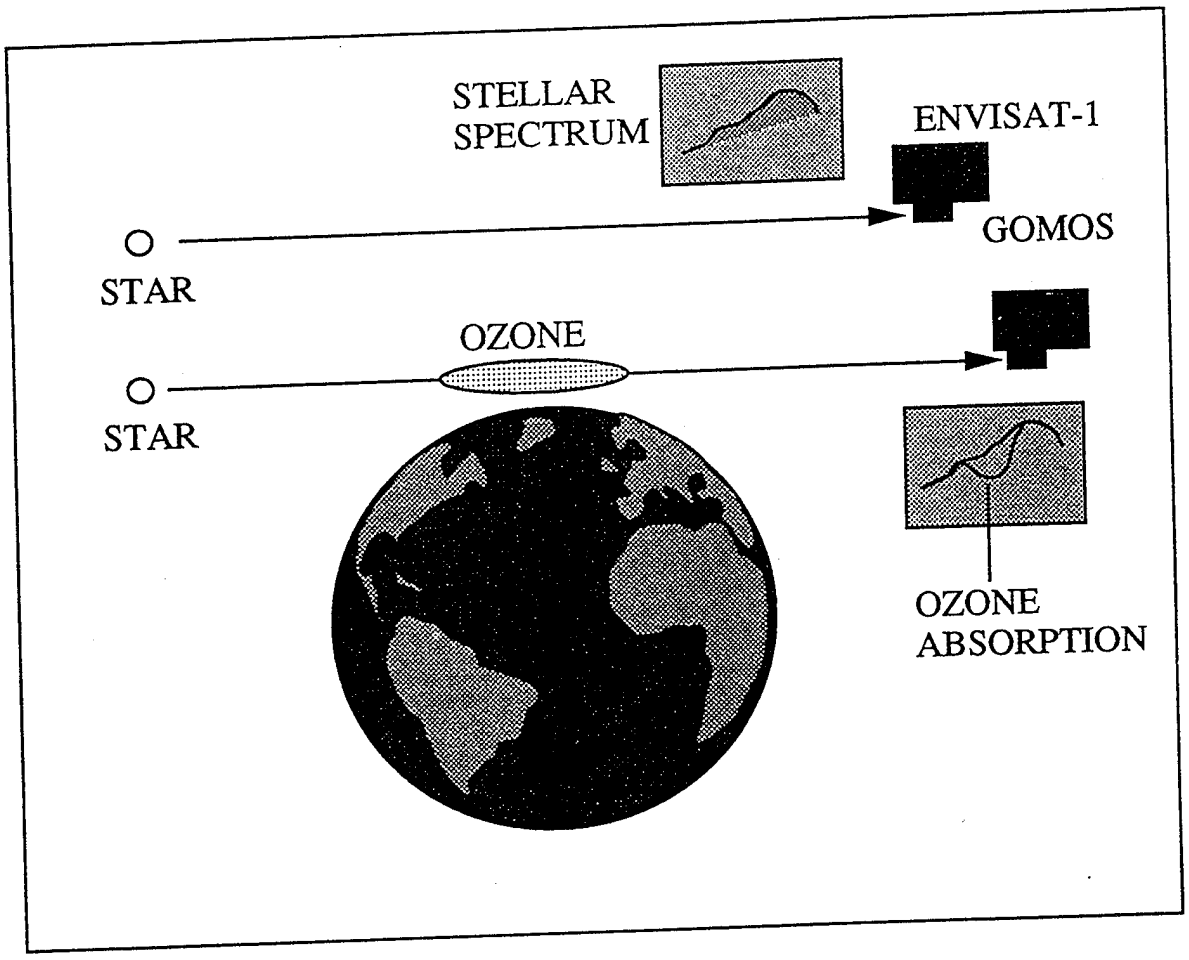

Tangent height 15 - 100 km
Vertical resolution 2 km (CCD integration time 0.5 s)
Stars up to magnitude 4 are used (bright limb up to 2)
Heliosynchronous polar orbit, altitude 800 km
Nominal orbit period 100 min
25 - 40 occultations per orbit

Global coverage of GOMOS measurements

15 orbit periods (25.3 h) in rectangular co-ordinates, in March

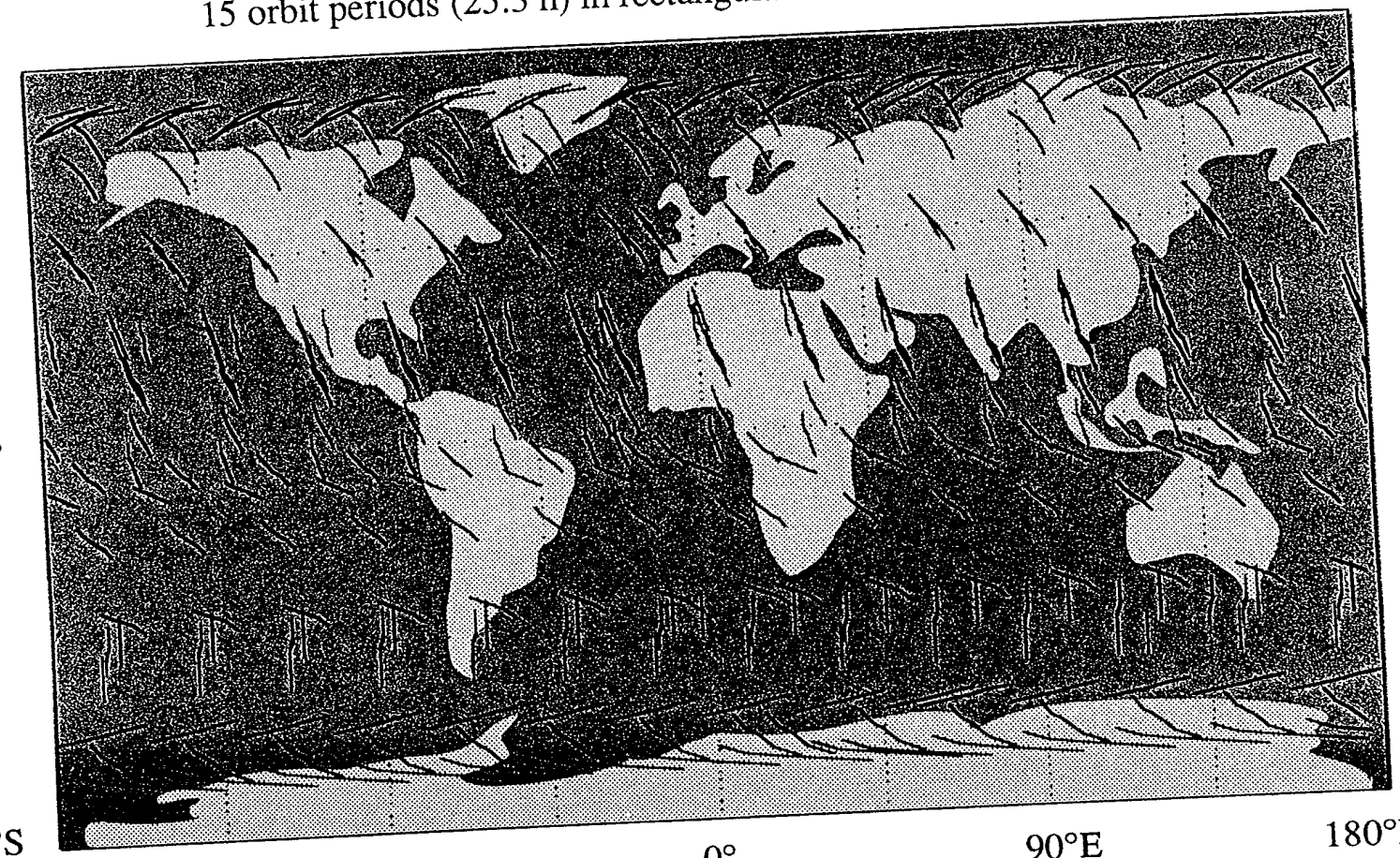

GOMOS INSTRUMENT

UVIS-spectrometer:

- Large spectral width: 250 - 675 nm,
  both Chappuis and UV-bands can be exploited:
  ozone can be retrieved at 15 - 90 km

- A good spectral resolution (1 nm), i.e., many pixels:
  Counteracts faintness of stars;
  Several trace gases can be retrieved: O_3, NO_2, NO_3,...

- Two dimensionality of CCD:
  Solar scattered backgroung can be measured,
  daytime measurements feasible;
  Pointing errors counteracted;
  Refractive bending counteracted

IR-spectrometer:

- O_2 and H_2O measurement (756 - 773 and 926 - 952 nm, 0.06 nm resolution)

- From O_2 neutral density and temperature to support UVIS-analysis

Photometers:

- 470 - 520 nm and 650 - 700 nm, maximum sampling rate 1 kHz

- Measurement of scintillations: The stellar signal can be corrected

- Studies of turbulence

Why stellar occultation?

Calibration stability
Global coverage
Altitude resolution

Solar occultation - SAGE

+ relative measurement
- only two occultations per orbit
- night/day terminator measurements
+ good altitude resolution (1 km)

SBUV-TOMS, TOVS

- absolute measurement
+ good coverage
- only dayside measurements
- poor altitude resolution (8 km)

Stellar occultation-GOMOS

+ relative measurement
+ global coverage (night and day)
+ sufficent altitude resolution (2 km)

GOMOS simulation

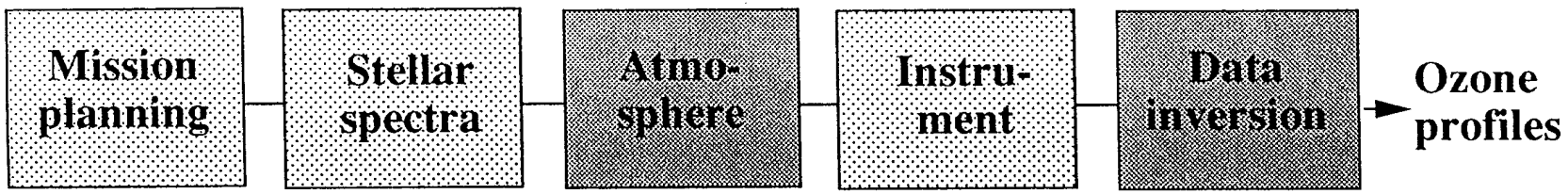

ATMOSPHERIC PHYSICS FOR GOMOS

Phenomena that should be simulated:

- Absorption by O_3, NO_2, NO_3, OClO, SO_2, BrO, H_2O, O_2
- Scattering out of the beam by Rayleigh and aerosol scattering
- Scattering of solar light by molecules and aerosols into the FOV of the instrument
- Emission into the FOV (aurora etc.)
- Refraction: bending of the ray, refractive attenuation
- Turbulence: scintillations

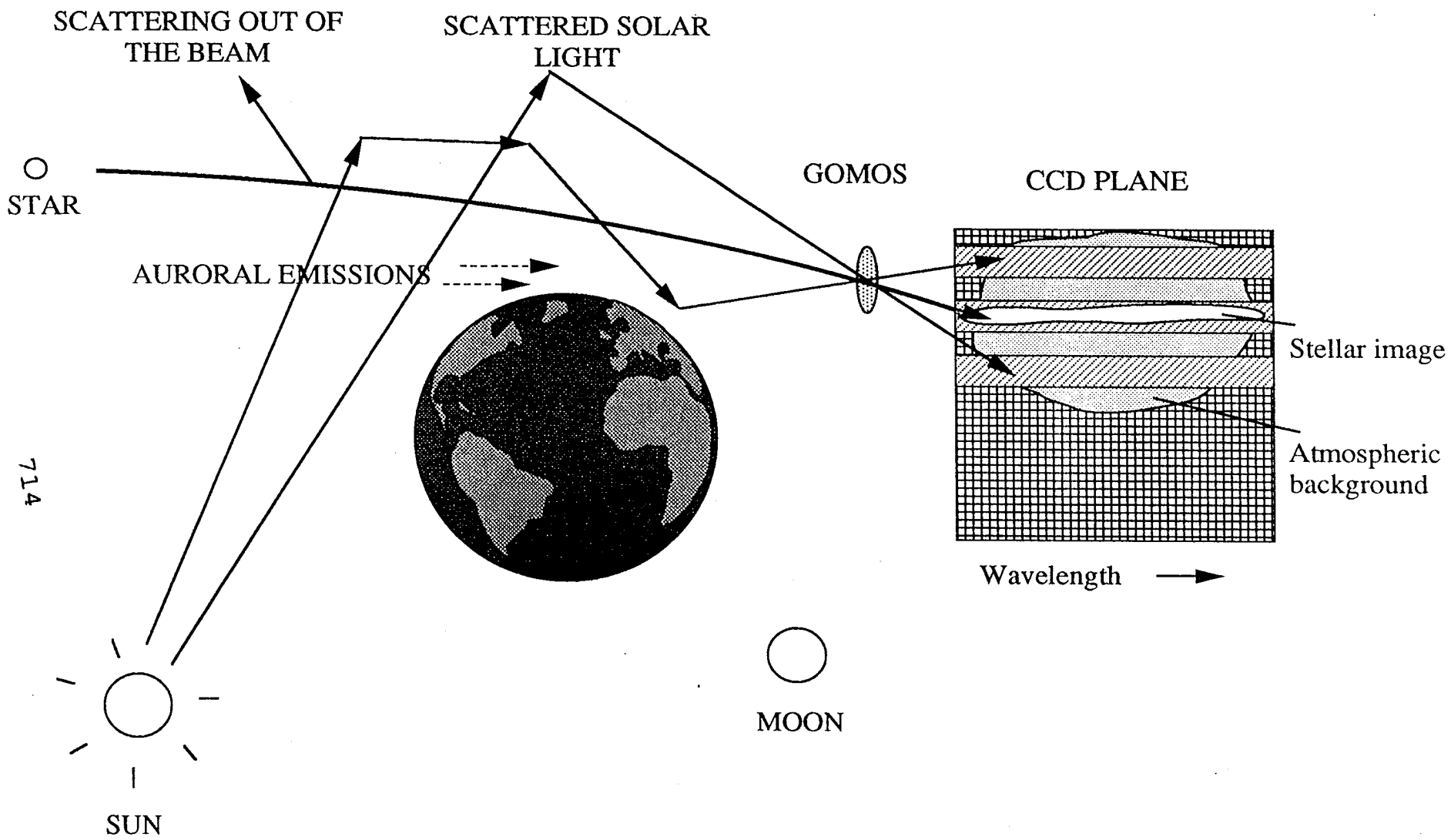
SCATTERING OUT OF THE BEAM
SCATTERED SOLAR LIGHT
STAR
GOMOS
CCD PLANE
AURORAL EMISSIONS
Stellar image
Atmospheric background
Wavelength
MOON
SUN

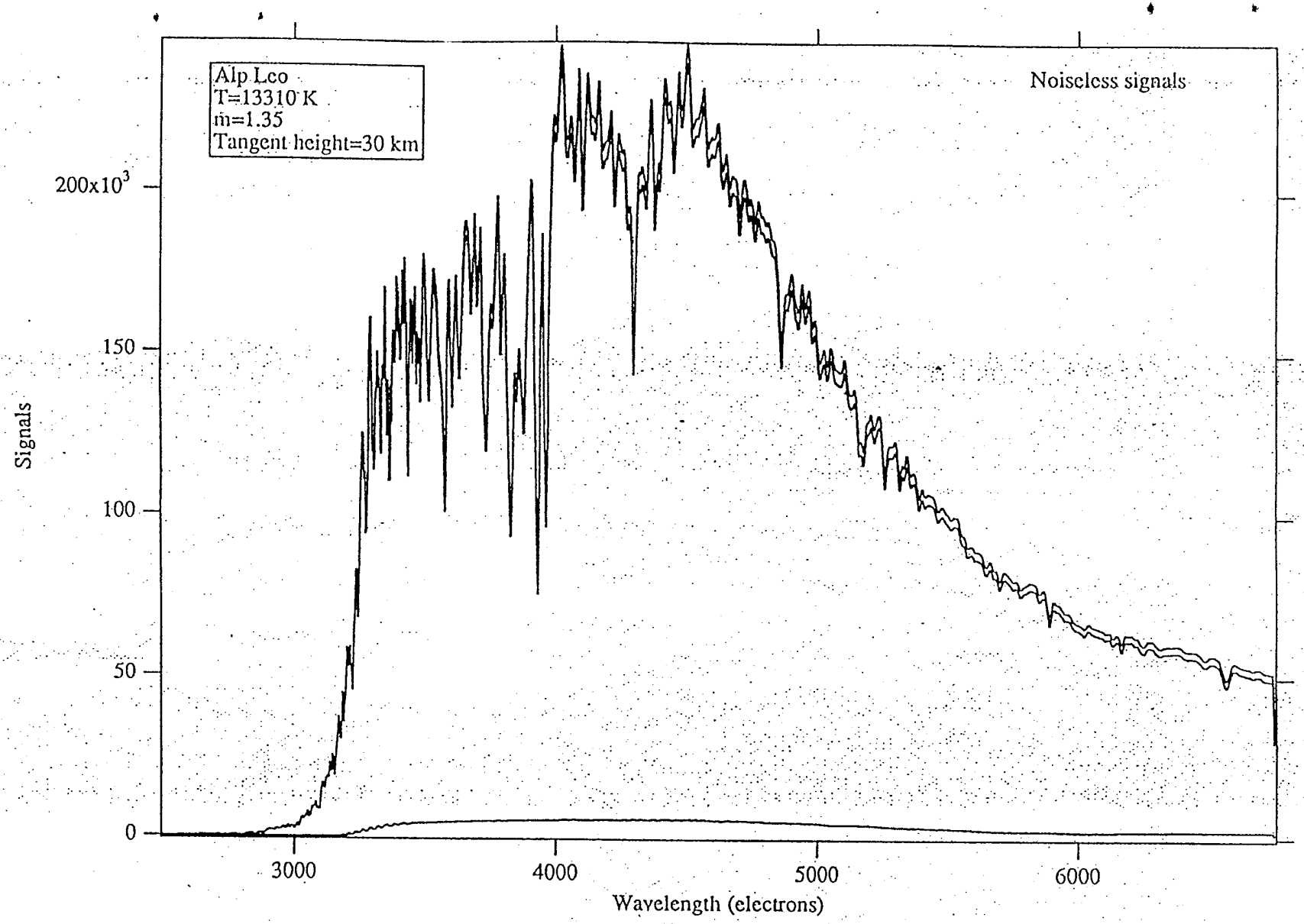
Alp Lco
T=13310 K
m=1.35
Tangent height=30 km
Noiseless signals
200x10^3
150
100
50
0
Signals
3000
4000
5000
6000
Wavelength (electrons)

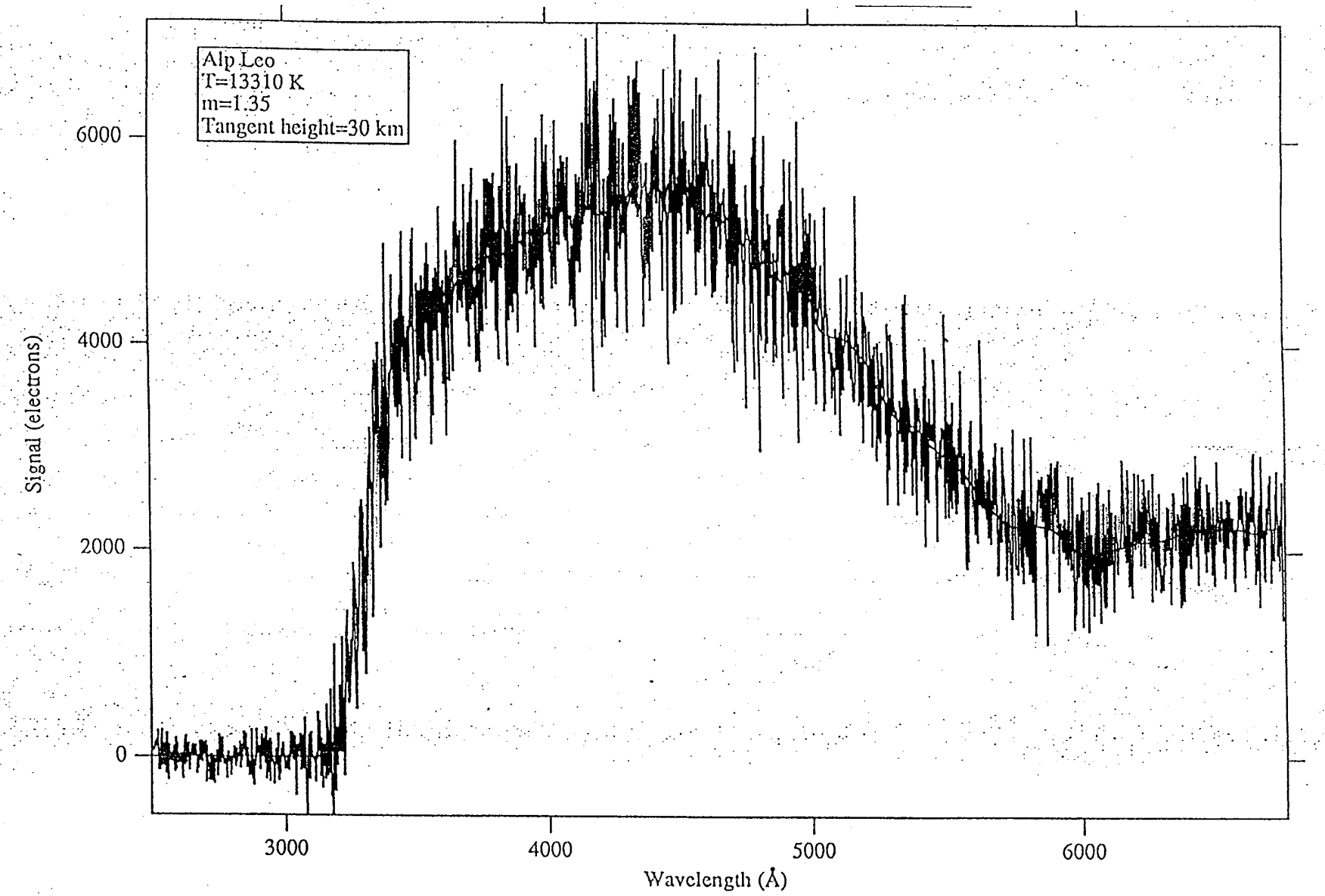
Alp Leo
T=13310 K
m=1.35
Tangent height=30 km
6000
4000
2000
0
Signal (electrons)
3000
4000
5000
6000
Wavelength (Å)

SPECIAL REQUIREMENTS OF GOMOS ATMOSPHERIC SIMULATION MODEL

- compactness (analytical density distributions etc.)

- the code should be easy to modify

- realistic variations in constituent distributions (ultimate conditions, eg. the ozone hole, required in addition to average atmospheres)

- occultation geometry

Comparison of FINGOM (a code specially designed for GOMOS by FMI) and LOWTRAN

model	**FINGOM**	**LOWTRAN**
absorbers in the vis.	O_3, NO_2, NO_3, SO_2, BrO, OClO	O_3
constituent profiles	3-D, seasonal, diurnal, latitudinal variations	local geographical-seasonal atmospheres
atmospheric model description	analytic	tables
refractive attenuation	included	not included
scattered solar background	single scattering	single- and multiple scattering
aerosol model	simple	models for various aerosol conditions

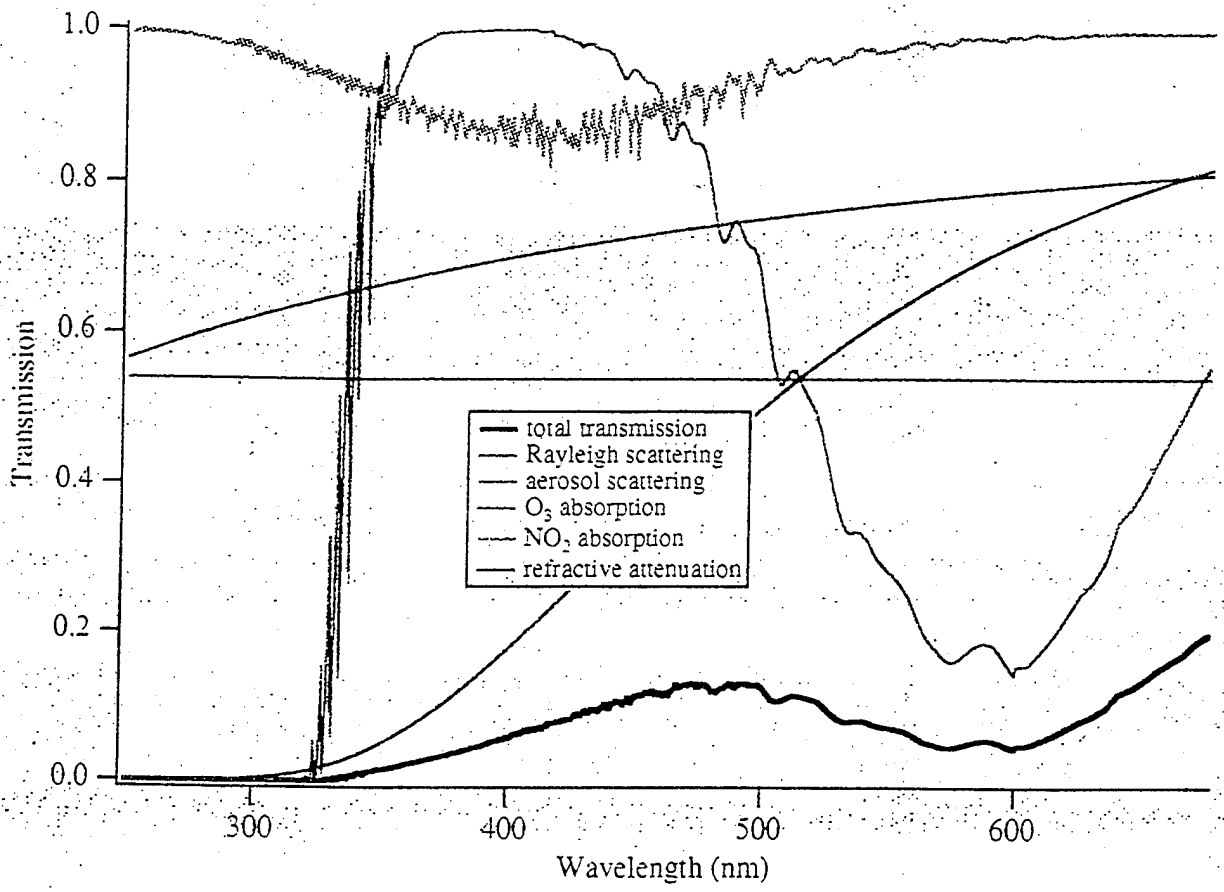

Atmospheric transmission for a ray path of tangent height 20 km. Total transmission is divided into the main extinctive components $T_{tot} = T_{O_3} T_{Rayl} T_{aer} T_{NO_2} T_{refr}$.

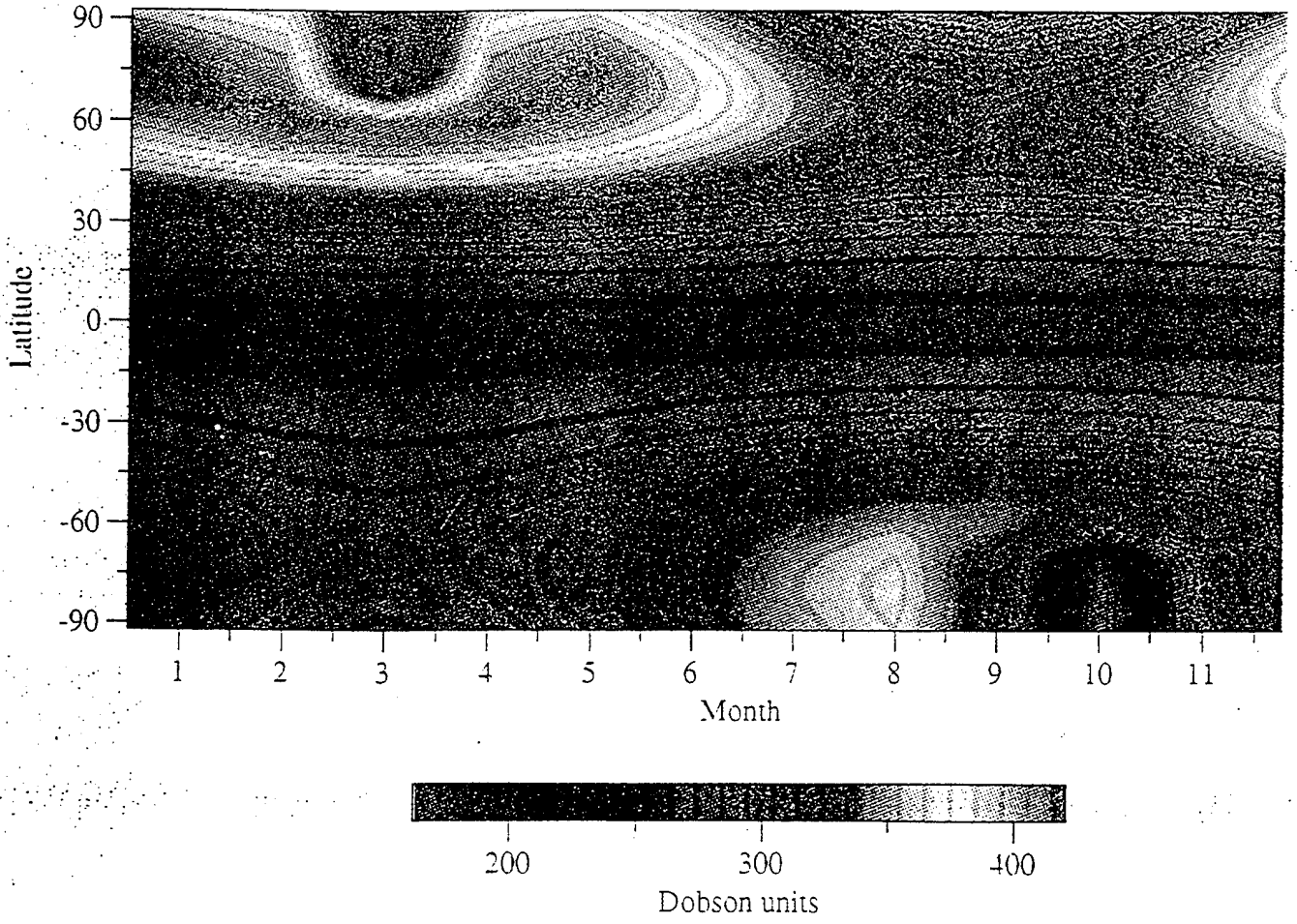

Total ozone distribution model as a function of latitude and season.

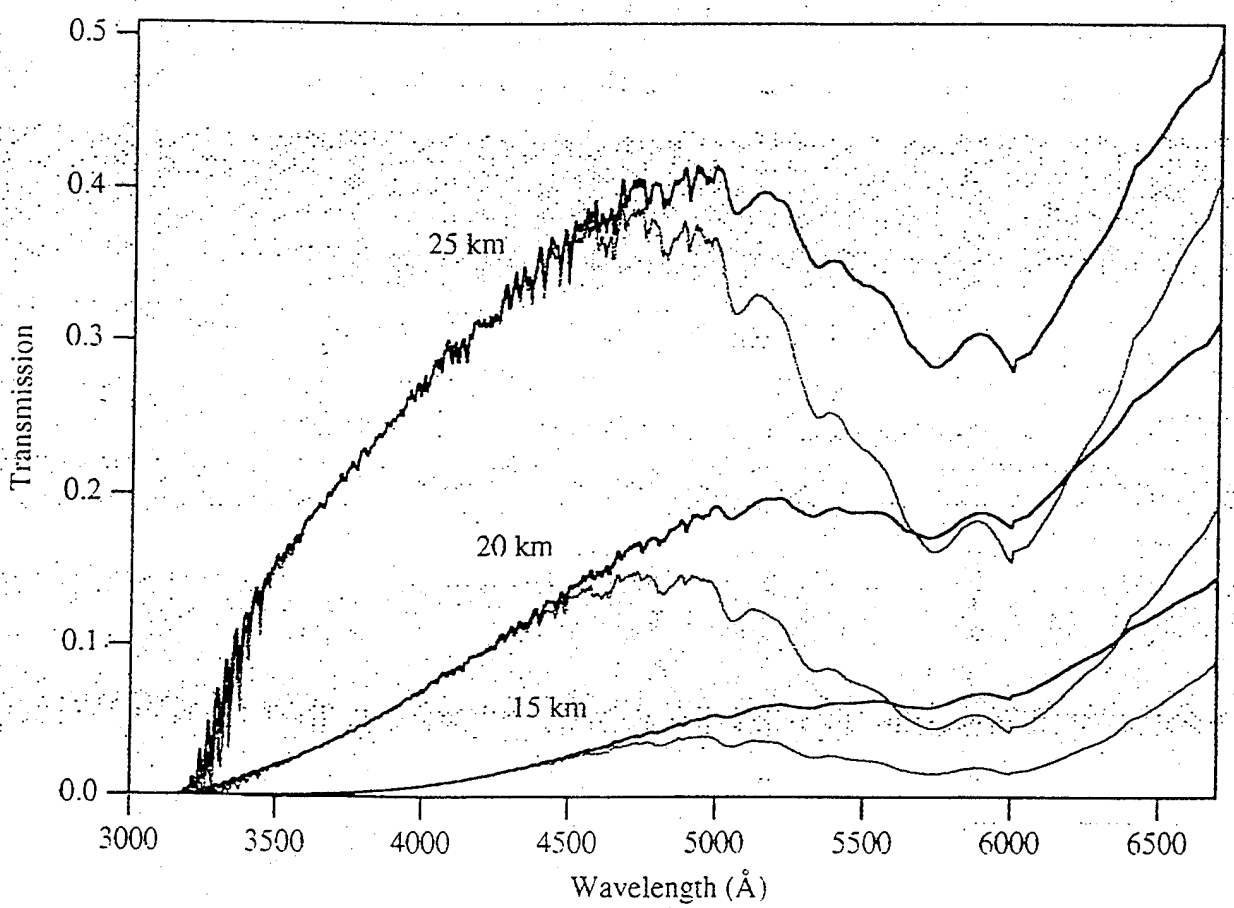
0.5
0.4
0.3
0.2
0.1
0.0
Transmission
25 km
20 km
15 km
3000
3500
4000
4500
5000
5500
6000
6500
Wavelength (Å)

INVERSION

$$T(l) = e^{-\tau(\lambda,l)}$$

$$\tau(\lambda,l) = \int_l k(\lambda,s)ds = \int_l \sum_i \rho_i(s)\sigma_i(\lambda,T(s))ds$$

Discretization:

(1) 1° $\tau(\lambda,l) = \sum_i N_i(l)\sigma_i(\lambda,T_i(l))$

The same temperature $T(l)$ is used for the whole ray l

2° $N_i(l) = \sum_j \rho_i(s_j)\Delta s_j$; N_i=line density of constituent i

The atmosphere is discretized into layers j

(2) $\tau(\lambda,l) = \sum_i \sum_{j\in l} \rho_i(s_j)\sigma_i(\lambda,T(s_j))\Delta s_j$

(3) 1° $\tau(\lambda,l) = \sum_{j\in l} k(\lambda,s_j)\Delta s_j$

2° $k(\lambda,s_j) = \sum_i \rho_i(s_j)\sigma_i(\lambda,T(s_j))$

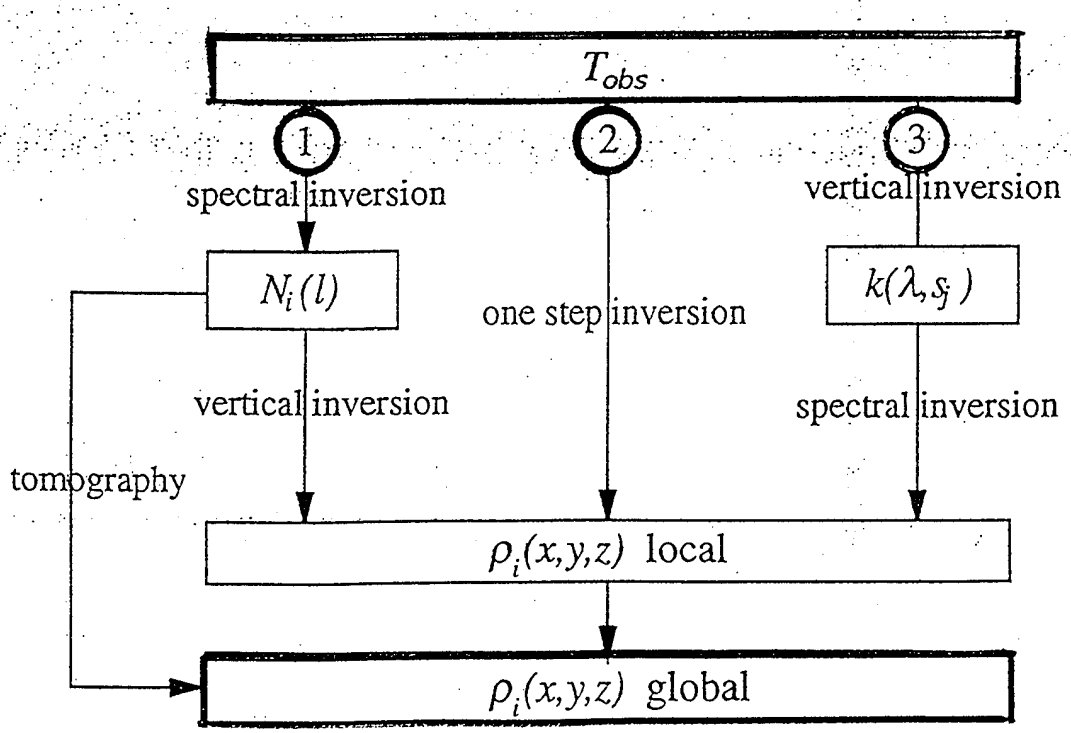

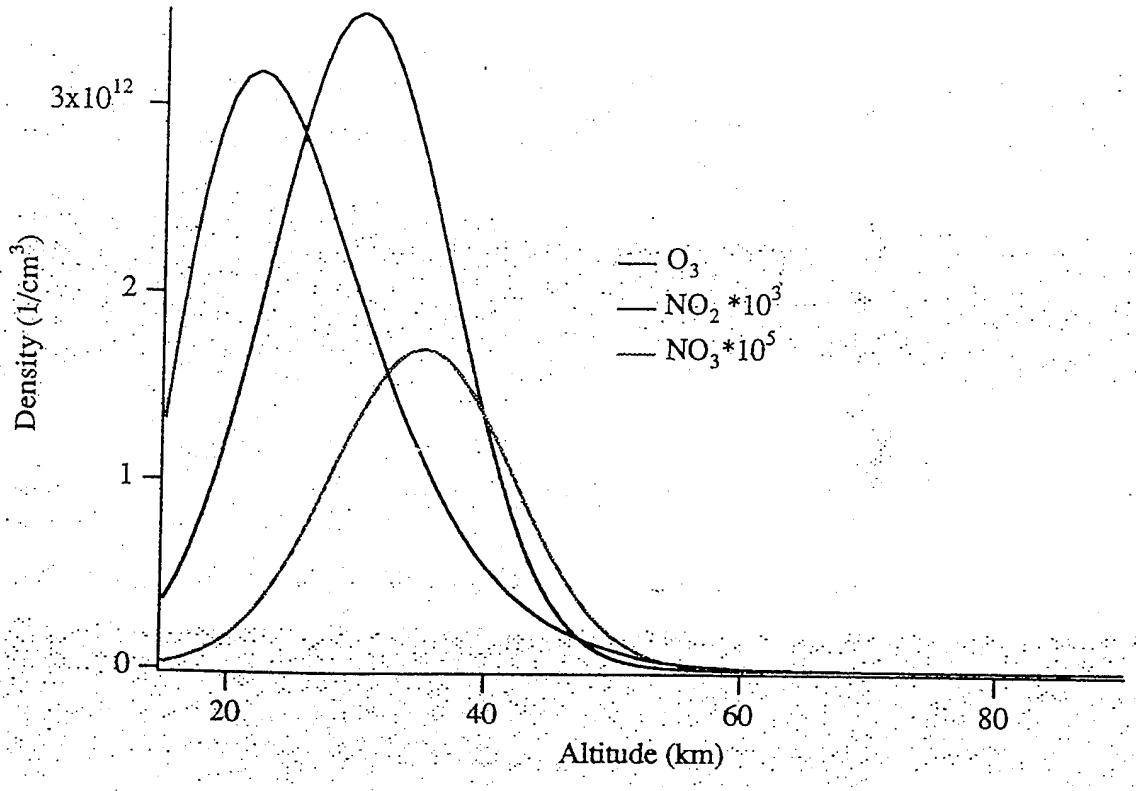

Ozone, NO2, and NO3 density profiles.

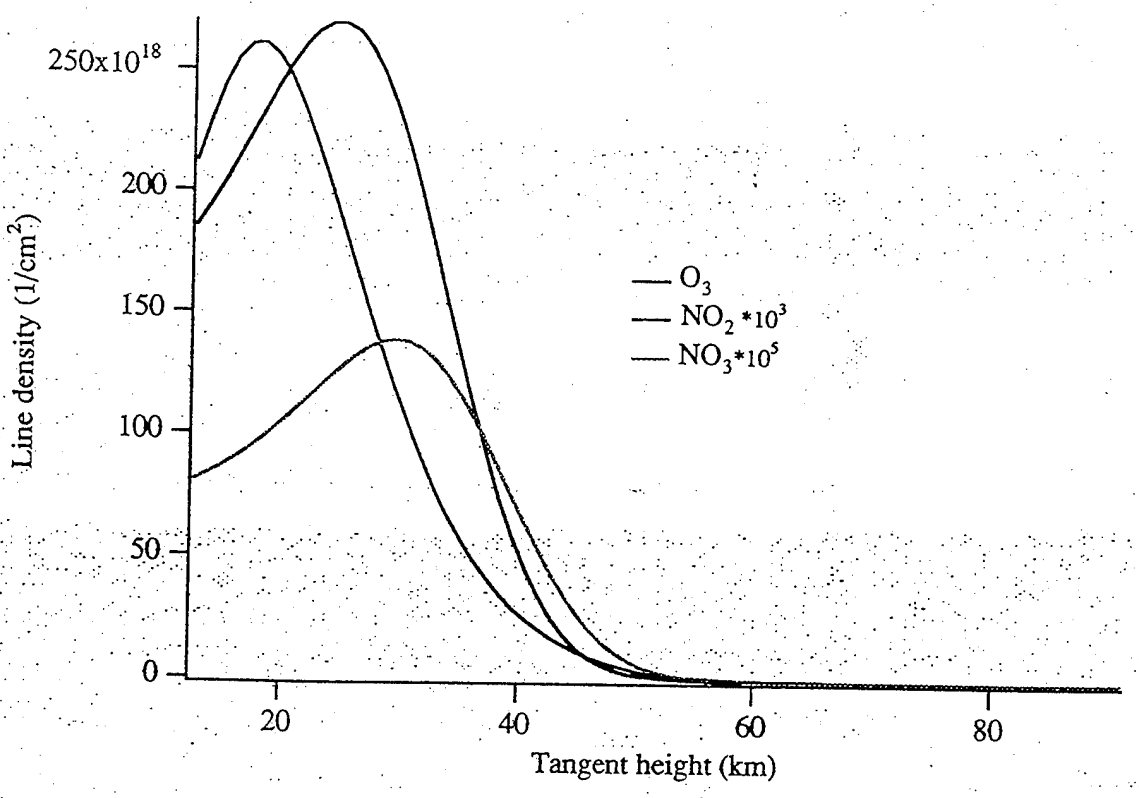

Integrated line density for ozone, NO2, and NO3 as a function of the tangent heigth of the path.

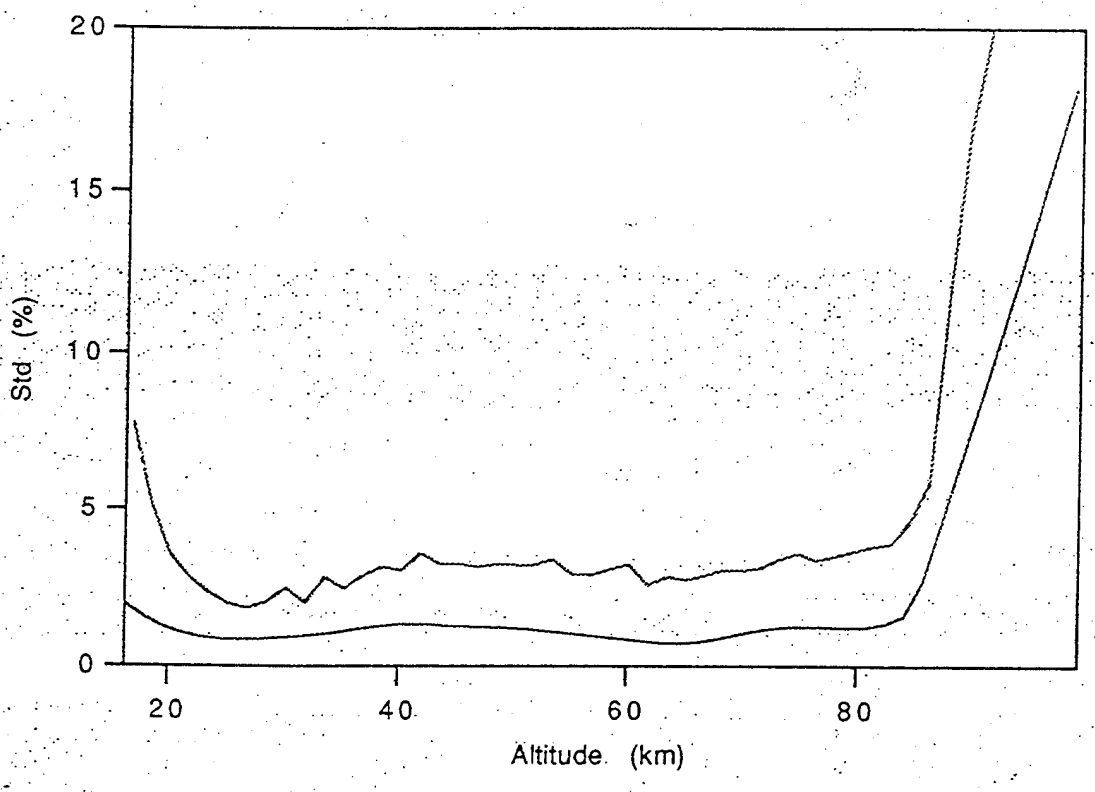

The standard deviation in vertical inversion (upper line). The lower line is the std in the data.

CONCLUSIONS

An atmospheric model with analytical density distributions has been constructed at FMI.

Realistic simulations of occultation measurements are possible with the model.

Problems:

- 3-D time dependent models are difficult to construct from the existing data
  (exception: O_3 and temperature)

- Absorber cross-sections are required at 160-280 K, not available at the moment

Open points:

- simulation of scintillations

- simulation of auroral emissions

aer

Line by Line Calculation of Atmospheric Fluxes and Cooling Rates: Application to Water Vapor, Carbon Dioxide, Ozone, Methane, Nitrous Oxide, and the Halocarbons

S. A. Clough, and M. J. Iacono
Atmospheric and Environmental Research, Inc.

Overview/Objectives

Line-by-line Model

- LBLRTM, (Line By Line Radiative Transfer Model)
- Vectorizable, 10-20x faster (based on FASCODE)
- Extensively validated against observed spectral radiance data (HIS)

Water Vapor, Carbon Dioxide, and Ozone:

- Mid-latitude summer, Mid-latitude winter, Tropical atmospheres
  - Calculate line-by-line upwelling, downwelling, and net (up-down) clear-sky fluxes at 5 cm-1 resolution for the full IR spectrum (10-3000 cm-1)
  - Cooling rates computed from the divergence of the net flux
  - Current US standard profiles used for H_2O and O_3; CO_2 = 355ppm
- Doubled carbon dioxide considered for CO_2 = 710 ppm

CH_4, N_2O, and the Halocarbons

- Halocarbons considered include CFC-11, CFC-12, CFC-22, and CCL4
- Profiles for Methane, Nitrous Oxide, and Halocarbons derived from a 2D chemistry model

1990-2000 Changes

- Ten-year profile changes in all trace species considered for their impact on fluxes and cooling rates
- Changes in water vapor have not been considered

Rapid Radiative Transfer Model

- Apply LBL flux and cooling rate results to the selection of appropriate spectral bands for use in k-distribution model and the verification of the rapid model output.

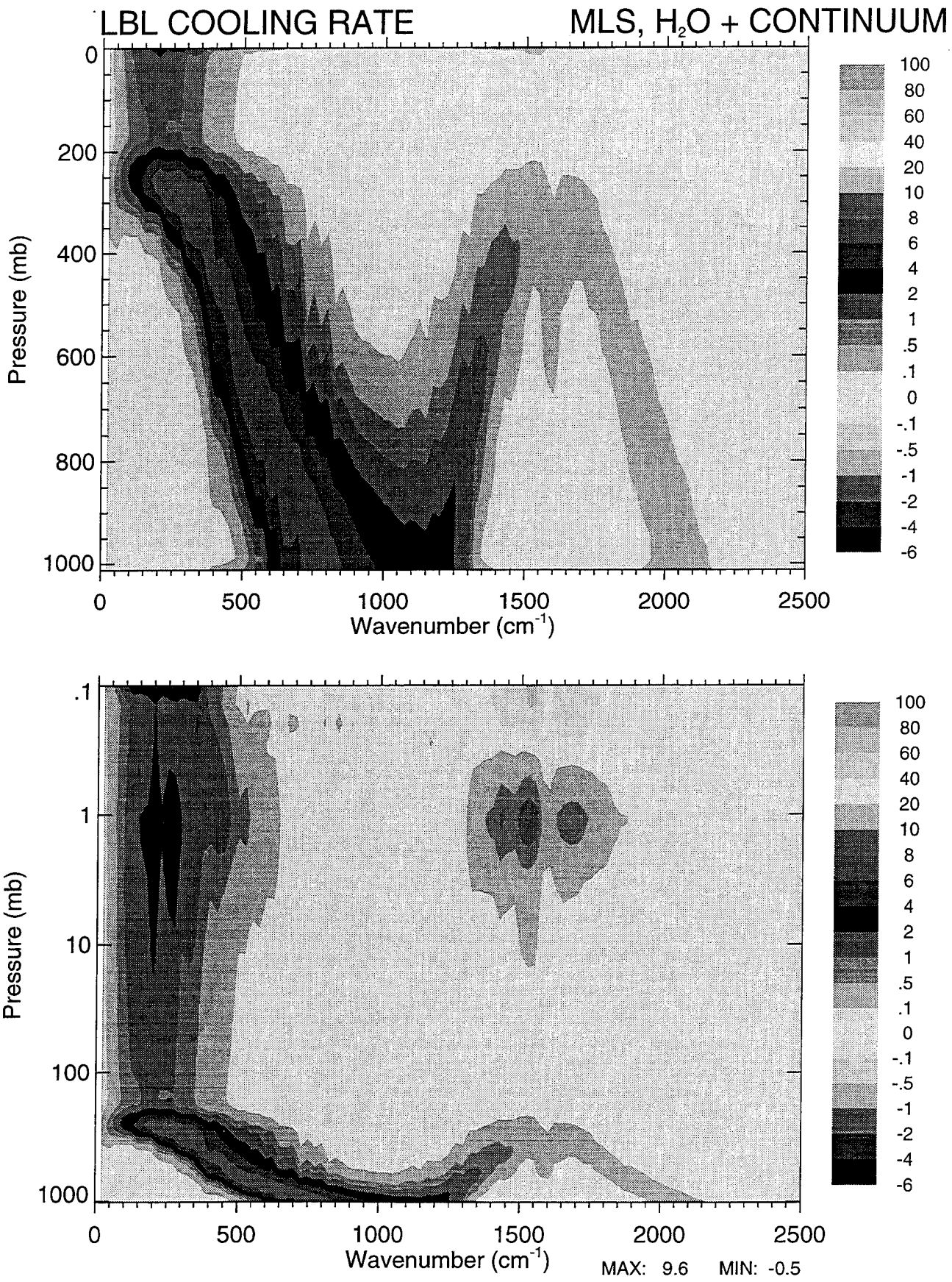

Shepard A. Clough, and Michael J. Iacono
Atmospheric and Environmental Research, Inc.

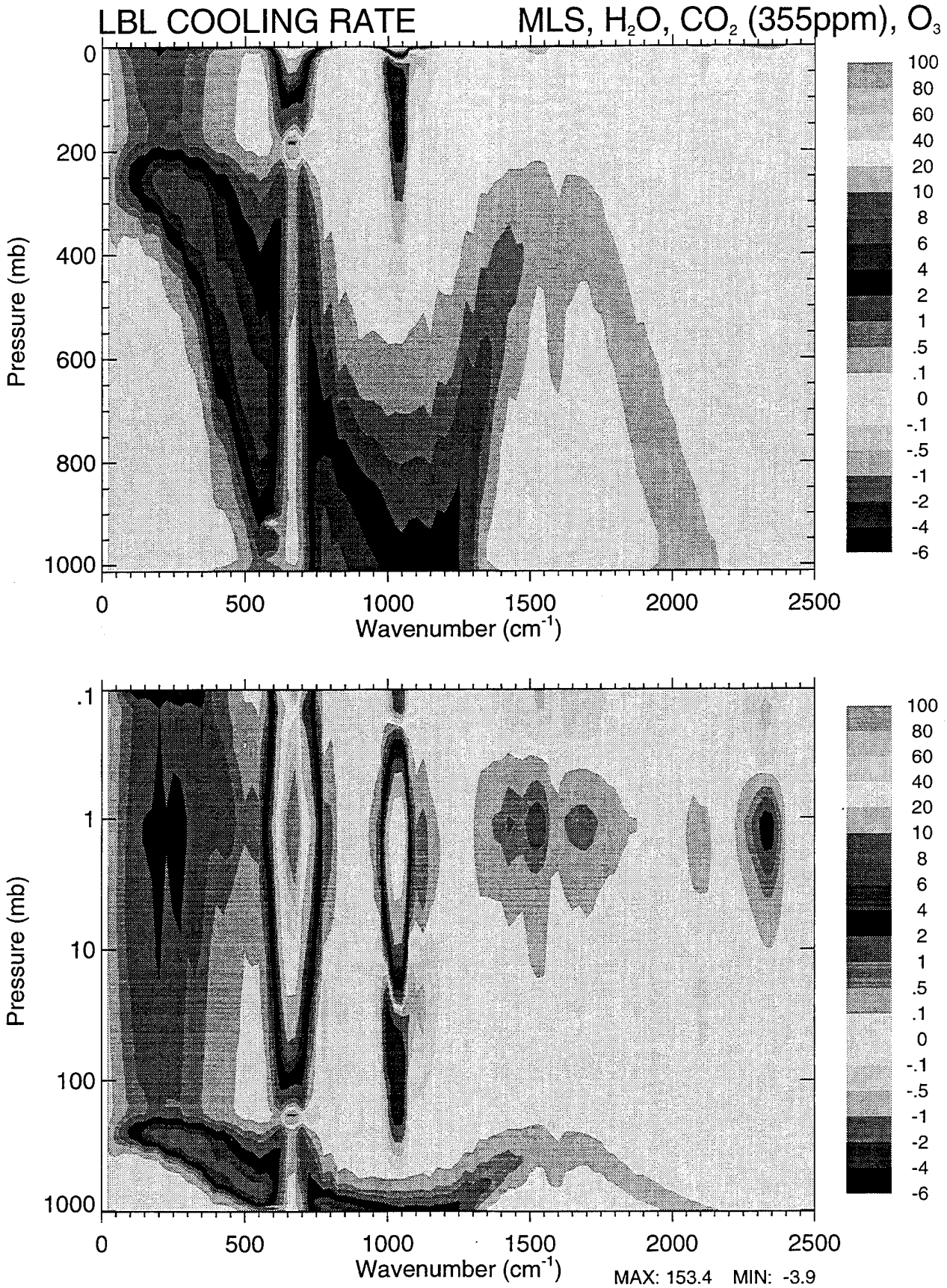

Shepard A. Clough, and Michael J. Iacono
Atmospheric and Environmental Research, Inc.

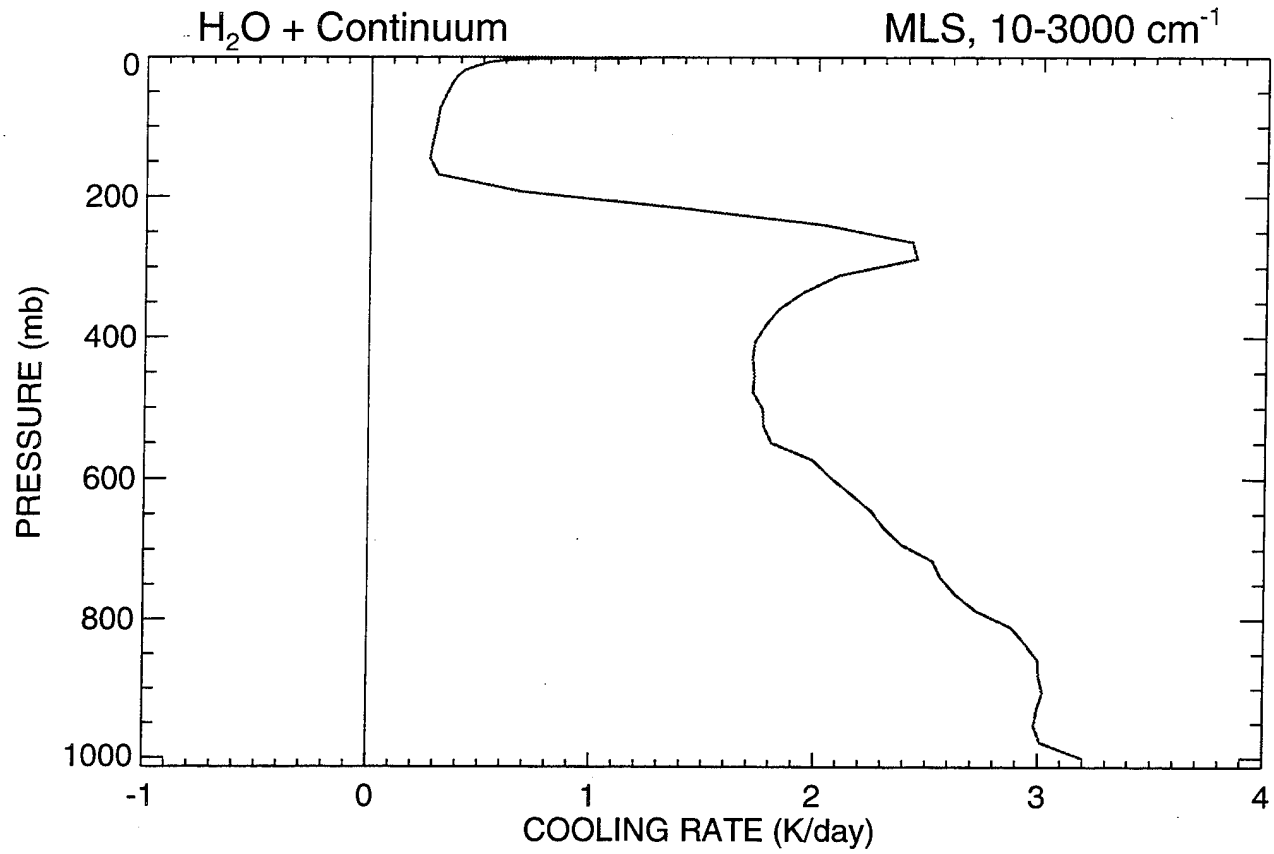
H_2O + Continuum
MLS, 10-3000 cm^{-1}
PRESSURE (mb)
0
200
400
600
800
1000
-1
0
1
2
3
4
COOLING RATE (K/day)

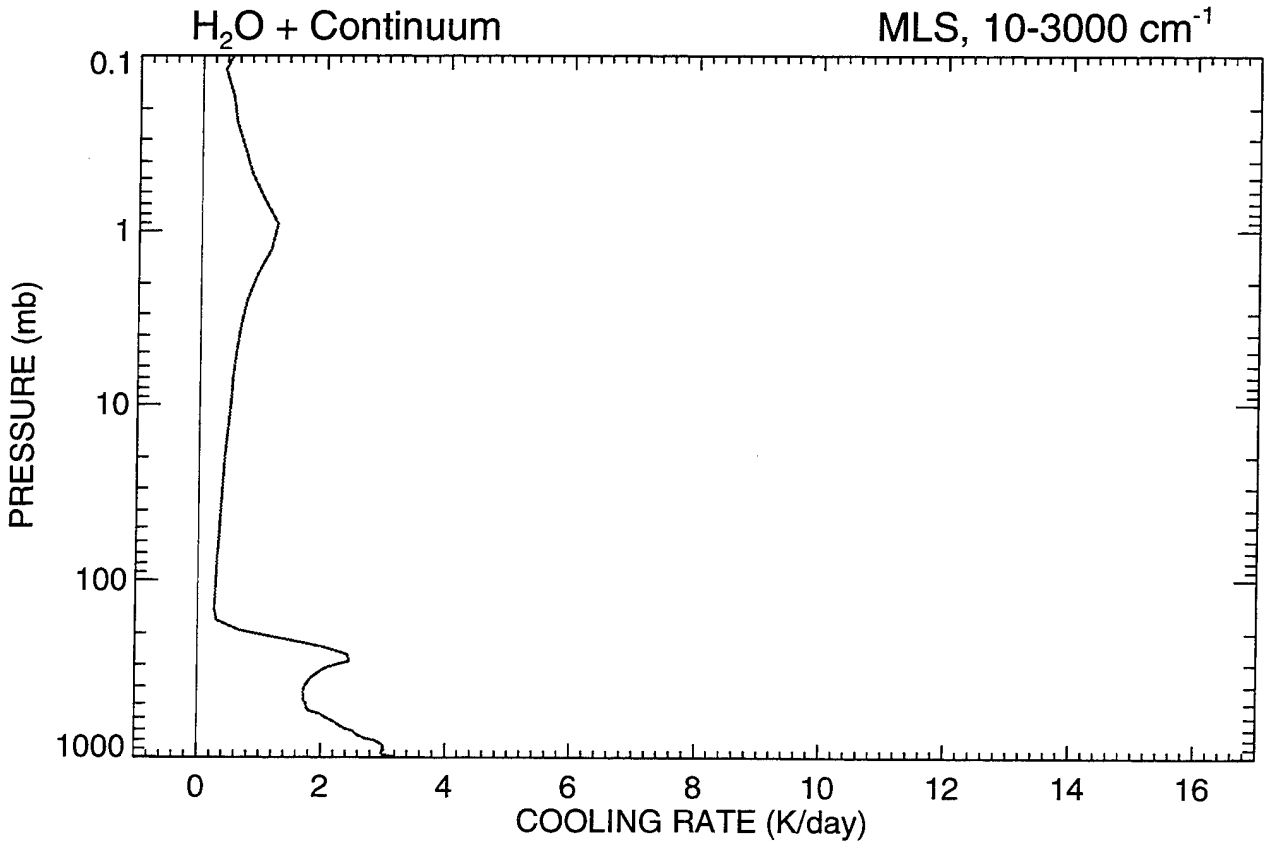
H_2O + Continuum
MLS, 10-3000 cm^{-1}
PRESSURE (mb)
0.1
1
10
100
1000
0
2
4
6
8
10
12
14
16
COOLING RATE (K/day)

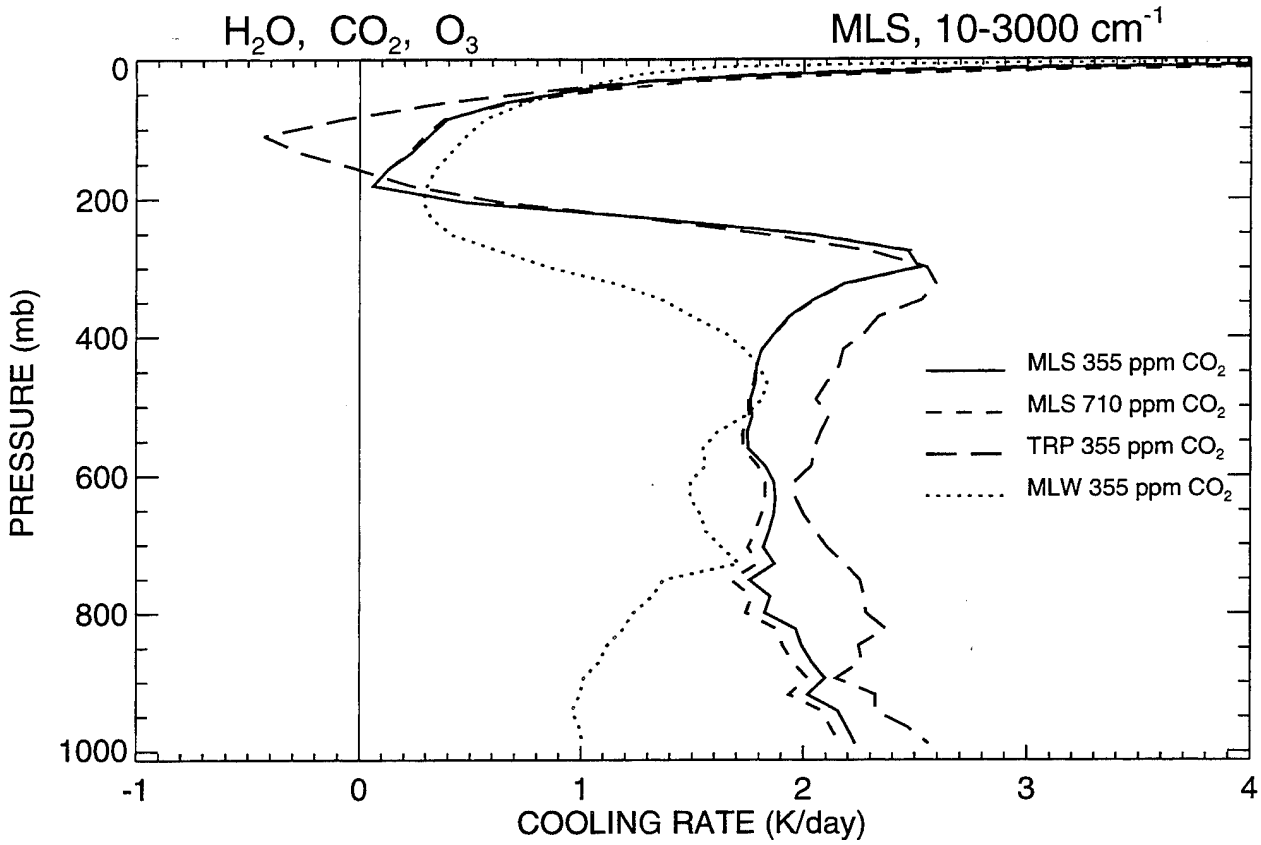
H2O, CO2, O3
MLS, 10-3000 cm-1
PRESSURE (mb)
0
200
400
600
800
1000
-1
0
1
2
3
4
COOLING RATE (K/day)
MLS 355 ppm CO2
MLS 710 ppm CO2
TRP 355 ppm CO2
MLW 355 ppm CO2

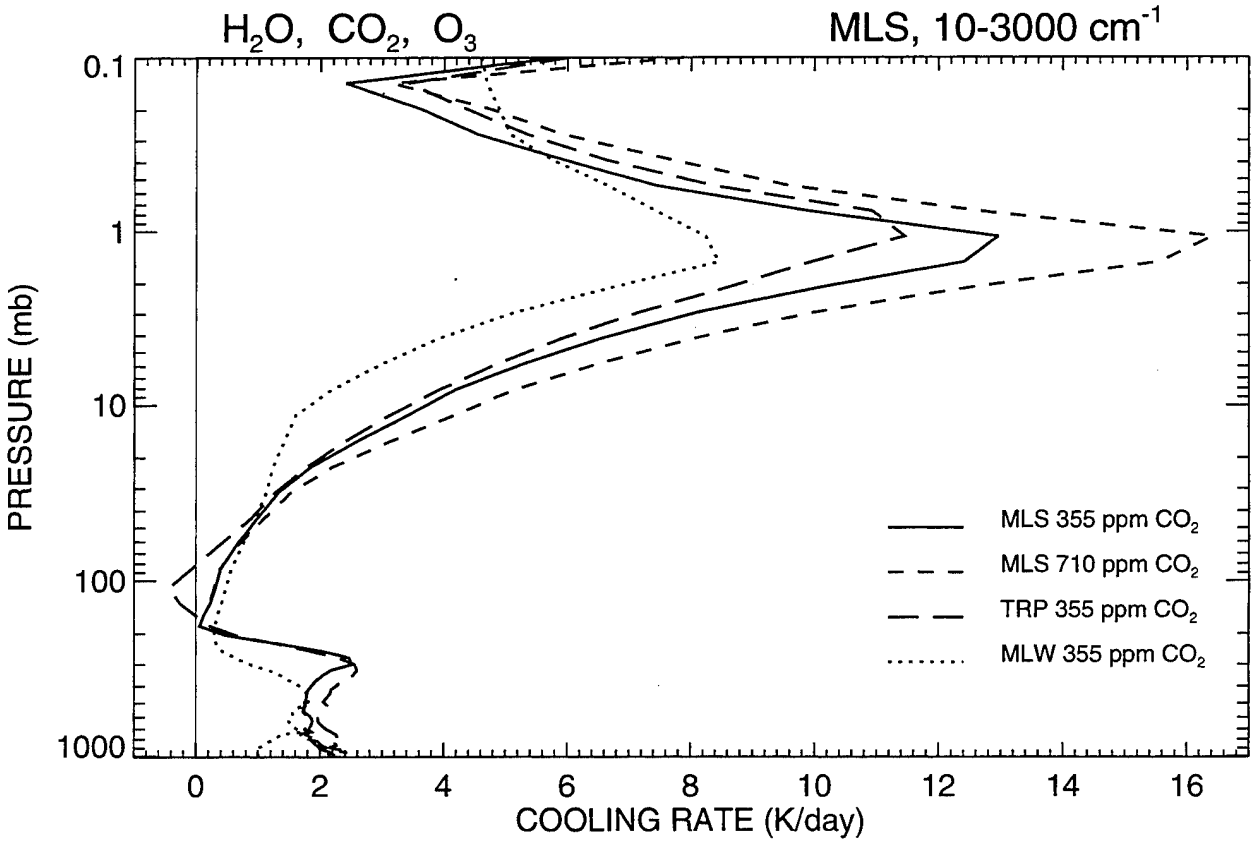
H2O, CO2, O3
MLS, 10-3000 cm-1
PRESSURE (mb)
0.1
1
10
100
1000
0
2
4
6
8
10
12
14
16
COOLING RATE (K/day)
MLS 355 ppm CO2
MLS 710 ppm CO2
TRP 355 ppm CO2
MLW 355 ppm CO2

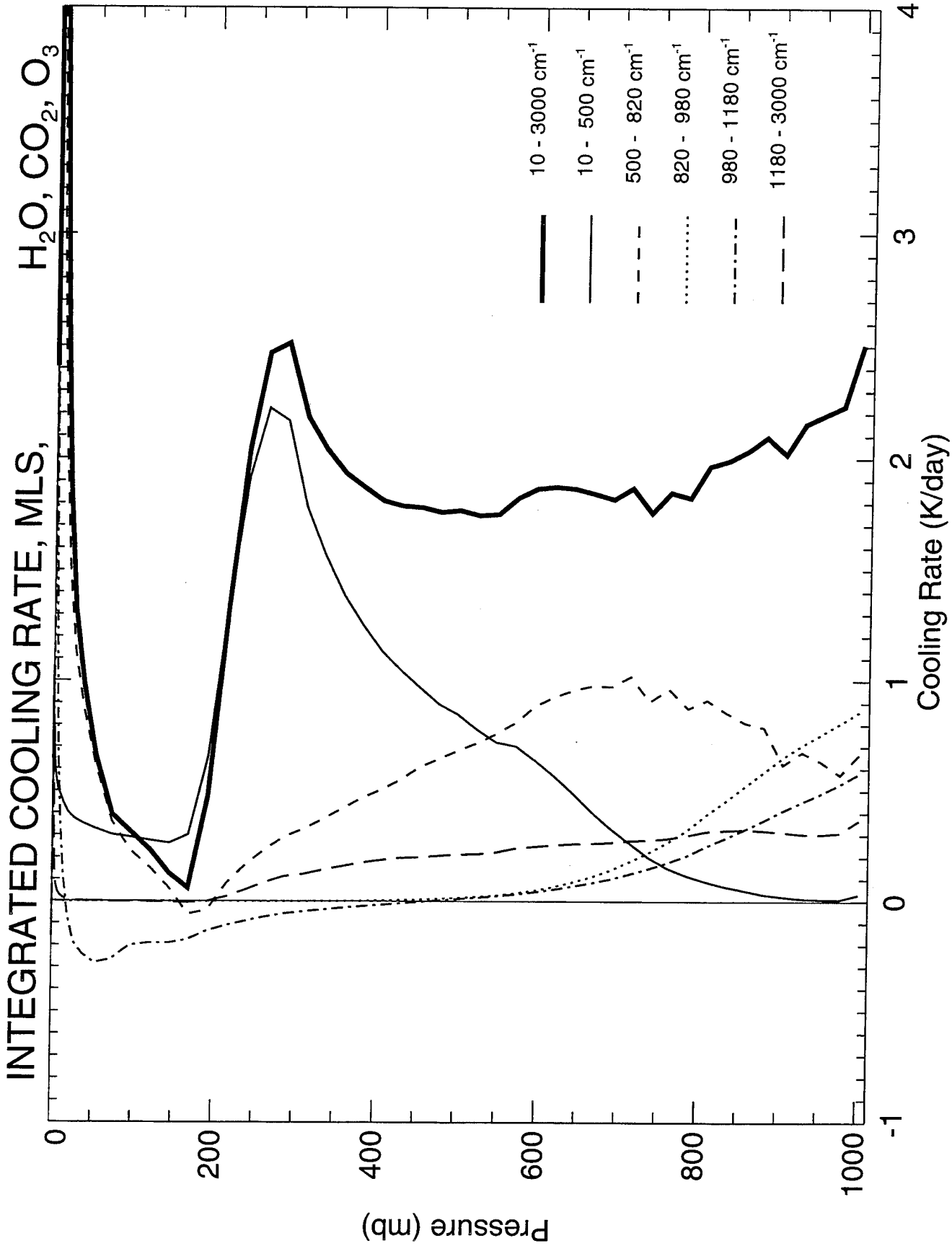
INTEGRATED COOLING RATE, MLS, H_2O, CO_2, O_3
10 - 3000 cm^{-1}
10 - 500 cm^{-1}
500 - 820 cm^{-1}
820 - 980 cm^{-1}
980 - 1180 cm^{-1}
1180 - 3000 cm^{-1}
Pressure (mb)
Cooling Rate (K/day)
0
200
400
600
800
1000
-1
0
1
2
3
4

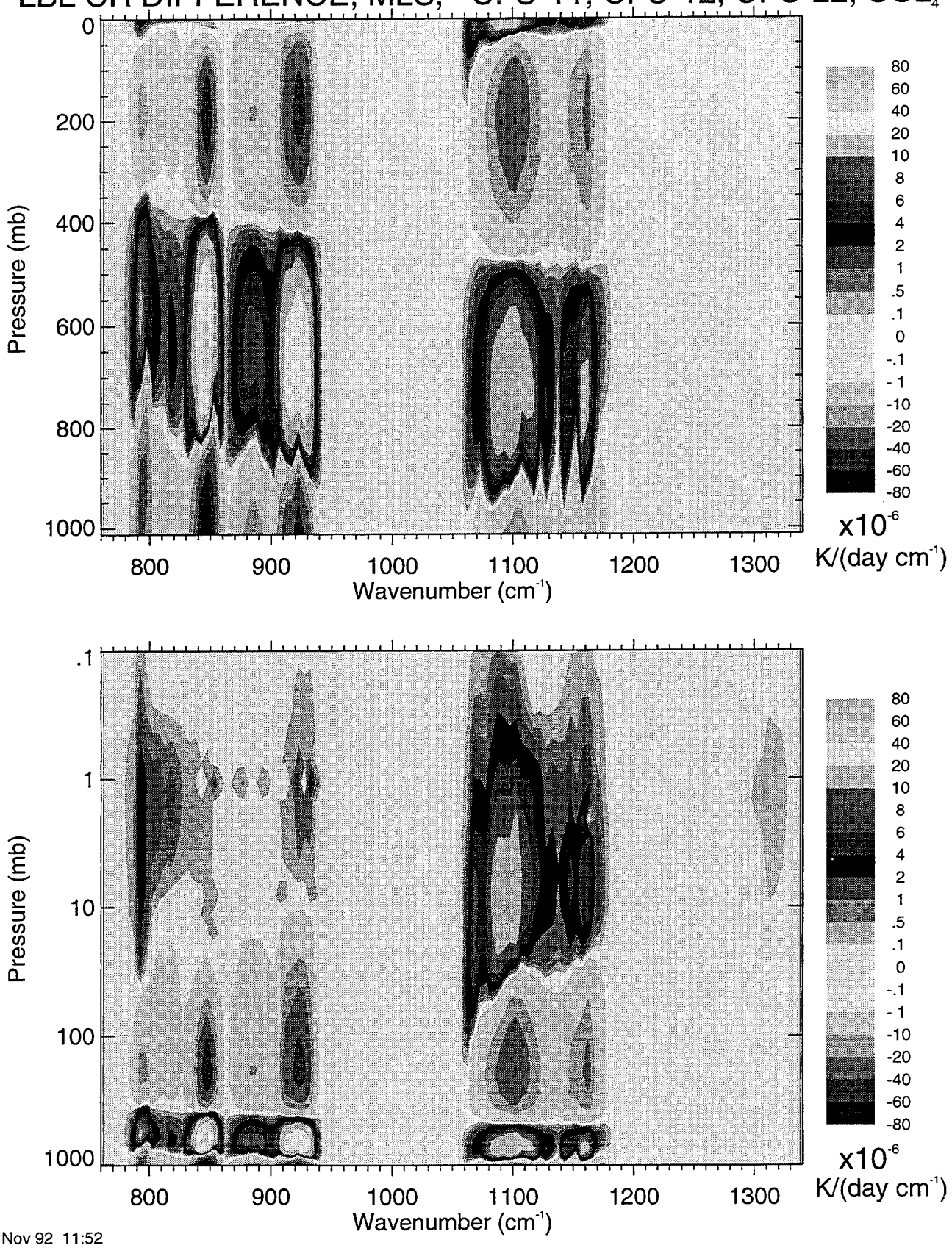
LBL CR DIFFERENCE, MLS, CFC-11, CFC-12, CFC-22, CCL4
Pressure (mb)
0
200
400
600
800
1000
800
900
1000
1100
1200
1300
Wavenumber (cm-1)
80
60
40
20
10
8
6
4
2
1
.5
.1
0
-.1
-1
-10
-20
-40
-60
-80
x10-6
K/(day cm-1)
Pressure (mb)
.1
1
10
100
1000
800
900
1000
1100
1200
1300
Wavenumber (cm-1)
80
60
40
20
10
8
6
4
2
1
.5
.1
0
-.1
-1
-10
-20
-40
-60
-80
x10-6
K/(day cm-1)
03 Nov 92 11:52

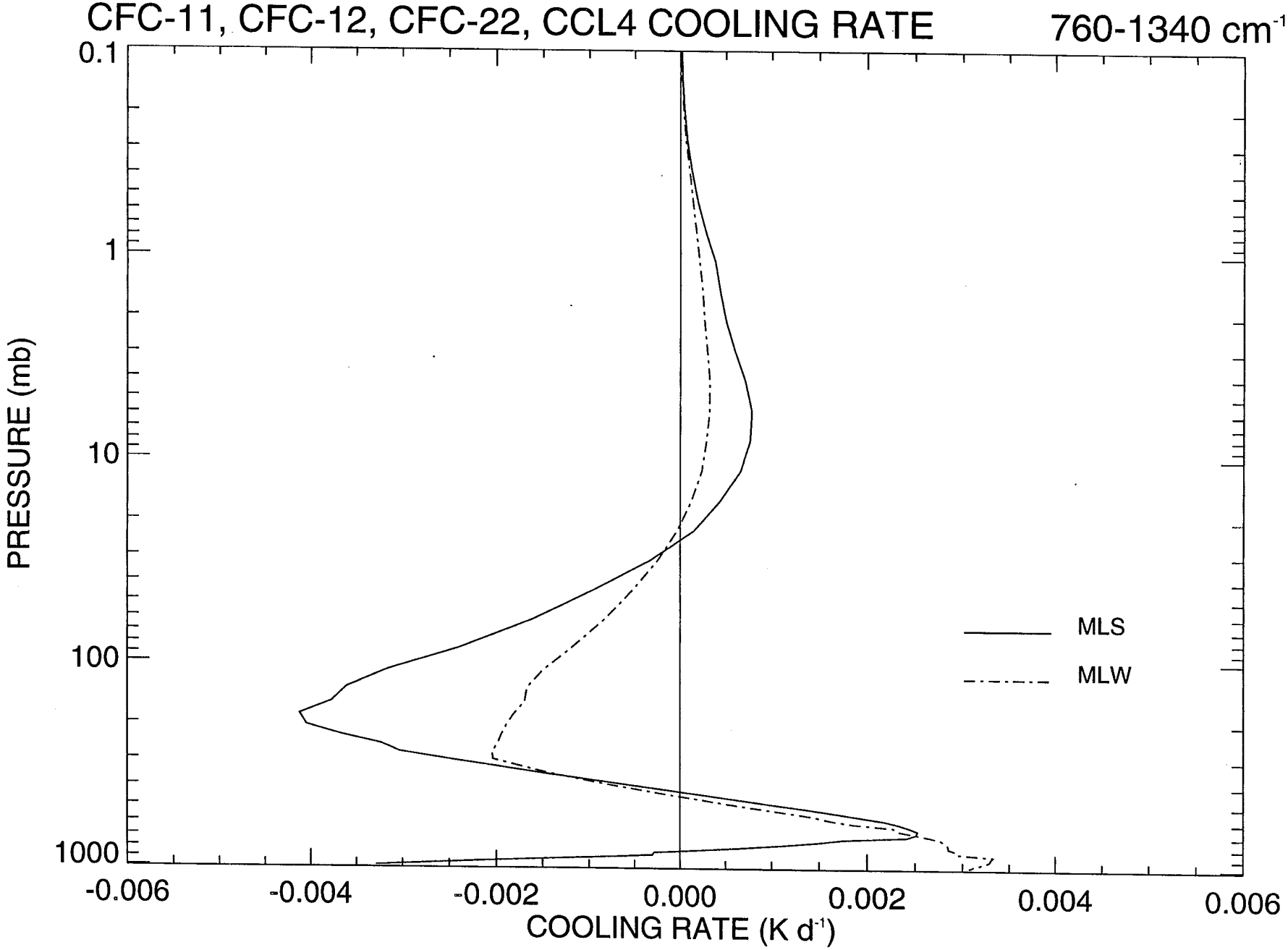
CFC-11, CFC-12, CFC-22, CCL4 COOLING RATE
760-1340 cm-1
PRESSURE (mb)
0.1
1
10
100
1000
-0.006
-0.004
-0.002
0.000
0.002
0.004
0.006
COOLING RATE (K d-1)
MLS
MLW

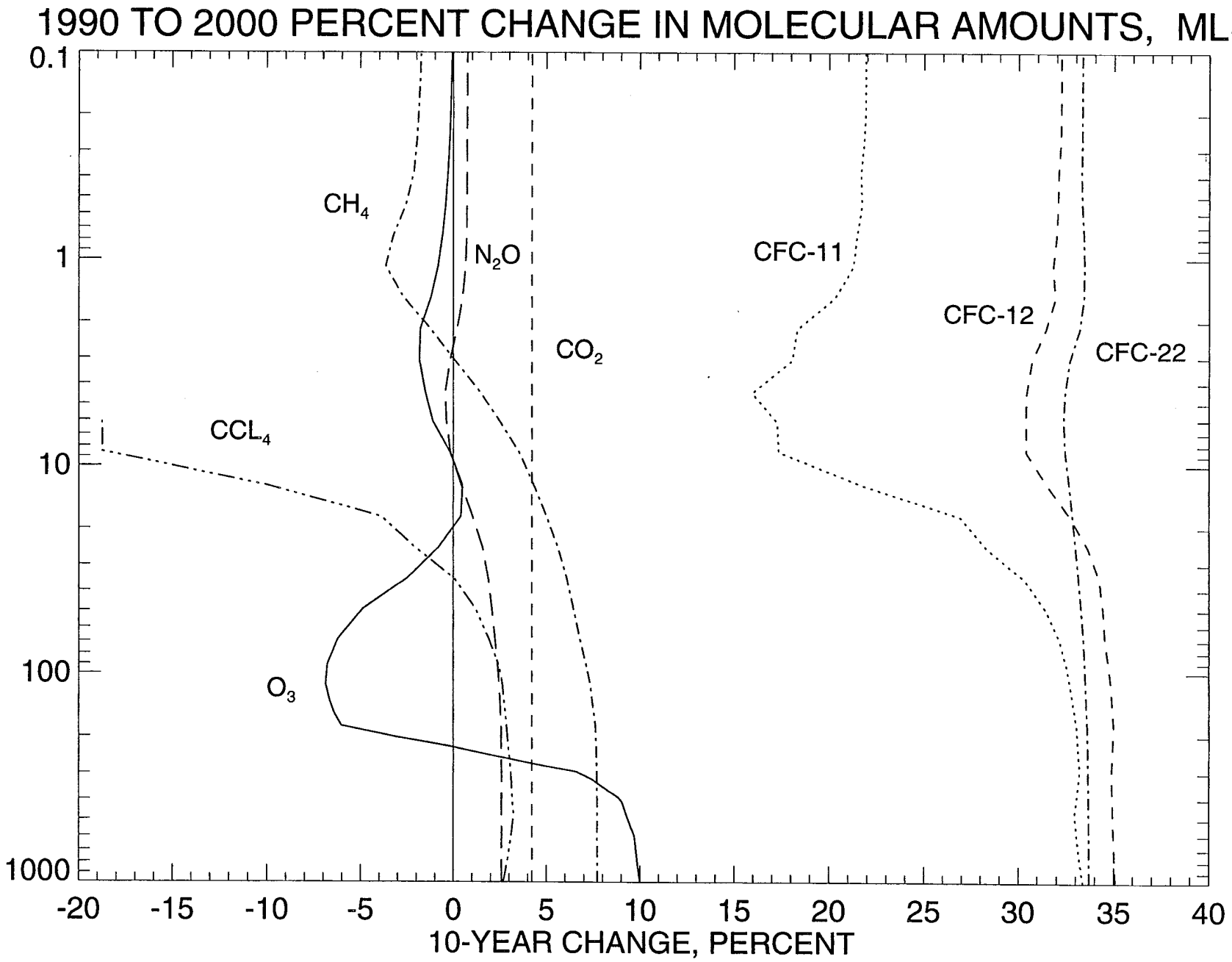
1990 TO 2000 PERCENT CHANGE IN MOLECULAR AMOUNTS, MLS
0.1
1
10
100
1000
CH4
N2O
CO2
CCL4
O3
CFC-11
CFC-12
CFC-22
-20
-15
-10
-5
0
5
10
15
20
25
30
35
40
10-YEAR CHANGE, PERCENT

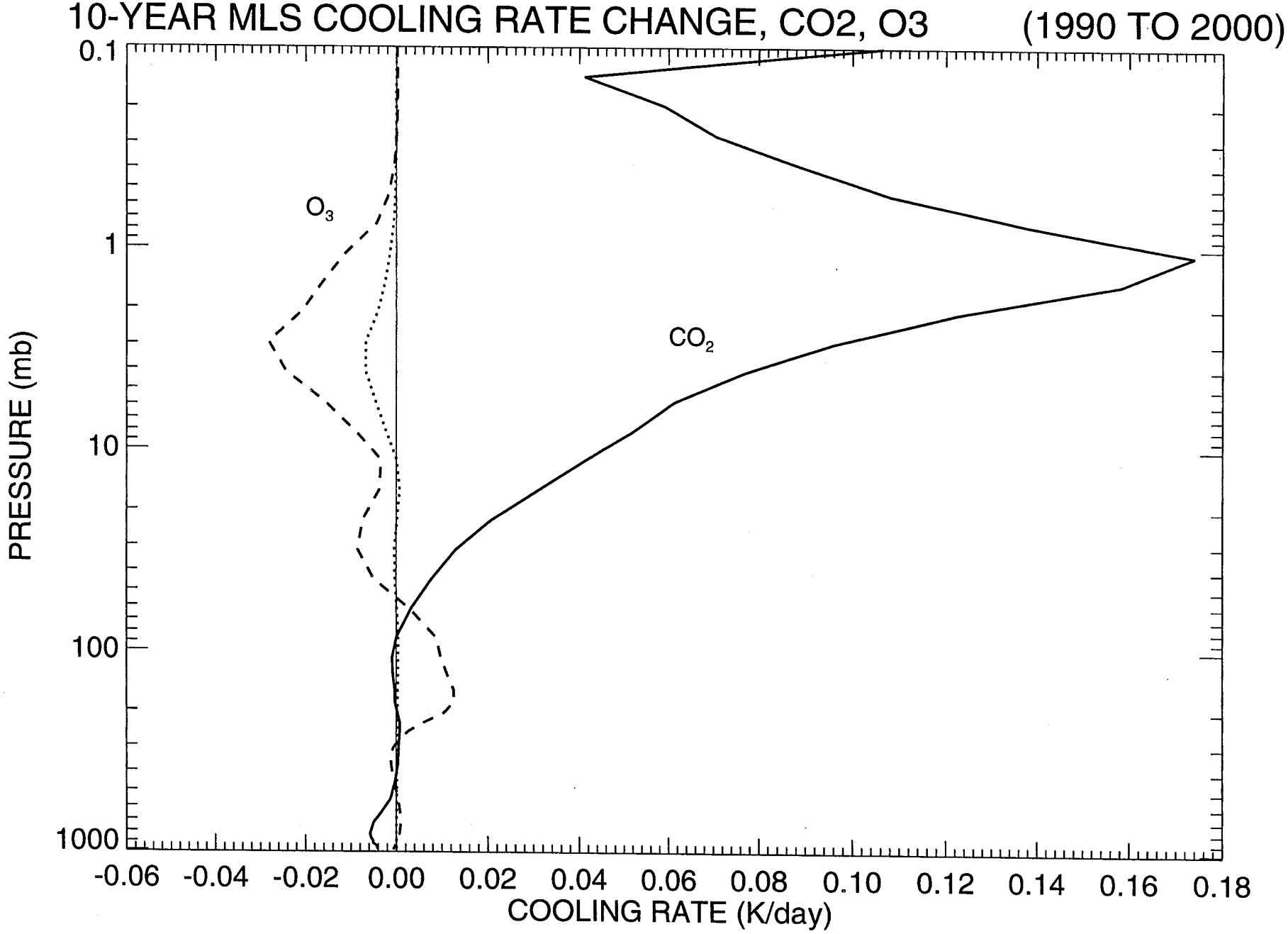
10-YEAR MLS COOLING RATE CHANGE, CO2, O3
(1990 TO 2000)
PRESSURE (mb)
0.1
1
10
100
1000
O3
CO2
-0.06
-0.04
-0.02
0.00
0.02
0.04
0.06
0.08
0.10
0.12
0.14
0.16
0.18
COOLING RATE (K/day)

10-Year Changes in Cooling Rate from 1990 to 2000

MLS Cooling Rate Change from 1990 to 2000 for CO_2, O_3 CFC-11, CFC-12, CFC-22, and CCL_4

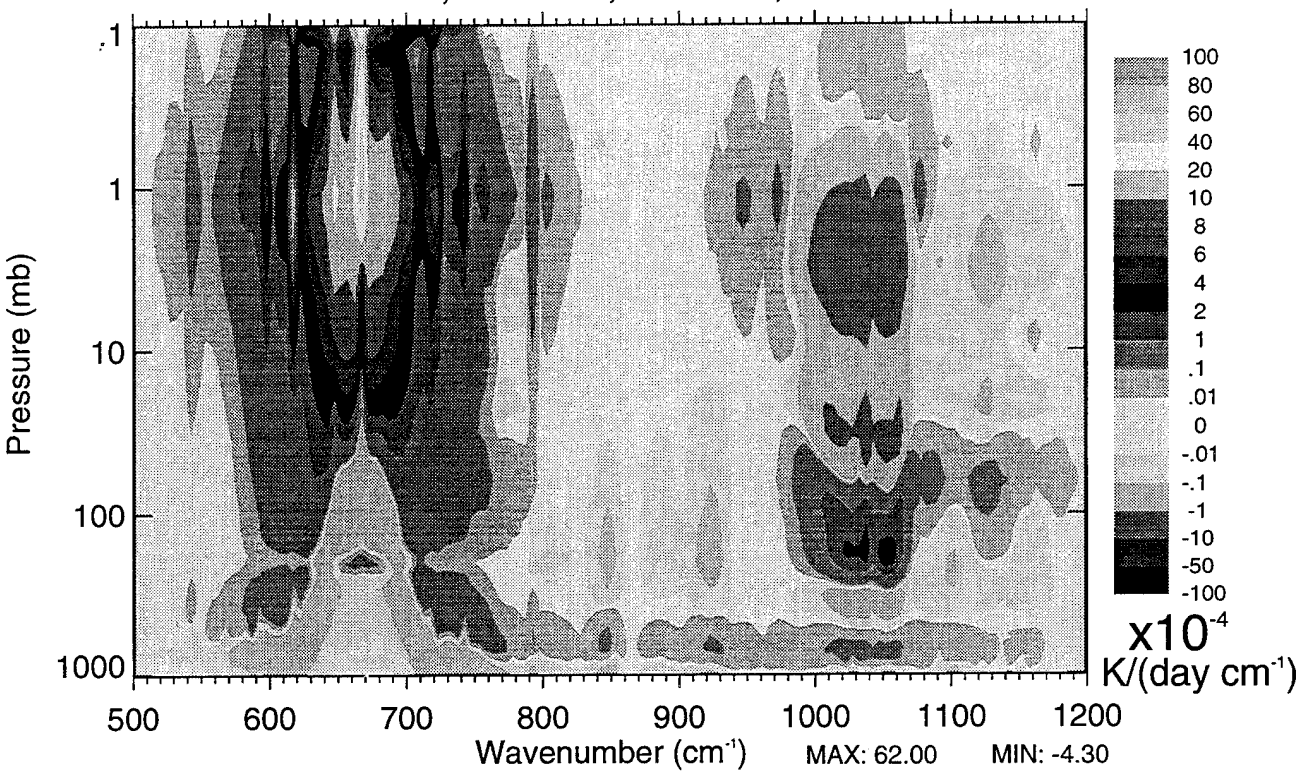

MLS Cooling Rate Change from 1990 to 2000 for Ozone Only

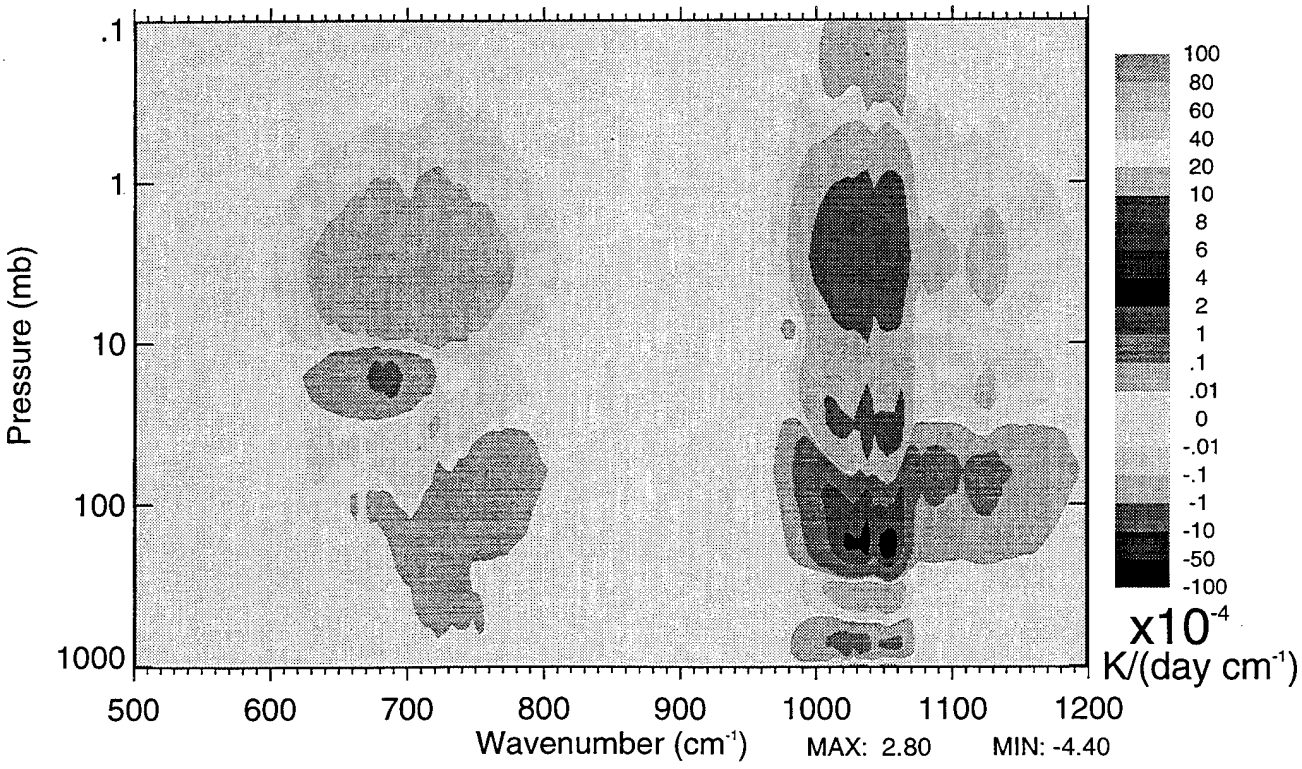

Shepard A. Clough, and Michael J. Iacono
Atmospheric and Environmental Research, Inc.

Plates 9 & 10

Conclusions

Water Vapor:

- The dominant greenhouse gas on a global basis for the troposphere
  - For atmospheres with significant amounts of water vapor, increases in concentration of a uniformly mixed gas result in a reduction in the atmospheric cooling in the lower troposphere
- Cooling in the upper troposphere is dominated by water vapor in the pure rotation region (0-400 cm^{-1}),

Carbon Dioxide and Ozone:

- Strong absorbers, but only over narrow spectral regions
  - CO_2 eliminates cooling below 500mb due to water vapor
  - from 640-690 cm^{-1}
- Doubling of carbon dioxide causes decreased cooling in the lower troposphere of about 5%
- Ozone exchange heating occurs from 500 to 20 mb; peaks at 0.3 K/day at 50 mb level

Halocarbons, CH_4, and N_2O

- These gases diminish H_2O cooling in lower troposphere in moist atmospheres, but have little affect on cooling in dry atmospheres
- Effects on outgoing flux and surface downwelling flux are non-negligible

1990-2000 Changes

- Radiative effects of ozone are highly dependant on depletion profile
- Stratospheric heating effect of ozone depletion offsets about 16% of the total cooling effect of carbon dioxide at this level
- 700 cm-1 ozone band is significant; contributes a maximum of 25% of the total ozone cooling response to ozone profile perturbations

VERY NARROW BAND MODEL CALCULATIONS OF ATMOSPHERIC FLUXES AND COOLING RATES USING THE MODTRAN CODE[$]

Presented By

L. S. BERNSTEIN, A. BERK, P. K. ACHARYA,
AND D. C. ROBERTSON
SPECTRAL SCIENCES, INC.

G. P. ANDERSON, J. H. CHETWYND, AND L. M. KIMBALL
GEOPHYSICS DIRECTORATE, PHILLIPS LABORATORY

Presented At

ANNUAL REVIEW CONFERENCE ON ATMOSPHERIC TRANSMISSION MODELS

June 8, 1994

$ Funded by Phillips Laboratory, Hanscom AFB, Bedford, MA.

PRESENTATION OVERVIEW

- VERY NARROW BAND MODEL(VNBM), $\Delta\omega = 1\ cm^{-1}$, YIELDS LINE-BY-LINE(LBL) QUALITY ATMOSPHERIC FLUX AND COOLING RATE PREDICTIONS.
  - $\approx$ 100 TIMES FASTER THAN LBL
  - NOT TUNED TO LBL CALCULATIONS
  - INTEGRATED INTO MODTRAN

- MODTRAN UPGRADES FOR IMPROVED ACCURACY.
  - SUB-LAYER INTEGRATION
  - LINE-OVERLAP CORRECTION
  - 3-PARAMETER CG(GOODY) FOR O_3

- DETAILED COMPARISONS TO ICRCCM LBL RESULTS FOR H_2O, CO_2, AND O_3.

SUB-LAYER INTEGRATION APPROACH*

- FINE LAYERING CONVERGES SLOWLY.
- SIMPLE AND ACCURATE ANALYTICAL APPROXIMATIONS FOR BEER'S LAW ABSORPTION.
- NO SIMPLE ANALYTICAL RESULT FOR BAND MODELS.
- RATIONAL POLYNOMIAL REPRESENTATION FOR INTERVAL ABSORPTION WITH NUMERICAL INTEGRATION OF R-T EQ.
  - MOLECULAR LINE
  - 2nd ORDER PADE APPROXIMANT
  - FAST AND FLEXIBLE
  - FIVE PARAMETER FIT

* L. S. Bernstein, Applied Optics, Accepted, May 1994.

SUB-LAYER INTEGRATION ERROR ESTIMATION

$\Delta\omega = 1\ cm^{-1}$ Single Line 10% Planck Function Variation

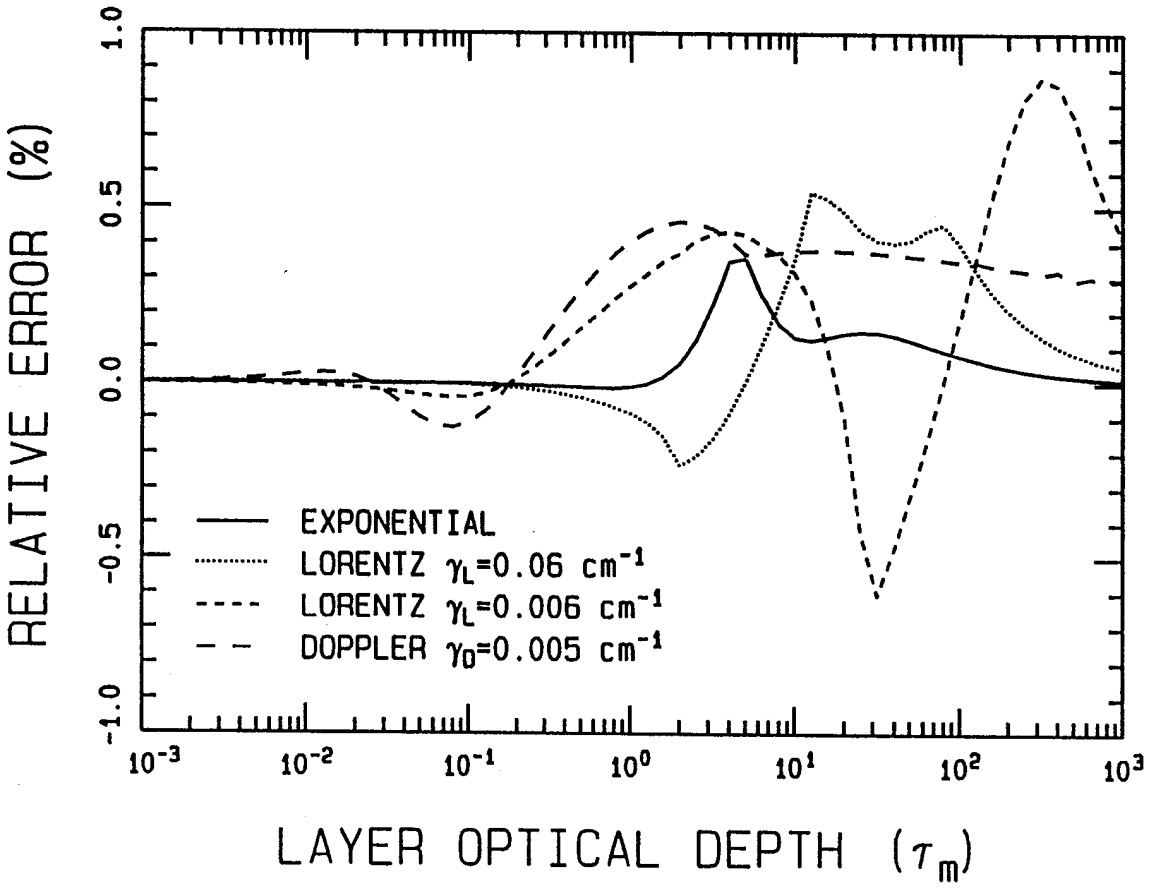

LINE-OVERLAP CORRECTION APPROACH

- EXACT AND NEAR-EXACT LINE OVERLAPS TREATED IN COMPUTING THE LINE DENSITY PARAMETER(1/d).
  - LINES WITHIN $\delta\omega$ COINCIDENT
  - REDUCES LINE DENSITY AND OPACITY
  - LOCAL CORRELATION APPROXIMATION(LCA)
  - $N = \Delta\omega/d$

- STATISTICAL OVERLAP CORRECTION APPLIED TO N EFFECTIVE LINES IN $\Delta\omega$.
  - NO POSITIONAL CORRELATION

- A SINGLE ALTITUDE AND FREQUENCY-INDEPENDENT VALUE OF $\delta\omega = 0.01$ cm^{-1} WORKS WELL FOR FLUX AND COOLING RATE CALCULATIONS.

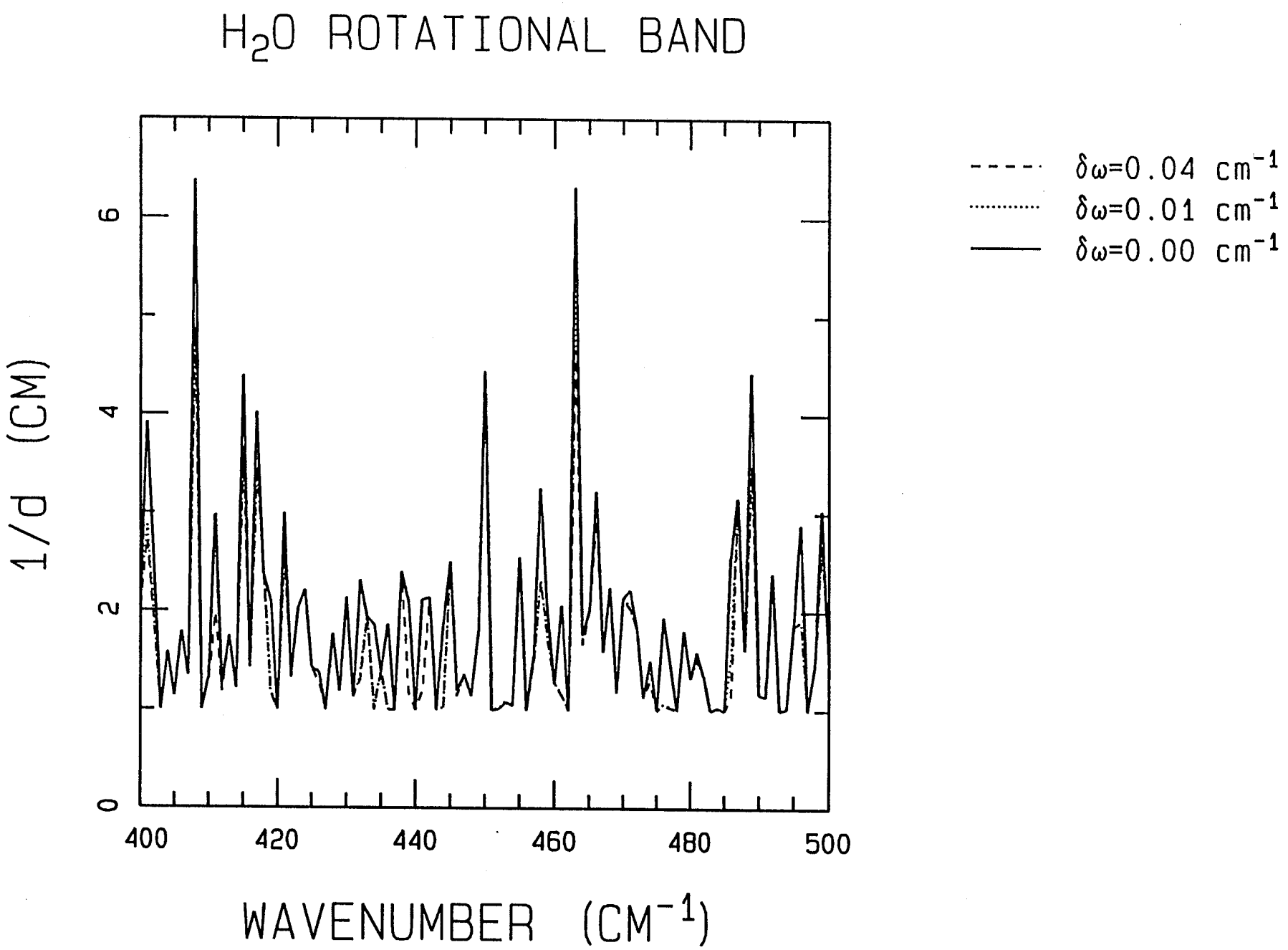
H2O ROTATIONAL BAND
1/d (CM)
0
2
4
6
400
420
440
460
480
500
WAVENUMBER (CM-1)
δω=0.04 cm-1
δω=0.01 cm-1
δω=0.00 cm-1

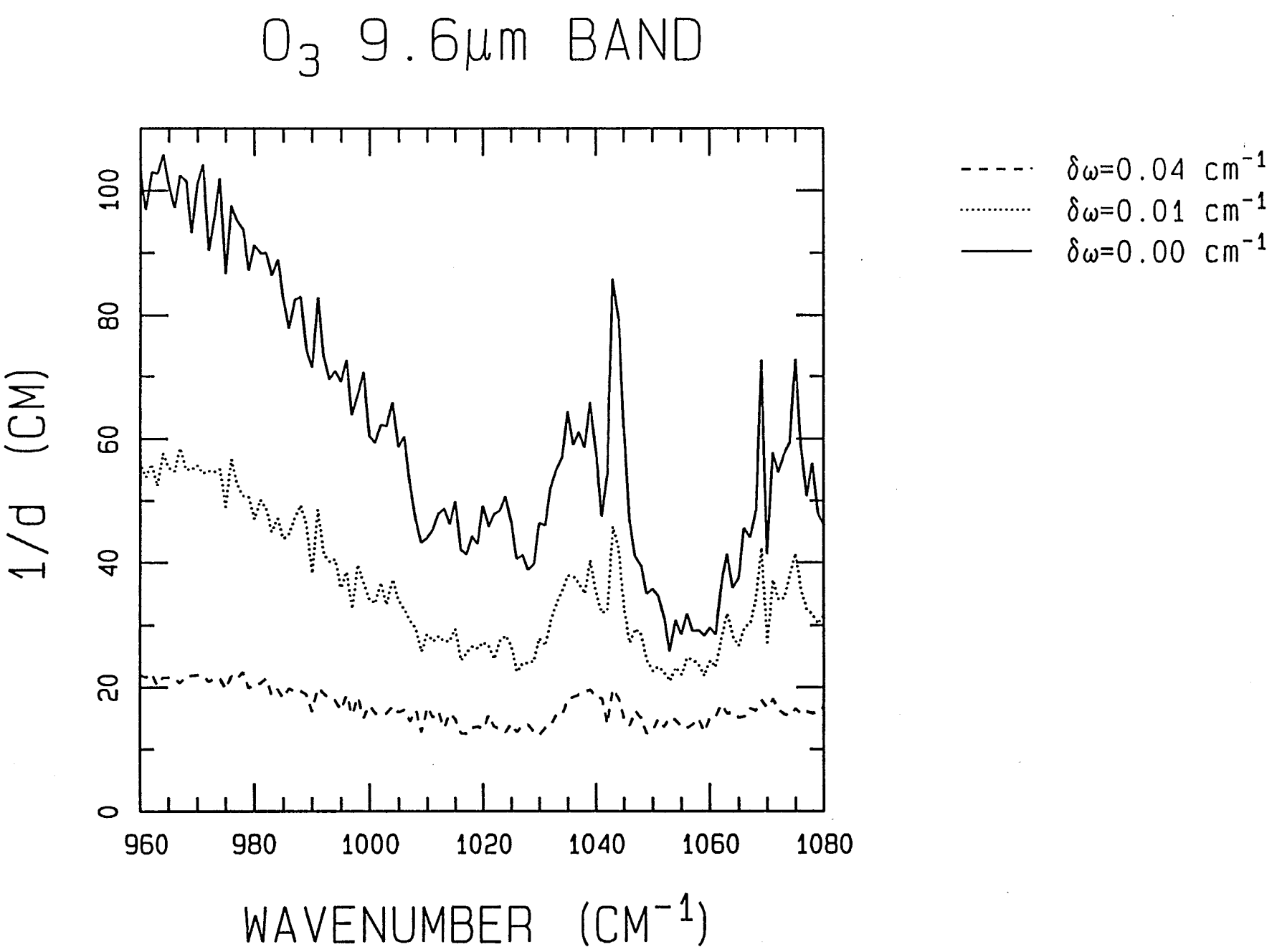
O_3 9.6μm BAND
1/d (CM)
0
20
40
60
80
100
960
980
1000
1020
1040
1060
1080
WAVENUMBER (CM^{-1})
δω=0.04 cm^{-1}
δω=0.01 cm^{-1}
δω=0.00 cm^{-1}

FLUX AND COOLING RATE COMPUTATIONAL OVERVIEW*

- 60 LAYERS.
- FLAT EARTH.
- 2 ANGLE 1st-MOMENT GAUSSIAN QUADRATURE.
- 0 - 3,000 cm^{-1}.
- 10 AND 25 cm^{-1} LINE TAILS.
- 27 MIN. ON HP-9000/735 WORKSTATION.
  - UNDER 10 MIN. ANTICIPATED

* L. S. Bernstein et. al., JGR, To Be Submitted, July 1994.

ICRCCM DATA BASE

- ATMOSPHERIC AND ENVIRONMENT RESEARCH(AER)
  - CLOUGH ET. AL., JGR, 15, 761, 1992.
  - RES = 0.0005 cm^{-1}
- NASA GODDARD LABORATORY FOR ATMOSPHERES(GLA)
  - RIDGWAY ET. AL., JGR, 96, 8969, 1991.
  - RES = 0.01 cm^{-1}
- NASA GODDARD INSTITUTE FOR SPACE STUDIES(GISS)
  - LACIS AND OINAS, JGR, 96, 9027, 1991.
  - RES = 0.0005 cm^{-1}
- NOAA GEOPHYSICAL FLUID DYNAMIC LABORATORY(GFDL)
  - SCHWARZKOPF AND FELS, JGR, 96, 9075, 1991.
  - RES = 0.005 cm^{-1}

Table I. Summary of Line-by-Line and MODTRAN Flux Calculations.

Atmospheric Case	Flux Model	Surface (W/m^2)		Tropopause[a] (W/m^2)		Top (W/m^2)
		UP	DOWN	UP	DOWN	UP
Tropical H_2O with Continuum	MODTRAN	459.12	389.21	331.43	3.22	331.13
	AER	458.92	385.88	332.39	3.19	332.59
Mid-lattitude Summer H_2O with Continuum	MODTRAN	423.51	335.84	321.09	7.56	320.80
	AER	423.53	333.92	321.17	7.32	320.96
Subartic Winter H_2O with Continuum	MODTRAN	247.72	138.05	222.49	16.59	221.35
	AER	247.61	138.23	222.55	16.78	221.52
Mid-lattitude Summer H_2O without Continuum	MODTRAN	423.51	269.58	334.98	7.15	334.77
	MODTRAN[b]	423.51	269.35	335.34	6.98	335.12
	AER	423.32	269.02	335.77	6.89	335.66
	GLA	423.48	267.28	336.59	6.25	336.50
	GFDL	423.56	266.77	336.61	6.71	336.32
Mid-lattitude Summer CO_2 (300 ppm)	MODTRAN	423.49	76.38	382.60	12.48	383.09
	GLA	423.48	76.48	383.08	12.14	383.65
	GISS[c]	422.85	76.35	382.01	12.22	382.68
	GFDL	423.56	76.28	383.26	12.15	383.72
Mid-lattitude Summer CO_2 (600 ppm)	MODTRAN	423.49	84.40	377.67	14.23	378.99
	MODTRAN[b]	423.49	76.22	382.75	12.38	383.22
	GLA	423.48	84.66	377.95	13.91	379.37
	GLA[d]	421.29	83.70	376.67	13.89	378.03
	GFDL[d]	421.38	83.60	376.83	13.92	378.07
Subarctic Winter CO_2 (300 ppm)	MODTRAN	247.71	44.17	231.50	14.52	229.83
	GLA	247.71	44.22	231.64	14.15	230.17
	GFDL[d]	247.36	43.90	231.44	14.16	229.94
Mid-lattitude Summer O_3	MODTRAN	433.49	6.33	419.34	3.26	411.64
	MODTRAN[b]	423.49	6.16	419.40	3.06	412.11
	GLA	423.48	6.00	419.60	3.10	412.02
	GISS[c]	422.85	6.40	418.61	3.31	410.84
	GFDL	423.56	6.18	419.43	3.04	412.06

(a) 99.7 mbar (TROP), 179 mbar (MLS), 282.9 mbar (SAW).
(b) $\delta\omega = 0.01$ cm^{-1} ($\delta\omega = 0.0$ cm^{-1} for all other MODTRAN runs).
(c) 0 - 2,500 cm^{-1} spectral interval.
(d) 0 - 2,200 cm^{-1} spectral interval.

Fig. 1

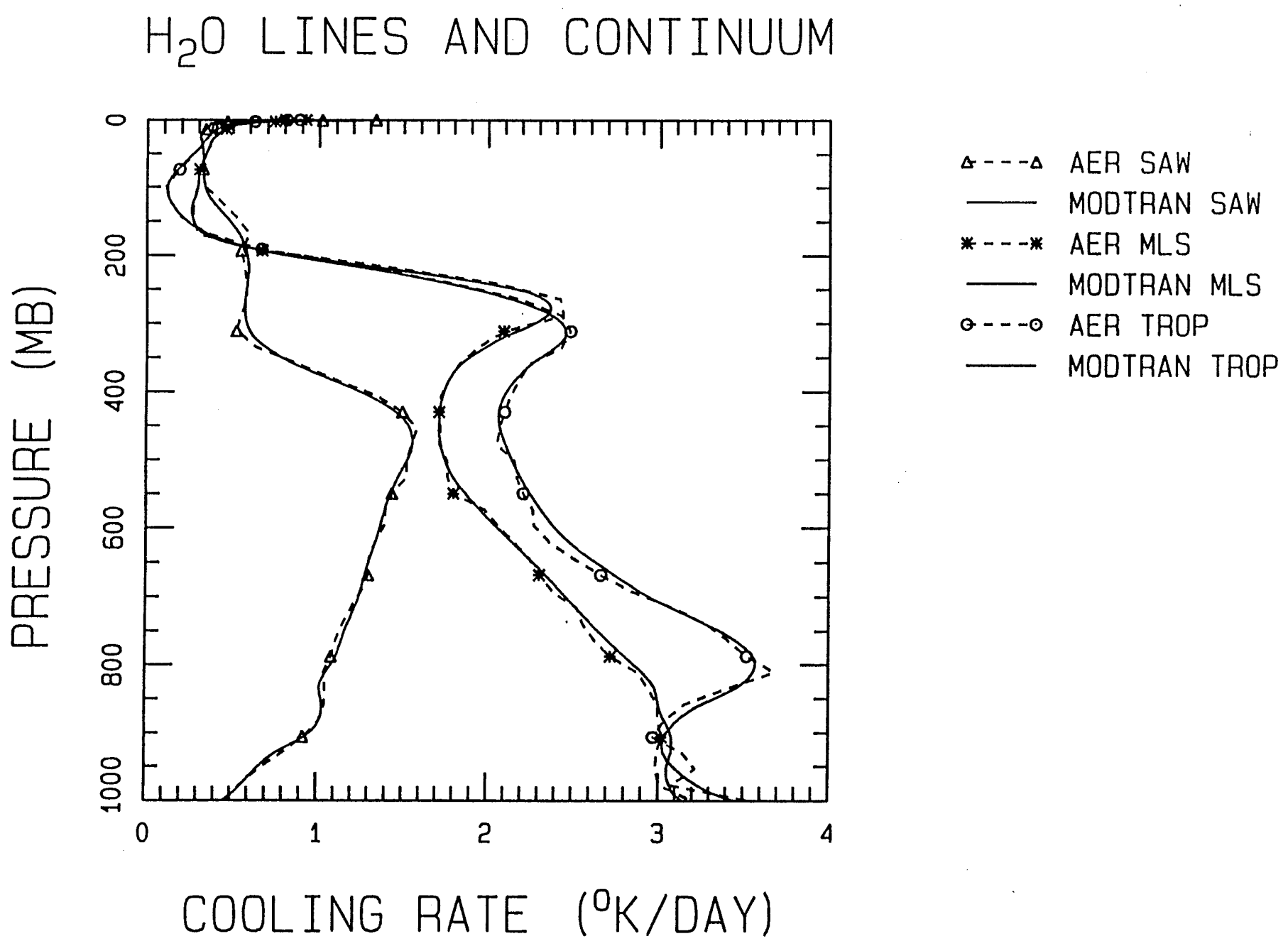
H_2O LINES AND CONTINUUM
PRESSURE (MB)
0
200
400
600
800
1000
0
1
2
3
4
COOLING RATE (°K/DAY)
AER SAW
MODTRAN SAW
AER MLS
MODTRAN MLS
AER TROP
MODTRAN TROP

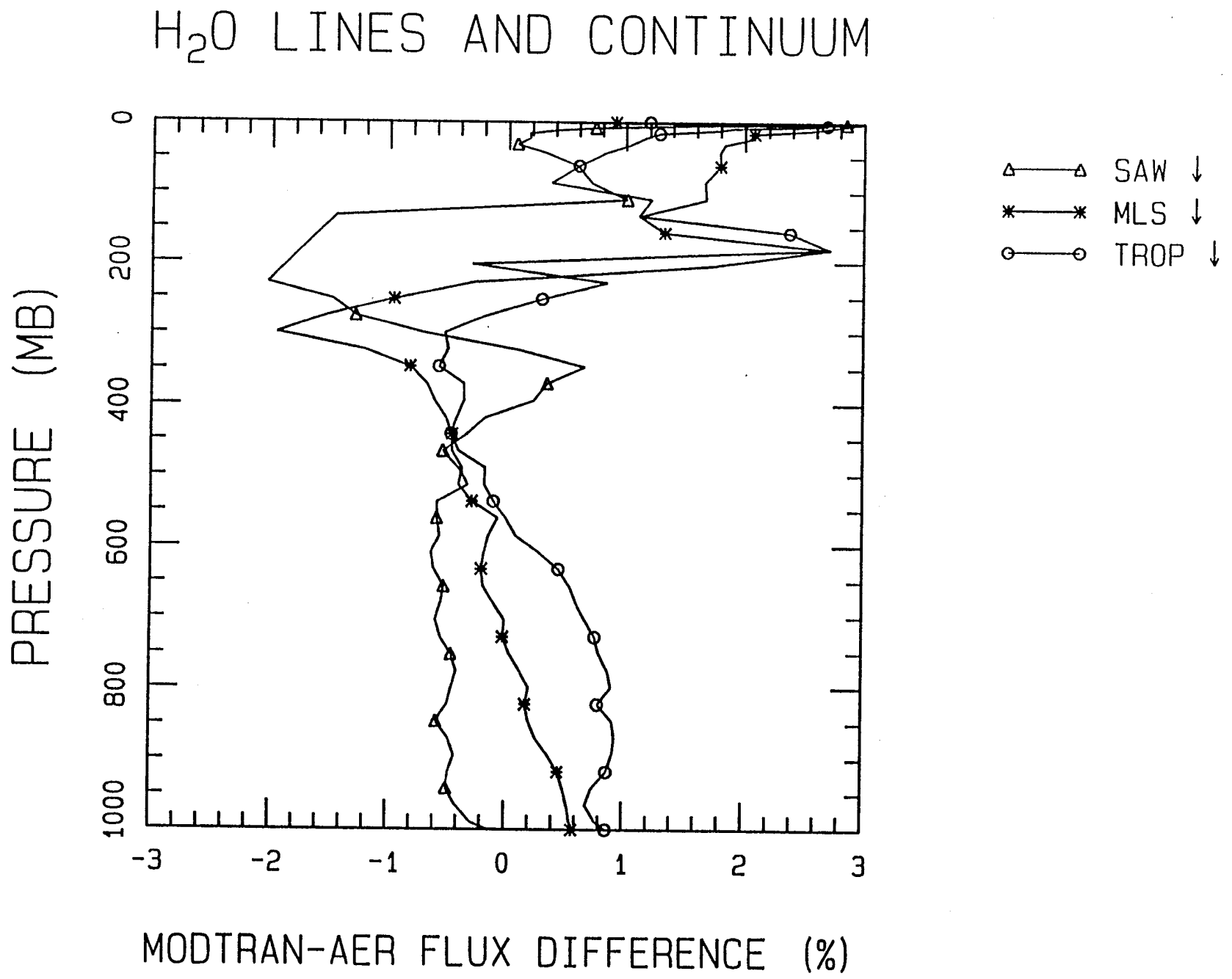
H2O LINES AND CONTINUUM
PRESSURE (MB)
0
200
400
600
800
1000
-3
-2
-1
0
1
2
3
MODTRAN-AER FLUX DIFFERENCE (%)
SAW ↓
MLS ↓
TROP ↓

Fig. 4

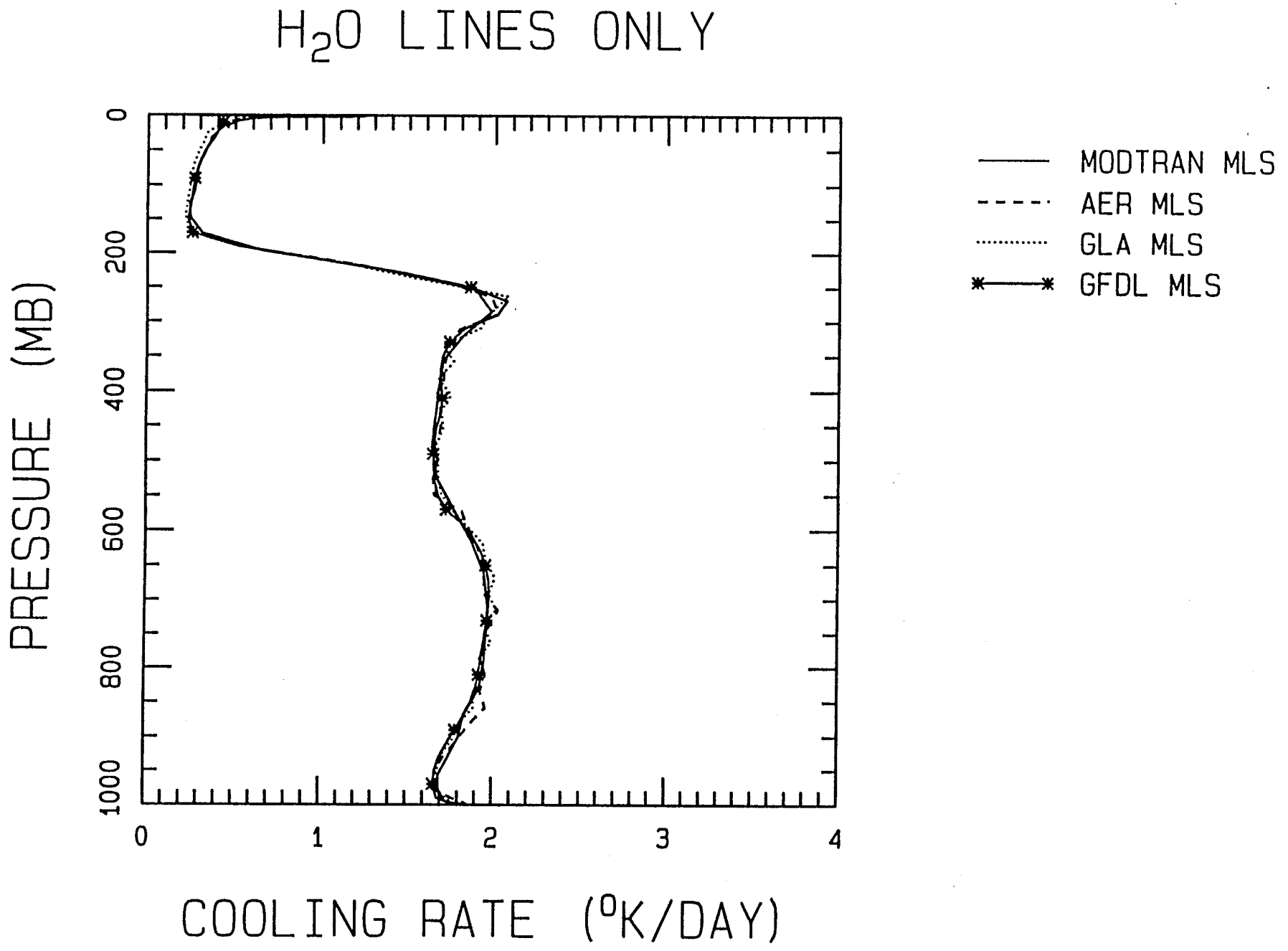
H2O LINES ONLY
PRESSURE (MB)
0
200
400
600
800
1000
0
1
2
3
4
COOLING RATE (°K/DAY)
MODTRAN MLS
AER MLS
GLA MLS
GFDL MLS

Fig. 6

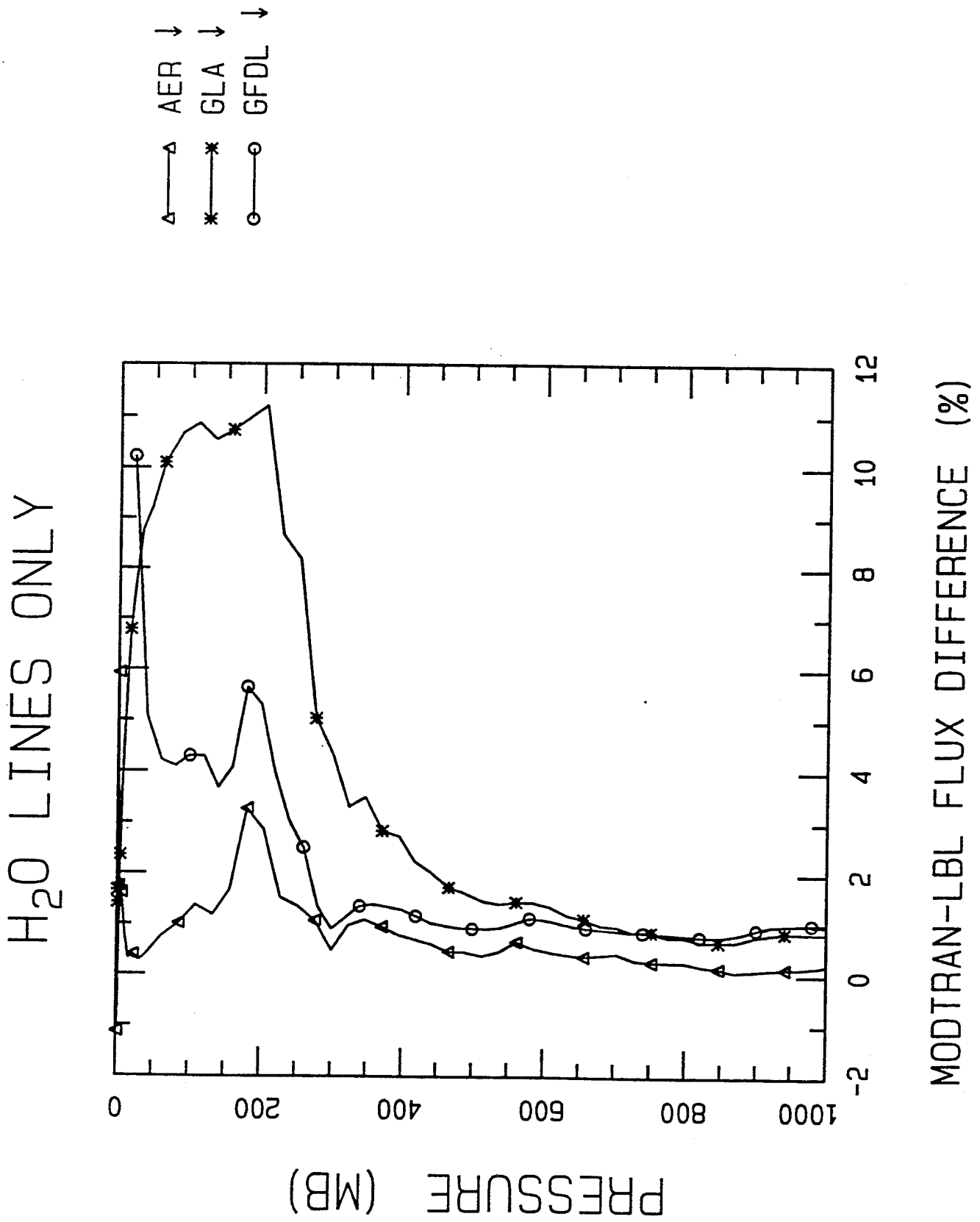
AER
GLA
GFDL
H2O LINES ONLY
PRESSURE (MB)
MODTRAN-LBL FLUX DIFFERENCE (%)
0
200
400
600
800
1000
-2
0
2
4
6
8
10
12

Fig. 21

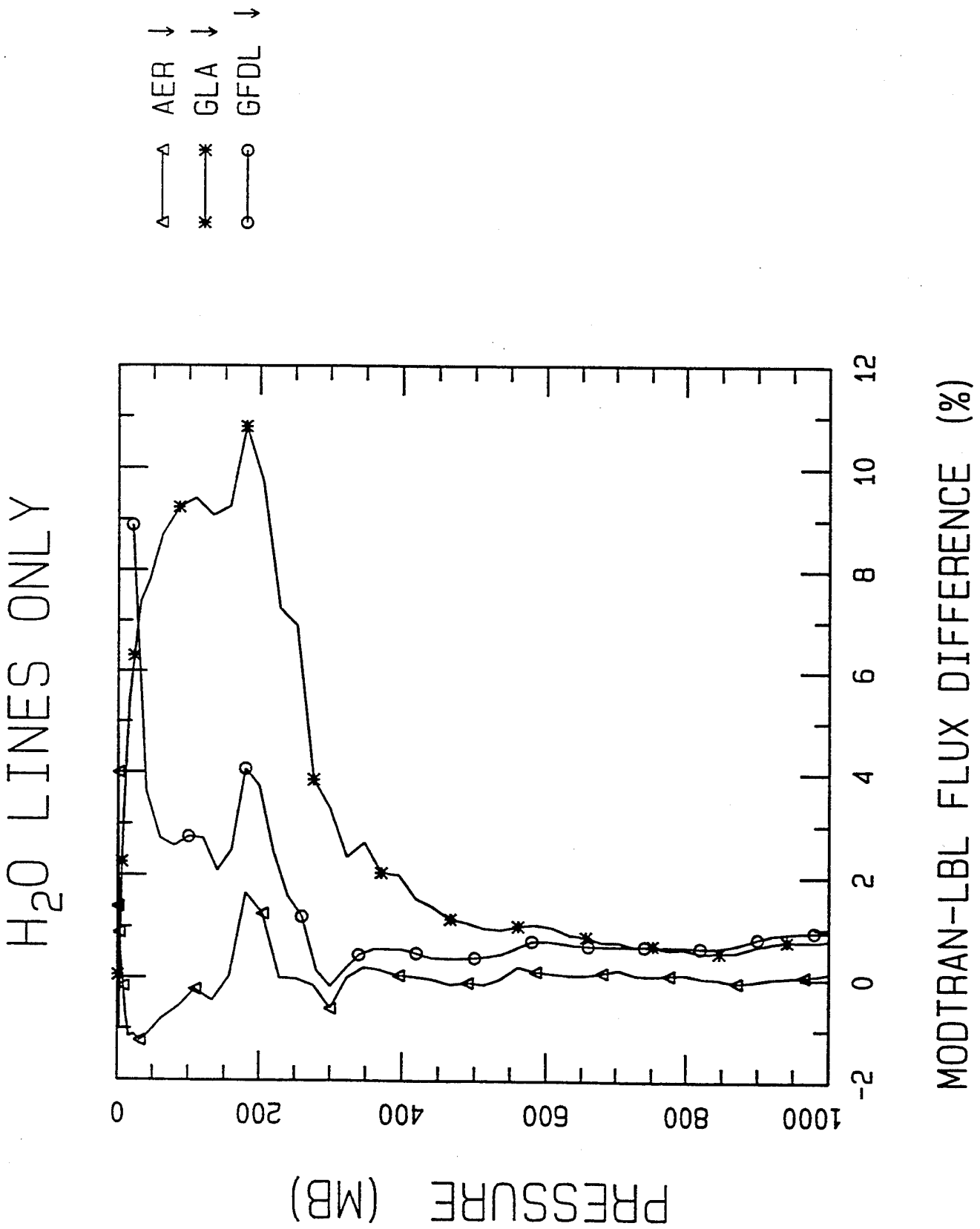
AER
GLA
GFDL
H2O LINES ONLY
PRESSURE (MB)
MODTRAN-LBL FLUX DIFFERENCE (%)
0
200
400
600
800
1000
-2
0
2
4
6
8
10
12

Fig. 7

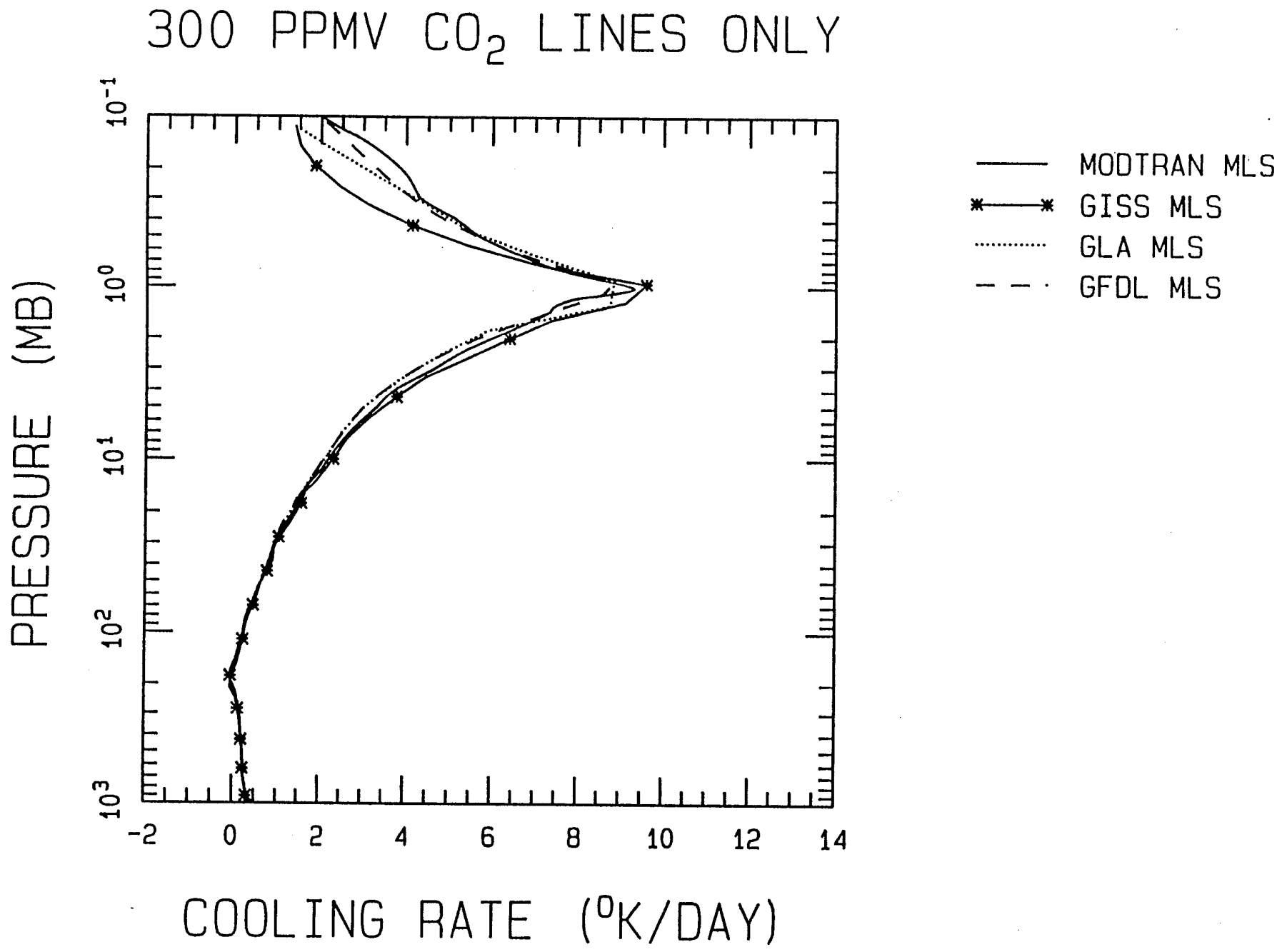
300 PPMV CO_2 LINES ONLY
PRESSURE (MB)
10^{-1}
10^{0}
10^{1}
10^{2}
10^{3}
-2
0
2
4
6
8
10
12
14
COOLING RATE (^{0}K/DAY)
MODTRAN MLS
GISS MLS
GLA MLS
GFDL MLS

Fig. 22

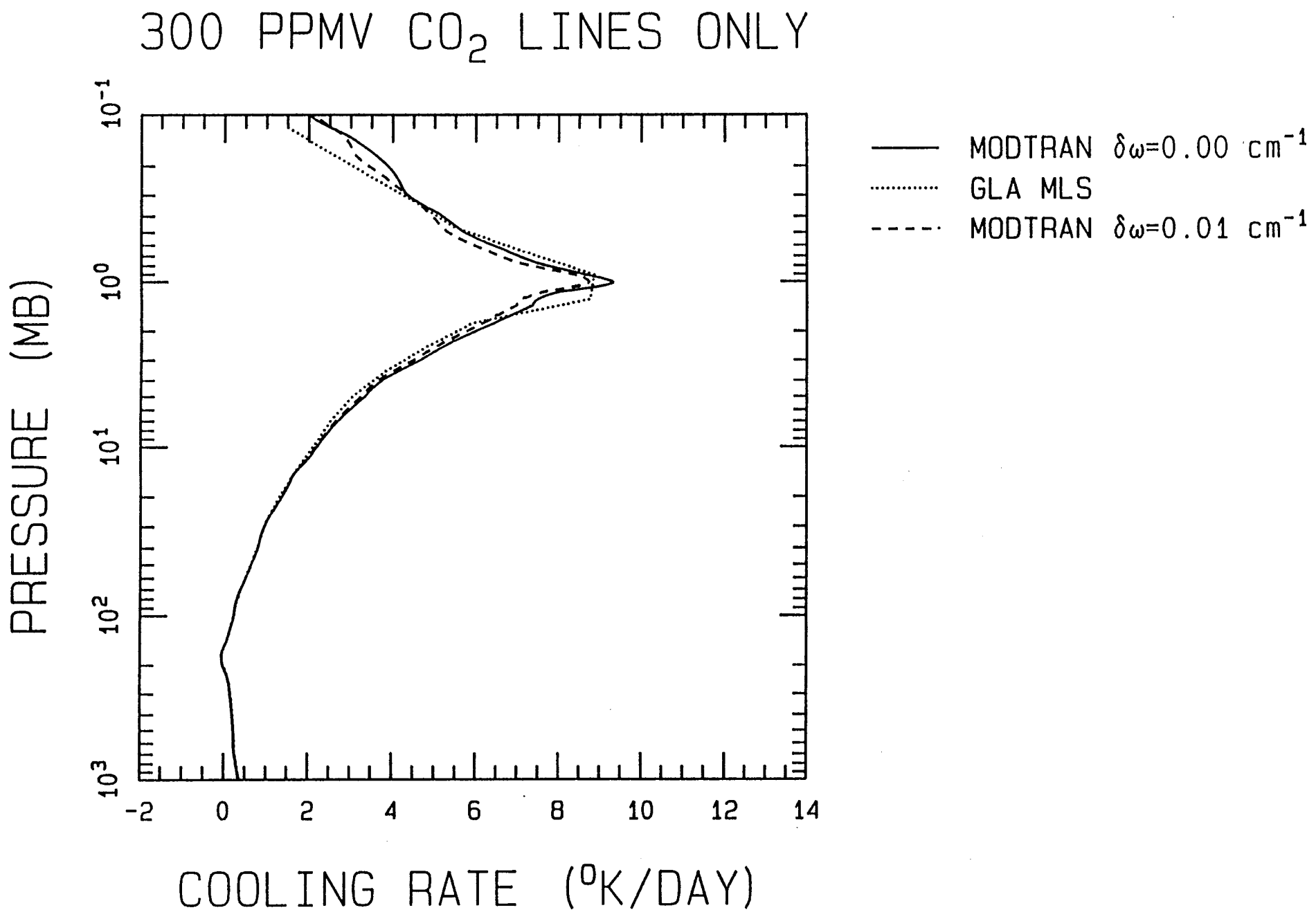
300 PPMV CO_2 LINES ONLY
PRESSURE (MB)
10^{-1}
10^{0}
10^{1}
10^{2}
10^{3}
-2
0
2
4
6
8
10
12
14
COOLING RATE (^{0}K/DAY)
MODTRAN $\delta\omega$=0.00 cm^{-1}
GLA MLS
MODTRAN $\delta\omega$=0.01 cm^{-1}

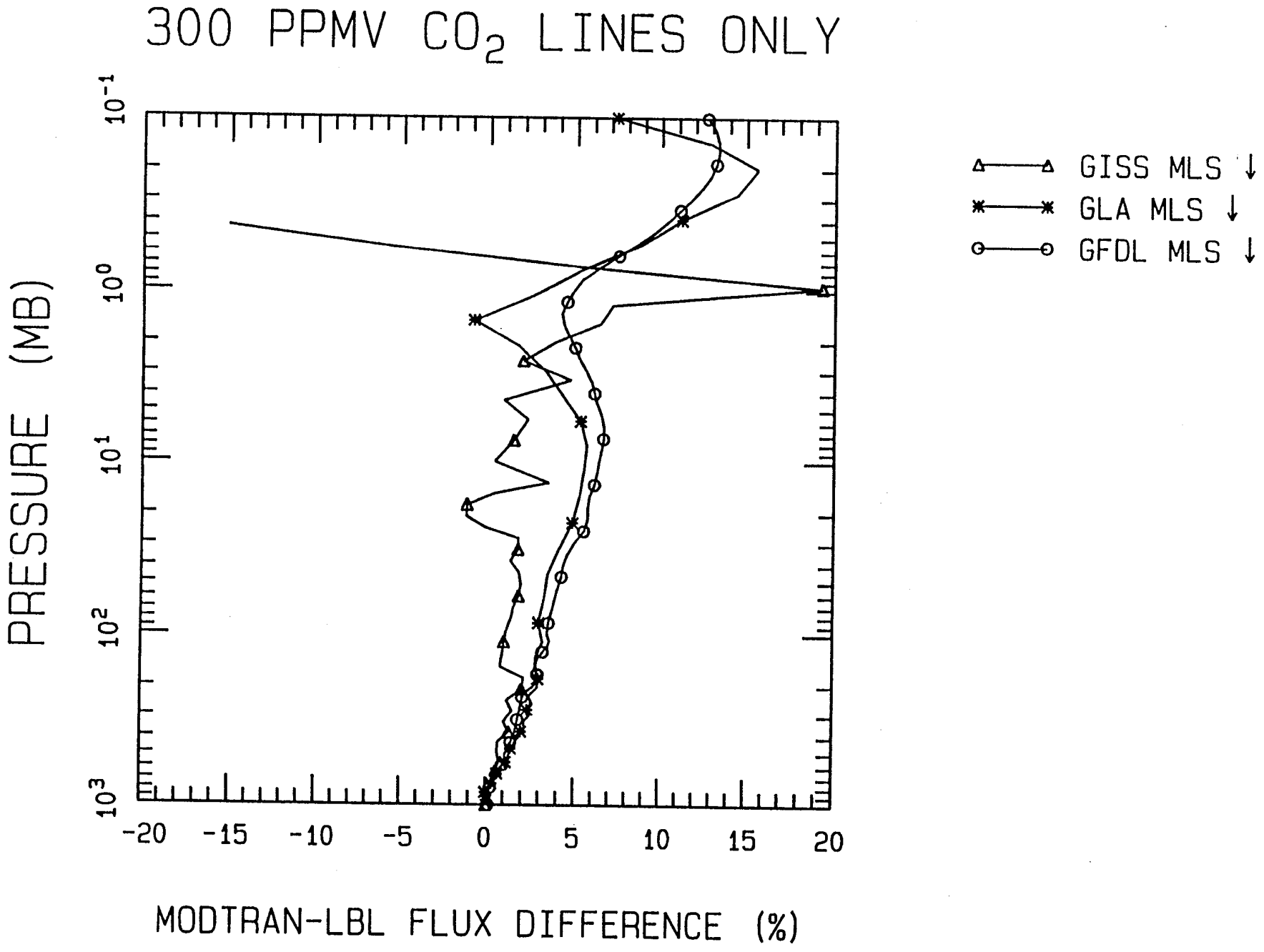
300 PPMV CO_2 LINES ONLY
PRESSURE (MB)
10^{-1}
10^{0}
10^{1}
10^{2}
10^{3}
-20
-15
-10
-5
0
5
10
15
20
MODTRAN-LBL FLUX DIFFERENCE (%)
GISS MLS ↓
GLA MLS ↓
GFDL MLS ↓

Fig. 23

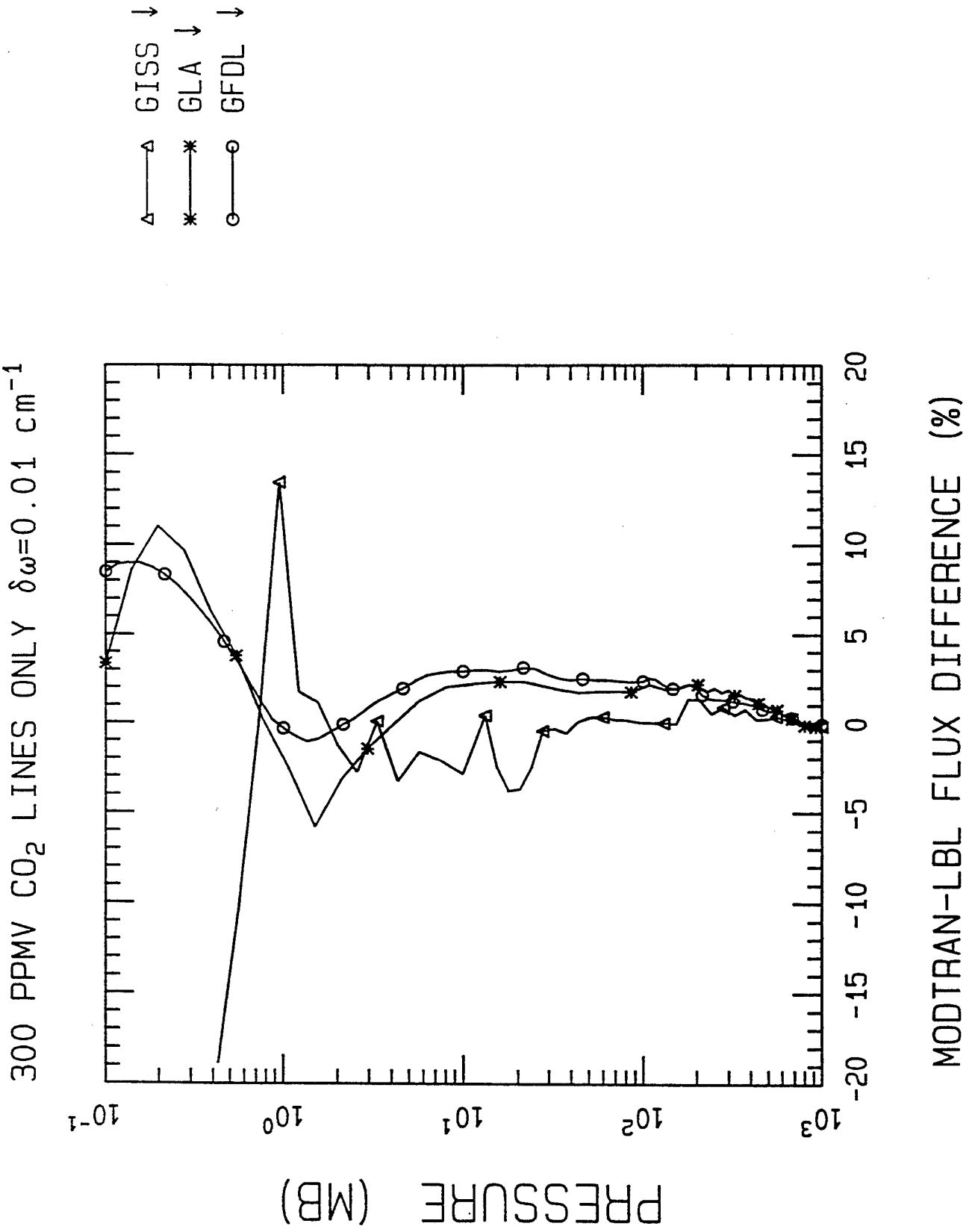
GISS
GLA
GFDL
300 PPMV CO_2 LINES ONLY $\delta\omega$=0.01 cm^{-1}
PRESSURE (MB)
10^{-1}
10^{0}
10^{1}
10^{2}
10^{3}
-20
-15
-10
-5
0
5
10
15
20
MODTRAN-LBL FLUX DIFFERENCE (%)

Fig. 15

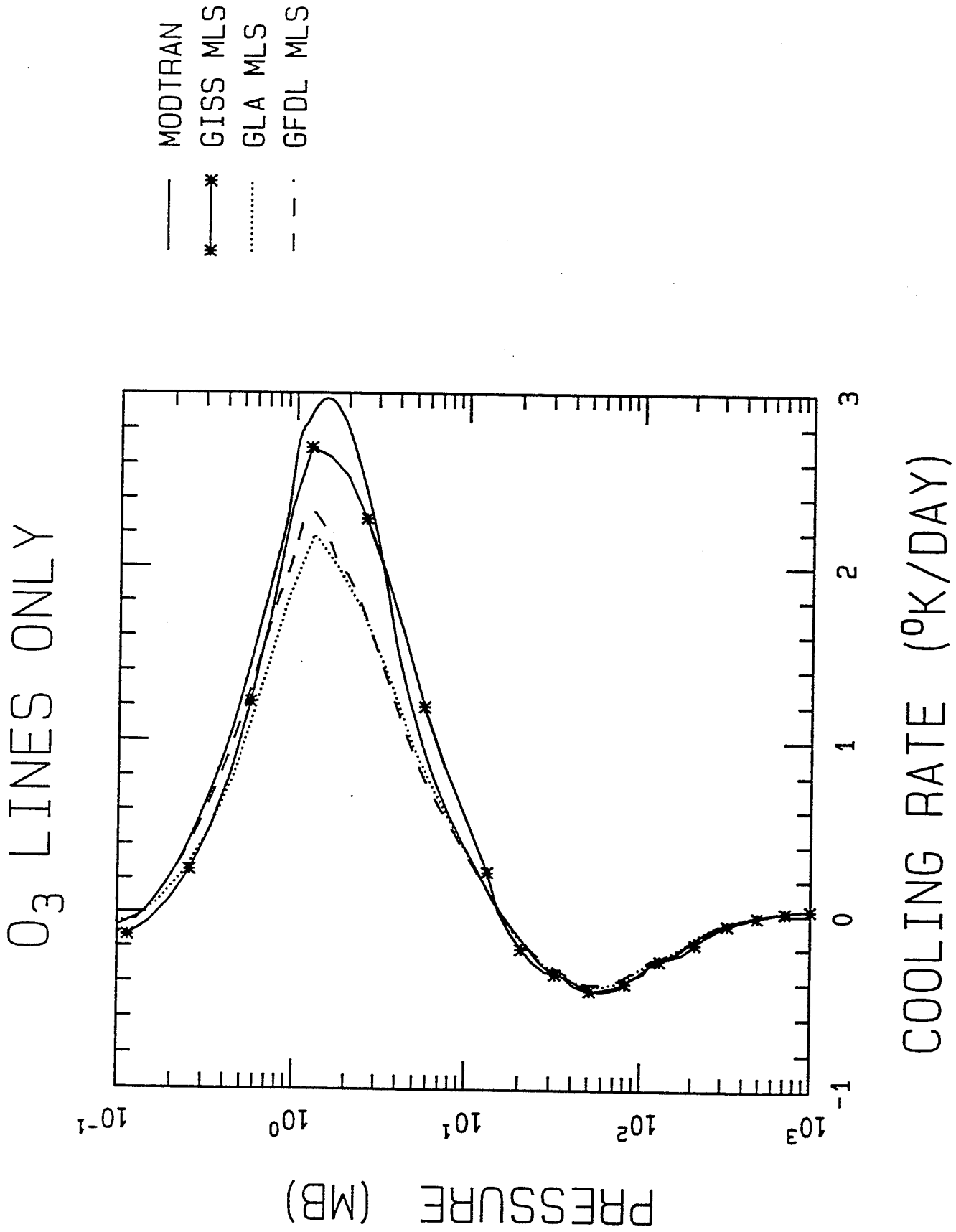
MODTRAN
GISS MLS
GLA MLS
GFDL MLS
O_3 LINES ONLY
PRESSURE (MB)
COOLING RATE (^oK/DAY)
10^{-1}
10^0
10^1
10^2
10^3
-1
0
1
2
3

Fig. 24

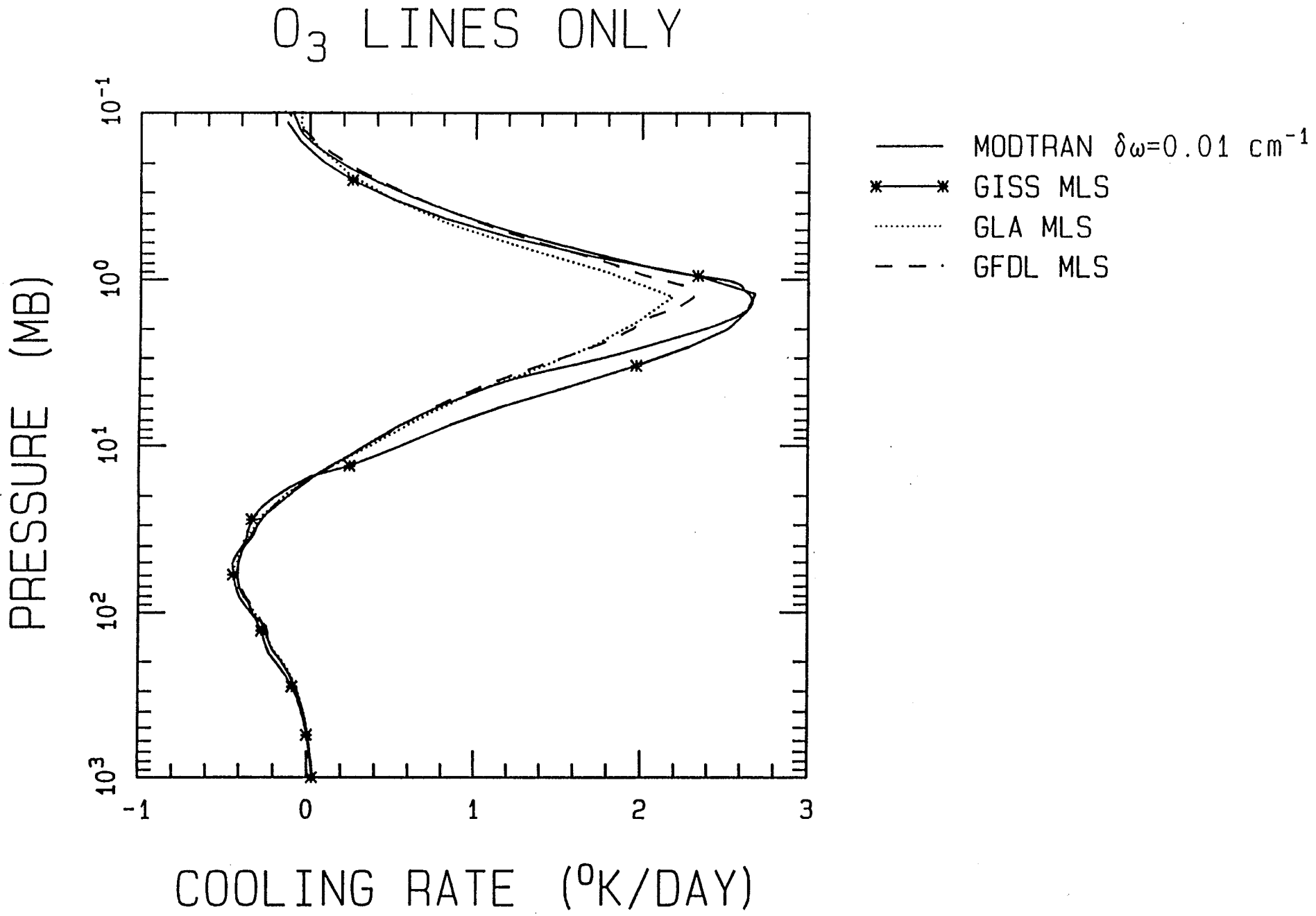
O_3 LINES ONLY
PRESSURE (MB)
10^{-1}
10^{0}
10^{1}
10^{2}
10^{3}
-1
0
1
2
3
COOLING RATE (^{o}K/DAY)
MODTRAN $\delta\omega$=0.01 cm^{-1}
GISS MLS
GLA MLS
GFDL MLS

759

Fig. 17

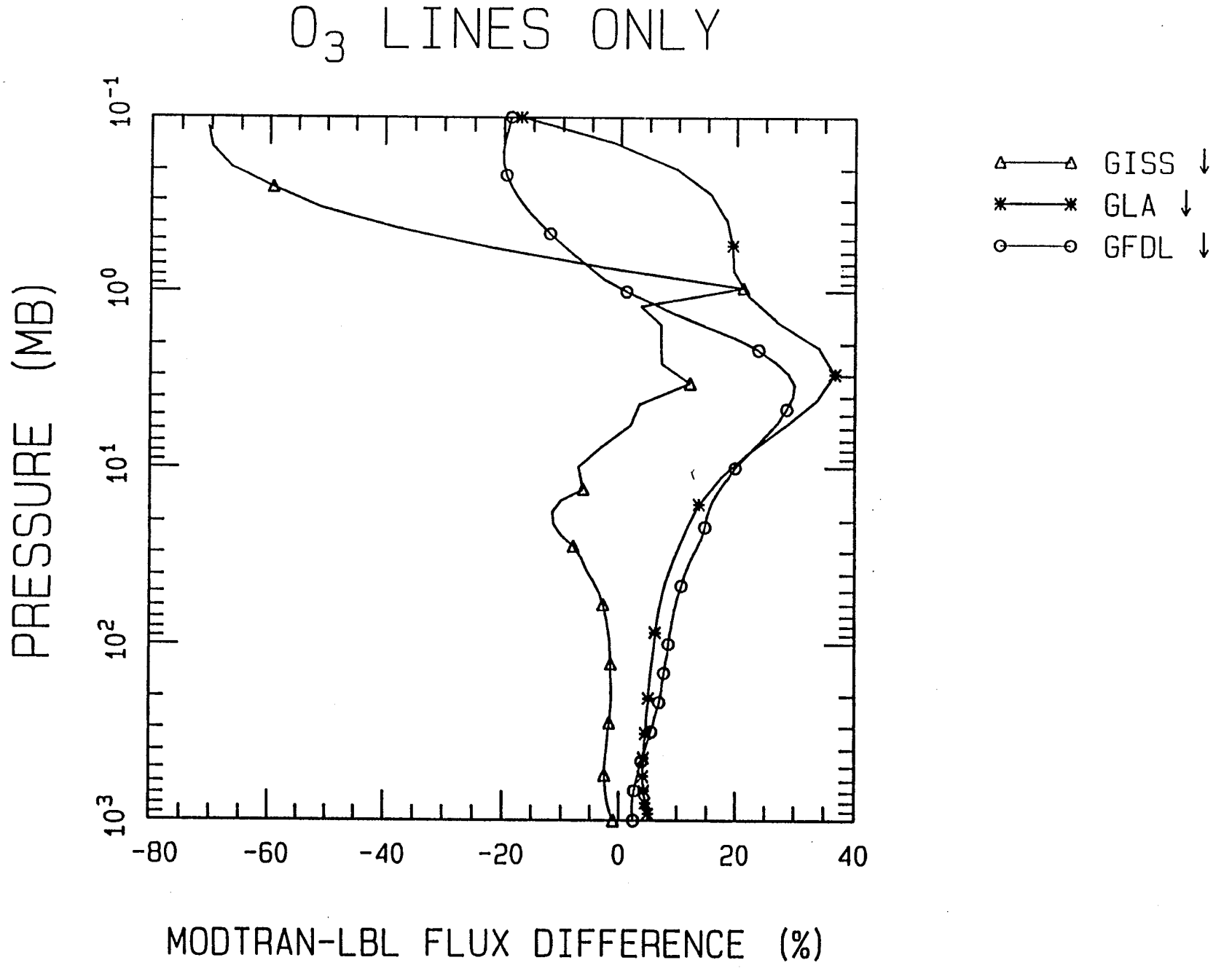
O_3 LINES ONLY
PRESSURE (MB)
10^{-1}
10^{0}
10^{1}
10^{2}
10^{3}
-80
-60
-40
-20
0
20
40
MODTRAN-LBL FLUX DIFFERENCE (%)
GISS ↓
GLA ↓
GFDL ↓

Fig. 25

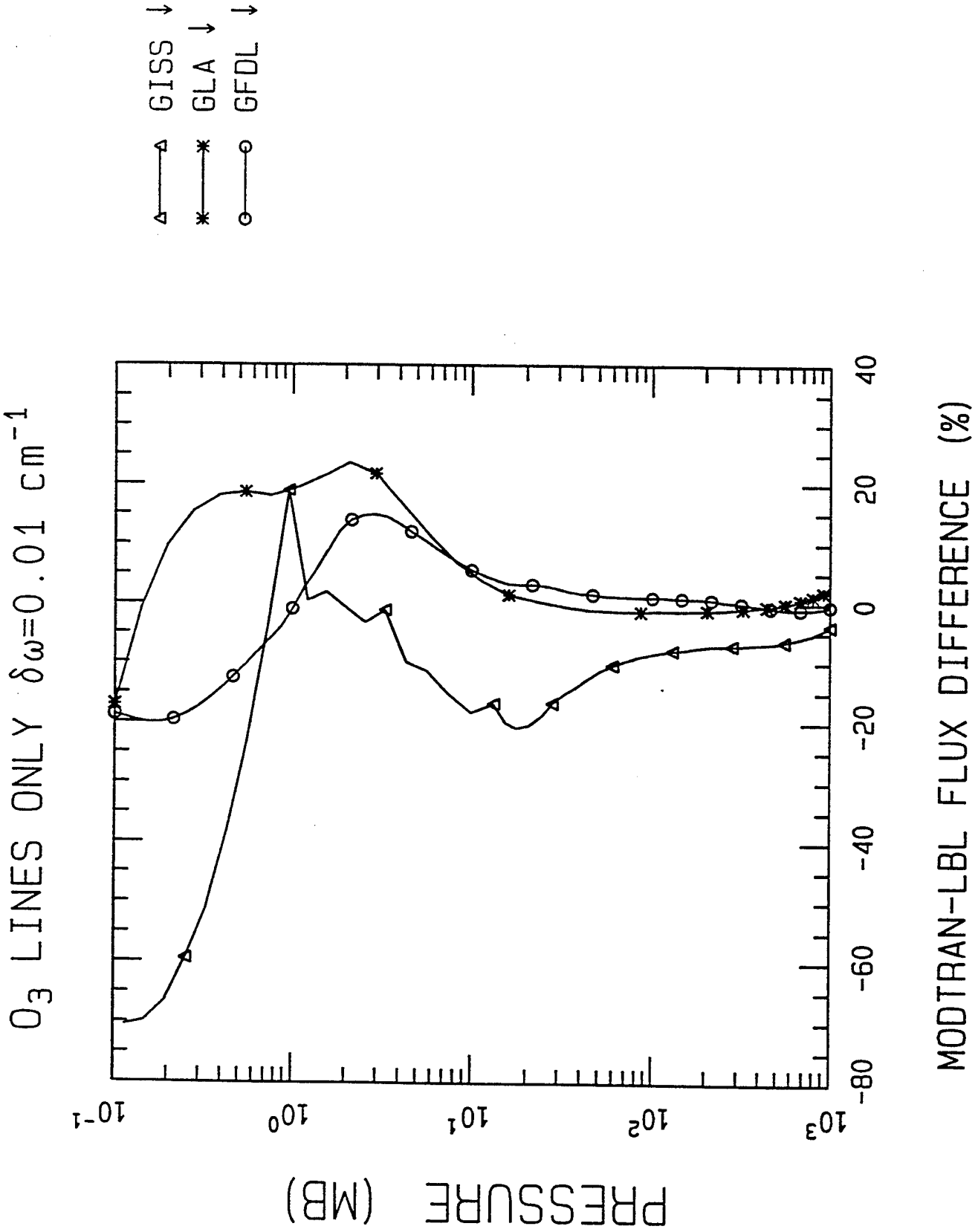
GISS ↓
GLA ↓
GFDL ↓
O_3 LINES ONLY $\delta\omega$=0.01 cm^{-1}
PRESSURE (MB)
10^{-1}
10^0
10^1
10^2
10^3
40
20
0
-20
-40
-60
-80
MODTRAN-LBL FLUX DIFFERENCE (%)

CONCLUSIONS

- 1 cm^{-1} VNBM INCORPORATED INTO MODTRAN.
- MODTRAN-PREDICTED FLUXES AND COOLING RATES WITHIN SPREAD OF LBL RESULTS FOR H_2O, CO_2, AND O_3.
  - HIGH ALTITUDE ISSUES
- FUTURE MODTRAN DEVELOPMENTS.
  - LCA REFINEMENTS
  - SCATTERING
  - SPECTRAL RESOLUTION

ACKNOWLEDGEMENTS

W. L. RIDGWAY
APPLIED RESEARCH CORPORATION

M. J. IACONO
ATMOSPHERIC AND ENVIRONMENTAL RESEARCH

Greenhouse Gas Concentration Profiles Retrieved from CIRRIS-1A Measurements in the 7-13 μm window during STS-39

G E Bingham, D K Zhou, and A J Steed
Space Dynamics Laboratory, Utah State University, Logan, UT 84341

G P Anderson and R M Nadile
Geophysics Directorate,Phillips Laboratory, Hanscom Air Force Base, MA 01731

Abstract

The spectral and spatial distributions of the greenhouse gas infrared emissions are measured by the CIRRIS-1A (Cryogenic Infrared Radiance Instrumentation for Shuttle) interferometer sensor during STS-39 flight (28 Apr - 6 May, 1991). The spectra in the important 7-11 μm infrared window were recorded. High resolution spectral scans ($\sim$1.5 cm^{-1} instrument resolution) and FASCOD-3 with HITRAN92 database and NMC temperature and pressure profiles are used in an onion peel routine to retrieve gas concentrations from absolutely calibrated radiance data. Scan to scan and profile to profile variability are compared to show the measurement capability of the cryogenic infrared interferometer. The local aerosol is estimated by comparing the modelled and measured CO_2 hot band (10.5 μm) spectra. The results of concentration profiles retrieved from the spectra (30° south latitude 9° East longitude, local time of 1.2 hr.) are shown in the figure. Profiles of CFC-11, CFC-12, HNO_3, and O_3 developed in this fashion and at different locations are compared with ATMOS (Atmospheric Trace Molecule Spectroscopy), LIMS (Limb Infrared Monitor of the Stratosphere), and situ mean data for these gases.

Conclusion

The infrared emissions from greenhouse gases were successfully measured as part of the STS-39 mission and the calibrated spectra used to obtain the spatial distribution of some of these gases. As an example, the vertical concentration profiles of O_3, HNO_3, CFC-12, CFC-11, and aerosols were retrieved from one of the CIRRIS-1A measured spectral profiles collected in the southern hemisphere (30° S, 9° E). Specific errors in the retrieval routine are shown. Other data profiles are in preparation to be published separately.

The CIRRIS-1A data set demonstrates the capability of a moderate resolution interferometer to monitor global distributions of the most prominent greenhouse gases in the 7-13 μm window. Since these gases are also active in the ozone reduction cycle, these data are doubly important. Use of the CO_2 laser band at 940 cm^{-1} provides an effective way to estimate aerosol emissions in the region where these emissions segregate offset trace gas retrieval. A

major limitation of the CIRRIS-1A instrument complement, as it was flown, was the specific instrumentation with the lack of capability to measure gas temperature and pressure while simultaneously collecting spectral signatures. One of the large error sources in the retrieval may be associated with the temperature and pressure fields of the NMC model. The accuracy of the tangent height determinations associated with this type of measurement was found to be extremely critical in the accuracy of the analysis, but was controlled in the CIRRIS-1A measurements.

Scientifically, the CIRRIS-1A data set fills an important gap in the measurements between the ATMOS and UARS data sets. The CIRRIS-1A data set does not provide a comprehensive global sampling; it is significant because it was collected only a few weeks before the Pinatubo eruption. The density profiles retrieved from other trace gases and other locations measured by CIRRIS-1A have also been performed and a detailed comparison between CIRRIS-1A profiles and comparisons with other measurements are in preparation.

Figure 1. An example of greenhouse gas emission spectrum collected at 22.4 hours local time on April 29, 1991, and tangent height of 14.08 km, latitude of 42° S longitude of 32° W, by interferometer detector 5 filter 3 (770-2100 cm^{-1}). The primary emitters are shown in this region, with indication of analysis and retrieval regions used.

Figure 2. The spectral distribution, collected in one stair-step mode in the wavenumber region of 800-1100 cm^{-1} and spatial region of 10-55 km. The data were taken at latitude 30° S and longitude 9° E, at local time 1.2 hours on April 29, 1991. This data set was used to present the VMR profiles in Figure 9.

Figure 3. CFC-11, CFC-12, and HNO_3 spectral overlapping are shown in the region of 830-960 cm^{-1}; the HNO_3 spectral emission is taken off of CFC-11 and CFC-12 spectrum by using spectra of different tangent heights. The major radiance peaks are identified. The data were collected at 22.4 hours local time on April 29, 1991, latitude of 42° S longitude of 32° W.

Figure 4. CFC-12 υ_8 Q branch at 1161 cm^{-1} is obtained by subtracting two different tangent height scans; N_2O spectrum is also shown in the same manner. The data were collected at 22.4 hours local time on April 29, 1991, latitude of 42° S longitude of 32° W.

Figure 5. An example of comparison of CIRRIS-1A and modelled spectra in the CO_2 laser band region at a tangent height of 17.93 km which is used to retrieve the aerosol extinction.

Figure 6. The temperature and pressure data (from NMC) plotted in (a) and (b) at same time and location of the CIRRIS-1A data collection (30° S, 9° E). The temperature and pressure profiles show the vertical error bar of altitude, and horizontal error bar of temperature. The data points were the chosen boundaries of the onion-peel layers. (c) the retrieved aerosol extinction at 0.55 μm is plotted as open cycles which are actual measured points. Some other measurements are reproduced for comparison.

Figure 7. Examples of comparison of CIRRIS-1A and modelled spectra in the (a) O_3, (b) HNO_3, (c) CFC-12, and (d) CFC-11 band regions which are used to retrieve their VMR profiles.

Figure 8. The comparison between measured and modelled spectra in the large spectral region of 800-1100 cm^{-1} by using retrieved VMR profiles of O_3, HNO_3, CFC-12, CFC-11, and aerosol.

Figure 9. The VMR profiles of (a) O_3, (b) HNO_3, (c) CFC-12, and (d) CFC-11 retrieved from 30° S and 9° E, Midnight April 29, 1991 data collection (plotted in Figures 2 and 8). The open triangle data points were the chosen boundaries of the onion-peel layers, and open cycles which are actual measured points with VMR error bar. Some other measurements are reproduced for comparison.

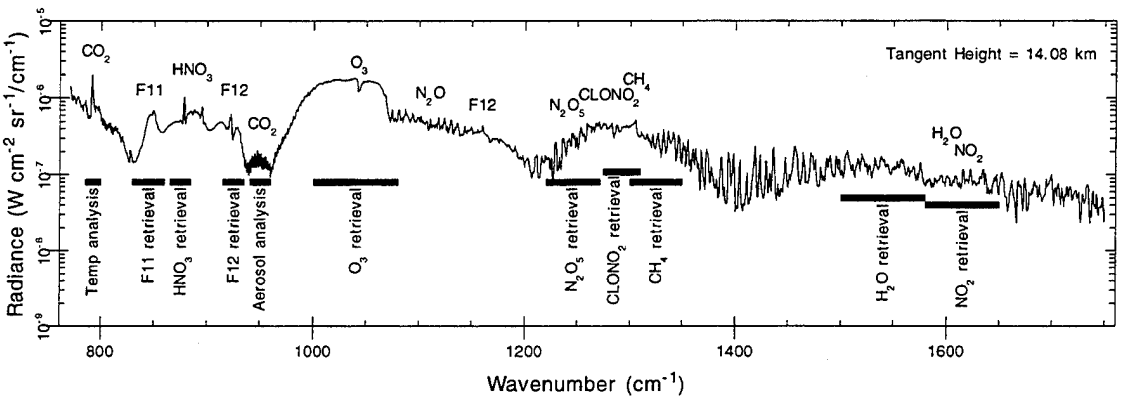
Radiance (W cm^{-2} sr^{-1}/cm^{-1})
Wavenumber (cm^{-1})
Tangent Height = 14.08 km
CO$_2$
F11
HNO$_3$
F12
CO$_2$
O$_3$
N$_2$O
F12
N$_2$O$_5$
CLONO$_2$
CH$_4$
H$_2$O
NO$_2$
Temp analysis
F11 retrieval
HNO$_3$ retrieval
F12 retrieval
Aerosol analysis
O$_3$ retrieval
N$_2$O$_5$ retrieval
CLONO$_2$ retrieval
CH$_4$ retrieval
H$_2$O retrieval
NO$_2$ retrieval

Figure 1

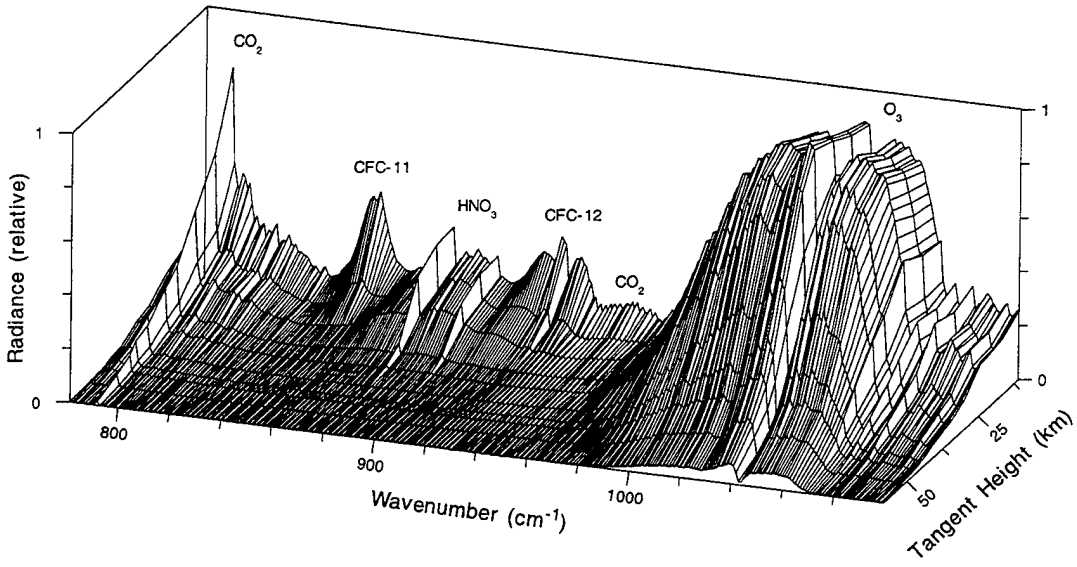
CO2
CFC-11
HNO3
CFC-12
CO2
O3
Radiance (relative)
1
0
800
900
1000
Wavenumber (cm-1)
1
0
25
50
Tangent Height (km)

Figure 2

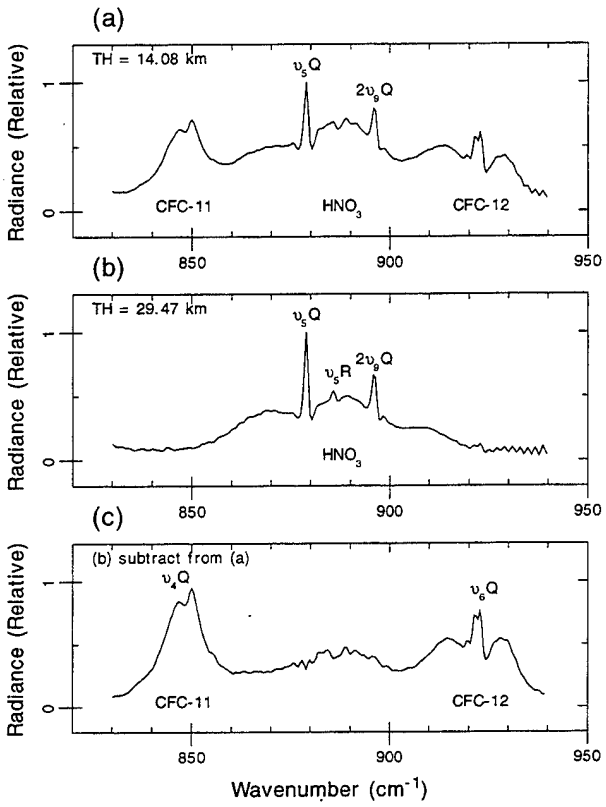
(a)
TH = 14.08 km
υ_5Q
$2\upsilon_9$Q
CFC-11
HNO_3
CFC-12
Radiance (Relative)
1
0
850
900
950
(b)
TH = 29.47 km
υ_5Q
υ_5R
$2\upsilon_9$Q
HNO_3
Radiance (Relative)
1
0
850
900
950
(c)
(b) subtract from (a)
υ_4Q
υ_6Q
CFC-11
CFC-12
Radiance (Relative)
1
0
850
900
950
Wavenumber (cm^{-1})

Figure 3

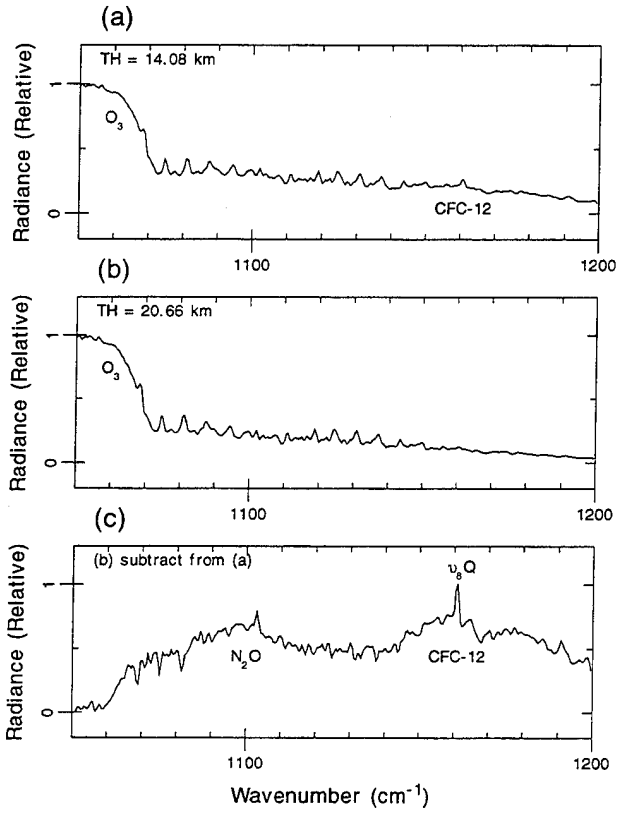
(a)
TH = 14.08 km
O_3
CFC-12
Radiance (Relative)
1
0
1100
1200
(b)
TH = 20.66 km
O_3
Radiance (Relative)
1
0
1100
1200
(c)
(b) subtract from (a)
$\nu_8 Q$
N_2O
CFC-12
Radiance (Relative)
1
0
1100
1200
Wavenumber (cm^{-1})

Figure 4

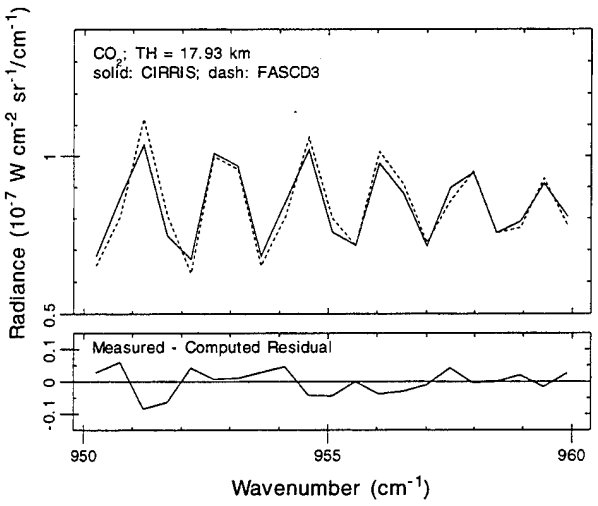
CO_2; TH = 17.93 km
solid: CIRRIS; dash: FASCD3
Radiance (10^{-7} W cm^{-2} sr^{-1}/cm^{-1})
1
0.5
Measured - Computed Residual
0.1
0
-0.1
950
955
960
Wavenumber (cm^{-1})

Figure 5

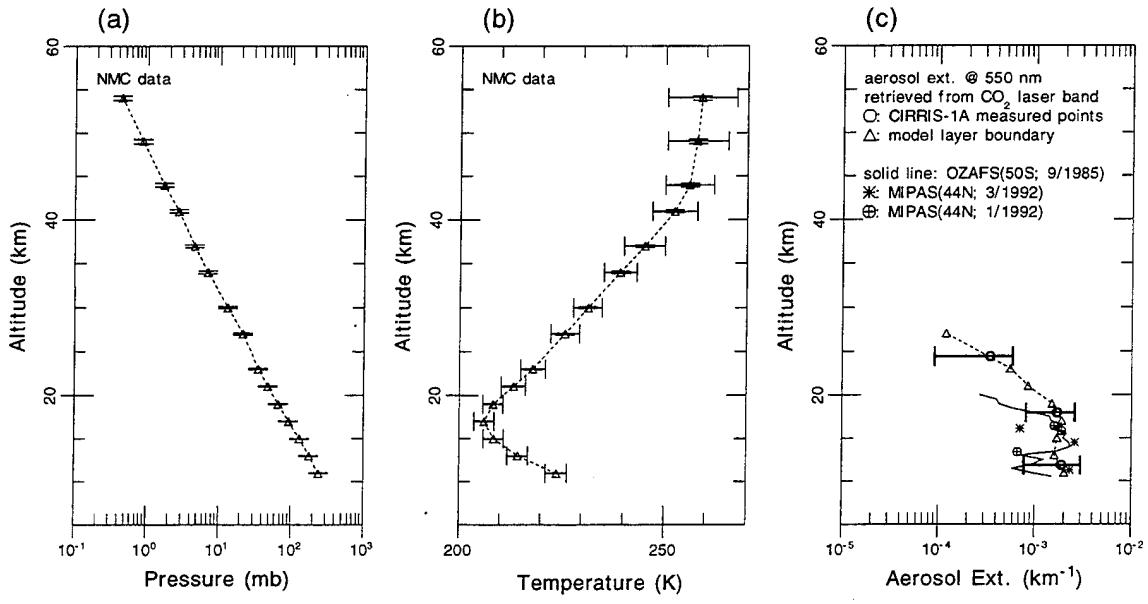
(a)
NMC data
Altitude (km)
Pressure (mb)
(b)
NMC data
Altitude (km)
Temperature (K)
(c)
aerosol ext. @ 550 nm
retrieved from CO_2 laser band
○: CIRRIS-1A measured points
△: model layer boundary
solid line: OZAFS(50S; 9/1985)
✳: MIPAS(44N; 3/1992)
⊕: MIPAS(44N; 1/1992)
Altitude (km)
Aerosol Ext. (km^{-1})

Figure 6

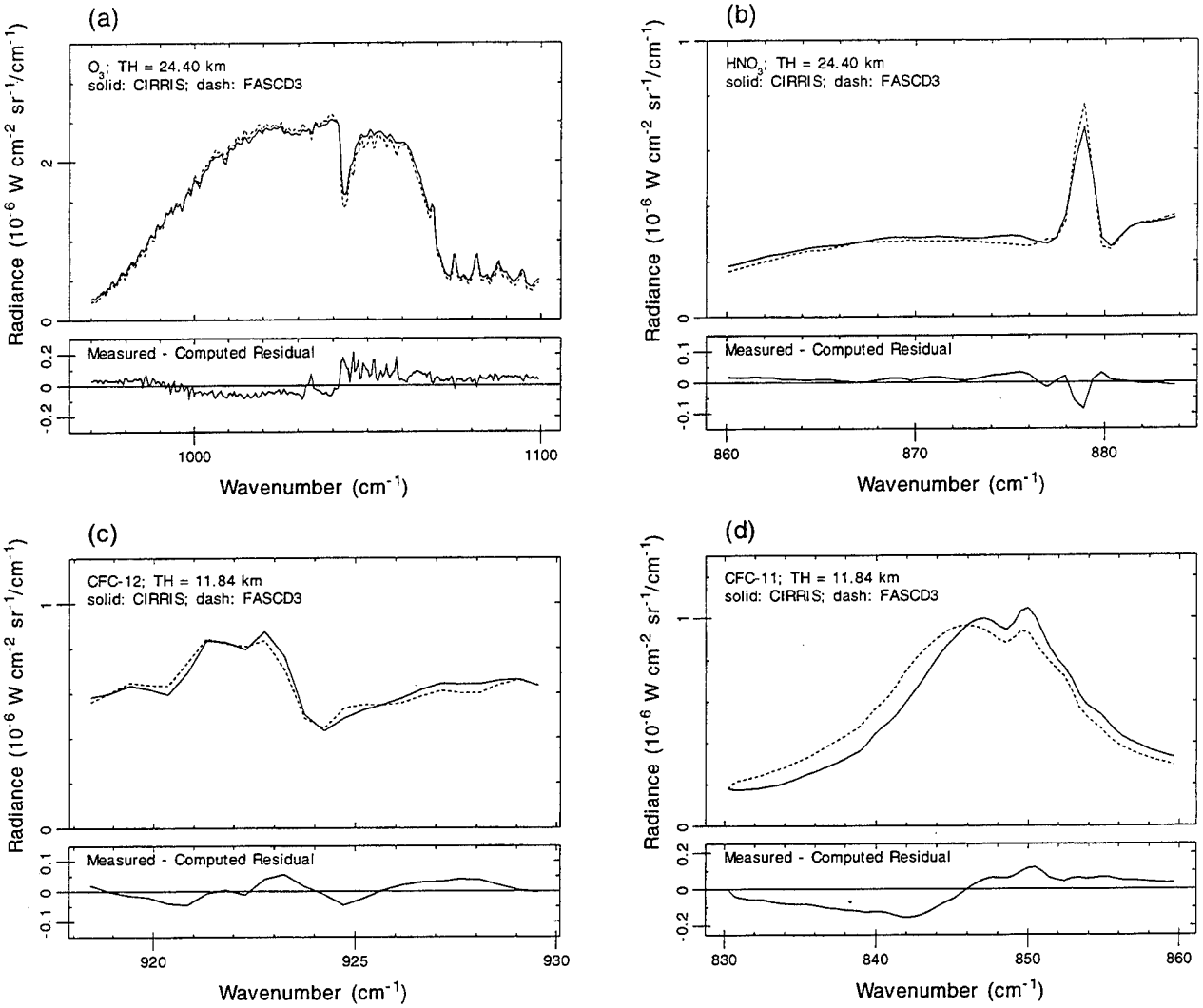
(a)
O_3; TH = 24.40 km
solid: CIRRIS; dash: FASCD3
Radiance (10^{-6} W cm^{-2} sr^{-1}/cm^{-1})
Measured - Computed Residual
Wavenumber (cm^{-1})
(b)
HNO_3; TH = 24.40 km
solid: CIRRIS; dash: FASCD3
Radiance (10^{-6} W cm^{-2} sr^{-1}/cm^{-1})
Measured - Computed Residual
Wavenumber (cm^{-1})
(c)
CFC-12; TH = 11.84 km
solid: CIRRIS; dash: FASCD3
Radiance (10^{-6} W cm^{-2} sr^{-1}/cm^{-1})
Measured - Computed Residual
Wavenumber (cm^{-1})
(d)
CFC-11; TH = 11.84 km
solid: CIRRIS; dash: FASCD3
Radiance (10^{-6} W cm^{-2} sr^{-1}/cm^{-1})
Measured - Computed Residual
Wavenumber (cm^{-1})

Figure 7

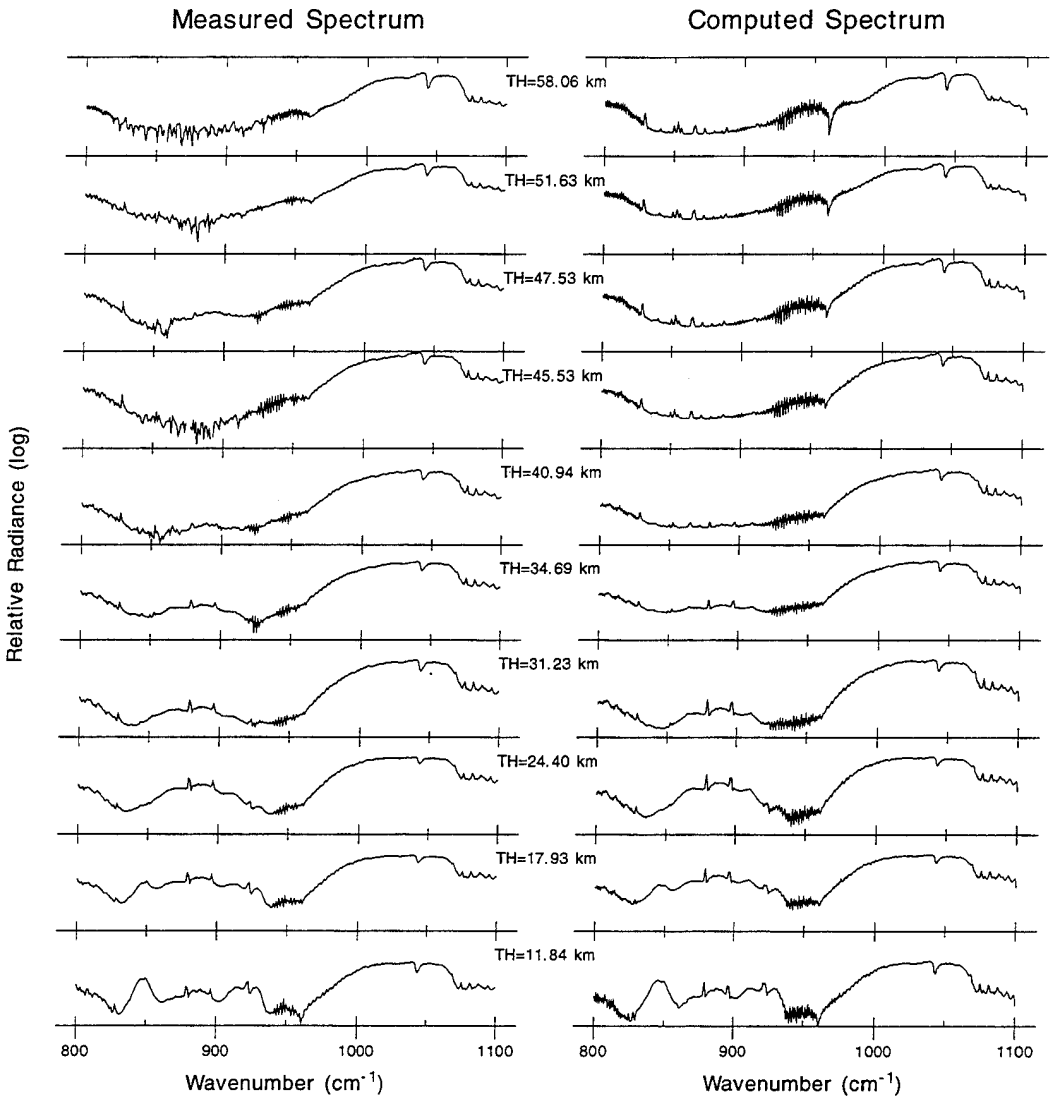
Measured Spectrum
Computed Spectrum
TH=58.06 km
TH=51.63 km
TH=47.53 km
TH=45.53 km
TH=40.94 km
TH=34.69 km
TH=31.23 km
TH=24.40 km
TH=17.93 km
TH=11.84 km
Relative Radiance (log)
800
900
1000
1100
Wavenumber (cm-1)

Figure 8

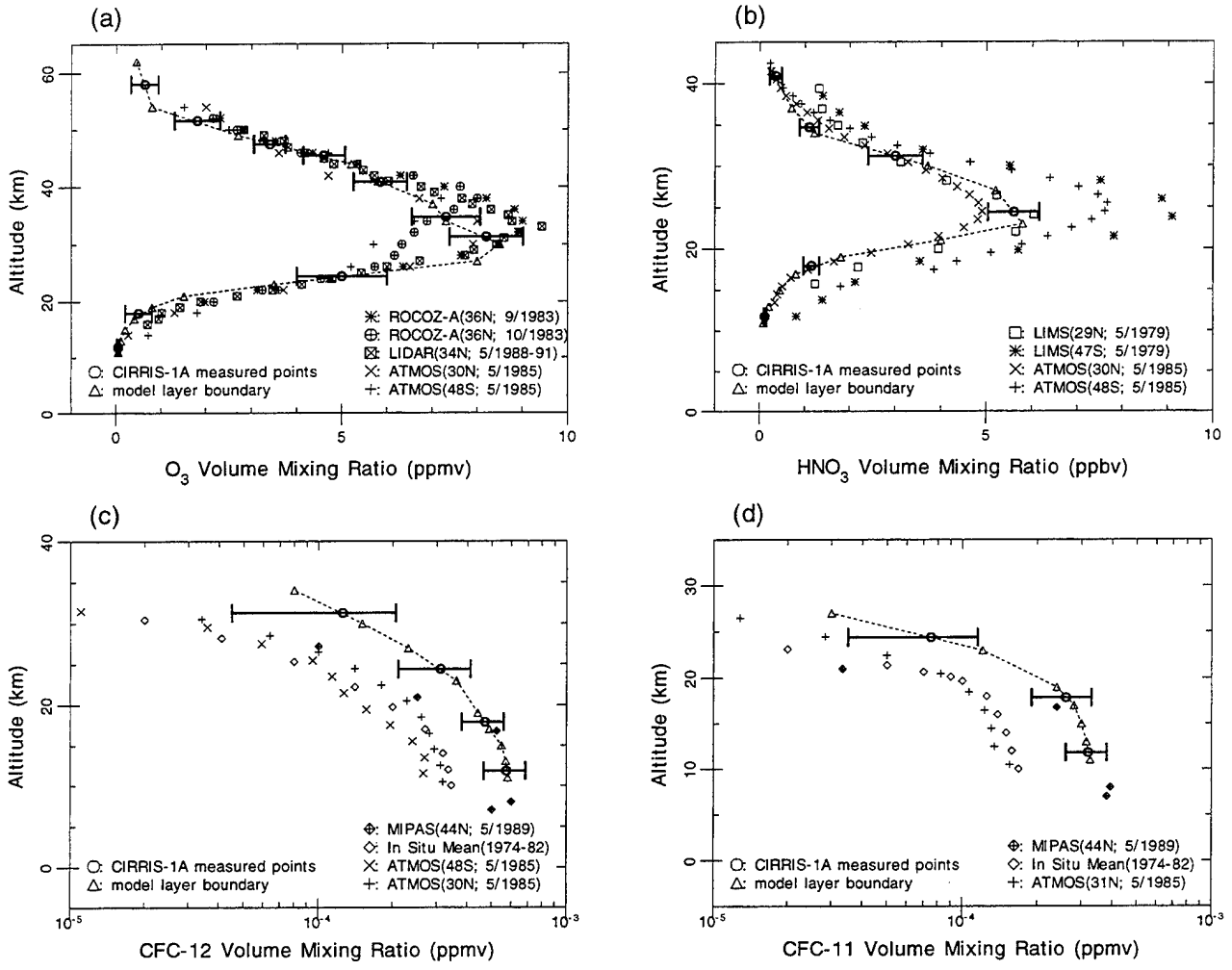
(a)
Altitude (km)
O3 Volume Mixing Ratio (ppmv)
O: CIRRIS-1A measured points
Δ: model layer boundary
✳: ROCOZ-A(36N; 9/1983)
⊕: ROCOZ-A(36N; 10/1983)
⊠: LIDAR(34N; 5/1988-91)
×: ATMOS(30N; 5/1985)
+: ATMOS(48S; 5/1985)
(b)
Altitude (km)
HNO3 Volume Mixing Ratio (ppbv)
O: CIRRIS-1A measured points
Δ: model layer boundary
□: LIMS(29N; 5/1979)
✳: LIMS(47S; 5/1979)
×: ATMOS(30N; 5/1985)
+: ATMOS(48S; 5/1985)
(c)
Altitude (km)
CFC-12 Volume Mixing Ratio (ppmv)
O: CIRRIS-1A measured points
Δ: model layer boundary
⊕: MIPAS(44N; 5/1989)
◇: In Situ Mean(1974-82)
×: ATMOS(48S; 5/1985)
+: ATMOS(30N; 5/1985)
(d)
Altitude (km)
CFC-11 Volume Mixing Ratio (ppmv)
O: CIRRIS-1A measured points
Δ: model layer boundary
⊕: MIPAS(44N; 5/1989)
◇: In Situ Mean(1974-82)
+: ATMOS(31N; 5/1985)

Figure 9

Indirect Global Warming Effects Of Ozone and Stratospheric Water Vapor Induced By Surface Methane Emission

D.J. Wuebbles
A.S. Grossman
J.S. Tamaresis
K.O. Patten
A. Jain
K.E. Grant

July 1994

Abstract

Methane has indirect effects on climate due to chemical interactions as well as direct radiative forcing effects as a greenhouse gas. We have calculated the indirect, time-varying tropospheric radiative forcing and GWP of O_3 and stratospheric H_2O due to an impulse of CH_4. This impulse, applied to the lowest layer of the atmosphere, is the increase of the atmospheric mass of CH_4 resulting from a 25 percent steady state increase in the current emissions as a function of latitude. The direct CH_4 radiative forcing and GWP are also calculated. The LLNL 2-D radiative-chemistry-transport model is used to evaluate the resulting changes in the O_3, H_2O and CH_4 atmospheric profiles as a function of time. A correlated k-distribution radiative transfer model is used to calculate the radiative forcing at the tropopause of the globally-averaged atmosphere profiles. The O_3 indirect GWPs vary from ~27 after a 20 yr integration to ~4 after 500 years, agreeing with the previous estimates to within about 10 percent. The H_2O indirect GWPs vary from ~2 after a 20 yr integration to ~0.3 after 500 years, and are in close agreement with other estimates. The CH_4 GWPs vary from ~53 at 20 yrs to ~7 at 500 yrs. The 20 year CH_4 GWP is ~20% larger than previous estimates of the direct CH_4 GWP due to a CH_4 response time (~17 yrs) that is much longer than the overall lifetime (10 yrs). The increased CH_4 response time results from changes in the OH abundances caused by the CH_4 impulse. The CH_4 radiative forcing results are consistent with IPCC values. Estimates are made of latitude effects in the radiative forcing calculations, and UV effects on the O_3 radiative forcing calculations (10%).

I. *Introduction*

The current concerns about global warming and ozone depletion have necessitated detailed studies of the potential greenhouse effects of various trace gases that have been introduced into the atmosphere. The mechanism usually used for comparison of the greenhouse potential of trace gases is the global warming potential or GWP as defined by IPCC (1990). The GWP is the ratio of the radiative flux change at the tropopause caused by the introduction of a unit mass impulse of a trace gas into the atmosphere to the radiative flux change at the tropopause caused by the introduction of a unit mass impulse of CO_2. An essential part of the GWP determination is the calculation of the radiative forcing, which is defined as the radiative flux change at the tropopause produced by a unit change in the number of molecules of a particular gas with all other abundances held constant. Usually the amount of abundance change used in a radiative forcing calculation is chosen such that the change is just enough to produce a numerically significant flux change value at the tropopause. Parameterized experiments for radiative forcing have been published, for example, in IPCC (1990, 1992), and by Ramanathan et al. (1987). A model for determining GWPs has been developed by Wuebbles et al. (1992). This model approximates GWP's with an accuracy of a few percent and has been published by Wuebbles and Grossman (1992) for CF_4, and Grossman and Wuebbles (1993) for SF_6. In addition to the direct GWP and radiative forcing discussed above, there is the indirect GWP and radiative forcing. The indirect effects are caused when the atmospheric chemical processes produce a change in the abundance of species 2 after the introduction of an impulse of species 1. A GWP and radiative forcing effect results from the indirect abundance changes of species 2 as well as the direct GWP and forcing effect of the change in abundance of species 1. Indirect GWP effects of ozone and stratospheric water vapor have been discussed in IPCC (1990,1992). IPCC (1990) gives an indirect ozone GWP, due to methane introduction, of 24 at a time of 20 years. IPCC (1992) gives an indirect water GWP of between 5 and 30 percent of the direct methane GWP. IPCC (1992) recommended that the indirect GWP's should be withdrawn due to incomplete understanding of the atmospheric chemical processes which cause the ozone changes. Yet, according to IPCC (1990), the indirect ozone forcing due to methane introduction could represent one of the main contributions to indirect GWP effects.

The main purpose of this paper is to reexamine the indirect effect on O_3 and stratospheric H_2O due to a tropospheric impulse of CH_4 and to determine the resulting GWPs. The LLNL 2-D radiative-chemistry-transport model is used to generate a set of annually and globally averaged model atmospheres which contain the perturbed O_3, H_2O, and CH_4 abundances as a function of time. A correlated k-distribution model for the atmospheric transmission is used to calculate the tropospheric radiative forcing for CH_4, O_3, H_2O, and CO_2. These forcing values are then used to calculate the direct GWP for CH_4, and the indirect GWP for O_3 and H_2O. Estimates are made for the UV contributions to the indirect O_3 radiative forcing values and latitude effects on the radiative forcing calculations for O_3, H_2O, and CH_4. Lastly, we make suggestions for future, more advanced, indirect O_3 and H_2O, GWP calculations.

II. *Model Atmospheres*

A. *Model Structure*

The version of the LLNL zonally-averaged two-dimensional chemical-radiative-transport model (Kinnison et al., 1994, Patten et al., 1994, Wuebbles et al., 1991) used for these calculations determines the atmospheric distributions of 44 chemically active atmospheric trace constituents in the troposphere and stratosphere. The model domain extends from pole to pole, and from the ground to 60 km. The sine of latitude is used as the horizontal coordinate, with uneven increments corresponding to approximately 10 degrees in latitude. The vertical coordinate corresponds to the natural logarithm of pressure; the scale height is 7.2 km and the surface pressure is 1013 mb. The vertical resolution is 1.5 km in the troposphere and 3 km in the stratosphere.

B. *Model Transport*

In the dynamics portion of the two-dimensional code, the circulation field is obtained following the approach of Garcia and Solomon (1983). Since this approach is only partially implemented in the model at the present time, we use climatological temperature and mean zonal wind fields. Both the temperature and mean zonal wind field vary continuously over the annual cycle. The temperature field is based on the reference model of Barnett and Corney (1985), while the mean zonal wind is based on data from Fleming et al. (1988). The method used to obtain the circulation is based on combining the zonal mean momentum equation and the thermodynamic equation into a form that, along with the thermal wind equation, yields a second order diagnostic equation for the residual mean meridional stream function. The net heating rate is calculated knowing the temperature and chemical species distribution and includes latent heating. The present code does not include a separate planetary or gravity wave calculation, but instead calculates the Eliassen-Palm flux directly from the zonal mean momentum equation. This is done by solving the zonal mean momentum equation.

The transport of chemical species is accomplished through both advection and turbulent eddy transport. Advection terms are treated using the second order, two dimensional transport algorithm of Smolarkiewicz (1984). The transport caused by eddy motion is parameterized through the diffusion coefficients, K_{yy} and K_{zz}. Values of K_{zz} do not vary with season, but are different between the troposphere and stratosphere. The value of K_{zz} in the troposphere is 4 m^2 sec^{-1}, while K_{zz} in the stratosphere has values of 0.1 m^2 sec^{-1} in the lower stratosphere increasing to 0.25 m^2 sec^{-1} near the middle stratosphere and returning to 0.1 m^2 sec^{-1} at the stratopause. Values of K_{yy} in the stratosphere are calculated using a similar method to that of Newman (1988) by dividing the zonal mean momentum equation (i.e., the Eliassen-Palm flux) by the horizontal gradient of the quasi-geostrophic potential vorticity. In the stratosphere, a minimum value of K_{yy} has been established as 1×10^5 m^2 sec^{-1}. The values of K_{yy} in the troposphere are assigned a value of 2×10^6 m^2 sec^{-1}. The tropopause is determined from the latitude

dependent annual mean temperature field. The height of the tropopause varies from 8 km near the poles to 14 km at the equator.

Two physical removal processes are included in the model. Surface deposition occurs in the first layer of the model. Most species are assigned a standard deposition velocity of 1 cm/sec. Nitric oxide, nitrogen dioxide, ozone, molecular hydrogen, and formaldehyde are assigned unique deposition velocities. Also, source gases emitted at the surface (e.g. methane) are assigned a deposition velocity of zero. Rainout is parameterized in the model as a first-order loss process that occurs in the first 6–7 altitude layers.

C. *Solar Radiative Transfer Model*

To capture the spectral detail needed for photodissociation calculations, the two-stream multiple-layer UV-visible model uses 126 wavelength bins between 175 nm and 735 nm. The two-stream approach was chosen because of the requirements for computational efficiency placed on radiative transfer models designed for inclusion in atmospheric chemistry models. In this approach, solar radiation is effectively divided into direct solar radiation, downward diffuse radiation, and upward diffuse radiation. The scattering of energy from the direct solar beam within each individual layer is treated using the delta-Eddington algorithm (Joseph et al. 1976), which includes the dependence of scattering and absorption on the solar zenith angle. The scattering of diffuse radiation (i.e., previously scattered radiation) from each individual layer is modeled using the simpler Sagan-Pollack (1967) algorithm. Both algorithms allow inclusion of the bulk optical properties of clouds and aerosols. Finally, the adding method is used to calculate irradiances throughout the vertically inhomogeneous atmosphere.

D. *Infrared Radiative Transfer Model*

The infrared model is a version of the model described by Harshvardhan et al. (1987). For our usage, it has been modified to improve the accuracy in the upper stratosphere. It includes absorption and emission by CO_2, O_3, and H_2O. It is based on wide-band parameterizations fit to line-by-line calculations. Inhomogeneous absorption paths are included by pressure and temperature weighted scaling of trace gas absorber amounts. The model provides for specification of fractional cloud cover within each vertical model layer. Separate fractions can be specified for convective (deep, overlapping) and randomly overlapped clouds.

E. *Model Chemistry*

The mechanism we are currently using in the LLNL two-dimensional model has the following characteristics:

- A total of 44 species are allowed to vary with time in the troposphere and stratosphere. Four additional species (O, $O(^1D)$, N, H) are treated as steady-state.

- There are 103 thermal (two- and three-body) reactions and 48 photolytic reactions in the mechanism.

- A complete representation of known stratospheric chemical processes.

The mechanism is listed in its entirety in Table 1. The reactions are classified by type: two-body, three-body, and photolytic. The kinetic parameters for two-body reactions are included as well.

The basic photochemistry represents the tropospheric and stratospheric interactions of actinic solar flux with the individual species in the families O_x, NO_y, ClO_y, HO_y, BrO_y, as well as with CH_4 and its oxidation products. This part of the mechanism incorporates 44 transported species and 4 species for which abundance is determined through the assumption of instantaneous equilibrium. The thermal reactions considered number 103, the photolytic reactions number 48. Source gases used include NO_x, N_2O, CH_4, CO_2, CO, the chlorine compounds CFC-11, CFC-12, CFC-113, CFC-114, CFC-115, HCFC-22, CCl_4, CH_3CCl_3, CH_3Cl, and the bromine compounds CH_3Br, CF_2ClBr, and CF_3Br. Most of the thermal reaction rates were taken from the NASA Panel recommendations provided in DeMore et al., (1992). The rate constant for $CH_4 + OH$ calculated by Vaghjiani and Ravishankara (1991) was used because it represents the most recent work. Absorption cross section information has been assembled primarily from DeMore et al. (1992) and Gillotay and Simon (1991a,b). Water vapor is dealt with in a unique way compared to the other chemical species. The level of water vapor is assigned its climatological value, following the specific humidity of the Oort climatology, everywhere below the hydropause. Above the hydropause, water vapor treated as a transported species; methane oxidation is its major source in this region of the atmosphere.

The photolytic loss rate constants are calculated by integrating the product of absorption coefficient, quantum yield, and solar flux over wavelength (i.e. from 175 nm to 760 nm). The exoatmospheric solar flux is from WMO, 1985. The solar flux is then calculated as a function of altitude, latitude, and season at each time step, including the effects of absorption by O_2 and O_3 and multiple molecular (Rayleigh) scattering. The absorption cross sections and quantum yields include temperature and pressure dependence where appropriate and available. The Schumann-Runge band region of the O_2 absorption is treated using the technique of Allen and Frederick (1982), modified to match the more recent lower cross sections of the O_2 Herzberg continuum region. The photolysis of NO is also treated through the parameterization technique of Allen and Frederick (1982).

The nonlinearity of the photochemistry with respect to diurnal averaging is accounted for through the calculation of individual altitude, latitude, and seasonally varying factors for each photochemical process. Full diurnal variability of each species is calculated off-line for four seasons. The factors, relating individual process rates from the full diurnal calculation to the diurnally-averaged values, are then spline-interpolated for each time step.

Members of the ClO_y family currently thought to play a role in the Antarctic spring, such as the ClO dimer, are included in this version of the model. Polar stratospheric aerosol surface has not been included. A representation of background stratospheric sulfuric acid aerosol surface is incorporated into the model, following the recommendations from the WMO, 1989 report. The reactions of N_2O_5 and $ClONO_2$ with H_2O on the aerosol surface are parameterized as first-order loss processes with rate constants determined by specified surface area density, collision frequency, and reaction probability.

F. *Emission and Boundary Conditions*

In our modeling of current and possible future atmospheres, we need to represent the surface (and atmospheric emissions) and/or surface concentrations of a number of constituents that affect tropospheric and stratospheric chemistry. A great deal of evidence indicates that surface emissions and concentrations of globally important trace gases are increasing (see WMO, 1991 for an overview). During the last ten years, scientists have been determining the atmospheric concentrations and emission rates of a variety of trace species (e.g. nitrogen oxides, carbon monoxide, and hydrocarbons) on a regional as well as global scale. These trace gases can affect the tropospheric oxidizing capacity due to changes in the levels of ozone and hydroxyl. To quantify these effects, researchers use global atmospheric models to investigate the effects of trace species. Emission inventories and measurements of the source gases are required for the initialization as well as validation of these models. The source gas fluxes must be estimated correctly in order for the models to calculate accurate species concentrations. Discrepancies between measured and calculated species concentrations can be used to check the consistency of emissions inventories, assuming all other model parameters are correct. The emphasis up to now has been to use global models to study these effects. One goal of these studies is to investigate the impact on the troposphere—ozone, hydroxyl, and oxidizing capacity.

The surface boundary conditions for the ambient version of the two-dimensional model consist of fixed concentration for nitrous oxide, molecular hydrogen, hydrochloric acid, and the halogenated organics and fluxes for methane, nitrogen dioxide, and carbon monoxide. The emission rates are specified for each latitude zone in Table 2.

Methane emissions are distributed latitudinally according to the recommendations of Fung et al., (1991). Carbon monoxide emissions are distributed latitudinally according to the emission categories defined by Hough (1991). The methane and carbon monoxide emission rates used for these calculations are obtained by determining the steady state chemical loss rate from a previous ambient model run. However, seasonal variations in the source gas emissions are not included in the results presented here. This can lead to discrepancies between the magnitudes of the calculated and observed species distributions. Another potential source of discrepancy is the representation of advective and diffusive transport in the troposphere. This would adversely affect short-lived species such as nitrogen oxides. In the current model, the diffusion coefficients are constant across all latitudes and seasons in the troposphere. We currently use diffusive transport to represent fast vertical transport processes such as convection. If the diffusivities are too

low, then species will undergo very slow vertical mixing. Fast vertical transport is often implicated in explaining unusually high levels of short-lived species in the middle and upper troposphere.

G. *Ambient Atmosphere*

The 2-dimensional model-derived ambient atmosphere used for these calculations is based on 1990 emissions of the source gases. The two-dimensional (i.e. latitude, altitude) distributions of the radiatively important trace gases—water vapor, carbon dioxide, ozone, nitrous oxide, and methane—are averaged over the annual cycle and from pole to pole. The resulting globally- and annually-averaged altitude profiles for water vapor, ozone, and methane are depicted in Figure 1. Carbon dioxide is constant at 350 ppmv throughout the model atmosphere. Nitrous oxide decreases monotonically from 308 ppbv near the surface to 1.2 ppbv at 59 km. The pressure-temperature profile for the model atmosphere is shown in Figure 2. The tropopause in the globally-averaged atmosphere, is specified as the altitude at which the temperature gradient in the troposphere decreases to 2K/km. As indicated in Figure 2, this occurs at 166 mb (~13.2 km).

H. *Time Dependent Atmosphere Calculations*

The two-dimensional model is used to determine the changes in ozone following the pulse increase in the abundance of methane. Due to its long lifetime in the troposphere, the assumed latitude and season of the methane pulse should not impact significantly the derived changes in ozone. Therefore, the pulse is distributed latitudinally at the start of the run as a percentage increase of the ambient methane concentrations. The pulse needs to be sufficiently large for the chemical model to determine an ozone change providing a significant change in radiative forcing, yet sufficiently small for the nonlinear effects on atmospheric chemistry to be minimal. Based on the analysis of ozone radiative forcing in Lacis et al. (1990), we estimate that a sufficiently large change in tropospheric average ozone concentration should be approximately 4%. This corresponds to a 25% increase of current methane emissions in our model. For the calculations in this paper we estimate the equilibrium change in the total atmospheric mass of methane for a 25% emission increase based on model results for several increased flux scenarios. The difference between the perturbed and ambient burdens, 1702.9 teragrams, is added to the surface layer in the model. We then run the model for thirty years using ambient CH_4 emission fluxes and initial concentrations for the other species.

Figure 3 shows the integrated change in the mass of methane calculated in the model as a function of time before and after the initial pulse as well as the ambient value of the methane mass. The methane pulse decays approximately, exponentially in time with a lifetime of the order of 17 years. The decay function with time indicates that significant nonlinear feedbacks with hydroxyl have occurred. The methane depletion rate is proportional to both the concentration of methane as well as the concentration of hydroxyl. Since the hydroxyl lifetime is of the order of five minutes, it can be assumed that the hydroxyl concentration is in equilibrium. The equilibrium hydroxyl concentration is an inverse function of the methane concentration,

$$d[CH_4]/dt = -k_1[CH_4]/(k_2 + k_3[CH_4]) + S_0 \quad , \tag{1}$$

where S_0 is the background methane flux input into the atmosphere, and $[CH_4]$ is the concentration of methane. The value of $[CH_4]$ is the sum of the background atmosphere methane plus the extra methane due to the pulse. Eventually the methane added in the pulse will decay back to the background atmosphere methane abundance. Equation 1 implies that the methane pulse decay will be a complex function of the instantaneous methane abundance, but it will closely approximate an exponential decay with a lifetime of the order of 17 years. While the instantaneous methane lifetime in the ambient atmosphere is 10–12 years, the conjecture made in IPCC (1990) that a methane pulse will decay exponentionally with a 10 year lifetime will not be the case for real methane pulses. Other analyses (Fisher, 1993, Prather, 1993) have determined that an equivalent lifetime of the order of 17 years appropriately describes the lifetime of a methane pulse in the atmosphere. We emphasize the point here that we do not use an exponential decay function in this paper, we use a direct integration of the actual radiative forcing which contains the actual value of the methane abundance at any particular time. Since the IPCC (1990) GWP numbers were based on an exponential methane decay function with a 10 year lifetime, we expect differences in the GWP values. This will be discussed in Section V. below.

Figure 4 depicts the annually-averaged change, with time, of the total ozone column calculated after the methane pulse. Figure 5 shows the calculated change with time of the annually-averaged tropospheric ozone column. Ambient values of the total and tropospheric values of the ozone column are shown in Figures 4 and 5. Total global ozone takes about six years before reaching the maximum effect while the troposphere responds within two years. The change in the ozone column abundance is a result of methane oxidation. In tropospheric regions characterized by high nitric oxide concentrations, the net methane oxidation reaction is (cf. Wuebbles and Tamaresis, 1993):

$$CH_4 + 7.2 - 7.5O_2 \rightarrow CO_2 + 0.4 - 0.5OH + 3.6 - 3.8O_3 + 1.2 - 1.4H_2O + 0.5 - 0.6H_2 \quad .$$

We see that complete methane oxidation results in net production of ozone. The difference in response times between the troposphere and stratosphere is due to transport, particularly across the tropopause. Since the pulse is emitted in the surface zone, dynamical processes will transport the methane upwards. Typically, it takes a long-lived gas emitted at the surface about four years to mix into the stratosphere. Furthermore, we observe that the tropospheric ozone column peaks two years after the pulse. Thus if the time constant for chemistry (two years) is added to that for transport (four years), we estimate that it should take six years for the stratospheric ozone column to peak.

Figure 6 shows the time variation of the increase in the annually and globally averaged stratospheric water vapor burden (kg). The peak value of the H_2O change occurs at a time of 10–11 years after the methane pulse. According to Lelieveld et al. (1993) the H_2O levels in the lower stratosphere are largely dependent on transport of CH_4 and O_3 from the troposphere. Since the stratospheric ozone peaks approximately 6 years

after the methane we expect the stratospheric water vapor to take at least this amount of time and possibly more to reach its peak value.

It is also important to consider the uncertainties in these calculations that may result both from the using a two-dimensional model in the analysis of tropospheric (and stratospheric) chemistry effects and from uncertainties in the chemistry itself. We are not able to define precisely the limits on the uncertainties at this time; however, we provide a range as a representation of overall uncertainties.

One major uncertainty is in the amount of production of ozone, in the troposphere, per unit oxidation of methane. This uncertainty depends on the reaction of CH_3O_2 + NO to produce NO_2 which then photolyzes (in the troposphere) and produces ozone. The primary uncertainty in the rate of ozone formation will then largely depend on the amount of NO_x in the troposphere (we argue that the well-recognized nonlinear relationship between NO_x and ozone is unimportant to the effect of methane oxidation to produce ozone, as the production of ozone depends only on the NO conversion reaction given above). Unfortunately, tropospheric NO_x concentrations are poorly characterized globally. The two-dimensional model gives a range in the tropospheric concentrations of NO_x of 1.8–416 pptv. By comparison, the MLOPEX study (Mauna Loa Observatory Photochemistry Experiment) over the Pacific Ocean found a range of 2.4–358 pptv (Carroll et al., 1992). Measurements over polluted areas can be much larger, giving NO_x levels ≥1 ppbv. Therefore, the model appears to represent the expected values in the clean troposphere reasonably well, but may greatly underestimate the values in polluted areas. The impact of these polluted areas on the derived effects of methane will not be known until we are able to better characterize the global amounts of NO_x. Most of the uncertainty in the model representation of NO_x should be in underestimating the effects of polluted areas, but this will also depend on how well the model represents the variability of NO_x in less polluted areas of the troposphere. At this time, we believe that we can safely assume that the total uncertainty is no more than a factor of two.

III. *Radiative Forcing Models*

A. *Infrared Radiative Transfer Model*

We have used an infrared radiative transfer model based on the correlated k-distribution algorithm (Grant et. al., 1992, Grossman and Grant, 1992) to calculate the radiative forcing at the tropopause. Calculations were done for a globally averaged atmosphere for CH_4 and O_3 at times between 1 and 30 years after a CH_4 impulse has been applied at the bottom of the atmosphere. Calculations have been made of the radiative forcing for CO_2, in the globally-averaged atmosphere and at five different latitudes, 2 years after the pulse. This was done in order to determine the scaling factor with respect to the IPCC (1990) expression for CO_2 radiative forcing at the tropopause. Calculations have also been made at five different latitudes for CH_4 and O_3, at a time of 2 years, in order to determine the differences between the radiative forcing in the globally-averaged atmosphere and latitude averaged radiative forcing. The tropospheric radiative forcing of H_2O, caused by the methane pulse, has been calculated at five different

latitudes for times of 5, 10, 15, and 20 years after pulse. An appropriate latitudinal average is calculated to determine the globally-averaged tropospheric radiative forcing. The parameters of the calculations are;

O_3, CH_4, wave number range of 900–1650 cm^{-1}, 25 cm^{-1} subintervals,

CO_2, wave number range of 550–1200, 2000–2525 cm^{-1}, 25 cm^{-1} subintervals,

H_2O, wave number range of 25–3000 cm^{-1}, 25 cm^{-1} subintervals,

Tropopause of globally averaged atmosphere at 166 mb,

Ground Temperature of 291K (Peixoto and Oort, 1992).

The radiative forcing is defined as the difference between the net infrared flux at the tropopause in the ambient, globally averaged atmosphere, and the net flux at the tropopause in the atmosphere with changed CH_4, H_2O, and O_3 profiles calculated at the various times after the CH_4 impulse.

A test of the ability of correlated k-distribution model to calculate O_3 tropospheric forcing was performed using an LLNL generated model for an annually-averaged, mid latitude, clear sky atmosphere. A perturbation of 15% of the tropospheric O_3 was added and the tropospheric forcing calculated. The result of 0.266 W/m^2 agreed to within about 10 percent of the Ramanathan et al. (1987) value for a similar test case, assuming a 20 percent correction factor for clouds. A test calculation for CH_4 radiative forcing in a mid-latitude summer, clear sky approximation, was made by Grossman et al. (1993) and the result agreed with the Ramanathan et al. (1987) value to within about 4 percent. A calculation of the tropospheric radiative forcing for CH_4 in a globally and annually averaged atmosphere both with and without a representative cloud distribution was made by Grossman and Grant (1993). The results with clouds agreed to within 1 percent of the IPCC (1990) value. These tests indicate that our correlated k-distribution model has the ability to provide consistent tropospheric radiative forcing results. Table 3 shows the radiative forcing values in W/m^2 at representative times between 1 and 30 years after the CH_4 impulse for both the direct CH_4 and the indirect O_3 radiative forcing. Also shown are the results of direct CO_2 tropospheric radiative calculations for year 2 (maximum O_3 radiative forcing) using CO_2 concentrations of 1.29 and 2 times normal CO_2 abundance. The CO_2 calculations were made to test the systematic differences between the IPCC (1990) formula for CO_2 tropospheric radiative forcing and the results obtained using the LLNL model atmosphere. For both cases shown in Table 3 the results of our calculation produce a radiative forcing which is approximately 25 percent higher than that calculated using the IPCC (1990) formula. IPCC (1990) notes that calculations which do not use a cloud cover model, which is the case for our calculations, will result in radiative forcing values which are of the order of 20 percent too high. Thus the agreement of our CO_2 radiative forcing values with the IPCC (1990) values would be of the order of 5 percent if we had included a cloud cover model in our calculations. It is important for the GWP calculations, which will be discussed later, that the CO_2 forcing values derived from the IPCC (1990) formula contain a 25 percent adjustment in order to be comparable with the

O_3 and CH_4 forcing values given in Table 3. The results for the time variation of the indirect O_3 radiative forcing, given in Table 3 show that the peak forcing occurs at a time of 2 years after the initial methane impulse. This is indicative of the radiative forcing being correlated with the time variation of the tropospheric ozone column density which peaks at a time of two years (Fig. 5) rather than the total ozone column density which peaks at a time of about 6 years (Fig. 4). The reason for this behavior of the O_3 radiative forcing is that the upward IR flux change is much larger than the downward flux difference at the tropopause at all times and this drives the temporal behavior of the O_3 forcing even though the change in the stratospheric ozone column is much larger than the change in the tropospheric ozone column.

Two interesting aspects of the use of a 2-D latidudinally averaged model atmosphere are the question of the variation of the tropospheric radiative forcing as a function of latitude and the difference between the latitudinally averaged value of the tropospheric radiative forcing and the tropospheric radiative forcing calculated for the globally averaged model atmosphere. We have calculated the direct CH_4 and indirect O_3 tropospheric for five different latitudes between +71 deg. and –71 deg for the time at which maximum O_3 radiative forcing occurs, year 2 after the CH_4 impulse. The results are shown in Table 4. The radiative forcing for O_3 and CH_4 has been shown, for a CH_4 impulse of 2.83 times the concentration of the lowest atmospheric level for each latitude (25 percent of the total tropospheric CH_4 mass), at the actual tropopause at that latitude. There are significant differences between the radiative forcing values calculated in the polar regions and those calculated for the mid latitude and the equatorial regions. The polar values are lower and the mid latitude values are higher than the average value of the forcing. The maximum latitudinal variations are +12, –9 percent for the CH_4 forcing and +29, –49 percent for the O_3 forcing. These excursions from the average may have significant climatalogical consequences which will be discussed later from the point of view of the GWP results. It is interesting to note that the results shown in Table 4 indicate that the radiative forcing values calculated for the globally averaged atmosphere, 0.2455 for CH_4 and 0.1180 for O_3, differ by ~5 percent (CH_4) and ~9 percent (O_3) with the average of the forcing values for each latitude. We consider these differences to be small and thus the use of the globally averaged atmosphere to determine the average radiative forcing is a reasonable approach to the GWP calculation.

Table 5 shows the latitude effect of the tropospheric CO_2 radiative forcing for a CO_2 impulse of twice the normal concentration (350 ppm). The CO_2 factor in Table 5 is the ratio of the IPCC (1990) value of the CO_2 forcing (4.3668 W/m^2) to the CO_2 forcing obtained in this paper (Column 2, Table 5). This factor must be applied to the CH_4 and O_3 forcing results to make them compatible with the IPCC (1990) CO_2 formulation for the GWP calculations to be discussed later. In addition to this factor, the results shown in Table 4 indicate a latitude variation of the direct CH_4 and indirect O_3 radiative forcing. The CH_4 and O_3 factors shown in Table 5 are the product of 1, the ratio of the value of the CH_4 and O_3 tropospheric radiative forcings at the various latitudes to the global average values (Table 4), and 2, the CO_2 factor of Table 5. The variation of these factors represent a rough estimate of the latitude variation of the radiative forcing part of the GWP calculation. The results indicate roughly a $\pm$ 10 percent variation of the CH_4 GWP

with latitude and a larger effect for the O_3 forcing of about 50 percent at the high latitudes.

Table 6 shows the latitude variation of the H_2O radiative forcing due to changes in the stratospheric H_2O as well as the latitude averaged value of the radiative forcing. Since H_2O is a very strong greenhouse gas, the tropopause must be carefully defined since the H_2O tropospheric radiative forcing will strongly depend on the height of the tropopause. The lower the tropopause the smaller the radiative forcing. In order to compare the latitude averaged radiative forcing for H_2O with the radiative forcing in a globally averaged atmosphere a test calculation of the radiative forcing in the global averaged atmosphere at year 10 was made. The tropospheric radiative forcing for H_2O in the globally averaged atmosphere (166 mb tropopause) was approximately 30 percent less than the globally averaged radiative forcing for year 10 given in Table 6. Since the location of the tropopause is a critical factor in the radiative forcing it is recommended, for the case of H_2O forcing, that the radiative forcing should be calculated as a function of latitude and then averaged as opposed to the calculation of the radiative forcing in the globally averaged atmosphere.

B. *UV Effects On O_3 Radiative Forcing*

Since O_3 has an absorption band in the UV spectral region the possibility exists that there may be a significant contribution to the total radiative forcing by the differential UV absorption. We make an estimation of the UV radiation forcing contribution in the following manner. The atmosphere is considered as a two component system. The stratosphere is taken to be a pure absorption region while the troposphere is taken to be a scattering and absorbing layer. The spectral region over which the UV radiative forcing will be calculated is taken to be 250–340 nm in 5 nm spectral sub intervals. The O_3 absorption cross sections and Rayleigh scattering cross sections are given by WMO-16 (1985). The radiative forcing calculation is done for the year 2 model atmosphere (the maximum O_3 forcing model). The downward UV flux at the tropopause is calculated using a simple Beer's Law exponential attenuation of the zero air mass solar flux (Goody and Yung, 1989). The upward flux at the tropopause is calculated using a delta-Eddington scattering model in the troposphere which takes the troposphere as a single scattering layer. In addition to the diffuse, reflected flux component from the troposphere additional upward flux components due to the attenuated direct and downward scattered beams that are reflected from the ground are also considered. The ground albedo was taken to be 0.2. The UV radiative forcing calculated in this way amounted to about 9 percent of the IR radiative forcing. Thus UV forcing effects should be a 10 percent effect at most.

IV. *Carbon Cycle Model and CO_2 Response Curves.*

Unlike many of the greenhouse gases emitted to the atmosphere, CO_2 does not have a chemical or photochemical sink within the troposphere or stratosphere. Removal of CO_2 is therefore dependent on exchanges with other carbon reservoirs. Following the emissions of a hypothetical pulse of CO_2 into the atmosphere, about 10% will be removed within 2 to 3 years through gaseous diffusion into the mixed layer of the ocean.

Subsequent removal is dependent on downward mixing into the deeper ocean. Ultimately, the rest of the initial pulse can be removed by mixing into the ocean, but only over a time period of hundreds of years (Maier-Reimer and Hasselmann, 1987). To avoid the need to use a single lifetime for CO_2, we have used a coupled climate-carbon cycle model of Jain and Bach (1994) to calculate the decay rate of CO_2. This model contains a box-diffusion carbon cycle model consisting of three reservoirs, namely the atmosphere, the mixed ocean layer (ca. 75 m) and the deep ocean (ca. 4000 m). The model ocean is treated as a diffusive medium with constant vertical eddy diffusivity. The model also takes into account the interaction with the biosphere. The biospheric emissions are calculated by a multi-box globally aggregated terrestrial biosphere submodel developed by Harvey (1989). The model includes stimulation of net photosynthesis or net primary productivity by enhanced atmospheric CO_2 using the fertilization factor ß.

To correctly estimate the GWP values and the past and future CO_2 concentrations, it is important to use carbon cycle models that properly balance the carbon budget. To balance the carbon cycle means to remove any inconsistencies between model output and observations. When a balanced model is run from pre-industrial times to the current date using the observed emissions, it will give the correct history or CO_2 concentration changes. However, the carbon cycle model used to calculate the GWPs given by IPCC (1990, 1992) does not properly balance the carbon budget. In a separate study (Wuebbles et al., 1993) we have assessed the effects of balancing the carbon budget on GWP values. The CO_2 variations can be made to fit observations by assuming the larger ocean flux, and/or accounting for feedbacks in the terrestrial component of the carbon cycle and/or assuming the existence of an additional CO_2 sink. The present model is sufficiently flexible that all three methods may be used; we chose to use only the first two methods. In Figure 7, the observed CO_2 concentrations are compared with the results of the carbon cycle model. The carbon cycle model including the biospheric feedbacks satisfactorily reproduces the observed atmospheric CO_2 concentration (balanced case). Excluding the effects of the biosphere (i.e. unbalanced case) results in an overestimation of CO_2 concentration. The time variation of the fraction of CO_2 concentration remaining after an atmospheric impulse is shown in Figure 8. It will be used in the GWP calculation described in the following section.

V. *Global Warming Potential Model*

A. *Basic Model*

Global warming potentials (GWPs) are evaluated according to the concept of IPCC (1990). A concentration change of trace gas X, arising from an impulse of a unit mass of the trace gas X (for direct GWPs) or from chemical processing due to an impulse of gas Y (for indirect GWPs), in the atmosphere produces a tropospheric radiative forcing change Δf_X (t), which decreases with time as X is removed from the atmosphere. This radiative forcing change is considered as directly proportional to the temperature change at the surface via a climate sensitivity factor. Commitment to radiative forcing from a unit mass of X is the integral of Δf_X (t) from the time of an impulse to the user-selected GWP time horizon, T. The GWP of X is the radiative forcing commitment from a unit mass of

X divided by the radiative forcing commitment from a unit mass of CO_2, or a CO_2 like molecule,

$$GWP_X = \frac{\int_0^T \Delta f_X(t)dt}{\int_0^T \Delta f_{CO_2}(t)dt} \tag{2}$$

The IPCC (1990)-derived GWPs assume that the background atmosphere is in equilibrium (that background concentrations are constant over the GWP integration period). In our calculations, the chemical processes are allowed to operate on the background concentrations for the trace gases that are present in the atmosphere just before the impulse. This has, as will be discussed later, a significant effect on the equivalent lifetime of the decay of the impulse of the trace gas X to the atmosphere.

The definition of GWP (1990) requires integration of radiative forcing (or tropospheric temperature change) resulting from a unit mass release of trace gas, usually one kilogram, and of CO_2. A small change in atmospheric concentration resulting from such a small release can produce computational errors, so larger mass releases are usually applied and then the radiative forcing is scaled to a one kilogram release. Radiative forcing scales linearly for many gases at reasonable concentrations (IPCC, 1990); only for releases of gas much greater than one gigaton of CO_2, CH_4, or N_2O does nonlinearity occur (Wuebbles *et al.*, 1993). The radiative forcing of CO_2 is obtained from the IPCC (1990) formula,

$$\Delta F_{CO_2} = 6.3\log_e\left(\frac{c_{CO_2}(t)}{c^0_{CO_2}}\right) \tag{3}$$

for which $c_{CO_2}(t)$ is the concentration of CO_2 at time t and $c^0_{CO_2}$ is the concentration of CO_2 which would exist in the absence of the pulse. In the equilibrium case used here, $c^0_{CO_2}$ is constant with respect to time, so that the argument of the $\log_e$ is replaced by one plus the impulse response function for CO_2, i_{CO_2} (t):

$$\Delta F_{CO_2} = 6.3\log_e\left(1+i_{CO_2}(t)\right);$$
$$i_{CO_2}(t) = \frac{c_{CO_2}(t) - c^0_{CO_2}}{c^0_{CO_2}} \tag{4}$$

The impulse response function used in this study was discussed in the previous section (Figure 8). Mass-scaled, integrated radiative forcing for CO_2 is then calculated by the procedure described in Wuebbles *et al.* (1993) at time horizons of 20, 50, 100, 200, and 500 yr.

B. *Extrapolation and integration of radiative forcing*

The radiative forcing values of Tables 3 and 6 must be fitted before numerical integration in Equation 2 due to the uneven timestep required by computer limitations and to time horizons exceeding the longest time after pulse for which the atmospheric and line models were run. IPCC (1990) states that CH_4 radiative forcings are proportional to $c_{CH_4}(t)^{1/2}$, while tropospheric O_3 radiative forcings are linear in c_{O_3} (t). In turn, the concentration perturbations of the two trace species may be taken as negative exponentials in time t. However, as seen by Figures 9 and 10, the initially perturbed atmosphere produces concentrations inconsistent with a negative exponential in t. Points for which this is the case, the first year of the CH_4 radiative forcings and years 1–4 after the pulse for O_3, are excluded from fitting for this reason. The fits after weighting by CH_4 mass are:

$$\Delta f_{CH_4} = \left(\exp(-58.841 \pm 0.028 - 0.1189 \pm 0.0024 t)\right)^{1/2} \quad , \tag{5a}$$

$$\Delta f_{O_3} = \exp(-30.0410 \pm 0.0035 - 0.05663 \pm 0.00022 t) \quad , \tag{5b}$$

$$\Delta f_{H2O} = \exp\left(-3.9645 \pm 0.040 - (0.05991 \pm 0.0017) t\right) \quad . \tag{5c}$$

For the integration of the radiative forcing of CH_4, the value in Table 3 is used for the first year after the pulse. Years 1 to 3 after the pulse also are used in the O_3 Δf integration, and the value at year 4 is replaced by a linear interpolation of years 3 and 5. Fit values are used for all years afterward. Simpson's Rule (Press et al., 1992, equ. 4.1.13) is then applied to integrate the radiative forcing over time. The radiative forcing for zero time after the pulse is set to zero in each case for integration. Integrated radiative forcings for CH_4, H_2O, and O_3 are each multiplied by a factor of 0.8 to reconcile the clear sky approximation with the IPCC (1990) cloud parameterization as discussed previously. Table 7 lists the integrated radiative forcings per kilogram derived for each of the gases.

C. *GWP Results*

Table 8 shows the results of the GWP calculations. The CH_4 GWP values are significantly larger than those given by IPCC (1990, 1992) and Wuebbles et al. (1993). In the IPCC calculations the CH_4 lifetime was given as 10.5 years, which implies that the OH abundance was held fixed at the ambient value. In the present calculation, the chemical processes which affect CH_4, O_3, and H_2O abundances are allowed operate and as a result the OH abundance changes as the chemical equilibrium is perturbed by the CH_4 pulse. Equation 1 predicts a lifetime of CH_4 which is dependent on the OH abundance. This long apparent lifetime of the pulse is the result of the slower destruction of all CH_4 from the decrease in OH. The radiative forcing fits for CH_4 given by Equation 5a and shown in Figure 9 indicate an apparent lifetime on the order of 17 years for the decay of the CH_4 pulse. Wuebbles et al. (1992) showed that when the CH_4 lifetime is increased, the GWP values also increase towards the results obtained in the present

calculation. For a lifetime of 12.6 years, GWP's at 20, 100, and 500 years of 41.7, 15.9, and 7.1 were obtained. A simple extrapolation of the GWP vs. CH_4 lifetime results Wuebbles et al. (1992) predicts a GWP of approximately 52 at 20 years which is the same as that obtained in this paper. The results obtained for the O_3 indirect radiative forcing are on the order of 10 to 20 percent higher those given in IPCC (1990) and Wuebbles et al. (1993). Given the uncertainties of the calculations, at least 20 to 30 percent, this is a reasonable agreement. The indirect GWP's for stratospheric H_2O obtained in this paper are lower by factors of 3 to 5 than those given in IPCC (1990). This is probably due to an overestimation of the tropospheric radiative forcing of H_2O in IPCC (1990). The ratio of the indirect H_2O GWP to the direct CH_4 GWP, for the calculations in this paper is about 4 percent and agrees quite well with the results obtained by Lelieveld and Crutzen (1992) who give a value of 5 percent for this ratio. This effect is strongly dependent on the height of the tropopause since H_2O is such a strong IR absorber and should have a sharp mixing ratio gradient at the tropopause. The overall uncertainty in the GWP calculations is due to the uncertainties in the lifetime of CH_4, the amount of NO_x present in the atmosphere, and the radiative forcing calculations. The best estimate of the overall uncertainty in the calculations is on the order of 20 percent.

VI. *Conclusions*

We have calculated the direct CH_4 GWP and the indirect O_3 and stratospheric H_2O GWPs resulting from a CH_4 pulse equal to ~36 percent of the total atmospheric mass of CH_4. The direct CH_4 GWP is significantly larger than previous estimates as a result of the effect on the pulse response time due to the variation of the OH abundance. The agreement of the indirect O_3 GWP effect with previous estimates is within the uncertainty bounds of the calculation. The indirect H_2O GWP is much less than the estimate given in IPCC (1990, 1992) but agrees very well with more recent calculations Lelieveld and Crutzen (1992). The H_2O effect is very strongly dependent on the location of the tropopause because of the strong IR absorption of H_2O. Future calculations need to be made to determine the effect of the magnitude of the CH_4 impulse on the impulse decay time and the effect of the presence of hydrocarbons and NO_x on the direct and indirect GWP's.

Acknowledgment

Work was performed under the auspices of the U.S. Department of Energy by the Lawrence Livermore National Laboratory under contract No. W-7405-Eng-48 and was supported in part by the Department of Energy Environmental Sciences Division and the Gas Research Institute under contract No. 5091-254-2167. One of us K. P. wishes to acknowledge the support of a Global Change Distinguished Postdoctoral Fellowship sponsored by the U. S. DOE, Office of Health and Environmental Research and administered by Oak Ridge Associated Universities.

References

Allen, M. and J.E. Frederick, 1982: Effective photodissociation cross sections for molecular oxygen and nitric oxide in the Schumann-Runge bands, *J. Atmos. Sci.*, 39, 2066–2075.

Barnett, J.J., and M. Corney, 1984: A middle atmosphere temperature reference model from satellite measurements, *Adv. Space Res.*, 5, 125–134.

Carroll, M.A., B.A. Ridley, D.D. Montzka, G. Hubler, J.G. Walega, R.B. Norton, B.J. Huebert, and F.E. Grahek, 1992: Measurement of nitric oxide and nitrogen dioxide during the Mauna Loa Observatory Photochemistry Experiment, *J. Geophys. Res.*, 95, 10361–10374.

DeMore, W.B., S.P. Sander, R.F. Hampson, M.J. Kurylo, D.M. Golden, C.J. Howard, A.R. Ravishankara, C.E. Kolb, and M.J. Molina, 1992: *Chemical kinetics and photochemical data for use in stratospheric modeling: Evaluation number 10*, Jet Propulsion Laboratory, California Institute of Technology, Pasadena, California.

Fisher, D. A., 1993, NASA/NOAA/AFEAS Workshop, Boulder Co. and *Geophys. Res. Letts.* (in press).

Fleming, E.L., S. Chandra, M.R. Schoeberl, and J. J. Barnett, 1988: Monthly mean global climatology of temperature, wind, geopotential height, and pressure for 0–120 km, NASA Technical Memorandum 1000697.

Fung, I., J. John, J. Lerner, E. Matthews, M. Prather, L.P. Steele, and P.J. Fraser, 1991: Three-dimensional model synthesis of the global methane cycle, *J. Geophys. Res.*, 96, 13033–13065.

Garcia, R. R., and S. Solomon, 1983: A numerical model of the zonally averaged dynamical and chemical structure of the middle atmosphere, *J. Geophys. Res.*, 88, 1379–1400.

Gillotay D. and P.C. Simon, 1991a: Temperature-dependence of ultraviolet absorption cross-sections of alternative chlorofluoroethanes, *Journal of Atmospheric Chemistry*, 12, 269–285.

Gillotay D. and P.C. Simon, 1991b: Temperature-dependence of ultraviolet absorption cross-sections of alternative chlorofluoroethanes: 2. The 2-chloro-1,1,1,2-tetrafluoro ethane—HCFC-124, *Journal of Atmospheric Chemistry*, 13, 289–299.

Goody, R.M., and Y.L. Yung, 1989: *Atmospheric Radiation, Theoretical Basis, 2nd. Ed,* 519 pp., Oxford, New York, NY.

Grant, K. E., A. S. Grossman, R. Freedman, and J. B. Pollack, 1992: A correlated k-distribution model of the heating rates for CH_4 and N_2O in the atmosphere between 0 and 60 km., *Proceedings of the 15th Annual Review Conference on Atmospheric Transmission Models*, in press, LLNL Report UCRL-JC-110364.

Grossman, A. S., and Grant, K. E., 1992: A correlated k-distribution model of the heating rates for H_2O and a molecular mixture in the 0–2500 cm^{-1} wavelength region in the atmosphere between 0 and 60 km., LLNL Report UCRL-ID-112296.

Grossman, A. S., K. E. Grant, 1993: Tropospheric radiative forcing of CH_4, LLNL Report UCRL-ID-116533.

Grossman, A. S., and D. J. Wuebbles, 1992: Global warming potential of SF_6., LLNL Report UCRL-ID-112944.

Grossman, A. S., K. E. Grant, and D. J. Wuebbles, 1993: Radiative forcing calculations for SF_6 and CH_4 using a correlated k-distribution transmission model., LLNL Report UCRL- ID-115042.

Harshvardhan, R. Davies, D.A. Randall, and T.G. Corsetti, 1987: A fast radiation parameterization for atmospheric circulation models, *J. Geophys. Res.*, 92, 1009–1016.

Harvey, L. D. D., 1989: Managing atmospheric CO_2, Climatic Change, 15, 343–381.

Hough, A.M., 1991: The development of a two-dimensional global tropospheric model: the model chemistry, *J. Geophys. Res.*, 96, 7325–7362.

Intergovernmental Panel on Climate Change (IPCC): Climate Change; The IPCC Scientific Assessment, Cambridge University Press, Cambridge, UK, 1990.

Intergovernmental Panel on Climate Change (IPCC): Climate Change 1992; The Supplementary Report to the IPCC Scientific Assessment, Cambridge University Press, Cambridge, UK, 1992.

Jain, A. K. and W. Bach, 1994: The effectiveness of measures to reduce the man-made greenhouse effect: the application of a climate-policy-model. *Theoretical and Applied Climatology* (in press).

Joseph, J. H., W. J. Wiscombe, and J. A. Weinman, 1976: The delta eddington approximation for radiative flux transfer. *J. Atmos. Sci.,* 33, 2452–2459.

Kinnison, D.E., K.E. Grant, P.S. Connell, and D.J. Wuebbles, 1994: The chemical and radiative effects of the Mt. Pinatubo eruption, submitted to *J. Geophys. Res.*, in revision.

Lacis, A. A., D. J. Wuebbles, and J. A. Logan, 1990: Radiative forcing by changes in the vertical distribution of ozone, *J. Geophys. Res.*, 95, 9971–9981.

Lelieveld, J., and P. J. Crutzen, 1992: Indirect effects of methane in climate warming. *Nature,* 355, 339–342.

Lelieveld, J., P. J. Crutzen, and C. Bruhl, 1993: Climate effects of atmospheric methane. *J. Chemosphere*, 26, 739–768.

Maier-Reimer, E. and K. Hasselmann, 1987: Transport and storage of CO_2 in the ocean-an inorganic ocean circulation carbon cycle model, Climate Dynamics, 2, 63–90.

Newman, P.A., M.R. Schoeberl, R.A. Plumb, J. Rosenfield, 1988: Mixing rates calculated from potential vorticity, *J. Geophys. Res.*, 93, 5221–5240.

Patten, K.O., P.S. Connell, D.E. Kinnison, D.J. Wuebbles, L. Froidevaux, and T.G. Slanger, 1994: Effect of vibrationally excited oxygen on ozone in the upper stratosphere, *J. Geophys. Res.*, 99, 1211–1223.

Peixoto, J. P., and A. H. Oort, 1992: *Physics Of Climate,* 520pp, AIP, New York.

Prather, M., 1993: Lifetimes and eigenstetes in atmospheric chemistry. *Geophys. Res. Letts.* (in press).

Press, W. H., S. A. Teukolsky, W. T. Vetterling, B. P. Flannery, 1992: *Numerical Recipes in C: The Art of Scientific Computing*, 2nd ed. (Cambridge Univ. Press, Cambridge, UK), 134.

Ramanathan, V., L. Callis, R. Cess, J. Hansen, I. Isaksen, W. Kuhn, A. Lacis, F. Luther, J. Mahlman, R. Reck, and M. Schlesinger, 1987: Climate-chemical interactions and effects of changing atmospheric trace gases. *Revs. of Geophys.*, 25. NO. 7, pp 1441–1482.

Sagan, C., and J. B. Pollack, 1967, On isotropic nonconservative scattering and the clouds of Venus. *J. Geophys. Res.*, 72, 469–477.

Smolarkiewicz, P. K., 1984: A fully multidimensional positive definitive advection transport algorithm with small implicit diffusion, *J. Comput. Phys.*, 54, 325–362.

Vaghjiani, G.L. and A.R. Ravishankara, 1991: New measurement of the rate coefficient for the reaction of OH with methane, *Nature*, 350, 406–409

World Meteorological Organization, Atmospheric Ozone, 1985: WMO Global Ozone Research and Monit. Proj. Report 16, Geneva.

World Meteorological Organization, Scientific Assessment of Stratospheric Ozone, 1989: Global Ozone Research and Monit. Proj. Report 20, Geneva.

World Meteorological Organization, 1991: Scientific Assessment of Ozone Depletion: 1991, Global Ozone Research and Monitoring Project Report 25, Geneva.

Wuebbles, D.J., D.E. Kinnison, K.E. Grant, and J. Lean, 1991: The effect of solar flux variations and trace gas emissions on recent trends in stratospheric ozone and temperature, *J. Geomag. Geoelectr.*, 43, 709–718.

Wuebbles, D. J., and A. S. Grossman, 1992: Global warming potential for CF_4., LLNL Report UCRL-ID-112295.

Wuebbles, D.J. and J.S. Tamaresis, 1993: The role of methane in the global environment, in *Atmospheric Methane: Sources, Sinks, and Role in Global Change*, edited by M.A.K. Khalil, Springer-Verlag, Germany.

Wuebbles, D. J., K. O. Patten, K. E. Grant, A. K. Jain, 1993: "Sensitivity of Direct Global Warming Potentials to Key Uncertainties", submitted for publication to *Climatic Change*, LLNL Report UCRL-ID-111461.

Wuebbles, D. J., J. S. Tamaresis, and K. O. Patten 1993: Quantified estimates of total GWP's for greenhouse gases taking into account tropospheric chemistry, LLNL Internal Document UCRL-ID-115850.

Figure Captions

Figure 1. Globally and annually averaged profiles of water vapor, ozone, and methane as a function of altitude for the ambient atmosphere.

Figure 2. Pressure-temperature profile for the ambient atmosphere. The temperatures are globally and annually averaged.

Figure 3. Total mass of methane (in units of teragrams) in the model atmosphere as a function of time before and after a pulse emission of methane equal to the equilibrium increase of CH_4 produced by a constant 25% increase in total emissions. Feedbacks in the lifetime of methane result in about a 36% peak increase in total atmospheric methane. The ambient value of the methane mass is indicated by the dashed line.

Figure 4. Annual average total ozone column after the pulse increase of methane. The ambient value of the ozone column is indicated by the dashed line.

Figure 5. Annually averaged tropospheric ozone column after the pulse increase of methane. The ambient value of the troposperic ozone column is indicated by the dashed line.

Figure 6. Increase in annually averaged stratospheric water vapor burden (kg) before and after the pulse emission of methane.

Figure 7. The time variation of the observed CO_2 concentration (+), the carbon cycle model prediction including biospheric feedbacks (_____), and the carbon cycle model prediction excluding the biosphere (--------).

Figure 8. The response of atmospheric CO_2 to a pulse of 1 GTC (gigatons of Carbon).

Figure 9. Radiative forcing of methane vs. time (years) after the pulse emission of methane. The correlated k-distribution radiative forcing model calculations are denoted by the symbols. The solid line is the fit to the model calculations given by Equation 4.

Figure 10. Radiative forcing of ozone vs. time (years) after the pulse emission of methane. The correlated k-distribution radiative forcing model calculations are denoted by the symbols. The solid line is the fit to the model calculations given by Equation 4.

Table 1. Chemical reaction mechanism for LLNL two-dimensional model. The reference used for all photochemical data is Demore et al. (1992).

(a) Two-body reactions (Arrhenius rate constant expression $k = A \cdot \exp\left(\frac{-E}{RT}\right)$)

No.	Reaction	A[1]	E/R[2]
1	$O + O_3 \rightarrow 2*O_2$	8.00E-12	2,060
2	$O_1D + N_2 \rightarrow O + N_2$	1.80E-11	–110
3	$O_1D + O_2 \rightarrow O + O_2$	3.20E-11	–70
4	$O_1D + O_3 \rightarrow 2*O_2$	1.20E-10	0
5	$O_1D + O_3 \rightarrow O_2 + 2*O$	1.20E-10	0
6	$H_2O + O_1D \rightarrow 2*OH$	2.20E-10	0
7	$H2 + O_1D \rightarrow OH + H$	1.00E-10	0
8	$N_2O + O_1D \rightarrow N_2 + O_2$	4.90E-11	0
9	$N_2O + O_1D \rightarrow 2*NO$	6.70E-11	0
10	$CH_4 + O_1D \rightarrow CH_2O + H2$	1.40E-11	0
11	$CH_4 + O_1D \rightarrow CH_3O_2 + OH$	1.40E-10	0
12	$CF_2Cl_2 + O_1D \rightarrow 2*Cl$	1.12E-10	0
13	$CF_3CCl_3 + O_1D \rightarrow 3*Cl$	1.60E-10	0
14	$CF_3CFCl_2 + O_1D \rightarrow 2*Cl$	1.28E-10	0
15	$CF_3CF_2Cl + O_1D \rightarrow Cl$	7.12E-11	0
16	$CHF_2Cl + O_1D \rightarrow Cl$	7.00E-11	0
17	$H + O_3 \rightarrow OH + O_2$	1.40E-10	470
18	$H2 + OH \rightarrow H_2O + H$	5.50E-12	2,000
19	$OH + O_3 \rightarrow HO_2 + O_2$	1.60E-12	940
20	$OH + O \rightarrow O_2 + H$	2.20E-11	–120
21	$HO_2 + O \rightarrow OH + O_2$	3.00E-11	–200
22	$HO_2 + O_3 \rightarrow OH + 2*O_2$	1.10E-14	500
23	$HO_2 + OH \rightarrow H_2O + O_2$	4.80E-11	–250
24	$H_2O_2 + OH \rightarrow H_2O + HO_2$	2.90E-12	160
25	$N + O_2 \rightarrow NO + O$	1.50E-11	3,600
26	$N + NO \rightarrow N_2 + O$	3.40E-11	0
27	$NO + O_3 \rightarrow NO_2 + O_2$	2.00E-12	1,400
28	$NO + HO_2 \rightarrow NO_2 + OH$	3.70E-12	–250
29	$NO_2 + O \rightarrow NO + O_2$	6.50E-12	–120
30	$NO_2 + O_3 \rightarrow NO_3 + O_2$	1.20E-13	2,450
31	$N_2O_5 + H_2O \rightarrow 2*HNO_3$	5.00E-22	0
32	$HO_2NO_2 + OH \rightarrow H_2O + NO_2 + O_2$	1.30E-12	–380
33	$Cl + O_3 \rightarrow ClO + O_2$	2.90E-11	260
34	$Cl + HO_2 \rightarrow HCl + O_2$	1.80E-11	–170
35	$Cl + HO_2 \rightarrow OH + ClO$	4.10E-11	450
36	$ClO + O \rightarrow Cl + O_2$	3.00E-11	–70
37	$ClO + OH \rightarrow HO_2 + Cl$	1.10E-11	–120
38	$ClO + HO_2 \rightarrow O_2 + HOCl$	4.80E-13	–700
39	$ClO + NO \rightarrow NO_2 + Cl$	6.40E-12	–290
40	$ClO + ClO \rightarrow Cl + ClOO$	4.00E-13	1,250
41	$ClO + ClO \rightarrow Cl_2 + O_2$	4.00E-13	1,250

[1] Units are cm^3/molecule-sec.

[2] Unit is degrees Kelvin.

No.	Reaction	A[3]	E/R[4]
42	$OClO + Cl \rightarrow 2*ClO$	3.40E-11	–160
43	$OClO + O \rightarrow O_2 + ClO$	2.50E-12	950
44	$OClO + OH \rightarrow HOCl + O_2$	4.50E-13	–800
45	$OClO + NO \rightarrow NO_2 + ClO$	2.50E-12	600
46	$ClOO + Cl \rightarrow Cl_2 + O_2$	2.30E-10	0
47	$Cl_2O_2 + Cl \rightarrow Cl_2 + ClOO$	1.00E-10	0
48	$HCl + OH \rightarrow H_2O + Cl$	2.60E-12	350
49	$HOCl + OH \rightarrow H_2O + ClO$	3.00E-12	500
50	$ClONO_2 + O \rightarrow ClO + NO + O_2$	3.19E-13	800
51	$ClONO_2 + O \rightarrow ClO + NO_2 + O$	2.58E-12	800
52	$ClONO_2 + OH \rightarrow HOCl + NO + O_2$	1.32E-13	333
53	$ClONO_2 + OH \rightarrow HOCl + NO_2 + O$	1.07E-12	333
54	$ClONO_2 + Cl \rightarrow Cl_2 + NO + O_2$	7.48E-13	–160
55	$ClONO_2 + Cl \rightarrow Cl_2 + NO_2 + O$	6.05E-12	–160
56	$Br + O_3 \rightarrow BrO + O_2$	1.70E-11	800
57	$Br + HO_2 \rightarrow HBr + O_2$	1.50E-11	600
58	$Br + NO_3 \rightarrow BrO + NO_2$	1.60E-11	0
59	$Br + OClO \rightarrow BrO + ClO$	2.60E-11	1,300
60	$Br + Cl_2O_2 \rightarrow BrCl + ClOO$	3.00E-12	0
61	$Br + CH_2O \rightarrow HBr + HO_2 + CO$	1.70E-11	800
62	$BrO + O \rightarrow Br + O_2$	3.00E-11	0
63	$BrO + HO_2 \rightarrow HOBr + O_2$	6.20E-12	–500
64	$BrO + OH \rightarrow Br + HO_2$	1.10E-11	0
65	$BrO + NO \rightarrow Br + NO_2$	8.80E-12	–260
66	$BrO + NO_3 \rightarrow NO_2 + Br + O_2$	1.00E-12	0
67	$BrO + ClO \rightarrow Br + OClO$	1.60E-12	–430
68	$BrO + ClO \rightarrow Br + ClOO$	2.90E-12	–220
69	$BrO + ClO \rightarrow BrCl + O_2$	5.80E-13	–170
70	$BrO + BrO \rightarrow 2*Br + O_2$	1.40E-12	–150
71	$HBr + O \rightarrow Br + OH$	5.80E-12	1,500
72	$HBr + OH \rightarrow Br + H_2O$	1.10E-11	0
73	$CH_4 + OH \rightarrow CH_3O_2 + H_2O$	2.90E-12	1,820
74	$CH_2O + OH \rightarrow H_2O + HO_2 + CO$	1.00E-11	0
75	$CH_3O_2 + O \rightarrow CH_2O + HO_2$	3.00E-11	0
76	$CH_2O + O \rightarrow HO_2 + OH + CO$	3.40E-11	1,600
77	$CH_3O_2 + NO \rightarrow HO_2 + CH_2O + NO_2$	4.20E-12	–180
78	$Cl + CH_4 \rightarrow CH_3O_2 + HCl$	1.10E-11	1,400
79	$Cl + CH_2O \rightarrow HCl + HO_2 + CO$	8.10E-11	30
80	$CH_3Cl + OH \rightarrow Cl + H_2O + HO_2$	2.10E-12	1,150
81	$CH_3CCl_3 + OH \rightarrow H_2O + 3*Cl$	1.80E-12	1,550
82	$CHF_2Cl + OH \rightarrow Cl + H_2O$	1.20E-12	1,650
83	$CH_3Cl + Cl \rightarrow HO_2 + CO + 2*HCl$	3.30E-11	1,250
84	$CH_3Br + OH \rightarrow Br + H_2O$	3.60E-12	1,430

[3]Units are cm^3/molecule-sec.

[4]Unit is degrees Kelvin.

(b) Three-body reactions (special rate constant expressions such as Troë equation)

Number	Reaction
1	$O + O_2 \rightarrow O_3$
2	$H + O_2 \rightarrow HO_2$
3	$HO_2 + HO_2 \rightarrow H_2O_2 + O_2$
4	$HO_2 + HO_2 + H_2O \rightarrow H_2O_2 + O_2 + H_2O$
5	$NO_2 + HO_2 \rightarrow HO_2NO_2$
6	$NO_3 + NO_2 \rightarrow N_2O_5$
7	$N_2O_5 \rightarrow NO_2 + NO_3$
8	$NO_2 + OH \rightarrow HNO_3$
9	$HNO_3 + OH \rightarrow H_2O + NO + O_2$
10	$HNO_3 + OH \rightarrow H_2O + NO_2 + O$
11	$HO_2NO_2 \rightarrow HO_2 + NO_2$
12	$ClO + NO_2 \rightarrow ClONO_2$
13	$ClO + ClO \rightarrow Cl_2O_2$
14	$ClOO \rightarrow Cl + O_2$
15	$Cl_2O_2 \rightarrow 2*ClO$
16	$BrO + NO_2 \rightarrow BrONO_2$
17	$CO + OH \rightarrow H$
18	$N_2O_5 \rightarrow 2*HNO_3$
19	$ClONO_2 \rightarrow HOCl + HNO_3$

(c) Photolysis reactions

Number	Reaction
1.	$O_2 + h\nu \rightarrow 2*O$
2.	$O_3 + h\nu \rightarrow O + O_2$
3.	$O_3 + h\nu \rightarrow O_1D + O_2$
4.	$H_2O_2 + h\nu \rightarrow 2*OH$
5.	$H_2O + h\nu \rightarrow H + OH$
6.	$NO_2 + h\nu \rightarrow NO + O$
7.	$N_2O + h\nu \rightarrow N_2 + O_1D$
8.	$NO + h\nu \rightarrow N + O$
9.	$NO_3 + h\nu \rightarrow NO_2 + O$
10.	$NO_3 + h\nu \rightarrow NO + O_2$
11.	$N_2O_5 + h\nu \rightarrow NO_2 + NO + O_2$
12.	$N_2O_5 + h\nu \rightarrow 2*NO_2 + O$
13.	$N_2O_5 + h\nu \rightarrow NO_2 + NO + 2*O$
14.	$N_2O_5 + h\nu \rightarrow 2*NO + O_2 + O$
15.	$HNO_3 + h\nu \rightarrow OH + NO_2$
16.	$HO_2NO_2 + h\nu \rightarrow OH + NO + O_2$
17.	$HO_2NO_2 + h\nu \rightarrow OH + NO_2 + O$
18.	$HO_2NO_2 + h\nu \rightarrow HO_2 + NO_2$
19.	$Cl_2 + h\nu \rightarrow 2*Cl$
20.	$ClO + h\nu \rightarrow Cl + O$
21.	$ClO + h\nu \rightarrow Cl + O_1D$
22.	$OClO + h\nu \rightarrow O + ClO$
23.	$ClOO + h\nu \rightarrow ClO + O$
24.	$Cl_2O_2 + h\nu \rightarrow Cl + ClOO$
25.	$HOCl + h\nu \rightarrow OH + Cl$
26.	$ClONO_2 + h\nu \rightarrow Cl + NO + O_2$
27.	$ClONO_2 + h\nu \rightarrow Cl + NO_2 + O$
28.	$ClONO_2 + h\nu \rightarrow Cl + NO_2 + O$
29.	$BrCl + h\nu \rightarrow Br + Cl$
30.	$BrO + h\nu \rightarrow Br + O$
31.	$HBr + h\nu \rightarrow H + Br$
32.	$HOBr + h\nu \rightarrow Br + OH$
33.	$BrONO_2 + h\nu \rightarrow Br + NO_2 + O$
34.	$BrONO_2 + h\nu \rightarrow Br + NO + O_2$
35.	$CH_2O + h\nu \rightarrow CO + H2$
36.	$CH_2O + h\nu \rightarrow HO_2 + CO + H$
37.	$CH_3Cl + h\nu \rightarrow CH_3O_2 + Cl$
38.	$CCl4 + h\nu \rightarrow 4*Cl$
39.	$CH_3CCl_3 + h\nu \rightarrow 3*Cl$
40.	$CFCl_3 + h\nu \rightarrow 3*Cl$
41.	$CF_2Cl_2 + h\nu \rightarrow 2*Cl$
42.	$CF_3CCl_3 + h\nu \rightarrow 3*Cl$
43.	$CF_3CFCl_2 + h\nu \rightarrow 2*Cl$
44.	$CF_3CF_2Cl + h\nu \rightarrow Cl$
45.	$CHF_2Cl + h\nu \rightarrow Cl$
46.	$CH_3Br + h\nu \rightarrow Br + CH_3O_2$
47.	$CF_3Br + h\nu \rightarrow Br$
48.	$CF_2ClBr + h\nu \rightarrow Br + Cl$

Table 2. Surface emission inventory for the LLNL two-dimensional model. (teragrams per year)

Model Zone	Latitude Center	Methane	Carbon Monoxide	Nitrogen Dioxide
1	–80.1	0.00	0.60	0.00
2	–70.9	0.00	1.00	0.00
3	–62.3	0.00	8.45	0.00
4	–53.1	0.15	18.64	1.98
5	–42.5	4.08	35.62	7.27
6	–30.0	18.99	84.83	10.35
7	–17.5	24.67	136.09	15.63
8	–5.7	39.25	154.50	11.67
9	5.7	42.43	145.11	12.67
10	17.5	54.99	167.10	10.69
11	30.0	81.71	197.88	20.37
12	42.5	70.41	209.05	27.09
13	53.1	57.51	126.63	8.88
14	62.3	30.00	34.40	4.83
15	70.9	15.92	5.02	0.00
16	80.1	12.77	3.01	0.00
	TOTALS (Tg/yr):	452.9	1328	131.4

Table 3. Radiative Forcing W/m^2

Year	Direct CH_4	Indirect O_3	CO_2 (1.29)	CO_2 (2.0)
1	0.2500	0.0947		
2	0.2455	0.1180	1.956	5.453
3	0.2312	0.1165		
6	0.1950	0.1013		
7	0.1844	0.0957		
8	0.1744	0.0909		
9	0.1649	0.0861		
10	0.1558	0.0818		
15	0.1176	0.0614		
20	0.0884	0.0462		
25	0.0665	0.0348		
30	0.0500	0.0261		

Table 4. Latitude Variation Of Radiative Forcing (W/M^2) For Year 2

LATITUDE (DEG)	DIRECT CH_4 (P. TROP.)	INDIRECT O_3 (P. TROP.)
–71	0.2403 (292mb)	0.0625 (292mb)
–30	0.2755 (139mb)	0.1518 (139mb)
+5.7	0.2628 (123mb)	0.1516 (123mb)
+30	0.2659 (135mb)	0.1406 (135mb)
+71	0.2244 (302mb)	0.0603 (302mb)
Avg.	0.2603	0.1297
% Diff.	+5 (0.2455)	+9 (0.1180)

Table 5. Latitude Effect Of CO_2 Forcing For An Impulse Doubling Of CO_2

LATITUDE	FORCING (W/m^2)	CO_2 FACTOR	CH_4 FACTOR	O_3 FACTOR
Average	5.453	0.8	0.8	0.8
–71	4.418	0.988	0.967	0.523
–30	5.735	0.76	0.852	0.977
+5.7	5.976	0.73	0.781	0.939
+30	5.773	0.76	0.823	0.906
+71	4.624	0.944	0.863	0.482

Table 6. Latitude Variation Of H_2O Radiative Forcing (W/M^2)

LATITUDE (DEG)	H_2O Forcing		
	Year 5	Year 10	Year 20
–60 (278mb)	2.085 (–3)	5.302 (–3)	3.761 (–3)
–30 (139mb)	4.179 (–3)	1.021 (–3)	7.270 (–3)
Eq. (123mb)	2.995 (–3)	6.456 (–3)	4.715 (–3)
+30 (135mb)	5.295 (–3)	1.251 (–2)	8.911 (–3)
+60 (278mb)	1.741 (–3)	4.032 (–3)	2.932 (–3)
Avg.	3.629 (–3)	8.535 (–3)	6.099 (–3)

Table 7. Radiative Forcing Integrals per Kilogram Mass of the Trace Gases

	20 yr	50 yr	100 yr	200 yr	500 yr
CH_4	1.505e-12[a]	2.074e-12	2.183e-12	[b]	[b]
O_3 (CH_4)	7.931e-13	1.127e-12	1.198e-12	[b]	[b]
H_2O(CH_4)	5.624e-14		1.012e-13		1.016e-13
CO_2	3.117e-14	6.303e-14	1.073e-13	1.832e-13	3.612e-13

[a]Read "e-" as an exponent, thus 1.505e-12 = 1.505×10^{-12}. Units are W yr m^{-2} kg^{-1} at the tropopause.

[b]Taken as identical to the value for time horizon of 100 yr.

Table 8. Global Warming Potentials and the Indirect GWP Total Uncertainty Estimate

	source	20 yr	50 yr	100 yr	200 yr	500 yr
CH_4	current	52.6		22.9		7.0
	a	37.7	21.7	12.9	7.5	3.8
	b	34		9		2
	c	35		11		4
O_3 (CH_4)	current	26.7		11.7		3.58
	b	24		8		3
	a	23.1		10.4		3.1
H_2O(CH_4)	current	1.9		1.01		0.31
	b	10		4		1

Sources:

(a) Wuebbles *et al.*, 1993

(b) IPCC, 1990

(c) IPCC, 1992.

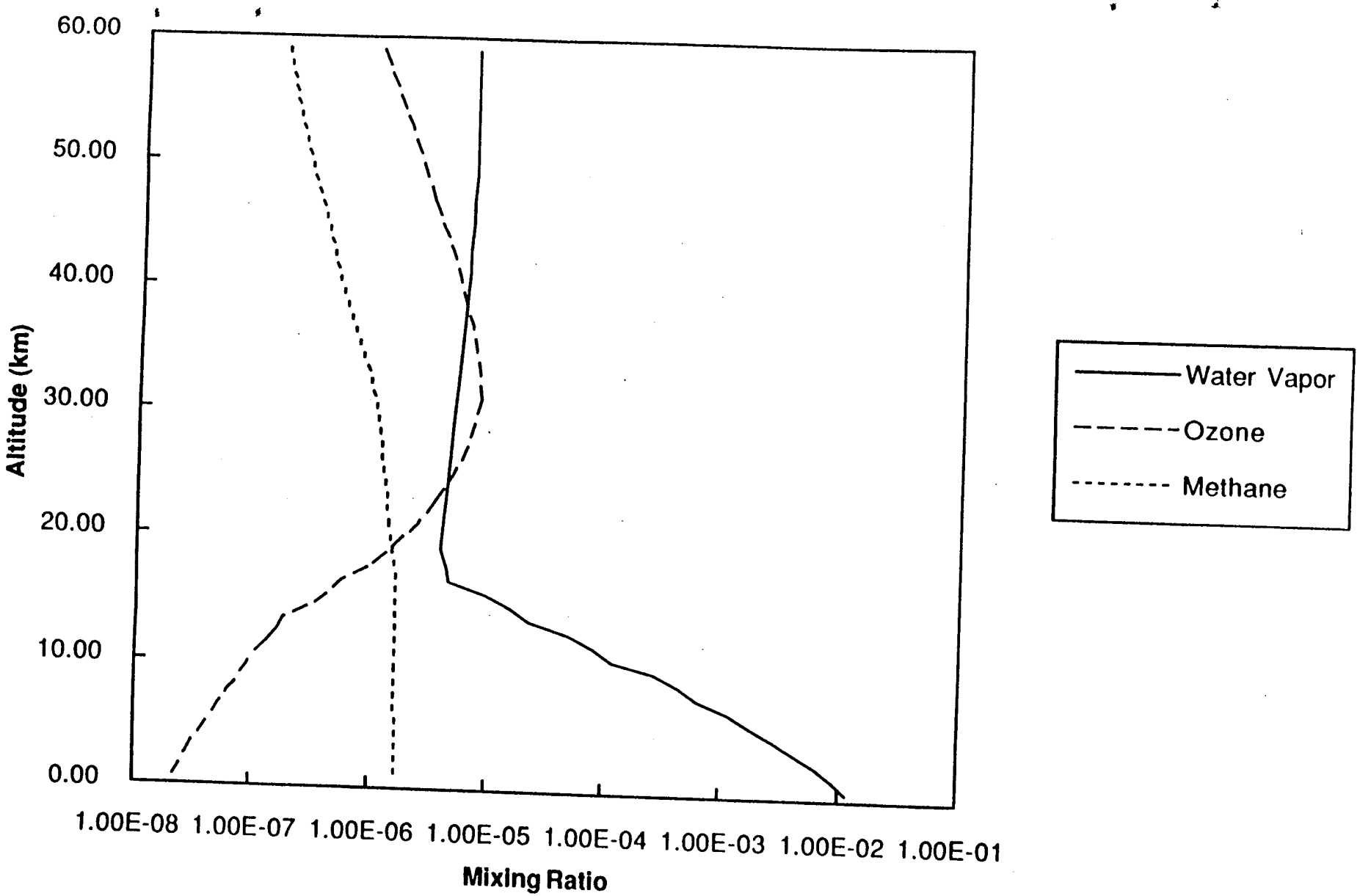

Figure 1 Globally- and annually-averaged profiles of water vapor, ozone, and methane as a function of altitude for the ambient atmosphere.

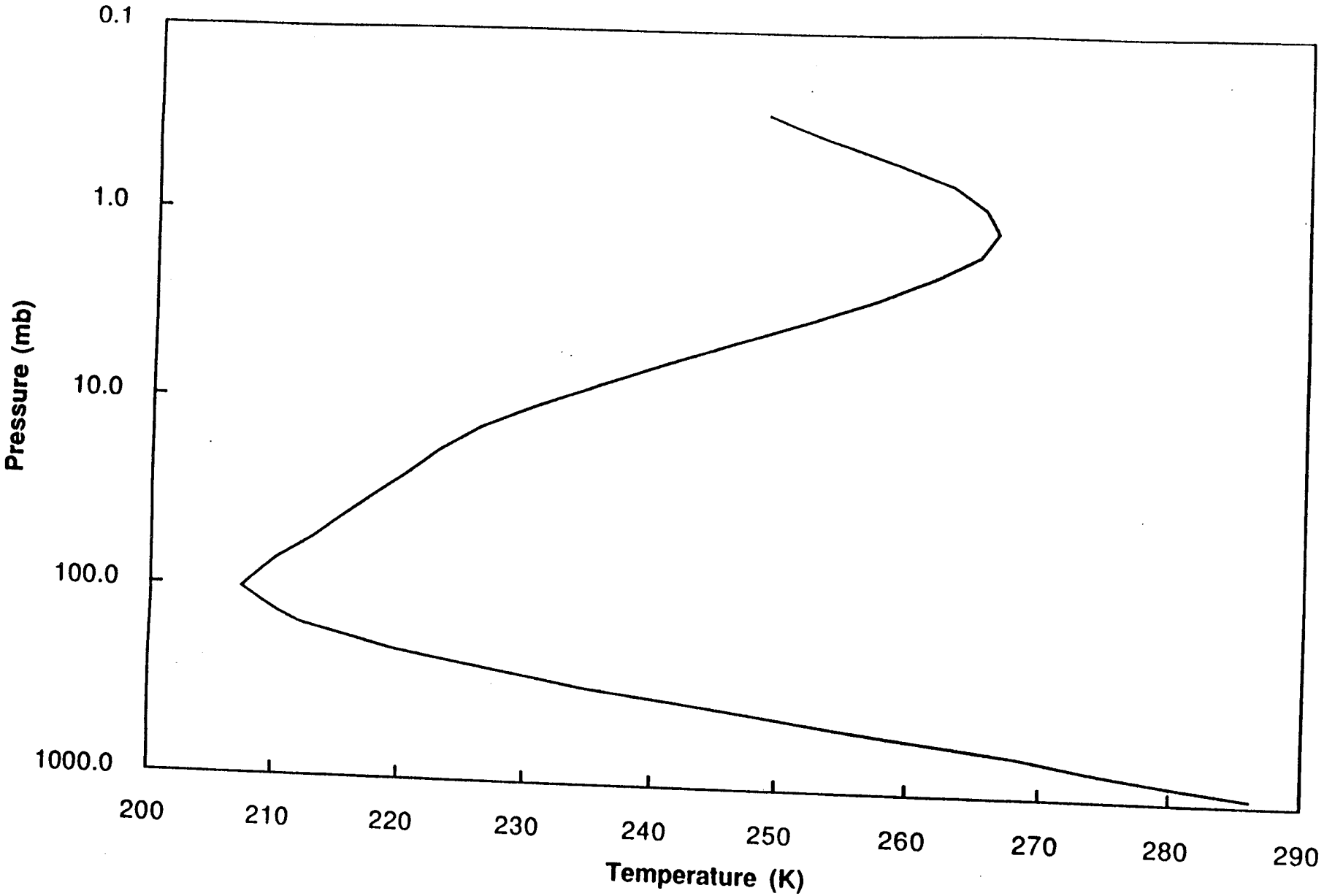

Figure 2 Pressure-temperature profile for ambient atmosphere. The temperatures are globally- and annually-averaged.

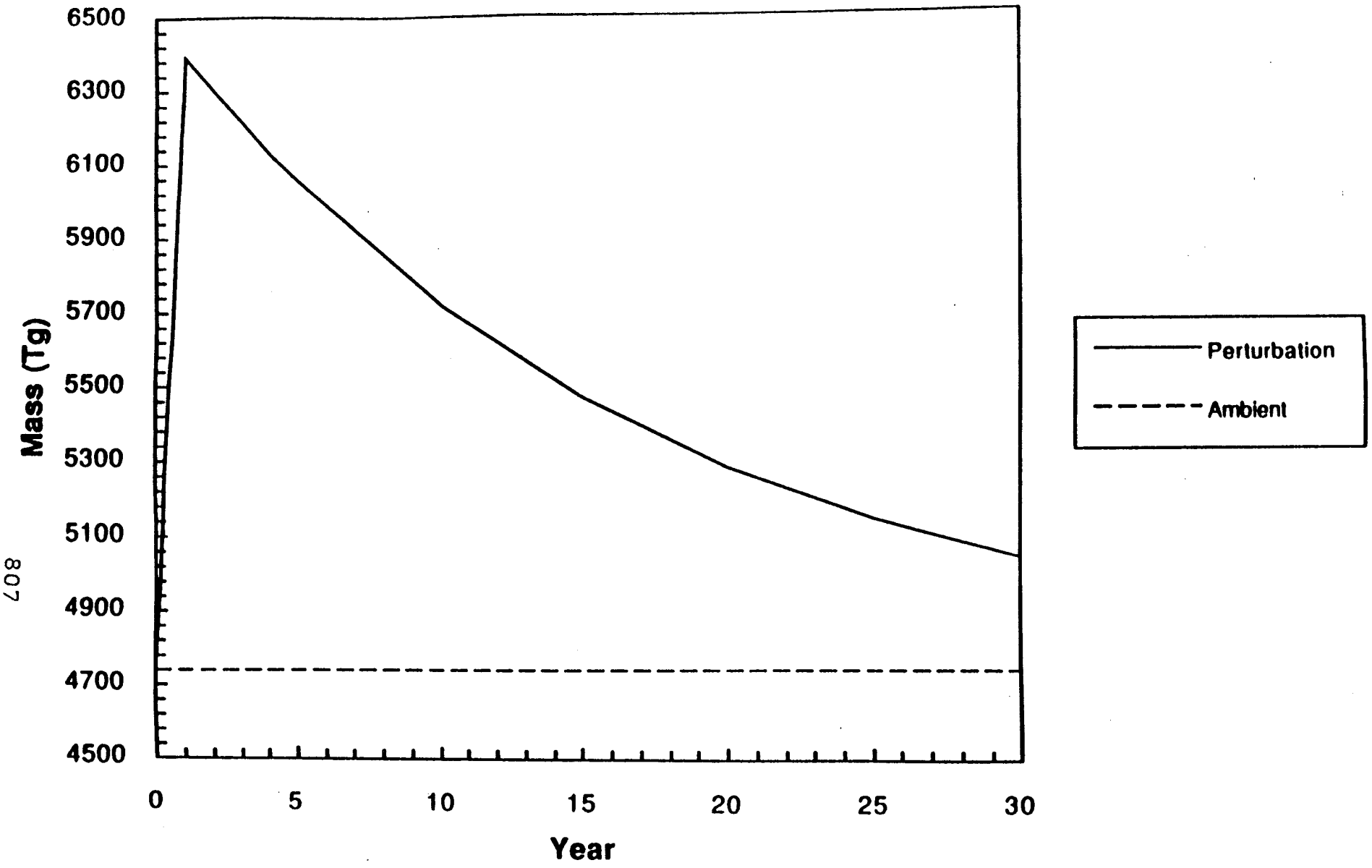

Figure 3 Total mass of methane (in units of teragrams) in the model atmosphere as a function of time before and after a pulse emission of methane equal to the equilibrium increase of CH_4 produced by a constant 25% increase in total emissions. Feedbacks in the lifetime of methane result in about a 36% peak increase in total atmospheric methane. The ambient value of the methane mass is indicated by the dashed line.

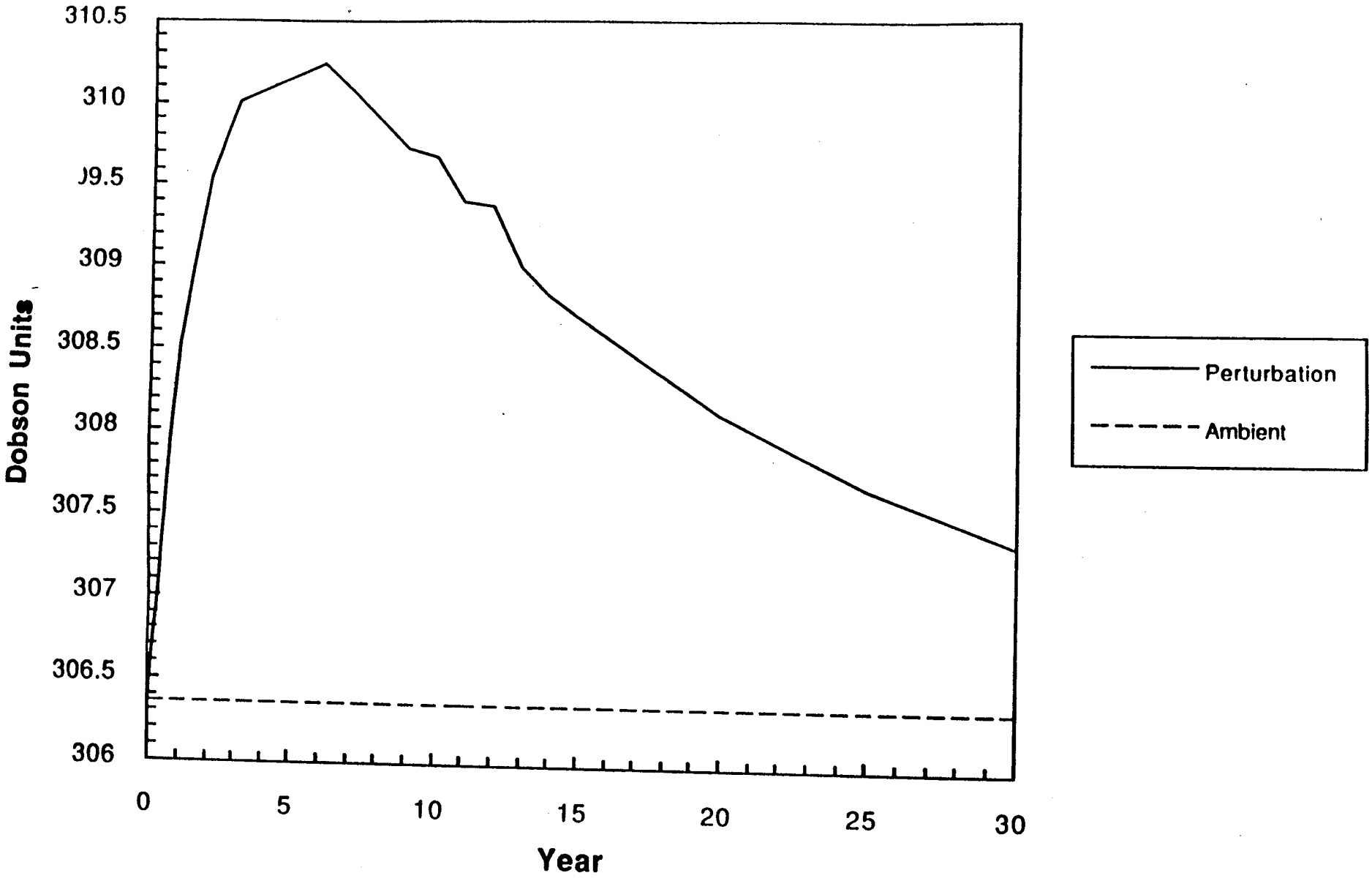

Figure 4 Annual average total ozone column after the pulse increase of methane.

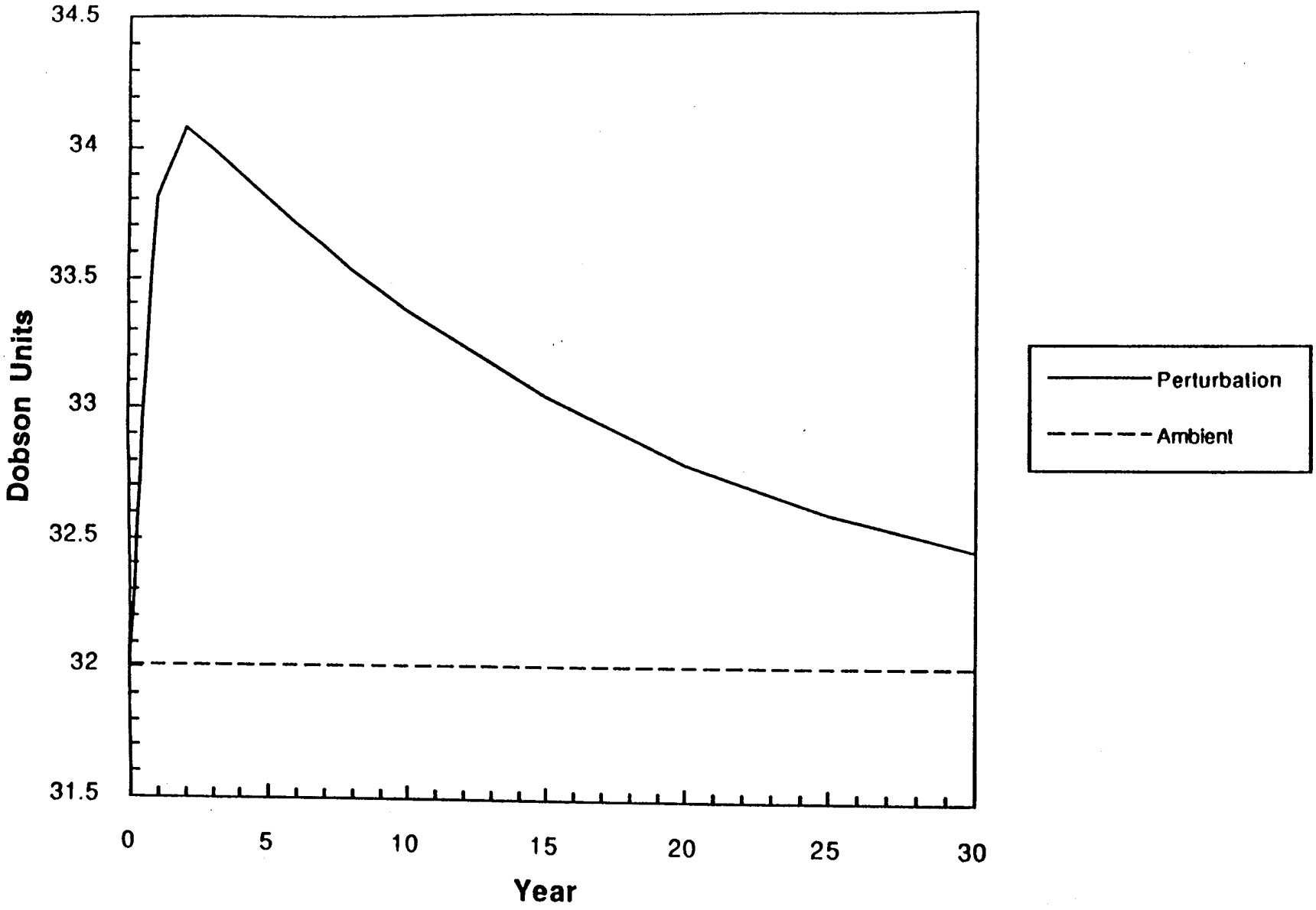

Figure 5 Annually averaged tropospheric ozone column after the pulse increase of methane.

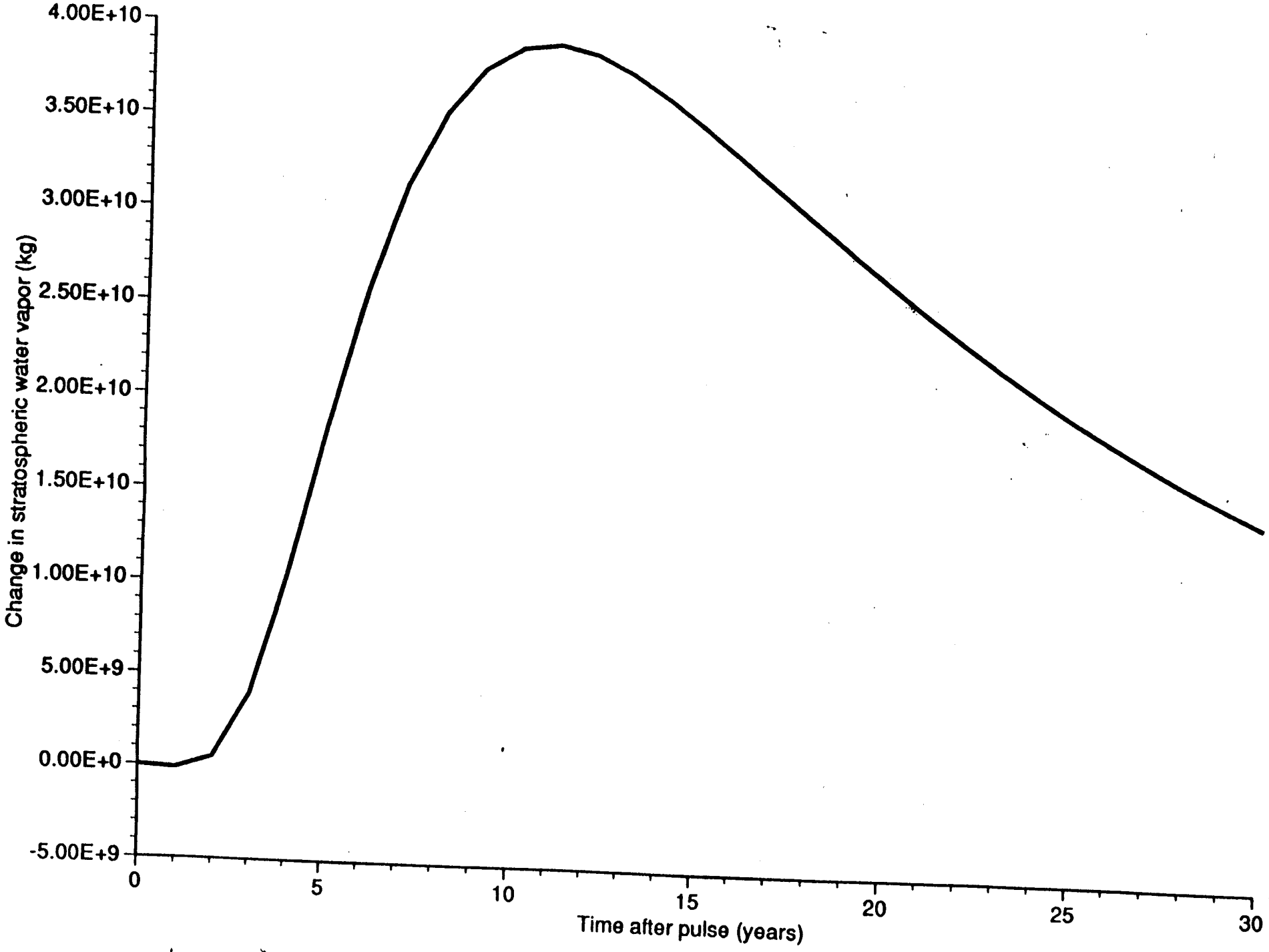
4.00E+10
3.50E+10
3.00E+10
2.50E+10
2.00E+10
1.50E+10
1.00E+10
5.00E+9
0.00E+0
-5.00E+9
Change in stratospheric water vapor (kg)
0
5
10
15
20
25
30
Time after pulse (years)

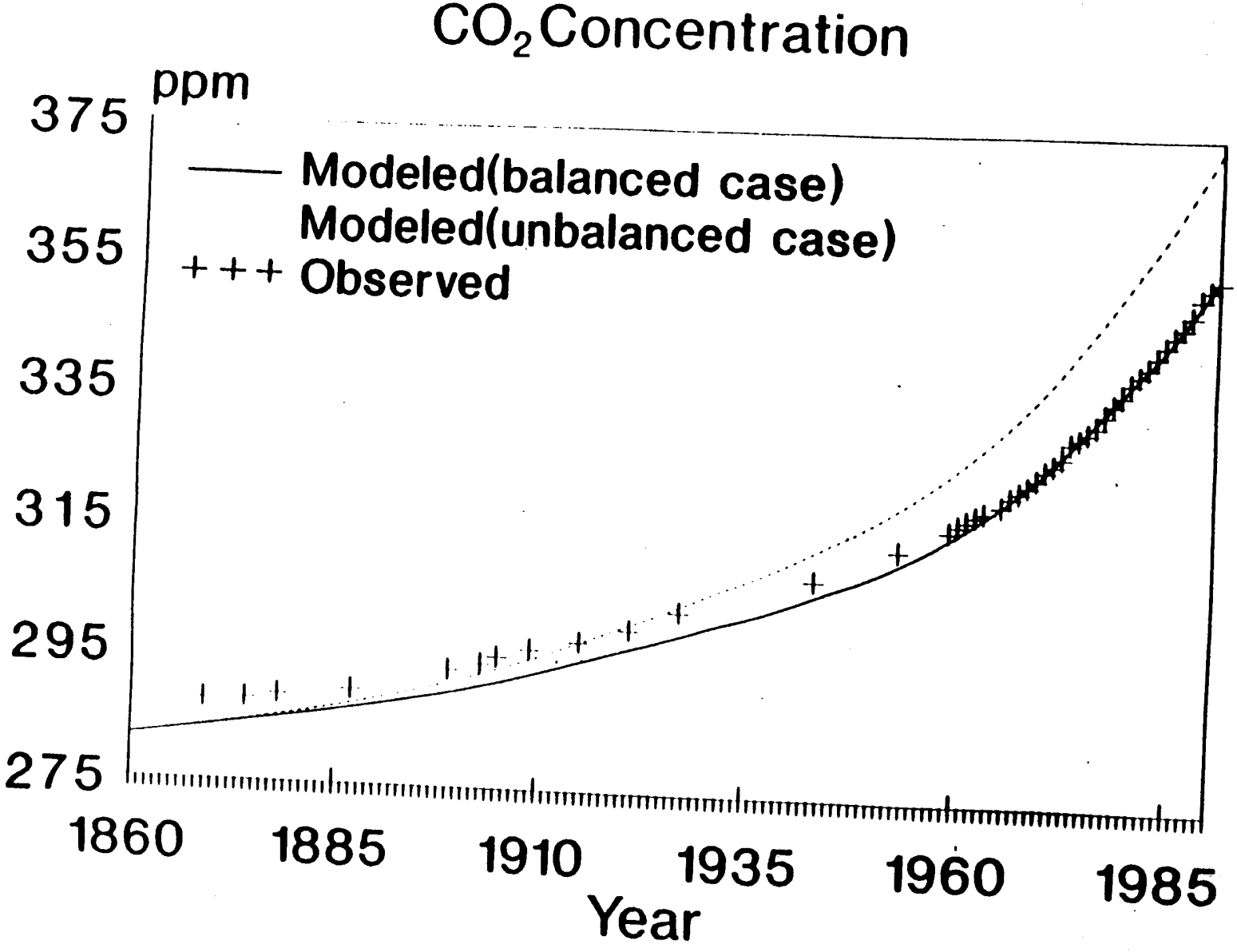
CO_2 Concentration
ppm
375
355
335
315
295
275
Modeled(balanced case)
Modeled(unbalanced case)
+++ Observed
1860
1885
1910
1935
1960
1985
Year

Figure 6

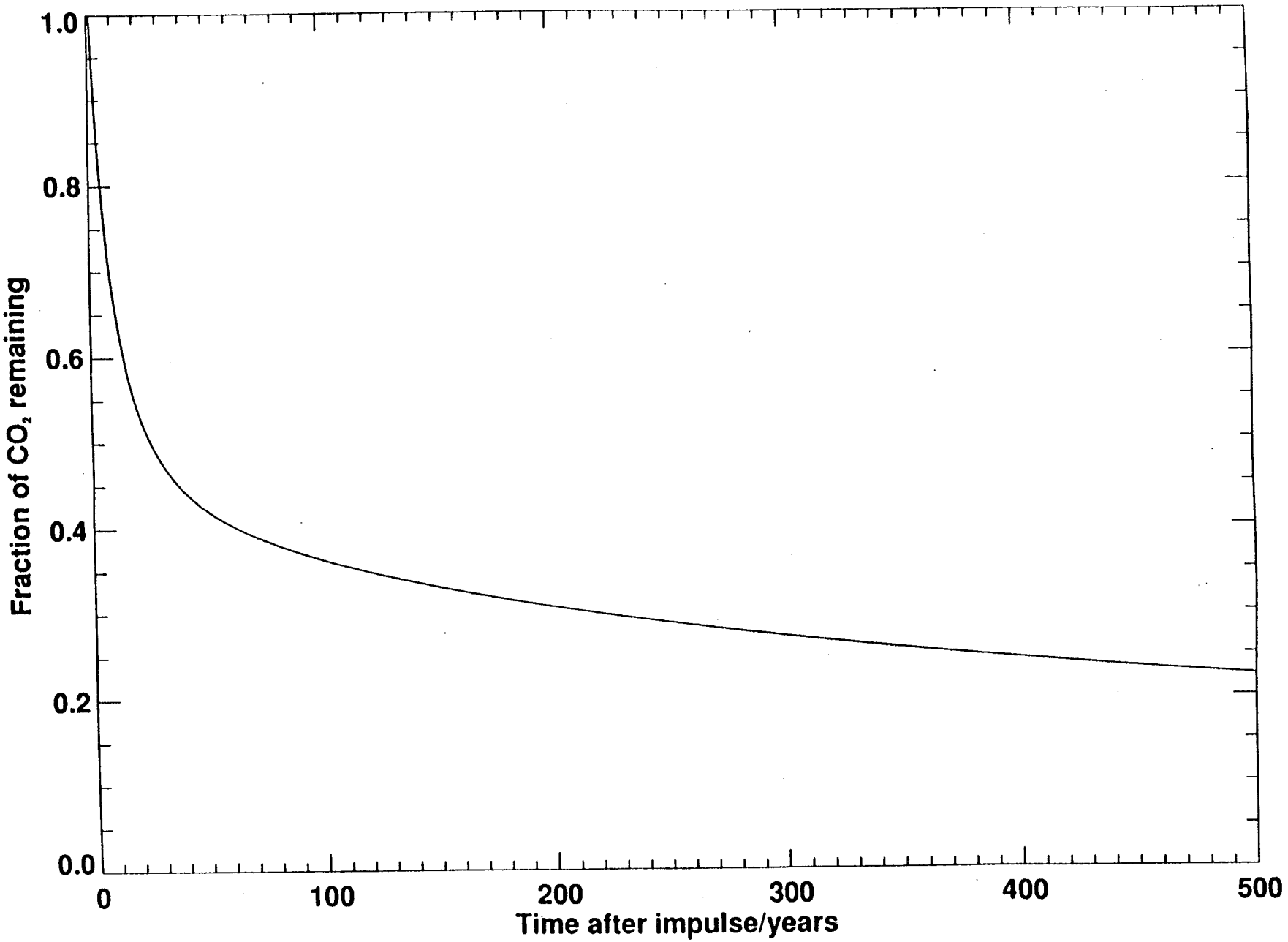
1.0
0.8
0.6
0.4
0.2
0.0
Fraction of CO_2 remaining
0
100
200
300
400
500
Time after impulse/years

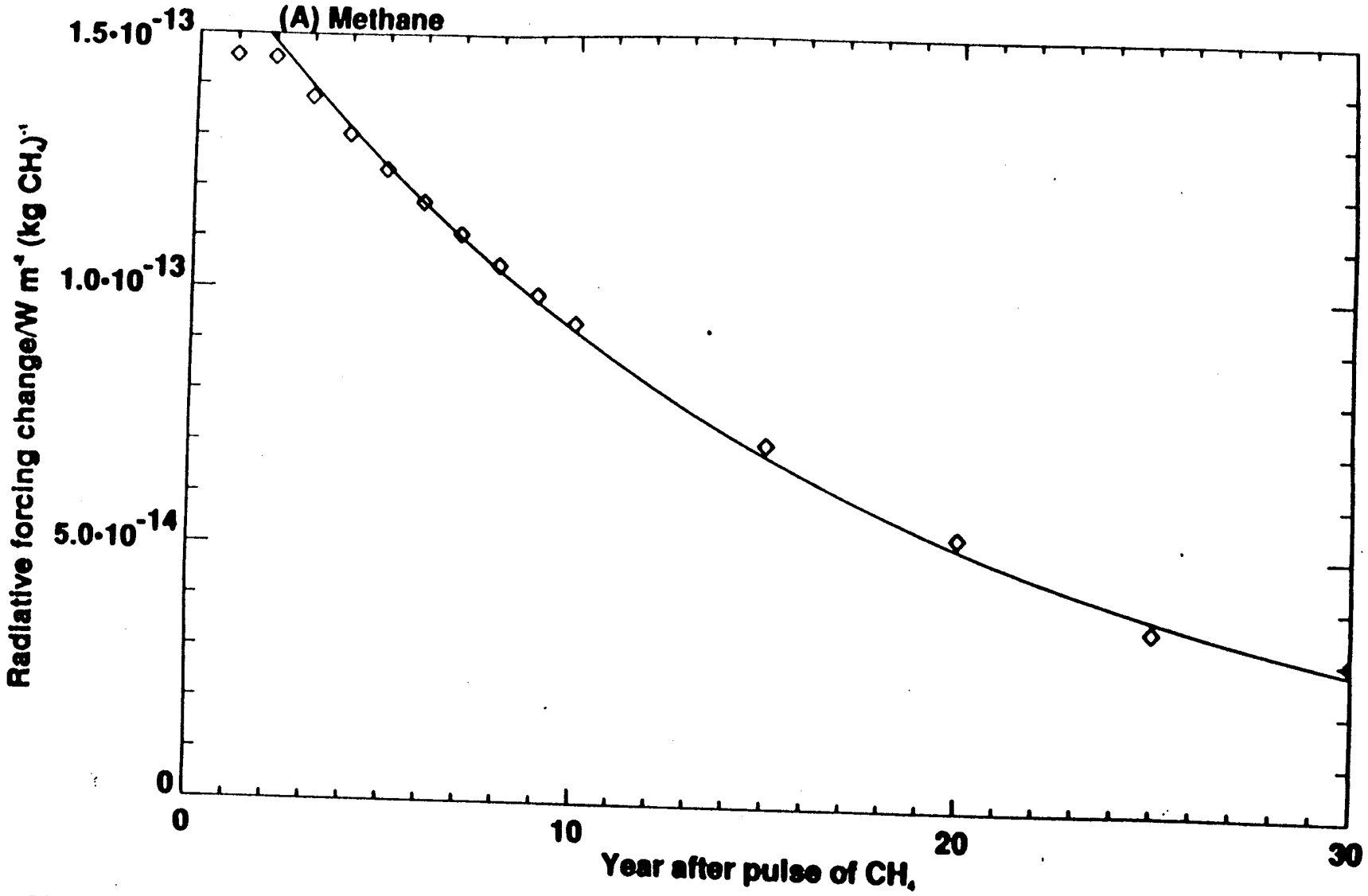

Figure B. Radiative forcing of CH_4 versus time after pulse release of CH_4. ◊: line model calculations. Solid line: fit of Equation 5.4a.

Name	Affiliation	Phone Number
Mr. Leonard Abreu	ONTAR Corporation	508-689-9622
Prabhat Acharya	Spectral Sciences, Inc.	617-270-5982
Steven Adler-Golden	Spectral Sciences, Inc.	617-273-4770
Ronald E. Alley	Jet Propulsion Laboratory	818-354-0751
Don Anderson	JHU/APL	
Gail P. Anderson	PL/GPOS	617-377-3687
Peter Armstrong	Stewart Radiance Laboratory	617-377-3626
Robert Beland	PL/GPOS	617-377-4604
Frank Bennett	Mitre Corporation	617-271-8712
Alexander Berk	Spectral Sciences, Inc.	617-273-4770
Larry Bernstein	Spectral Sciences, Inc.	617-273-4770
Mike Bossert	Boeing Computer Services	619-939-0667
Tyler Brown	JPL/NASA	818-354-6357
James T. Bunting	PL/GPAB	617-377-4854
Johnson Chan	ONTAR Corporation	508-689-9622
Kelly Chance	Smithsonian	617-495-7389
Michael Cheifetz	SPARTA	617-863-1060
Paola Ciarpallini	Smithsonian	617-495-7497
George Cipperly	Martin Marrietta Corporation	610-531-6266
F.O. Clark	PL	617-377-4139
John Conant	Aerodyne Research, Inc.	508-663-9500

Name	Affiliation	Phone Number
William Cornette	PRA	619-455-9741
Kathy Crow	SciTec, Inc.	609-921-3892x248
Gil Davidson	Photometrics	617-935-6500
Richard E. Davis	NASA-Langley Research Center	804-864-1647
Adam D. Devir	EORD/Technion/Israel	972-4-294233
Edmond Dewan	PL/GPOS	617-377-4401
Susan Downer	Mission Research Corporation	603-891-0070
Tom Dugan	NRL	
Martin Fair	DRA Farnborough UK	44-252-395344
Harry Finkle	MIT/LL	617-981-4905
John Feeley	Boeing/NAWC	619-939-0605
Grace E. Gagnon	PL/GPOS	617-377-2336
William Gallery	AER	617-547-6207
Richard Garner	Photometrics	617-935-6500
Stuart Gathman	NRnD	619-553-1418
Roy Goeller	Los Alamos National Laboratory	505-665-1107
Donald Grantham	PL/GPAA	617-377-2982
Allen Grossman	Los Alamos National Laboratory	510-923-6371
J.A. Hall	PL/GPIM	
Larrene Harada	WJSA	703-558-7900
Sabrina Harvey	ONTAR Corporation	508-689-9622

Name	Affiliation	Phone Number
Michael Iacono	AER	617-349-2208
Precila Ip	Mission Research Corporation	603-891-0070
Ken Jucks	Smithsonian Ast. Ops	617-496-7580
Simon Kaelin	Aerosols/Eth Zurich	
Brook Koffine	Aerospace Corporation	310-336-7412
Robert Kurucz	SAO	617-495-7429
Alex Kutepov	University of Munich	49-89-92209430
Tom Kyle	PL/XPG	617-377-7443
Olga Lado-Bordowsky	ENSSAT	
Steven Lipson	PL/GPOS	617-377-3626
U. Makhlouf	SRL	617-377-4203
Steve Mazuk	Aerospace Corporation	310-336-5614
Andy McCann	ONTAR Corporation	508-689-9622
Sue McKenzie	Mission Research Laboratory	603-891-0070
Joe Michalsky	SUNY	518-442-3809
Ferenc Miskolczi	UMD	301-799-7693
Mike Neer	SciTec, Inc.	609-921-3892x206
Meg Noah	Mission Research Laboratory	
Lüsa Oikarinen	Finnish Meteorological Institute	358-0-1929521
Clifford A. Paiva	NSWC/	703-663-4980
Brunel Pascal	Meteo France	33-96056765

Name	Affiliation	Phone Number
Richard Picard	PL/GPOS	617-377-2222
Russell Phillbrick	ARL/PSO	814-863-7682
Angela Phillips	Hughes Aircraft Company	310-616-0124
Behrooz Rezai		801-797-3564
Lt. Col. John Roadcap	PL/WE	505-846-4722
David Robertson	Spectral Sciences, Inc	617-273-4770
Ronald Rodney	WPAFB-Wright Lab.	513-255-1978
Larry Rothman	PL/GPOS	617-377-2336
John Schroeder	ONTAR Corporation	508-689-9622
Mark Schmitt	Los Alamos National Laboratory	505-667-0655
John E.A. Selby	Northrop-Grumman	516-575-6608
Dima Seliverstov	Mitre Corporation	617-377-5314
Eric Shettle	NRL	202-404-8152
Richard Shirkey	ARL/DED	505-678-5470
Lewis L. Smith	Northrop Grumman	516-575-2196
Roberta Smith	US Army Tecom	703-704-1762
Ned Snell	AER	617-547-6207
Pierre Simoneau	ONERA	33-46734850
Knut Stamnes	University of Alaska	907-474-7368
Tim Stevens	ARL/PSU	814-863-0851
William Stoner	SAIC	508-667-6365

Name	Affiliation	Phone Number
James Telford	University of Nevada	702-677-3201
David Tofsted	ARL	505-678-3039
Martine Voltaire	ONTAR Corporation	508-689-9622
Philip Walker	Naval Postgraduate School	408-656-2674
Zhengning Wan	University of California	805-893-4541
Jinxue Wang	PL/GPOS	617-377-4854
Alan Wetmore	ARL	505-678-5567
Robert C. Wilson	Boston College	617-552-8765
Peter P. Wintersteiner	ARCON	617890-3330x231
Rich Woodford	USAFETAC	618-256-5211
Kouichi Yoshino	CFA	617-495-2796
Douglas Youmans	W.J. Schafer	508-256-2070
Daniel Zhou	SDL/USU	301-953-5470

AUTHORS

17th Annual Review Conference on Atmospheric Radiation Models

ABSTRACTS

7-8 June 1994
PL/Geophysics Directorate
Science Center

FASCODE: AN UPDATE AND RECENT VALIDATIONS/APPLICATIONS

G.P. Anderson, J.H. Chetwynd, and J. Wang*

Phillips Laboratory
Geophysics Directorate
29 Randolph Road
Hanscom AFB, MA 01731-3010
*NRC Fellow (on leave from Univ. of Michigan)

FASCODE, the DoD standard line-by-line (LBL) code, has undergone only minor changes over the past two years, since the release of FASCOD3P in March 1992. Present/future capabilities and their driving requirements will be reviewed. In addition, the results of two recent comparisons of FASCODE against other LBL codes, both initiated by the WMO (World Meteorological Organization) will be presented: Intercomparison of Transmittance and Radiance Algorithms (ITRA) in the microwave region, and InterComparison of Radiation Codes used in Climate Models (ICRCCM) in the more historic infrared spectral range.

MODTRAN3, MODTRAN4, AND BEYOND

A. Berk[1], P.K. Acharya[1], L.S. Bernstein[1], D.C. Robertson[1], G.P Anderson[2], J.H. Chetwynd[2], F.X. Kneizys[2], L.A. Hall[2], L.M. Kimball[2], E.P. Shettle[3], L.W. Abreu[4], and K. Minschwaner[5]

[1]Spectral Sciences, Inc.
99 S. Bedford St. #7
Burlington, MA
01803-5169

[2]Phillips Laboratory
29 Randolph Road
Hanscom AFB, MA
01731-3010

[3]Naval Res. Lab
Code 7227
Washington, DC
20375-5351

[4]Ontar Corp.
9 Village Way
No. Andover, MA
01845

[5]NCAR
Box 7000
Boulder, CO

The MODTRAN code continues to be an invaluable tool for predicting and modeling radiation transport in the lower atmosphere (< 60km). The newest version, MODTRAN3, will be released shortly. Its enhancements include: (1) arbitrary layer resolution (2) improved treatments for single scatter solar and multiple scatter radiances (3) CFC, UV NO_2, UV SO_2 and new O_3 Chappius cross-sections (4) a spectrally varying surface albedo input option (5) HITRAN 94 based band model data. Current research which will lead to upgrades for MODTRAN4 and later include: improved cooling rate, vertical flux, and weighting function calculations; higher spectral resolution; an updated aerosol database; vector optimization; and incorporation of the NRL climatology database via the SAG code.

MOSART: AN UPDATE ON THE MODERATE SPECTRAL ATMOSPHERIC RADIANCE AND TRANSMITTANCE CODE

William M. Cornette

Photon Research Assoc. Inc.
10350 N. Torrey Pines Road
Suite 300
La Jolla, CA 92037-1020

Prabhat K. Acharya
David Robertson

Spectral Sciences, Inc.
99 South Bedford St.#7
Burlington, MA 01803

Gail P. Anderson

Phillips Laboratory
Geophysics Directorate
29 Randolph Road
Hanscom AFB, MA
01731-3010

The MOderate Spectral Atmospheric Radiance and Transmittance Code is currently undergoing beta testing and is scheduled for release in August 1994. Since the overview last year, a number of new capabilities have been added. These include an earthshine and skyshine model, improved classification for terrain types, and upgrades to the global terrain database and aerosol model. General verification and validation has been performed primarily with comparisons to MODTRAN, while limited direct validation has been performed with data comparisons.

PLEXUS

PHILLIPS LABORATORY EXPERT UNIFIED SOFTWARE

Dr. Frank O. Clark

Phillips Laboratory
Geophysics Directorate
29 Randolph Road
Hanscom AFB, MA 01731-3010

PLEXUS, or Phillips Laboratory Expert Unified Simulator, places PL Codes in a unified knowledge based interface. PLEXUS is intended for the intelligent non-expert as well as expert users. PLEXUS contains: the standard Atmospheric Generator (SAG), MODTRAN (& LOWTRAN), a validated integrated MODTRAN and SHARC pre- and post- processor combination, CBSD (Celestial Background Scene Descriptor). With a single set of input parameters from the user, the preprocessor automatically runs MODTRAN below 50 km and SHARC above 50 km and produces a single output, permitting sight paths which cross the equilibrium/non-equilibrium boundary. PLEXUS also contains the new Standard Atmospheric Generator which is based on NASA MSIS-90 and NRL lower atmosphere phenomenology data. This seamless model implementation is essential for modern space based, TMD, and GPALS applications. The single geometry interface applies to all codes.

EOSAEL92 UPDATE

Alan E. Wetmore
U.S. Army Research Laboratory
White Sands, Missile Range, NM 88002-5501, U.S.A.

Since the distribution of EOSAEL92 several of the modules have been updated and an acoustics module has been selected for incorporation. The TARGAC model has been extended and an interface to run the module under Microsoft Windows has been developed. The UVTRAN model also has a version that runs under Microsoft Windows. Both of these will be demonstrated at the conference. The millimeter wave module, NMMW, has been updated with a new gaseous absorption algorithm. The Scanning Fast Field Program (SCAFFIP) is an acoustics model that predicts acoustic propagation based on spherical spreading, molecular absorption, refraction, acoustically complex ground impedance, and diffraction over being terrain. We are in the process of making all of these modules and documentation available through the Test and Evaluation Community NETwork (TECNET). In addition the Validation and Verification of the laser transmission module, LZTRAN, has been performed.

THE NAVY OCEANIC VERTICAL AEROSOL MODEL IN A FORTRAN SUBROUTINE FORMAT

Stuart G. Gathman

NCCOSC RDTE DIV 543
53170 Woodward Road
San Diego, CA 92152

A FORTRAN version of the Navy Oceanic Vertical Aerosol Model, NOVAM, has been completed and is ready to be interfaced with other types of transmission models. The model is available in the form of a NCCOSC RDT&E DIV technical report #1634 which contains: (a) a written description of the model, (2) the printed code of the subroutine, (3) the printed code of the associated subroutines and functions, and (4) a sample driver which can be used for batch processing of data. The model requires meteorological data in the form of both surface and atmospheric sounding data files. NOVAM predicts the vertical distribution of aerosol in the first 6 km above the ocean. Outputs of the model include optical properties in the wavelength band from 0.2 to 40 micrometers at any altitude. These properties include the volume extinction and absorption coefficient, the relative humidity, as well as parameters describing the aerosol size distribution in terms of dN/dr at that altitude. This paper will describe the model and some sample applications.

THE NATURE OF DESERT AEROSOLS: SUMMARY OF CHINA LAKE STUDIES TO DATE

P.L. Walker
Physics Department, Naval Postgraduate School, Monterey, CA 93943-5117
and
L.A. Mathews retired from
Naval Air Warfare Center, China Lake, CA

The Naval Air Warfare Center has been conducting desert aerosol characterization measurements at China Lake at ground level in 1987; at 15,000 feet in connection with Long Jump in 1988; at ground level in the western Mojave including Edwards AFB and China Lake in 1990; and will be conducting further measurements in the western Mojave in the summer of 1994. This presentation will present an over view of the analysis of data to date. The properties of desert aerosol that are appearing are somewhat different than those proposed by Longtin and Shettle in that the accumulation mode is dominated by the presence of large numbers of organic carbon particles while dust is characterized by the presence of clay particles in the dust size distribution mode with few quartz particles being present and no quartz dominated blowing sand mode. We will compare particle size and composition at 15,000 feet and ground level, further micrographic studies of the composition of high altitude aerosols and the effect of wind speed on aerosol characteristics at ground level.

APPLICATION OF THE MODTRAN2 CODE TO THE MODELING OF SILICATE DUST CLOUDS.

S. Mazuk and D.K. Lynch
The Aerospace Corporation
P.O. Box 92957
Mail Code M2/255
Los Angeles, CA 90009-2957

The MODTRAN2 code has been used to model the thermal infrared radiance from a dust cloud formed during an explosives test at the White Sands Missile Range in 1993. High signal-to-noise infrared spectra of the dust cloud were measured, indicating the presence of silicate particles. A silicate dust cloud was defined as part of the model atmosphere, and MODTRAN was used to calculate radiance spectra between 6 and 16 microns. A description of the analysis, comparison with experimental data, and the problems encountered will be presented.

MODELIZATION OF CLOUD RADIATION AND COMPARISON WITH AIRBORNE MEASUREMENTS

C. Malherbe, P. Simoneau and A. Boischot

Office National d'Etudes et de Recherches Aerospatiales
BP 72, 92322 Chatillon Cedex
France

We have developed a computer code named NUALUM, dedicated to the computation of the atmospheric radiance in presence of clouds.

This radiance is the sum of three terms:

- the atmospheric radiance between the cloud and the observator
- the thermal radiance of the cloud
- the scattering by the cloud of the solar, the terrestrial and the atmospheric fluxes.

The bidirectional reflectivity and the emissivity of the cloud are computed with the DISORT program. The solar flux, the terrestrial flux, and the atmospheric flux are calculated by MODTRAN. Numerical results are compared with spectral and spatial infrared measurements performed by airborne devices.

OSIC - AN ULTRAVIOLET TRANSMISSION AND MULTIPLE SCATTERING MODEL

Michael Neer and Kathy Crow

SciTec, Inc.
100 Wall Street
Princeton, NJ 08540

A novel analytical approach is presented for predicting not only conventional transmission associated with molecular and aerosol scatter and absorption, but also the contribution of multiple scattering including angle of arrival. The approach has been implemented in a model called MWR and sample signature versus time predictions will be presented along with comparisons to experimental data. The program will run much faster than Monte Carlo models so it is better suited to carrying out missile signature parametric studies. The model can also be used to predict signatures when the source is not in the sensor field of view and the received signal comes only from scattered radiation.

ATMOSPHERE UV-VISIBLE RADIATION FIELD PERTURBATIONS PRODUCED BY CLOUDS AND AEROSOLS: COMPARISON OF RESULTS USING MONTE CARLO, DISORT AND INTEGRAL EQUATION METHODS

D.E. Anderson and R. DeMajistre

The Johns Hopkins University
Applied Physics Laboratory
Laurel, MD 20723

The UV-Visible stratosphere radiation can be strongly perturbed from the clear atmosphere case when clouds and/or aerosols are present. The clear atmosphere is, to within ~2% accuracy, isotropic. When clouds and/or aerosols are present the radiation field can become anisotropic to a degree that isotropy is no longer a useful assumption, an inclusion of these effects is necessary either by approximation or by a more representative numerical description. We compare the results from three different approaches to the calculation of the radiation field when clouds and/or aerosols are present. Results are presented for the 280-800nm wavelength region and for a range of solar zenith angles.

We find that the integral equation solution assuming isotropic scattering is accurate to ~2% for a clear atmosphere and when similarity transformations are included, accurate to ~5-20% when aerosols and/or clouds are present, the variation in accuracy depending on wavelength, solar zenith angle, altitude and cloud or aerosol extinction optical depth. The Monte Carlo and DISORT results employ either the actual phase function calculated from a Mie scattering code, or a Henyey-Greenstein representation of the phase function.

INCLUSION OF ACCURATE MULTIPLE SCATTERING IN MODTRAN

K. Stamnes, S. Tsay, N. Larsen

Geophysical Institute
University of Alaska
Fairbanks, AK 99775-7320

M. Yeh

Caelum Research Corp.
11229 Lockwood Drive
Silver spring, MD 20901

An accurate multiple scattering scheme has been incorporated into MODTRAN by merging it with the general-purpose multiple scattering algorithm DISORT. The multiple scattering source functions for solar as well as thermal radiation are computed in DISORT and fed into MODTRAN where they are combined with the single scattering solar and thermal source terms. The complete intensity distribution is then computed in MODTRAN by integrating along the line-of-sight. The importance of this improved multiple scattering computation is demonstrated by comparing results from the original MODTRAN with those produced by the merged MODTRAN/DISORT package for radiation in the solar, thermal, and solar/thermal crossover spectral regions. In the ultraviolet/visible region the improvements are significant even for clear sky conditions, while multiple scattering effects are important in the thermal region only in the presence of clouds and aerosols. Comparisons with experimental data will also be used to demonstrate the superior performance of the merged package.

AN APPLICATION OF RADIATIVE TRANSFER THEORY TO UNDERSTANDING AEROSOL MTF

David H, Tofsted
Alan E. Wetmore
Richard C. Shirkey
U.S. Army Research Laboratory
White Sands Missile Range, NM 88002-5501

Andrew Zardecki
Los Alamos National Laboratory
Los Alamos, NM 87544

Brian Davis
Physical Sciences Laboratory
Las Cruces, NM 88003

Aerosol forward scattering effects can significantly blur distant objects when the Mie size parameter becomes large (such as snow, rain, fog in the visible). Starting with previous radiative transfer forward scattering approximations, we have developed a new means for determining these effects on the aerosol MTF. This derivation allows for inclusion of horizontal inhomogeneities of aerosol densities and species, uses the aerosol forward scattering approximation of radiative transfer theory, and models the aerosol phase function forward peak as a sum of Gaussian components. Using Gaussian phase function components yields an exact solution to the radiative transfer function under the forward scattering approximation. The results of the radiative transfer calculation have been translated directly into terms compatible with a linear filter interpretation of incoherent imaging. Thus the aerosol MTF derived directly from the radiative transfer analysis and does not depend on system characteristics.

MOLECULAR AND AEROSOL EFFECTS ON AIRBORNE LASER PROPAGATION

Larrene Harada and Daniel Leslie

W.J. Schafer Associates, Inc.
1901 North Fort Myer Drive, Suite 800
Arlington, VA 22209

Recent missions for lasers on airborne platforms require propagation through long, horizontal, high altitude slant paths. Propagation is affected by upper tropospheric and stratospheric molecules and aerosols. Extinction coefficients and tranmissions for specific high energy laser and laser radar wavelengths have been calculated using FASCOD3P/HITRAN92. The relative importance of various molecular constituents are affected because the influence of water vapor is significantly less than it is near the surface. Stratospheric aerosols can cause considerable attenuation following a major volcanic eruption. We have used NASA SAGE (Stratospheric Aerosol and Gas Experiment) satellite data to evaluate the effects of the Mount Pinatubo eruption on airborne laser propagation at certain wavelengths. We have also determined probability of occurrences of cirrus at the air-to-air mission path altitudes for different seasons.

GROUND-TO-SPACE ATMOSPHERIC TRANSMITTANCE MEASUREMENTS IN THE 3-5 AND 8-12μm SPECTRAL REGIONS: COMPARISON WITH LOWTRAN 7

Adam D. Devir, N. Brandman, B. Barzilai and A. Ben Shalom
Electro Optics R& Division (EORD)
Technion R&D Foundation, Haifa 32000, ISRAEL

The computer code LOWTRAN is widely and extensively used for the prediction of the propagation of IR radiation through the atmosphere. The latest version of this code, the LOWTRAN 7, is assumed to be the most elaborate and accurate one. Hence it was decided to test its validity by comparing its prediction for ground-to-space slant paths with actual transmittance measurements with the sun as a blackbody source. A good agreement between the theoretical predictions and the experimental results was obtained in the 8-12μ m spectral region for all zenith angles between 90° and 60° (0° to 30° above the horizon). In the 3 -5μm spectral region some spectral discrepancy was observed though the value of the integrated measured transmittance agreed well with the predicted one. The reasons for this can be assumed to be in the new band model absorption parameters (in the 3-4μm region) and in the water continuum model (in the 4.4-5.2μm region).

WEATHER AND ATMOSPHERIC VISUALIZATION EFFECTS (WAVES) FOR SIMULATION

Richard Shirkey
David Tofsted
Alan Wetmore
Army Research Laboratory
Battlefield Environment Directorate
White Sands Missile Range, NM

Andrew Zardecki
Los Alamos Consulting
Los Alamos, NM

The WAVES suite of codes ascertains and visualizes environmental effects due to natural clouds/haze and fog. WAVES determines the illumination passing through multiple inhomogeneous cloud layers and the resulting radiance field. The effects of aerosol forward scattering and optical turbulence are also included.

SPARTA'S LIDAR SIMULATION CODE, BACKSCAT VERSION 4.0

D.R. Longtin, M.G. Cheifetz, J.R. Jones, J.R. Hummel

SPARTA, Inc.
24 Hartwell Avenue
Lexington, MA 02173

Since 1988, SPARTA, Inc. has been developing a lidar simulation package for the IBM PC environment called BACKSCAT. The package simulates the backscatter return from lidar systems of different designs, viewing geometries, and atmospheric conditions. This paper will describe the latest version, BACKSCAT Version 4.0, and present sample results. The package will be available for distribution within a few months. BACKSCAT Version 4.0 includes many new technical features. Foremost is the ability to evaluate signal-to-noise performance for direct detection and coherent Doppler lidar systems. Signal-to-noise ratios are then used to estimate the accuracy of range and wind speed measurements for the chosen lidar configuration. These capabilities transform BACKSCAT into a more general purpose lidar simulation tool for users who want to design a lidar system to explore specific aspects of the atmosphere. In response to the user community, the second new feature is the ability to include water clouds in lidar simulations. Although the existing user-defined aerosol option could be used to represent water clouds, it required detailed cloud particle size distribution data that might not be available to some users. Thus, as an alternate approach, water clouds now can be "clicked on" automatically as a built-in cloud model. The third new feature is auxiliary software that estimates the molecular absorption profile for a particular lidar wavelength. Although previous versions of BACKSCAT provided the means to include molecule absorption in a simulation, the code did not provide a tool to calculate it. The molecular absorption package has been nicknamed MABS and generates output that can be directly used in a lidar simulation. It must be noted that the spectral resolution in MABS probably exceeds that of most lidars, so the package is not intended to be a complete treatment of the molecular absorption problem.

* Work Performed Under Contract F19628-C-91-0093

THE SOLAR IRRADIANCE BY COMPUTATION

Robert L. Kurucz

Harvard-Smithsonian Center
for Astrophysics
60 Garden Street
Cambridge, MA 02138

I am now able to compute a purely theoretical model photosphere that reproduces the irradiance measurements of Neckel and Labs in the visible for bandpasses of approximately 2 nm. That model and Avrett's empirical quiet sun model are used to predict the irradiance out to 200 microns. At 200 microns the chromosphere in the empirical model is responsible for most of the flux. Actually, monochromatic irradiance is required to determine the absorption by molecular lines in the atmosphere. I am producing atlases of the solar flux, central intensity, and limb spectra taken by James Brault at Kitt Peak. One atlas "Solar Flux Atlas from 294 to 1300 nm" by Kurucz, Furenlid, Brault, and Testerman (1984), has been published thus far. I also have the "Photometric Atlas of the Solar spectrum from 1,850 to 10,000 cm-1" by Delbouille, Roland, Brault, and Testerman (1991) also taken at Kitt Peak. In addition I have the ATMOS central intensity atlas from 650 to 4800 cm-1 taken by Farmer and Norton (1989) from Spacelab 3. Parts of the flux atlases directly give the irradiance spectrum but much is confused or obscured by terrestrial lines. The intensity atlases can be used as guides for deconvolving blends because the solar lines are narrower. One path I am pursuing is fitting the transmission spectrum empirically and simply dividing it out. However, the regions where the transmission is too low, there is no alternative but to compute a purely theoretical solar spectrum. I use these atlases to test the pure calculations of solar spectra and of transmission spectra. I identify problems with the line data and I try to make generic corrections that improve hundreds or thousands of lines at a time. If the spectrum calculations look good in the regions that have high transmission are computed accurately. The main problem has been continuum placement. Ozone and 01 "dimer" features are difficult to determine because the atlases are each made up of a number of sharply peaked FTS scans. The continuum placement affects the appearance of line wings and the apparent depth of weak features. To get a feel for the scope of the monochromatic irradiance problem I have computed the spectrum from 150 nm to 200 microns at a resolution of 500000 using 58 million lines, both predicted and observed. These are the same lines that went into computing the opacity for the model photosphere. If this spectrum is degraded to the resolution of the model it looks like the model. At any given monochromatic point the spectrum is not reliable. But at a resolution of 10000, say, it approaches measurement accuracy. In regions of low transmission it is more reliable than existing measurements. I will publish tables of these irradiance spectra at various resolutions.

NEW VISIBLE AND NEAR IR OZONE ABSORPTION CROSS-SECTIONS FOR MODTRAN

Eric P. Shettle, Code 7227, Remote Sensing Div., NRL, Washington, DC 20375
and
Stuart M. Anderson, Dept. of Physics, Augsburg College, Minneapolis, MN 55454

Knowledge of the ozone absorption cross-sections is important for modeling the propagation of radiation through the atmosphere, and is critical for deriving the atmospheric ozone concentration from measurements of the spectral character of transmitted or scattered radiation. While the ultraviolet cross-sections for ozone were completely replaced in LOWTRAN 7, the visible cross-sections are unchanged since the original version of LOWTRAN and the cross-sections are not given at all for wavelengths longer than 769 nm. Recently there have been a several new spectroscopic studies of the ozone Chappuis and Wulf absorption bands, along with measurements of the absolute cross-section at selected wavelengths. We have normalized the spectral measurements to the absolute cross-section data, and smoothly joined the different sets of measurements, to provide the ozone cross-section from 407 to 1089 nm. The temperature dependence is also given for 407 to 762 nm. It is anticipated that these cross-sections will be included in MODTRAN 3.

ABSORPTION CROSS SECTION MEASUREMENTS OF CARBON DIOXIDE IN THE WAVELENGTH REGION 118.7-175.5 nm AND THE TEMPERATURE DEPENDENCE

K. Yoshino, J.R. Esmond and W.H. Parkinson

Harvard-Smithsonian Center
for Astrophysics
60 Garden Street
Cambridge, MA 02138

K. Ito and T. Matsui

Photon Factory, KEK
Tsukuba, Ibaraki 305
Japan

In absorption, CO_2 is transparent down to at least 210 nm. Photoabsorption cross section measurements of CO_2 in the UV to VUV region have been made by several investigators. Because of lack of resolution, none of the studies in the period 1950-70 resolved the structures in the CO_2 absorption cross sections. After investigating photographic plates of CO_2 absorption spectra taken in high resolution, we confirmed that structures in the CO_2 are broad enough to allow the use of a medium resolution instrument. The 3-m spectrometer on the BL-20A beam line at the Photon factory, Japan was used in the first order of a 1200 l/mm grating to obtain absorption cross sections of CO_2. The background continuum is provided by the synchrotron radiation source without any order separation, because any high order radiation is cut off by MgF_2 windows. The absorption cross sections of CO_2 were obtained at two temperatures, 195 K and 295 K, in the wavelength region 120-175 nm for every 0.005 nm step. Almost no temperature dependency was observed in the peak cross sections in the wavelength region 125-143 nm, however, the ratio of peak cross sections are down to 0.7 around 175 nm. This work is supported by NASA Upper Atmospheric Research Program under the Grant No. NAGS-494 to the Smithsonian Astrophysical Observatory.

FASCODE ENVIRONMENT (FASE)

J.L. Moncet and W.O. Gallery
Atmospheric and Environmental Research, Inc.
840 Memorial Drive, Cambridge, MA 02139
and
G. P. Anderson
Phillips Laboratory, 29 Randolph Road, Hanscom AFB, MA 01731-3010

The Optical Physics Division of the Phillips Lab is developing a state-of-the-art line-by-line atmospheric transmittance/radiance model as the successor to FASCODE. Under a joint program with DoE's Atmospheric Radiation Measurement (ARM) project, the best features of FASCODE and the DoE's standard radiative transfer program **LBLRTM** will be merged and new capabilities developed. While retaining all of FASCODE's capabilities, FASE will specifically address environmental applications such as atmospheric heating rates and temperature and species inversion.

The main features of FASE will be:

- Highly modular all the basic function--l-b-l optical depth, radiative transfer, atmospheric profile, filtering, scanning and plotting--will be broken out into independent programs These program can be run together through a driver just as FASCODE is now, run separately, or incorporated into customized applications: e.g., multiple scattering codes or inversion routines

- Core module: line-by-line calculation of optical depth: incorporate best Physics: including continuua, line coupling, cross-sections of heavy molecules.

- Optimized: for vectorized and/or parallel processing

- Interface: improved user-friendliness

- Improved packaging: makefile for easy installation on a wide variety of platforms.

- Configuration controlled: for ease of maintenance

SSGM: THE STRATEGIC SCENE GENERATION MODEL

S. McKenzie and R. Armstrong

Mission Research Corp.
One Tara Blvd., Suite 302
Nashua, NH 03062

The Strategic Scene Generation Model generates viewer-perspective pixel apparent radiance maps and point-source intensity data. These scenes are computed from the output of state-of-the-science phenomenology codes and their authenticated input databases. Scenes consist of quiescent and enhanced natural and perturbed backgrounds with embedded targets and target related events. Backgrounds include terrain, clouds, earthlimb, space, aurora, horizon, and nuclear events. Targets include boosting missile plumes and hardbodies, fuel vents, and post-boost objects including RV and decoys. A review of the robust Earthlimb Capabilities in Release 6.0 will be presented.

LIDAR MEASUREMENTS OF ATMOSPHERIC OPTICAL PROPERTIES

C.R. Philbrick, T.D. Stevens, and S. Maruvada

Penn State University
Dept. of Electrical Engineering and
Applied Research Laboratory
University Park, PA 16802

The LAMP (Lidar Atmospheric Measurements Program) lidar instrument has been used to develop and refine techniques for measurements of atmospheric properties. The initial measurements primarily focused on the measurement of middle atmsophere dynamics and structure. More recent efforts have concentrated on measurements of tropospheric water vapor and temperature. The vibrational and rotational Raman scatter signals used for these lower atmospheric profiles can also be used to determine the backscatter and extinction profiles. The optical extinction profiles determined from the Raman scatter signals at several wavelengths provide a measure of the wavelength dependence of aerosol and cloud layers in the troposphere. Several examples of the optical extinction profiles have been examined and comparisons with inversion techniques from the backscatter have shown limitations of the inversion analysis. The inversion of backscatter profiles does not generally yield satisfactory results. These investigations show that the Raman lidar measurements provide a most useful way to measure the atmsoheric optical properties.

GROUND-BASED MEASUREMENTS OF HF AND HCI

Hilary E. Snell and Paul B. Hays
University of Michigan

This poster describes remote sensing observations of HF and HCI column densities over Ann Arbor, Michigan. Spectra were collected between October 1992 and July 1993 using a ground-based Michelson Interferometer and the technique of solar absorption spectroscopy. While the column densities computed from these spectra agree with other groups' measurements of these species, we have noticed that the HCI spectral line at 2925.897 cm^{-1} appears strongly asymmetric. It is our belief that this is due to spectral contamination by another chemical species and not instrumental phase errors as previously reported by other groups.

AN ATMOSPHERIC MODEL FOR GRAVITY WAVE INDUCED TURBULENT LAYERS (BLINI) BASES ON THE SATURATED CASCADE MODEL

E.M. Dewan

Geophysics Directorate
Phillips Laboratory
29 Randolph road
Hanscom AFB, MA
01731-3010

N. Grossbard

Boston College

T. VanZandt

NOAA

Turbulence in the atmosphere above the boundary layer occurs in thin, pancake-shaped horizontal layer called "blini". These are generated by gravity waves whenever the Richardson number is less than a critical value. A theory which seems to accurately predict atmospheric gravity wave spectra was recently published in GRL (Dewan, May 1, 1994, vol. 21, p.817). This theory also implies wave number-period relationships used below. On the basis of this theory, simulations were made of gravity wave fields by means of a superposition of random (phase and amplitude) sine waves consistent with the vertical wave number spectrum of horizontal wind fluctuations. Whenever shears exceeded critical values, the computer program graphed the locations on an altitude-plot. As a result, realistic blini appear which, as was anticipated, "blink" on and off. Subsequently this model will go by the name "The blinking blini model for atmospheric turbulence". It will be used, in the future, together with laser propagation codes to ascertain the effects of wave induced turbulence on ABL systems.

PRELIMINARY RESULTS FROM A RECENT ICRCCM INITIATIVE

F. Miskolczi, M. Bonzagni, R. Guzzi
University of Maryland

In this paper high resolution measured and computed atmospheric downward radiance spectra are compared. The spectral measurements were taken during the SPECTRE experiment (Coffeywille, Kansas 1991) using the UWI AERI fourier spectrometer. The radiance modeling is based on the High-Resolution Atmospheric Radiance-Transmittance Code (HARTCODE) (F. Miskolczi, M. Bonzagni andR. Guzzi, 1990). In this comparison the seven major absorbers, F11, F12, N2 and CCL4 were included.

Reference:

F. MISKOLCZI, M. BONZAGNI, R. GUZZI (1990)
High Resolution Atmospheric Radiance-Transmittance Code (HARTCODE).
Meteorology and Environmental Sciences, World Scientific
Pub. Co., 1990, pp. 743-790

STRUCTURE IN RADIATIVE EXCITATION AS A SOURCE OF HIGH ALTITUDE RADIANCE STRUCTURE: CO(v=1) RADIANCE

J.R. Winick[1], R.H. Picard[1], P.P. Wintersteiner[2], and J.A. Dodd[3]

[1]Phillips Laboratory
29 Randolph Road
Hanscom AFB, MA
01731-3010

[2]Arcon Corp.
Waltham, MA

[3]Stewart Radiance Laboratory
129 Great Road
Bedford, MA 01730

We discuss a largely overlooked source of upper atmosphere structured radiance, structure in the earthshine pumping rate caused by a structured lower boundary. The 4.7 μm radiance from CO(v=1) is a good example of a non-LTE emission that is dominated by radiative processes. The analysis of limb spectra of both the $^{12}C^{16}O$ and $^{13}C^{16}O$ from CIRRIS 1A data (Dodd et al., GRL, 20, 2683, 1993) clearly indicated how the differing opacity of the isotopes controlled the effect of pumping from the lower boundary. We examine some limiting cases that show that nighttime earthlimb radiance variations of factors greater than 2 can be caused by cold clouds at the tropical tropopause.

INFRARED RADIANCE FLUCTUATIONS IN THE UPPER ATMOSPHERE

J. Gruninger[1], R.L. Sundberg[1], P. De[1], and J. Brown[2]

[1]Spectral Sciences, Inc.
99 S. Bedford St. #7
Burlington, MA 01803

[2]Phillips Laboratory
29 Randolph Road
Hanscom AFB, MA 01731-3010

Simulation of infrared radiance fluctuations in the atmosphere depends on detailed descriptions of fluctuations in atmospheric species number densities, vibrational state populations, and the kinetic temperatures along the sensor line-of-sight. In the upper atmosphere, where nonequilibrium effects (LTNE) become important, a small fluctuation in the kinetic temperature can result in correlated, anti-correlated, or no change in the vibrational temperature of states. The relationship between kinetic and vibrational temperature fluctuations depends on the subtle interplay between changes in the total number densities, changes in the temperature-dependent kinetic rates, and the relative contribution of the radiative relaxation. The model developed in this paper predicts the two-dimensional radiance covariance function for LTNE conditions. The radiance statistics are non-stationary and are explicitly bandpass and sensor FOV dependent. The SHARC model is used to calculate mean LOS radiance values and radiance derivatives which are necessary to determine the radiance statistics. Inputs to the model include the statistical parameters of a non-stationary atmospheric temperature fluctuation model and an atmospheric profile. The radiance statistics are used in a simple model for synthesizing images. The model has been applied to calculate the radiance structure for the OH(Δv=1) swir band and the CO2(ν_3) MWIR band under nighttime conditions.

SYNTHETIC 3-D ATMOSPHERIC TEMPERATURE STRUCTURE: A MODEL FOR KNOWN GEOPHYSICAL POWER SPECTRA USING A HYBRID AUTOREGRESSION AND FOURIER TECHNIQUE

James H. Brown
Phillips Laborarory
29 Randolph Road
Hanscom AFB, MA 01731-3010

Neil Grossbard
Boston College

Within a defined domain, geophysical phenomena often are characterized by smooth continuous power spectral densities having a negative power law slope dependence. Frequently, Fourier transform analysis has been employed to generate synthetic scenes from pseudorandom arrays by passing the stochastic data through a Fourier filter having a desired correlation structure and power spectral dependency. This report examines the possibility of producing synthetic structure by invoking autoregression analysis in conjunction with the Fourier method. Since computations that apply multidimensional fast Fourier transforms to large data arrays consume enormous resources and time, the goal of this study is to seek an alternative method to reduce the computational burden. Future editions of the Phillips Laboratory Atmospheric Radiance Codes will feature an ability to calculate structured radiance. The methods explored herein provide a process that can complement or in some cases supplement methods presently being used. Line of sight computations using the three-dimensional database will be presented.

PLANE WAVE SCINTILLATION IN AN ONION SKIN MODEL

Robert R. Beland

Phillips Laboratory
29 Randolph Road
Hanscom AFB, MA 01731-3010

The geometry of an onion skin model for atmospheric optical turbulence is presented for application to near horizontal propagation. This is then used to derive analytic expressions for the log amplitude variance of a plane wave in the weak turbulence (Rytov) framework. The geometrical effects on the altitude weighting function are investigated and used to define the limit of validity of the flat earth model. The formalism is then extended to include the effects of aperture averaging and non-zero inner scale. It is found that Rytov theory should be applicable to zenith angles of less than approximately 85°. It is also established that inner scale and aperture averaging are much less important for near horizontal than for vertical propagation in the weak turbulence case. Predictions of log amplitude variance are presented for calculations using the CLEAR t model as well as individual Cn2 profiles derived from balloon measurements. This formalism is readily extended to provide analytic expressions for other turbulence effects.

COMPARISON OF A MODEL DESCRIBING PROPAGATION THROUGH OPTICAL TURBULENCE (PROTURB) WITH FIELD DATA

Robert W. Smith
U.S. Army Test and Evaluation Command
Ft. Belvoir Meteorological Team
Ft. Belvoir, Virginia 22060

Jennifer C. Ricklin
U.S. Army Research Laboratory
Battlefield Environment Directorate
White Sands Missile Range, New Mexico 88002

Kevin E. Cranston and John P. Cruncleton
Physical Science Laboratory
New Mexico State University
Las Cruces, New Mexico 88003-0002

The PROTURB model, developed by the Battlefield Environment Directorate of Army Research Laboratory, calculates an estimate of optical turbulence strength and its effects on visible and infrared imaging and laser system performance. The PROTURB model was compared to data supplied by the Army Test and Evaluation Command Ft. Belvoir Meteorological Team. Here we present a comparison using data from three locations that differ greatly in meteorological conditions and in site characteristics. We discuss the data collection and reduction effort, and show how this data compares with PROTURB predictions.

THE ROLE OF TURBULENCE IN CLOUD DROPLET FORMATION AND OUTSIDE CLOUDS

by James W. Telford
Atmospheric Sciences Center
Desert Research Institute
P.O. Box 60220
Reno NV 89506

Turbulence, it is becoming increasingly clear, contains organized structures which carry fluid from one place to another through the turbulent medium. Much of the atmosphere is in a stable stratified state. In these conditions two dimensional vortices form, and smaller swirls can coalesce to feed larger scale motion. The Red Spot on Jupiter appears to be such a structure. In clouds, cooled parcels near cloud tops generate descending spherical vortices which carry diluted cloud parcels deep into the cloud. This phenomena drives the microphysical development in both cumulus and stratus clouds, and hence controls the droplet spectra and the distribution of ice, which in turn plays a large role in the radiative characteristics of the cloud. It seems likely that the mammatus protruding into the clear air below shelf clouds are of this form of motion.

SHARC-3: A MODEL FOR INFRARED ATMOSPHERIC RADIANCE AT HIGH ALTITUDES

R.D. Sharma[1], J.H. Brown[1], J.H. Gruninger[2], R.L. Sundberg[2], J.W. Duff[2], L.S. Bernstein[2], M.W. Matthew[2], S.M. Adler-Golden[2], D.C. Robertson[2], and R.J. Healey[3]

[1]Phillips Laboratory
29 Randolph Road
Hanscom AFB, MA

[2]Spectral Sciences Inc.
99 South Bedford St.,#7
Burlington, MA 01803

[3]Yap Analytics, Inc.
594 Marrett Road
Lexington, MA 02173

SHARC-3 is the latest version of Strategic High Altitude Radiance Code. This talk describes new SHARC features like its ability to simulate changing atmospheric conditions along the line-of-sight (LOS) paths being calculated. SHARC has been developed by the Air Force to meet systems requirements for a simulation code that is both suitable for systems studies and which provides: rapid and accurate calculations of upper atmospheric IR radiance and transmittance spectra; has a spectral resolution of better than 1 cm^{-1}; spans the 2 to 40 μm (250 to 5,000 cm^{-1}) wavelength region; and accommodates arbitrary lines of sight in the 50-300 km altitude regime. SHARC accounts for the production, loss, and energy transfer processes among the molecular vibrational states important to this spectral region. Auroral production and excitation of CO_2, NO, and NO^+ are included in addition to quiescent atmospheric processes. Calculated vibrational temperatures are found to be similar to results from other non-LTE codes, and SHARC's equivalent-width spectral algorithm provides very good agreement with much more time-consuming "exact" line-by-line methods. Calculations and data comparisons illustrating the features of SHARC-3 are presented.

NON-LTE IN CO_2 IN THE MIDDLE ATMOSPHERE

A.A. Kutepov

V.P. Ogibalov
G.M. Shved

Institute for Astronomy & Astrophysics
University of Munich
Germany

Dept. of Atmospheric Physics
University of St. Petersburg
Russia

A new line-by-line ALI (accelerated lambda iteration) technique, initially designed to solve multilevel non-LTE line formation problem in stellar atmospheres, is applied to study effects of the non-LTE on the populations, source functions and limb radiances in various infrared CO_2 bands in Earth's middle atmosphere. Approximations used in previous studies of non-LTE in CO_2 are analyzed. Implications for remote sensing with high spectral resolution instruments are discussed.

COMPARISON OF LINE-BY-LINE AND MODIFIED CURTIS MATRIX NARROW-BAND MODEL APPROACHES TO RADIATIVE TRANSFER IN THE CO_2 15 μm BANDS

P.P. Wintersteiner[1], M. Lopez-Puertas[2], J.R. Winick[3], and R.H. Picard[3]

[1]Arcon Corp.
Waltham, MA 02154

[2]Instituto de Astrofisica
de Andalucia
Granada, Spain

[3]Phillips Laboratory
29 Randolph Road
Hanscom AFB, MA 01731-3010

We have undertaken a detailed comparison of two different models for calculating non-LTE populations in the terrestrial atmosphere, for the purpose of studying the effects of the radiative transfer algorithms that are embodied in them. The models are the iterative line-by-line RAD model that forms the basis of the PL ARC code and the inverse modified Curtis matrix (MCM) model, developed by Lopez-Puertas and co-workers. They have been used to calculate the vibrational temperatures and cooling rates in the CO_2 15 μm bands. The comparison covers the altitude range 40-160 km, includes strong and weak bands, uses model atmospheres having extreme temperature structures, and also tests the effect of changing kinetic parameters. The models' vibrational temperatures and cooling rates generally agree to within 2 K and 0.5 K/day, respectively. We will show these results, discuss those aspects of the radiative transfer algorithms responsible for the small differences that do appear, and mention the implications for non-LTE code validation.

SUBTHERMAL NO($^2\prod_\Omega$) SPIN-ORBIT DISTRIBUTIONS IN THE THERMOSPHERE

S.J. Lipson, P.S. Armstrong[1], J.A. Dodd[1], J.R. Lowell[1], W.A.M. Blumberg, and R.M. Nadile

Optical Environment Division, Geophysics Directorate, Phillips Laboratory. Hanscom AFB. MA 01731
[1]Stewart Radiance Laboratory, 139 Great Road, Bedford, .MA 01730

The populations in the two NO($X^2\prod$,v=1,Ω=1/2, 3/2) spin-orbit manifolds in the Earth's thermosphere have been found to depart by as much as a factor of two from the ratio expected from thermal equilibrium. The effective temperature describing the observed population distribution is hundreds of degrees Kelvin lower than the kinetic or rotational temperatures. Absolute spin-orbit specific column densities of NO(v=1) were derived from high-resolution (1 cm^{-1}) IR earthlimb spectra in the 100 to 200-km region, obtained in the CIRRIS 1A Space Shuttle experiment. Nonlinear least-squares synthetic spectral fitting was used to analyze the NO Δv=l fundamental band emissions near 5.3μm. The spin-orbit distribution represents a third degree of freedom, along with vibration and rotation. that is not in equilibrium with the local kinetic temperature. These observations may significantly impact the remote sensing of NO in the upper atmosphere. The subthermal distribution is most likely produced in the collisional uppumping of NO(v=0) by O atoms, which is the major source of NO(v=1) in the thermosphere. Thus, spin-orbit distribution measurements may provide a means of distinguishing NO produced by chemical reaction from NO excited by collisional uppumping.

This work was supported by the Air Force Office of Scientific Research and the Ballistic Missile Defense Organization.

COMPARISON OF GLOBAL VARIATION OF THE RADIANCE OF THE STRATOSPHERIC O_3 CH_4 SPECTRA AS VIEWED CIRRIS 1A FORM DISCOVERY-103 WITH CLAES EXPERIMENT ON BOARD OF UARS

B.K. Rezai[1], G.E. Bingham[2], L.R. Megill[1], D.K. Zhou[2], M. Mergenthaler[3], A.E. Roche[3], J.B. Kumar[3], and G.P. Anderson[4]

[1]Center for Atmospheric & Space Sciences
Utah State University
Logan, UT 84322-4405

[2]Space Dynamic Laboratory
Utah State University
Logan, UT 84322-9710

[3]Lockheed Palo Alto Research Lab
Palo Alto, CA 94304

Phillips Laboratory/GP/GPOS
29 Randolph Road
Hanscom AFB, MA 01731-3010

We report on meaurements of these species by the Cryogenic Infrared Radiation Instrumentation for shuttle (CIRRIS 1A) which flew aboard the Discovery OV-103, STS-39 on April 28 to May 6, 1991. By looking in the limb, it was possible to obtain approximately a thousand interferograms. This made possible a certain identification of many important stratospheric gases, including O_3, CH_4, HNO_3, and chlorine source species CCL_2F_2, and CCL_3F. The accuracy of the CIRRIS 1A measurements is therefore of interest in polar ozone depletion studies, and validation is a major consideration. This paper will review the CIRRIS 1A observations of O_3, CH_4, and HNO_3 spectra and of vertical profiles concentration and discuss their accuracy and precision. We will compare the CIRRIS 1A measurements with the Cryogenic Limb Array Etalon Spectrometer (CLAES) on board the Upper Atmosphere Research Satellite. Specifically we will compare CIRRIS 1A and CLAES spectra in the wavelength regions targeted for O_3, CH_4, and HNO_3 concentration retrievals, and we will compare the retrieved quantities for species in the southern and northern hemispheres. Since CIRRIS 1A data were collected shortly before, and CLAES data shortly after, the Pinatubo eruption, such comparisons are of significant value both scientifically and from a validation standpoint.

THE POAM EXPERIMENT AND EARLY MEASUREMENT RESULTS

E.P.Shettle, R.M.Bevilacqua, J.S.Hornstein (Code 7227, NRL, Washington, DC 20375)
W.J.Glaccum (ARC, Landover, MD)
S.Krigman, J.Lumpe, M.Fromm, and D.Debrestian (CPI, Fairfax, VA)
and the POAM II Science Team

NRL's Polar Ozone and Aerosol Measurement (POAM II) instrument was developed to measure the distribution of atmospheric aerosols, PSC's, and several molecuIar species critical for understanding ozone chemistry in the polar stratosphere. It was launched on France's SPOT 3 satellite on 25 September 1993. It makes solar occultation measurements in nine narrow-band channels from the visible to the near IR. From the measured transmissions, it is possible to determine the densities of aerosols at altitudes of 10-40 km, ozone at altitudes of I0-60 km, water vapor at altitudes of 15 -40 km, and nitrogen dioxide at altitudes of 20-40 km. The SPOT 3 satellite is in a 98° inclined sun-synchronous orbit at an altitude of 833 km. This results in all the POAM II measurements being in the Polar regions. We will discuss the POAM II instrument design, the retrieval algorithm, and the preliminary results of the measurements, including early data validation studies. POAM II is sponsored by the Innovative Science and Technology Office of BMDO (BMDO/DTI) and the DoD Space Test Program (STP).

LARGE-SCALE RETRIEVAL OF ATMOSPHERIC PARAMETER PROFILES

L. Sparks
J. L. Fanselow
J. McComb
S. Nandi
J. Parker
J. E. Patterson
H. Worden

Jet Propulsion Laboratory
Pasadena. California

We have developed and tested SEASCRAPE (Sequential Evaluation Algorithm for Simultaneous and Concurrent Retrieval of Atmospheric Parameter Estimates), a code designed to automate and expedite the retrieval of atmospheric profiles from large quantities of remote sensing data generated by nadir and limb soundings. Our algorithm uses a *sequential* parameter estimation method known as the Square Root Information Filter, a numerical technique for solving least squares problems that is particularly suited for handling large volumes of data. The algorithm permits *simultaneous* retrieval of many atmospheric profiles. By implementing the algorithm in a parallel processing environment, *concurrent* data analysis will achieve a dramatic increase in the rate at which the data can be processed.

GENERAL INVERSION PACKAGE FOR RETRIEVAL OF ATMOSPHERIC SPECIES FROM HIGH RESOLUTION SPECTRAL MEASUREMENTS

J.L. Moncet and W.O. Gallery

Atmospheric & Environmental Research, Inc.
840 Memorial Drive
Cambridge, MA 02139

A general inversion algorithm based on the Rodgers (1976, 1990) optimal inversion approach is being developed. The algorithm is applicable to the simultaneous retrieval of any ensemble of selected molecular species as well as atmospheric temperature from down-looking, up-looking or limb measurements. The algorithm has been designed to use FASCODE for the molecular optical depths calculations but can be modified to run with faster transmittance models (e.g. MODTRAN). Substantial computational gain is achieved over the existing "Path Characterization" algorithm (Isaacs et al. 1990), by performing the K-matrix calculation analytically and by making the code fully vectorizable. The algorithm has been applied successfully to the simultaneous retrieval of temperature and water vapor from the ground based interferometric measurements (Theriault et al. 1993). The algorithm will be applied to CIRRIS data and to MSX data when available.

SIMULATION OF STELLAR OCCULTATION MEASUREMENTS

L. Oikarinen

Finnish Meteorological Institute
Dept. of Geophysics
P.O. Box 503, FIN-00101
Helsinki, Finland

An instrument for monitoring stratospheric ozone, GOMOS (Global Ozone Monitoring by Occultation of Stars), will be launched by ESA on the ENVISAT-1 satellite in 1998. The instrument measures atmospheric UV-visible transmission spectra in 250 - 675 nm at a resolution of 0.6 nm. Absorption spectra of O_2 and H_2O are detected by two IR channels of spectral resolution 0.12 nm located around 760 and 930 nm. Transmission along slant paths of tangent heights down to 15 km is measured. Solar light scattered into the instrument FOV forms a background signal. Simulation of both the transmittance and the scattered background are required in developing the instrument and data analysis methods. Special requirements of occultation measurements are the modeling of scintillations and refractive attenuation of light (dilution of the flux density due to the decreasing of refractive index with altitude). In the case of GOMOS absorption by minor species, such as NO_2, NO_3, BrO, and OCIO, should also be simulated.

LINE-BY-LINE CALCULATIONS OF ATMOSPHERIC FLUXES AND COOLING RATES II: APPLICATION TO CARBON DIOXIDE, OZONE, METHANE, NITROUS OXIDE, AND THE HALOCARBONS

M. J. Iacono, and S. A. Clough
Atmospheric and Environmental Research, Inc.
840 Memorial Drive
Cambridge, MA 02139

Tel: 617-547-6207
FAX: 617-661-6479

Determining the spectral contribution of atmospheric molecular components to the total longwave fluxes and cooling rates is a necessary step toward understanding the effect and response of these gases to global climate change. Clear-sky longwave computations using a line-by-line radiative transfer model (LBTRTM) have been completed for several atmospheric profiles. We have previously presented results for both water vapor [Clough et al. , 19921] and the water vapor continuum [Clough et .a1., 1989]. In the current paper we present the effects of carbon dioxide, ozone, methane, nitrous oxide and the most important halocarbons in addition to water vapor. Both the spectral and spectrally integrated flux and cooling rate contributions from each of these significant greenhouse gases are evaluated. Carbon dioxide, an extremely strong atmospheric absorber, is generally saturated in the troposphere with the exception of two narrow spectral bands with the result that carbon dioxide plays an anomolously small role in this altitude regime. Additional studies include the effect on the longwave cooling rates and fluxes due to the anticipated ten year changes in C02, 03, CFC-ll, CFC-12, GFC-22, and CCL4 from 1990 to 2000 as well as due to the doubling of carbon dioxide

---

Clough, S.A ., F.X. Kneizys, and R. W. Davies Line shape and the water vapor continuum, Atmos. Res., 23, 229-241, 1989.
Clough, S. A, M. J. Iacono, and J-L. Moncet. Line-by-line Calculations or Atmospheric Fluxes and Cooling Rates: Application to water Vapor. J Geophys. Res ., 97, 15761-15785, 1992.

VERY NARROW BAND MODEL CALCULATIONS OF ATMOSPHERIC FLUXES AND COOLING RATES USING THE MODTRAN CODE

L. S. Bernstein, A. Berk, P. K. Acharya, and D. C. Robertson
Spectral Sciences, Inc., Burlington, Massachusetts
and
G. P. Anderson, J. H. Chetwynd, and L. M. Kimball[1]

Geophysics Directorate, Phillips Laboratory
Hanscom AFB, Bedford, Massachusetts

Because of the large computational speed advantage afforded by band models over line-by-line (LBL) models the development and application of band models to the calculation of atmospheric radiative fluxes and cooling rates continues to be an active area of research. A wide variety of narrow band model (NBM) and wide band model(WBM) approaches have been developed. Typically the calculation of spectral resolution, Δw, of the NBMs falls within the $5 \leq \Delta w \leq 20$ cm^{-1} range, while for the WBMs $\Delta w \geq 100$ cm^{-1}. Direct application of these band models to the calculation of atmospheric fluxes and cooling rates usually results in poor to only fair agreement with LBL calculations. In order to circumvent this problem the band models are treated as parameterizations rather than as first principles models. These tuned band models can yield atmospheric flux and cooling rate predictions of LBL-like quality. This paper discusses a new first principles based very narrow band model (VNBM) approach with $\Delta w = 1$ cm^{-1} which yields atmospheric flux and cooling rate predictions of near LBL quality. The VNBM is incorporated in the Phillips Laboratory MODTRAN atmospheric transmittance-radiance code which enables general specification of the atmospheric species, concentration and thermodynamic profiles, calculational spectral interval, and path geometry. The relatively high spectral resolution of this approach combined with separation of the transmittance algorithm into truncated line and line wing components treats the problem of line correlation in a physically realistic manner. In order to evaluate the VNBM approach comparison is made to LBL benchmark atmospheric flux and cooling rate calculations.

---

[1] Mathematics Department, Worcester Polytechnic Institute

GREENHOUSE GAS CONCENTRATION PROFILES RETRIEVED FROM CIRRUS 1A MEASUREMENTS IN THE 7-13 μm WINDOW DURING STS-39

G.E. Bingham, D.K. Zhou, Y. Yang, and A.J. Steed (All at Space Dynamics Lab., Utah State University, Logan, UT 84322: 801 770 0256: e-mail: cirrus@cc.usu.edu)
G.P. Anderson and R.M. Nadile (Geophysics Directorate, Phillips Laboratory, Hanscom Air Force Base, MA 01731)

The spectral and spatial distributions of the greenhouse gas infrared emissions are measured by the CIRRUS 1A (Cryogenic Infrared Radiance Instrumentation for Shuttle) inferometer sensor during STS-39 flight (28 Apr - 6 May, 1991). The spectra in the important 7-11 μm infrared window were recorded. High resolution spectral scans (~1.5 cm^{-1} instrument resolution) and FASCOD-3 with HITRAN92 database and NMC temperature and pressure profiles are used in an onion peel routine to retrieve gas concentrations from absolutely calibrated radiance data. Scan to scan and profile to profile variability are compared to show the measurement capability of the cryogenic infrared interferometer. The local aerosol is estimated by comparing the modelled and measured CO_2 hot band (10.5 μm) spectra. The results of concentration profiles retrieved from the spectra (42° south latitude 32° west longitude, local time of 22.4 hr.) are shown. Profiles of CFC-11, CFC-12, HNO_3, O_3 and CH_4 developed in this fashion and at different locations are compared with ATMOS (Atmospheric Trace Molecule Spectroscopy), LIMS (Limb Infrared Monitor of the Stratosphere), and situ mean data for these gases.

INDIRECT GLOBAL WARMING EFFECTS OF TROPOSPHERIC OZONE INDUCED BY SURFACE METHANE EMISSION

A.S. Grossman, D.J. Wuebbles, J.S. Tamaresis
K.O. Patten, A. Jain, and K.E. Grant

Global Climate Research Division
Lawrence Livermore National Laboratory
P.O Box 808
Livermore, CA., 94550

June 1994

Changing concentrations of atmospheric methane can significantly affect the concentration and distribution of ozone in the troposphere and stratosphere. Changes in the concentrations of these gases can thus influence the radiative forcing on climate. In this study we determine the indirect, time-varying tropospheric radiative forcing and Global Warning Potential (GWP) of O_3 due to an impulse of CH_4 that is equivalent to 36 percent of the atmospheric mass of CH_4. The direct CH_4 radiative forcing and GWP are also calculated. The LLNL 2-D radiation-chemistry-transport code is used to evaluate the resulting changes in the O_3 and CH_4 atmospheric profiles as a function of time. A correlated k-distribution radiative transfer model is used to calculate the radiative forcing at the tropopause of the globally-averaged atmosphere profiles. The O_3 indirect GWPs vary from ~ 25 after 20 yr integration to ~3 after 500 years. The direct CH_4 GWP vary from ~48 at 20 yrs to ~ 6 at 500 yrs. The 20 year direct CH_4 GWP is ~20% larger than previous estimates due to an increased CH_4 lifetime resulting from the applied impulse. Estimates are made of latitude effects in the radiative forcing calculations.